Biochemie

Non-Invasive Biosensors to Characterize the Cell-Material Interface

Inaugural-Dissertation
zur Erlangung des Doktorgrades
der Naturwissenschaften im Fachbereich Chemie und Pharmazie
der Mathematisch-Naturwissenschaftlichen Fakultät
der Westfälischen Wilhelms-Universität Münster

vorgelegt von
Stefanie Michaelis
aus Solingen

- 2010 -

Dekan:	Prof. Dr. A. Hensel
Erster Gutachter:	Prof. Dr. J. Wegener
Zweiter Gutachter:	Prof. Dr. H.-J. Galla
Tag der Disputation:	16.07.2010
Tag der Promotion:	16.07.2010

Meiner Familie und Michael

Contents

1 Introduction

The interaction of living mammalian cells with technical surfaces is of crucial importance for a wide field of applications in life sciences – ranging from fundamental research in cell biology and biotechnology to certain applications in medical technology aiming for the integration of medical devices in human tissue. Biological fields of research that depend on a close contact between cells and the technical material surface encompass for example development of commercial biosensors, cell arrays or diagnostic assays. In medical technology, the design of biomaterials for use as short-term or permanent tissue implants aims for materials which not only mimic the biomechanical and chemical properties of the host tissue, but also support essential tissue-specific cell functions. These functions may include cell adhesion, growth, differentiation, motility as well as the expression of tissue-specific genes. A general requirement for a certain technical material in contact with a biological system is its biocompatibility in order to avoid toxic reactions and adverse immune responses, like inflammatory and foreign-body responses. Thus, it is of crucial importance to evaluate a material's biocompatibility by studying the interaction of the material surface with the complex biological environment consisting of physiological fluids, proteins and cells (chapter 1.3).

A successful integration of a biomaterial into the human body usually not only requires the colonization of its surface with cells – moreover, a strong and mechanically stable cell-substrate contact is needed. The formation of these specific cell-substrate contacts, which is a prerequisite for proper and mechanically stable attachment and spreading of mammalian cells upon technical surfaces, both in the body and *in vitro*, is a rather complex and versatile process. Cells do not interact directly with a substrate surface; cell binding usually requires the presence of extracellular matrix (ECM) molecules pre-adsorbed onto the surface. After the adsorption of proteins, which *in vitro* either originate from the culture medium and/or are synthesized and secreted by the cells themselves, cell attachment and spreading are initiated by unspecific interactions of the cells with the material surface. Later on specific receptor-mediated cell-surface interactions with the surface immobilized proteins provide mechanically stable substrate anchorage of the cells (Bongrand, 1998; Pierres et al., 2002). These specific cell-surface interactions are mediated by cell-surface receptors, so-called integrins, which bind at one end to the corresponding ECM proteins and are linked to the cytoskeleton of the cell at the other end. Via their transmembrane domain, integrins serve as a mechanical link between extracellular and intracellular domains. In most cell types, certain intracellular signaling cascades essential for cell growth, function, and survival are triggered by integrins upon attachment and spreading. Without a functional attachment to a growth substrate, the

cell undergoes apoptosis (Meredith and Schwartz, 1997). Furthermore, cell-surface interactions are involved in processes like cell differentiation, cell migration, wound healing and tumor metastasis.

Cell-surface interactions predominantly determine the biocompatibility of biomaterials and their potential use in biomedical applications. Despite the widespread use of artificial mainly polymeric materials as cell culture substrates in biology or implants in medicine, it is still a challenging task to understand the interactions of the components of a biological system, like proteins or anchorage dependent cells, and man-made surfaces with defined chemical and physical properties. Surface chemistry as well as surface topography are both important surface properties influencing the cellular response. However, only a better basic understanding of the interaction between a material's surface and the components of the biological system will allow for the development of suitable biomaterials and their successful use as implant materials or biosensors. These requirements drive the development of reliable measurement techniques to analyze the complex and dynamic cell-biomaterial interface.

Two techniques that are capable of specifically addressing the cell-biomaterial interface in a non-invasive manner were applied in this study: the quartz crystal microbalance (QCM) and the electric cell-substrate impedance sensing (ECIS) technique. Both are based on impedance spectroscopy and provide quantitative information about cell-substrate interactions with a high time resolution. In both techniques, cells are cultured on planar gold film electrodes, which serve as growth substrate and sensoric surface at the same time. On the basis of these two techniques, a biosensor was developed to characterize cell-material interactions developing during the adhesion of mammalian cells upon special substrates. The study comprises different polymers as well as patterned silicon substrates exhibiting different topographical features. The QCM technique (chapter 1.6.1), which monitors the mechanical interactions between cells and their growth substrate, was applied to obtain valuable information on the cytocompatibility of chemically different polymer films. The ECIS technique (chapter 1.6.2), capable of monitoring the passive electrical properties of cells during formation and modulation of cell-substrate interactions, was applied to substrates with different surface topographies that were modeled by mesoporous silicon surfaces to evaluate the impact of surface topography on cell-substrate interactions.

1.1 Molecular Composition of the Cell-Material Interface

The cell membrane is not in direct contact with the underlying surface. The adhesion of cells to a surface is mediated by specific cell-surface receptors, which anchor via their extracellular domain to ligands pre-adsorbed onto the substrate surface (Fig. 1.1). Usually, these surface immobilized ligands belong to a macromolecular network of various adhesive proteins, also referred to as the extracellular matrix (ECM) (Davies, 2001). The major class of these cell-surface receptors is the integrin family. They are specialized to recognize and specifically bind to adhesion-promoting proteins anchored to the surface. Besides these specific cell-surface interactions, there are also many non-specific interactions involved in cell adhesion, such as electrostatic, electrodynamic, steric or entropic interactions. These are founded in the presence of fixed charges, i.e. ionic or polar groups, on both the cell surface and the substrate surface, leading to attractive or repulsive forces between the cell and the surface. As specific cell-surface interactions are considered as being mainly responsible for the final strength and the dynamic properties of the cell-substrate adhesion sites (Bongrand, 1998; Pierres et al., 2002), non-specific cell-surface interactions are not discussed in any more detail.

1.1.1 Cell-Surface Receptors Involved in Cell-Substrate Adhesion

The most prominent type of transmembrane receptors responsible for specific cell-substrate interactions are the integrins (Arnaout et al, 2005). Integrins are a family of non-covalently associated, α, β-heterodimeric transmembrane glycoproteins that stick out of the cell membrane by roughly 20 nm (Hynes, 1992). To date, 24 different integrins have been identified, resulting from different combinations of 18 α- and 8 β-subunits (Barczyk et al., 2010).

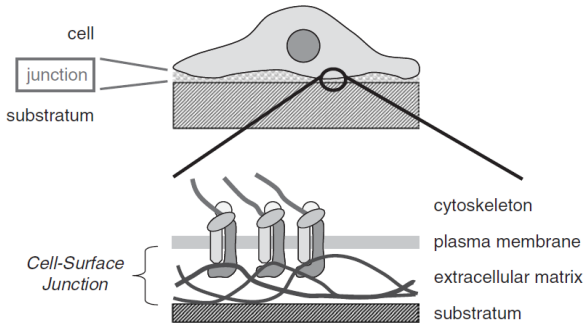

Fig. 1.1 Schematic of the contact area between lower cell membrane and substrate surface. Adhesion is provided by cell-surface receptors that specifically bind to components of the ECM on the substrate surface and are intracellularly linked to the cytoskeleton (adapted from Wegener, 2006).

Both subunits exhibit some structural similarity: each is composed of a long stalk-like extracellular segment, with the N-terminal portion combining to form a globular domain, which mediates the binding to the ECM components in the presence of divalent cations (Mg^{2+} or Ca^{2+}), and a hydrophobic domain, which spans the cell membrane. On the intracellular side, the β-subunit of the integrins is linked to the actin cytoskeleton (Krissansen and Danen 2006 and 2007) by means of cytoskeletal adapter proteins, such as talin, vinculin, α-actinin and paxillin. In contrast to all other integrins, the $\alpha_6\beta_4$ integrin associates with the keratin intermediate filaments (hemidesmosomes). Thus, integrins interconnect the intracellular protein filaments of the cytoskeleton with the protein filaments of the ECM and serve as a transmembrane bridge between these two macromolecular networks, ensuring mechanical stability of the cell-surface junction. The distribution of integrins in the plasma membrane of adherent cells is very often not homogeneous. Upon cell adhesion to the ECM, the integrins tend to cluster locally forming so-called focal adhesions or focal contacts (Davies, 2001; Wozniak et al., 2004). At these adhesion sites, the cells are believed to have the closest distance to the surface.

Dependent on their subunit composition, integrins differ significantly in their binding specificity to different ECM proteins. Molecular recognition of and binding to individual ECM proteins are generally mediated via rather short amino acid sequences (~ 4 – 10 amino acids) on ECM proteins. The most well-known amino acid sequence involved in integrin recognition is the tetrapeptide binding motif Arg-Gly-Asp-Ser (RGDS), a sequence found in many ECM ligands including the ECM proteins fibronectin and vitronectin (Pierschbacher and Ruoslahti, 1984; Krissansen and Danen, 2007). Many integrins are multispecific receptors meaning they can bind several different ECM proteins as long as these carry a suitable recognition sequence. On the other hand, one particular ECM protein may interact with various integrins by carrying more than one recognition sequence in its primary structure.

Apart from their crucial functional role in cell adhesion and linkage of the cytoskeleton to the ECM (Hynes, 1992), integrins act as bi-directional signaling receptors that mediate information transfer across the plasma membrane, thereby regulating various cellular processes. Integrins participate in outside-in signaling, when an integrin-ligand interaction triggers transmission of signals into the cell interior, mediating cell growth, differentiation, proliferation, migration, morphology and survival signals from the ECM (Cox and Huttenlocher, 1998; Davies, 2001; Bökel and Brown, 2002; Hynes 2002; Krissansen and Danen, 2006; Luo et al., 2007). In addition, integrins transfer signals from the cells to the ECM, a process termed inside-out signaling. This process mainly acts to regulate integrin conformation and ligand-binding affinity from inside the cell (Hynes, 2002).

1.1.2 The Extracellular Matrix

The extracellular matrix (ECM) is a complex, highly organized macromolecular network of various extracellular components, which surrounds the cells in mammalian tissue. It consists

of proteins, polysaccharides, low-molecular-weight components, salt and water. The ECM is a component of the environment of all cell types, but it differs with respect to composition and architecture of its molecular components between tissues and sometimes also developmental age, ranging from rock-hard bone to elastic ligament and skin. The common property of all ECM macromolecules is their ability to form suprastructural aggregates, like fibrils, microfibrils, filaments or networks. These, in turn, are assembled into a supramolecular meshwork, such as interstitial matrices or basement membranes, providing structural support, organization and orientation to tissues (Bosman and Stamenkovic, 2003).

The major macromolecular components of ECMs include glycoproteins and proteoglycans. Specific binding interactions between unique glycoproteins and proteoglycans create the macromolecular, highly crosslinked architecture of the ECM. The process of assembly is complex, involving both reversible interactions as well as covalent stabilizations and crosslinks. Important ECM proteins recognized by cell-surface receptors are the collagens, fibronectins, vitronectin, fibrinogen and laminins. Collagens, being the most abundant glycoproteins, belong to the structural components of the ECM. They provide the backbone scaffolding essential for the interaction of ECM components, as well as tissue structure and structural integrity (tensile strength, mechanical stability). A second structural component crucial for ECM architecture is the protein elastin, which forms a random network of elastic fibres, imparting much of the required tissue elasticity. The ratio between elastic fibres of elastin and relatively inelastic fibres of collagen varies between different ECMs dependent on the individual mechanical requirements of the tissue. It is thought to be a key regulator of the mechanical properties of ECMs (Davies, 2001). The remaining glycoproteins such as laminins, fibronectins or vitronectin have little structural role but mediate cell-ECM interactions. Non-protein ECM ligands comprise proteoglycan polysaccharides, such as heparan sulfate, chondroitin sulfate and keratan sulfate, and the non-proteoglycan polysaccharide hyaluronan. Proteoglycans are large macromolecules composed of a specific multidomain core protein to which very large and complex polysaccharides, so-called glycosaminoglycans (GAG), are covalently attached. Proteoglycans are structurally very diverse, due to variations in length and sequence of the core protein as well as differences in abundance, distribution and composition of the GAG chains (Schwartz, 2009). Because of the water-storage capacities of most proteoglycans, they form hydrated gels, thus filling interstitial space into which ECM fibres are embedded.

The ECM does not only serve as an inert structural scaffold upon which cell and tissue development takes place. As mentioned above, cells interact with ECM components via integrins, which recognize specific structural features of ECMs and mediate critical cellular functions by triggering intracellular signaling cascades. It is known that the ECM plays a crucial role in a number of different cellular processes, including cell growth, differentiation, migration and proliferation as well as wound healing (Ingber et al., 1986; Adams and Watt, 1993; Kalluri, 2003). In addition to these direct roles in signaling, the ECM is capable to specifically store and sequester biologically active compounds, such as growth factors, cytokines and developmental control factors required for organ and tissue development,

thereby controlling their local concentration (bioavailability) (Davies, 2001). The ECM is not a static structure, but is constantly remodeled by the cells within and around it. This is done either by endogenous synthesis and secretion of ECM components or the production and release of restriction enzymes like, for instance, matrix metalloproteinases, that are capable of cutting and digesting ECM components (Davies, 2001; Mott and Werb, 2004).

1.2 Protein Coatings Provide Cytocompatibility

For a successful cell adhesion *in vitro*, a technical surface has to be decorated with adhesive proteins that provide binding sites for the cell-surface receptors. By binding to these proteins, the cells get connected to the substrate. In order to provide a cytocompatible surface, proteins are often pre-deposited experimentally from a protein solution upon the surface before cells are seeded. The following paragraph will introduce some typical proteins as applied in this thesis and will describe important aspects of their structures and functions.

1.2.1 Bovine Serum Albumin

Bovine Serum Albumin (BSA) is the most abundant soluble protein constituent found in bovine blood plasma and shows a typical blood concentration of 50 mg/mL. In addition to blood plasma, serum albumins are also found in tissues and bodily secretions. The extravascular protein comprises 60 % of the total amount of albumin (He and Carter, 1992).
BSA is a globular multi-domain protein with a molecular weight of 66 kDa and an isoelectric point at pH 4.7. It is composed of a single polypeptide chain consisting of 583 amino acids (He and Carter, 1992; Hirayama et al., 1990). The protein possesses a high cysteine content. At pH 5 – 7 BSA shows a total of 17 intrachain disulfide bridges and a single free thiol group (cysteine in position 34). The disulfides are arranged in a repeating series of nine loop-link-loop structures around eight sequential Cys-Cys pairs and are mainly responsible for the stabilization of the 3D structure of BSA (Kragh-Hansen, 1981; Hirayama et al., 1990; He and Carter, 1992). The tertiary conformation of BSA is believed to be very similar to the well-known structure of human serum albumin (HSA), because the two proteins share a 76 % homology with respect to their amino acid sequence. The serum albumin molecule is made up of three homologous domains (I, II, III) with high α-helical content that assemble to form a heart-shaped molecule. Each domain is a product of two subdomains (A and B) that possess common structural motifs (Kragh-Hansen, 1981; He and Carter, 1992; Huang et al., 2004).
Serum albumins have many physiological functions: they contribute significantly to the colloid osmotic pressure of the blood and are involved in the transport, distribution and metabolism of a wide variety of endogenous and exogenous compounds including fatty acids, amino acids, steroid hormones, xenobiotics and metal ions (Carter et al., 1989).

The interaction of BSA with water insoluble compounds such as long-chain fatty acids results in a masking of their hydrophobic nature, thus ensuring an increased solubility in plasma and their transport to the different target organs.
Because of these extraordinary characteristics, albumins from various sources have triggered extensive interest in numerous biomedical and industrial applications. For instance, BSA is used as a blocking agent in enzyme-linked immunosorbent assays (ELISA), immunoblots and immunohistochemistry. In restriction analysis BSA is used to stabilize some enzymes during digestion of DNA and to prevent adhesion of the enzyme to the walls of the reaction tubes. It is also commonly used as a standard in protein calibration studies. Regarding the interaction of BSA with mammalian cells, the protein is classified as being non-adhesive. It lacks integrin-specific peptide sequences and is thus often used to passivate blood contacting materials.

1.2.2 Collagens

Collagens (Col) are structural macromolecules of the ECM. They represent a family of glycoproteins with currently 28 identified collagen types (Gordon and Hahn, 2010). The collagen family members form a wide range of different structures and can be grouped into fibrillar collagens (collagen I, II, III, V, XI, XXIV, XXVII), fibril-associated collagens (collagen IX, XII, XIV, XVI, XIX, XX XXI, XXII), network-forming collagens (collagen IV, VIII, X) and transmembrane collagens (collagen XIII, XVII, XXIII, XXV) (van der Rest and Garrone, 1991; Kadler et al., 2007; Gordon and Hahn, 2010). Collagen fibrils are found in most connective tissues, such as skin, bone, tendon, ligament, cartilage and inner organs, where they provide structural integrity. They often consist of alloys of fibrillar collagens. Collagen IV forms an interlaced network constituting basement membranes. Other collagens present in smaller quantities in tissues play a role as connecting elements between these major scaffolding structures and other tissue components. The fibril-associated collagens are non-fibrillar types of collagen which associate with the surface of collagen fibrils in order to connect fibrils to other matrix elements or to allow the fusion of fibrils, leading to larger diameter structures. They are often found in cartilage or tendon (van der Rest and Garrone, 1991).
Collagens are trimeric molecules sharing a characteristic molecular structure: the triple helical constitution. Three distinct polypeptide (α) chains, each of which displaying a left-handed helical structure, are assembled to form a right-handed triple helix stabilized through interchain hydrogen bonds and covalent crosslinks (Brodsky and Ramshaw, 1997). The length of the triple helix and the type and position of non-helical domains depend on the collagen type. A structural prerequisite for the assembly of the collagen molecule into a triple helix is a special amino acid sequence: a glycine residue, the smallest amino acid, occurs in every third position of each polypeptide chain resulting in repeating tripeptide units of the amino acid sequence glycine-X-Y which characterizes the triple helical part of all collagens. The α chains

assemble around a central axis in a way that all glycine residues are positioned in the center of the triple helix, while the more bulky side chains of the other amino acids occupy the outer positions. This allows a close packaging along the central axis of the collagen molecule. Any other amino acid composition would interfere with the triple helical conformation due to steric reasons. The accompanying amino acids X and Y in these triplets are often proline and 4-hydroxyproline, respectively, which stabilize the helical structure due to the buildup of hydrogen bonds. In each collagen molecule, the triple helical region is flanked by non-triple helical (non-glycine-X-Y) domains. These domains are called non-collagenous (NC) and are involved in the covalent crosslinking of the collagen molecules as well as linking to other molecular structures of the ECM (Gelse et al., 2003; Gordon and Hahn, 2010). All members of the collagen family are able to form supramolecular aggregates that are stabilized in part by interactions between triple helical domains (van der Rest and Garrone, 1991).

In this study, the collagens type I, III and IV were studied with respect to their adsorption characteristics on different polymers and will thus be considered in more detail.

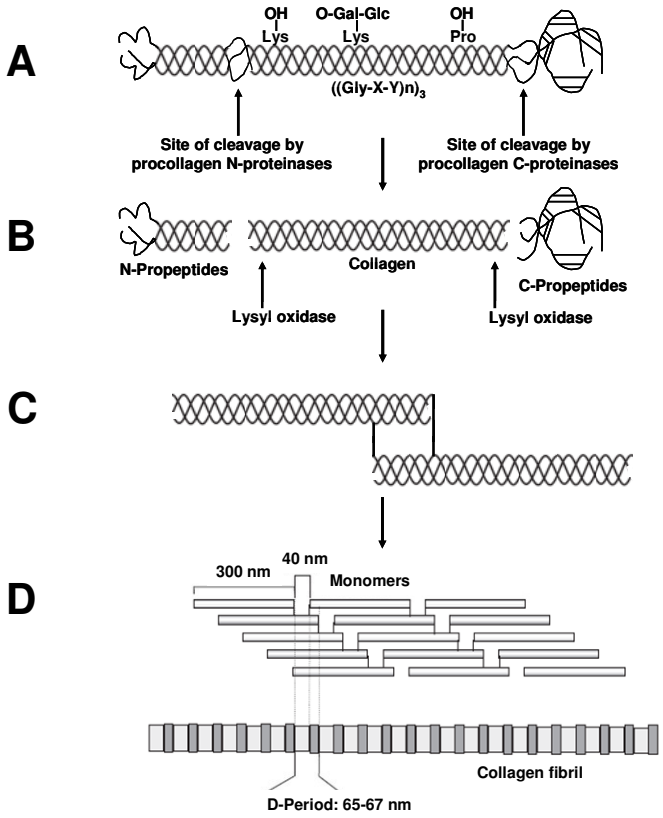

Fig. 1.2 Schematic representation of the supramolecular assembly of trimeric collagen I molecules resulting into a formation of quarter-staggered collagen fibrils. **A** Type I procollagen after triple helix formation, **B** cleavage of N- and C-propeptides, **C** intermolecular covalent crosslinking of two trimeric collagen molecules in a quarter-staggered arrangement, **D** quarter-staggered fibril-array. Each monomer is 300 nm long and is separated by 40 nm from its neighbor, causing the characteristic banding pattern of collagen I fibrils with a periodicity of about 70 nm (D-period), which is visible in the electron microscope (adapted from Gelse et al., 2003; Kadler et al., 2007; Gordon and Hahn, 2010).

Collagen I is a fibrillar heterotrimer with the chain composition $[\alpha1(I)]_2\alpha2(I)$ and a molecular weight of 285 kDa. The three α chains form trimeric molecules which are secreted by mammalian cells as large precursors, so-called procollagens (Fig. 1.2 A). Procollagens possess extra domains at each end of a mature collagen, so-called N- and C-propeptides. These domains are cleaved off outside the cell by specific proteinases, upon which the collagen chains can associate with each other to form fibrils in a quarter-staggered arrangement (Fig. 1.2 B – D). The fibrils in turn line up with one another to form larger fibres (Davies, 2001). The quarter-staggered arrangement, i.e. triple helices are staggered within a collagen fiber in the longitudinal direction by a quarter of their chain length, ensures an optimal overlap between hydrophobic glycine-proline-hydroxyproline rich, rigid structure elements and hydrophilic domains, which account for a certain flexibility of the macro-structure. The fibrillar structure is additionally stabilized by the formation of non-reducible covalent lysine- and hydroxylysine-derived crosslinks which are located at the overlap position connecting the N- or C-telopeptides with specific lysine and hydroxylysine residues within the triple helical part of adjacent collagen molecules (Gelse et al., 2003; Kadler et al., 2007).

Collagen III is a homotrimeric molecule with the chain composition $[\alpha1(III)]_3$ and also belongs to the family of fibrillar collagens. As molecules of type I and type III collagen exhibit the same length and diameter as well as a similar crosslinking mechanism, the formation of copolymers is possible, resulting in mixed fibrils of type I and type III collagen (Henkel and Glanville, 1982). Collagen G, which was also used in this study, is a copolymer formed between collagen I (90 %) and collagen III (10 %). In living organisms, most individual fibrils are composed of a mixture of type I, II and III collagens and may also include small amounts of other fibrillar collagens (V, XI).

Collagen IV, the most abundant collagen of the epithelial basement membranes, is a heterotrimer with a molecular weight of 550 kDa. There are six different α chains that can be arranged into the trimer. The most common chain composition is $[\alpha1(IV)]_2\alpha2(IV)$.

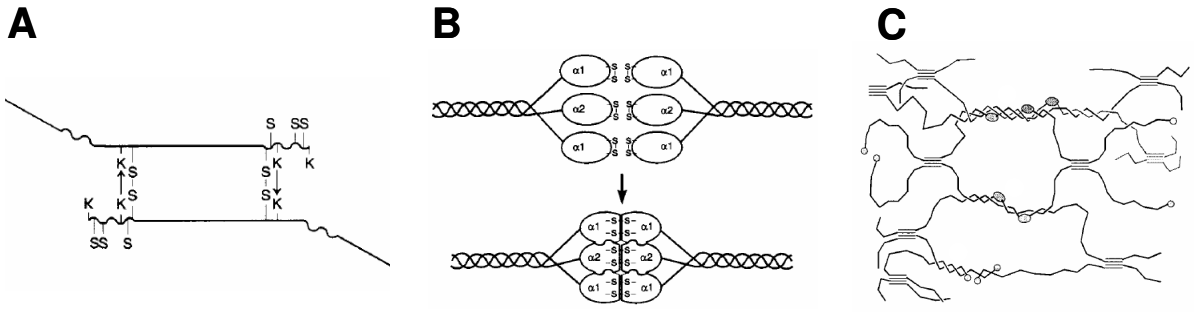

Fig. 1.3 Assembly of collagen IV molecules into a complex macromolecular network. **A** N-terminal association forming a dimer (K: lysine, S-S: disulfide bonds). The assembly to tetramers is not shown for reason of clarity, **B** C-terminal association, **C** lateral association and formation of superhelices (adapted from Kühn, 1994).

Collagen IV can self-assemble into a stable three-dimensional macromolecular network, forming a covalently stabilized polygonal framework via three types of interactions, N-terminal, C-terminal and lateral association (Fig. 1.3). Unlike the fibrillar collagens, the C- and N-terminal ends of collagen IV are not processed before self-assembly.
During assembly and crosslinking via the N-terminus, four triple helical domains from four different molecules assemble in an antiparallel manner to form a tetramer, the structure known as a spider. They form 25 nm, end-overlapped domains which – stabilized by hydrophobic interactions – are connected by intermolecular bonds, i.e. disulfide and lysine-derived aldimine bonds (Fig. 1.3 A). Pairs of C-terminal disulfide-stabilized globules unite to form a hexameric C-terminal complex, responsible for the tail-to-tail binding of collagen IV. This complex is formed by complete disulfide exchange between corresponding cysteins of the two monomeric domains and leads to linear dimers (Fig. 1.3 B). In addition to tail-to-tail aggregation, collagen IV self-interacts through lateral (side-by-side) associations between its triple-helical domains, whereby superhelices are formed (Fig. 1.3 C). This interaction is characterized by a thermally reversible and concentration dependent assembly in which extensive irregular networks form (Yurchenco and Schittny, 1990; van der Rest and Garrone, 1991; Kühn, 1994).

In the clinical field, collagen is used for the reconstruction of bone and soft tissue or as an implant during plastic surgery in order to fill up tissue defects (artificial skin). As a principal component of the ECM, collagen not only provides a biochemically stable scaffold, into which other compounds of basement membranes can be integrated, it also interacts directly with integrins. It has been shown that a number of different cell lines show an improved adhesive and migratory behavior on collagen surfaces. Various cellular recognition sites have been identified within the triple-helical regions of collagen I, II, III and IV (Brodsky and Ramshaw, 1997).

1.2.3 Gelatin

Gelatin (Gel) is a collagen-derived protein with a molecular weight between 13.5 kDa and 500 kDa, depending on the raw material and the extraction conditions. Gelatin is obtained by chemical degradation and thermal denaturation of collagen, predominantly collagen I, which is extracted from animal raw material like bones and skins (thermal partial hydrolysis). The conversion of collagen to gelatin involves the breaking of the triple-helix structure of the water-insoluble collagen molecule into single peptide chains, each having the disordered random-coil configuration. The acid-catalyzed degradation is dominated by hydrolytic cleavage within single chains of collagen and is applied for collagens with a low degree of crosslinking. If an alkaline hydrolysis is used, mainly intermolecular and intramolecular crosslinkages are destroyed, which is more suitable for highly crosslinked collagen (Babel,

1996). Subsequent to the acidic or alkaline hydrolysis, gelatin is extracted using hot water and a step-wise increase of the extraction temperature (55 – 100 °C).
An inherent property of aqueous gelatin solutions is to perform thermoreversible sol/gel transformations at a given temperature. At a temperature of about 40 °C, aqueous gelatin solutions are in the sol state and form physically thermoreversible gels if cooled down to RT. During cooling, the chains undergo a conformational disorder-order transition and tend to partly recover their collagen triple-helix structure by associating helices in junction zones stabilized by hydrogen bonds (Bigi et al., 2004).

Due to its biodegradable properties, gelatin has been used for various applications in the clinical as well as the biomedical research field. Drug encapsulation using hard or soft capsules, microspheres, sealants for vascular prostheses as well as three-dimensional tissue regeneration are among the most common use cases. In food industry, gelatin is often used as a stabilizer, thickener and texturizer. Since gelatin exhibits poor mechanical properties and is soluble in aqueous solution, gelatin materials must be subjected to chemical crosslinking if they are used for long-term biomedical purposes. Crosslinking improves both the thermal and the mechanical stability of the biopolymer. Among the crosslinking agents, glutardialdehyde is by far the most widely used, due to its high efficiency of collagenous material stabilization. In the field of *in vitro* research, gelatin is widely used to coat cell culture dishes in order to generally increase the surface's biocompatibility for mammalian cells. However, it has been shown that a number of different cell lines show strong adhesion and migration on native collagen surfaces while their attachment is hampered by a gelatin coating.

1.2.4 Laminins

Laminins (Lam) are quite large and complex adhesion-promoting proteins which are synthesized and secreted by mammalian cells during the production of endogenous ECM. The family of laminins comprises the most abundant structural non-collagenous glycoproteins of the ECM. Their molecular weight ranges from under 500 kDa to nearly 1000 kDa, depending on the type of laminin. Laminins are heterotrimers, composed of three different peptide chains – one α, one β and one γ chain – that are interconnected via disulfide bridges in the shape of a cross or a T (Aumailley and Smyth, 1998). There are several types of α, β and γ chains, which can associate to generate different types of laminins. In mammals, five α, three β and three γ chains have been identified (Colognato and Yurchenco, 2000; Schéele et al., 2007), but only 18 different laminin isoforms have been described to date (Durbeej, 2010).
Most laminins have a cross-shaped structure, composed of a long α chain and two similar but not identical shorter chains, β and γ (Engvall, 1995). The three short arms of the cross represent the N-terminal ends of each chain, while the middle and the C-terminal portions of the chains run together down the long arm of the cross. The most widely studied laminin type, i.e. laminin I, which was used in this study, exhibits the subunit composition α1β1γ1

(Fig. 1.4). The cross-shaped protein has a molecular weight of ~ 800 kDa (α1: ~ 400 kDa, β1 and γ1: ~ 200 kDa each). The three short arms exhibit a length of 48 nm, 34 nm and 34 nm, while the long arm has a length of 77 nm (Aumailley and Smyth, 1998).
The structure of the laminins, which all share a common domain structure, is described on the basis of laminin I (Fig. 1.4 A). The three short arms of laminin I are composed of two or three types of globular domains (domains IV and VI), respectively, separated by rod-like spacers formed by epidermal growth factor-like cystein-rich domains (domains III and V). The long arm is formed by the C-terminal domains of all three chains, giving a triple α-helical coiled coil domain (domains I and II). The C-terminal end of the α-chain is composed of a tandem of five homologous globular domains (domain G) (Durbeej, 2010).

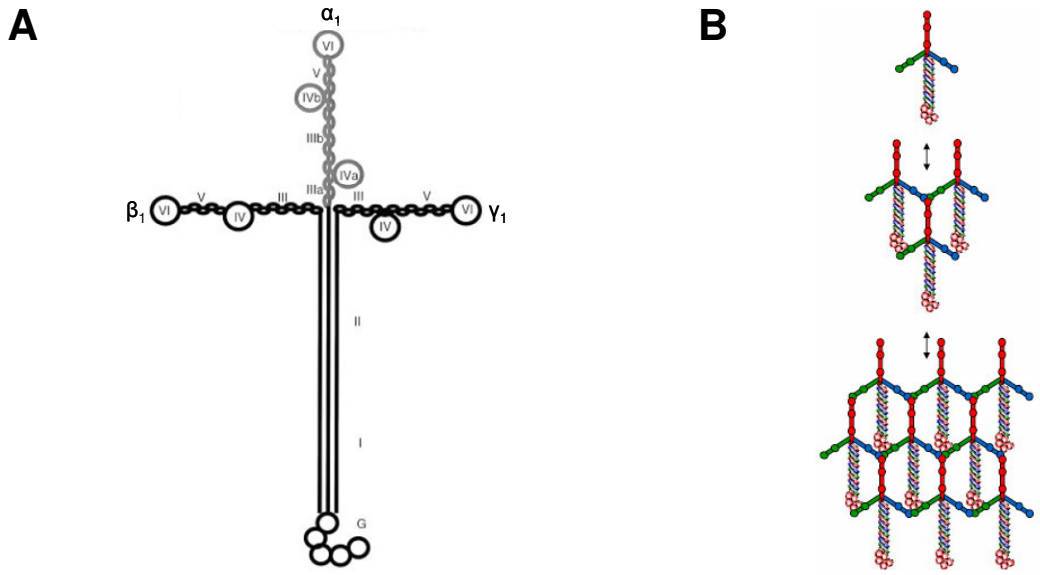

Fig. 1.4 A Schematic drawing of the laminin I structure and **B** laminin network formation through polymerization, in which the primary interactions lead to a trimer by the assembly of three different globular N-terminal domains (adapted from Aumailley and Smyth, 1998 and Durbeej, 2010).

Most laminins are able to self-assemble by means of interactions between the globular N-terminal domains VI from all three short arms, forming independent grossly hexagonal networks (Yurchenco and Schittny, 1990, Cheng et al., 1997). The globular N-terminal domain of each chain non-covalently binds other globular N-terminal domains so that three chains meet (Fig. 1.4 B). The laminin polymerization is a divalent cation, calcium in particular, dependent process. Laminins serve as interconnector between other ECM molecules due to their ability to bind several ECM macromolecules, like proteoglycans or collagen IV in order to form a highly crosslinked ECM. The glycoprotein nidogen, also called entactin, which interacts with laminin I but can also bind to collagen IV, may mediate the formation of ternary complexes that can stabilize the ECM (Colognato and Yurchenco, 2000). Besides interacting with various ECM molecules, laminin I also binds several cell-surface receptors and thereby tightly connects the cells to the ECM (Aumailley and Smyth, 1998). The major cell binding domains of laminin I are the globular C-terminal domains: most

integrins bind to the G-domains 1 – 3 of the α chain, although some integrins also bind to the globular N-terminal domains of the α chain (Durbeej, 2010). As a principal component of the ECM, laminin promotes the attachment and spreading of cells *in vitro*, their migration and neurite outgrowth and even changes their pattern of gene expression and state of differentiation (Colognato and Yurchenco, 2000).

1.2.5 Normal Calf Serum

Normal calf serum (NCS) is the fluid phase of clotted calf blood and contains a complex and ill-defined mixture of macromolecular serum proteins, low molecular weight nutrients, carrier proteins for water-insoluble components, electrolytes and other compounds such as growth factors, hormones and adhesion factors. Serum proteins can be classified by five fractions: albumins, α1-, α2-, β- and γ-globulins. α- and β-globulins are involved in the transport of lipids, hormones, vitamins and metal ions. Furthermore, they include protease inhibitors and the proteins of the complement system. The soluble antibodies compose the γ-globulin fraction.
Since serum is a rich source of growth factors and contains a high amount of adhesive proteins, such as vitronectin and fibronectin, it promotes the attachment and spreading of mammalian cells. Thus, it can be used as a supplement to basal growth medium (2 – 20 % v/v) to promote the survival and growth of mammalian cells in cell culture. In combination with DMSO (10 % v/v), NCS is often used as freezing medium for the cryopreservation of mammalian cell lines. Its cryoprotective capability is based on its high protein content, protecting the cells from cytoplasmic protein leakage due to transient lesions of the cell membrane and thus from freeze-induced cell death due to chemoosmotic stress.

1.3 Interactions of Technical Materials with a Biological Environment

Technical materials that come in direct contact with a biological system – be it only temporary or for long-term exposure – have to meet various requirements in order to fulfill structural or functional tasks. These important characteristics required for biomaterials in their numerous operational areas are often subsumed under the two terms biofunctionality and biocompatibility (Wintermantel, 2002).
Biofunctionality comprises a set of physical properties, such as strength, rigidity, permeability, weight and force transfer, resistance to wear, or optical, electrical and acoustic transmission. These functional requirements have to be fulfilled effectively for a given period of time without any deterioration. However, for biomaterials to be successfully applied and to perform optimally in the biological environment, their biocompatibility is a must.

As defined by Williams (1986), *biocompatibility* is “the ability of a material to perform with an appropriate host response in a specific application”. This definition is rather abstract and provides no insight into what kinds of materials are biocompatible, how they work or how to design improved materials. A definition given by Ratner (1993) describing biocompatibility as “the exploitation by materials of the proteins and cells of the body to meet a specific performance goal” emphasizes the central role of proteins and cellular recognition processes in biocompatibility while also stressing the active role of the biomaterial itself. Thus, a biocompatible material is a technical material that is able to interact with cells and liquids of a biological system causing a desired reaction.
Since the interactions between the biological environment and the technical material take place on the material’s surface (outermost atomic layers of ~ 1 nm) (Kasemo and Lausmaa, 1986), the chemical and physical properties of the biomaterial’s surface influence many of the biological reactions that occur in response to the biomaterial, such as protein adsorption, cell adhesion, cell growth or blood compatibility. Thus, surface properties are crucial for a material’s biocompatibility. These surface properties include chemical composition, wettability (hydrophilicity, hydrophobicity), charge and texture (topography). Among these, wettability is one of the most important parameters known to have an impact on biological surface reactions (Lee et al., 1998).
Surface biocompatibility aims for adapting the chemical, physical, biological and morphological (topography) surface properties of the technical material to the biological system in order to obtain a desired interaction. While resistance to bacterial colonization as well as the suppression of inflammatory and foreign-body responses are *generally* required basic properties of a biocompatible material, *particular* properties of biocompatible polymers can include various requirements arising from the specific application: in many cases, the concept of biocompatibility can be interpreted in the way that a material is well accepted by cells, which show a strong and mechanically stable adhesion to the surface, such as required for the proper functionality of long-term dental implants or soft tissue replacements. However, in cases when a material must be kept free from adsorbing proteins or adhering cells, for example intraocular or contact lenses, where these processes would lead to haze of the material, the term biocompatibility may also mean that an implant surface prohibits protein adsorption and cell growth. Especially in contact with blood, biocompatibility means that no coagulation takes place. Thus, in order to evaluate the biocompatibility of a certain material, knowledge about the surface nature as well as the interactions between the biomaterial’s surface and the biological system are required and have to be taken into account with respect to the intended use.

When a technical material is brought in contact with a biological system, the first interaction of the surface on the molecular level takes place with water molecules (Fig. 1.5 A). These bind rapidly to the surface, establishing a water mono- or bilayer. The specific arrangement of water molecules depends on the surface properties on the atomic level. Highly reactive surfaces lead to the dissociation of H_2O and form a hydroxylated, i.e. OH-terminated surface.

On the other hand, H_2O molecules can also be bound strongly by hydrogen bonds, but as intact, undissociated molecules. Surface types following these kinds of reactions are termed wetting or hydrophilic surfaces. Surfaces displaying a weak tendency for binding H_2O are termed non-wetting or hydrophobic. After the formation of the water overlayer which occurs within nanoseconds, hydrated ions such as Cl^- and Na^+ are incorporated into the water overlayer. The specific arrangement of these ions and their water shells is influenced by the properties of the surface.

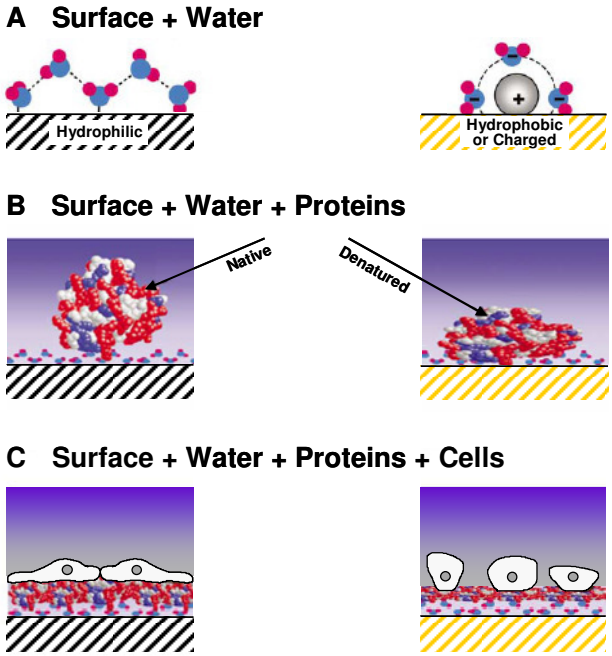

Fig. 1.5 Schematic illustration of the sequence of events following after a technical material has been brought in contact with a biological system. **A** Formation of a water overlayer dependent on the surface properties on the atomic level, **B** protein adsorption with native or denatured conformation, **C** cell adhesion dependent on the adsorbed protein layer (adapted from Kasemo, 2002).

Subsequently, proteins from the bioliquid (e.g. blood, lymphatic fluid, tears, etc.) in contact with the technical material reach the surface and adsorb in a complex series of events, including initial adsorption, conformational changes (denaturation) and/or replacement of typically smaller proteins by larger ones (Fig. 1.5 B). Since most physiological fluids are multi-component systems containing a wide range of proteins, the composition of the protein layer is usually a mixture of proteins reaching the surface early and those arriving later but exhibiting a higher affinity to the surface. Depending on the surface properties of the technical material, the mixture of proteins on the surface, their conformational state as well as their orientation will be different (Ziats et al., 1988). A common observation is that hydrophilic and hydrophobic surfaces bind proteins differently, i.e. proteins may adsorb intact or may denaturate to minimize the free energy of the system. Water-soluble proteins exhibit complex structures with a hydrophobic core and hydrophilic side chains exposed to the protein surface. Thus, on very hydrophilic surfaces, it is more likely that proteins bind intact with their hydrophilic parts oriented towards the surface and with intact water shells (native

conformation), while on very hydrophobic surfaces, the proteins are more likely to bind with their hydrophobic segments closest to the surface and without intervening water shells (denaturation) (Fig. 1.5 B). The adsorbed protein layer which forms within the first few seconds controls all further reactions like the adhesion of cells.
The cells that arrive at the surface after protein adsorption are well adapted to responding to the protein layer coating the material: they interact with the protein covered surface via specific cell-surface receptors (integrins). The surface specificity of the cell-surface interaction derives from the composition of the protein layer, i.e. the types of adsorbed proteins, as well as from its biological activity, i.e. the respective protein conformation. This in turn depends on how the surface binds water, ions and different biomolecules. The biological activity of proteins on the surface will depend upon whether specific active peptide sequences in the respective proteins are accessible for the arriving cells. This finally determines the fate of attached cells upon a technical surface: cells may either remain rounded, unaffected and poorly adhesive in case of few accessible recognition sequences in the protein or will start to firmly attach and spread, maximizing their surface areas (Fig. 1.5 C). While hydrophilic surfaces promote cell adhesion due to the coating with a native protein layer, hydrophobic surfaces covered with a denatured protein layer mostly counteract cell adhesion.
In summary, surface properties of a technical material may influence the nature of the water layer, which in turn determines the protein-surface and cell-surface interactions. All these interactions determine the biocompatibility of a certain technical material in contact with a biological system, like, for instance, the ultimate success or failure of an implant.

1.4 Relevance of Synthetic Polymers in the Life Sciences

Being a product of the 20th century, synthetic polymers nowadays play an essential part in many areas of life, in the private as well as in the industrial sector. Synthetic polymers are also widely used in contact with biological systems – application fields are in medicine, biotechnology or cell biology. Materials used for these purposes are often referred to as biomaterials (Ratner, 1997 in d'Agostino et al., 1997). However, most of the polymers used today were not originally engineered for biomaterial applications, but were widely available before they found their way into medical technology at the end of the 1960s. Even though they were initially applied for sterile medical disposables such as syringes or catheters, synthetic polymers nowadays are used for a variety of sophisticated biomedical devices including orthopedic implants, cardiovascular products, or instruments for surgery. Table 1.1 presents a selection of the most abundant polymers and their current field of application.

Tab. 1.1 Selection of synthetic polymers used in biomedical technology (Ratner, 1993; Klee and Höcker, 2000; Ratner et al., 2004).

Polymer	**Application**
Polyethylene	hip or knee joint replacement
Polypropylene	finger joint replacement, heart valves, suture materials
Polyethylenterephthalat	vascular grafts, ligament reconstruction, suture materials
Polyamide	suture materials, catheters, artificial kidney (extracorporal)
Polytetrafluorethylene	vascular grafts, catheters
Polymethylmethacrylate	bone cement, intraocular lenses and hard contact lenses, dental implants
Polyurethane	vascular grafts, catheters, heart valves, dialyzer membranes
Polysiloxanes	breast implants, artificial tendons, heart valves, artificial skin, bladder prosthesis, tubings and seals for medical devices, contact lenses
Polycarbonates	dialyzer components, tubings, flasks
Polystyrene	cell culture dishes, flasks, reaction tubes, multiwell plates

As shown in Tab. 1.1, synthetic polymers play an important role in many extracorporal devices, from contact lenses to kidney dialyzers, and are essential components of complex long-term implants within the human body, like vascular grafts or heart valves. A variety of materials has been designed for the contact with blood, as replacements for soft and hard tissues or as dental materials. In addition, polymers serve as drug-delivery systems and are essential for organ reconstruction by tissue engineering (Ratner, 1993; Peppas and Langer, 1994; Ratner et al., 2004).

In cell biology, synthetic polymers have become indispensable due to their outstanding properties and price. They serve as culture substrates to grow mammalian cells, like, for instance, polystyrene culture dishes or culture flasks and are used as a basic material of disposable lab equipment such as reaction tubes, pipette tips, cryovials, multiwell plates, etc.

Besides their usefulness for medical applications, polymers are also of growing importance in the fabrication of biosensors and lab-on-a-chip devices. These miniaturized systems serve as powerful platforms for the rapid detection and screening of new drugs, i.e. for the development of high throughput screening systems, especially when combined with integrated microfluidics and sensitive detection technologies (Bashir, 2004). Prominent examples are DNA or protein chips, which have led to recent advancements in genomics and proteomics during the last decade. Biochips exhibiting antibody or specific receptor functionalized surfaces can play a key role as disease markers in search for disease-specific proteins and for the determination of a predisposition to specific disease via genotypic screening (receptor-ligand, immunological, metabolism studies). Many of these micro-fabricated devices are being developed for onetime use assays to prevent a possible cross-contamination and to ensure the reproducibility. Thus, the use of polymer biochips is very

prevalent compared to traditional biosensoric setups consisting of glass or silicon. Synthetic polymers such as PMMA, PDMS, PEG or PTFE are a suitable alternative base material for biochips (Tanaka et al., 2006; Ko et al., 2003; Müller et al., 2003; Lin et al., 2001).

Regarding the versatile and wide-spread applications of synthetic polymers in biology and biomedical technology, it is obvious that diverse polymeric properties are required. In order for these polymers to be successfully applied in a biological environment consisting of proteins and cells, they must have the chemical and physical attributes that most closely match those required for a particular application. Thus, the choice of the polymer depends on the desired functionality including optical properties, a sufficient thermal and mechanical (long-term) stability, sterilizability and surface charge/chemistry. A common indispensable property of all polymeric materials in contact with a biological system is that they are long-term biocompatible. Though the requirements that are associated with the term "biocompatibility" strongly depend on the specific application, a common prerequisite for the biocompatibility of polymers is the absence of certain additives within the bulk polymer, like, for instance, plasticizers, antioxidants or stabilizers, as they might be toxic to cells or denature biomolecules.

As presented above, polymers constitute a broad, diverse family of materials, valuable for many biological and clinical applications. This is due to their easy and low-cost production and processability in a variety of forms and geometries as well as their wide spectrum of physical and chemical properties. In biomedical technology, they are a viable alternative to metallic and ceramic materials due to their low specific weight as well as their simple deformability. Moreover, polymeric materials can be designed to exhibit the appropriate mechanical properties, durability and functionality, which makes them an interesting material for life science applications. Whereas in former decades, the engineering process of polymers was bypassed in favor of trial-and-error-optimization, a multitude of tailor-made synthetic polymers are available nowadays (Ratner, 1993). Material properties can be easily adapted by varying the chemical structure of the polymer such as changing the chain length, the respective monomers or the chain architecture (linear, branched, crosslinked) itself. Advances in material engineering made the production of polymers containing specific hydrophilic or hydrophobic entities possible as well as biodegradable repeating units or multifunctional structures that can become points for the build-up of 3D networks. The presence of functional groups on the backbone or side chains of a polymer also means that polymers can be readily modified chemically or biochemically at their surface without affecting the polymer bulk structure, and thus, the physical properties. Since biological responses to biomaterials are dominated by the polymer surface chemistry and surface structure (chapter 1.5), many researchers have successfully altered the chemical and biological surface properties of polymers by immobilizing anticoagulants such as heparin, proteins such as albumin for passivation and fibronectin for cell adhesion, as well as cell-receptor peptide ligands to enhance cell adhesion, thereby greatly expanding the range of applications for polymers (Thorslund et al., 2005; Tourovskaia et al., 2003; Toworfe et al., 2004).

The following paragraph introduces the synthetic polymers which were applied in this study with their inherent properties as well as the current methods of synthesis.

1.4.1 Polystyrene

Polystyrene (PS) is a vinyl polymer and one of the most widely used kinds of polymers. Structurally, it consists of a long hydrocarbon chain with a phenyl group attached to every other carbon atom (chain-like structure). PS is commercially synthesized by addition polymerization of styrene in a typical chain reaction. In addition polymerization, unsaturated monomers react through the stages initiation, propagation and termination to give the final polymer product. Initiation requires an activated species to attack and open the double bond forming a newly activated species. The initiators can be free radicals, anions, cations or stereospecific catalysts. However, free radical polymerization is still the most commonly used method to synthesize PS. Widely used radical initiators for PS synthesis are peroxides or certain azo compounds. The formulas of two common initiators, dibenzoylperoxide and azo(bis)isobutyronitrile (AIBN) as well as the formation of radical species from these initiators are presented in Fig. 1.6.

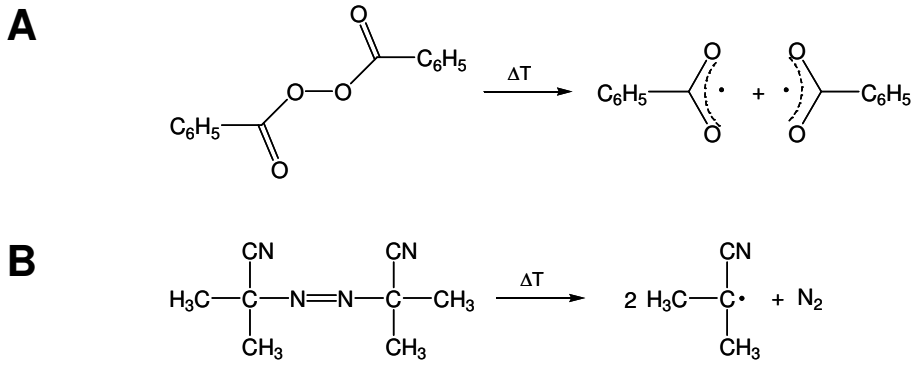

Fig. 1.6 Formulas of the radical initiators dibenzoylperoxide (**A**) and azo(bis)isobutyronitrile (**B**).

Added to the monomer, the initiator undergoes homolytic disproportionation induced by thermal or light energy resulting in free radicals. These free radicals open the double bond of the styrene monomer, presenting an initiation site in the monomer for ensuring continuing growth (Fig. 1.7 A). Rapid chain growth up to thousand monomer molecules ensues during the propagation step by adding one monomer after the next to the free electron of the active end of the polymer chain (Fig. 1.7 B). Each monomer unit adds to the growing chain in a manner that generates the most stable radical until chain terminating reactions take place. The most common termination processes are radical combination and disproportionation. In both cases, two reactive radical sites are removed by simultaneous convertion to stable products. In the former, two polymer radicals combine to form a single molecule. In the latter case, a hydrogen atom is transferred from one polymer radical to the other to form two polymer

chains, one of which has a terminated double bond. The polymerization can also be terminated by reaction with a solvent molecule, an initiator or an added chain transfer reagent. Since the concentration of radical species in a polymerization reaction is small compared to other reagents (e.g. monomers, solvents and terminated chains), the rate at which these radical-radical termination reactions occur is very small, and most growing chains achieve moderate length before termination.

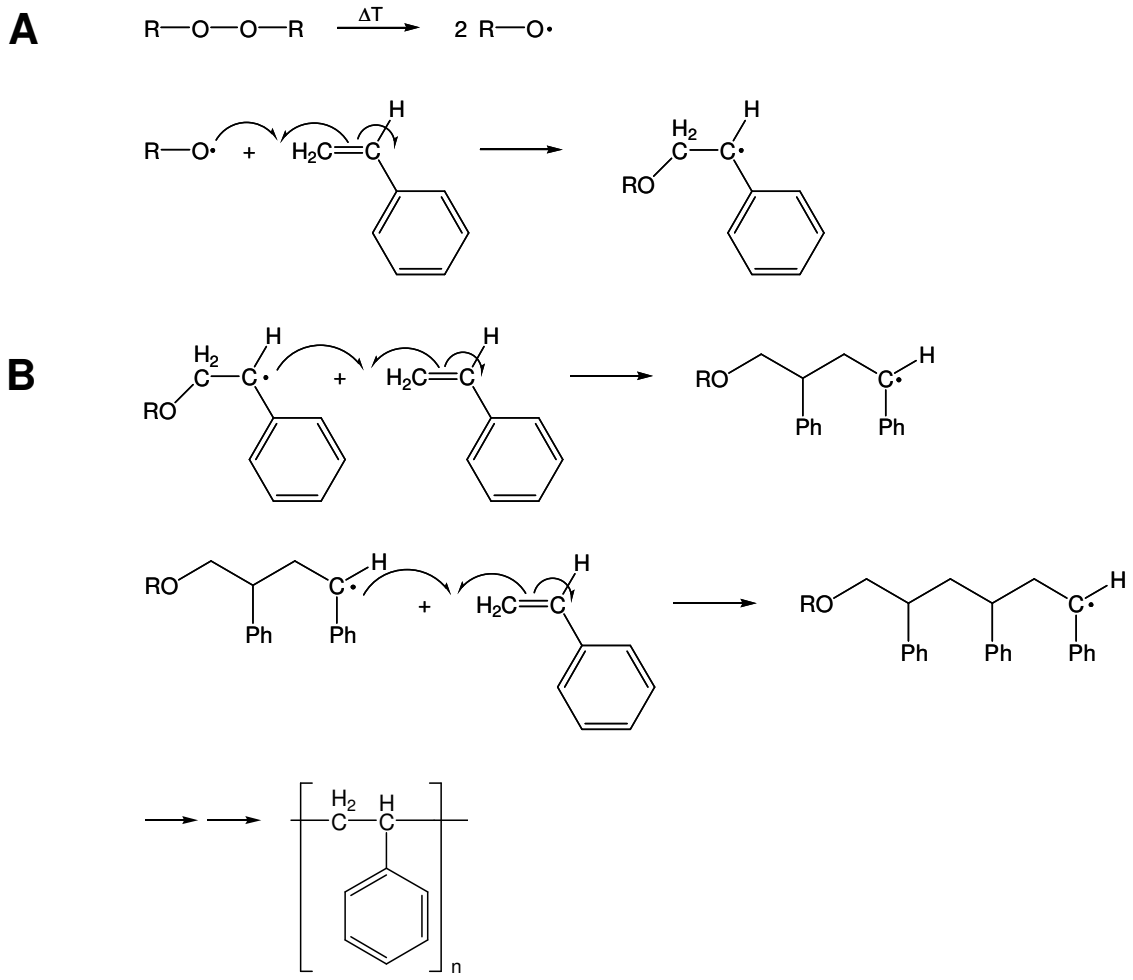

Fig. 1.7 Radical polymerization of styrene forming polystyrene. **A** Free radical formation and chain initiation, **B** chain propagation. Chain termination processes are not shown.

An essential method to control the molecular weight, i.e. the chain length, of polymers during polymerization is the use of regulators, so-called chain transfer reagents. Chain transfer reagents induce termination of one growing polymer chain and simultaneous initiation of a new chain. The polymer radical abstracts a radical – usually a hydrogen atom but sometimes a halogen – from the chain transfer reagent, turning it into a radical, which initiates a new polymerization chain. Common chain transfer reagents include mercaptans, especially dodecyl mercaptan, and halocarbons, such as carbon tetrachloride or carbon tetrabromide. In technical radical polymerizations, transfer reagents are often added in small concentrations (< 0.1 % referring to the monomer) to the monomer (Wünsch, 2000). To a minor extent, the

molecular weight can also be influenced by the adjustment of the reaction temperature or the monomer-to-initiator ratio. Similar to most polymers, PS is not composed of identical molecules. The length of the individual polymer chains may vary by thousands of monomer units. Thus, polymer molecular weights are usually given as averages. The PS used in this study has an average molecular weight of M_w = 230000 g/mol.

PS is a hard, rigid and clear solid with limited flexibility at RT (thermoplastic substance). It is chemically resistant against acids, aqueous base and alcohols, but it is soluble in most organic solvents. PS is susceptible to UV degradation. The thermal stability of PS is low – it is only usable at temperatures up to 70 °C. Above its glass transition temperature (T_g = 94 °C), PS can be readily deformed, i.e. softened and molded with the addition of heat (Sigma-Aldrich, 2009). The properties of PS can be adjusted by copolymerization, for example to fabricate toughened PS, the so-called high impact PS.
PS is commonly produced as extruded PS or PS foams. Extruded PS is used, for example, for the production of disposable cutlery, plastic models, CD cases, casing parts for electric devices, bottles and toys. Products made from foamed PS include food and non-food packaging materials or building insulation materials, since PS foams are good thermal insulators (Wünsch, 2000).
In cell biology and biomedical technology, PS has become indispensable. It plays a key role in the fabrication of cell culture dishes, culture flasks as well as reaction tubes and multiwell plates. Before brought into contact with biological material, PS is sterilized either by gamma irradiation or treatment with ethylene oxide. Surface modification by subjection to UV light (Welle and Gottwald, 2002; Welle, 2004) or to an oxygen plasma is prevalent to introduce polar groups, thus increasing surface hydrophilicity (see chapter 1.4.5 for more details).

1.4.2 Poly(methyl methacrylate)

Poly(methyl methacrylate) (PMMA) is a linear chain polymer and the most important member of the acrylate family. It may more easily be recognized by its trade name „Plexiglas“. PMMA is produced by radical polymerization of methyl methacrylate. The molecular chain reaction is similar to the one previously described for the synthesis of PS (Fig. 1.7). Once thermally initiated using the homolytical disproportionation of the radical starter dibenzoylperoxide or AIBN, the polymerization follows the stages of chain propagation and termination resulting in the final PMMA product (Fig. 1.8). Most of the industrial processes for the synthesis of PMMA are based on free radical polymerization. However, anionic polymerization of PMMA can also be performed.

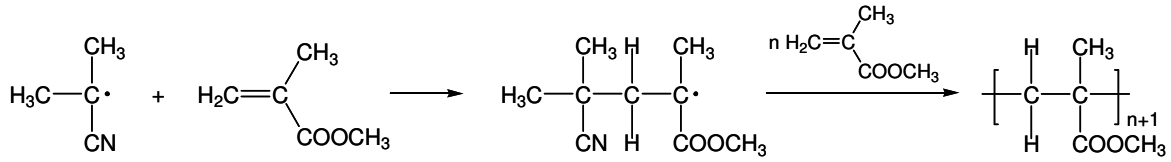

Fig. 1.8 Radical polymerization of methyl methacrylate forming poly(methyl methacrylate).

The PMMA used in this study has an average molecular weight of M_w = 120000 g/mol. PMMA is a hard, transparent solid at RT (thermoplastic substance). It is mainly known for its exceptional optical properties (92 % visible light transmission) and its high molding precision. It is chemically resistant against low concentrated acid and base as well as unpolar solvents, but it is not stable in contact with strong acid and base as well as polar solvents. Polar solvents are known to swell and easily dissolve the polymer. PMMA exhibits a low thermal stability with a glass transition temperature of T_g = 105 °C, above which it can be softened and molded (Sigma-Aldrich, 2009).
PMMA is a technically important polymer used for many commercial applications. Due to its high light transmission, it is often used as an impact resistant substitute for glass, for example in the glazing of automobiles. It is also an ideal material for the use in ophthalmological devices, especially hard contact lenses and intraocular lenses (Brinen et al., 1991). PMMA is a major ingredient in bone cement for orthopedic implants, filling the spaces between the implant and the bone to prevent motion and is used for the fabrication of dentures and dental fillings (Glasmacher, 2006). PMMA can be easily used under sterile conditions after treatment with gamma irradiation or ethylene oxide.
Pure PMMA homopolymer is rarely sold as an end product, but modified formulations with varying amounts of other comonomers, additives and fillers are used to easily adapt the properties of PMMA to various purposes. For example, the addition of plasticizers, like phthalates, provides PMMA with elastic properties. In cell biology and biomedical technology, PMMA is important for the fabrication of biosensors and microfluidic lab-on-a chip devices (Harsanyi, 1996; Ko et al., 2003; Lin et al., 2001).

1.4.3 Poly(dimethyl siloxane)

Poly(dimethyl siloxane) (PDMS) is a silicon-based organic polymer consisting of repeat units of $[Si(CH_3)_2O]$. Depending on the number of these repeat units in the polymer chain and the degree of crosslinking, polysiloxanes can occur in a variety of forms, such as fluids, emulsions, compounds, lubricants, resins and elastomers. Linear polysiloxanes occur as viscous oils, compounds or lubricants. Crosslinked polysiloxanes are soft elastomers, whose bulk rigidity depends on the degree of crosslinking.
The PDMS used in this study is a crosslinked, high molecular weight PDMS, resulting from the reaction of two components: a base and a curing agent (Campbell et al., 1999). The base component contains siloxane oligomers terminated with vinyl groups, i.e. vinyl endcapped

oligomeric dimethyl siloxane. The curing agent includes a (30 – 35 %) methylhydro-(65 – 70 %) dimethylsiloxane copolymer and a platinum divinyltetramethyl disiloxane complex used as a reaction catalyst. The Si–H groups in the siloxane backbone are the prerequisite for the following crosslinking reaction. When both components are mixed together, the Si–H bonds of the curing agent are inserted across the double bond of the base oligomer in a platinum-catalyzed hydrosilylation reaction, resulting in $Si–CH_2–CH_2–Si$ linkages (Fig. 1.9). The multiple reaction sites on both the base and the curing agent oligomers allow for three-dimensional crosslinking. The rigidity of the PDMS elastomer can be readily adjusted by varying the curing agent-to-base ratio leading to a modified degree of crosslinking. As this ratio increases, a more rigid, i.e. higher crosslinked, elastomer results. Heating the polymer mixture can additionally accelerate the curing.

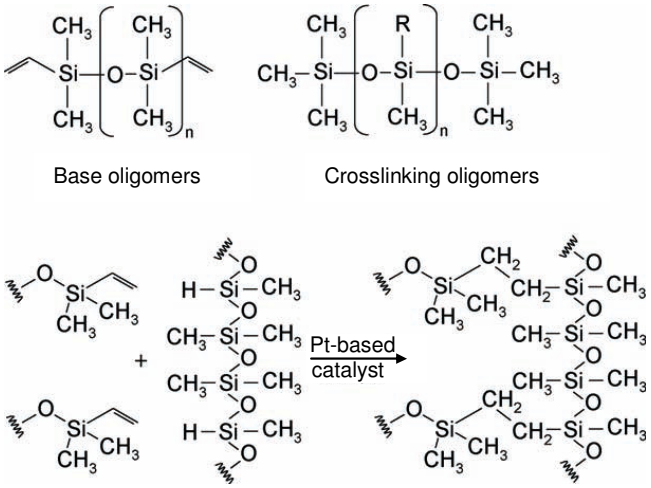

Fig. 1.9 Reaction diagram of platinum catalyzed PDMS curing. R = CH_3 (30 – 35 % H); base oligomers: n = ~ 60, crosslinking oligomers: n = ~ 10 (adapted from Thorslund, 2006).

Cured, crosslinked PDMS is a soft elastomer at RT. Besides its low cost and ease of fabrication, the physical and chemical properties of the polymer include its self-sealing capability, interness – thermal (temperature range: – 45 °C to 200 °C) as well as chemical –, high gas permeability, high hydrophobicity (advancing contact angle ~ 122°) and optical transparency. However, it is incompatible with many non-polar organic solvents, since they swell the polymer (Dow Corning, 2009). Because of its special properties such as high chemical and thermal stability as well as low toxicity, PDMS is used in a wide range of commercial applications including rubbers, resins, water repellents, antifouling materials, corrosion inhibitors, mold release agents, dielectric fluids, antifoams, polishes, lubricants as well as for medical and pharmaceutical purposes. In the construction industry, the polymer is used as a sealing compound, in the electronics field it serves as an electrical insulant and potting compound for electronic equipment exposed to water. In medical technology, PDMS is utilized for catheters and soft implant material (Tab. 1.1).

Whitesides et al. have demonstrated the usefulness of this elastomer for a technique called soft lithography, i.e. non-photolithographic methods for replicating a pattern (Xia and

Whitesides, 1998; Xia et al., 1999). Soft lithography starts with the replication of a submicron-scale pattern in PDMS by casting a negative relief image from a master template. Using inks which consist of molecular adsorbates, it is possible to print with the patterned PDMS stamp, a process termed microcontact printing (Mrksich et al., 1997; Chen et al., 1998; Tien et al., 2002; Folch et al., 2000). Thus, it is possible to generate certain motifs and structures with feature sizes ranging from few tens of nanometers to centimeters. The contact transfer of the material of interest from the PDMS stamp onto a surface only on the areas contacted by the stamp is a convenient way of chemically (micro)patterning a material surface. It allows to selectively deposit proteins (adhesive, non-adhesive) from solution or cells on designated areas of the culture substrate guided by regional differences in adhesiveness of the substrate. The patterning of cell attachment sites on PDMS devices has found relevance for studies of cell growth as well as for high-throughput cell-based assays (Toworfe et al., 2004; Li et al., 2003; Taylor et al., 2003; Tourovskaia et al., 2003; Tan et al., 2004; Raghavan and Chen, 2004).

PDMS has also been widely used in the fabrication of microdevices designed for biological applications, such as microfluidic systems to study the behavior of cells under flow conditions (McDonald and Whitesides, 2002). PDMS-based microfluidic devices have proven of value for ultra-small-volume reagent delivery, microscale chemical reactions (microreactors) and cell manipulations (Sia and Whitesides, 2003; Whitesides et al., 2001; Effenhauser et al., 1997; Chiu et al., 2000; Leclerc et al., 2003). These microfluidic systems can be used as research and diagnostic devices to approximate the size and flow conditions found *in vivo* in capillaries (McDonald et al., 2000).

Furthermore, polysiloxanes are applied as sensitive layers in chemosensors. Since the polymer is gas-sensitive, changes in the polymer film upon gas exposure can be used to monitor organic components in the gas phase (Haug et al., 1993; Harsanyi, 1996).

1.4.4 Photopolymer Microposit® SC® 1827

Photopolymers (PhoP), also called photoresists, are a class of photosensitive polymers which are widely used for microelectronics processing in the semiconductor industry (Rai-Choudhury, 1997; Li et al., 2003). Upon exposure to light they undergo a change in their physical and/or chemical properties. This allows for the formation of a relief pattern in the material by means of a technique termed photolithography. Photolithography describes the patterning of a thin layer of PhoP by means of light. The PhoP is usually spin coated onto a flat substrate from organic solution resulting in an uniform thin film (~ 1 µm) and dried before light exposure to remove residual solvent (soft bake). After the soft bake, the resist coated substrate is exposed patternwise to radiation which is typically UV light. Therefore, a special mask is used, containing the desired pattern in the form of clear and opaque features, thus defining a map of exposed and unexposed regions in the photoresist. The light exposure chemically alters the PhoP by modifying its solubility in a certain developer solution.

Depending on the nature of the resist, the developer solution selectively dissolves either the exposed or unexposed areas. The areas of the substrate that are no longer covered by photoresist can subsequently be subjected to further processing such as plasma etching or ion implantation, while the remaining resist serves as a barrier protecting the underlying substrate. Once the substrate is processed, the photoresist layer can be easily stripped from the surface by organic solvents, e.g. aceton (see chapter 3.6.4.2, Fig. 3.33 for the photolithographic scheme). Using photolithography, physical micropatterns can be produced in various material surfaces.

PhoPs can be classified into two main groups: positive and negative photoresists. They mainly differ with respect to their reaction upon UV light. Negative PhoPs crosslink in areas exposed to UV light during a subsequent baking step and remain on the substrate after development. The unexposed part of the PhoP can be removed in the developer. Positive PhoPs develop where they have been exposed to UV light, while the unexposed areas remain on the substrate after development.

Since a multitude of photoresists comprising different features are commercially available, all following considerations will be made with respect to the PhoP used in this study, Microposit® SC® 1827. Microposit® SC® 1827 is a positive, fluid photoresist with a reddish-brownish color. Its detailed chemical composition is described in Tab. 1.2.

Tab. 1.2 Composition of the positive photopolymer Microposit® SC® 1827.

Component	**Concentration [%]**
Diazo Photoactive Compound	1.0 – 10.0
Nonionic Surfactant	< 1.0
Mixed Cresol Novolak Resin	10.0 – 30.0
Propylene Glycol Monomethyl Ether Acetate	65.0 – 76.0
Cresol	< 0.9

The PhoP is composed of three main ingredients: i) the resin, ii) the photoactive compound and iii) the solvent.

i) The PhoP resin is a cresol novolak copolymer. Novolak is a name generally given to a phenol resin which is polymerized from formaldehyde and phenol via acidic condensation (Fig. 1.10). However, commercial resists do not use phenol itself but rather contain mixtures of *meta*- and *para*-cresol. In a typical novolak production run, a mixture of *m*- and *p*-cresol isomers, formaldehyde and an oxalic acid catalyst are reacted in the ratio 1:0.75:0.08-0.01 (Dammel, 1993). The resin molecular chain length – typically 8 to 20 monomer units – determines many physical properties of the resist: long chains increase the thermal stability or decrease the development rate of exposed resist. Short chains increase the resist adhesion to the substrate. This allows for a designable resin with desired physical and chemical properties by adjusting the chain length. Due to the presence of the acidic phenolic functionalities on the

polymer backbone, the resin is soluble in aqueous base. This issue is exploited in the photolithographic process.

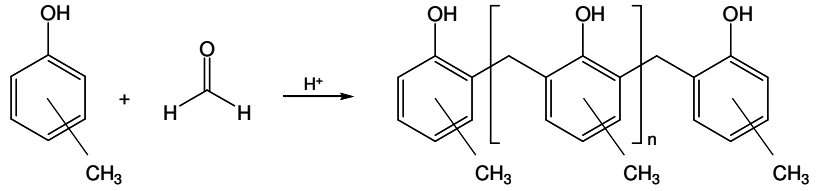

Fig. 1.10 Acid-catalyzed novolak formation as obtained by condensation of formaldehyde and cresol (*m*- or *p*-cresol). All condensations have been arbitrarily chosen to occur in *ortho*-position. This is not true for actual novolaks containing for example *m*-cresol (R = CH_3, n = ~ 8 – 20; modified after Dammel, 1993).

ii) The photoactive compound or sensitizer in the resist belongs to the group of diazonaphthoquinone (DNQ) sulfonates. It determines the resist's sensitivity to light or more precisely, it is responsible for the ability of the resist to change its dissolution behavior in aqueous base upon exposure to UV light. The addition of DNQ-sulfonate to the resin leads to a reduction in the alkaline solubility of the polymer film relative to the alkaline solubility of the pure polymer by 1 – 2 orders of magnitude (MicroChemicals, 2007). DNQ is therefore termed a dissolution inhibitor. During the exposure to UV light (typically $\lambda < 440$ nm), DNQ converts into indene carboxylic acid by releasing N_2 while consuming an H_2O molecule (Fig. 1.11). This carboxylic acid is soluble in aqueous base and its presence in the polymer film increases the alkaline solubility of the novolak 3 – 4 orders of magnitude relative to the pure novolak polymer. The carboxylic acid formed during UV light exposure moves from the hydrophobic to the hydrophilic part of the polymer chain and promotes the deprotonization of the OH-group, increasing the resist solubility in aqueous alkaline developers (MicroChemicals, 2007). It is this change in the dissolution rate of the novolak film due to the reaction of DNQ with light that allows for the applicability of this PhoP in the formation of relief images in the resist film.

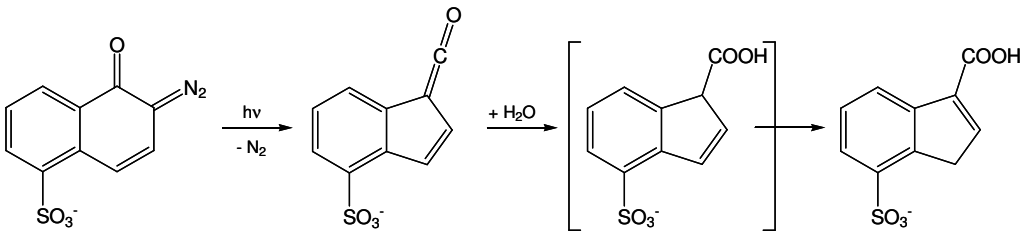

Fig. 1.11 The photo reaction of DNQ-sulfonate. Upon exposure to UV light, DNQ-sulfonate releases a N_2 molecule to form an indenylidene ketene. By consuming an H_2O molecule, the ketene converts into indene carboxylic acid. The intermediate indene-1-carboxylic acid rearranges to the preferred conjugation stabilized 3-isomer (modified after Dammel, 1993).

iii) Propylene glycol monomethyl ether acetate (PGMEA) is a commonly applied solvent of almost all photoresists due to its low vapor pressure which prevents fast evaporation during dispense and its suppression of particle formation in the resist. It determines the viscosity of the resist and can be additionally added as thinner to the resist.

Moreover, specific polymer additives can be compounded into the PhoP to enhance or improve specific resin characteristics like resistance to oxidation or thermal degradation, dependent upon the required purpose. PhoP additives are typically present in rather small quantities (< 1 % w/v) and include material classes such as antioxidants, wetting and leveling agents as well as thermal stabilizers. A wetting and leveling agent present in Microposit® SC® 1827 is the nonionic surfactant listed in Tab. 1.2. Fluorocarbon based surfactants, so-called fluorosurfactants, are commonly applied since they provide low surface tensions, ensuring a complete and homogeneous coating with PhoP.

Depending on the nature of the substrate surface, it can be sometimes necessary to pretreat the surface with a so-called adhesion promoter in order to improve the adhesion of the photoresist to the substrate surface. Especially on substrates such as silicon or glass, polar OH-groups are formed by oxygen and humidity, rendering the substrate surface hydrophilic, thus preventing good wetting and adhesion of the unpolar PhoP. Common adhesion promoters are hexamethyldisilazane (HMDS) or TI-Prime.

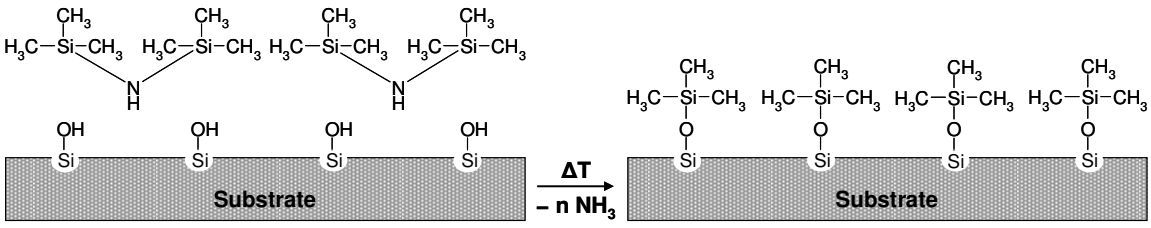

Fig. 1.12 Mechanism of the adhesion promotion of HMDS. By releasing NH_3, the Si atom of the cleaved trimethylsilicon groups chemically binds to oxygen contained in hydroxyl-groups of the glass surface. The methyl groups of the HDMS fragment exposed on the surface provide a hydrophobic surface (modified after Dammel, 1993).

The Si atom of HMDS chemically binds to the oxygen atoms exposed on oxidized surfaces, thereby releasing NH_3. The OH-groups which render the surface hydrophilic are broken. The resulting methyl groups of the HDMS fragment on top of the substrate form a hydrophobic surface, thus improving resist wetting and adhesion (Fig. 1.12).

The adhesion promoter TI-Prime which was applied in this study contains a titanium complex in an organic solvent, which, similar to HDMS, converts the hydrophilic surface into a hydrophobic surface. TI-Prime is applied to the substrate surface by spin coating, forming a physically bonded monolayer of the active compound after solvent evaporation. A subsequent baking step of the primed substrate chemically activates the adhesion promoter. Details concerning the mechanism of the adhesion promotion were not available in the literature.

Besides being widely used in the semiconductor industry, photolithographic processes based on PhoP are also applied in the fabrication of microsystems essential for biotechnological applications, such as microelectromechanical systems (MEMS) or DNA chips (Chrisey et al., 1996; Urban, 1999). PhoPs have also been successfully developed as master templates for replica molding using PDMS, as required for the fabrication of microfluidic devices (Duffy et al., 1998; O'Brien et al., 2001; Cao et al., 2002; Ng et al., 2002).

1.4.5 Surface Modification of Polymers

Polymers play an important role in many areas of biomedical and biotechnological sciences, mainly due to their mechanical characteristics, chemical stability, low specific weight and many design possibilities adaptable to a specific purpose. Their successful application in a biological environment, for example as implants or in diagnostic and biosensing devices, is highly dependent on their surface characteristics. These comprise surface chemistry and topography and govern the biological responses to polymers, like protein-polymer and cell-polymer interactions (chapter 1.3 and 1.5). Hence, it is of crucial importance to design biomaterials with good biocompatible surface properties. In parallel, these biomaterials must possess bulk properties, especially mechanical ones, in order to function properly in a biological environment. As it is quite difficult to synthesize polymers fulfilling both needs – good bulk properties and suitable surface characteristics for a given application – a common approach is to fabricate biomaterials with adequate bulk properties followed by a selective surface modification, thus enhancing the polymers' performance. In this way, it is possible to create ideal custom-made biomaterials with surface properties that are decoupled from the bulk properties.

In general, surface modifications fall into two categories: i) overcoating the existing surface with a material having a different composition (coating, grafting, thin film deposition) or ii) chemically or physically altering the atoms, compounds, or molecules in the existing surface (etching and chemical modification) (Ratner and Castner, 1997). Surface modifications may either be aimed to engineer cell-adhesive surfaces or cell-repellent surfaces depending on the specific purpose. Since many cell biological or biomedical applications require a surface that favors protein adsorption as well as a mechanically stable attachment and spreading of cells, surface modification of polymers is usually aimed for improving surface wettability, as this is regarded as one of the most important surface parameters influencing both protein adsorption and cell adhesion to biomaterials (Lee et al., 1998). The native hydrophobicity of certain polymer surfaces has been one of the biggest limitations in biological applications, as this enhances nonspecific adsorption of biomolecules, limits cell attachment and presents a poor wettability for aqueous solutions. Thus, surface modification of polymers has been a matter of research for a long time and a broad spectrum of surface modification techniques has been applied to tailor the surface properties of polymers in order to control protein adsorption and

cell adhesion. The approaches described below will only address the creation of surfaces which favor cell attachment and spreading.

i) A cell-adhesive polymer surface can be engineered by immobilizing various types of biomolecules on the surface. The strategies for immobilizing biomolecules can consist of physisorption, i.e. simple physical adsorption of biomolecules to the substrate surface mainly via van der Waals forces (weak bonding), or chemisorption, i.e. immobilization of biomolecules via covalent or ionic bonds (usually strong bonding). In the former, the surface can be coated for example with adhesive ECM proteins like fibronectin or laminin, whereas in the latter, cell adhesion can be improved by covalently linking integrin ligands to the surface, like short synthetic peptides mimicking parts of the ECM proteins such as RGD or GRGDS peptides (Klee and Höcker, 2000; Massia and Hubbell, 1990 and 1990a).
A different approach to modify polymer surfaces for an enhanced cell attachment and spreading is to deposit thin layers of various hydrophilic organic polymers onto an existing polymer surface, a method called surface grafting. In graft polymerization, radicals are generated on the polymer surface, where they initiate polymerization reactions when put in contact with monomers in the liquid or gas phase. As a result, grafted copolymers are formed on the surface (Chu et al., 2002).

ii) Chemical or physical surface modifications of polymers aiming to increase surface hydrophilicity include wet chemical treatments (chemical oxidation), photochemical treatments and plasma treatments. Photochemical modifications of polymer surfaces usually employ UV irradiation, which results in the formation of instable peroxide species and different kinds of stable oxidized groups on the polymer surface. Welle and Gottwald (2002) and Welle (2004) exposed different polymer samples (PS, PMMA and polycarbonate) to short wavelength UV light (λ = 185 nm) and observed that hepatocytes and fibroblasts attach and spread upon the UV irradiated polymer surfaces, whereas on non-irradiated regions hardly any cell adhesion was detected. UV/ozone (UVO) treatment is also extensively used to modify polymer surface properties, thereby controlling the wettability to improve cell attachment and spreading. Toworfe et al. (2004) recognized an increase in PDMS wettability upon exposure to a combination of UV light and ozone and Sordel et al. (2007) described an enhanced adhesion of CHO cells upon PDMS coatings after UVO treatment when compared to unmodified PDMS.
Plasma treatment of polymers is another established technique in order to efficiently increase the wettability of a polymer surface thus improving cell attachment and spreading. It is a valuable means for the generation of desired surface properties since plasma treatments have been shown to chemically modify only the outermost molecular layers in the surface region of the polymer (~ 100 Å) while leaving the bulk properties unchanged (Liston, 1989; Li et al., 1997; Beake et al., 1998; Johansson et al., 2002; Chai et al, 2004). Four major effects of plasma on surfaces can be observed: cleaning of organic contamination from the surfaces, material removal by ablation (micro-etching), crosslinking or branching and surface chemistry modification (Liston, 1989). These four effects occur concurrently and depending

on substrate chemistry, gas chemistry and processing conditions, one or more of these effects may dominate.

The increase in wettability of polymer surfaces due to plasma treatment is a well-known phenomenon and can be in part referred to simply cleaning the surface from impurities, contaminants and other weakly bound layers that may impair adhesion, but mainly results from physical and chemical alterations of the surface region. In particular, new polar functional groups originating from the plasma gas or from subsequent exposure to selected gases and vapors are incorporated into the polymer surface, leading to an increase in surface free energy (Fritz and Owen, 1995; Davies et al., 2000). The effect of plasma surface modification mainly depends on the combination of the type of gas as well as the chemical structure of the polymer (Grace and Gerenser, 2003). Common plasma gases are argon, helium, oxygen and nitrogen. Particularly oxygen plasmas have been widely used to modify the surfaces of polymers by introducing new oxygen functionalities into the polymer surface, thus improving surface wettability (Chu et al., 2002; Ferguson et al., 1993). For most untreated polymers, the contact angle of water ranges between 95° and 60°. After plasma treatment with an oxidizing gas the contact angle often decreases to less than 40°, with some surfaces being so wettable that the contact angle cannot be measured (Liston, 1989). Since in this study an argon plasma treatment was chosen as the standard treatment in order to improve surface wettability of different polymers, the mechanism of inert gas plasma induced polymer surface modification will be explained in detail below.

A plasma which is regarded as the fourth state of matter is composed of a broad spectrum of reactive species, resulting from ionization, fragmentation and excitation processes. These include positive and negative ions, electrons, radicals and highly excited neutrals, whose decay leads to the emission of electromagnetic radiation, usually UV and vacuum UV (VUV) radiation (Liston 1989), being responsible for the characteristic glow of the plasma. When a polymer sample is exposed to an argon plasma, the primary effect is the deposition of energy from the plasma species to the polymer surface. The argon ions accelerated from the plasma to the polymer surface as well as VUV photons are thought to be the predominant reactive species in an argon plasma (Beake et al., 1998; Liston 1989; France and Short 1997 and 1998). The energy input leads to the creation of excited state species at the polymer surface and with the decay of these species, to homolytical C–C and C–H bond breaking (Poll et al., 1981; Wilken et al., 1998). This creation of surface free radicals upon plasma exposure is called plasma activation. In inert gas plasmas, the dominant process is hydrogen abstraction from the polymer chain by breaking C–H bonds (Clouet and Shi, 1992). Since the plasma gas argon is an inert gas, it cannot chemically react with the surface radicals, thus leaving a large number of stable radicals at the surface that will persist until being exposed to some reactive gas. Subsequent exposure of the polymer sample to the surrounding atmosphere after venting the reactor vessel leads to surface functionalization: argon plasma treated polymer samples are observed to incorporate instantaneously and almost exclusively oxygen at their surfaces, which accounts for the increase in surface wettability (France and Short, 1997). An increase in oxygen content with non-oxygen containing plasmas is a common phenomenon that has

been reported in various studies (Inagaki et al., 1989; France and Short 1997 and 1998) and is thought to occur mainly by the reaction of surface free radicals created during plasma exposure with atmospheric oxygen when the sample is exposed to air. Besides atmospheric oxygen incorporation after plasma treatment, any traces of oxygen within the reactor vessel during plasma treatment, like oxygen-containing plasma species arising from residual H_2O, are also thought to be responsible for some functionalization (Coopes and Gifkins, 1982). The incorporation of oxygen, as illustrated in Fig. 1.13, leads to the formation of intermediate metastable peroxy radicals, which are prone to further reactions. These peroxy radicals further react to hydroperoxide groups, which slowly convert to the more stable moieties such as carbonyl, carboxyl or hydroxyl groups. These new oxygen containing groups impart wettability to the surface (Clouet and Shi, 1992; Teng and Yasuda, 2002).

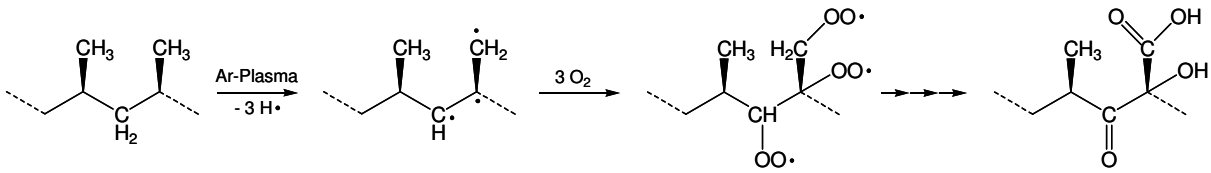

Fig. 1.13 Mechanism of argon plasma induced surface modification of polymers. The energy deposition of reactive plasma species leads to hydrogen abstraction resulting in the formation of free radicals at the surface (plasma activation). The plasma-induced surface radicals can react with atmospheric oxygen forming peroxy radicals which finally convert to the more stable hydroxyl, carbonyl or carboxyl groups.

In addition to the introduction of new hydrophilic functionalities into the polymer surface, intermolecular crosslinking reactions between near-surface polymer chains may also occur as a possible side reaction due to the recombination of the plasma induced polymer radicals, in particular if no oxygen is present which might otherwise serve as a reaction partner (Friedrich et al., 1979) (Fig. 1.14).

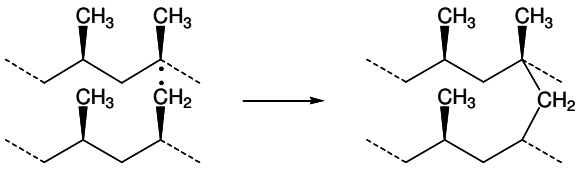

Fig. 1.14 Crosslinking reaction by recombination of two macroradicals under exclusion of oxygen.

By using reactive gas plasmas instead of noble gases, further functionalities can be introduced to the surface. Ammonia and oxygen are widely used gases for plasma treatment because of the high hydrophilicity of amine, amide, carbonyl and carboxyl groups which are created on the surface (Inagaki et al., 1989; Moy et al., 1994; Steele et al., 1995). Reactive gas plasmas are expected to functionalize the surface during the course of the plasma process, while for inert gas plasmas, functionalization is thought to mainly occur on atmospheric exposure subsequent to plasma treatment and second in the plasma chamber during the plasma

treatment process. In contrast to plasma activation using inert gases, which usually do not alter the surface topography of the polymer, reactive gas plasmas are also known to cause ablation or etching, resulting in the formation of small volatile degradation products (Clouet and Shi, 1992).

Plasma treatment is a highly versatile technique due to the adaptivity of various plasma parameters like the gas type, the gas pressure or the temperature, allowing for a designed surface modification. It offers the advantages that almost every polymer can be modified, the modification can be controlled and varied by the choice of the utilized gas and a relative large area of the material's surface can be modified homogeneously, independent of its geometry. Thus, the chemical functionality, wettability and bondability of polymer surfaces can be selectively influenced by plasma treatments (Hegemann et al, 2003). However, a variety of plasma treated polymer surfaces are unstable in air and show an aging effect: the acquired surface hydrophilicity (wettability) is often only a temporary effect and decreases with increasing storage time in air (Lai et al., 1996). This phenomenon has been described by the term *hydrophobic recovery*. Whereas for plasma treated PS, oxygenation seems to be permanent (Davies et al., 2000), PDMS exhibits hydrophobic recovery. It has been reported that plasma treated PDMS reverts to being hydrophobic within less than 1 h (Lai et al., 1996; Sia and Whitesides, 2003). Ginn and Steinbock (2003) detected a loss of the induced hydrophilicity of the PDMS surface within a period of 2 – 3 h, but the surface never fully regained its initial hydrophobicity (water contact angle on unmodified PDMS: (112 ± 2)°, directly after plasma exposure: (15 ± 2)°, 3 h after plasma exposure: 79°). Possible mechanistic explanations for the observed decay of wettability can be attributed to the following phenomenons (Fritz and Owen, 1995; Lai et al., 1996; Kim et al., 2001):

i) thermodynamically driven reorientation of surface hydrophilic (polar) groups away from the surface to the bulk phase
ii) migration (diffusion) of the untreated polymer chain from the bulk to the surface
iii) formation of unpolar low-molecular-weight (LMW) species in the sub-surface during plasma exposure and their subsequent migration to the surface
iv) external contamination of the polymer surface
v) changes in surface roughness
vi) loss of volatile oxygen-rich species to the atmosphere

In the case of PDMS, hydrophobic recovery has been shown not be caused by the adsorption of organic contaminants from the surrounding atmosphere. Instead, it was reported by various authors that processes which increase the relative amount of hydrophobic molecules (groups) at the surface thus lowering the surface free energy are attributed to the rearrangement processes under i) – iii) (Sia and Whitesides, 2003; Kim et al., 2000): hydrophilic groups generated at the polymer surface reorient from the surface into the bulk of the polymer. Additionally, low-molecular-weight polymer chains migrate from the bulk material to the surface (passive transport) (Hillborg et al., 2000; Fritz and Owen, 1995). The rate of hydrophilicity loss is related to the thermal motion of the polymer chains and hydrophilic

groups (Lai et al., 1996). Keeping the oxidized surface in contact with a polar liquid (e.g. water or polar organic solvents) immediately after oxidation maintains the hydrophilic nature, although its long-term stability is unknown (Morra et al., 1990; Duffy et al., 1998).

1.5 Influence of Surface Topography on Cell Attachment and Spreading

In addition to surface chemistry, both protein adsorption and cell-substrate interactions are also influenced by the surface micro- or nanotopography of the substrate to which they are attached, i.e. the topographical surface features (Curtis and Wilkinson, 1998). Curved surfaces, pits, protrusions or cavities that have sizes or radii of curvature comparable to the size of biological entities (proteins ~ 1 – 10 nm, cells ~ 1 – 100 μm) can induce biological interactions different from those on a flat surface. Engineering approaches to modulate the topography of a substrate are based on micropatterning technology or photolithography. Historically, photolithography is the most widely used technique to imprint distinct topographical patterns on planar surfaces, such as pits and grooves of controlled size and shape. Depending on the photomask resolution, the size of the features can be precisely controlled down to micrometer dimensions, a size domain comparable or smaller than a single cell. The smallest feature size obtainable by conventional photolithography is approximately 0.3 μm, while electron beam lithography can produce features down to below 10 nm, depending on processing procedures and the specific materials used (Kasemo and Gold, 1999; Wilkinson et al., 2002).

Via distinct surface patterns, the response of a biological system can be controlled. As addressed in several studies, micro- and nanostructures can be used to influence cell attachment, morphology, growth and proliferation. The most prominent response of cells to surface topography is the phenomenon of contact guidance, describing the process whereby oriented surface features such as grooves and ridges in the dimension of micrometers direct cell orientation and migration (Weiss, 1945; Curtis and Wilkinson, 1998). Cells tend to align themselves in the direction of the grooves on a patterned surface without any chemical coatings to the surface itself, leading to an altered often very elongate morphology (Walboomers et al., 1999). Especially fibroblasts, but also epithelial cells, show this phenomenon. On microgrooves (1 μm deep and 0.5 – 10 μm wide) in PMMA films, created by electron beam microlithography, human fibroblasts showed a strong orientation along the groove direction, independent of the groove width (Alaerts et al., 2001). On 10 μm and 5 μm wide grooves, the cells were within the grooves. On grooves of 1 μm and 2 μm width, the cells resided on top of the ridges and elongated along the grooves and on 0.5 μm wide grooves the cells were also oriented while covering several grooves. Walboomers et al. (1998) investigated the contact guidance phenomenon for rat dermal fibroblasts on microgrooved PS

substrates of the same dimension used by Alaerts et al. and obtained similar results. The microgrooves in PS were supposed to induce a pattern of mechanical stress on fibrous cellular components, especially in the filopodium, influencing cell spreading and orientation and causing the cells to be aligned with the surface microgrooves (Walboomers et al., 1998).
Using PS microgrooved substrates with groove widths between 1 – 20 µm and depths between 0.5 – 5.4 µm, Walboomers et al. (1999) not only confirmed an orientation of fibroblasts on most microgrooved surfaces independent of groove width, the rate of orientation was also effectively increased by an increase in groove depth.
Clark et al. compared the alignment of BHK (baby hamster kidney) fibroblasts with the behavior of epithelial MDCK cells and chick embryo cerebral neurons on parallel gratings made in fused quartz with feature sizes ranging from 0.13 µm to 25 µm in width (0.1 – 1.9 µm in depth). The authors found that the influence of topography is dependent on cell type, cell-cell interactions and the geometry of the micropatterns. While all gratings induced alignment of BHK cell populations, the degree of alignment was dependent on the depth and the pattern period. Single MDCK cells aligned to all patterns in the direction of the gratings and elongated, their elongation being depth and period dependent, whereas colonies of MDCK cells were mainly unaffected. The outgrowth of neurites from chick embryo neurons was also predominantly unaffected by the grating surfaces (Clark et al., 1990, 1991 and 1992).
Topographical micropatterning of substrates has also been applied to control or spatially dictate the adhesion and polarization of neurons. Well-defined neuronal networks, where the relative position of cells and their axons or dendrites are determined by the artificial design, could give valuable insigths into the effect of cell-cell communication on basic processes such as synapse development, synaptic transmission and potentiation. Here, special emphasis lies on the arrangement of cells on surfaces of sensor devices, like microelectrode arrays, detecting the electrical activity of a large number of neurons. Using micropatterning of a polymer substrate, the preferential orientation of Schwann cells can be controlled (Miller et al., 2001). Horizontal microgrooves with a width of 10 – 20 µm and thus ranging in the same dimension as the cell width (5 – 10 µm) were found to promote the alignment of the Schwann cells along the direction of the grooves. While groove width was found to be a key parameter for alignment of the cells, groove depth (1.4 – 3.3 µm) did not seem to play a significant role.
Micromachined grids of so-called “neurowells” in silicon were used to mechanically trap neurons onto electrodes and yet allow them to directed outgrowth of neural processes and synapse with each other (Tatic-Lucic et al., 1997; Maher et al., 1999). Since the neurons are confined to the electrodes, the access, i.e. electrical recording and stimulation, to each neuron in a small cultured network is unambiguous and well isolated, allowing for a one-to-one correspondence of neurons to electrodes. Living neuronal circuits based on surface micropatterning are widely studied in biosensoric applications, medical devices and neural computing (Matsuzawa et al., 1997).
The microtopography of the substrate can also indirectly alter cellular functionality at the genetic level by affecting changes in cell shape. Using human fibroblasts, fibronectin mRNA level, mRNA stability and the secretion and assembly of fibronectin in the ECM could be

related to cell shape changes on microgrooved surfaces (Chou et al., 1995). Cells on grooved surfaces showed an untypical elongated morphology and were oriented along the grooves of the substrate, while cell height was increased by a factor of about 1.5 compared to cells on smooth surfaces.

Control of surface topography using microfabrication has also potential applications in tissue engineering. Van Kooten et al. (1998) studied the effect of surface structures on the proliferation of human skin fibroblasts cultured on 0.5 μm-deep grooved PDMS substrates using cell cycle analysis. PDMS surfaces used were either textured with 2, 5 and 10 μm wide grooves or left unmodified as a smooth substrate. Cells on smooth surfaces got into the S-phase of the cell cycle earlier than cells on microtextured surfaces, indicating a faster proliferation. Proliferation was groove width-dependent, revealing a slower proliferation on 10 μm-wide grooves than on 2 μm or 5 μm ones.

Besides cell adhesion and proliferation, cell migration is an additional important factor which can be influenced by surface topography. Titanium-coated grooved silicon substrates (40 μm wide, 3 μm deep, separated by 40 μm wide ridges) have been found not only to control the direction of migration of fibroblasts and epithelial cells, but fibroblasts moved significantly faster – increasing their speed by a factor of two – on grooved than on smooth surfaces (Damji et al., 1996). However, the speed of epithelial cell migration was not significantly altered. Since fibroblasts as well as their cytoskeletal elements including microfilaments and microtubules have been shown to be aligned in the direction of the grooves (Oakley and Brunette, 1993), these polarized cells were expected to move more rapidly because the organization of their cytoskeleton would not have to be reoriented, as it would be necessary when cells change their direction of migration as they do on smooth substrates.

Kaiser et al. (2006) demonstrated that 3T3 fibroblasts cultured on titanium alloy surfaces with groove and ridge patterns of different dimensions (depth: 5 – 22 μm, spacing: 5 – 30 μm) show a 1.5 – 2.6 higher migration velocity when moving parallel to the grooves/ridges than perpendicular to the structures.

Berry et al. (2004) studied the interaction of fibroblasts with a micro-pit patterned quartz surface, consisting of a regular array of pits with diameters of 7, 15 and 25 μm and spacings between the pits of either 20 μm or 40 μm (depth: 4.8 μm). They demonstrated that fibroblasts are sensitive to a pitted topography, in particular to the diameter of the pits. The 25 μm pits combined with both spacings allowed cells to completely enter the pits. Conversely, the 7 μm pitted surface allowed the majority of cells to move over the pits completely. The 15 μm pits were in between the two extremes. This cellular reaction was ascribed to the fact that cells may sense differences in radius of curvature.

Titanium surfaces exhibiting hemispherical cavities of 10, 30 or 100 μm in diameter, arranged in a hexagonal pattern, were chosen to study the role of the microtopography on osteoblast cell behavior (Zinger et al., 2004). On substrates with cavities of 30 μm and 100 μm in diameter, the cells were found preferentially inside the cavities. On the other hand, on 10 μm surfaces, the cells entirely or partly spread over one or several cavities. The cells inside the

30 µm cavities showed a higher cell thickness, contrary to those inside the 100 µm cavities, which were flat and more spread out.
The topographic pattern of the substrate surface may also play a role in the distribution and deposition, i.e. the composition, spatial arrangement and conformation, of endogenous and exogenous ECM proteins. On microgrooved silicon surfaces (width: 2, 5 and 10 µm; depth: 0.5 µm), fibronectin and vitronectin were found to be aligned along the surface grooves and ridges (den Braber et al., 1998). The topographic discontinuities were supposed to have a different surface charge and surface free energy and to act as sites of preferred protein deposition, resulting in the creation of protein patterns along the topographic patterns. This could in turn play a role in the contact guidance of cells. A difference in protein adsorption along the edges of ridges may cause the formation of focal adhesions preferably at this site, possibly resulting in an oriented cell shape.

In summary, surface topography, meaning ordered and continuous topographical surface structures, is an important and powerful modulator of cellular behavior and thus can be used to optimize substrates for medical and *in vitro* applications. Unlike some other approaches that influence cellular behavior such as the use of chemical coatings that might be present only transiently, topographical features in the range of the size of a cell can exert abiding influence on cells. Surface topography can have an impact on cellular behavior in many ways, including their morphology, orientation, motility and adhesion. The ability to control and guide the placement and properties of cells in an organized pattern on a substrate has become increasingly important for the development of applications ranging from cellular biosensor technology to tissue engineering. Concerning the phenomenon of contact guidance, it has been shown that the interaction of cells with substrates presenting nonplanar surfaces depends on the dimensions of the underlying topography. For groove/ridge patterns, it was found that groove width was more important for cellular alignment than groove depth, leading to cells becoming polarized and elongated in the direction of the grooves. The response to topography is also dependent on the cell type and can be different for the same cell depending on whether or not cell-cell interactions are allowed. The effects on cell growth and cellular properties appear to be mediated via modulation of cell shape by the surface features.

1.6 Experimental Techniques to Study the Cytocompatibility of Biomaterial Surfaces

The constant improvement in biomaterial synthesis and surface treatments have led to the elaboration of sophisticated synthetic materials designed to be used for a wide field of biomedical purposes in applied and fundamental research. Consequently, highly sensitive methods are required to characterize, evaluate and analyze the biocompatible properties of these surfaces. Specific physical and chemical surface characterization techniques may be

helpful to understand the surface properties of certain materials. The non-destructive determination of the surface energy state can be achieved by direct measurement of contact angles of pure, physiological test fluids on the surfaces. The surface texture can be investigated using a scanning electron microscope and possible degradation problems can be detected performing long-term exposure to aqueous electrolyte solutions. However, in order to evaluate the potential of technical materials for applications in contact with living cells, special attention should be paid to the interface between the cells and the biomaterial surface. One crucial issue in the research and development of biomaterials with tailored surface properties is the *in vitro* evaluation of real-time cell-surface interactions, giving valuable information on the material's cytocompatibility. These interactions mainly determine the successful performance of a technical material in a biological environment and are of great importance to find materials which favor cell adhesion, which is desirable for many medical implants, and to develop materials which prevent cell adhesion, e.g. to stop biofouling.

A number of different approaches to study the cytocompatibility of certain biomaterials are available nowadays. Some less sophisticated methods include proliferation studies, which allow for a measurement of the cell density several days after seeding by simple cell counting. The amount of vital cells can be determined by intracellular uptake of membrane-permeable dyes, by the use of particular staining techniques or biochemical assays. An established *in vitro* assay to evaluate the cytocompatibility of biomaterials, based on measuring the metabolic activity of cells in contact with the material, is the colorimetric MTT assay. It is based on the transformation (reduction) of a colorless tetrazolium salt to colored formazan, which only occurs in the presence of the mitochondrial enzyme succinate-dehydrogenase which is active only in vital cells. The amount of the colored formazan is proportional to the number of living cells and can easily be quantified spectrophotometrically. In addition to cell viability and metabolic activity assays, the morphology of attached and spread cells on substrates can be determined by scanning force microscopy (SFM) or scanning electron microscopy (SEM), both providing nanoscopic detailed images of the upper cell surface with a high spatial resolution. Additionally, the application of functionalized tips enables biospecific chemical force microscopy. Video microscopy and fluorescence microscopy are also suitable in order to determine morphological changes occurring in a cell after seeding on a specific biomaterial surface.

All methods mentioned above are able to address the cytocompatibility issue in a rather indirect manner, since they have no direct access to the interface between the lower cell membrane and the substrate that the cell is attached to, i.e. the adhesion zone. However, most of the crucial processes important for the adhesion, spreading, differentiation or migration of cells happen in the subcellular cleft. A second disadvantage of most methods is the inherent destruction of the probed cell layer, regarding for example flow-chambers for quantifying the strength of cell adhesion to surfaces or fixing/staining techniques affecting the cell vitality. Moreover, as in the case of microscopic evaluation of morphological aspects such as the study of the physical appearance of cytoskeletal features in adhered cells, the interpretation of the results may be subjective dependent on the operator. Thus, non-invasive techniques directly

addressing the contact zone between lower cell membrane and substrate surface are of valuable importance. However, the number of such experimental techniques is rather limited. Two microscopic techniques, capable of imaging the contact area of adherent cells, shall be described below.

Reflection interference contrast microscopy (RICM) allows to visualize the contact area between living cells and a transparent substrate, the so-called "footprints" of cells. It is also used to study cell adhesion dynamics (Verschueren, 1985). Cells are grown on a glass coverslip which is placed under an inverted microscope and is illuminated from below by a monochromatic light cone with a rather big apex angle. The RICM image results from light reflected at interfaces between media of different refractive indices like the glass/liquid and the liquid/cell membrane interface. When the incident light hits a cell-free area, a fraction is reflected at the glass/liquid interface. The intensity of the reflected light depends on the difference in the refractive indices of the two adjacent media. Since this difference is rather significant for the glass/liquid interface compared to any of the other interfaces of the sample, the reflection is relatively strong, which results in cell-free areas appearing bright in RICM images. In cell-covered areas the incident light is also reflected but its intensity is modulated by interference. The fraction of the incident light passing through the glass/liquid interface is reflected at the liquid/cell membrane interface. Due to the close proximity of these two interfaces, both reflected light beams are partly coherent and interfere so that the intensity of the reflected light and thus the overall brightness of the image in cell-covered areas depend on the optical path difference of the two reflected light beams. This opens up the possibility to determine the cell-substrate separation distance (Curtis, 1964). In the corresponding RICM image, the contact area of a cell with a substrate appears dark against a homogeneous grey and cell-free background, whereas the intensity of the dark regions themselves depends on the local distance of the lower cell membrane from the substrate surface. Besides providing static information about the area of contact between cell and substrate, this technique also allows for real-time recordings of dynamic cell processes, such as cell motion, when being combined with videomicroscopic techniques and digital image processing (Schindl et al., 1995). However, the absolute distances determined by RICM have to be handled with care as the refractive indices of the liquid underneath the cell, of the cell membrane itself and of the cytoplasm are highly critical parameters for the determination of such distances and can not be measured with high precision.

Another microscopic technique addressing the cell-substrate adhesion zone is the so-called fluorescence interference contrast microscopy (FLIC), which was introduced by Braun and Fromherz in 1997. This technique is capable of quantifying the exact cell-substrate separation distance (Braun and Fromherz, 1997). Cells are grown on oxidized silicon substrates that have been designed to exhibit special topographical features: steps made from silicon dioxide of at least four different, well-known heights – ranging between 20 nm and 200 nm – are introduced to the substrate surface using photolithography. After the attachment and spreading of cells on the FLIC substrate, the cell membranes are stained with a lipophilic,

fluorescent dye. FLIC microscopy is based on the effect that the resulting fluorescence intensity of the fluorophore close to the silicon/silicon dioxide interface is modulated by the reflection of excitation and emission light at this interface and the resulting interference. When the cell-covered FLIC substrate is placed in the incident light beam, the light excites the fluorophore either directly or indirectly after reflection at the silicon/silicon dioxide interface. This interface behaves as a rather ideal mirror and standing waves of the incident light are formed with a node at the silicon surface. Thus, the intensity of fluorophore excitation is dependent on the distance between fluorophore (cell membrane) and silicon. In a similar manner, the fluorescent light emitted by the fluorophore upon excitation is collected from the objective lens of the microscope either directly or after reflection at the silicon/silicon dioxide interface. Since both, the direct and the reflected fluorescent light are partly coherent, interference occurs so that the intensity of the resulting light beam is also modulated by the optical path difference and thus, the distance between fluorophore (cell membrane) and silicon. The intensity of the fluorophore excitation and the intensity of the resulting fluorescence light are a function of the cell-substrate separation distance. However, the relation between the relative fluorescence intensity and the distance of the fluorophore to the silicon substrate surface is not unique. Thus, four different steps of silicon dioxide, serving as well-defined spacers between the cell membrane and the reflecting silicon surface, are used to provide four data pairs. The four different fluorescence intensities are analyzed using an optical theory, providing a distinct cell-substrate separation distance.

Substrate-Integrated Biosensors

Substrate-integrated biosensors are a promising research tool to study cell-surface interactions. In this approach, mammalian cells are cultured directly on the sensor surface. Thus, the technical surface serves as a growth substrate for the cultivation of cells and as a sensory element. The technical material for the sensor should be selected properly, since it should withstand the cell culture conditions (37 °C, 95 % relative humidity) and show biocompatibility. Additionally, the material needs to be sterilizable, what necessitates either the tolerance of high temperatures or the resistance against radiation (electron beams, gamma rays, UV light). For the sensor to be functional, the interactions between the cells and the sensor surface need to be converted into a measurable signal. Consequently, appropriate analytical techniques are required, which have direct access to the cell-substrate adhesion zone. Optical, impedimetric (electrical) or gravimetric (mechanical) approaches are in use. A crucial requirement for time-resolved measurements is the non-invasiveness of biosensors – the measurement should not interfere with the system under study. Substrate-integrated biosensors are often applied to quantitatively analyze the reaction of cells upon biochemical or physical stimuli and to serve as screening methods for drugs, diagnostic information from clinical samples related to diseases and biomaterials research. Especially in the field of large-scale screening, substrate-integrated biosensors have made the process of testing much more

comfortable, objective and even faster by recording data in a quantitative manner and with a high time resolution.

Two impedimetric techniques are applied in this thesis in order to follow the cellular responses, like cell adhesion and differentiation, to technical surfaces, and to gain quantitative insight into cell-substrate interactions: the quartz crystal microbalance (QCM) technique (chapter 1.6.1) and the electric cell-substrate impedance sensing (ECIS) technique (chapter 1.6.2). Both techniques can be subsumed under the generic term "substrate-integrated biosensor": in the basic form of both techniques, cells are cultured on planar gold film electrodes, with serve as a growth substrate and a sensory element at the same time. The QCM technique monitors the mechanical interactions between cells and their growth substrate, while the ECIS technique follows the establishment and modulation of cell-substrate interactions by means of measuring the passive electrical properties of the adhesion contact.

1.6.1 Micromechanical Analysis of the Cell-Substrate Contact Using the QCM Technique

The QCM (quartz crystal microbalance) technique is a sensitive analytical tool which allows to monitor and quantify the formation and modulation of cell-substrate contacts in a non-invasive manner and in real time. The core component of the QCM technique is a thin disk-shaped piezoelectric (AT-cut) quartz crystal sandwiched between two metal electrodes. When an oscillating potential difference is applied between the surface electrodes, the piezoelectric resonator is excited to perform mechanical shear oscillations parallel to the crystal faces at the resonator's resonance frequency. This mechanical oscillation is highly sensitive to the deposition of any foreign material upon the resonator surface, so that adsorption processes can be followed from readings of the characteristic shear wave parameters.
For many years, the QCM technique was used as an established means to study deposition processes of thin material films in the gas phase or in vacuum. As the QCM detects any mass loading with nanogram sensitivity, it is a valuable tool to probe the thickness of even thin material films. A rigid, homogeneous and sufficiently thin adsorbed mass layer deposited in air or vacuum causes the resonance frequency to decrease proportionally to the amount of mass deposited on the sensor surface, a relation found by Sauerbrey (Sauerbrey, 1959). Recent progress in designing oscillator circuits which are capable of coping with high viscous damping of the shear displacement paved the way to monitor adsorption processes even in an aqueous environment – a prerequisite for the detection of protein adsorption or cell adhesion processes.

The most sensitive operational mode for a quartz resonator is the active oscillator mode. Here, the quartz resonator is integrated as the frequency-controlling element in an oscillator circuit and the resonance frequency of the crystal is recorded with a high sensitivity and a time

resolution of less than 1 s. The oscillator circuit only compensates for energy losses and supports the quartz resonator on its resonance frequency.
The general applicability of the QCM technique in the active oscillator mode for cell biology has been demonstrated by many authors addressing various bioanalytical issues. Gryte et al. (1993), Redepenning et al. (1993) and Wegener et al. (1998) monitored the attachment and spreading of initially suspended mammalian cells on the resonator surface in real time by readings of the resonance frequency. They showed that the attachment and spreading of mammalian cells upon the resonator surface induce a decrease in resonance frequency proportional to the fraction of the surface area covered with cells. Thus, time-resolved measurements of the resonance frequency can be used to follow the kinetics of cell attachment and spreading to the resonator surface. Wegener et al. (1998), who studied the adhesion of different mammalian cell types, have additionally found that confluent monolayers of different cell types produce individual shifts in resonance frequency, possibly reflecting individual molecular architectures of their cell-substrate contacts.

Since the resonance frequency of the quartz resonator is highly sensitive to both mass deposition and changes in the density or viscosity of the contacting liquid (Kanazawa and Gordon, 1985), a differentiation between both contributions by measuring the resonance frequency alone is not possible. This becomes highly important when the resonator is loaded with a complex material which does not behave like a rigid mass, such as living cells, which have to be treated like viscoelastic bodies and for which the linear relation between the adsorbed mass and the change in frequency is not valid (Janshoff et al., 1996; Rodahl et al., 1997). Rodahl et al. (1996, 1997) developed an extension of the traditional QCM technique, the so-called QCM-D technique, allowing simultaneous measurements of the change in the dissipation factor D in addition to the common measurement of the resonance frequency f. The dissipation factor quantifies the damping of the quartz oscillation and is defined as the ratio of the dissipated energy and the energy that is elastically stored during one period of oscillation. Simultaneous f and D measurements are performed by periodically switching off the driving power to the quartz oscillator and subsequently recording the free decay of the quartz oscillation. The measured decay time of the damped sine wave is expressed as the dissipation factor to which it is inversely proportional. Readings of D indicate whether the recorded shift in resonance frequency is affected by dissipation processes, as prevalent for viscous loading of the resonator surface (Rodahl et al., 1997) and thus facilitates the interpretation of the measured resonance frequency shift in terms of mass uptake.
The QCM-D has been established as a useful tool for evaluating interactions between various biological and non-biological systems as well as for monitoring cellular behavior. Fredriksson et al. (1998) and Nimeri et al. (1998) used this approach to characterize the attachment and spreading of mammalian cells and the interaction of neutrophils with a protein-coated surface. Reiß et al. (2003) used functionalized (biotin-doped) lipid vesicles and studied their adhesion onto a resonator surface coated with specific ligands (avidin) as a simple model system to mimic cell attachment and spreading. The adhesion of mammalian cells and liposomes gave

rise to very similar shifts in resonance frequency, whereas the viscous energy dissipation was at least one order of magnitude higher for cellular loading.

The second operational mode for a quartz resonator is termed the passive mode, since the quartz resonator is not oscillating freely. A sinusoidal voltage is applied to the surface electrodes and the crystal is thereby forced to oscillate at frequencies determined by the frequency of the applied AC (alternating current) voltage. The quartz is excited sequentially along a narrow frequency band around its resonance frequency, while recording the respective electrical impedance. Because of the electromechanical coupling within quartz crystals, the mechanical oscillation can be described by an electrical equivalent circuit model. Martin et al. (1991) introduced an electromechanical model for the quartz oscillation in an aqueous environment, which allows to discriminate and quantify pure mass loading as well as a simultaneous liquid loading by means of electrical impedance elements. Equivalent circuit modeling of the recorded impedance spectra allows to quantify the characteristic electrical parameters of the shear oscillation, which can be related to the mechanical, material-specific properties of the quartz and the load material on the resonator surface. Thus, impedance analysis provides a more detailed description of the shear oscillation than simple frequency recordings.

Wegener et al (1998, 2000) demonstrated that QCM readings only report on specific, integrin-mediated cell adhesion to the resonator surface. Sedimentation and loose attachment of cells to the resonator surface via unspecific interactions do not influence the shear displacement of the quartz resonator. This has been shown by the authors via the addition of the soluble pentapeptide GRGDS to a cell suspension. GRGDS is known to compete with the adhesive ECM proteins immobilized on the quartz surface for the binding sites of the integrins, thus preventing cells from forming specific integrin-mediated cell-substrate contacts. Cells that are not allowed to adhere to the resonator surface via specific cell-substrate contacts have no influence on the QCM readout. Wegener et al. (2000) also showed that the QCM is only sensitive to those parts of the cellular body that are involved in making cell-substrate contacts and are therefore close to the resonator surface. Changing the mechanical properties of the culture medium on top of a confluent cell layer by increasing the medium viscosity had no impact on the quartz oscillation of the cell-covered resonator. Reiß (2004) examined the particular impact of different mammalian cell types on the parameters of the shear oscillation and observed that the presence of a confluent cell layer on top of the resonator surface leads to a significant increase in energy dissipation, usually many times (2 – 10-fold) larger than the increase in the stored energy. The impact of cells on energy dissipation was shown to be individual and dependent on the particular cell type, reflecting the different acoustic properties of the respective cell types as well as a possible individual anchorage to the resonator surface. A major contributor to the QCM signal of adherent cells was identified to be the actin cytoskeleton (Wegener et al., 2000). Its disruption via cytochalasin D, which is known to inhibit the polymerization of actin monomers and thus results in a shortening and finally disappearance of actin filaments, had a considerable impact on the shear wave

parameters. The signal decreased by more than 40 % of the signal for a confluent cell layer. Energy dissipation as well as energy storage was affected.

Besides being operated in the sensor mode to monitor cell adhesion non-invasively, the QCM can also be used as an actuator to disturb molecular recognition at the solid-liquid interface, like the formation of stable cell-substrate contacts. In the actuator mode, the resonator is used at elevated lateral shear amplitudes, which can be controlled by the voltage applied to the surface electrodes to excite the crystal. Heitmann and Wegener (2007) and Heitmann (2008) studied the impact of elevated lateral oscillation amplitudes on the adhesion kinetics of different mammalian cells. By gradually increasing the amplitude of the resonator's shear displacement during cell attachment, the authors were able to determine a threshold lateral oscillation amplitude of ~ 20 nm in the center of the resonator (driving voltage: > 5 V) beyond which cell adhesion to the quartz surface was retarded or even entirely blocked. A maximum shear amplitude of 35 nm (driving voltage: 10 V) was sufficient to completely inhibit cell adhesion for all cell lines under study. However, shear oscillations of similar amplitudes applied to already established confluent cell layers were not able to disrupt existing cell-surface contacts and displace the attached cells from the surface.

In summary, the QCM technique is a highly sensitive tool to monitor and quantify the formation or modulation of cell-substrate interactions, like the attachment and spreading of mammalian cells to *in vitro* surfaces, or their reorganization under the influence of biological, chemical or physical stimuli, in real time and in a non-invasive manner.

1.6.2 Electrochemical Analysis of the Cell-Substrate Contact Using the ECIS Technique

Another powerful and sensitive method to monitor the formation and modulation of cell-substrate interactions of adherent mammalian cells *in vitro* with a time resolution down to seconds is the electrochemical ECIS (electric cell-substrate impedance sensing) technique. Thus, the kinetics of cell attachment and spreading as well as cell motion and cell morphology changes can be followed in real time. The basic principle of this technique was introduced by Giaever and Keese in 1984 (Giaever and Keese, 1984). In this approach, adherent cells are cultured directly on the surface of planar gold film electrodes, deposited on the bottom of a cell culture chamber. The gold films serve as a growth substrate for the cells and electrodes for the electrochemical measurement, thus allowing for a highly sensitive measurement due to the close proximity between cells and the underlying electrode. The measurement system contains two electrodes: a small working electrode (5×10^{-4} cm^2) and a substantially larger (~ 500-fold) counter electrode, which are electrically connected via the culture medium. ECIS is based on measuring changes in the AC impedance of the small gold film electrodes, upon which cells are deposited, as a function of AC frequency used for excitation. A low amplitude alternating voltage is applied across the cell layer to excite the system, ensuring a non-

invasive examination of the living cells. The measurement of the steady-state current resulting from the excitation allows for the determination of the electrical impedance of the system as a function of frequency. The difference in surface area of working and counter electrode provides a much higher current density and voltage drop at the small electrode. Thus, the total impedance of the system is dominated by the impedance of the small working electrode, whereas the counter electrode provides only negligible contributions. The presence of cells on the electrode surface causes a significant increase in the measured electrical impedance of the system compared to a cell-free electrode, since the cells behave like insulating particles, forcing the current to flow around them. This change in impedance is sensitive to changes in cell shape and can be used to analyze cellular behavior.

Since the introduction of this technique, ECIS has found many applications in cell biology and biotechnology and has been continuously optimized to follow the behavior of mammalian cells in general or their response to chemical, mechanical or electric stimuli in particular in real time.
Due to the close proximity of cells and electrode and the resulting sensitivity of this approach, the ECIS technique can be applied to quantify changes in cell shape as they happen for example during apoptosis (Arndt et al., 2004). During apoptosis, or programmed cell death, severe changes in cell shape occur, such as cell shrinkage and disintegration of cell-cell contacts. The authors monitored cycloheximide-induced apoptosis in endothelial cells in real time by recording the impedance change. From impedance readings along a broad frequency range, it could be deduced that disassembly of cell-cell contacts (tight junctions) precedes changes in cell-substrate contacts.

The ECIS technique is also a valuable means to study the barrier function of epithelial and endothelial cells as well as its physiological regulation. DePaola et al. (2001) applied ECIS to detect dynamic changes in the barrier function of endothelial cells during exposure to fluid flow, simulating the blood stream *in vivo*. The authors developed an “ECIS/Flow” model system, in which a confluent monolayer of bovine aortic endothelial cells was exposed to physiological fluid shear stress for various time periods, while simultaneously recording the electrical impedance of the system. The impedance of the endothelial monolayer changed dynamically depending on the onset and stop of flow, indicating cell morphological changes. The observed changes in impedance were reversible upon flow removal with a recovery rate that varied with the duration of the preceding flow exposure.

The ECIS technique can also be applied to analyze the interaction of endothelial cells with other cell types present in blood. Thus, the invasive activities of metastatic tumor cells could be demonstrated *in vitro* (Keese et al., 2002). Different metastatic cells were added to a confluent monolayer of human umbilical vein endothelial cells (HUVECs), cultured on ECIS gold film electrodes. In accordance with preceding microscopic observations in which metastatic cells have been shown to attach to and invade the endothelial cell layer, large impedance changes were observed in response to the metastatic cells. Highly metastatic cells, in contrast to cells with a weaker metastatic potential, caused a significant decrease of the

impedance measured for the confluent HUVEC cell layer within one hour after addition. The extent of the impedance decrease could be correlated with the known metastatic potential of the tumor cell lines under study.

An additional field of application for ECIS is *in vitro* cytotoxicity testing, allowing for the quantification of the dose-dependent cytotoxicity of diverse substances harmful for adherent cells. In a study conducted by Xiao et al. (2002), an adherent cell layer of fibroblasts was subjected to different concentrations of cadmium chloride, sodium arsenate and benzalkonium chloride and the percentage inhibition of cell proliferation was determined as a function of the inhibitor concentration. The concentration required to achieve 50 % inhibition as deduced from ECIS measurements agreed well with the results obtained using a conventional dye uptake assay (neutral red assay).

Wegener et al. (2000) studied the attachment and spreading kinetics of MDCK-II cells on different ECM protein coatings in a time-resolved manner. The individual kinetics reveal information on the cell-adhesive properties of the protein coating. The authors also quantified the dose-dependent influence of short soluble peptides (RGDS), which mimic a common recognition sequence of integrins, on cell attachment and spreading.
Furthermore, impedance spectra which are recorded in a broad frequency range can provide multi-parametric morphological information about the cell layer on the electrode surface. Data modeling of the recorded impedance spectra following Wegener et al. (2000) allows for the deconvolution of the overall impedance signal into individual (subcellular) impedance contributions arising from different portions of the cell bodies. The impedance contribution from the sub-cellular region (cell-substrate adhesion zone) can be quantified by the parameter α. The parameter R_b describes the impedance contribution arising from the intercellular cleft and is a measure for the strength of the cell-cell contacts. The specific cell membrane capacitance C_m contains information about the area of the cell surface, such as membrane protrusions or folding. These quantitative parameters deduced from ECIS measurements can also be used – similar to microscopic techniques – to analyze cell shape changes upon external stimuli, but allow for a much more detailed analysis.

Besides cellular processes such as cell adhesion and spreading, transient cell shape changes in the sub-nanometer range can be monitored quantitatively using the ECIS technique due to its high sensitivity accompanied by a time resolution of less than a second. This metabolically driven cell motion was termed micromotion (Giaever and Keese, 1991). Micromotion has been electrically recorded as small and rapid fluctuations of the impedance signal of cell-covered ECIS electrodes, when the impedance is tracked as a function of time at a single frequency sensitive for these movements. Micromotion was observed to be a fundamental property of living cells and could be correlated with their metabolic activity (Giaever and Keese, 1991; Lo et al., 1993). Lo et al. (1993) monitored cellular micromotion in a confluent cell layer of fibroblasts for various experimental conditions. The impedance fluctuations were recorded for cells cultured at different temperatures (27 °C and 37 °C), in serum-free medium and under addition of cytochalasin D and could be directly related to the metabolic activity

and vitality of the cells. Crosslinking of the cells by fixatives like formaldehyde (10 %), inducing cell death, caused the fluctuations to vanish (Giaever and Keese, 1991).

The ECIS technique can not only be used to monitor cell morphological changes, it is also possible to apply electric fields that are able to manipulate the cells on the electrode surface.
Extracellular membrane-impermeable probes (macromolecules like DNA constructs, proteins, antibodies or drugs) can be loaded into the cytoplasm of adherent mammalian cells cultured on ECIS electrodes using *in situ* electroporation, i.e. reversible permeabilization of the plasma membrane (Wegener et al., 2002). After applying the electroporating voltage pulse to the cells cultured on the small ECIS electrode for several hundred milliseconds, subsequent non-invasive ECIS recordings provide the real time documentation of the cell recovery. The authors reported that already one hour after the electroporation pulse the ECIS measurements indicated a complete morphological recovery of the cells.
Wound healing experiments constitute another possible application for the ECIS technique. In order to assess the migration and proliferation of mammalian cells *in vitro*, a defined mechanical wound is often applied to a confluent cell monolayer and its subsequent reclosure is monitored microscopically over time (scratch assay). A weakness of this scratch assay is the time-consuming microscopic readout and the fact that the applied mechanical wounds are often hardly reproducible. The mechanical wounding can be replaced by electrical wounding and the closure of the wound can be followed in real time when using the ECIS technique (Keese et al., 2004). The cells cultured on the small gold electrode are subjected to an invasive electric field of a few volts for several seconds, which causes irreversible damage and permeabilization of the cell membranes, leading to subsequent cell death. By recording the impedance of the electrode after the wounding pulse non-invasively, the migration of cells from the electrode periphery to the center of the electrode can be followed quantitatively and in an automated fashion. In contrast to the mechanical scratch assay, ECIS-based wound healing studies take advantage of a defined and highly reproducible wound.

In summary, the ECIS technique can be used in many ways to obtain quantitative and time-resolved information on mammalian cell behavior *in vitro*, including cell attachment and spreading, micromotion and cell migration (wound healing) as well as changes in the barrier function or the cell-substrate contact of epithelial and endothelial cell layers in response to biological, chemical or physical stimuli.

2 Objective

Great efforts are put into the design and optimization of technical materials to ensure their appropriate biofunctionality and biocompatibility. In order to guarantee functional biomaterials which exert perfect long-term biocompatibility, understanding the interactions which take place between a material surface and the various components of a biological system is indispensable. In particular, the interactions between technical materials and mammalian cells are a key factor for a material's biocompatibility. A valuable tool for addressing these interactions *in vitro* are cell-based, substrate-integrated biosensors, which allow to monitor the cellular response to a given material surface in real time and in a non-invasive manner.

Against this background, the objective of this thesis was to optimize and evaluate cell-based, substrate-integrated biosensors relying on two well-established impedimetric techniques – the quartz crystal microbalance (QCM) and the electric cell-substrate impedance sensing (ECIS) technique – to analyze the biocompatibility of different substrates with respect to their molecular and cellular interactions with a biological system in quantitative terms. The substrates addressed here were on the one hand chemically different polymers and on the other hand patterned silicon substrates exhibiting different topographical features. These substrates were chosen in order to explore new sensors capable of reading the impact of *surface chemistry* and *surface topography* on the nature and strength of interactions between a technical material and a biological system.

Based on the QCM technique, which has been shown to monitor the mechanical interactions between cells and their growth substrate, a biosensor should be developed in order to obtain valuable information on the biocompatibility of different polymers. For this purpose, model thin films of various polymers were deposited on the resonator surface and possible interfacial phenomena that occur on the polymer surface in response to a biological system should be investigated, such as the long-term stability in a physiological environment, protein adsorption as well as cell attachment and spreading. Various experimental parameters to selectively modify the polymer surface features should be studied in detail. The QCM measurements should be accompanied by some general physicochemical characterizations of the polymer surface as well as a microscopic study of cell adhesion upon the polymers. These different experimental studies should allow for a detailed correlation and evaluation of the QCM data and thus a validation of the polymer coated sensor system.

Based on the ECIS technique, known to monitor the passive electrical properties of adherent cells, a complementary biosensor should be developed in order to analyze the influence of surface topography on cell-substrate interactions, in particular during cell attachment and

spreading as well as cellular micromotion. The different surface topographies were modeled by mesoporous silicon surfaces which were coated with thin gold film electrodes in order to apply ECIS. The cellular response on porous substrates should be compared to the one on planar substrates.
Furthermore, an experimental setup combining both impedimetric techniques should be used to follow and analyze the electrical and mechanical properties of mammalian cells during attachment and spreading on the resonator surface simultaneously. The combined setup should also deliver insight into the local sensitivity of the mechanical quartz oscillation.

3 Materials and Methods

3.1 Cell Culture

This thesis includes experiments with the epithelial cell line MDCK (*Madin Darby Canine Kidney*, Strain II) and the epithelial-like cell line NRK (*Normal Rat Kidney*, Strain 52E).

MDCK cells are epithelial cells originating from the kidney of an adult female cocker spaniel and were isolated in 1958 by Madin and Darby (Fuller et al., 1984). From the heterogeneous parent line two different cell subtypes were cloned denominated MDCK-I and MDCK-II, both forming epithelial monolayers. Besides their individual morphology the two strains differ with respect to their ability to act as a selective diffusion barrier between two fluid compartments (Richardson et al., 1981). The subclone MDCK-I is classified as a tight epithelium with characteristics of tight epithelia of the renal collecting duct showing transepithelial electrical resistances between 400 and 4000 Ωcm^2 (Fuller et al., 1984). By contrast, MDCK-II cells are thought to originate from the distal tubule or collecting duct of the nephron and belong to the so-called leaky epithelia with moderate transepithelial resistances ranging between 40 and 200 Ωcm^2 (Stevenson et al., 1988; Hein et al., 1992; Wegener et al., 1996).
In confluent monolayers MDCK-II cells exhibit cobblestone morphology with an epithelia-typical membrane polarity. Microvilli on the apical side extend upward into the medium and tight junctions provide a continuous band of cell-cell contacts close to the apical pole of the cells, regulating both, the paracellular permeability of ions and hydrophilic molecules (Anderson and Van Itallie, 1995) and the exchange of membrane lipids and proteins between the apical and basolateral membrane domains, thus maintaining the membrane polarity (Dragsten et al., 1981; Van Meer and Simons, 1986). Besides these morphological qualities, the cell line even exhibits functional qualities of a transporting epithelium, regulating the exchange of solutes between two fluid compartments. The vectorial transport of ions from the culture medium or the cytosol into the subcellular space leads to a passive osmotic influx of water. As a result of the fluid accumulation, the monolayer detaches from the substrate at various positions, forming variable sized blisters or domes when the cells are cultured on impermeable supports (Leighton et al., 1969; Cereijido et al., 1981).

NRK cells originate from the kidney of normal rats. Two cell lines (NRK-52E and NRK-49F) cloned from a mixed culture of normal rat kidney cells exist, which are described to be distinct in growth properties and transforming abilities. Whereas NRK-49F cells exhibit contact inhibition and are very sensitive fibroblast-like cells with a fusiform shape, the cell

line used in this thesis, NRK-52E, is supposed to be more stable. These cells are epithelial-like and form monolayers with cobblestone morphology if adherently grown (de Larco and Todaro, 1978). They are thought to be derived from the proximal tubule and possess uncommon cell junctions containing components of both, tight junctions and adherens junctions, focused at sites of cell-cell adhesion (Li et al., 2005). Compared to MDCK-II cells, NRK-52E cells form a diffusion barrier which is much leakier. *In vivo*, mammalian proximal renal tubules form a leaky epithelium showing a transepithelial electrical resistance of 5 – 12 Ωcm^2 (Glube, 2007; Prozialeck et al., 2006).

3.1.1 General Culture Conditions

MDCK-II and NRK cells were obtained from the *Deutsche Sammlung von Mikroorganismen und Zellkulturen* (DSMZ) in Braunschweig. Any kind of cell culture work was carried out in a sterile flow hood (Holten, Gydevang, Denmark). All media and solutions were autoclaved (20 min, 120 °C) or passed through a sterile filter (pore diameter: 0.2 µm), respectively, if the products were not delivered in a sterile form. Stocks of both cell lines were generally grown in polystyrene culture flasks (growth area = 25 cm^2) and kept at 37 °C in incubators (Heraeus, Hanau, Germany) maintaining an atmosphere with 5 % CO_2 and 95 % relative humidity.

3.1.2 Subculturing

Both cell lines were subcultured once a week, following an identical standard protocol. For this purpose the confluent cell monolayers were washed twice with phosphate buffered saline (PBS^{--}, without divalent cations Ca^{2+} and Mg^{2+}) removing all traces of divalent cations, which would otherwise interfere with the proteolytic removal of the cells. Subsequently, the cells were incubated with an EDTA (ethylenediamine-tetraacetic acid, 1 mM in PBS^{--}) solution for 10 min at 37 °C, which serves as a chelating agent for the adhesion co-factors Mg^{2+} and Ca^{2+}. This step is necessary as both cell lines exhibit strong cell-substrate contacts. The cells were then removed from the stock flask by 0.25 % (w/v) trypsin supplemented with 1 mM EDTA (5 min at 37 °C). Trypsin digestion was terminated by the addition of an excess of the particular culture medium. Cells were spun down by a 110 x g centrifugation for 10 min at room temperature (RT). The supernatant was discarded and the cell pellet was resuspended in prewarmed fresh culture medium. Aliquots of the cell suspension were transferred into new culture flasks with a subcultivation ratio of 1:10 relative to the original cell density per cm^2. The medium of the stock cultures was exchanged twice a week or 24 h before starting any experiment, to provide the cells with nutrients as well as to remove cell fragments or non-adherent dead cells. After three to four days, the cells have formed a confluent monolayer.

PBS^{--}	140 mM NaCl 2.7 mM KCl 8.1 mM Na_2HPO_4 1.5 mM KH_2PO_4 in deionized water (DI-water)
MDCK-II culture medium	Earle's Minimal Essential Medium (MEM-Earle, 1x) 2.2 g/l $NaHCO_3$ 1 g/l D-glucose 10 % (v/v) fetal calf serum (FCS) 100 µg/ml penicillin 100 µg/ml streptomycin 4 mM L-glutamine
NRK culture medium	Dulbecco's Modified Eagle's Medium (DMEM) 3.7 g/l $NaHCO_3$ 4.5 g/l D-glucose 10 % (v/v) FCS 100 µg/ml penicillin 100 µg/ml streptomycin 2 mM L-glutamine

3.1.3 Cryopreservation

Mammalian cells can be preserved over a long period of time by cooling them down to low sub-zero temperatures, typically – 196 °C in liquid nitrogen. At this temperature, any biological activity is effectively stopped. Thus, the adherent monolayer of cells was detached from the bottom of the culture flasks by standard trypsinization protocols using 0.25 % (w/v) trypsin (chapter 3.1.2). After centrifugation, the cell pellet was resuspended in normal calf serum (NCS) containing 10 % DMSO (dimethyl sulfoxide). DMSO is a cryoprotective agent, which prevents intracellular ice crystal formation by simply penetrating the cell membrane thus reducing the water content in the cytoplasm. Ice crystals may otherwise lead to plasma membrane disruption and subsequent necrosis. The cryoprotective capability of NCS is based on its high protein content, protecting the cells from cytoplasmic protein leakage due to transient lesions of the cell membrane and, thus, from freeze-induced cell death due to chemoosmotic stress. Cells suspended in their cryopreservation solution were placed into cryovials and carefully frozen in a standard two-step process in which the cell suspension was first cooled down slowly to – 70 °C for 24 h by using a freezing container filled with isopropyl alcohol, which provides a cooling rate of 1 °C/min, before the cryovials were transferred into liquid nitrogen for long-term storage.

The thawing process of cells should be carried out carefully but quickly for maximal survival. Upon removal from the liquid nitrogen, the cryovial was exposed to – 20 °C for ~ 1 h followed by a transfer to a 37 °C warm water bath for ~ 4 min while agitating in order to achieve uniform thawing. The cell suspension was diluted by slowly adding 37 °C warm culture medium. Following centrifugation, the DMSO containing supernatant was removed, the cell pellet was resuspended in 37 °C warm fresh culture medium and the cell suspension was inoculated into new culture flasks.

Cryopreservation solution	normal calf serum (NCS) 10 % (v/v) DMSO

3.2 Preparation of Polymer Films

One part of this work is focused on the characterization of four types of technical polymeric surfaces from various perspectives. The respective polymers are polystyrene (PS), poly(methyl methacrylate) (PMMA), poly(dimethyl-siloxane) (PDMS) and the technical, commercially available photopolymer (PhoP) Microposit® SC® 1827, a positive photoresist often used in microelectronic related photolithographic processes, most notably for the production of sensor devices interfaced with mammalian cells.
For biocompatibility testing using the quartz crystal microbalance technique, shear wave resonators are used as carrier substrates (chapter 3.5) that the polymer surfaces were prepared on as thin films. A corresponding physicochemical characterization of the polymer surface as well as microscopic studies documenting the adhesion kinetics of mammalian cells on the regarding polymers were performed on coverslips as carrier substrates (chapter 3.3 and 3.7.1). The first step for characterizing a polymer surface was to coat the respective carrier substrates with a thin and uniform layer of the material of interest. This was achieved by spin coating the polymer from organic solution.

A prerequisite for any surface coating is a clean and dry surface of the carrier substrates. Therefore, the substrates were treated with a detergent solution (Mucasol, 5 mL/L in DI-water) at 70 °C for 15 min in an ultrasonic bath and washed twice in DI-water, thereafter (70 °C, 15 min). The cleaned substrates were dried in a stream of nitrogen or in an oven (37 °C over night).

3.2.1 The Spin Coating Technique

The term “spin coating” describes a process where a carrier substrate spins around an axis which is perpendicular to the coating area and an applied solution is spread evenly over the

substrate surface by using centrifugal force. The spin coating technique is often used in industrial processes for the application of thin, uniform material films on planar substrates. In the microelectronics industry, it is commonly employed for the deposition of photoresist layers (Wang and Yen, 1995).

A typical spin coating process consists of the three following steps: (i) deposition of a small amount of the fluid material onto the center of the substrate, (ii) rapid acceleration to the desired rotation speed (typically 1500 – 6000 rpm) in order to dispense and thin the material film due to the action of centrifugal force and (iii) evaporation of excess organic solvent from the resulting film by additional spinning of the substrate for a certain time (drying process). This is called the static method of dispense, whereas the dynamic one describes the deposition of the material while the substrate rotates at a certain, commonly low (~ 500 rpm) speed (Fig. 3.1). The rotation speed generally defines the final film thickness, which is mainly a balance between the force applied to shear the fluid material towards the edge of the substrate and the drying rate affecting its viscosity. As the solvent evaporates, the viscosity increases until the radial force of the spin process can no longer move the material over the surface. At this point, the film thickness will not decrease any more with increasing spin time (Hall et al., 1998).

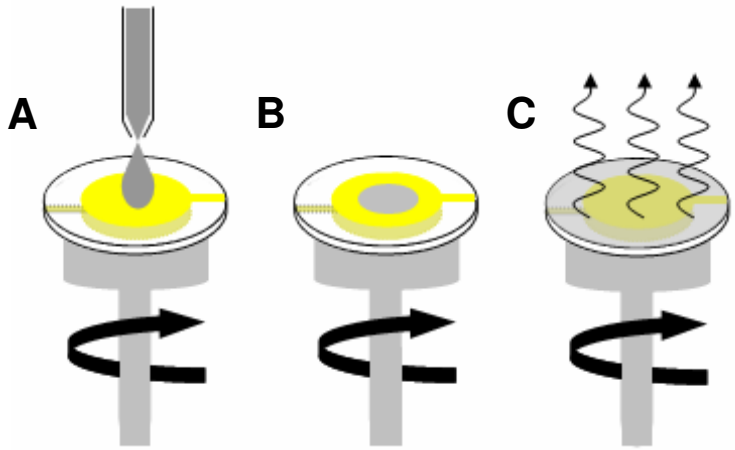

Fig. 3.1 Spin coating technique using the dynamic dispense method. **A** The substrate (here: a quartz disk) is fixed on the chuck and the polymer solution is deposited on the center of the substrate while rotating at full speed. **B** The solution is dispensed and gradually thinned by rotational motion. **C** Complementary solvent evaporation leads to a uniform and complete surface coverage with a thin polymer film.

The film thickness depends on several factors, such as viscosity, percentage of solids, solvents and surface tension of the coating material itself as well as parameters chosen for the spin coating process like rotation speed, acceleration and spin time (Hardeveld et al., 1995; Washo, 1977). Process parameters can vary greatly for different materials and substrates and need to be adapted to the respective spin coating situation to obtain a homogeneous and complete surface coverage with a material film in a designated thickness.

3.2.2 Experimental Procedure

For spin coating, a self-made spin coater on the basis of a hard disk drive[1] was applied (Fig. 3.2). The substrate was fixed on the chuck using BluTack®, a pressure-sensitive adhesive. All polymer films were deposited on the substrate surface via the dynamic dispense technique at full rotation speed (Fig. 3.1). After setting the individual spin coating parameters the spinner was started and the substrate was accelerated up to its final rotation speed (Tab. 3.1). While rotating, the polymer solution was placed on the center of the substrate, letting it spin at a constant rate for a certain time. Any excess of coating solution is expulsed from the substrate surface by the rotational motion and the fluid is gradually thinned. Nearly simultaneously, the volatile organic solvent evaporates, effectively immobilizing the coating in place. After the spin coating process, the coated substrate was dried to further stabilize the film by removing the residual solvent. This ensures a high chemical and physical stability of the polymer film before it is used in any experimental procedure.

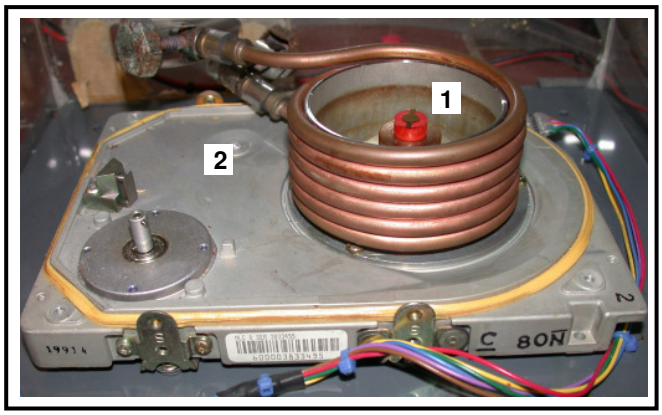

Fig. 3.2 Self-made spin coater. The sample stage **1** (chuck with a fixed quartz disk) consists of a small brass block attached to an electric motor taken from an old computer hard drive **2**.

Tab. 3.1 Spin coating parameters for the different polymer films.

Polymer	Rotation speed [rpm]	Rotation time [s]	Applied volume [µL]
PS	4000	60	20
PMMA	4000	60	20
PDMS	5000	30	20
PhoP	3500	60	40

Besides their individual process parameters in the spin coating step, the investigated polymers exhibit certain differences with respect to the film preparation procedure which are described in detail below:

[1] Created by Dr. F. Höhn (Institut für Biochemie, Münster, Germany)

Individual Protocol for PS Film Preparation

PS films were spun from a 1 % (w/v) solution in toluene onto the substrates using the respective spin coating parameters (Tab. 3.1). For this purpose, PS (M_w = 230.000 g/mol) was dissolved in toluene and the solution was subsequently stirred over a period of several hours (~ 6 h). Spun films were placed in an oven at 60 °C for 15 h to ensure that the solvent had been completely removed.

Individual Protocol for PMMA Film Preparation

PMMA (M_w = 120.000 g/mol) was spun from a toluene solution with a concentration of 1% (w/v) PMMA onto the substrates (Tab. 3.1) after being dissolved and stirred in toluene over several hours (~ 24 h). Subsequent to the spin coating process, the coated substrates were kept at 60 °C for 15 h in order to remove any residual solvent.

Individual Protocol for PDMS Film Preparation

For the preparation of the PDMS film, the Sylgard® 184 silicone elastomer kit (Dow Corning, Michigan, USA) was used, which comprises two liquid components, a base and a curing agent. PDMS pre-polymer was dissolved in hexane with a concentration of 1% (w/v) by sonication (5 min, RT). Afterwards, the curing agent (0.1 % (w/v)) was added and the solution was thoroughly mixed by a second sonication procedure (5 min, RT). The mixture was then stirred over a period of 15 min and subsequently spin coated onto the substrates (Tab. 3.1). Finally, the spin coated PDMS films were cured for 12 h at 70 °C to remove any residual hexane and to accelerate the crosslinking reaction of PDMS.

Individual Protocol for PhoP Film Preparation

The wetting and adhesion of a positive photoresist on substrates such as glass or many metals is often poor and the resist easily delaminates from such material surfaces during development. Since polar OH-groups are formed on these substrate surfaces by oxygen and humidity rendering the surface hydrophilic, good wetting and adhesion of the unpolar photoresist are prevented (MicroChemicals, 2007; Grosse et al., 2001). Therefore, the substrates had to be pretreated by applying an adhesion promoter before PhoP was spin coated. First of all, an additional cleaning step with acetone and isopropyl alcohol had to be performed after the standard cleaning procedure. Acetone removes organic impurities, whereas isopropyl alcohol removes the contaminated acetone thereby avoiding striations. The cleaned substrates were placed in an oven at 120 °C for 30 min to remove adsorbed water from the substrate surface. Immediately afterwards, the substrates were spin coated with the adhesion promoter TI-Prime (MicroChemicals, Ulm, Germany) at 3000 rpm for 20 s and baked in a drying oven at 130 °C for 10 min. TI-Prime contains a titanium complex in an organic solvent, forming a titanium monolayer on the substrate via spin coating, which is activated by the baking step at 130 °C. Thereby, the hydrophilic surface is converted into a

surface showing hydrophobic properties, which ensures a firm adhesion of PhoP to the substrate. Immediately afterwards, PhoP was spin coated onto the substrates (Tab. 3.1) followed by a soft bake for 30 min at 100 °C and a final hard bake for 2 h at 118 °C. Soft baking reduces the remaining solvent concentration in PhoP and prevents the sticking of PhoP to the mask during mask alignment, thus improving light exposure in photolithographic processes and the resist adhesion to the substrate. Though no photolithographic procedure was performed and soft baking would not have been necessary, this step was performed in order to achieve a uniform preparation process with respect to further applications (see below). The final hard bake increases the thermal, chemical and physical stability of PhoP regarding subsequent processes.

Individual Protocol for PhoP Film Preparation Containing a Certain Electrode Layout

For further studies addressing the sensitivity of the resonant oscillation, the surface area of the quartz gold electrode on the open resonators was gradually reduced. This was achieved by covering quartz disks with PhoP and opening up variously sized areas on the resonators using photolithographic techniques. The substrates were coated with PhoP following the protocol described above including the soft baking. After the soft bake, the polymer film was exposed to UV light for 2 min through a mask containing the electrode layout. Two different aluminium dot masks were applied – one mask with a hole diameter of ~ 3 mm and another with a diameter of ~ 0.5 mm. The masks were aligned in a way that the UV light exposed areas were either located centrally (for both hole diameters) or at the edge of the original surface electrode (for Ø ~ 0.5 mm) (Fig. 3.3). The subsequent development of the UV light exposed areas of PhoP was done by incubation with a NaOH (7 g/L) solution for 15 – 30 s, while gently shaking. The substrates were rinsed with DI-water afterwards and then placed in an oven at 118 °C for 2 h (hard bake). After the hard bake, the substrate could be used for following experiments.

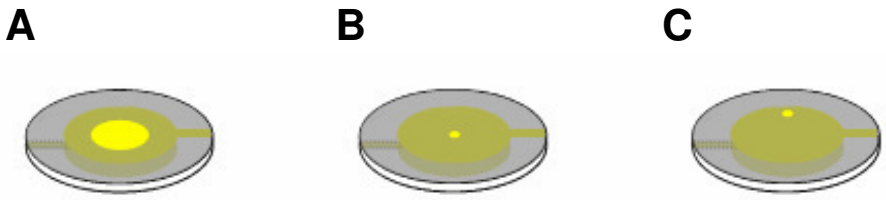

Fig. 3.3 Schematic illustration of the electrode layout established on top of the upper surface electrode of quartz resonators. **A**, **B** Circular openings are introduced into the PhoP film either at the centre (for Ø ~ 3 mm and Ø ~ 0.5 mm) or **C** at the edge (for Ø ~ 0.5 mm) of the original surface electrode.

Regeneration of Polymer Coated Substrates

Quartz resonators coated with one of the polymers, PS, PMMA and PhoP, could be regenerated by first sonicating them twice in the respective organic solvent used for spin coating (toluene for PS and PMMA, acetone for PhoP) for 15 min at RT, followed by a cleaning step with so-called "Piranha"-solution (H_2O_2 (30 %) : H_2SO_4 (97 %) = 1:3) for

1 – 2 min to remove any remaining organic residues. Afterwards, the resonators were rinsed in DI-water and sonicated in a detergent solution (Mucasol, 5 mL/L in DI-water) at 70 °C for 15 min and twice in DI-water, thereafter (70 °C, 15 min). The substrates were dried in a stream of nitrogen or in an oven (37 °C over night). PDMS coated resonators could not be recycled, as polymerized PDMS is completely inert and resistant against any kind organic solvent and inorganic acid, only showing swelling to some extent.

3.3 Physicochemical Surface Characterization

Before the polymer coated quartz resonators were used in protein adsorption and cell attachment and spreading studies, the polymer surface was analyzed regarding its physical and chemical properties. This allows for a correlation of surface properties on the one hand with cellular behavior on the other, providing a detailed description of the respective material's biocompatibility.

3.3.1 Time-of-Flight Secondary Ion Mass Spectrometry

The Time-of-Flight Secondary Ion Mass Spectrometry (ToF-SIMS) is a surface analytical technique that provides detailed information about the chemical composition of a surface on the atomic or molecular level. The penetration depth of this approach is limited to the uppermost three monolayers of the object under study. Since analysis and identification by mass spectrometry requires free ions in the gas phase, the surface constituents have to be ionized and transformed into the gas phase.

3.3.1.1 Basic Principle

For ToF-SIMS analysis, a solid surface is bombarded with a focused beam of primary ions with energies in the keV range (Fig. 3.4). When the fast ions hit the substrate surface, they penetrate into the surface up to a certain depth, usually a few tens of nanometers, transferring their kinetic energy to the atoms of the solid in a succession of individual atomic collisions, called collision cascade. Subsequent collisions cause some of the energy to be transported back to the surface, where it may cause surface particles, i.e. atoms and molecular compounds, to be desorbed. These compounds originate almost entirely from the uppermost monolayer of the surface and are observed as neutral particles (90 %) or as positively or negatively charged secondary ions. Thus, the subsequent mass analysis of the secondary ions allows for direct conclusions about the chemical composition of the uppermost monolayer of a surface (Benninghoven, 1994). As the determination of mass depends on charged particles,

desorbed neutrals are not detected by the SIMS analysis. In order to detect them, they would have to be postionized before mass determination (mass spectrometry of sputtered neutrals), which is an inefficient process, reducing the originally larger number of secondary neutrals to the same order of magnitude as the originally charged species (Hagenhoff, 2000).

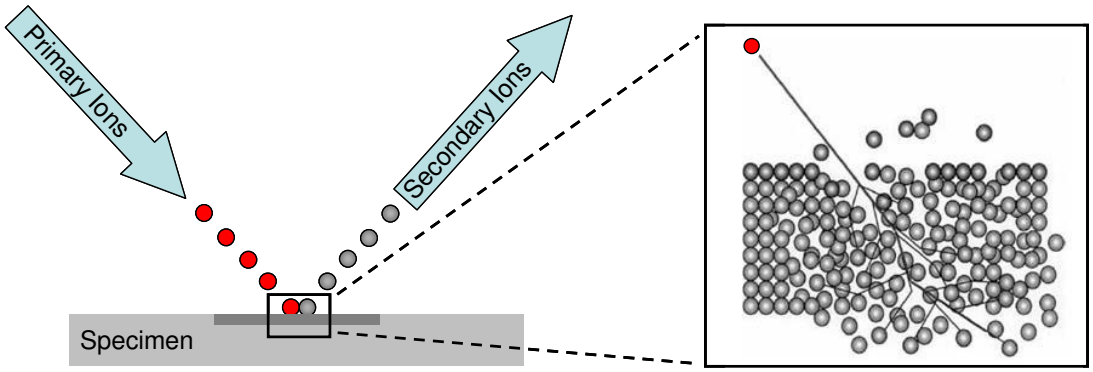

Fig. 3.4 Schematic of secondary ion formation. Upon surface bombardment with primary ions a collision cascade causes secondary ions originating from the uppermost monolayer (dark grey) of the specimen's surface to be desorbed (modified after Hagenhoff (2000)).

It is not only the uppermost monolayer that is altered or removed during ion bombardment. Besides implantation of the primary ions in the material, additional changes in the neighborhood of the primary ion tracks occur, causing severe radiation damage in the underlying layers. This comprises, for example, alterations in the crystalline or molecular structure, which have to be taken into account when analyzing the chemical composition of a surface.

The emitted secondary ions are analyzed by a time-of-flight mass spectrometer, which contains several ion-optic elements: a secondary ion extractor, an ion lens which focuses the secondary ion beam onto the detector and a reflectron or ion mirror. Since it is of great importance that the secondary ions enter the flight path quasi simultaneously, the investigated surface area is bombarded with short pulses of primary ions. All secondary ions generated by such a pulse are accelerated into the flight path by passage through a fixed electric field with the potential difference U_{ac} (± 2 kV) applied between target and extractor. The accelerating electrostatic field can be operated with different polarities, allowing for the detection of either positively or negatively charged secondary ions. The velocity of the accelerated ions depends on the relation between their molecular mass m and their charge z. In the case of identically charged secondary ions, they theoretically enter the field-free flight path of length L with the same kinetic energy, drifting towards the detector with constant velocity, which is only dependent on their mass. Lighter ions travel faster and therefore hit the detector at the end of the drift region earlier than havier ones, resulting in a mass spectrum. This sequential arrival of different ion types at the detector allows the detection of all secondary ions of a given polarity. Measuring the flight time from the sample to the detector for each ion allows the determination of its mass-to-charge ratio, which is given by:

$$\frac{m}{z} = \frac{2U_{ac}T^2}{L^2}. \tag{3.1}$$

In general, secondary ions of the charge ± 1 are obtained, providing a direct correlation of mass with the square of the measured time of flight T (for $z = 1 \Rightarrow m \propto T^2$).

Theoretically, all ions of the same charge receive the same kinetic energy by the accelerating potential, which then drift along the field-free flight path where they will be separated, so that all ions of the same m/z value should arrive at the detector simultaneously. In practice, secondary ions with an identical m/z value can possess a relatively small, but diverse initial kinetic energy and will thus acquire a total kinetic energy which is larger than the one imposed by the accelerating potential. Another point is that they are emitted from the sample surface with an angular distribution. Time-of-flight spectrometers nowadays therefore not only separate ions according to their mass-to-charge ratio but also compensate for the initial kinetic energy and angular distributions (Schueler, 1992). This is achieved by using combinations of linear drift paths and electrostatic sectors or ion mirrors (reflectrons) which guarantee a high mass resolution (Fig. 3.5).

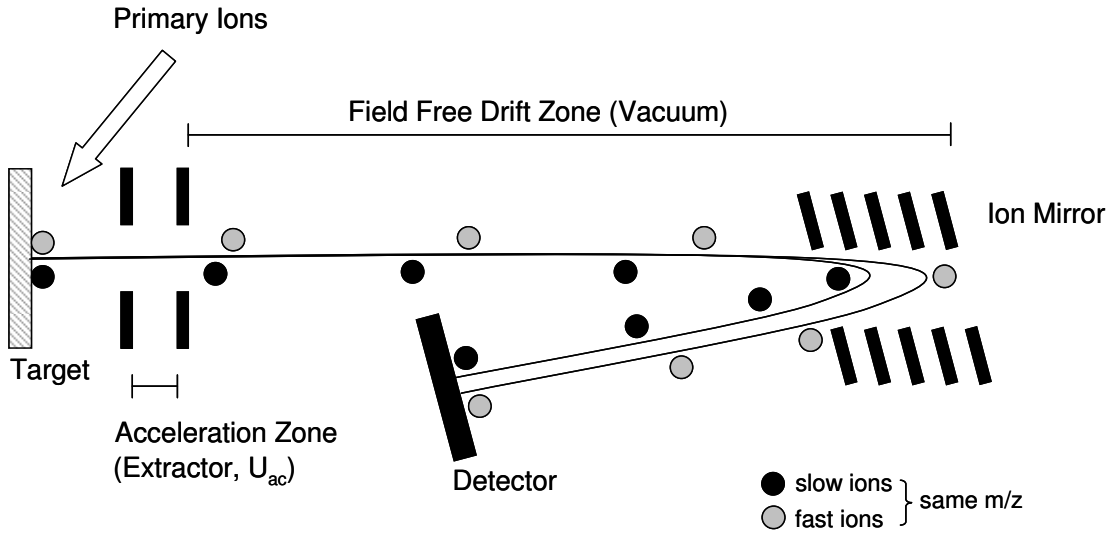

Fig. 3.5 Schematic illustration of a time-of-flight analyzer equipped with an ion mirror (reflectron) for improved mass resolution. Here, only ions with the same mass-to-charge ratio are considered. After having been emitted from the target's surface upon primary ion bombardment, the secondary ions are electrostatically accelerated up to a certain kinetic energy into a field-free drift zone, where they approach the ion mirror. Due to their initial energy distribution before passing the acceleration zone, some ions will possess lower kinetic energy (moving with lower velocity) and some higher energy (moving with higher velocity). The ion mirror compensates for the difference in flight time, focusing the ions with the same m/z value to arrive at the detector simultaneously.

The ion mirror, located at the end of the field-free drift zone, uses a constant retarding electrostatic field to reflect the secondary ions towards the detector. Faster, more energetic ions penetrate deeper into the ion mirror and take a slightly longer path before they are reflected back to the detector, compared to less energetic ions of the same m/z ratio. The net

effect is an energy focusing of the ion species at the detector plane, eliminating the negative effect of their initial energy spread on the final mass resolution.

3.3.1.2 Experimental Procedure

ToF-SIMS measurements of polymer coated quartz resonators were performed in order to verify a complete surface coverage. Areas of incomplete coverage or pin holes and cracks in the polymer films could interfere with subsequent electrochemical measurements or provide artificial data. A resonator was classified as being completely covered as long as the gold electrode of the quartz resonator underlying the polymer film could not be detected by ToF-SIMS measurements. Besides serving as quality control for surface coverage, the chemical composition of the uppermost layer of the polymer films could be analyzed with respect to the desorbed secondary ions. As the chemical composition and structure of the uppermost layer of atoms or molecules determines the surface properties, like adsorption behavior, wettability, or biocompatibility of a given material (Benninghoven, 1994), the chemical composition could allow for a correlation with physical and cytocompatible properties of the polymer films as obtained from further measurements using other techniques.

Any kind of ToF-SIMS measurements were carried out in cooperation with the Tascon GmbH (Münster, Germany). For ToF-SIMS measurements using the *ION-TOF "TOF-SIMS IV" SIMS* instrument, quartz resonators were spin coated with different polymer films, i.e. PS, PMMA, PDMS or PhoP, according to the procedure described in chapter 3.2.2. Ion bombardment of the surface was performed using a pulsed ion beam of Bi_3^+ primary ions at an energy of 25 keV over a surface area of 100 x 100 μm^2. Both, positively and negatively charged secondary ions were detected from the given area and presented as intensity spectra plotted against the mass-to-charge ratio.

3.3.2 Optical Profilometry

Optical profilometry is a surface analytical technique for non-contact three-dimensional (3D) monitoring of the micro- and nanoscopic surface topography. It provides information about surface roughness or discontinuities, e.g. steps or cavities, in the form of a height map. Thus, it is often used to characterize surfaces, for example for quality control in the production process of computer chips, or to measure film thicknesses. The optical profiling method used in this study is vertical scanning interferometry (VSI), which uses optical interference to image the surface in 3D.

3.3.2.1 Basic Principle of Vertical Scanning Interferometry

Interferometry in general is a technique based on interference. Interference describes the process of superposition of two or more coherent light waves of the same frequency when overlapping at the point of detection. A difference in the optical path of two light beams derived from the same light source causes a phase difference. The resultant light intensity at any point of detection depends on whether the light waves reinforce or cancel each other, called constructive and destructive interference, respectively. These maxima and minima of light intensity can be seen in the microscope as light and dark bands, called interference fringes. For light having the same phase at the origin, a sample that is hit reflects the beams in an individual manner dependent on its surface topography, causing a difference in the optical path and thus a phase difference between the initially identical beams, which results in an interference pattern at the point of detection.

VSI is a technique in which an optical path difference (OPD) between two beams of light, a reference beam and a sample beam, is used to produce contour maps of the surface (Lüttge et al., 1999). In order to allow the detection of microscopic topographic structures, an optical arrangement is applied, combining the interferometer with a microscope, as shown in Fig. 3.6. The main supplementations to a standard light microscope comprise specific interferometric objectives, e.g. Michelson, Mirau and Linnik – all are modifications of the Michelson interferometer – a motorized stage to vertically move the interference objective, a charge-coupled device (CCD) camera and a white light source. Figure 3.6 shows a typical system using a two-beam Mirau interferometer as the microscope objective, usually applied for magnifications between 10x and 50x.

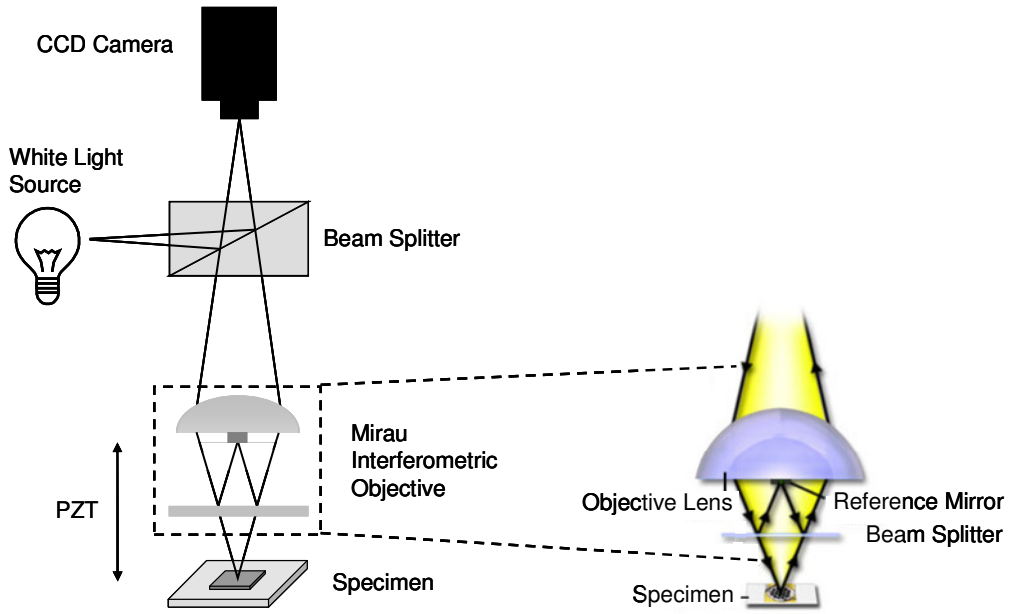

Fig. 3.6 Schematic drawing of the optical profiling system used in this study, operating in the VSI mode. The components needed for interferometry include a white light source, a CCD camera, a beam splitter, a piezoelectric stage (PZT) as well as a Mirau interferometric objective. The magnification on the right hand side illustrates the light path between the Mirau interferometer and the sample surface (modified after Lüttge et al. (1999) and www.microscopyu.com).

Incoming white light emitted from a single conventional light source (halogen lamp, LED) is divided into two separate beams by a beam-splitter inside the interferometric objective: one beam is directed to an internal reference surface while the other one is directly transmitted to the sample surface. The reference surface is a small mirror on the objective front lens which has the same area as the illuminated area of the sample. After reflection at the respective sample and reference surface, the beams are recombined inside the interferometer, thereby undergoing constructive or destructive interference. This produces maxima and minima of light intensity, which appear in the microscope as a pattern of light and dark fringes representing the surface topography of the sample. This so-called interferogram is recorded by a high resolution CCD camera and transferred to a computer which allows the calculation of a topographic surface map using interferometric phase-mapping programs.
In VSI a broad spectral width light source with a short coherence length of the light is used, so that good contrast interference fringes will be obtained only when the two paths of the interferometer are closely matched in length (Wyant, 2002). A basic principle of optics is that the peak contrast for white light fringes in an interferometer occurs when the optical path difference is zero. This fact is utilized by the VSI technique, which uses fringe contrast to identify the surface height (Fig. 3.7): The interference objective is continuously moved along the vertical axis in discrete steps, mechanically varying the path length of the sample arm and thus the OPD, while a digital camera stores the intensity data for each pixel in the field of view.

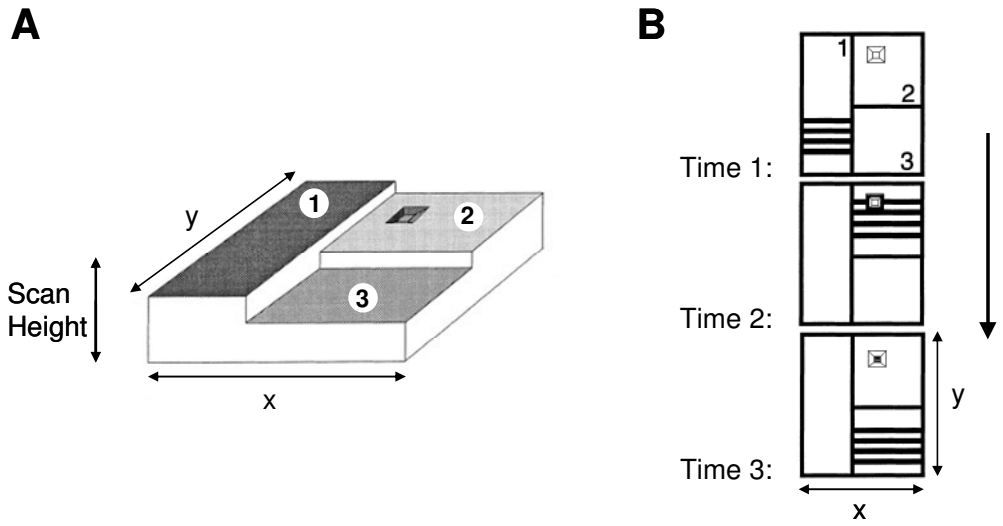

Fig. 3.7 Schematic drawing illustrating the basic principle of VSI (modified after Lüttge et al. (1999)). **A** Sample surface with different step heights. The interference objective is continuously moved along the vertical axis in discrete steps. **B** During this scan process a series of interferograms is taken by a digital camera. Due to the complex focal conditions for white light, there is only a small range of fringes observable at any time, i.e. only for the respective surface point in focus.

By varying the OPD, the relative height of a particular surface point in the field of view can be determined by looking at the sample (scan) position for which the fringe contrast is at its maximum. For a properly adjusted interferometer the sample is in focus when the maximum

fringe contrast is obtained (Harasaki et al., 2000), meaning the z-value of a specific xy-position on the sample surface corresponds to the z-value of the motorized stage, allowing its determination by moving the objective relative to the sample surface. Thus, the surface topography is completely vertically scanned. The data aquired during the scan process consist of a series of interferograms, representing the variation in intensity as a function of scan position. All interferograms are automatically overlayed using the respective software. From the stack of interferograms the topographic information can be extracted resulting in a height profile and thus, the topography of the investigated surface.

3.3.2.2 Experimental Procedure

Optical profilometry was used to study the thickness of different spin coated polymer films, i.e. PS, PMMA, PDMS and PhoP. Polymer film thickness measurements were performed in cooperation with nanoAnalytics GmbH (Münster, Germany) using the optical 3D profiling system *Wyko NT3300* (Veeco Instruments, NY, USA) operating in VSI mode to map out the surface. Prior to any measurement, the system was calibrated with an appropriate calibration standard ((10.10 ± 0.085) µm, step height value SHV1654). Coverslips were spin coated with the polymer of interest according to the procedure described in chapter 3.2.2. The thickness of the polymer films was examined by removing parts of the polymer film in order to have a height difference in the polymer surface that corresponds to the polymer film thickness. This was done with a pair of tweezers, scraping away parts of the polymer film. In the case of PhoP, the step was generated by applying photolithography. Subsequently, the prepared substrates were completely covered with a 10 nm thin gold film to provide a chemical homogeneous surface for the reflection of the illuminating beam. The illuminating beam was adjusted to the step within the sample surface and two to four different regions on each surface were chosen for film thickness measurements. At least two different coverslips spin coated for each polymer were measured. All measurements were performed in air at (22 ± 1) °C using a magnification of 2.6x and 10.2x, respectively, over a field of view of 736 x 480 μm^2. The aquired data were further analyzed using the *Veeco Vision 3.43* software in two different ways. While a 3D rendering of the surface area allows for further calculations of roughness or waviness, a 2D analysis displays profile slices taken from the height data. 3D height maps produced from the interferometric raw data were used to determine the thickness of the polymer films. Therefore, line profiles were chosen which cut the experimental step in the polymer film. The depth of the experimental scratch was then measured relative to the neighboring polymer surface area at the right and the left edges of the step. The data were averaged for different regions of the surface.

3.3.3 Contact Angle Measurements

Hydrophilic or hydrophobic properties of a solid surface, which is also referred to as its wettability, are characterized by the contact angle which is formed between a liquid surface and a solid support. Often, techniques measuring the contact angle even allow for the determination of the surface energy of a certain solid material.
When a drop of liquid is placed on a perfectly smooth solid surface, three different interfaces, solid/liquid, solid/vapor and liquid/vapor are involved, each interface having its own specific surface energy content. The three interfacial tensions γ_{SL}, γ_{SV} and γ_{LV} can be viewed as forces acting along the perimeter of the drop. They depend only on the chemical composition of the three phases, the pressure and the temperature und are related via the following Young equation (de Gennes, 1985; Dörfler, 2002):

$$\gamma_{LV} \cos\theta = \gamma_{SV} - \gamma_{SL}\,. \tag{3.2}$$

The Young equation describes the force balance of the three phases in the horizontal direction at equilibrium, relating the interfacial tensions (Fig. 3.8) to the angle θ. The angle θ between the vectors γ_{SL}, the solid/liquid interface, and γ_{LV}, the liquid/vapor interface, has its vertex where the three phases meet and is termed the contact angle.

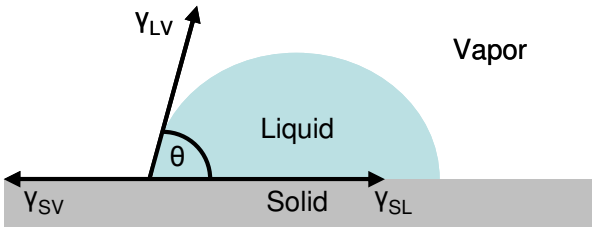

Fig. 3.8 Schematic illustration of interfacial tension components which determine the contact angle θ for the liquid/vapor/solid system according to Young, with the indices s for “solid”, l for “liquid” and v for “vapor”. The symbols γ_{LV}, γ_{SV} and γ_{SL} represent the interfacial tension between the respective two phases.

The Young equation is only valid for the state in which the interfaces are not moving and the phase boundary line exists in equilibrium. It is also based on the assumption of an ideal surface, i.e. a solid surface that is flat, smooth and chemically homogeneous. Real solid surfaces are quite different from the idealized one, often rough and chemically heterogeneous, causing a deviation in the contact angle from the one predicted by Young’s equation. Thus, empirical corrections are often used in order to adapt Young’s equation to the actual surface situation.

When a liquid comes in contact with a solid surface, two distinct equilibrium regimes, determined by the resultant between adhesive and cohesive forces, like partial wetting with a finite contact angle $0° < \theta \leq 180°$ or complete wetting $\theta = 0°$ can be found (Palzer et al., 2001; de Gennes, 1985). In the case of partial wetting, various cases, depending on the wetted portion of the surface, can be distinguished (Fig. 3.9). In general, the tendency of a drop to spread out over a flat, solid surface increases as the contact angle decreases. A surface is termed hydrophilic, if the value of the water contact angle is less than 90° (Fig. 3.9 B). Many highly hydrophilic surfaces reveal water contact angles between 0° and 30°. The border case of $\theta = 0°$ implies complete wetting, i.e. spreading of the drop to a thin film (Fig. 3.9 A). Hydrophobic surfaces exhibit contact angle for water droplets which are greater than 90° (Fig. 3.9 C). Surfaces with a contact angle between 150° and 180° are called superhydrophobic with hardly any contact between the liquid drop and the surface, whereas $\theta = 180°$ implies perfectly non-wetting (Fig. 3.9 D). The contact angle depends on several factors, such as surface energy, roughness, surface preparation and surface contaminations (Jung et al., 2006).

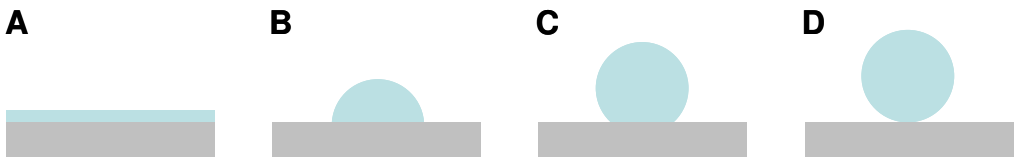

Fig. 3.9 Different wetting situations for a water drop on a solid surface. **A** Complete wetting, i.e. spreading by forming a thin film ($\theta = 0°$). Partial wetting on a hydrophilic ($0° < \theta < 90°$) (**B**) and a hydrophobic (**C**) surface ($90° \leq \theta < 180°$). **D** Non-wetting ($\theta = 180°$) behavior on a superhydrophobic surface.

The calculation of contact angles in this study was based on the sessile drop method, meaning a drop of liquid was deposited on a solid, smooth and horizontal surface. Two distinct ways of measuring the contact angle then exist: (i) in a static measurement the drop is produced before readings of the contact angle are performed and is kept at a constant volume during the whole measurement and (ii) in a dynamic approach the contact angle is measured while the drop is being enlarged or reduced. In the latter case, the boundary surface is being constantly newly formed during the measurement. Contact angles measured on increasing drops are termed advancing angles (θ_A), whereas those measured on reducing drops are called receding angles (θ_R).

In a static contact angle measurement the size of the drop does not alter during the measurement. Nevertheless, considerable changes in the size of the contact angle are possible due to interactions at the interface, like evaporation of the liquid or dissolving or swelling of the solid support by the liquid, leading to an increase or decrease with time (Kwok et al., 1997). It is a disadvantage of the static method that it is restricted to the measurement of the contact angle only on a single spot on the sample, being unable to detect local irregularities. Additionally, a measurement of the static contact angle only provides an angle somewhere

between θ_A and θ_R. For a complete surface characterization it is important that both advancing and receding contact angles are determined (Gao et al., 2006).
For this reason, usually dynamic contact angle measurements are used. Dynamic contact angles describe the processes at the liquid/solid interface during the increase (θ_A) or decrease (θ_R) of the drop volume, following the wetting and dewetting processes. In order to establish a dynamic equilibrium between the new boundaries, the flow rates must be sufficiently slow. In contrast to the static method, the syringe needle by which the volume of the drop is altered remains in the drop throughout the process of the measurement. A small drop is deposited by a syringe needle on the solid surface and liquid is carefully added to the drop. At the beginning, the measured contact angle is not independent from the drop size because of adhesion of the drop to the needle and the accompanying drop distortion. If additional liquid is added, the drop volume and the contact angle further increase, maintaining the same contact area until the contact angle stays constant and the drop begins to expand over the surface with a constant advancing contact angle θ_A. Since the expanding drop wettens a fresh surface, measurements of θ_A are the most reproducible way of measuring contact angles. Thus, θ_A is used for the calculation of surface energies. During the measurement of the receding angle the size of the drop is being reduced with a constant flow rate. The drop decreases in volume and contact angle, maintaining the same contact area with the surface until it begins to recede with a constant angle θ_R. Receding angles are measured on an already wetted surface and are usually smaller than advancing angles.
The difference between advancing and receding contact angles is termed contact angle hysteresis, a phenomenon mainly due to deviations from the ideal behavior. Real surfaces do not exhibit perfect smoothness, rigidity or chemical homogeneity thus usually showing a contact angle hysteresis different from zero (Jung et al., 2006; Extrand, 2003). By analyzing the contact angle hysteresis it is possible to evaluate properties of a surface like roughness and chemical contaminations or chemical inhomogeneities (de Gennes, 1985). Though there is no direct relation of the contact angle hysteresis to roughness certain assumptions can be made.

Experimental Procedure

Contact angle measurements were performed on all polymer coated coverslips. Prior to the measurements, some polymer films were argon plasma treated for 60 s and/or additionally incubated in buffer solution over a period of 20 h. The wettability of the individually coated polymer films was evaluated by measuring advancing and receding water contact angles using a video-based drop shape analysis system *DSA 100* (Krüss, Hamburg, Germany). An integrated high resolution camera takes images of the sessile drop on the substrate during the measurements. A DI-water droplet of about 3 – 5 µl was dispensed by a microsyringe and needle pointing vertically down onto the sample surface with a velocity of 30 µL/min to a final volume of about 10 µL and thereafter reduced in size with the same velocity. All measurements were performed at RT ((22 ± 1) °C) in air. The contact angle was calculated

using the automatic *DSAII* image analysis software (Krüss, Hamburg, Germany), which fits a mathematical model (polynomial function) to the experimental shape of the drop (*tangent method 2*). The slope of the tangent to the drop at the liquid/vapor interface line and the respective contact angle are determined using the iteratively optimized parameters of the polynomial. Advancing and receding water contact angles were measured on one (plasma treated polymer) to three (unmodified polymer) different regions of each surface – at least two coated coverslips per polymer were analyzed – on both sides of the drop and averaged over the constant regions of the contact angle.

3.4 Impedance Spectroscopy

Impedance spectroscopy (IS) is a versatile method for investigating and characterizing the electrical characteristics of a wide variety of materials and devices (Mcdonald, 1992). The technique is based on measuring the impedance of a conducting system, i.e. the ability of the system to resist flow of alternating current (AC), depending on the frequency of the excitation signal (Ende and Mangold, 1993). IS makes use of low amplitude alternating current or voltage to excite the system, ensuring a non-invasive examination without affecting the system under study. This allows for an application even in the biological and biomedical field, enabling a non-invasive investigation of living cells and tissues with respect to their stationary and dynamic electrical properties (Freiesleben de Blasio and Wegener, 2006). The data obtained from IS measurements are analyzed by modeling the electrical properties of the system with a suitable equivalent circuit. The equivalent circuit consists of electrical elements, like resistors or capacitors, which represent the electrical frequency response of the system under study. Fitting the transfer function of the equivalent circuit to the experimental data reveals the electrical parameters characterizing the studied system (Wegener, 1998).

Theoretical Background

There are two distinct methods to record impedance spectra: In the continuous wave method, a low amplitude sinusoidal current $I(t)$ or voltage $U(t)$ signal with the angular frequency ω ($\omega = 2\pi f$) is passed through or imposed on the sample. The steady-state voltage $U(t)$ or current $I(t)$ resulting from the excitation is measured, revealing the inherent impedance of the system. A given frequency range is scanned sequentially at well-defined individual frequencies between hertz and gigahertz. Plotting the impedance magnitude against the corresponding frequency results in a so-called impedance spectrum. The Fourier transform impedance spectroscopy uses transient pulses or white noise as excitation signal. The white noise excitation signal can be considered as a superposition of sine waves with distinct frequency, providing a simultaneous excitation of the system at all frequencies. Fourier analysis is then

used to transform the impedance data from the time domain to the frequency domain. In this thesis the continuous wave method was applied to record impedance data, as described in the following chapters in more detail.
According to Ohm's law for direct current, the resistance R is given by the ratio of the applied voltage U to the resulting current I. Consistently, the impedance Z in an AC electric circuit is defined by the ratio of the applied alternating voltage and the resulting alternating current. Except for a purely resistive system, for which the current is in-phase with the voltage, electric circuit elements like capacitors or inductors induce a current response which is sinusoidal at the same frequency ω as the applied voltage signal but shifted in phase φ. This can be best described using a complex notation.

The alternating voltage $U(t)$ at a frequency ω is defined by:

$$U(t) = U_0 e^{i\omega t} . \tag{3.3}$$

$U(t)$ is the voltage at a certain time t with the amplitude of the voltage U_0 and the angular frequency ω ($i = \sqrt{-1}$ imaginary unit).
The corresponding alternating current is defined by:

$$I(t) = I_0 e^{i(\omega t - \varphi)} , \tag{3.4}$$

with $I(t)$ being the actual value of the current at a certain time t with the amplitude of the current I_0. φ is the phase angle between voltage $U(t)$ and current $I(t)$.
The impedance Z is defined by the ratio of voltage $U(t)$ and current $I(t)$:

$$Z = \frac{U(t)}{I(t)} = \frac{U_0 e^{i\omega t}}{I_0 e^{i(\omega t - \varphi)}} = \frac{U_0}{I_0} e^{i\varphi} = |Z| e^{i\varphi} . \tag{3.5}$$

The impedance at each frequency of interest is described by its magnitude $|Z|$, which is the ratio of the amplitudes of $U(t)$ and $I(t)$ and the phase angle φ between them.
Using the Cartesian form, the measured complex impedance Z can be separated into its real and imaginary components, i.e. the impedance contribution arising from current in-phase with the voltage and 90° out-of-phase with the voltage. The real part is called resistance R and the imaginary part is termed reactance X:

$$Z = R + iX . \tag{3.6}$$

The complex impedance can be geometrically presented in the Gauss plane, a modified Cartesian plane consisting of the real axis and the orthogonal imaginary axis. The real part is reflected by a displacement along the x-axis, whereas the imaginary part is reflected by a

displacement along the y-axis. The relation between the polar coordinates |Z|, φ and the Cartesian coordinates R, X is illustrated in the following diagram (Fig. 3.10).

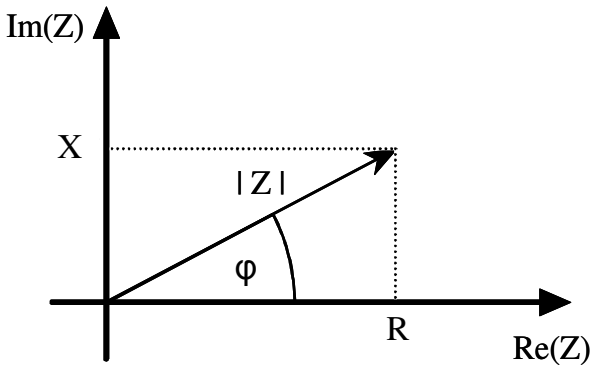

Fig. 3.10 The impedance Z plotted as a planar vector using Cartesian and polar coordinates in the Gauss plane.

The two polar coordinates |Z| and φ can be converted to the Cartesian coordinates R and X as follows:

$$R = \mathrm{Re}(Z) = |Z| \cos\varphi \qquad X = \mathrm{Im}(Z) = |Z| \sin\varphi . \tag{3.7}$$

In an analogous manner, the Cartesian coordinates R and X can be reconverted to yield the magnitude |Z| and the phase φ of the impedance as follows:

$$|Z| = \sqrt{R^2 + X^2} \tag{3.8}$$

$$\varphi = \arctan\frac{X}{R} . \tag{3.9}$$

|Z| and φ as well as R and X are separate pairs of parameters which can serve independently to describe and analyze the electrical properties of a studied system.

Impedance data are generally analyzed in terms of an equivalent circuit model, consisting of a collection of common electrical elements such as ideal resistors, capacitors and inductors. The crucial point is to find a model whose theoretical electrical frequency response matches the measured electrical frequency response of the studied system. By fitting the transfer function of an appropriate equivalent circuit to the experimental impedance spectra the electrical parameters of the system are obtained. Table 3.2 provides a list of circuit elements commonly used in this thesis to describe the systems under study with respect to their individual impedance and phase shift.

Tab. 3.2 Ideal and empirical equivalent circuit elements and their individual impedance contributions.

Component of Equivalent Circuit	Impedance Z	Phase Shift φ
Resistor R	R	0
Capacitor C	$(i\omega C)^{-1}$	$-\pi/2$
Inductor L	$i\omega L$	$+\pi/2$
Constant Phase Element (CPE) A, n $(0 < n < 1)$	$(i\omega)^{-n} \cdot A^{-1}$	$-n \cdot \pi/2$, $[0,1] = n$

The impedance of an ideal resistor is completely frequency-independent. A resistor R only affects the amplitude of the current response upon voltage application and the current is always in-phase with the voltage. The impedance of a capacitor or an inductor is frequency-dependent: a capacitor's impedance decreases, while the impedance of an inductor increases as frequency increases. Capacitors and inductors have only an imaginary impedance component. The current through a capacitor is phase shifted by $-90°$ with respect to the voltage while the one through an inductor is phase shifted by $+90°$.

In order to fit the equivalent circuit model impedance to the impedance of the system under study, it is often necessary to include non-ideal circuit elements, i.e. elements with real and imaginary components. Such elements are not accurately described by standard electronic elements due to the fact that ions transporting charge in electrochemical systems show a different behavior compared to electrons in common electrical elements. A closer look at the electrode-electrolyte interface, for example, reveals that it is usually not ideally smooth and uniform. A large number of surface defects like irregularities in the electrode topography or variations in the chemical composition of the electrolyte close to the surface lead to local charge inhomogeneities. The non-ideal circuit element which can cope with this phenomenon is the constant phase element (CPE), an empirical impedance element. It describes a non-ideal capacitor and was originally introduced to describe the interface impedance of noble metal electrodes immersed in electrolytic solutions. In living tissue and at electrode interfaces, its physical basis is not fully understood so far. The parameters A and n characterize the electrical properties of the CPE (Tab. 3.2). Depending on the parameter n the CPE causes a frequency-independent, constant phase shift between voltage and current, ranging between $-\pi/2$ and 0. If $n = 0$ the CPE can be described as an ideal resistor, with the value $R = A^{-1}$, whereas for $n = 1$ it turns into an ideal capacitor with the capacitance $C = A$. For all values in between $-\pi/2$ and 0, the CPE has resistive as well as capacitive properties. The parameter n has been linked to the degree of surface roughness – it decreases with growing surface roughness (McAdams et al., 1995; Kurtyka and de Levie, 1992).

For a given equivalent circuit model, the total impedance is calculated by combining the impedances of the individual components using Kirchhoff's laws. For impedance elements in series the equivalent impedance is equal to the sum of their individual impedances, whereas in

a parallel combination of circuit elements the total impedance is equal to the reciprocal of the sum of the reciprocals of their individual impedances (admittance).
The parameters of the electric circuit components are determined using least-square algorithms to fit the transfer function to the experimental impedance spectrum. The best estimates for the parameters are used to characterize the electrical properties of the system.

In order to analyze the cytocompatibility of certain technical surfaces, two different techniques, both based on IS, were applied in this study.
The first part of this work addresses the biocompatibility of different polymer films. Here, the quartz crystal microbalance (QCM) technique was the most important biophysical tool. Shear wave resonators were used as microgravimetric sensors on which the polymer of interest was deposited. Using the QCM technique the polymer surface was analyzed regarding its long-term stability in a physiological environment, protein adsorption as well as cell attachment and spreading, monitoring the mechanical interactions between the cells and their growth substrate.
The second part focuses on the characterization of cell-surface interactions, i.e. cell adhesion and micromotion, on different surface topographies that were modeled by mesoporous silicon surfaces. This analysis was performed by the electric cell-substrate impedance sensing (ECIS) technique. To apply ECIS the mesoporous silicon surfaces were coated with thin gold films that served as a culture substrate for mammalian cells and as a measuring electrode at the same time.

3.5 Quartz Crystal Microbalance

The quartz crystal microbalance (QCM) technique is a surface-analytical device that reads changes in the resonant oscillation of a piezoelectric shear wave resonator in response to any surface alteration. Due to the sensitivity of the mechanical oscillation for changes that occur at the crystal's surfaces, it is possible to determine and quantify adsorption or desorption processes of material from reading the resonance frequency f (Schumacher, 1990) or analyzing the shear oscillation of the resonator using principles of impedance analysis (Kipling and Thompson, 1990; Yang and Thompson, 1993; Buttry and Ward, 1992). The QCM was first introduced as a microgravimetric sensor to study adsorption processes at solid surfaces in the gas phase and in vacuum. According to Sauerbrey, mass loading onto a quartz surface causes a proportional shift in the resonance frequency of the quartz resonator (Sauerbrey, 1959). However, this is only valid in the case of a thin, homogeneous and rigid mass film which is strongly coupled to the resonator. The development of oscillator circuits capable of exciting shear vibrations of quartz resonators under liquid loading paved the way for new applications of this technique in chemical and biological research and allowed to follow adsorption processes at the solid/liquid interface. Most studies are focused on the

molecular level, comprising ligand-receptor recognition (Ebato et al., 1992), immunological recognition (Muramatsu et al., 1987), protein-membrane interactions and protein adsorption to technical or functionalized surfaces (Lord et al., 2006). Besides the detection of small amounts of adsorbed molecules, the QCM technique can also provide more detailed information about the viscoelastic properties of the adsorbed material. This makes the QCM technique an interesting non-invasive tool for cell biology, being able to monitor cell-substrate interactions of mammalian cells *in vitro* under physiological conditions. Cell attachment and spreading can be followed in real-time (Wegener et al., 2000) as well as cytotoxicity/biocompatibility screenings can be performed (Modin et al., 2006).

3.5.1 Basic Principle of the QCM Technique

The core component of this technique is a thin disk made from α-quartz. Single crystals of α-quartz are piezoelectric in nature, due to an inversion center in the crystal lattice and a non-zero fraction of ionic binding between silicon and oxygen. The arrangement of the binding dipoles shows a spatially preferred orientation, giving the crystal a polar axis (Fig. 3.11 A). If the quartz crystal is mechanically deformed, i.e. torsion, pressure or bending along an appropriate direction, electrical charges are generated on the opposing surfaces of the crystal. This is due to a change in the orientation of the binding dipoles and termed the piezoelectric effect. The piezoelectric effect is proportional to the strength of the mechanical deformation.

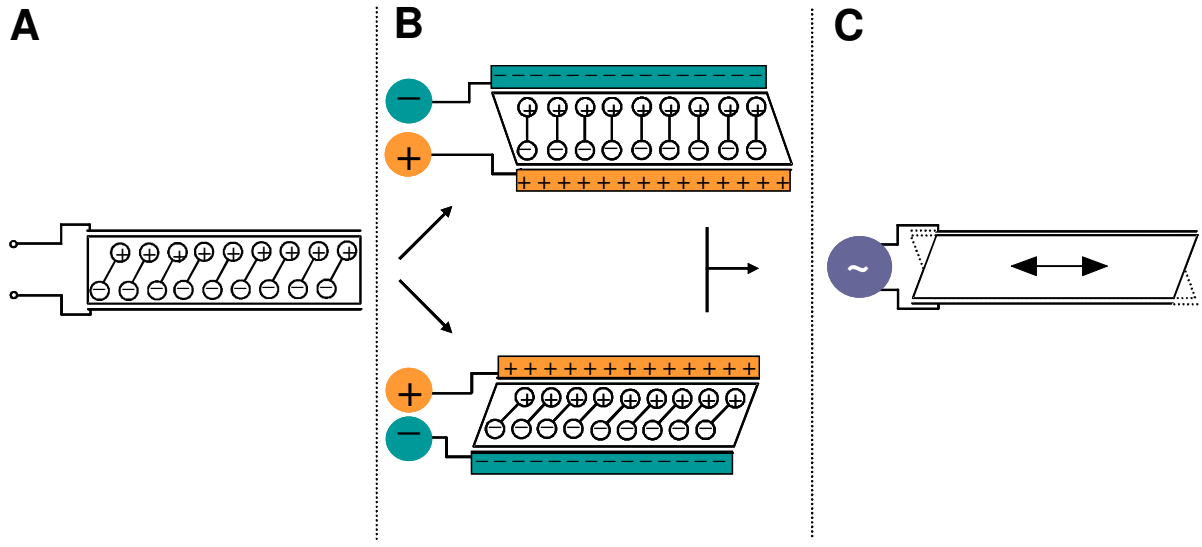

Fig. 3.11 Schematic diagram of the converse piezoelectric effect of quartz crystal. **A** A thin, AT-cut α-quartz disk in the unstressed state is shown. **B** The quartz disk is exposed to an external electric field (direct current), which leads to a mechanical deformation of the quartz crystal depending on the polarity of the electric field. **C** An alternating potential difference induces mechanical shear displacements of the resonator around its steady-state position.

Conversely, the piezoelectric quartz crystal mechanically deformes when an external electric field is applied to the crystal faces. The applied electric field induces a displacement of the binding dipoles, leading to a deformation of the whole crystal (Fig. 3.11 B). The induced mechanical deformation is proportional to the strength of the applied electric field and its direction depends on the polarity of the electric field. If an alternating potential difference is applied, the crystal undergoes a shear oscillation, mechanically oscillating around its steady-state position (Fig. 3.11 C). This effect is termed converse piezoelectricity and it is the fundamental basis of the QCM technique. The sensitivity of the mechanical oscillation for any surface loading can be used analytically to follow adsorption processes.

The quartz resonators, as aforementioned, originate from a single crystal of α-quartz. Dependent on the cut angle relative to the crystal lattice, different resonator types, like thickness shear mode, face shear mode or flexural shear mode resonators can be obtained, revealing different wave propagation modes. The resonators which are used for QCM measurements are AT-cut crystals, operating in the thickness shear mode. They are commonly used as microgravimetric sensors in QCM applications and are prepared by slicing a quartz disk with an angle of 35°10' to the optical z-axis from the mother crystal (Fig. 3.12 A). For the application of an alternating potential difference at the crystal faces, a gold film electrode is evaporated on each side of the resonator (Fig. 3.12 B).

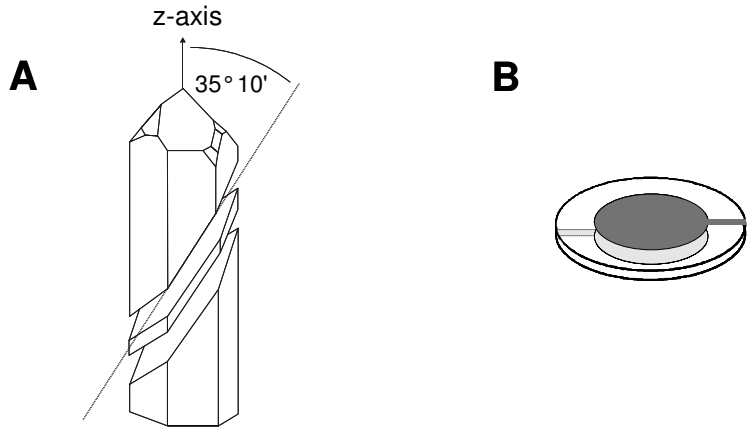

Fig. 3.12 A AT-cut of a quartz crystal with an angle of 35°10' to the optical z-axis to obtain a thickness shear mode resonator. **B** AT-cut disk-shaped quartz resonator sandwiched between two evaporated gold film surface electrodes.

The application of an alternating potential difference to the surface electrodes results in a shear displacement of the resonator which travels as two transverse (acoustic) waves in opposite direction through the solid perpendicular to the crystal surfaces. The waves traverse the quartz thickness, are reflected at the opposing crystal face and return to their origin. When the frequency of the applied alternating electric field is adjusted in a way that the crystal thickness d_q is an integer multiple of half the acoustic wavelength λ (Eq. 3.10), constructive interference of incident and return waves occurs. This forms a standing acoustic wave within the crystal, also termed resonant oscillation (Fig. 3.13).

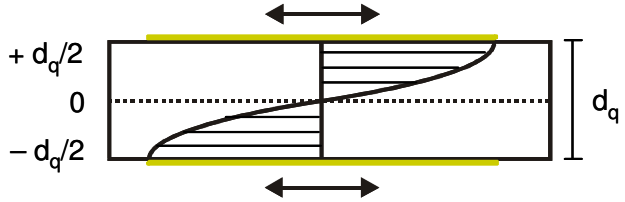

Fig. 3.13 Quartz resonator of thickness d_q coated with evaporated gold electrodes on opposing surfaces (yellow).

$$d_q = \frac{n\lambda}{2}, \qquad \text{with } n = 1, 3, 5, 7, \ldots \tag{3.10}$$

For the fundamental frequency ($n = 1$), the standing acoustic wave exhibits a maximum amplitude at the crystal's surfaces (at $z = \pm d_q/2$ maximum particle displacement) and a displacement node in the center of the resonator ($z = 0$).
The resonance frequency f_0 of the quartz resonator depends on the thickness of the quartz resonator d_q and with the propagation velocity of acoustic waves v_{at} travelling in an AT-cut crystal, f_0 can be expressed by:

$$f_0 = \frac{v_{at}}{2d_q} = \frac{\sqrt{\overline{c_{66}} / \rho_q}}{2d_q} = \frac{K_R}{d_q}. \tag{3.11}$$

f_0 increases with decreasing thickness of the crystal. K_R denotes the frequency constant of AT-cut quartz, $\overline{c_{66}}$ the piezoelectrically stiffened elastic modulus and ρ_q the mass density of quartz.

The shear amplitude along the crystal surface is not uniform. The amplitude is maximum at the center of the gold surface electrode at $r = 0$ and decreases with increasing distance from the center in a Gaussian-like manner to a value of zero at and beyond the electrode boundary (Martin et al., 1989). The reason for this exponential damping is based on the fact that the particles, surrounding the electrode-covered region, are not moving. This is due to different resonance conditions of the quartz crystal for the electrode-covered and the electrode-free region, making the center of the resonator the most sensitive part for adsorption processes.

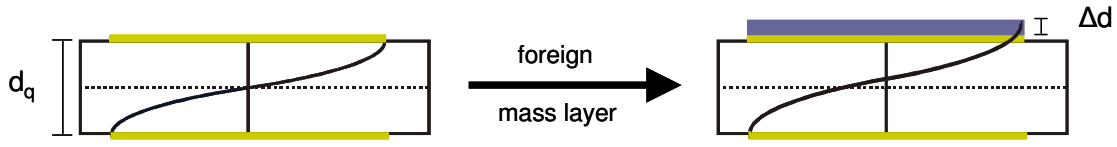

Fig. 3.14 Sauerbrey relationship. The deposition of an ideal foreign mass layer on the crystal surface increases the crystal's thickness to ($d_q + \Delta d$).

Sauerbrey theoretically described the application of quartz resonators as a microbalance for rigidly deposited mass films, if the resonator is operated in air or vacuum (Sauerbrey, 1959). The deposition of an ideal foreign mass layer on the crystal surface leads to an increase Δd of the resonator's thickness (Fig. 3.14). An ideal mass layer denotes a layer of foreign mass that is rigid, thin and of uniform thickness. As a consequence of the mass deposition, the resonance frequency of the resonator is decreased (Eq. 3.11), allowing the detection of the deposited mass from reading the resonant frequency.
Assuming that the density of the mass layer is similar to the density of the quartz, the frequency decrease Δf is proportional to the deposited mass Δm (Sauerbrey, 1959):

$$\frac{\Delta f}{f_0} = -\frac{\Delta d}{d_q} = -\frac{2 f_0}{A\sqrt{\overline{c_{66}}\rho_q}} \cdot \Delta m \Rightarrow \Delta f = -\frac{2 f_0^{\,2}}{A\sqrt{\overline{c_{66}}\rho_q}} \cdot \Delta m = -S_f \cdot \frac{\Delta m}{A}, \tag{3.12}$$

with A being the piezoelectrically active area, i.e. the surface area of the surface electrodes. The integral mass sensitivity, or Sauerbrey constant S_f, is a measure for the sensitivity of the quartz resonator and depends on the square of the fundamental frequency (Eq. 3.12). According to Eq. 3.11, an increase in the fundamental frequency and therefore the integral mass sensitivity S_f can be realized when decreasing the crystal thickness d_q. However, the use of resonators with high fundamental frequencies and intrinsic high sensitivities is limited by the mechanical fragileness of the quartz resonators when getting increasingly thin. The quartz resonators used in this thesis are 5 MHz quartzes with a corresponding thickness of 330 µm. Following the Sauerbrey equation (Eq. 3.12) the integral mass sensitivity S_f for these 5 MHz resonators is given by:

$$S_f = 0.057 \frac{Hz \cdot cm^2}{ng}. \tag{3.13}$$

If the device is not operated in air or vacuum but in a liquid environment, viscous effects play an important role, which cause an additional frequency shift and therefore cannot be neglected. The fluid in contact to the resonator is treated like an ideal Newtonian liquid with the viscosity η_{fl} and the density ρ_{fl}. Based on the Sauerbrey equation Kanazawa and Gordon (1985) derived an equation for the impact of Newtonian liquids on the resonance frequency of quartz resonators:

$$\Delta f_{fl} = -\frac{f_0^{3/2}}{\sqrt{\pi \overline{c_{66}}\rho_q}} \cdot \sqrt{\eta_{fl}\rho_{fl}}. \tag{3.14}$$

The shift in resonance frequency depends on the square root of the density-viscosity product of the liquid. Kanazawa and Gordon did not consider the damping of the quartz resonator

caused by viscous loading. Damping and energy losses can be characterized by the quality factor Q_0, following the definition by Rodahl et al. (1996):

$$\Delta Q_{fl} = \frac{1}{\Delta D_{fl}} = -2\pi \cdot \Delta\left(\frac{E_{stored}}{E_{dissipated}}\right) = -2Q_0^2 \sqrt{\frac{f_0}{\pi \overline{c_{66}} \rho_q}} \cdot \sqrt{\eta_{fl} \rho_{fl}} \,. \tag{3.15}$$

The quality factor Q_0 is proportional to the ratio of the energy stored to the energy dissipated during one period of oscillation. The quality factor is the inverse of the often used dissipation factor D.

3.5.2 Electromechanical Coupling

In order to analyze the oscillation of a quartz resonator in a more detailed manner and to discriminate between mechanically different load material such as a rigidly deposited mass layer or a viscous liquid, the shear displacement has to be described by an appropriate mechanical model. Due to the piezoelectric coupling within the quartz resonator, the mechanical oscillation is always accompanied by an electrical oscillation, so that the mechanical surface load can be expressed by an electrical equivalent circuit. Impedance measurements and subsequent analysis of the obtained spectra give access to the electrical parameters of the equivalent circuit and thus allow a complete description of the mechanical oscillation in the presence of any load material.
Following Buttry and Ward (1992), the mechanical oscillation of a quartz resonator can be described by the model of a mass-on-a-spring (Fig. 3.15 A), consisting of a mass m connected to a spring with the Hooke's constant k in parallel to a dashpot that represents energy losses of the oscillation, e.g. damping of the oscillation due to friction of the mass in a viscous liquid.

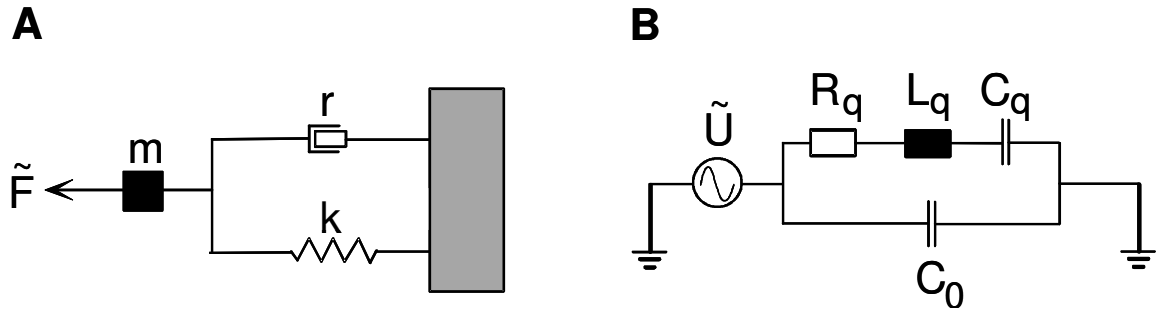

Fig. 3.15 A The mechanical model and **B** the corresponding electrical model describing the shear motion of an oscillating quartz resonator.

By applying an external force F the mass is displaced (displacement x) and starts to oscillate. In the mechanical model, the moving mass m holds a certain kinetic energy and mirrors the particle displacement within the oscillating quartz crystal. The Hooke's constant k is

equivalent to the elastic properties of the quartz and determines the energy stored during oscillation (potential energy), whereas the friction coefficient r represents the energy dissipation during oscillation due to internal friction and friction between the resonator and the material in contact with its surface (e.g. medium). The corresponding mechanical model that includes damping can be described by the following equation of motion:

$$m \cdot \frac{d^2x}{dt^2} + r \cdot \frac{dx}{dt} + k \cdot x = F \; . \tag{3.16}$$

In the case of an ideal mass-on-a-spring ($r = 0$), the resonance frequency of the mechanical oscillation is equivalent to the fundamental frequency:

$$f_0 = \frac{1}{2\pi}\sqrt{\frac{k}{m}} \; . \tag{3.17}$$

Analogous to the mass-on-a-spring model to describe the mechanical oscillation of the quartz, Dye and Butterworth (Bottom, 1982) developed a corresponding model to describe the electrical oscillation. The electrical equivalent circuit (Fig. 3.15 B) consists of lumped impedance elements – an ohmic resistance R_q in series to an inductance L_q and a capacitance C_q, connected in parallel to a capacitance C_0. The equation of motion for the electrical oscillation of series R_q, L_q and C_q is given by:

$$L_q \cdot \frac{d^2Q}{dt^2} + R_q \cdot \frac{dQ}{dt} + \frac{Q}{C_q} = U \; , \tag{3.18}$$

with Q being the amount of charge and U the applied voltage.
When comparing the equations of motion for both models (Eq. 3.16 and Eq. 3.18), it can be noted that the external force F in the mechanical model is equivalent to the applied voltage U in the electrical model and the particle displacement x corresponds to the amount of charge Q. A comparison of the coefficients reveals the correspondence of (i) displaced mass m and inductance L_q, (ii) friction factor r and ohmic resistance R_q as well as (iii) Hooke's spring constant k and the inverse of the capacitance $1/C_q$. This allows the conversion of the mechanical model to an electrical model and therefore analysis of the mechanical properties of the system by determining the electrical parameters of the equivalent circuit. The serial connection of R_q, L_q, and C_q represents the electrical (piezoelectric) properties of the quartz at frequencies close to resonance and is termed the motional branch of the equivalent circuit. The analogy of both models is consistently reflected in the resonance frequency of an ideal serial oscillating circuit ($R_q = 0$):

$$f_{s,0} = \frac{1}{2\pi}\sqrt{\frac{1}{L_q \cdot C_q}} \tag{3.19}$$

The extra capacitance C_0, which is connected in parallel to the other impedance elements of the equivalent circuit, has no mechanical analog. It describes the electrical properties of the quartz away from resonance, when the dielectric properties dominate the piezoelectric properties. The parallel capacitance C_0 comprises the static capacitance C_s, representing the dielectric quartz material between the two surface electrodes and a parasitic capacitance C_p, originating from the experimental setup like wiring, contacts and the mounting system:

$$C_0 = C_s + C_p . \tag{3.20}$$

In the case of an unloaded quartz resonator, its electrical oscillation is described by the Butterworth-van Dyke (BVD) equivalent circuit (Fig. 3.16).

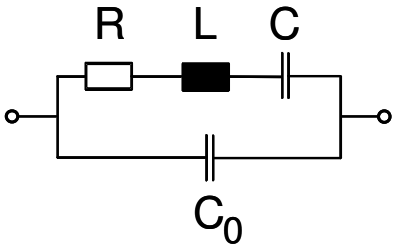

Fig. 3.16 Butterworth-van Dyke (BVD) equivalent circuit with lumped impedance elements for an unperturbed quartz resonator.

Impedance analysis of shear wave resonators near resonance and subsequent fitting of the transfer function of the BVD network to the recorded impedance spectra allows the quantification of characteristic parameters of the shear oscillation.

3.5.2.1 The Electrical Parameters of the BVD Equivalent Circuit and their Impact on the Bode Diagram

The entire Butterworth-van Dyke equivalent circuit combines a series and a parallel resonant circuit, each revealing a distinct resonance frequency. When the impedance magnitude $|Z|$ and the phase shift φ of the BVD equivalent circuit for an unperturbed resonator ($R \approx 0$) are plotted against the frequency f in a so-called Bode diagram (Fig. 3.17), general features of the recorded spectrum are revealed. The phase spectrum is similar to a rectangular function, showing a phase shift of – 90° between current and voltage at low frequencies, followed by a steep increase to + 90° for slightly higher frequencies before falling back to – 90° again. In the frequency range producing – 90° phase shift, the impedance is dominated by the parallel

capacitance C_0. The Bode diagram shows that the resonator possesses two resonance frequencies for $R \approx 0$, one at a phase shift of $\varphi = 0$ and minimal impedance magnitude $|Z_{min}|$ and the other one at $\varphi = 0$ and maximal impedance magnitude $|Z_{max}|$.

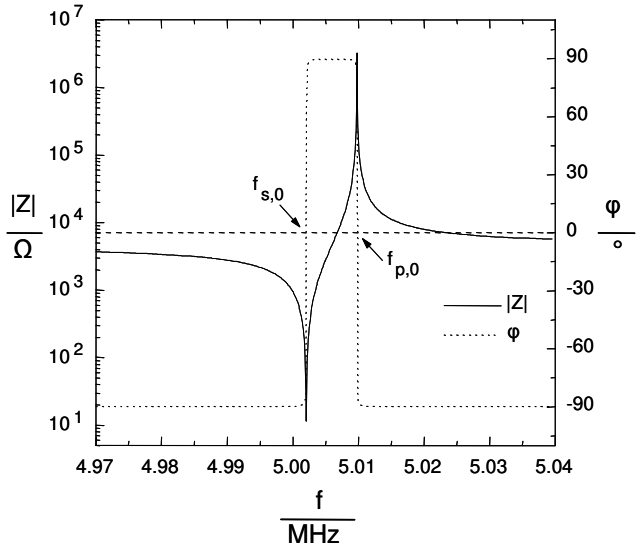

Fig. 3.17 Simulated Bode diagram presenting the impedance and phase spectra of the BVD equivalent circuit for an unperturbed quartz resonator ($R \approx 0$) by plotting log $|Z|$ and φ against f.

The respective resonance frequencies are termed series frequency $f_{s,0}$ and parallel or antiresonant frequency $f_{p,0}$, the latter being the higher one:

$$f_{s,0} = \frac{1}{2\pi}\sqrt{\frac{1}{LC}} \qquad f_{p,0} = \frac{1}{2\pi}\sqrt{\frac{1}{L}\left(\frac{1}{C}+\frac{1}{C_0}\right)}. \tag{3.21}$$

They are obtained from the Bode diagram either by extracting the frequencies of $\varphi = 0$, $|Z_{min}|$ and $|Z_{max}|$ from the experimental data or indirectly by fitting the transfer function of the BVD equivalent circuit to the measured impedance spectra by means of least-square methods and a subsequent computation of the respective frequencies using Eq. 3.21.

Discrete variations in the impedance elements R, L, C, and C_0 of the BVD equivalent circuit induce characteristic changes in the course of the impedance and phase spectra of a quartz resonator (Fig. 3.18). Figure 3.18 A presents the Bode diagrams of the BVD equivalent circuit when the motional resistance R is varied, while the remaining parameters are kept constant. $R = 10\ \Omega$ reflects an almost undamped resonator oscillating loss-free. An increase of the motional resistance R induces a broadening of the phase spectrum, characterized by a stepwise decrease of the phase maximum φ_{max} accompanied by a decrease in steepness of $d\varphi/df$ (Fig. 3.18 A2). The respective impedance spectrum shows an increase of the magnitude of the minimal impedance $|Z_{min}|$ and a concomitant decrease of the maximal impedance $|Z_{max}|$ with increasing R (Fig. 3.18 A1).

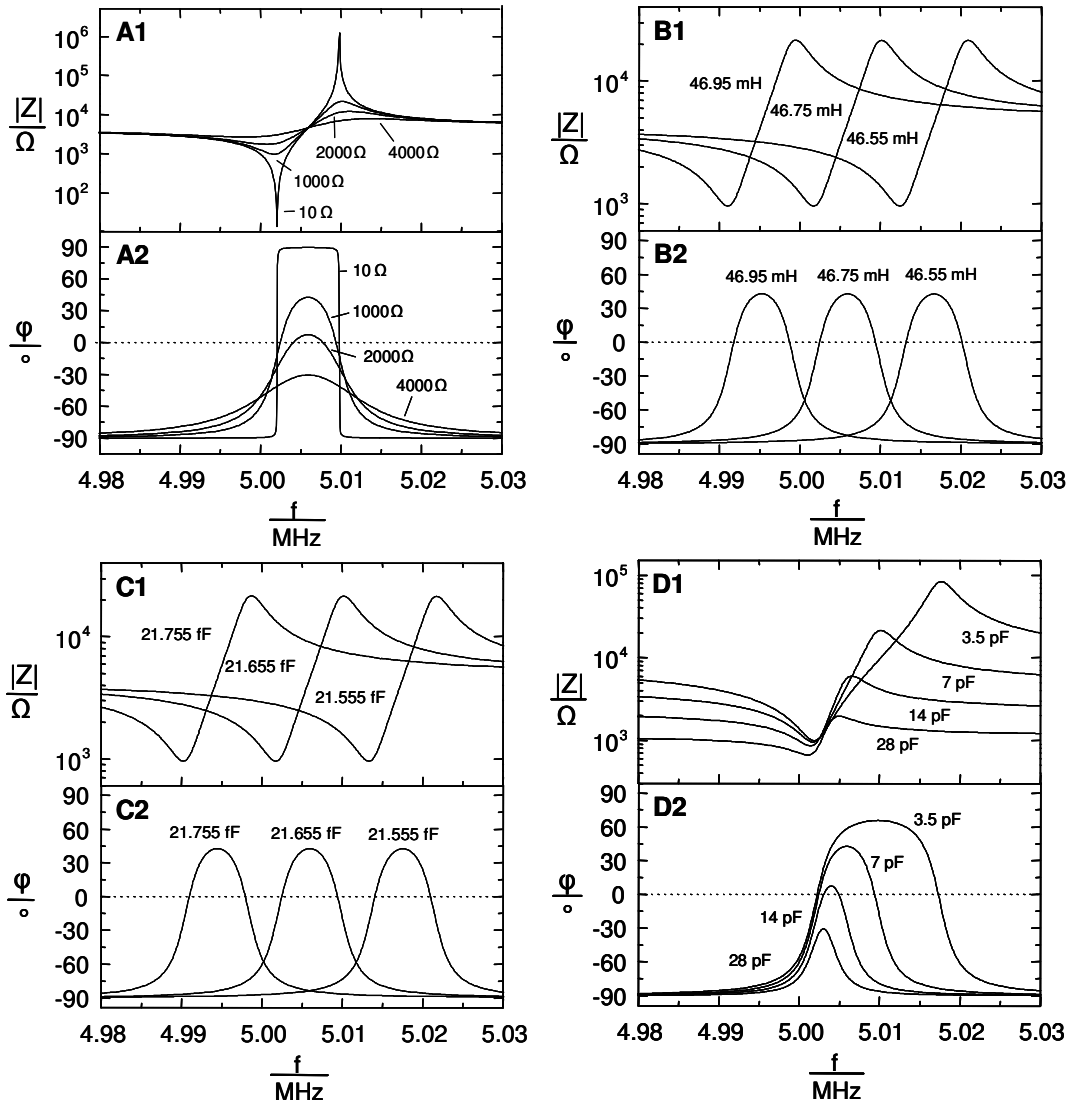

Fig. 3.18 Simulated Bode diagrams for the impedance magnitude $|Z|$ and the phase shift φ, as computed from the transfer function of the BVD equivalent circuit, when single impedance elements (**A**) R, (**B**) L, (**C**) C and (**D**) C_0 are discretely varied while keeping the remaining parameters constant (R = 1000 Ω, L = 46.75 mH, C = 21.655 fF, C_0 = 7 pF) (Wegener, 1998).

Furthermore, each of the resonance frequencies for $R = 0$, $f_{s,0}$ and $f_{p,0}$, are split symmetrically in a low- and a high-frequency part each, due to the fact that the resonance frequency at 0° phase shift does not overlap anymore with the one of the minimal and maximal impedance, respectively (Fig. 3.19). $f_{s,0}$ separates into f_s, the frequency of 0° phase shift at the low frequency end, and f_{Zmin}, the frequency at minimal impedance. $f_{p,0}$ separates into f_p, the frequency of 0° phase shift at the high frequency end, and f_{Zmax}, the frequency at maximal impedance. If the resonator is loaded with a viscous mass and damped accordingly ($R > 0$), the quartz resonator exhibits four characteristic resonance frequencies. An increased damping causes f_s and f_{Zmax} to rise, whereas f_p and f_{Zmin} decrease, till the two resonance frequencies f_s and f_p finally meet at $\varphi_{max} = 0$ with increasing R.

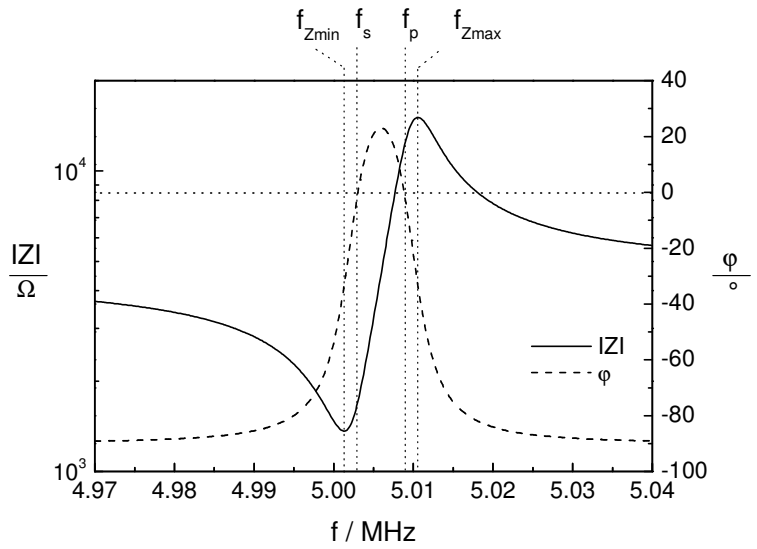

Fig. 3.19 Simulated Bode diagram presenting the impedance and phase spectra of the BVD equivalent circuit for a damped quartz resonator ($R > 0$). The oscillation of the resonator can be described by four characteristic frequencies, f_{Zmin}, f_s, f_p and f_{Zmax}.

Discrete variation of the motional inductance L results in a translation of the impedance and phase spectra along the frequency axis, though leaving the course of the spectra unchanged. An increase of L shifts both spectra to lower frequencies (Fig. 3.18 B). This translation has an equal impact on all characteristic resonance frequencies, making them all equally well suited to monitor inductive changes of a quartz resonator.

An increase of the motional capacitance C has a similar effect on the impedance and phase spectra like an increase of L has. Both spectra are translated along the frequency axis to lower frequencies, without their internal course being affected (Fig. 3.18 C). This prevents an independent determination of the parameters L and C during fitting of the transfer function of the BVD network to the recorded impedance spectra. Thus, in order to characterize a pure mass deposition on a quartz resonator, the capacitance C is set to a constant value, since it describes the intrinsic elastic properties of the quartz, which should not be influenced by any surface loading. Following Noël and Topart (1994), the computed capacitance for 5 MHz quartz resonators used in this thesis is 21.655 fF.

Discrete variation of the parallel capacitance C_0 results in unsymmetrical distortions of the impedance and phase spectra. An increasing parallel capacitance C_0 causes the phase maximum to decrease and the center of the phase spectrum to be shifted to lower frequencies (Fig. 3.18 D).

All characteristic frequencies of the quartz resonator are affected by the parameters of the BVD equivalent circuit in an individual way, what can be seen in the simulated Bode diagrams. Only an impedance analysis is capable of differentiating between the single parameters of the quartz oscillation.

3.5.2.2 Influence of the Surface Loading on the Electrical Parameters of the Shear Oscillation

The BVD equivalent circuit can be used to model the parameters of the electrical oscillation of an unperturbed quartz resonator. Any surface loading of the resonator can be characterized by an additional impedance element, added to the motional branch in series to *R*, *L* and *C*. This extra impedance element is termed load impedance Z_L, arising from the load material in contact with the resonator surface (Fig. 3.20).

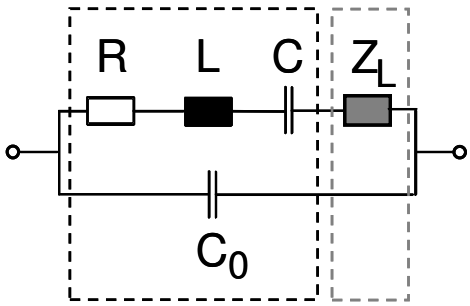

Fig. 3.20 General BVD equivalent circuit for any load situation of the quartz resonator. The load impedance Z_L denotes the additional impedance, arising from the load material in contact with the resonator surface.

The electrical impedance Z_L of the load material on the resonator surface is directly proportional to its acoustic impedance. Thus, reading Z_L gives access to the mechanical properties of the surface load. Z_L can exhibit ohmic, inductive or capacitive properties, depending on the mechanical properties of the load material coupled to the resonator surface.

Pure Mass Loading

A thin and homogeneous mass layer which is rigidly coupled to the resonator surface follows the oscillation of the resonator synchronously and loss-free. Because of the correlation of displaced mass with inductance, the deposited mass can be described by a load impedance $Z_L = \omega L_m$ added to the motional branch of the BVD equivalent circuit. The change of L_m in the course of an experiment is directly proportional to the deposited mass per unit area, analogous to the Sauerbrey equation (Eq. 3.12), with S_l being the integral mass sensitivity:

$$L_m = S_l \cdot \frac{m}{A}. \tag{3.22}$$

Liquid Loading

The influence of a liquid load on the shear oscillation can be approximated by an ideally viscous Newtonian liquid, whose first molecular layer adsorbs tightly to the resonator surface, moving synchronously with the oscillating surface (no slip behavior). Viscous coupling of

adjacent liquid layers results in a transfer of the shear oscillation into the bulk medium, leading to a loss of kinetic energy and thus to damping of the shear oscillation (Martin et al., 1991) (Fig. 3.21).

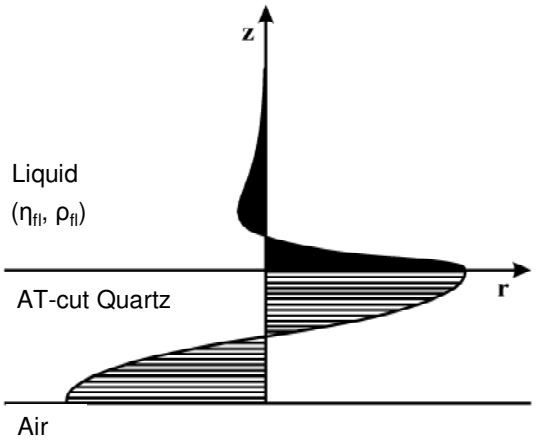

Fig. 3.21 Schematic cross-section of a quartz resonator loaded on one side with an ideal Newtonian liquid. The shear displacement causes a synchronous motion of the first adsorbed liquid layer and an entrainment of adjacent liquid layers. As a consequence, a damped shear wave is radiated into the bulk medium (Martin et al., 1991).

The decay length δ of the shear wave radiated vertically to the quartz surface into the bulk phase depends on the density and viscosity of the investigated liquid. For a 5 MHz quartz resonator, the decay length δ of the shear wave in water is approximately 250 nm at room temperature:

$$\delta = \sqrt{\frac{\eta_{fl}}{\pi \cdot f \cdot \rho_{fl}}} \,. \tag{3.23}$$

In the corresponding BVD network, Z_L denotes a serial connection of an inductance L_{fl} to account for the tightly adsorbed first molecular layer of the liquid and a resistance R_{fl} for the energy dissipation due to the propagation of the shear wave into the bulk medium. L_{fl} and R_{fl} are directly proportional to the square root of the density-viscosity product of the liquid, thus they can be related with mechanical properties of the liquid.

Mass and Liquid Loading

When loading the quartz resonator simultaneously with a rigid, homogeneous mass layer covered with an ideal Newtonian liquid, the impedance contributions of both surface loadings can be added (Martin et al., 1991). In the respective extended equivalent circuit (Fig. 3.22), Z_L represents a serial connection of L_m for the deposited mass, L_{fl} for the liquid layer tightly adsorbed to the surface and R_{fl} for the energy dissipation due to viscous coupling.

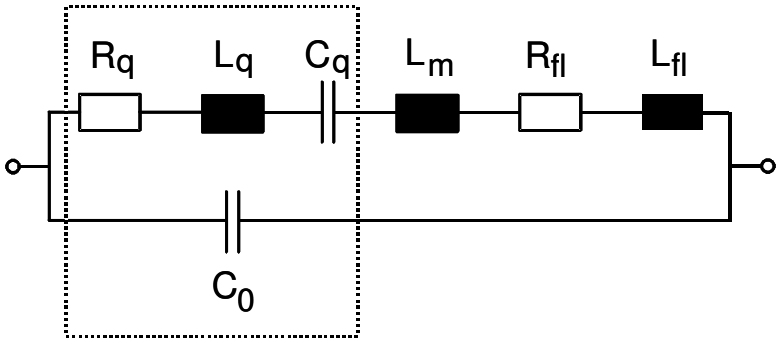

Fig. 3.22 Extended equivalent circuit derived from the BVD equivalent circuit for simultaneous loading of the resonator with a rigid mass and a Newtonian liquid (Martin et al., 1991).

However, it is noteworthy that impedance analysis only reveals the sum of all inductive, resistive and capacitive contributions, respectively, within the motional branch of the extended BVD equivalent circuit, including those of the resonator itself. They cannot be determined separately as the equivalent circuit implies:

$$L_{total} = L + L_m + L_{fl} \qquad R_{total} = R + R_{fl} \qquad C_{total} = C \qquad C_0 = C_s + C_p . \tag{3.24}$$

Loading the Resonator with Living Cells

The acoustic behavior of cells in contact to a quartz resonator is quite complex and does not fit to one of these categories described above. For this reason, the load material, i.e. the cell layer in contact with the resonator surface, is described by the complex load impedance Z_L. Reiß (2004) analyzed the impact of various cell types attached to a quartz resonator on the load impedance Z_L. A decomposition of Z_L into its real and imaginary part revealed that for all but one investigated cell lines the dissipated energy is always many times larger than the stored energy, showing a ratio between two and ten. A confluent cell layer apparently increases the energy dissipation from the shear oscillation whereas the impact on the stored energy is small, as just a minor shift of the impedance spectra to lower frequencies could be found. An appropriate theoretical model to describe the complex viscoelastic behavior of attached cells is still lacking (Li et al., 2005).

3.5.3 Experimental Procedure

Two different operational modes of the quartz resonators were used in this thesis. The active oscillator mode was used to monitor the adsorption of different proteins upon a polymer film spin coated onto a quartz resonator surface. In active mode, the resonator was integrated as the frequency-controlling element in an oscillator circuit, which compensates for energy losses thus allowing a stationary oscillation, and the series resonance frequency of the

oscillation was recorded with time. The decrease in resonance frequency was assumed to be proportional to the adsorbed mass of protein on the resonator surface.
In the case of a more complex load material, like mammalian cells, viscous damping must be taken into account. Therefore, the passive mode QCM or impedance analysis of the oscillation was used to characterize the long-term stability of spin coated polymer films in a physiological environment as well as the subsequent attachment and spreading of mammalian cells on these polymer surfaces. In passive mode, the resonator is forced to mechanically oscillate at a frequency which is determined by the frequency of the applied AC voltage, typically in the range of 4.97 – 5.05 MHz. Reading the impedance in the vicinity of the resonance frequency of 5 MHz provides detailed information about the shear oscillation and thus the mechanical properties of the load material.

3.5.3.1 The Measuring Chamber

All measurements were performed using the measuring chamber shown in Fig. 3.23. The core component of the QCM-measuring chamber is an AT-cut quartz resonator (Ø = 14 mm) with a fundamental resonance frequency of 5 MHz coated with circular gold film surface electrodes (Ø = 6 mm, piezoelectrically active area = 0.28 cm^2) on both sides (KVG, Neckarbischofsheim, Germany). A planar gold contact line on each side that leads from the circular electrode to the periphery of the resonator provides the electrical connection of the electrodes with the measuring hardware. The gold contact line on the upper side of the resonator is guided around the rim to the bottom of the resonator, allowing the electrical connection from the bottom side of the quartz plate. The measuring chamber itself consists of two main Teflon® elements: an upper part (Fig. 3.23 **2**) forming the culture vessel and a lower part (Fig. 3.23 **1**) containing spring-mounted gold contacts, so-called pogo pins. The quartz resonator is fixed between both Teflon elements via two Kalrez®-sealing rings on each side of the disk in order to prevent medium leakage. The two Teflon elements including the embedded quartz resonator are integrated in a massive Teflon housing (Fig. 3.23 **3**), enabling a stable oscillation.
When mounted in the measuring chamber, the upper side of the quartz resonator is exposed to the load material, serving as the sensing substrate, while the bottom is only in contact to air. The measuring chamber is mounted on a special holder connecting the surface electrodes via the contact pins to either the impedance analyzer (passive mode) or the oscillator circuit (active mode). The measuring chamber holds a total volume of 1.9 mL while the accessible surface area is 1.13 cm^2. In order to avoid evaporation and subsequent changes in the height of the meniscus, the complete chamber was closed airtight by a special stopper, as a stable oscillation can not be maintained otherwise due to the reflection of longitudinal waves at the liquid/air interface (Lin and Ward, 1995). These waves may result either from non-uniform velocity profiles along the shear direction or from non-ideal contributions from longitudinal or flexure acoustic modes in the quartz resonator which are coupled to the shear mode.

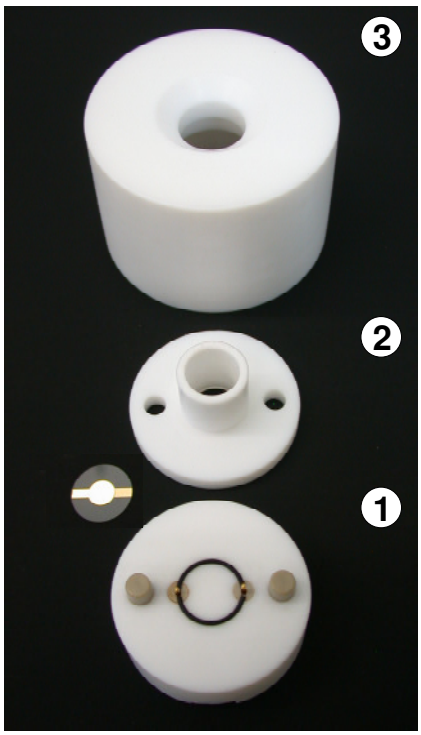

Fig. 3.23 Assembly of the measuring chamber as it is used for QCM measurements. The quartz resonator forming the bottom plate of the chamber is fixed between the Teflon elements **1** and **2**. The embedded contact pins in **1** electrically connect the surface electrodes of the quartz resonator via the electrical gold contact lines from the bottom side of the quartz plate.

With respect to the operational mode, the experimental setup differs regarding the sealing of the measuring chamber and the connection of the gold electrodes to the electrical driver units. Detailed information concerning these setups are given in the following chapters. Prior to any QCM experiment, the measuring chamber was sterilized and cleaned with ethanol. At the end of each experiment, parts of the measuring chamber were cleaned by sonication in Mucasol (5 mL/L in DI-water) and twice in DI-water for 15 min at 40 °C each.

3.5.3.2 Monitoring Protein Adsorption Using the Active Oscillator Mode QCM

In order to follow the adsorption of different proteins from solution upon a certain polymer film in a quantitative manner, the quartz resonator surface was spin coated with the respective polymer (chapter 3.2.2) before being mounted into the measuring chamber. All measurements were performed at (18 ± 1) °C in a closed experimental setup. The plastic (Teflon/Polyetherketone (PEEK)) stopper that seals the chamber is equipped with an inlet and an outlet. The first connects the chamber to a reservoir containing the protein solution while the latter is attached to a syringe. This allows the addition of protein solution at any given time by drawing it from the reservoir into the measuring chamber while monitoring the resonance frequency. Figure 3.24 shows a schematic of the experimental setup that was used to measure the change in resonance frequency versus time during protein adsorption.

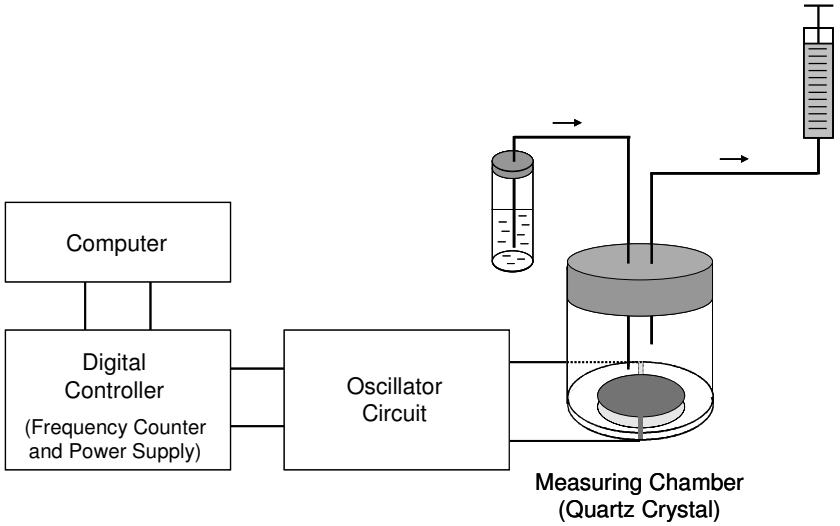

Fig. 3.24 Schematic diagram of the experimental setup used to monitor protein adsorption. The process was followed by reading the resonance frequency of the quartz resonator being operated in the active oscillator mode. An exchange of protein solution is performed by a transfer mechanism using a reservoir and a syringe. The measurement is controlled via a personal computer, which also records and stores the data. The measuring chamber is connected via shielded wires to the oscillator circuit.

The measurements were performed using the *SRS QCM200* system (Standford Research Systems, Sunnyvale, Canada) with C_0 compensation, which allowed simultaneous measurement of resonance frequency and energy dissipation in form of an equivalent loss resistance. The system includes a digital controller as well as the oscillator electronics. The oscillator circuit placed close to the resonator stabilizes the oscillation at series resonance frequency. The digital controller provides power to the oscillator electronics and contains a frequency counter for frequency measurements. The instrument is controlled with a personal computer, which collects and stores the experimental data with a time resolution of 1 s using the *QCM2000 main* software.

Protein Adsorption Assay

Protein adsorption was analyzed for polymer films of PS, PMMA, PDMS and PhoP. Except for PDMS, the polymers were used in two different modifications – an unmodified hydrophobic form as well as an argon plasma treated form, with the coated resonator being exposed to an argon plasma for 1 min before the measurement. This treatment renders the polymer surface hydrophilic to a certain extent, dependent on the respective polymer.

First, the measuring chamber was filled with DI-water, closed airtight by the plastic stopper and flushed with DI-water to get rid of remaining air bubbles which would otherwise influence the resonator's oscillation in a negative way. In order to prevent polymer swelling to interfere with protein adsorption, equilibration of each polymer was a prerequisite before starting protein adsorption measurements. Additionally, protein adsorption is supposed to be different upon a non-hydrated film compared to a liquid-incubated, swollen polymer surface, since the surrounding liquid can alter the polymer surface, for instance, its surface

homogeneity. After equilibration, which usually took about 1 h, the protein dissolved in DI-water was added from solution by injecting it into the reservoir and drawing it into the measuring chamber using the syringe. The respective protein was introduced to the measuring chamber with sequentially increasing concentrations exchanging the solution via the transfer mechanism described above every 30 min, i.e. the moment, when the resonance frequency had reached a stable value.

The protein solutions studied were bovine serum albumin (BSA), gelatin (Gel), collagen G (Col G), collagen IV (Col IV) and laminin I (Lam I) dissolved in DI-water at concentrations of 5, 10, 25, 50, 100 µg/mL (Lam I: 5, 10, 25, 50 µg/mL). NCS was diluted with SFM in order to obtain working concentrations of 0.1, 0.5, 1, 5 and 10 % (v/v). Here, polymer swelling was performed in SFM for a period of 1 h and the incubation time with each NCS concentration took 1.5 h.

Data Analysis

Protein adsorption was quantified from readings of the series resonance frequency over time (Fig. 3.25 A). The resonance frequency of the equilibrated polymer coated resonator after swelling was chosen as the basis relative to which the change in resonance frequency Δf due to protein adsorption was expressed.

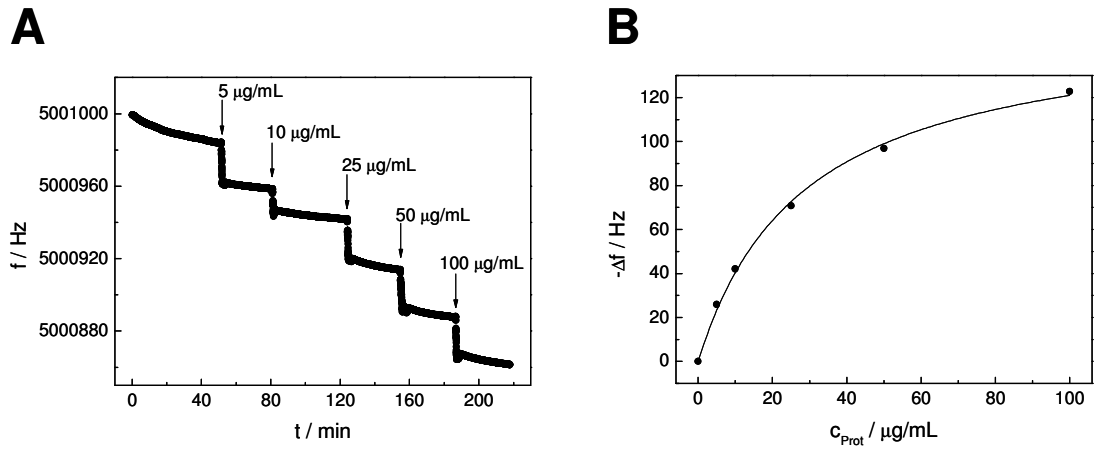

Fig. 3.25 A Time course of the resonance frequency of a PDMS coated quartz during the adsorption of Col IV from differently concentrated bulk solutions in water. The protein solution was added after a constant baseline was reached (arrow) and exchanged every 30 min by an increasingly higher concentrated solution. **B** Dependence of the resonance frequency shift on the protein concentration. The frequency shift Δf of the resonator as obtained by A is plotted against the respective protein concentration in the bulk solution. The frequency shift rises with increasing protein concentration up to a saturation level of $\Delta f_{max} = -(155 \pm 5)$ Hz. The solid line represents the fit according to the Langmuir adsorption isotherm (Eq. 3.25).

The shift in resonance frequency Δf upon protein adsorption was plotted against the respective protein concentration in the bulk solution for each protein of interest (Fig. 3.25 B). A Langmuir adsorption isotherm was chosen as a suitable model to analyze the experimental data. The respective equation has been found to describe with reasonable accuracy a large

number of adsorption reactions on plane surfaces if a monolayer of adsorbates is formed (Langmuir, 1932). The basic prerequisites for employing the Langmuir isotherm are a perfectly plane surface with no irregularities, energetic equivalence of all binding sites and the absence of interactions between adsorbate molecules on adjacent sites. Additionally, adsorption and desorption are assumed as being elementary processes and at dynamic equilibrium (Langmuir, 1932).
The Langmuir isotherm relates the adsorption of molecules on a solid surface to the concentration of the adsorbant in the bulk at a fixed temperature:

$$q = q_{\max} \cdot \frac{K_{ad} \cdot c_{prot}}{1 + K_{ad} \cdot c_{prot}}, \tag{3.25}$$

where q is the fractional coverage of the surface, $q_{\max}$ the coverage upon saturation, K_{ad} the Langmuir adsorption constant and c_{Prot} the protein concentration in the bulk solution.
Assuming the decrease in frequency to be proportional to the adsorbed mass of protein on the respective surface (Steinem et al., 1997), q can be related to the frequency shift Δf and $q_{\max}$ to the maximal frequency shift $\Delta f_{\max}$ upon saturation. The inverse of the adsorption constant K_{ad} describes the bulk protein concentration required for half-maximal coverage of the polymer surface with protein and is termed the $c_{50\%}$ value. The parameters were fitted to the experimental data and $c_{50\%}$ as well as $\Delta f_{\max}$ were used to characterize and compare the protein adsorption upon the various polymer surfaces.

3.5.3.3 Measurements Using the Passive Mode QCM

When dealing with a mechanically more complex load material than a simple rigid mass film, the load situation was analyzed by impedance analysis, using the passive mode QCM. This includes an analysis of the long-term stability of a polymer film in a physiological environment (PBS^{--} and SFM) as well as cell attachment and spreading upon these polymer surfaces. Additionally, experiments addressing the local sensitivity of the quartz oscillation to cell adhesion were performed.
The experimental setup which was applied to perform impedance analysis of the shear displacement of the resonator is depicted in Fig. 3.26. It allows impedance analysis of the shear displacement of the quartz resonator, termed **quartz mode**, and an impedimetric analysis of the passive electrical properties of the load material on the upper surface electrode, termed **ECIS mode** (electric cell-substrate impedance sensing; for further details see chapter 3.6). The combined approach is therefore called **double mode** impedance analysis. Thus, the mechanical and electrical properties of the load material on the resonator surface can be monitored in one experimental setup.

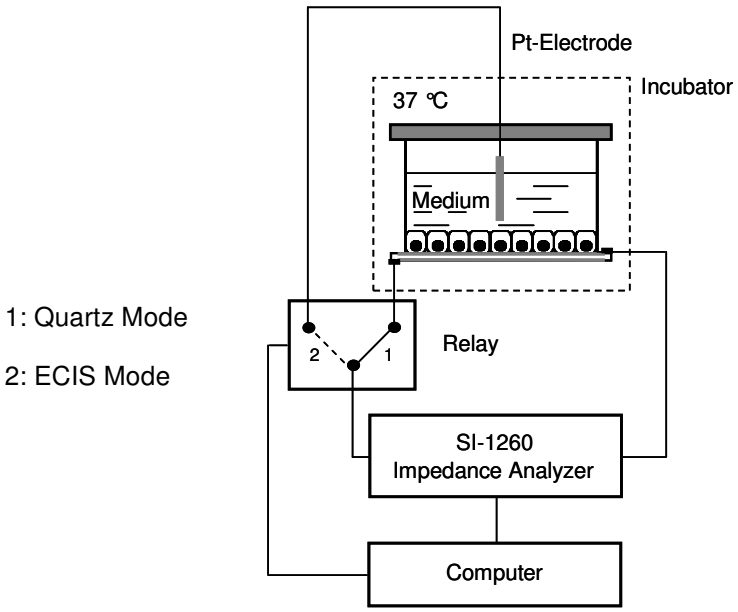

Fig. 3.26 Experimental setup used to perform double mode impedance analysis of a loaded quartz resonator. The measuring chamber is connected to an impedance analyzer (Solartron Instruments, SI-1260) via a relay switch, which allows to address two different measuring modes, i.e. the quartz mode **1**, recording the impedance spectrum of the quartz resonator close to its resonance frequency and the ECIS mode **2**, recording the electrochemical impedance spectrum of the top electrode facing the bulk electrolyte. The impedance analyzer as well as the relay is controlled via a personal computer, which records and stores the data.

For impedance analysis of the shear displacement (**quartz mode**) both, the upper and the lower surface electrode of the resonator were connected to the impedance analyzer (Solartron Instruments, SI-1260, UK) (Fig. 3.26 **1**). The impedance analyzer has a build-in frequency generator operating in the continuous-wave mode in a wide frequency range of 10 µHz to 32 MHz. Impedance data were continuously recorded in a way that the frequency range symmetrically embraced the resonance frequency of the quartz, usually using the frequency range of 4.97 MHz to 5.05 MHz. The amplitude of the applied sinusoidal AC voltage was adjusted to 150 mV. Within the given frequency range, 150 equally spaced data points were collected. The frequency-dependent complex impedance $Z(f)$ returned by the impedance analyzer is expressed as the magnitude of impedance $|Z|(f)$ and the phase shift $\varphi(f)$ between voltage and current (Fig. 3.27 A). The impedance analyzer was controlled via a personal computer using a custom-made *LabView* software (J. Wegener, Regensburg, Germany). The computer additionally collects and stores the experimental data.

In **ECIS mode** measurements, the upper surface electrode and a platinized platinum electrode dipping into the medium from above were connected to the impedance analyzer (Fig. 3.26 **2**). The gold electrode on the top side of the quartz disk serves as working electrode and the platinum electrode as the counter electrode. Further details for **ECIS mode** measurements, the respective parameters and the underlying principle are given in chapter 3.6.

Quartz mode followed by ECIS mode impedance spectra were recorded in a time interval of 2 min, using a computer controlled relay, which allows to sequentially switch between the two different measuring modes.

All measurements were performed in a humidified incubator at 37 °C with an atmosphere containing 5 % CO_2 and 95 % air. Only the analysis of the long-term stability of the polymer films in PBS^{--} was performed inside a temperature-controlled Faraday cage at 37 °C in order to maintain pH stability. All measurements were performed in a closed experimental chamber in order to avoid evaporation of fluid or bacterial contamination. The sealing of the chamber consists of a polycarbonate disk which is fixed to the measuring chamber using silicon grease. A hole in the middle of the plate allows for the platinized platinum electrode to be introduced into the medium. The electrode is mechanically fixed to the polycarbonate disk with silicon glue, sealing the measuring chamber and ensuring a constant depth of immersion.

Impedance spectra recorded in **quartz mode** were either analyzed by fitting the transfer function of the BVD equivalent circuit (Fig. 3.27 B) to the recorded phase spectra by means of a non-linear-least-square fit or the magnitude of the minimal impedance $|Z_{min}|$ was extracted from the raw data without any fitting routine (Fig. 3.27 A). Fitting routines were performed using a *LabView*-based software written by Joachim Wegener (university of Regensburg, Germany).

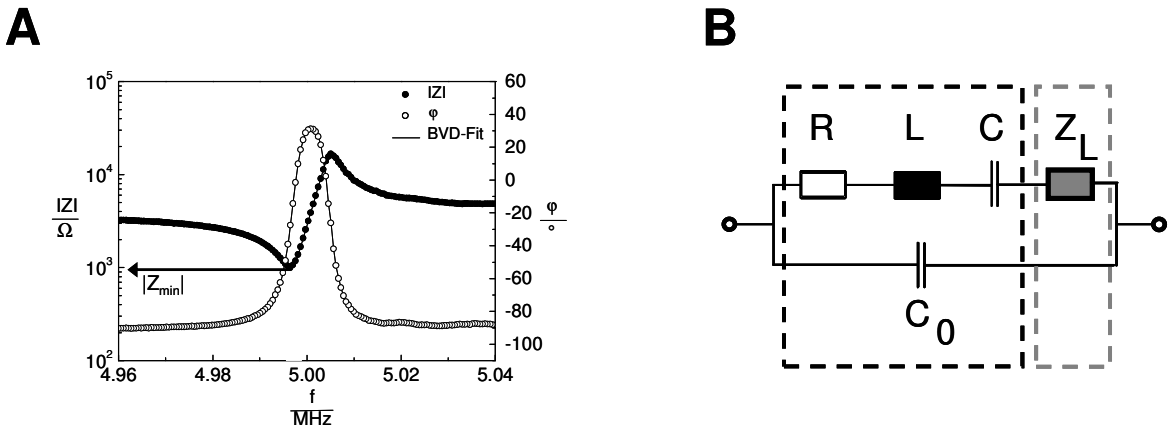

Fig. 3.27 A Bode presentation of the impedance and phase spectrum of a cell-covered quartz resonator near its fundamental resonance frequency of 5 MHz. The solid line represents the transfer function of the BVD equivalent circuit after parameter fitting. The arrow marks the magnitude of minimal impedance $|Z_{min}|$ which was used to follow cell attachment and spreading upon the resonator surface. **B** BVD equivalent circuit with the lumped impedance elements C_0, R, L, C and Z_L.

Figure 3.27 A shows an impedance spectrum in the Bode presentation as it is typically recorded for a quartz resonator covered with a confluent monolayer of MDCK-II cells. It is expressed in $|Z|(f)$ (filled circles) and $\varphi(f)$ (open circles). The corresponding BVD equivalent circuit (Fig. 3.27 B) contains the lumped impedance elements C_0, R, L, C and Z_L. As aforementioned, the serial connection of R, L and C represents the piezoelectric properties of the unperturbed quartz at frequencies close to resonance, whereas C_0 represents the dielectric properties of the quartz material away from resonance completed by parasitic contributions due to the experimental setup. The complex impedance Z_L represents the load material in contact with the resonator surface.

The surface loading was analyzed either in terms of changes of the real (load resistance R_L) and the imaginary components (load reactance X_L) of the complex load impedance Z_L or in terms of changes in magnitude of the minimal impedance $\Delta|Z_{min}|$ with respect to the values of the same fluid-loaded (PBS^{--}, SFM or culture medium) resonator which was the beginning of any QCM experiment.

Double Mode Impedance Analysis of Cell Attachment and Spreading upon an Uncoated Resonator

Prior to any cell inoculation the resonators were mounted in the measuring chamber and treated in an argon plasma for one minute providing both, an intense cleaning of the electrode surface from adsorbates and sterilization of resonator and chamber. Subsequently, the cell suspension was added to the measuring chamber. Suspensions of MDCK-II cells and NRK cells in culture medium were routinely prepared from confluent cell layers by standard trypsinization techniques (chapter 3.1.2). The cell density was monitored using a standard Bürker hemacytometer (LO-Laboroptik, Friedrichsdorf, Germany) and adjusted to yield 450.000 cells/cm^2. This guarantees a complete coverage of the entire quartz surface just by adhesion without the necessity of further cell division. The measuring chamber was subsequently closed with the platinum electrode containing cover and placed in an incubator at 37 °C (see also Fig. 3.26). Impedance data were continuously recorded to follow cell attachment and spreading with time as described before. The first spectrum after cell inoculation served as a cell-free control. Details about the recording of impedance spectra in ECIS mode are given in chapter 3.6.5.1.

Double Mode Impedance Analysis of the Long-Term Stability of Polymer Films

The long-term stability of polymer films was investigated by exposing the polymer coated quartz resonators to a physiological fluid at 37 °C while monitoring the impedance of the system using double mode impedance analysis. Polymer films on quartz resonators were prepared by spin coating the polymer from organic solution (chapter 3.2.2), yielding a quartz resonator whose upper surface was completely covered with a homogeneous mass film of one of the polymers: PS, PMMA, PDMS or PhoP. With the exception of PDMS, the long-term stability was analyzed for both the hydrophobic and the hydrophilic (plasma treated) form of the polymer. By contrast, PDMS was applied only in its unmodified form.
Each polymer film was subjected to two different physiological fluids – on the one hand PBS^{--} and on the other hand serum-free culture medium (SFM). The polymer coated resonators were mounted in the measuring chamber, the chamber was filled with the respective fluid (1.9 mL), closed with the electrode containing sealing and placed in an incubator (SFM) or a temperature-controlled Faraday cage (PBS^{--}) at 37 °C. The impedance data were recorded in double mode over a period of 20 h. The complementary ECIS mode measurements are described in chapter 3.6.5.2.

Quartz Mode Impedance Analysis of Cell Attachment and Spreading upon a Polymer Coated Resonator

The attachment and spreading of initially suspended MDCK-II and NRK cells on polymer films was followed with time. The resonator surface was first spin coated with the polymer of interest. Cell attachment and spreading was studied under a variety of processing conditions: i) unmodified polymer, ii) unmodified polymer + PBS^{--}/SFM incubation over 20 h, iii) plasma modified polymer or iiii) plasma modified polymer + PBS^{--}/SFM incubation over 20 h.

In the case of category i) and iii), cell suspensions were seeded on the polymer coated quartz resonators without any preceding incubation in a physiological fluid. The resonators were either argon plasma treated (1 min) or left untreated and mounted in the measuring chamber. MDCK-II or NRK cell suspensions were transferred into the measuring chamber as described for an uncoated resonator and impedance spectra were continuously recorded.

In the case of category ii) and iiii), cell suspensions were seeded on the polymer coated quartz resonators after the resonators had been incubated in a physiological fluid (PBS^{--} or SFM) over a period of 20 h. For all polymers under study, a period of 20 h was sufficiently long to finish the swelling process and was usually kept constant to provide identical conditions for QCM measurements. After swelling of the polymer films was complete, the respective fluid was removed and the cell suspension was transferred into the measuring chamber before data acquisition was started. Cell inoculation and other experimental parameters were as previously described. Since a polymer film electrically behaves like an insulator and therefore prevents the detection of a cellular monolayer on top of the polymer, additional ECIS mode measurements were therefore omitted.

As aforementioned, the polymer PDMS was analyzed only in the categories i) and ii), PhoP in the categories ii) and iiii), and PS and PMMA in all four categories (Tab. 3.3).

Tab. 3.3 Various processing conditions for spin coated polymer films upon which cell attachment and spreading was investigated.

Polymer	No Plasma, No Incubation	No Plasma, Incubation	Plasma, No Incubation	Plasma, Incubation
PS	✓	✓	✓	✓
PMMA	✓	✓	✓	✓
PDMS	✓	✓	–	–
PhoP[1]	–	✓	–	✓

Double Mode Impedance Analysis of Cell Attachment and Spreading upon Resonators with Partly Covered Surface Electrode

In order to address the sensitivity of the mechanical oscillation with respect to the location and size of the piezoelectrically active part of the surface electrode while simultaneously

[1] Processing conditions were omitted for technical reasons.

increasing the sensitivity of ECIS mode measurements, the upper gold electrode was completely coated with PhoP. By means of photolithography well-defined circular holes were introduced into the insulating PhoP film to expose the surface electrode to the bulk only at certain positions and with a fraction of the total electrode area (chapter 3.2.2, Fig. 3.3): (i) circular openings of either ~ 3 mm or ~ 0.5 mm diameter were introduced at the center of the surface electrode, or (ii) circular openings of ~ 0.5 mm diameter were introduced at the edge of the surface electrode. The exact size of the active electrode area was determined by taking a microscopic reflection image using the confocal laser scanning microscope.
These specially prepared resonators were similarily treated and analyzed with respect to their long-term stability as described before. Subsequently, the respective fluid (PBS^{--}/SFM) was removed and a suspension of MDCK-II cells was inoculated into the measuring chamber. Cell attachment and spreading upon the resonator surface was followed with time by recording impedance spectra in double mode, using the frequency range of 4.95 – 5.03 MHz in quartz mode.

Double Mode Impedance Analysis of Adherent Cells after Partial Removal of the Cell Layer

Another approach to address the local sensitivity of the mechanical oscillation of the quartz resonator to the surface load was to sequentially remove parts of a confluent MDCK-II cell monolayer, beginning with a small circular wound introduced in the cell layer in the center of the electrode while sequentially extending the wounded area to the edge of the electrode. For this purpose, stainless steel stamps with a PEEK (polyetheretherketone) head of variable diameters were pressed on the surface to generate centrally located wounds of a certain size in the cell layer. The procedure is depicted in Fig. 3.28:

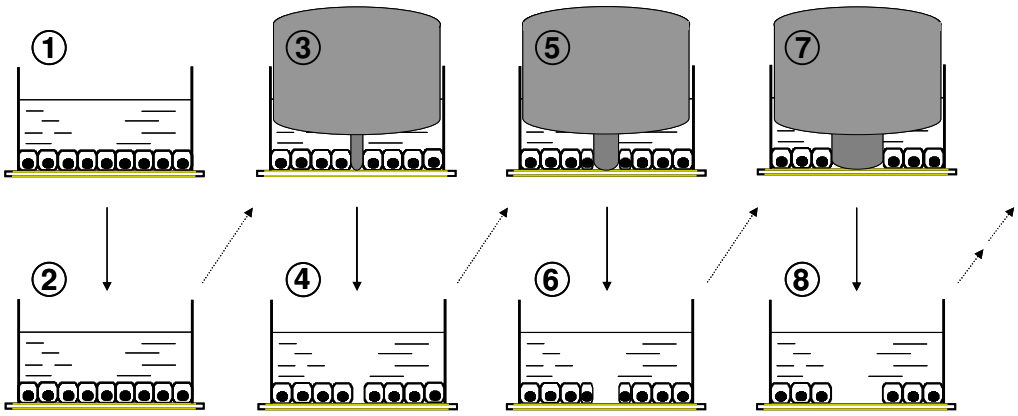

Fig. 3.28 Experimental setup to address the local sensitivity of the mechanical oscillation. A confluent monolayer of MDCK-II cells on the surface of a quartz resonator is removed stepwise, beginning with a small wound in the middle of the resonator. The wound is generated and sequentially extended using stamps of different diameters. The respective load situation on the quartz resonator is documented between successive steps using microscopic techniques and double mode impedance analysis.

MDCK-II cells were grown to confluence on a quartz resonator which was already mounted in the measuring chamber. 20 h after inoculation, the load situation on the quartz resonator was documented via a stereomicroscopic picture (chapter 3.7.3.2) and an impedance spectrum recorded in double mode (**2**). Thereafter, a wound was generated in the cell layer in the center of the electrode by pressing a stamp with a head of 1.0 mm diameter on the cell layer and turning it around (**3**). The stamp was removed, followed by documentation of the load situation via stereomicroscopy and impedance analysis (**4**). In a similar manner, the wound was sequentially extended to the rim of the gold electrode by using stamps of 2.0 mm and 3.0 mm diameter (**5**, **7**). Between each step the load situation on the resonator surface was documented (**6**, **8**). For further extensions of the wounded area and the final removal of the complete cell layer from the resonator surface, a rubber policeman was wiped across the resonator surface.

Double Mode Impedance Analysis of Wound Healing of NRK Cells on Resonators with Partly Covered Surface Electrode

The migratory properties of NRK cells on the small gold electrode (surface area ~ $2.2 \cdot 10^{-3}$ cm^2) designed on the quartz resonator by means of photolithography (chapter 3.2.2) were followed in double mode. NRK cells were seeded on the quartz resonator and their attachment and spreading was followed with time by continuously recording impedance spectra in double mode. After the formation of a confluent cell monolayer with stable electrical properties, the cells on the small gold electrode were wounded by applying an invasive electric field across the cell layer using an external frequency generator (for details see chapter 3.6.5.5). Subsequent to the wounding pulse the migration of intact cells from the electrode periphery onto the electrode was followed with time, using the frequency range of 4.95 – 5.03 MHz in quartz mode. Details about the recording of impedance spectra in ECIS mode are given in chapter 3.6.5.5.

3.5.3.4 Regeneration of Quartz Resonators

Depending on the load material, the resonators could be reused for several experiments. Resonators which were covered with a cell or a protein layer were cleaned by sonication in a detergent solution (Mucasol, 5 mL/L in DI-water) at 40 °C for 15 min, followed by two rinsing steps in DI-water (40 °C, 15 min). The resonators were dried under nitrogen flow or in an oven (37 °C, 24 h). In the case of polymer coated resonators, the polymer film was removed as described in chapter 3.2.2.

3.6 Electric Cell-Substrate Impedance Sensing

Electric cell-substrate impedance sensing (ECIS) is a versatile technique to monitor mammalian cells *in vitro* with important applications in various fields of biomedical research, since it is non-invasive and allows online monitoring with a high time resolution. The ECIS technique is capable of detecting morphological changes of adherent cells (cell behavior) caused by biological, chemical or physical stimuli, providing quantitative data with a time resolution down to seconds in a continuous, automated (computer-controlled) manner. The technique was introduced by Giaever and Keese in 1984 and has been continuously optimized (Giaever and Keese, 1984). It is based on measuring changes in AC impedance of small gold film electrodes upon which cells are deposited as a function of AC frequency used for excitation. The experimental setup comprises two electrodes: a small one termed working electrode (Ø = 250 µm) and a so-called counter electrode, which is approximately 500 times larger than the working electrode (Fig. 3.29; Wegener, 2003). Both electrodes – working and counter electrode – are electrically connected via the culture medium providing a closed electric circuit.

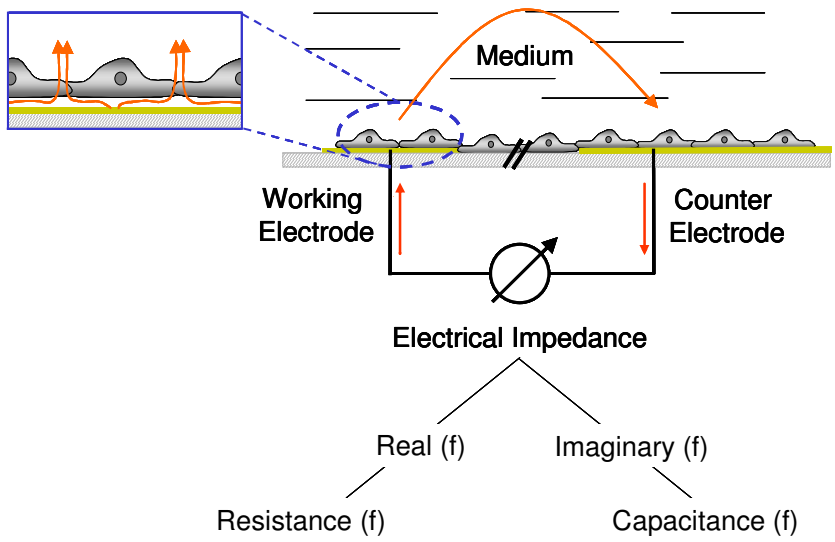

Fig. 3.29 Schematic of the ECIS principle, indicating AC current flow between the small working electrode and the larger counter electrode, using normal culture medium as the electrolyte. The arrows, which indicate AC current flow, are drawn unidirectional for clarity. Cells deposited on the electrode behave like insulating particles, constricting the current flow thus leading to an alteration in the impedance of the system.

The gold films serve as a growth substrate for the cells and electrodes for the electrochemical measurement, which results in a close proximity between cells and the underlying electrode, which is deceisive for the sensitivity of this technique. When current flows between the two electrodes, the difference in surface area of both electrodes (~ 500-fold) provides a much higher current density and voltage drop at the small electrode. Thus, the total impedance of the system is determined mainly by the impedance of the small working electrode. The

impedance of the counter electrode relative to the total impedance of the system is a fraction of a percent and can be ignored (Wegener, 2003).
Without cells, the current flows unrestrained from the surface of the electrodes. As cells attach and spread on the electrode surface, they act like insulting particles, forcing the current to flow around the cellular bodies on paracellular pathways at low frequencies. As a consequence, the impedance of the system increases compared to a cell-free electrode, dependent on the size of the remaining electrolyte-filled clefts between and under the cells. At high frequencies, the predominant part of the current passes through the cell membranes giving rise to capacitive reactance. These changes mainly reflect the capacitive nature of the non-conducting lipid-bilayer membrane of the cells. By scanning the sample impedance over a broad range of frequencies, it is possible to differentiate between impedance contributions arising from the cell-substrate contact and the cell-cell contact. The continuously repeated recording of impedance spectra allows to follow morphological changes of cells in real-time by calculating cell membrane capacitances and barrier resistance of epithelial cell layers.

3.6.1 Model of the Electrode-Cell Interface

The measured total impedance of a biological system has to be analyzed by using a physical model in order to allow for a detailed interpretation of the data. In 1991, Giaever and Keese developed a physical model to analyze the impedance spectra of cell-covered gold film electrodes as a function of frequency and to pinpoint impedance contributions from various cellular structures (Giaever and Keese, 1991). The model is shown in Fig. 3.30 and can be further described in physical detail by a corresponding equivalent circuit model (Wegener, 2003). Three individual circuit elements are combined in series, representing the individual impedances arising from the electrolyte, the confluent cell layer and the electrode. The ohmic resistor R_{bulk} represents the electrolyte resistance of the bulk electrolyte on top of the cell layer, whereas the CPE describes the interface impedance of the gold film electrode immersed in the electrolyte solution (equivalent to the specific impedance of a cell-free electrode). The additional impedance Z_{Cl} arising from the presence of the cells on the electrode can be further divided into three individual impedance parameters.

At low and medium frequencies ($f < 10$ kHz) the main part of the current takes the paracellular pathway, flowing through the cleft between the basal membrane of the cells and the electrode. This cleft underneath the cells has an average width between 10 and 200 nm (often < 100 nm), giving rise to one main part of the measured total impedance of the system in this frequency range. The impedance contribution from the subcellular region can be quantified by the parameter α. The intercellular cleft between two adjacent cells has similar dimensions as the space between cell and substrate. Thus, an additional resistance arises from the constriction of the current when flowing out between the cells, accounting for the second main impedance contribution described by the parameter R_b. When dealing with barrier-

forming epithelial cells, tight junctions are mainly responsible for the barrier function of the cells, which can therefore be quantified by the parameter R_b.

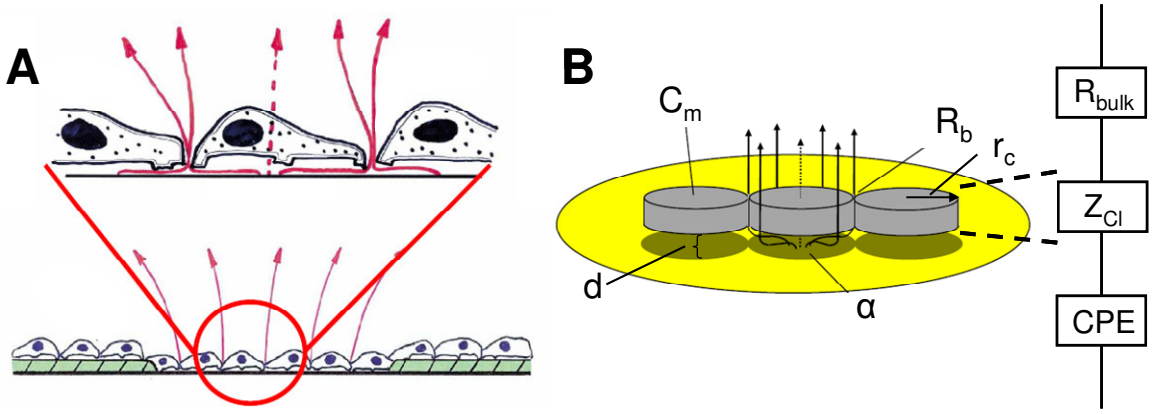

Fig. 3.30 A Model of the current flow from a cell-covered working electrode in electrolyte solution. The solid arrows represent the current flow at low and medium frequencies through the subcellular and intercellular cleft. The broken arrow represents the capacitive current flow at high frequencies through the cellular bodies taking the transcellular way right through the cell membranes (www.biophysics.com). **B** Model used for calculating the specific impedance of a cell-covered electrode (Giaever and Keese, 1991) and the corresponding equivalent circuit model (Wegener, 2003). The cells are treated like circular disks with the radius r_c that are separated an average distance d from the electrode surface. The cell-associated impedance Z_{CI} can be further divided into the impedance contribution arising from cell-substrate contacts quantified by the parameter α, the ohmic barrier resistance R_b of cell-cell contacts and the specific cell membrane capacitance C_m. R_{bulk} is the electrolyte resistance and the CPE describes the interface impedance between the electrode and the electrolyte.

At high frequencies ($f > 10$ kHz) the main part of the current passes capacitively through the cells, passing the basal and the apical cell membrane (transcellular pathway). The specific cell membrane capacitance C_m which can be extracted from impedance readings in this frequency region reveals information about the area of the cell surface, thus allowing to monitor time dependent changes of membrane protrusions or folding.

The model developed by Giaever and Keese allows the determination of the individual impedance arising from the cell-substrate contact and the cell-cell contact. The model parameters α, R_b and C_m can be used to describe morphological properties of the cells and their changes in a quantitative way.

The geometrical assumptions in the model about the shape of the cells are that they are treated as circular disks of radius r_c, that are separated an average distance d from the electrode surface. This approach is a valid approximation for the epithelial MDCK-II and epithelial-like NRK cells used in this thesis, which both reveal cobblestone morphology. With respect to the model as aforementioned, the total impedance of the cell-covered electrode Z_{total} is given by the following transfer function:

$$Z_{total} = \left[\frac{1}{Z_{CPE}} \left(\frac{Z_{CPE}}{Z_{CPE} + Z_m} + \frac{\frac{Z_m}{Z_{CPE} + Z_m}}{\frac{1}{2} \gamma r_c \frac{I_0(\gamma r_c)}{I_1(\gamma r_c)} + R_b \left(\frac{1}{Z_{CPE}} + \frac{1}{Z_m} \right)} \right) \right]^{-1} + R_{bulk} \qquad (3.26)$$

where

$$Z_{CPE} = \frac{1}{(i\omega)^n A_{El}} \qquad (3.27)$$

and

$$\gamma = \frac{\alpha}{r_c} \sqrt{\frac{1}{Z_{CPE}} + \frac{1}{Z_m}}, \qquad (3.28)$$

where Z_{CPE} is the specific impedance of the empty electrode and Z_m the total membrane impedance, i.e. the sum of impedance contributions arising from the apical and the basal side of the cell membrane.

$$Z_m = \frac{2}{i\omega C_m} \qquad (3.29)$$

where

$$Z_m = \frac{1}{i\omega C_{Cl}} \qquad (3.30)$$

and

$$C_m = 2C_{Cl}. \qquad (3.31)$$

C_m describes the specific membrane capacitance of a single cell membrane, whereas C_{Cl} is the specific capacitance of two cell membranes – apical and basal – in series. The ECIS experiment only allows to calculate the parameter C_{Cl}. By combining equation (3.30) and (3.31) the capacitance of one cell membrane C_m is calculated from Z_m. The fact, that many mammalian cells do not possess the same surface area or do not exhibit equal capacitance contributions for their apical and basal membranes is not accounted for. Thus, C_m is a measure for an average membrane capacitance across the cellular body. I_0 and I_1 are modified Bessel functions of the first kind of the order zero and one. A_{El} is the electrode surface area and R_b is the specific barrier resistance as described before. The parameter α, which is essential to evaluate the constraint of current flow under the cells, is given by:

$$\alpha = r_c \cdot \sqrt{\frac{\rho_{sub}}{d}}. \qquad (3.32)$$

It depends on the radius of the cells r_c, the average distance d of their basal membrane from the electrode surface, i.e. the width of the subcellular cleft, and the specific resistivity ρ_{sub} of

the electrolyte in the adhesion cleft underneath the cells. Thus, it is possible to draw conclusions from the experimental parameter α about the dimension of the cleft between cells and the underlying substrate.

In order to calculate the electrical parameters α, R_b and C_m, the transfer function of the equivalent circuit model is fitted to the experimental impedance spectra based on a method described by Wegener et al. (2000), using a non-linear least-square fit according to the Levenberg-Marquardt-algorithm. Fig. 3.31 shows a typical impedance spectrum of an empty electrode immersed in cell culture medium and the same electrode covered with a confluent monolayer of MDCK-II cells. The magnitude of the impedance is plotted versus the frequency in a double logarithmic manner. The solid line represents the transfer function after optimization of the model parameters.

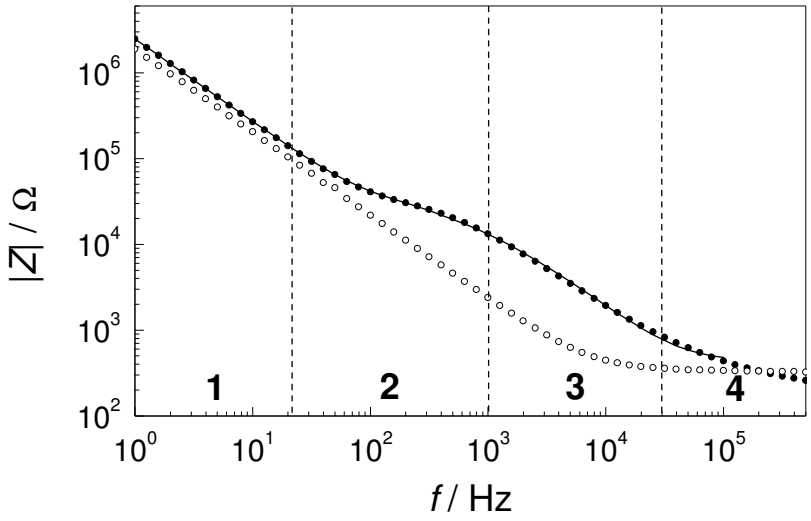

Fig. 3.31 Typical impedance spectrum of a cell-covered (●) compared to an empty (○) electrode only immersed in cell culture medium. The solid line represents the course of the fitted transfer function. The complete impedance spectrum can be separated in four different frequency bands (broken vertical lines), characterizing individual contributions to the total impedance. 1: CPE, 2: α, R_b, 3: C_m, 4: R_{bulk}.

At low frequencies (band 1) the impedance of the system is completely determined by the interface impedance of the electrode (CPE). At medium frequencies (band 2), the current flows paracellularly and the parameters α and R_b dominate the impedance spectrum. The fact that R_b is a frequency-independent parameter is reflected by the formation of a plateau in the impedance spectrum of the cell-covered electrode, which is typical for a confluent monolayer of barrier-forming cells. The parameter α can be inferred from the slope of this plateau. It exhibits resistive as well as capacitive behavior and characterizes impedance contributions arising from current flow underneath the cells. In the band of higher frequencies (3) the current passes through the cell membrane (transcellular path). Impedance analysis in this frequency regime provides the cell membrane capacitance C_m. The resistivity of the electrolyte R_{bulk} determines the total impedance in the frequency range between 10^5 and

10^6 Hz (band 4). Using the mathematical model, impedance data allow the determination of cell morphological parameters including the distance between the basal cell membrane and the substrate, the barrier resistance, and the cell membrane capacitance of confluent cell layers.

3.6.2 Micromotion

Living adherent cells in a confluent monolayer do not behave completely static, but they exhibit motility, performing continuous movements, i.e. small vertical motion in the sub-nanometer range, altering the distance between the basal cell membrane and the substrate as well as cellular shape (diameter). These movements have been electrically recorded by Giaever and Keese (1991) and are called micromotion. They are a major characteristic of living cells and can be correlated with their metabolic activity (Lo et al., 1993).
Due to its high sensitivity and a sub-second time resolution the ECIS technique is capable of detecting and quantifying the cellular micromotion. When the impedance is tracked as a function of time at a frequency sensitive for these movements, fluctuations in the impedance can be observed and directly attributed to cellular movement on the electrode (Giaever and Keese, 1991). The fluctuations in impedance are due to small variations in the parameters that describe the cell-substrate contact (α) as well as the resistance between cells (R_b).

Numerical Analysis of Micromotion Data

Micromotion data obtained from ECIS measurements can be analyzed by several different numerical methods (Lo et al., 1993). Prominent methods for analyzing the measured fluctuations and thus the cell motion comprise a variance analysis, a Fast Fourier transform (FFT) or an increment analysis. The latter was chosen in this thesis as it turned out to be the most sensitive method for the quantification of the impedance fluctuations. It is based on the calculation of the standard deviation of the increments between the subsequent data points for different time resolutions. By means of a typical data set (Fig. 3.32), showing the normalized impedance of a porous gold film electrode confluently covered with MDCK-II cells and measured at 500 Hz each second, the numerical method applied in this thesis is described in detail:

1. Each element of the recorded data set is divided by the time mean of all data points, which results in normalized values without dimension (Fig. 3.32 A).
2. Then, the increments are calculated by subtracting successive data points. For an original data set which consists of N points N-1 increments are obtained (Fig. 3.32 B). The mean and the standard deviation of all increments are calculated and the standard deviation of

the increments (SDI) is used as a measure to describe the impedance fluctuations of the original data set. Strong impedance fluctuations result in a high SDI value.

3. Subsequently, the data is treated as if it had been sampled every 2 s – in contrast to the original data which are sampled each second. Thus, every second element of the normalized data set is discarded. The remaining data set consists of *N*/2 elements. The increments are now calculated for this new data set. The standard deviation of the increments describes the impedance fluctuations for a time resolution of 2 s.

4. This process can be repeated for sampling intervals of 4, 8, 16, 32, 64, 128 or 256 seconds, continuously reducing the time resolution from 1 s to 256 s. The standard deviation of the increments can be calculated for each sampling interval plotted against the time resolution. This results in a versatile characterization of impedance fluctuations on different time scales. Dependent on the cells under study and the respective impedance fluctuations, a distinct sampling interval turns out to be the most sensitive one and is used to quantify the cellular micromotion under various conditions.

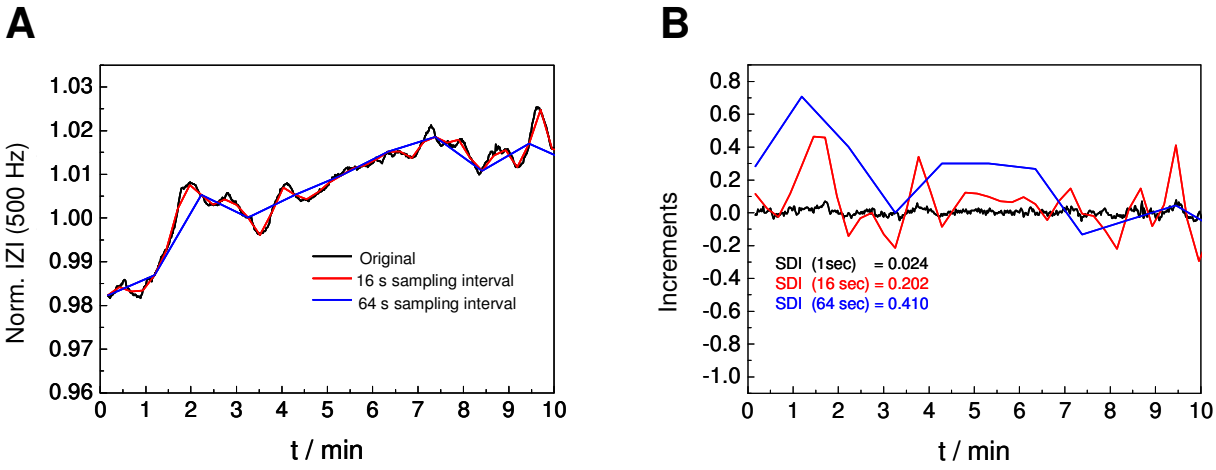

Fig. 3.32 Increment analysis of a typical micromotion data set. **A** Normalized impedance of an electrode confluently covered with MDCK-II cells as a function of time measured at 500 Hz with different sampling intervals (1 s, 16 s, 64 s). The original impedance data are sampled each second, whereas the other curves result from a reduction in the time resolution with sampling intervals of 16 s and 64 s, respectively. **B** Time course of the standard deviation of the increments calculated for the respective sampling intervals (1 s, 16 s, 64 s).

The numerical analysis of the standard deviation of increments – in contrast to the variance analysis – is less sensitive to certain trends caused by e.g. thermal drifting, which may influence the general course of the impedance fluctuations.

In this thesis, the micromotion of MDCK-II cells on different topographically structured surfaces in comparison to planar gold film surfaces was analyzed by looking at the averaged standard deviation of the increments for a sampling interval of 64 s, what revealed to be the most sensitive parameter to interpret the cellular impedance fluctuations.

3.6.3 Wound Healing

Wound healing assays are a widespread method to monitor and quantify the migration and proliferation of mammalian cells *in vitro*. A common way to wound cells *in vitro* is to apply a scratch wound to a confluent monolayer by mechanically disrupting the cell sheet with e.g. a small pipette tip. Subsequently, the migration of cells from the edge to the center of the wound is followed microscopically with time. Other means for applying an artificial well-defined wound to cells involve photochemical methods or an electroporation to insert membrane impermeable cytotoxic agents. Besides these techniques, the ECIS technique described above also provides the opportunity to wound cells in a confluent cell layer by applying an invasive electric field to the small electrode (Keese et al., 2004). Only cells directly bound to the small gold electrode (working electrode) are electrically wounded by being exposed to the invasive AC field for a short time of several seconds. The cell membranes are irreversibly damaged and permeabilized resulting in a subsequent cell death. The neighboring cells close to the electrode are not permeabilized and stay intact due to the restriction of the electric field to the active electrode. They start to close the wound by migrating from the periphery to the center of the electrode, thereby replacing the dead cell bodies. As the coverage of the gold film electrode is proportional to the capacitance change of the electrode at 40 kHz, the healing process can be followed with time in a quantitative way by recording the electrode impedance after the wounding pulse via the ECIS technique (Keese et al., 2004).
In order to achieve a complete, homogeneous and reproducible wounding of cells on the small electrode, it is necessary to choose the ideal wounding frequency, where the contribution of the cell layer to the total impedance of the system is most pronounced. This ensures that the major part of the voltage drops across the cell layer and not across the electrode-interface or the electrolyte. Thus, the most sensitive wounding frequency is exactly the frequency at which the cell layer contributes the most to the impedance spectrum. This can be determined by dividing the impedance spectrum of a cell-covered electrode by the spectrum of the respective cell-free electrode. The resulting impedance spectrum is called normalized impedance spectrum ($|Z|_{\text{cell-covered}}/|Z|_{\text{cell-free}}$) and shows a characteristic peak whose frequency indicates the frequency at which the electrical wounding is supposed to be most effective. The sensitive frequency is an adjustable parameter depending on the electrode size or the individual electrical properties – α, R_b and C_m – of the cells under study and was accordingly determined and adjusted with respect to the experimental situation.

In this thesis, NRK cells cultured on a small electrode (surface area = $2.2 \cdot 10^{-3}$ cm^2) prepared on a quartz resonator (chapter 3.2.2 and 3.5.3.3) were used for wound healing studies. The normalized impedance spectrum revealed a peak at the most sensitive wounding frequency, which in accordance to established wound healing assays for NRK cells on small ECIS electrodes ($5 \cdot 10^{-4}$ cm^2) was determined to 40 kHz. By using a 5 V pulse at 40 kHz, a 30 s application has been verified to result in a complete wounding of NRK cells on the small

electrode on the quartz resonator. ECIS measurements as well as a specific live/dead assay at different time points of the healing process (chapter 3.7.2.1) were used to follow the migration of intact cells from the periphery to the center of the electrode with time.

3.6.4 ECIS Measurements using Mesoporous Gold Film Electrodes

One part of this thesis was focused on the establishment of mesoporous silicon substrates to be used as a sensor system in order to characterize the interaction of cells with a topographically structured growth surface. Cellular behavior on topographically different substrates was biophysically analyzed in terms of cell adhesion and micromotion as well as cell morphology, quantified by the parameters α, R_b and C_m. MDCK-II cells were used as a model epithelial cell line, whose morphological parameters on different structured silicon substrates were quantified using the impedimetric ECIS technique. Cellular behavior on porous silicon substrates was compared to those on a planar, polycarbonate (Lexan®) surface used as a reference.

3.6.4.1 Mesoporous Silicon Substrates

The mesoporous silicon substrates used for ECIS measurements were kindly provided by Dr. Petra Göring (MPI for Mikrostrukturphysik, Halle, Germany) from the research group of Prof. Dr. Gösele. The mesoporous substrates are based on silicon wafers (1 cm x 1 cm) with pores on one side of the wafer. Two different types of mesoporous substrates were investigated. Type I contains pores that are arranged in a hexagonal lattice with a pore diameter of 1.3 µm, a depth of 10 µm and an interpore distance of 4.2 µm (lattice constant). Additionally, this substrate type exhibits inverted-pyramidal pre-etched areas that taper into a pore, so-called KOH-pits.

Tab. 3.4 Geometrical parameters of the mesoporous silicon substrates with (type I) and without (type II) KOH-pits.

Substrate Type	Pore Diameter [nm]	Ridge Width [nm]
I	1300	1700
II 1	700 – 750	1000
II 2	1000	750
II 3	1350 – 1400	360 – 400

Type II exhibits a lattice constant of 2 µm and a pore depth of 10 µm, but differences in pore diameter and width of the ridges. In contrast to the previously described substrate type I, here, the KOH-pits had been almost entirely removed. The parameters for all substrates are shown in Tab. 3.4. Corresponding SEM (scanning electron microscope) micrographs are presented in chapter 5.1 (Fig. 5.3).

3.6.4.2 Preparation of Gold Film Electrodes on Mesoporous and Planar Substrates

After cutting of the Lexan sheets (1 cm x 1 cm) and removal of the protection foils, the Lexan substrates as well as the silicon wafers were cleaned by sonication in Mucasol (5 mL/L in DI-water) for 15 min at 70 °C followed by a two time sonication in DI-water. Subsequently, they were dried in a nitrogen stream and stored in an oven at 37 °C over night.

Sputter Deposition of a Gold Film

In order to perform an electrical characterization, an electrode layout had to be applied on the surface of the mesoporous silicon as well as the planar Lexan substrates. Thus, the cleaned substrates were covered with gold by sputter deposition, using the sputter coater *Bal-Tec SCD 050* (Balzers, Liechtenstein). Sputter deposition describes a process, where some kind of material is ejected from a source (target), which then deposits onto a substrate. The substrates were placed on the specimen table in a sputtering chamber which was evacuated by a roughing pump. The chamber was flushed with argon several times in order to get rid of undesired gases and to get a pure argon atmosphere required for sputter deposition. Afterwards, the working pressure was adjusted to 0.05 – 0.1 mbar and the sputtering process was started by applying a high voltage field between the gold target (cathode) and the substrate holder (anode). The free electrons in this field collide with the argon atoms, knocking an electron out of the outer shell of an argon atom resulting in a positively charged argon ion. This cascading process leads to a glow discharge, which is called plasma. The positively charged argon ions are accelerated to the cathode (target) where they impinge, knocking out gold atoms due to the impact of the hit. These gold atoms ejected into the gas phase impinge on the substrate from all directions and condense evenly on it, forming a homogeneous gold layer. The sputtering process was conducted till the layer had reached a final thickness of 100 nm. The thickness of the sputtered film was controlled via a quartz crystal film thickness monitor inside the chamber, as the changes in resonance frequency are proportional to the deposited gold mass. After completion of the sputtering process, the chamber was flooded with argon and the substrates were removed.

Generation of the Electrode Layout using Photolithography

The electrode layout on the substrate surface was generated via photolithography (Fig. 3.33). Thus, the substrates were coated with PhoP (for detailed spin coating parameters see chapter 3.2.2). After spin coating, the substrates were baked for 30 min at 100 °C (soft bake). After the soft bake the photoresist was exposed to UV light for 2 min through a special mask containing the electrode layout. The mask was printed in black ink on a transparent film. The successive development of the UV exposed areas of the photoresist was performed by incubating the substrate in a NaOH (7 g/L) solution for 15 – 30 s, while gently moving it. The substrates were rinsed with DI-water and the exposed gold areas were now etched in an I_2/KI (4.7 g I_2 and 5.8 g KI in 70 mL DI-water) etch solution for 1 – 2 min. The etching process is based on:

$$I_{2\,(s)} + I^-_{(aq)} \rightarrow I_3^-{}_{(aq)} \tag{3.33}$$

$$2\,Au_{\,(s)} + I^-_{(aq)} + I_3^-{}_{(aq)} \rightarrow 2\,[AuI_2]^-_{(aq)} \tag{3.34}$$

The solubility of iodine in water is extremely low. Iodide promotes the solubility of iodine in aqueous solution by the formation of triiodide (Eq. 3.33). The triiodide ion serves as an oxidant for gold according to Eq. 3.34, leading to the dissolution of gold as the soluble Au(I)-diiodo complex (Qi and Hiskey, 1991; Davis and Tran, 1991). After rinsing the substrates with DI-water the remaining photoresist on the mesoporous substrates covering the gold electrode layout was stripped with acetone.

For polycarbonate (Lexan) substrates the last step of the procedure has to be changed as acetone would damage and dissolve the Lexan substrate. Thus, the dried substrates were exposed to UV light again for 2 min without any mask.

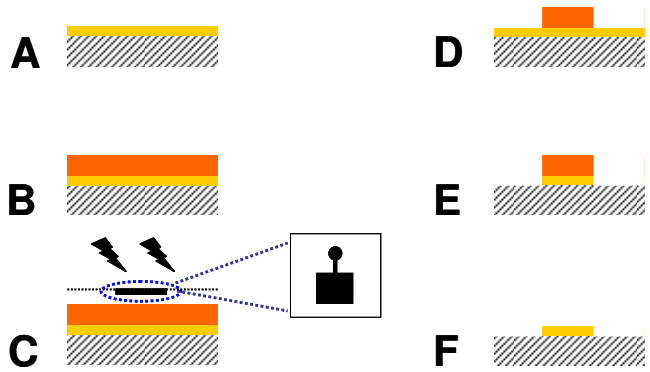

Fig. 3.33 Electrode preparation procedure. **A** Sputter deposition of gold (100 nm thickness) and the individual photolithographic steps to obtain the desired electrode layout on the mesoporous silicon as well as the planar polycarbonate surface (**B – F**). **B** Spin coating of the photoresist and successive soft baking. **C** UV light exposure of the photoresist with the attached mask. **D** Development of the exposed photoresist with basic solution. **E** Etching of gold with I_2/KI solution. **F** Stripping of the residual photoresist to free the gold electrode layout.

The substrates were subsequentially placed in the developing solution (7 g/L NaOH) for 2 min in order to strip the residual photoresist covering the gold electrode layout. After a final rinsing step with DI-water, the substrates were dried in a nitrogen stream or in an oven at 37 °C over night.

In order to guarantee gold electrodes with a definite surface area and to prevent that other parts of the gold film than the circular electrode contribute to the electrochemically active area, that part that led from the outer contact site to the small circular electrode inside the chamber (electrical connection) needed to be electrically insulated against the bulk electrolyte. Nail polish (top coat, Manhattan, USA) was used as a coating as it proved to be a suitable non-cytotoxic insulator in its cured state without affecting the electrode parameters during the electrical measurement. The electrical connection was insulated against the bulk with nail polish which was applied by using a thin brush and allowed to dry for at least 24 h at RT. In order to prevent leakage of the culture medium, only a small amount of nail polish was applied to insulate the gold path in the region where the sealing ring of the measuring chamber was located.
The electrode surface area was approximately 0.03 cm^2. The precise surface area of the electrode was determined from a microscopic reflection image recorded with a confocal laser scanning microscope.

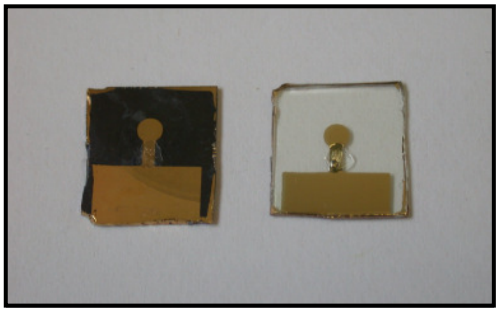

Fig. 3.34 Photographic image showing a mesoporous silicon substrate (left) and a planar Lexan substrate (right) with the gold electrode layout on top used for impedimetric ECIS measurements. The electrode layout consists of a small circular electrode (working electrode, 0.03 cm^2 surface area), an electrical connection and a big contact site. The electrical connection is insulated against the electrolyte by nail polish and connects the circular electrode, located inside the measuring chamber with the contact site, located outside the measuring chamber.

3.6.4.3 Experimental Setup and Instrumentation

In order to allow the cell-covered substrates to be electrically analyzed by the ECIS technique they were placed inside a self-made measuring chamber, forming a cell culture compatible vessel (Fig. 3.35). This chamber consists of a Teflon block containing three individual wells with a growth area of 0.14 cm^2 each and a supportplate, fixing the substrates to the Teflon block in a way that the circular gold electrode resides centrally under each well. In this ECIS

analog experimental setup, the circular electrode (0.03 cm^2) on the substrate surface serves as the working electrode. As a counter electrode a 200 µL pipette tip completely sputter coated with gold (thickness 100 nm) was used for each well, dipping into the culture medium from above.

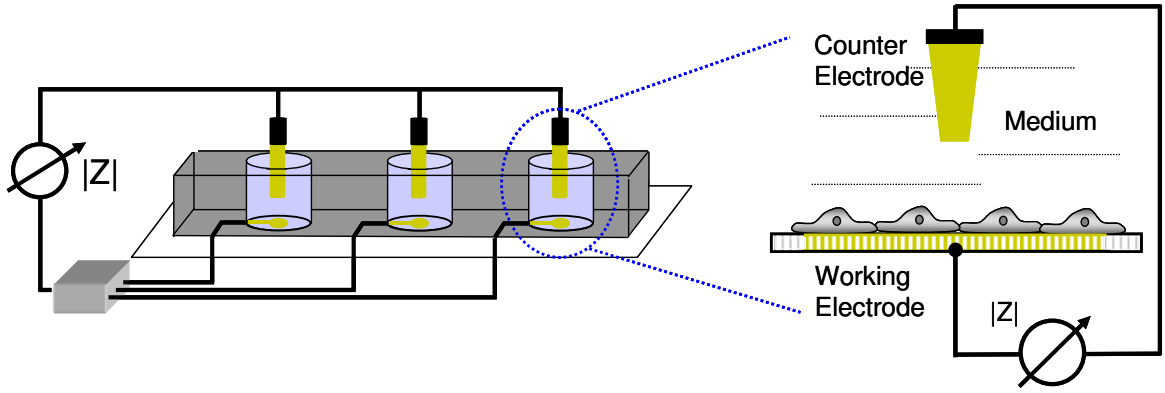

Fig. 3.35 Schematic drawing of the measuring chamber (left) and its magnification (right) for the impedimetric analysis of adherent MDCK-II cells on mesoporous and planar substrates. The counter electrodes dip into the culture medium from above and are connected in parallel with the impedance analyzer via a copper wiring. The polycarbonate lid covering the chamber is not shown for reason of clarity.

Due to the difference in surface area between working and counter electrode (~ 1000 fold) the contribution of the counter electrode to the total impedance can be neglected (chapter 3.6). The counter electrodes were fixed at the same distance between the individual wells with hot glue on the inner side of the polycarbonate lid of the chamber. Besides serving as a scaffold for the counter electrodes, the lid should also prevent evaporation of the culture medium. Additionally, the wells were covered with PDMS squares (1 cm x 1 cm) against evaporation (Fig. 3.36, 3). A stamped hole in the PDMS square allows the counter electrode to dip into the culture medium. PDMS sealing rings located between the Teflon chamber and the substrate were used to seal the medium from leakage. The three counter electrodes are connected in parallel to the impedance analyzer via copper wires, which were fixed to the pipette tips by hot glue and silver conductive adhesive. Spring-loaded gold contacts (pogo pins) embedded into the Teflon block of the measuring chamber and shielded copper wires are used to electrically connect the substrates to the impedance analyzer.

All measurements were performed in an incubator at 37 °C with a 5 % CO_2 atmosphere and 95 % relative humidity. A closed experimental setup was used (Fig. 3.36) in order to ensure sterile experimental conditions in the incubator. In order to allow an automated measurement of the three electrodes, a relay, connected to an impedance analyzer (SI 1260, Solartron Instruments, UK), was used to address the individual substrates in the measuring chamber. Relay and impedance analyzer were controlled via a personal computer, using a custom-made *LabView* software (written by J. Wegener, Regensburg, Germany). The computer additionally collects and stores the experimental data.

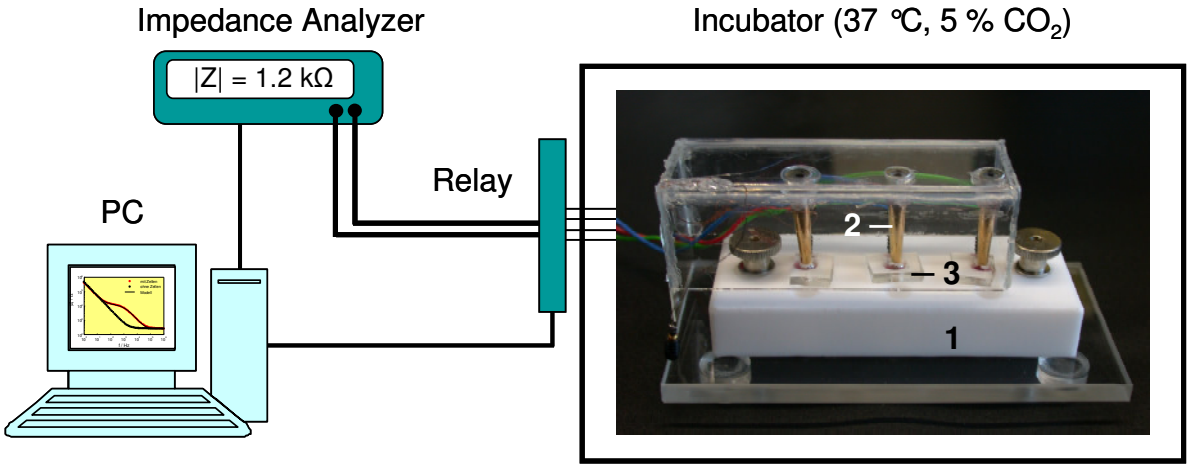

Fig. 3.36 The experimental setup used to perform ECIS measurements. The completely mounted measuring chamber consists of a supportplate, a Teflon block (**1**) with three individual openings and a polycarbonate lid containing the counter electrodes (**2**). The wells were additionally covered with PDMS squares to prevent evaporation (**3**). All measurements are performed in an incubator at 37 °C. The measuring chamber is connected via the relay with an impedance analyzer SI-1260 (Solartron Instruments). The impedance was followed in a frequency range from 0.1 Hz to 10^6 Hz.

3.6.4.4 Cell Attachment and Spreading on Mesoporous and Planar Substrates

Prior to any cell inoculation and subsequent ECIS measurements, the substrates as well as the sealing rings, the Teflon chamber and the lid containing the three counter electrodes were cleaned and sterilized in an argon plasma for one minute. Subsequently, the substrates were mounted into the measuring chamber in a sterile flow hood and the wells were filled with the cell suspension. Suspensions of MDCK-II cells in culture medium were routinely prepared from confluent cell layers by standard trypsinization protocols (chapter 3.1.2) and diluted to a final concentration of 1 Mio. cells/cm^2 after being counted using a standard Bürker hemacytometer (LO-Laboroptik, Friedrichsdorf, Germany). This ensures the establishment of a confluent cell layer without the necessity of further proliferation. The measuring chamber was subsequently closed with the electrode containing lid and placed in an incubator at 37 °C. Impedance data were continuously recorded to follow cell attachment and spreading over a frequency range of 10^{-1} – 10^6 Hz, with 10 points per decade and a time interval of 15 min. The amplitude of the applied sinusoidal AC potential was adjusted to 10 mV ensuring a sufficient signal-to-noise ratio while keeping the measurement non-invasive.

3.6.4.5 Micromotion Measurements on Mesoporous and Planar Substrates

After a confluent monolayer had been formed and the electrical properties remained stationary – which usually took 24 h after cell inoculation – the cellular micromotion was followed by tracking the impedance of one electrode as a function of time. The impedance of

the cell-covered electrode was recorded at a constant frequency of 500 Hz with the amplitude of the applied AC potential set to 20 mV. Two data sets were recorded over a time period of 20 min with a time resolution of one second for each electrode.

After the measurement the cells were removed by incubating the substrates in trypsin (2.5 % in PBS^{--} for 1 h at 37 °C), followed by an extensively rinsing with DI-water. The empty electrodes were characterized using fresh culture medium as electrolyte. The impedance was recorded over the frequency range from 10^{-1} to 10^{6} Hz and in the micromotion mode at 500 Hz using the same parameters as for cell-covered electrodes. The electrical parameters of the empty electrodes serve as a reference for the parameters of the cell-covered electrodes.

3.6.4.6 Regeneration of the Substrates

Due to their limited availability, the mesoporous substrates needed to be regenerated. As long as the electrode layout was undamaged, the substrates were reused for several experiments after being cleaned with detergent solution, DI-water and dried (37 °C, 24 h). Often, parts of the gold pattern were scratched, preventing a proper electrical connection in future experiments. In this case, the mesoporous substrates were completely regenerated, while first, the nail polish insulation was removed by incubation in acetone for 5 min. After a rinse cycle in DI-water, the gold film was removed by incubation in a I_2/KI etch solution for 2 min. The substrates were rinsed in DI-water several times, followed by a piranha solution cleaning (H_2O_2 (30 %) : H_2SO_4 (97 %) = 1:3) for 2 min to remove organic impurities. After a rinsing step with DI-water, the substrates were treated with a detergent solution (Mucasol, 5 mL/L in DI-water) at 40 °C for 15 min in an ultrasonic bath. The substrates were sonicated twice in DI-water (40 °C, 15 min) to wash residual inorganic acid as well as Mucasol out of the pores of the substrates. Finally, the substrates were dried in an oven (37 °C, 24 h). Lexan substrates with a damaged electrode layout were not recycled.

3.6.5 ECIS Measurements on Quartz Resonators

The principle of the ECIS technique can be transferred to bigger gold electrodes like the ones used for quartz resonators (surface area 0.33 cm^2), allowing for a combination of both impedimetric techniques, ECIS and QCM, in one experimental setup (chapter 3.5.3.3, Fig. 3.26). This opens up the possibility to follow and analyze the electrical and microgravimetric properties of the load material on the resonator surface simultaneously.
To perform electrochemical impedance analysis of the load material on the upper gold electrode of the quartz resonator using the **ECIS mode**, an additional platinized platinum dipping electrode was introduced into the QCM chamber that served as a counter electrode. The platinization of the counter electrode, i.e. the galvanic deposition of amorphous platinum,

causes an increase of the electrode's capacitance because the porous structure of the deposited metal causes an enormous increase in the electrode's surface area. This ensures a difference in surface area between working and counter electrode. In most cases, concomitant **quartz mode** measurements were performed (chapter 3.5.3.3) to complement the **ECIS mode** readings.

3.6.5.1 Cell Attachment and Spreading upon an Uncoated Resonator

Parallel to the impedance analysis in quartz mode (chapter 3.5.3.3.) attachment and spreading of initially suspended MDCK-II or NRK cells upon an uncoated quartz resonator (working electrode = 0.33 cm^2) were followed with time using ECIS mode. The experimental procedure is described in chapter 3.5.3.3. Impedance spectra were continuously recorded every 2 min using a sinusoidal AC voltage with an amplitude of 10 mV in the frequency range between 1 Hz and 10^6 Hz reading a total of 60 data points that were chosen to be equidistant on a logarithmic scale.

3.6.5.2 Long-Term Stability of Polymer Films

To address the long-term stability of PS, PMMA, PDMS and PhoP films, ECIS mode measurements on quartz resonators were performed by tracking the impedance of the polymer coated top electrode of the resonator while it was treated with a physiological fluid, i.e. PBS^{--} or SFM, at 37 °C. The polymers were investigated in their unmodified and their plasma modified form. Details concerning the experimental setup are described in chapter 3.5.3.3. ECIS mode measurements were performed over a period of 20 h using a sinusoidal AC voltage of 10 mV amplitude in the frequency range of 1 Hz to 10^6 Hz reading a total of 60 data points.

3.6.5.3 Cell Attachment and Spreading upon Resonators with Partly Covered Surface Electrode

The quartz resonators used in this study exhibit a gold electrode with a surface area of 0.33 cm^2. This is much larger than for working electrodes usually applied in ECIS experiments, leading to a reduced sensitivity of the recorded ECIS mode impedance signal. An increase in sensitivity of ECIS mode measurements could be achieved by covering the major part of the resonator surface with PhoP with exception of a small circular area of ~ 3 mm or ~ 0.5 mm diameter introduced by photolithography (chapter 3.2.2). This procedure reduced the area of the resonator's top electrode with access to the bulk electrolyte significantly. The circular opening in the PhoP overlayer was either centrally located or

resided at the edge of the underlying gold electrode. After having incubated the coated resonator in a physiological fluid, MDCK-II or NRK cells were seeded on the prepared quartz resonator according to chapter 3.5.3.3 and cell attachment and spreading was followed with time, recording impedance spectra using the same parameters as aforementioned.

3.6.5.4 Double Mode Impedance Analysis of Adherent Cells after Partial Removal of the Cell Layer

The partial removal of an initial confluent MDCK-II cell layer, grown on a quartz resonator, should give an insight into the local sensitivity of the mechanical quartz oscillation. The procedure to remove parts of the cell layer by gradually extending the wounded area is described in chapter 3.5.3.3. Parallel to the microgravimetric analysis the load situation on the resonator surface was documented by recording impedance spectra in ECIS mode after each step of the sequential cell layer removal. Experimental parameters were similar to those described above.

3.6.5.5 Double Mode Impedance Analysis of Wound Healing of NRK Cells on Resonators with Partly Covered Surface Electrode

The migratory properties of NRK cells on the small gold electrode designed on the quartz resonator (surface area = $2.2 \cdot 10^{-3}$ cm^2) were followed in ECIS mode.
NRK cells were seeded on the quartz resonator and their adhesion and spreading process was followed with time by continuously recording impedance spectra in double mode. After the formation of a confluent cell monolayer with stable electrical properties, the cells on the small gold electrode were wounded by applying an invasive electric field across the cell layer using an external frequency generator. The frequency for wounding the cell layer was set to 40 kHz according to established wound healing assays with NRK cells on commercially applied ECIS electrodes. Time and intensity of the elevated voltage were adjusted to 30 s and 5 V. Subsequent to the wounding pulse the migration of intact cells from the electrode periphery onto the electrode was followed with time via impedimetric ECIS measurements. Details concenring the concomitant quartz mode measurement are given in chapter 3.5.3.3.

3.7 Microscopic Techniques

3.7.1 Phase Contrast Microscopy

Phase contrast microscopy is a type of light microscopy which can be used to produce high-contrast images of thin, transparent objects such as living cells, which are otherwise almost invisible by bright-field transmitted-light microscopy. This is achieved optically without altering the cells by staining. Differences in the refractive index (density) or the thickness of a specimen are transformed in variations in light intensity, making a transparent specimen visible in contrast to its surrroundings.

Light that passes through a medium other than vacuum is altered in its amplitude or phase, depending on the properties of the medium. In the case of a thin, optically transparent specimen, an illuminating beam of light becomes divided into two components when it encounters the object: it either passes through and around structures in the specimen unaffected, termed direct or undeviated light, or is diffracted by structures present in the specimen, termed deviated light. Both, the specimen's refractive index as well as its thickness cause the light to be altered in velocity (http://www.microscopyu.com). Is, for example, the refractive index of the specimen greater than that of the surrounding medium, the propagation velocity of the wave is reduced, meaning the wavelength is reduced. Thus, the optical path (number of waves) increases while the geometric path remains constant. While passing through a transparent specimen, the deviated light travels a greater distance in comparison to direct light and is subsequently phase shifted when it emerges from the specimen. For most biological objects it lags behind the direct light by approximately ¼ wavelength and arrives at the image plane out of phase (Sanderson, 2001). This relative phase difference of ¼ wavelength between the direct and the deviated beam is due to local differences in density and composition of the specimen. However, it is not visible by eye, since the amplitude of the interference of direct and deviated light at the image plane is almost the same as that of direct light (http://www.mikroskopie.de). It is noteworthy that the detection of a high-contrast specimen image depends on the relative intensity difference, and therefore on the amplitudes of the direct and deviated light. This undiminished intensity results in very little specimen contrast, hardly detectable by eye or camera when superimposed against the bright background.

The phase contrast technique is based on an optical mechanism to translate these small invisible phase variations introduced by the specimen into visible amplitude variations of the light, which appear as differences in light intensity. To render these specimens visible two additional optical elements are added to the microscopic setup (Fig. 3.37): a phase plate is integrated into the objective and a condenser annulus is placed directly under the lens of the condenser. The phase plate increases the phase difference between the direct and deviated light by advancing the phase of the direct light by ¼ wavelength, while leaving the deviated light unaffected, leading to a net phase shift of ½ wavelength between the two beams. Thus,

the two sorts of beams recombine at the image level of the eyepiece by destructive interference, which leads to a significantly reduced amplitude of the resulting wave if the light originates from a stray center of the specimen. The contrast of the image is considerably increased, showing details of the transparent specimen in dark against a lighter background. The phase plate which shifts the phase of direct light by ¼ wavelength contains a narrow ring shaped area, termed phase ring, and resides in the rear focal plane of the objective. This area is optically thinner than the rest of the plate. Direct light passing through the phase ring travels a shorter distance in traversing the glass of the objective than does the deviated light.

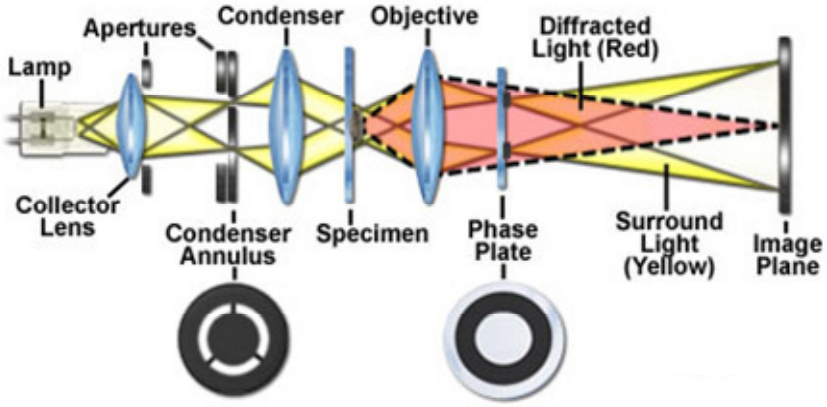

Fig. 3.37 Optical train of the phase contrast microscope (http://www.microscopyu.com). Light that passes through the specimen undeviated hits the phase ring where a phase shift of ¼ λ is introduced. The light deviated by the specimen remains predominantly unaffected by the phase ring.

To make sure that only the phase of the direct light is selectively advanced by ¼ wavelength while leaving the deviated light unaffected, it is of crucial importance to separate the two beams from one another at the rear focal plane of the objective. This is achieved by a condenser annulus, a ring annulus, placed directly under the lens of the condenser in its front focal plane, matched in diameter and optically conjugated to the phase plate. Thus, the beam illuminating the field of view is constrained, forming an annular image in the rear focal plane of the objective when passing through the specimen undeviated and hitting the phase ring. The light deviated by the specimen is spread over the entire rear focal plane of the objective and remains predominantly unaffected by the phase ring. The phase plate does not only alter the phase of the direct light, it also alters its amplitude. The direct light is much brighter than the deviated one because there are fewer deviated than undeviated photons at the image point. In order to adjust the intensities of the direct and the weaker deviated light which is equivalent to increasing contrast, a thin absorptive transparent metallic layer is deposited on the phase ring and reduces the amplitude of the undeviated beam travellling through the condenser annulus (Sanderson, 2001). Thus, a high contrast image is obtained when the deviated and the undeviated beams recombine by destructive interference at the image level.

In this study, phase contrast microscopy was applied to characterize the attachment and spreading of MDCK-II and NRK cells on various polymer surfaces with time. Phase contrast images were taken using the inverted *Leica DM IRB* microscope (Wetzlar, Germany) with the 10x magnification objective (N PLAN L 10x / 0.25).

Microscopic Study of the Adhesion Kinetics of Mammalian Cells on Polymer Films

A microscopic study documenting the adhesion kinetics of mammalian cells on the polymers PS, PMMA, PDMS and PhoP was performed by taking phase contrast images at regular time intervals after cell inoculation. This allows for a systematic correlation between microscopic observation of cell attachment and spreading (degree of confluence) with the impedance signal measured in quartz mode. Ordinary microscopic coverslips were used as substrates and spin coated with a thin layer of the respective polymer (chapter 3.2.2). The coated polymer films were thin enough to be transparent, so that cell growth on top of these polymers could be documented by an ordinary light microscope. Confluent monolayers of MDCK-II and NRK cells were removed from the culture flask by standard trypsinization protocols (chapter 3.1.2) and seeded onto the polymer coated coverslips residing in 24-well plates with a cell density of 450.000 cells/cm^2. The surface coverage of the polymer films (cell attachment and spreading) was documented by acquisition of phase contrast images after 2, 4, 6, 8, 10, 24 and 48 h.

3.7.2 Fluorescence Microscopy

Fluorescence microscopy is a type of light microscopy whose major use is to visualize fluorescence emission from a sample upon irradiation with excitation light of a specific wavelength. The principle of fluorescence is the following: certain atoms or molecules absorb light of a particular wavelength and thereby are excited from the lowest vibrational level of the electronic ground singlet state (S_0) to an accessible vibrational level in an electronic excited state (S_1). After excitation, the molecule is quickly relaxed to the lowest vibrational energy level of the excited electronic state. This process is called internal conversion (IC) and lasts between 10^{-13} s and 10^{-12} s. From this state, the system relaxes after a brief interval, termed the fluorescence lifetime (10^{-8} s), to an allowable vibrational level in the electronic ground state. The routes to loose the rest of the absorbed energy include a number of possible pathways, like radiative decay pathways, i.e. molecular deexcitation processes accompanied by photon emission, called fluorescence, and nonradiative relaxation processes where the excitation energy is dissipated by thermal processes such as vibrational relaxation and collisional quenching. Another possibility for certain molecules to relax to its ground state is the spin conversion to the lower energy first triplet state through intersystem crossing (ISC)

and relaxation to the singlet ground state accompanied by photon emission (phosphorescence). The fluorescent light which is emitted during the relaxation process possesses a longer wavelength than the absorbed light (Stokes shift). The process of photon absorption and subsequent fluorescence is illustrated in the following Jablonski diagram (Fig. 3.38).

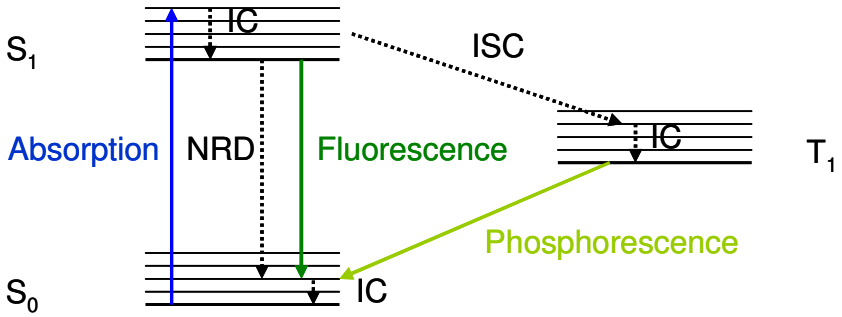

Fig. 3.38 Jablonski diagram illustrating electronic transitions including excitation, radiative and nonradiative decay (NRD) pathways. S_0 is the ground singlet state, S_1 is the successively higher energy excited singlet state and T_1 is the lowest energy triplet state. Each electronic state is split into multiple sublevels, representing the vibrational modes of the molecule. Upon irradiation, the molecule is excited from the ground state S_0 to any vibrational level of a higher energy S_1 state. IC is the rapid internal conversion to the lowest vibrational level in the excited state. From this state, energy is lost by nonradiative decay and by emission of a photon (fluorescence).

Light sources used for the excitation of fluorophores could be either lamps exhibiting a line spectrum like mercury vapor lamps (sometimes xenon arc lamps) or lasers which are applied in scanning systems. Mercury lamps have a relatively strong output (at 360, 405, 546 and 578 nm) and are therefore well-suited to excite multiple fluorophores of different spectral characteristics. The desired excitation wavelength, i.e. light in the region of the spectrum where the absorption maximum of the fluorophore is located, is adjusted by using a narrow-bandpass exciter filter. The emission is detected through an emission or barrier filter (longpass filter) that allows the emitted fluorescent light to pass while blocking all shorter wavelengths below the emission band. As a consequence, the fluorescing areas shine out against a dark background which can be detected by eye or camera.

In the most commonly used illumination system, the so-called epi-illumination, excitation and emission light are directed by the same lens: the objective thus also serves as a condenser. A dichroic beam splitting mirror separates the excitation from the emission light. The shorter wavelength excitation light is reflected through the back aperture of the objective onto the specimen. The longer wavelength emitted fluorescence light is also collected by the objective, passing through the dichroic mirror to either the eyepieces, a camera or an electronic multiplier where the image is formed (Jacobson, 2001). The selection of filter sets (exciter and barrier) is of crucial importance to obtain a good fluorescent image, as both, the specific brightness of the image of the fluorophore as well as the contrast between the fluorophores and the background are affected by this combination (Kramer, 1999). Fluorescence microscopy makes it possible to identify cells and cellular components with a high degree of

specificity. It is therefore the basis for various cell biological and immunological techniques like fluorescent or immunofluorescent stains.

In this study, fluorescence microscopy was used to perform wound healing studies of NRK cells on specially designed electrodes on quartz resonators as well as to document the status of the actin cytoskeleton of initially suspended MDCK-II cells, seeded on a gold or a PhoP surface. Fluorescence micrographs were taken with the upright *Leica TCS SL* microscope (Wetzlar, Germany) using 10x (HCX APO L 10x/0.30W) and 63x (HCX APO L 63x/0.90W) magnification water immersion objectives. For image documentation, the microscope is equipped with a digital video camera (*Leica DC 300 F*, Wetzlar, Germany) connected to a computer.

3.7.2.1 Live/Dead Assay of NRK Cells to Document Wound Healing after Electric Wounding

In parallel to ECIS mode measurements monitoring the migration of NRK cells to repopulate the small gold electrode prepared on the resonator surface (surface area = $2.2 \cdot 10^{-3}$ cm^2) after wounding (chapter 3.6.5.5), cell death as well as the subsequent migration of intact cells from the electrode periphery inward was followed using viability stainings at different time points of the healing process. The applied live/dead viability/cytotoxicity kit (Molecular Probes, Göttingen, Germany) is a two-color fluorescence assay that allows the simultaneous determination of live and dead cells. The kit consists of the bioactive calcein acetoxymethyl ester (CaAM) and ethidium homodimer-1 (EthD-1). The viability of cells is determined on the basis of intracellular esterase activity in the cytoplasm of living cells as well as plasma membrane integrity.

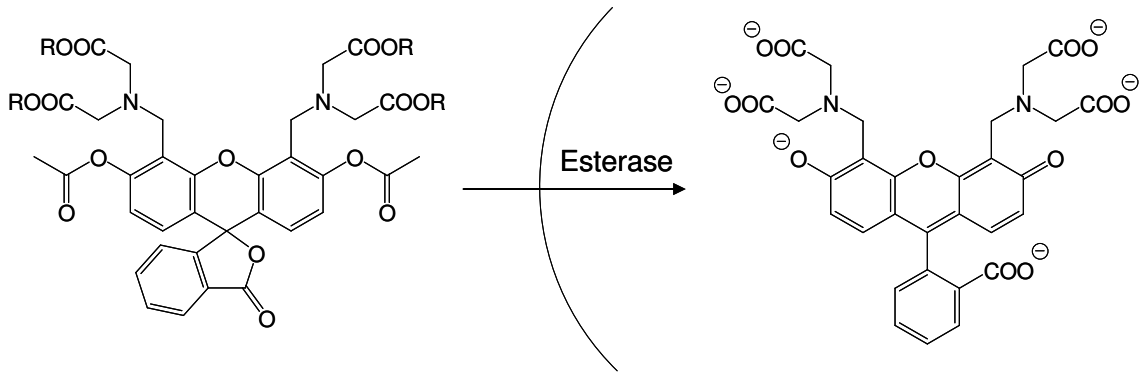

Fig. 3.39 Schematic illustration of the hydrolization of non-fluorescent CaAM to the green fluorescent calcein by intracellular esterases. Cleaved calcein is polyanionic and remains within the cells (R = CH_2OCOCH_3).

Vital cells have intracellular esterases that hydrolyze non-fluorescent, cell-permeable CaAM to the green fluorescent calcein (ex/em: ≈ 494 nm/≈ 517 nm). Calcein is polyanionic and thus

a membrane-impermeable substance which is retained inside the cytoplasm (Fig. 3.39). A green cytoplasmic fluorescence is therefore an indicator for cellular esterase activity as well as an intact membrane which retains the esterase products and therefore serves as viability marker.
EthD-1 was used together with CaAM to selectively stain non-viable cells with damaged membranes. EthD-1 is a high-affinity, red-fluorescent nucleic acid stain that is not able to cross an intact cell membrane. However, it is able to enter the cells by diffusing through damaged cell membranes as they can be typically found in dead cells. Once entered the cells, EthD-1 intercalates in the double-stranded DNA and forms a fluorescent complex. The DNA-EthD-1-complex produces a bright red-orange fluorescence (ex/em: ≈ 528 nm/617 nm) in damaged or dead cells. This combined approach allows for a selective staining of vital and dead cells which can be discriminated according to their specific fluorescence.

Usually 24 h after cell inoculation on the small gold electrode of the quartz resonator, the confluent monolayer of NRK cells was wounded by applying an invasive electric field as described in chapter 3.6.5.5. The wound healing process was documented directly after application of the elevated field pulse, at various points during wound healing and after closure of the wound. Therefore, the double mode measurement was stopped after a distinct time, the medium was discarded and the quartz dismantled from the measuring chamber. The quartz resonator was placed on a piece of parafilm in a petri dish and carefully rinsed with PBS^{++}. Thereafter, the cells were incubated in a freshly prepared PBS^{++} solution supplemented with 4 µM EthD-1 and 2 µM CaAM for 30 min at 37 °C in the dark. The dye solution was removed, the cells on the resonator were rinsed three times with PBS^{++} and thereafter investigated with a fluorescence microscope.

3.7.2.2 FITC-Phalloidin Staining of the Actin Cytoskeleton at Different Times after Cell Seeding

The cellular cytoskeleton is a cohesive meshwork of different protein filaments extending throughout the cytoplasm. It is involved in maintaining cell shape and movement. On the one hand, it mechanically provides the cell with structure and shape. On the other hand, it is also part of biochemical reactions, such as the polarized growth and shrinkage, their association through multiple linker proteins into larger structures and the directed motion of motor proteins walking along these protein polymers, playing an important role in cellular motion, intracellular transport and cellular division. The cytoskeleton comprises three main types of filaments: microfilaments, intermediate filaments and microtubules (Insall and Machesky, 2001). Microtubules are the thickest fibres (Ø = 25 nm), they have a hollow, cylindrical form and consist of the protein tubulin. They radiate from a point in the center of the cell and only occasionally extend as far as the edge of the cell. They act as a scaffold to determine cell shape and are involved in cell organelles and vesicles transport. Intermediate filaments form a

meshwork which spans the whole width of cells. With a diameter of 10 nm, they are smaller than microtubules and are composed of different types of monomers. Unlike microfilaments and microtubules, which are constantly remodeled and redistributed within the cell, intermediate filaments are very static structures which mainly provide tensile strength to the cellular body. Microfilaments, the thinnest filaments of the cytoskeleton (Ø = 8 nm), can be mainly found in the peripheral region, underlying the cellular plasma membrane, where they compose a dense two-dimensional meshwork of microfilaments. However, they can also be more regularly arranged into parallel bundels. Microfilaments, also called actin filaments, are composed of actin monomers, forming long linear chains of filamentous actin (F-actin). Each microfilament is made up of two helical interlaced strands of actin chains. Microfilaments are the basis for cellular movements and are responsible for resisting tension and maintaining cellular shape. This can be achieved by a continuous assembly and disassembly: polymerization of actin at one end of the filaments accompanied by depolymerization at the other end. The actin cytoskeleton itself reveals three prominent actin structures: the microvilli, which are finger-like protrusions of the apical membrane and typical of transporting epithelia, the junctional actin belt that follows the cell periphery and stabilizes cell-cell junctions and stress fibres, parallel bundels of microfilaments that run along the lower, substrate facing membrane interconnecting different sites of cell-substrate adhesion.

Since microfilaments underlie the plasma membrane and stabilize it by forming a dense meshwork, they are regarded as an important factor that determines the mechanical properties of the plasma membrane and thus contribute to the QCM response (Heitmann et al., 2007). It had been already shown that the actin cytoskeleton has a strong impact on the acoustic properties of the cell layer and that the QCM is capable of monitoring functional changes in the cytoskeleton (Heitmann et al., 2007). In this study, the status of the actin cytoskeleton of MDCK-II cells was checked for different growth surfaces. MDCK-II cells were freshly seeded on a gold or a PhoP surface and the formation of actin structures was followed at regular time intervals using fluorescence microscopy. These findings were correlated with time-resolved quartz mode measurements on the respective surfaces to analyze how the actin cytoskeleton contributes to the individual acoustic load of MDCK-II cells on the resonator surface.

MDCK-II cells were stained for their actin cytoskeleton by fluorescence-labeled phalloidin. Phalloidin belongs to the group of phallotoxins, isolated from the death cap (*Amanita phalloides*, Fig. 3.40) and specifically binds to F-actin without interacting with actin monomers. The bicyclic heptapeptide phalloidin laterally binds to actin filaments, thereby stabilizing the actin filaments against depolymerization into actin monomers. Thus, the dynamic polymerization equilibrium of F-actin assembly and disassembly is disturbed. *In vivo* the cellular toxicity of phalloidin is a result of this F-actin stabilization accompanied by changes in dynamic cell functions, what finally poisons the cell.

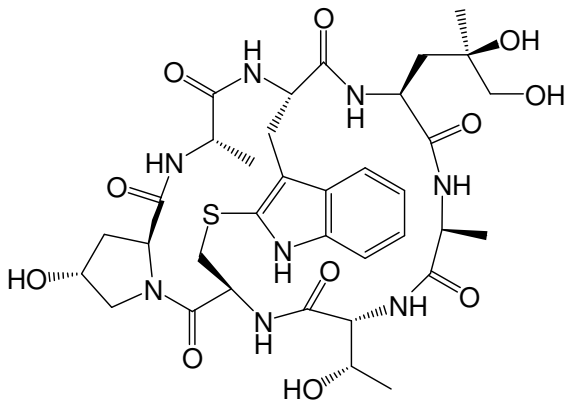

Fig. 3.40 Structure of the heptapeptide phalloidin.

A fluorescence label attached to the phalloidin molecule renders the actin cytoskeleton visible by fluorescence microscopy after the binding event of phalloidin. The used fluorescent derivative of phalloidin was Alexa Fluor® 488 phalloidin (ex/em: ≈ 495 nm/≈ 518 nm), allowing a specific detection of F-actin in the cells as a green fluorescence.

In order to document the status of the actin cytoskeleton, MDCK-II cells were seeded to confluence on gold coated coverslips (chapter 3.6.4.2) and PhoP coated coverslips (chapter 3.2.2), respectively. The gold coated coverslips were treated with an argon plasma for 1 min prior to cell inoculation. The PhoP coated coverslips were incubated in SFM for a period of 20 h prior to cell inoculation. The substrates were placed in a 24-well plate and a suspension of MDCK-II cells was added to the wells (450.000 cells/cm^2). At distinct intervals after cell seeding, the medium was discarded and the substrate was placed on a piece of parafilm in a petri dish. The cells were carefully rinsed twice with PBS^{++} and incubated in 4 % (w/v) paraformaldehyde (PFA) in PBS^{++} for 10 min at RT. This fixes the sample by linking the amino moieties of cellular proteins with the aldehyde moieties of PFA in an unspecific way, thus creating imin bonds. The proteins are stabilized and immobilized, thus conserving the structure of the cells. For fluorescent staining, the cells had to be permeabilized because the phalloidin molecule can not pass the intact cell membrane. The fixative was removed, the cells were carefully rinsed twice with PBS^{++} and subsequently permeabilized with a solution of the non-ionic detergent Triton X-100 in PBS^{++} (0.2 % (v/v)) for 10 min at RT. After two further rinsing steps in PBS^{++} the sample was incubated with Alexa Fluor® 488 phalloidin for 20 min at RT in the dark. The staining solution was freshly prepared from the stock solution (6.6 µM in methanol) by diluting it in a ratio of 1:40 in PBS^{++}. After 20 min, the staining solution was removed and the sample was rinsed three times with PBS^{++} in order to remove residues of the staining solution. To further stabilize the stained specimen, the cells were postfixed with 4 % (w/v) PFA in PBS^{++} for 10 min at RT and rinsed with PBS^{++} three times. For microscopic inspection at the fluorescence microscope using water immersion objectives, 2 mL PBS^{++} were added.

3.7.3 Stereomicroscopy

Stereomicroscopy is a technique which is often used to investigate the surfaces of solid specimens or for specimen preparation, e.g. dissections and micromanipulations. The design of a stereomicroscope differs from a standard light microscope. It uses two separate optical paths that provide slightly different viewing angles to the left and the right eye, usually between 10° and 12°. This allows for the observation of the specimen at an angle similar to the natural convergence angle of the human eyes, providing a spatial quasi three-dimensional image of the investigated specimen with a high degree of depth perception after the two images have been combined in the human brain.

Stereomicroscopes can be generally divided into two basic types: the Greenough type consists of two identical but separate optical systems, each containing a separate objective within twin body tubes that are inclined to produce the stereo effect. The common main objective (CMO) or parallel optics type uses a single large diameter objective that is shared between a pair of ocular tubes and lens systems (Nothnagle et al. on http://www.micros-copyu.com). The latter was the microscope type which was used in this study.

Depending on the object of interest, the selected illumination strategy may vary – either reflected (episcopic) illumination, or transmitted (diascopic) illumination or a combination of both. Using episcopic illumination, the specimen is illuminated from above and reflected light is used for examination. Commonly applied light sources are fibre optic illuminators, which are placed above the specimen and can be adjusted to different lighting angles to the specimen surface. This kind of illumination offers a bright illumination over the entire surface and allows for the examination of thick or opaque specimens. For transmitted light illumination, some microscopes are additionally equipped with a halogen lamp located beneath a transparent stage underneath the object.

The basic experimental setup for the CMO stereomicroscope which was used in this study is shown in Fig. 3.41. The single large central objective at the bottom of the microscope body is focused on the specimen and collects the two divergent light rays. Collimated light leaving the objective is taken up by two parallel arranged independent optical trains, i.e. the left and the right channel with two different viewing angles, and is split by a series of prisms redirecting the light to the respective oculars. In order to adjust the magnification level, the stereomicroscope makes use of a continuous zoom lens system, i.e. a minimum of three lens groups (zoom lenses), enlisting two or more elements for each group, which are positioned with respect to each other in the body tube between the CMO and the prisms. One element is fixed within the channel, while the other two are translated up and down within the channel by precision cams.

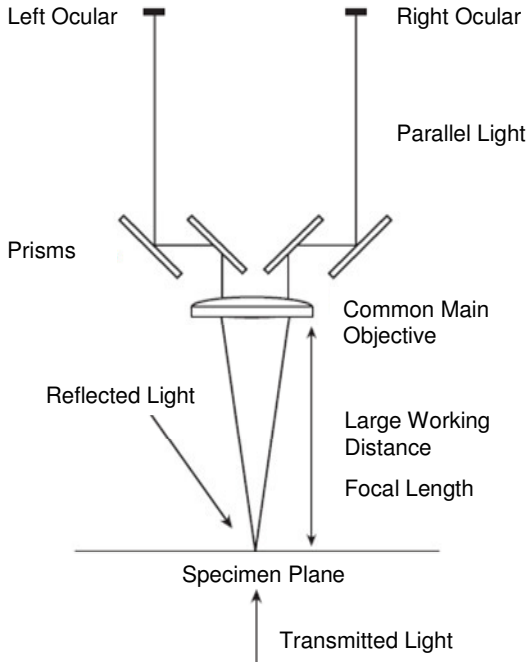

Fig. 3.41 Basic experimental setup and optical path for a CMO stereomicroscope (modified from http://www.media.wiley.com/product_data....pdf).

Stereomicroscopic images were taken using the *SMZ 1500 C-DSD230* CMO stereomicroscope (Nikon Instruments Europe, Amstelveen, Netherlands). The microscope allows for total magnifications of 3.75x to 540x with a zoom range of 0.75x to 11.25x, depending on the combination of objective lenses, zoom lenses and eyepiece. Additionally to an episcopic illumination, the stereomicroscope contains a diascopic stand for transmitted illumination. For image documentation, the microscope is equipped with a digital video camera which allows to visualize and store all data digitally on a standard computer using the Nikon software *NIS-Elements AR 3.0*.

3.7.3.1 Documentation of the Electrode Layout on Quartz Resonators

The electrode layout generated via photolithography on the upper surface electrode of quartz resonators (chapter 3.2.2), showing either centrally located gold electrodes (Ø ~ 3 mm and Ø ~ 0.5 mm) or an electrode at the edge of the PhoP covered surface electrode (Ø ~ 0.5 mm) was documented by taking stereomicroscopic images using reflected as well as transmitted light.

3.7.3.2 Documentation of Resonator Coverage after Partial Removal of the Cell Layer

In order to determine the load situation on the quartz resonator in addition to double mode impedance analysis (chapter 3.5.3.3), the size of the artificial wound applied to a MDCK-II cell layer confluently grown on a quartz resonator was documented using stereomicroscopy. The quartz resonator, mounted in the measuring chamber, was examined under the stereomicroscope using reflected light. The stereomicroscopic documentation was performed subsequent to the generation of a wound in the cell layer and repeated after each wound extension step (chapter 3.5.3.3).

4 A Microgravimetric Biosensor to Study the Biocompatibility of Polymer Surfaces

The aim of the study was to develop a biosensor to monitor the biocompatibility of polymer surfaces with respect to their molecular and cellular interactions with a physiological environment. A biosensor device capable of analyzing biocompatibility in quantitative terms is required in biomedical research for the development of anatomical implants and other devices that need to be in contact with living tissue.

The quartz crystal microbalance (QCM) technique was used as the key transducer element after the surfaces of the quartz resonators had been coated with the different polymer layers using thin-film technology. Since the resonance frequency of the quartz oscillation is highly sensitive to any surface modification, it provides a direct readout for adsorption or desorption of material like, for instance, proteins or cells. But is this also true for polymer coated quartz resonators? Are they applicable as a biosensor to monitor the anchorage of adherent cells upon the underlying polymer film by reading the parameters of the resonant oscillation? Using the QCM technique, the polymer surface was analyzed with respect to its long-term stability in a physiological environment, protein adsorption as well as cell attachment and spreading upon the surface.

In addition to QCM measurements, some general physicochemical characterizations of the polymer surface as well as a microscopic study documenting the adhesion kinetics of mammalian cells on the respective polymers were performed, allowing for a detailed correlation and interpretation of the QCM data and thus a validation of the polymer coated sensor system.

4.1 Physicochemical Surface Characterization of Spin Coated Polymer Films

In order to analyze the biocompatibility of a polymeric material using the QCM technique, all quartz resonators needed to be initially coated with a layer of the respective polymer. The challenge was to produce a homogeneous polymer film that covered the entire sensor surface while being thin enough not to cause any significant acoustic losses reducing the technique's sensitivity for further adhesion processes. For polymer film deposition, the spin coating technique was used. Since the parameters for the spin coating process, like the rotation speed or the spin time, can vary greatly for different materials and substrates, they needed to be optimized for the respective polymer in order to obtain a homogeneous and complete surface coverage in a designated thickness (chapter 3.2.2).
Before starting QCM measurements addressing protein adsorption as well as cell attachment and spreading upon these polymers, a preceding physicochemical surface analysis of the deposited polymer film was a prerequisite. Surface properties such as wettability, charge, rigidity and surface structure are known to profoundly influence cell-substrate interactions and have been widely studied by several authors (Lee et al., 1998). The physicochemical surface characterization in this study includes a quality control for complete surface coverage, a determination of the polymer film thickness, a quantification of the amount of polymer deposited on the sensor surface as well as a characterization of the wetting behavior of the polymeric material. The physical and chemical properties of the polymer film revealed by such a surface analysis may allow to correlate these findings with cellular behavior obtained from QCM experiments, leading to a detailed characterization of the respective material and its inherent biocompatibility. The following surface characterizations were performed for spin coated films of the polymers polystyrene (PS), poly(methyl methacrylate) (PMMA), poly(dimethyl siloxane (PDMS) and photopolymer (PhoP).

4.1.1 Completeness of Surface Coverage

The time-of-flight secondary ion mass spectrometry (ToF-SIMS) was applied to verify a complete surface coverage of the respective polymer coating on top of the quartz resonators. Pin holes or incomplete coverage of the polymer film could interfere with subsequent measurements or provide artificial data. A resonator was classified as being completely covered if the gold electrode underlying the polymer film was not detected by ToF-SIMS measurements, i.e. no gold atoms could be found in the uppermost layer.
Besides using ToF-SIMS as a quality control for complete surface coverage, it was also applied to gain detailed atomic and molecular information about the chemical composition of the polymer film in the region of the uppermost surface monolayer, as provided by the emitted secondary ions. Thus, possible surface contaminants can also be detected and identified. As the chemical composition and structure of the uppermost layer of atoms or

molecules determines the surface properties, the chemical composition should allow for a correlation with physical and biocompatibility properties of the polymer film.

Polymer films of PS, PMMA, PDMS and PhoP were prepared by solution spin coating onto the surface of quartz resonators (chapter 3.2.2) and were analyzed by ToF-SIMS (primary ion source: Bi_3^+, 25 keV) over a surface area of 100 x 100 μm^2 with respect to the chemical composition of the uppermost monolayer of the surface. The emitted secondary ions are presented in a secondary ion mass spectrum of one – positive or negative – spectral polarity by plotting the secondary ion intensity against the corresponding mass-to-charge ratio (Fig. 4.1). The intensity presents the added counts, i.e. the number of secondary ions of a distinct mass. It is noteworthy that the intensity for a certain ion does not only depend on its concentration on the surface. The ionization rate plays an important role, which is influenced by several factors like the nature of the primary ions or the ionization potential of the sample as well as its chemical environment (Guerquin-Kern et al., 2005). Thus, ToF-SIMS does not allow for a quantitative analysis of the polymer surfaces. The polymer surfaces were rather analyzed in a qualitative way with special attention to complete coverage of the quartz resonator.

A typical secondary ion spectrum from a polymer often contains numerous peaks. They arise from the macrochain fragmentation of the molecules at the surface and can extend to masses beyond $m/z = 10.000$. An analysis of the fragmentation pattern can allow for the identification of materials at a surface. Three regions can be distinguished in such a spectrum: the oligomer region, the fragment region and the fingerprint region. The former two are located in the high mass region ($m/z > 1000$) and arise from intact oligomer molecules emitted from the surface and fragments of these oligomers, respectively. The fingerprint region extends from the fragment region to low mass numbers ($m/z < 1000$) and arises from the fragmentation of the macromolecules to smaller fragment ions, which are commonly emitted with quite high intensities (Benninghoven, 1994). However, it is not necessary, or even possible, to identify all fragments. The prominence of high molecular mass fragment ions varies between different polymer types, and oligomer spectra have generally been observed only for polymers with $M_w < 10.000$ but not for all types of polymers. By contrast, all polymers give fingerprint spectra. In this low mass range ions consisting of end groups, fractions of repeat units or side chains are observed. They allow the unambiguous identification of most of the polymeric molecular compounds (Eynde et al., 1997, 1991; Eynde and Bertrand, 1997). Thus, the following identification process of the spin coated polymer films considers characteristic peaks only in the fingerprint region of the secondary ion mass spectra, which were related to specific secondary ion fragments.

Surface Analysis of Polystyrene

Figure 4.1 shows a section of a positive secondary ion mass spectrum confined to the low mass range $m/z \leq 230$ as obtained for the PS film spin coated on top of the quartz resonator. The spectrum is representative for the sample surface regardless of the region of data acquisition.

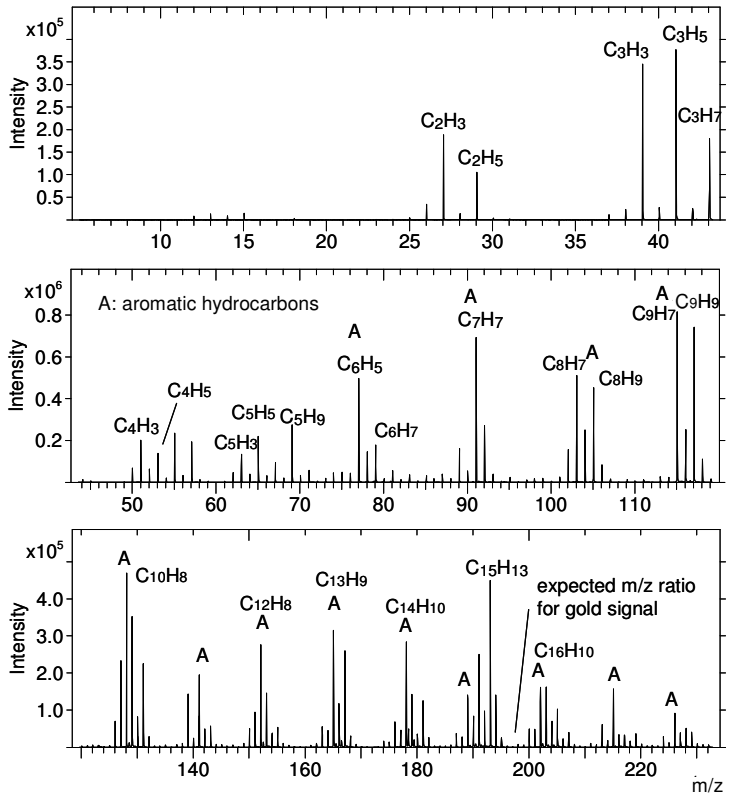

Fig. 4.1 Positive secondary ion mass spectrum of a representative PS surface in the mass range $m/z = 0 - 230$.

The positive secondary ion spectrum of the PS surface is dominated by a series of peaks due to aliphatic hydrocarbon fragments like $C_2H_3^+$ (27), $C_2H_5^+$ (29), $C_3H_3^+$ (39), $C_3H_5^+$ (41), $C_3H_7^+$ (43) ions. For the mass range above $m/z = 70$, the spectrum mainly contains peaks arising from aromatic hydrocarbon compounds including $C_6H_5^+$ (77), $C_7H_7^+$ (91), $C_8H_7^+$ (103), $C_8H_9^+$ (105) and $C_9H_7^+$ (115), produced by rearrangements between the main chain and the phenyl side chains. One important feature is the strong peak at 91 mass units, which is due to the cyclic tropylium ion $C_7H_7^+$, believed to form from styrene units at the hydrogen-terminated chain end. The remaining visible peaks (up to 230 mass units) at $m/z = 128$, 141, 152, 165, 178, 193, etc. are attributed to cyclic cations due to aromatic structures as well.

The fragmentation pattern observed in the positive ToF-SIMS spectrum of the sample is characteristic of PS (Zeng et al., 2001; Weng et al., 1995). A characteristic gold substrate signal which is expected at the mass range $m/z = 196.95$ in the spectrum can not be detected. Besides confirming the chemical identity of PS, ToF-SIMS is also capable of detecting possible surface contaminations of the polymer sample. Typical contaminants are mainly

polysiloxanes and salts, the latter being represented by alkali cations such as sodium (Na^+ at $m/z = 23$), potassium (K^+ at $m/z = 39$), lithium (Li^+ at $m/z = 6$ and 7), which are often concentrated at the polymer surface. Molecular sample contamination can arise during the preparation and spin coating procedure of polymer films. Siloxanes can originate from silicon oils used to lubricate the spin coater and are represented by its fragment ions Si^+ and $SiCH_3^+$. Salts which might contaminate the surface can be possibly contained in the organic solvent or can be introduced by impure film preparation conditions.
The spectrum of PS indicates neither metallic species (sodium, potassium) nor silicone contaminants to be present on the surface.

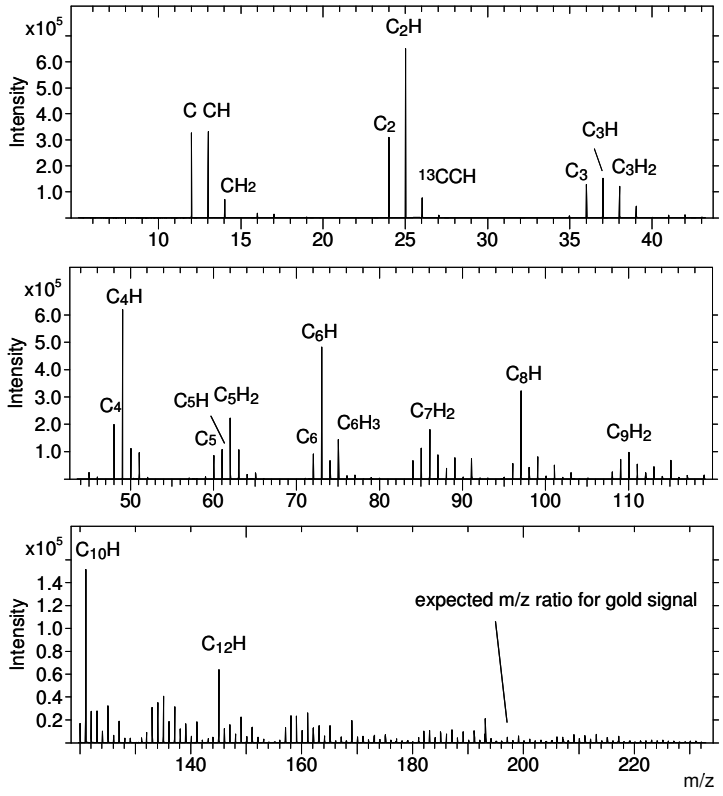

Fig. 4.2 Negative secondary ion mass spectrum of a representative PS surface in the mass range $m/z = 0 - 230$.

In addition to the positive secondary ions, the negative secondary ions can also provide an unequivocal fingerprint of the respective polymer. This is particularly true as the negative ion spectra do not suffer from the intense $C_xH_y^+$ clusters of ions which, although structurally important, often completely dominate the positive mode and in the case of polymers arise almost entirely from the side chain groups. Negative spectra often contain a number of very clear signals, diagnostic for the polymer repeat unit, main chain and side chain. Thus, negative ion spectra of polymer surfaces were additionally recorded, complementing and clarifying the information obtained from positive ion emission.

In the negative ion spectrum (Fig. 4.2), which was also analyzed in the mass range of $m/z = 0 - 230$, it is possible to detect in addition to hydrocarbon ions mainly atomic and

molecular anions such as C^-, C_2^-, C_3^-, C_4^-, C_5^- or C_6^-. Hydrocarbon ions of the general formula C_xH are found throughout the mass range. Prominent ones are for example CH^- (13), C_2H^- (25), C_3H^- (37), C_4H^- (49), C_5H^- (61) and C_6H^- (73), which are characteristic fragments of a PS surface (Zeng et al., 2001; Weng et al., 1995). As revealed in the positive secondary ion spectrum, the PS sample does not show a negatively charged gold species signal either.

The mass spectra of both spectral polarities reveal that gold atoms are not present in the uppermost monolayer of the PS sample, confirming a complete coverage of the sensor surface with PS. Pin holes, cracks or areas of incomplete coverage could not be detected. The secondary ion peaks observed in Fig. 4.1 and 4.2 can be assigned to the molecule from which they originate through the characteristic mechanism of fragmentation, thus confirming the chemical identity of PS. Elements and components which were detected on the surface of the PS sample in form of their secondary ions include aliphatic and aromatic hydrocarbons, in consistence with previous data. The PS sample surface was found to be free from any impurities like salts or polysiloxanes. Thus, the sample was considered to be contaminant free, providing a pure PS surface for further experiments.

Surface Analysis of Poly(methyl methacrylate)

The following figures (Fig. 4.3 and 4.4) present representative positive and negative secondary ion mass spectra of a PMMA film which was deposited on the surface of a quartz resonator by spin coating.

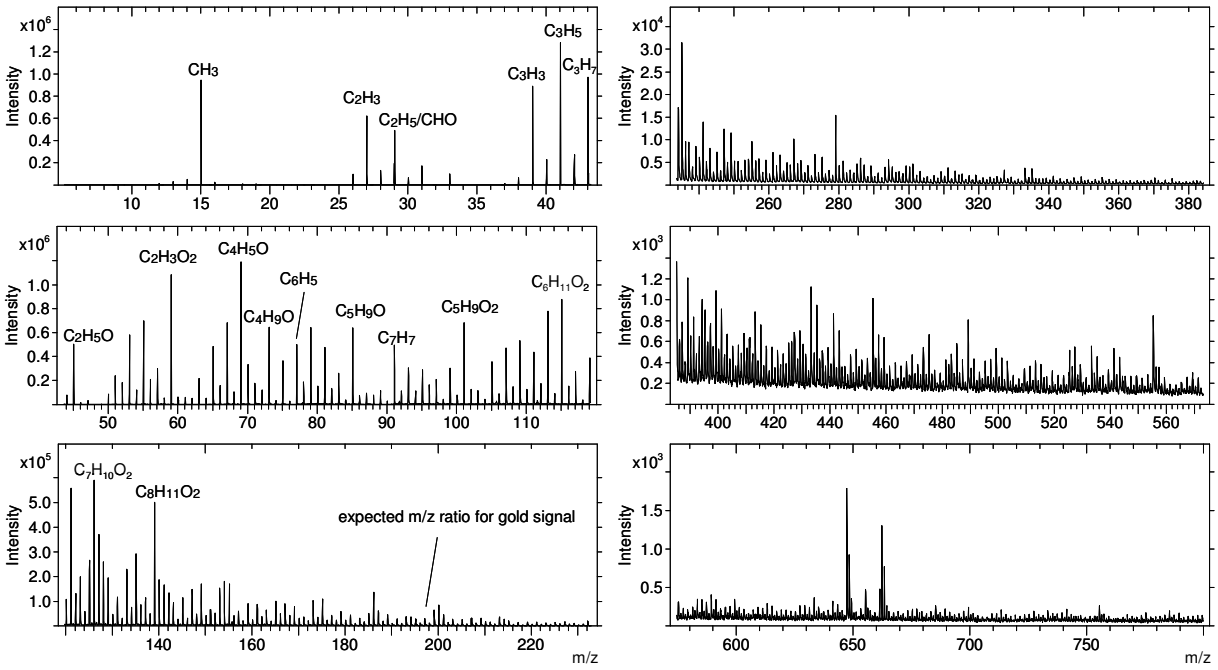

Fig. 4.3 Positive secondary ion mass spectrum of a representative PMMA surface in the mass range $m/z = 1 - 800$.

The positive mass spectrum of the spin coated PMMA film confined to the low-mass range of $m/z = 1 - 800$ (Fig. 4.3) contains prominent peaks which can be assigned to the ions CH_3^+ (15), $C_2H_3^+$ (27), $C_2H_5^+$ (29), $C_3H_3^+$ (39), $C_3H_5^+$ (41), $C_3H_7^+$ (43), $C_2H_3O_2^+$ (59) and $C_4H_5O^+$ (69). These peaks are characteristic of an ion beam-induced fragmentation pattern in PMMA (Zimmerman et al., 1993). It has been shown that the CH_3^+ species originates from the methyl group on the polymer side chain rather than from the methacrylate backbone. At higher mass, a series of characteristic ions appears at a mass-to-charge ratio of 105-115, 126, and 139. Conjugated five and six-membered ring systems have been proposed which account for most of these ions (Brown and Vickerman, 1986). Besides $C_2H_3O_2^+$ (59) and $C_4H_5O^+$ (69), the ions $C_6H_{11}O_2^+$ (115), $C_7H_{10}O_2^+$ (126) and $C_8H_{11}O_2^+$ (139) are key positive ions for an identification of PMMA (Leeson et al., 1997). No additional signals, in particular no gold signal, were observed in the spectrum, ruling out a surface contamination by salts and polysiloxanes as well as cracks or defects in the polymer coating.

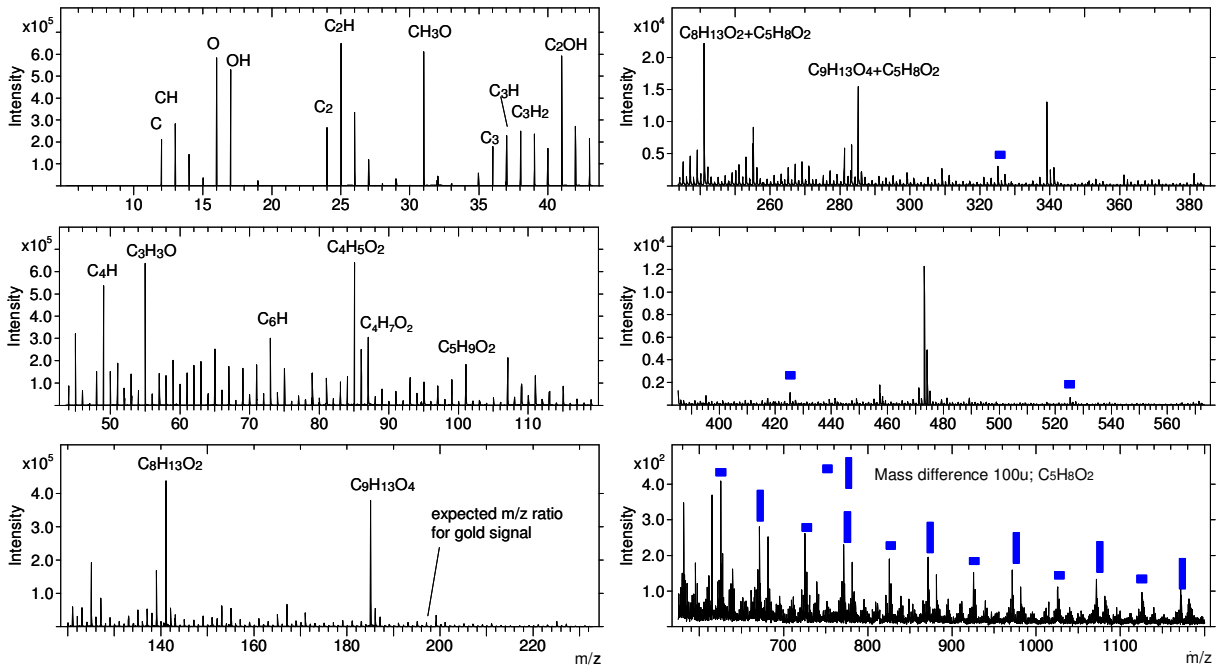

Fig. 4.4 Negative secondary ion mass spectrum of a representative PMMA surface in the mass range $m/z = 0 - 1200$.

The negative secondary ion mass spectrum of PMMA recorded over the mass range $m/z = 0 - 1200$ (Fig. 4.4) exhibits low mass fragments like C^-, CH^-, O^-, OH^-, C_2^- and C_2H^- with high peak intensity contributions in the mass range below $m/z = 30$. These ions are rather unspecific and convey no direct structural information. At higher mass, ions directly relatable to the polymer structure are found. These peaks are attributed to the ions CH_3O^- (31), C_2OH^- (41), $C_3H_3O^-$ (55), $C_4H_5O_2^-$ (85), $C_4H_7O_2^-$ (87), $C_5H_9O_2^-$ (101), $C_8H_{13}O_2^-$ (141) and $C_9H_{13}O_4^-$ (185). They are characteristic negative ions of PMMA and in good qualitative agreement with those reported previously by Leeson et al. (1997) as well as Lub and Benninghoven (1989). The anions relatable to the peaks at 31, 41, 55, and 85 are direct

fragments of the methacrylate unit. For example, the methanolate anion CH_3O^- (31) arises from cleavage of the side chain methoxy group, whereas the peak at $m/z = 85$ (methacrylate anion) is the result of cleavage of a monomer unit from the polymer with a concomitant loss of a methyl group from the side chain (Brown and Vickerman, 1986). For the peaks at 87, 101 and 141, 185, the formation of enolate anions is an important negative secondary ion formation process. These enolate anions arise from the chain ends and from side chain elimination followed by free radical rearrangement, respectively (Leeson et al., 1997; Lub and Benninghoven, 1989). The peaks labeled in blue correspond to a mass difference of $m/z = 100$ and are derived from the characteristic PMMA fragment $C_5H_8O_2^-$, the repeat monomer unit for PMMA.

The absence of a gold signal at $m/z = 196.95$ in the ToF-SIMS spectra recorded for both spectral polarities, i.e. gold atoms are not present in the uppermost monolayer of the PMMA sample, verifies that the polymer film covers the entire gold surface without any surface defects like, for instance, pin holes or cracks. The secondary ions which were detected on the sample surface are characteristic of a typical PMMA surface composition. In addition, the results from the ToF-SIMS spectra confirm that no contaminants are present on the surface of the PMMA film.

Surface Analysis of Poly(dimethyl siloxane)

Figure 4.5 depicts a positive secondary ion mass spectrum of the PDMS film surface in the mass range $m/z = 1 - 800$. Obviously, the spectrum is dominated by few, but characteristic peaks with high intensities.

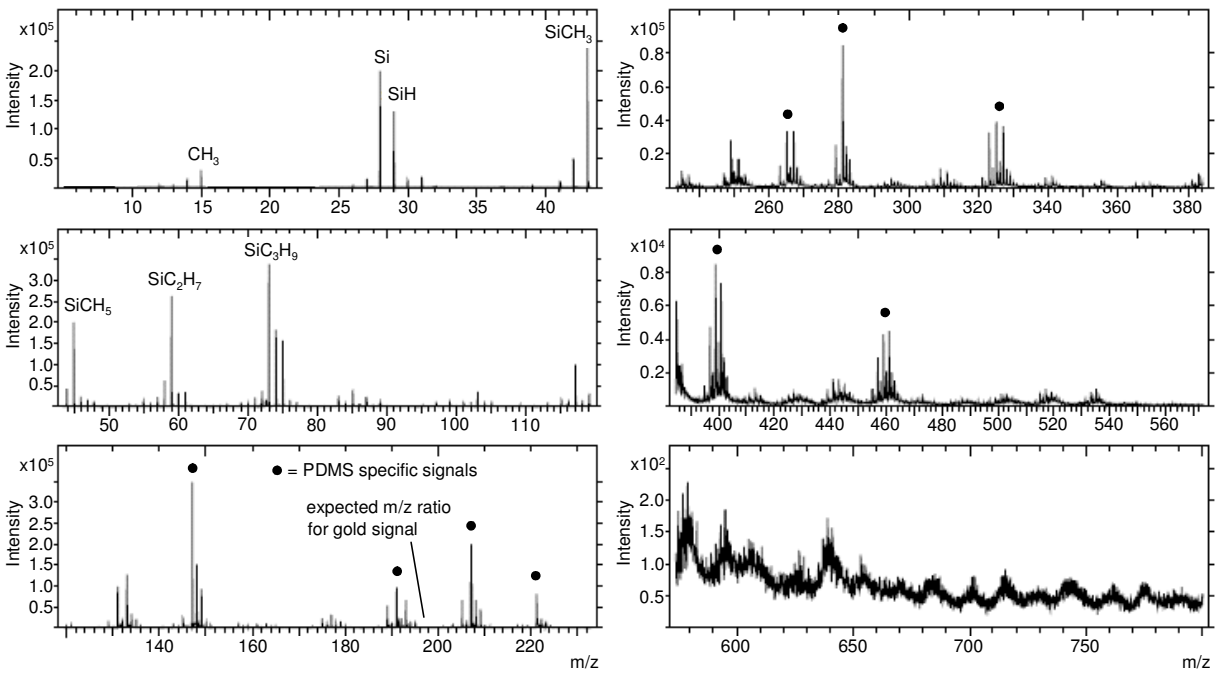

Fig. 4.5 Positive secondary ion mass spectrum of a representative PDMS surface in the mass range $m/z = 1 - 800$.

The spectrum contains peaks arising from Si^+ (28) and SiH^+ (29) as well as hydrocarbon-silicon complexes at $m/z = 43$ ($SiCH_3^+$), 45 ($SiCH_5^+$), 59 ($SiC_2H_7^+$), 73 ($SiC_3H_9^+$), with the last being the most intense one. Further PDMS specific signals in the spectrum are marked with a black dot. They are mainly found in the m/z range between 140 and 470, following the general formula $Si_wC_xO_yH_z$. For this mass range, the spectrum shows prominent peaks at $m/z = 147$, 191, 207, 221 and 281. The results are consistent with those obtained from previous ToF-SIMS studies of PDMS, which confirm the presence of peaks at $m/z = 28$, 43, 73, 147, 207, 221 and 281 as being highly indicative of PDMS (Eynde and Bertrand, 1997; Dong et al., 1997; Weng et al., 1995). Similar to other polymeric coatings, a gold signal which would be expected at $m/z = 196.95$ can not be detected, indicating the absence of gold atoms in the uppermost atomic monolayer of the PDMS sample and thus complete coverage of the surface. No typical impurities like salts (Na^+ at $m/z = 23$ and K^+ at $m/z = 39$) are present on the surface, providing a contaminant-free and pure PDMS surface for further experiments.

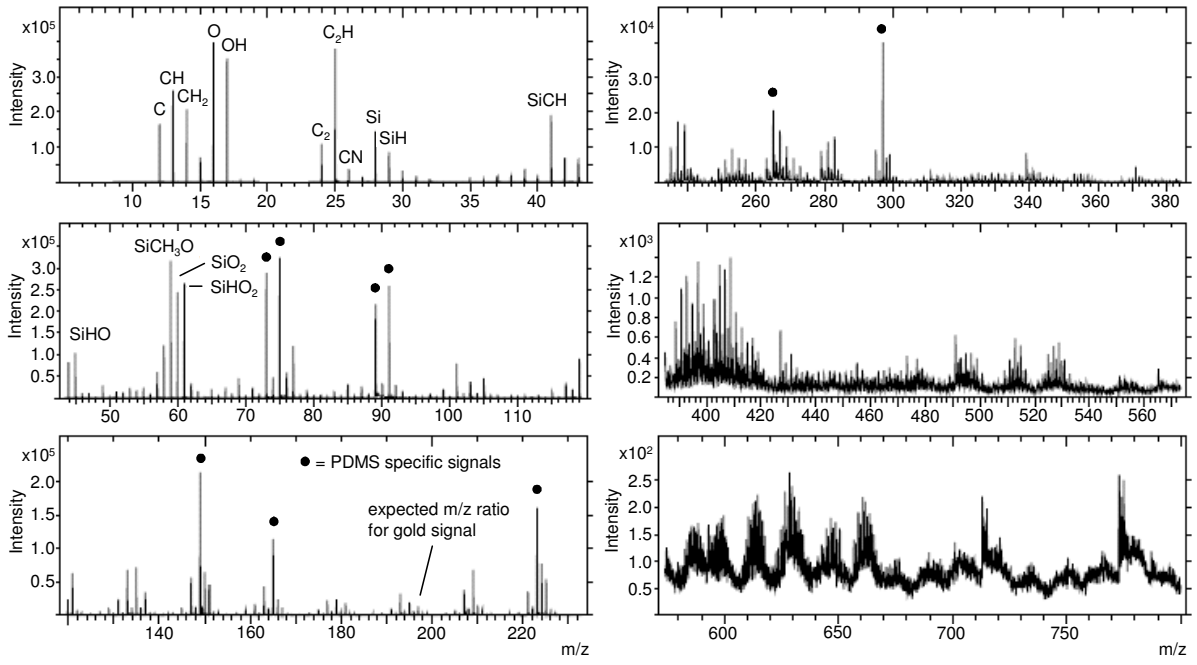

Fig. 4.6 Negative secondary ion mass spectrum of a representative PDMS surface in the mass range $m/z = 1 - 800$.

Figure 4.6 shows the negative secondary ion mass spectrum of PDMS. Peaks assigned to ionic silicon (28) and silicon containing ions like $SiCH^-$ (41), $SiHO^-$ (45), $SiCH_3O^-$ (59), SiO_2^- (60) and $SiHO_2^-$ (61) can be identified besides rather unspecific low mass fragments like C^-, CH^-, CH_2^-, O^-, OH^-, C_2^- or C_2H^- with high peak intensities. Just like in the positive spectrum, additional PDMS specific fragments, mainly occurring in the mass range between 70 and 300, are labeled with a black dot. The negative mass spectrum confirms the results of the positive spectrum with respect to a complete coverage of the sensor surface by the absence of a gold signal at $m/z = 196.95$.

The dominant fragment peaks which could be detected in the surface spectra of the PDMS sample were found to be Si and $Si_wC_xO_yH_z$ fragments as well as several hydrocarbon-silicon complexes. A comparison with published ToF-SIMS data for PDMS indicates that the spectra are consistent with those reported in literature, showing the expected chemical composition and thus confirming the chemical identity of PDMS (Dong et al., 1997; Feng et al., 2001). The complete coverage of the resonator's gold surface with a thin film of PDMS was confirmed by the absence of a gold signal at $m/z = 196.95$ in the positive as well as in the negative ion mass spectrum. The results shown above for the low mass range spectra of PDMS indicate that the sample surface is contaminant-free – no impurities were introduced during sample preparation.

Surface Analysis of Photopolymer

The following figures (Fig. 4.7 and 4.8) present a section of the secondary ion mass spectrum of a representative PhoP surface for the mass range m/z of 0 – 800.

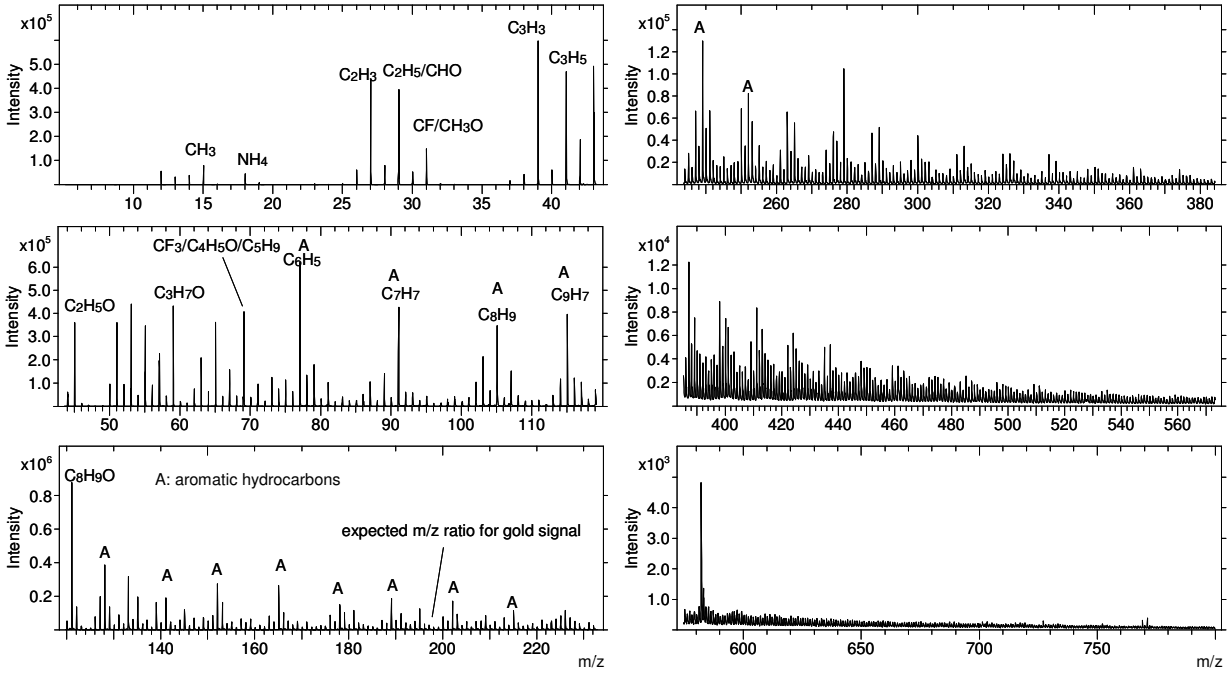

Fig. 4.7 Positive secondary ion mass spectrum of a representative PhoP surface in the mass range $m/z = 0 – 800$.

The positive spectrum of PhoP (Fig. 4.7) is characterized by a series of peaks in the low mass range due to hydrocarbon compounds like CH_3^+ (15), $C_2H_3^+$ (27), $C_2H_5^+$ (29), $C_3H_3^+$ (39) and $C_3H_5^+$ (41) as well as oxygen-containing complexes like $C_2H_5O^+$ (45), $C_3H_7O^+$ (59) and $C_4H_5O^+$ (69). Aromatic hydrocarbon signals are labeled with "A" and are mainly found in the mass range between 70 and 250. A prominent one is the peak at $m/z = 77$ ($C_6H_5^+$). Further prominent peaks that can be assigned to $C_8H_9O^+$ (121) and $C_{16}H_{17}O_2^+$ (241) are typical for a

Novolak® resin as applied in this study and originate from the polymer backbone (Saito et al., 1999; Winkelmann et al., 2003). No peak at m/z = 196.95 can be detected, indicating that no gold atoms are present on the surface. Additionally, no salt or polysiloxane contaminants are found in the spectrum.

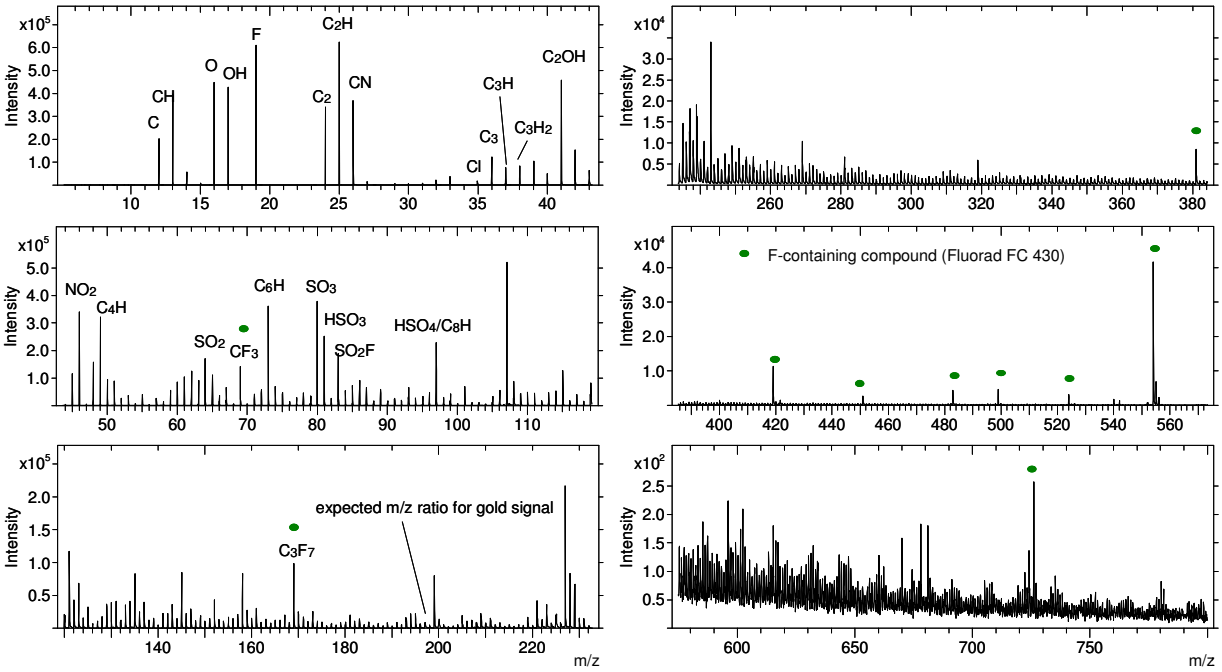

Fig. 4.8 Negative secondary ion mass spectrum of a representative PhoP surface in the mass range m/z = 0 – 800.

Besides the expected unspecific low mass fragments with high intensities which could also be detected in the negative spectra of PMMA and PDMS due to C^-, CH^-, O^-, OH^-, C_2^- and C_2H^-, the negative secondary ion spectrum (Fig. 4.8) is dominated by peaks due to CN^- (26), NO_2^- (46), SO_2^- (64), SO_3^- (80), HSO_3^- (81) and HSO_4^- (97) ions. They originate from the photosensitive additive (diazonaphthoquinone) and are characteristic of a typical *Novolak*® photopolymer sample (Saito et al., 1999). In addition to these compounds, atomic fluorine and fluorine containing ions are found at m/z = 19 (F^-), 69 (CF_3^-) and 169 ($C_3F_7^-$) as well as throughout the mass range of 380 – 570. These peaks are labeled with a green dot in the spectrum above and can be ascribed to the non-ionic surfactant which is contained to < 1.0 % by weight in the photoresist composition. Typical non-ionic surfactants which are commonly used as coating additives for photoresists in the coatings industry are fluorocarbon based surfactants, so-called fluorosurfactants like, for instance, *Fluorad*® *FC 430*. Since these surfactants provide low surface tensions, they serve as a wetting, leveling and flow control agent for a variety of organic polymer coating systems, ensuring a complete and homogeneous coating. The spectrum contains also peaks arising from hydrocarbon ions of the general formula C_xH at m/z = 37, 49, 73 and 97. A gold signal can not be detected.

In summary, a complete and defect-free coverage of the sensor surface with a PhoP film by means of spin coating could be achieved, as indicated by the absence of the gold substrate signal in the ToF-SIMS spectra. PhoP could be specifically identified by means of its molecular compounds, like aromatic hydrocarbon ions as well as ions originating from the photosensitive additive, being characteristic of a photopolymer. Characteristic signals from specific surface-adsorbed contaminants like salts or polysiloxanes are not detected.

4.1.2 Determination of the Polymer Film Thickness

The thickness of the polymer films deposited on the quartz resonator surface is a significant parameter since the spin coated polymer films should be compatible with the sensor's limits of operation. If the polymer layer is too thick, it is not possible to transfer the entire energy from the oscillating crystal to the outermost surface of the polymer, leading to a high loss of sensitivity and thus an incomplete quantification of further adsorption processes. Moreover, it is important to provide a polymer coating which exhibits a uniform film thickness in order to avoid local differences in sensitivity. The occurrence of slight variations in film thickness with radial distance from the center of the resonator is a well-known phenomenon and often depends on the concentration of the spin coating solution. Films exhibiting this phenomenon are thickest at the center of the resonator with progressively decreasing thickness moving radially away from the center. In order to rule out a loss of sensitivity for spin coated quartz resonators due to a polymer film that is either too thick or exhibits local thickness inhomogeneities and, as a consequence, to ensure a successful application of the sensor device for further adhesion studies, the thickness of spin coated polymer films was determined.
Film thickness measurements were performed using an optical profiler working in the VSI mode (chapter 3.3.2.2). Since this surface-analytical technique monitors the microscopic surface topography in 3D, it additionally provides information about surface roughness or possible discontinuities of the coating, like steps or cavities. Microscopic coverslips were used as substrates for the spin coated polymer films (chapter 3.2.2). A step that corresponds to the polymer film thickness was introduced into the polymer film either by scraping away parts of the polymer film with a pair of tweezers (PS, PMMA, PDMS) or by applying photo-lithography as in the case of PhoP. Subsequently, the whole surface was covered with a thin gold film (10 nm) in order to provide a homogeneously reflecting surface. The acquired data were analyzed with the *Veeco* software, yielding 3D height maps of the surface as well as 2D profile slices taken from the height data.

Figure 4.9 presents the 3D height map of a representative spin coated PS surface with the additional scratch introduced in the middle showing the polymer-free substrate surface (glass) and the intact polymer to the left and the right side. The PS surface is relatively smooth with only a few narrow spikes randomly distributed on the surface.

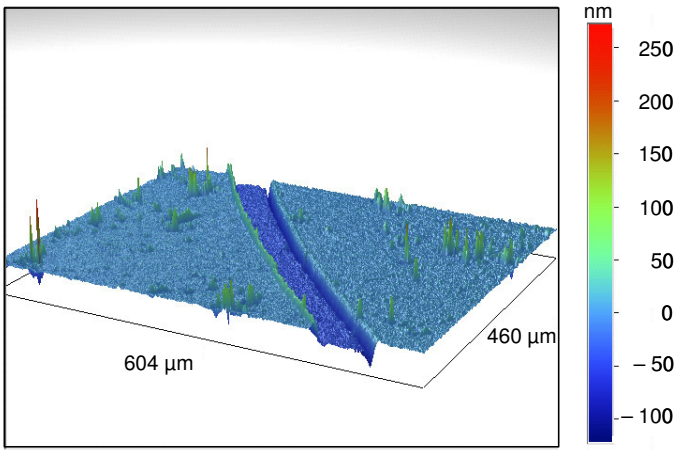

Fig. 4.9 3D VSI image of a representative spin coated PS surface with a scratch within the polymer film (dark blue line) from which the height profile can be derived.

From the 3D height map the thickness of the PS film was determined by choosing a line profile which cuts the experimental step in the polymer film. Thus, the depth of the experimental scratch relative to the intact polymer film at the right and the left edges of the step was measured and interpreted as film thickness.
In the following, one 2D height image as well as the corresponding height profile is representatively shown for each polymer film of the study.

Film Thickness of Polystyrene

Figure 4.10 A presents the 2D height image taken from the PS surface with the introduced step. As already presented above in the 3D height map, the predominant part of the PS surface appears smooth with only a few irregularities. A corresponding and representative phase contrast image taken from the PS film spin coated on a microscopic coverslip confirms the existence of a homogeneous polymer film of uniform thickness, revealing no microscopic irregularities or defects within the coating such as entrapped air bubbles, grains or areas of incomplete coverage (appendix A, Fig. A.1 A).
The height profile providing the film thickness along the red line is given in Fig. 4.10 B. The black and the white arrow heads mark the surface region which was used for thickness determination. The general course of the height profile recorded along the red line is as follows: The first ~ 250 µm of the line run across the PS surface. It is rather smooth, only showing height irregularities below 10 nm. The spikes recorded in the x-profile for the left and the right border of the scratch possibly arise from polymer accumulation due to the scraping process, causing an increase in polymer film thickness in this region. For PS, this can be observed mainly at the left border of the scratch – the thickness increases up to ~ 30 nm. Subsequently, the profile line reaches the substrate surface, causing the x-profile to drop to its minimal value. Having crossed the right border of the scratch, the profile line follows the PS surface again, showing small fluctuations in thickness.

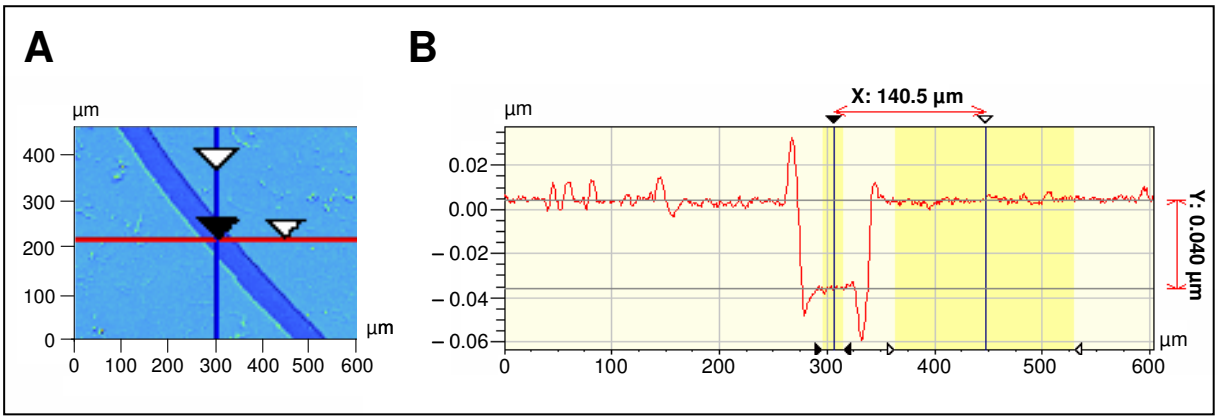

Fig. 4.10 Film thickness determination of spin coated PS. **A** 2D height image of PS with an experimental step within the polymer film (diagonal line). **B** Height profile taken over the step along the red line in A. The two arrow heads mark the region which was used for thickness determination.

In order to reduce the impact of local fluctuations, a certain region of the height profile (marked in yellow) from either the polymeric surface or the gap, i.e. the glass substrate surface, was averaged for thickness determination of the polymer film. For PS, a film thickness of (40 ± 1) nm is obtained (n = 7, with two measurements per sample) when being spin coated from a 1 % (w/v) solution in toluene at 4000 rpm and for 1 min on the substrate surface. This measured thickness is in good agreement with the literature. Hall et al. (1998) receive a thickness of approximately 30 nm for spin coating of a PS film from toluene on a silicon wafer, using the static method of dispense. Except for the method of dispense, the processing parameters are consistent with the ones applied in this study, i.e. the solution concentration of 1 % (w/v), the total spin time of 60 s and the spin speed of 4000 rpm.
In a similar manner as described for the PS sample, the thickness measurements were performed for the other polymer films.

Film Thickness of Poly(methyl methacrylate)

The 2D height image (Fig. 4.11 A) as well as a corresponding phase contrast image (appendix A, Fig. A.1 B) of a representative spin coated PMMA film indicate no surface irregularities, presenting a smooth and homogeneous surface of uniform thickness. This optical impression is further confirmed by the height profile (Fig. 4.11 B). Fluctuations in the height profile recorded for the PMMA coated region range in the order of only a few nanometers, i.e. 2 – 3 nm. The optical profilometry reveals a thickness of (19 ± 1) nm for PMMA spin coated at 4000 rpm and for 1 min on the substrate surface (n = 6, with three measurements per sample).
This is in good agreement with previously determined thickness data of PMMA coatings applied via spin coating. A thickness of approximately 20 nm is obtained for a PMMA film spin coated upon a silicon wafer using the same spin coating parameters as applied in this study but static dispense (Hall et al., 1998).

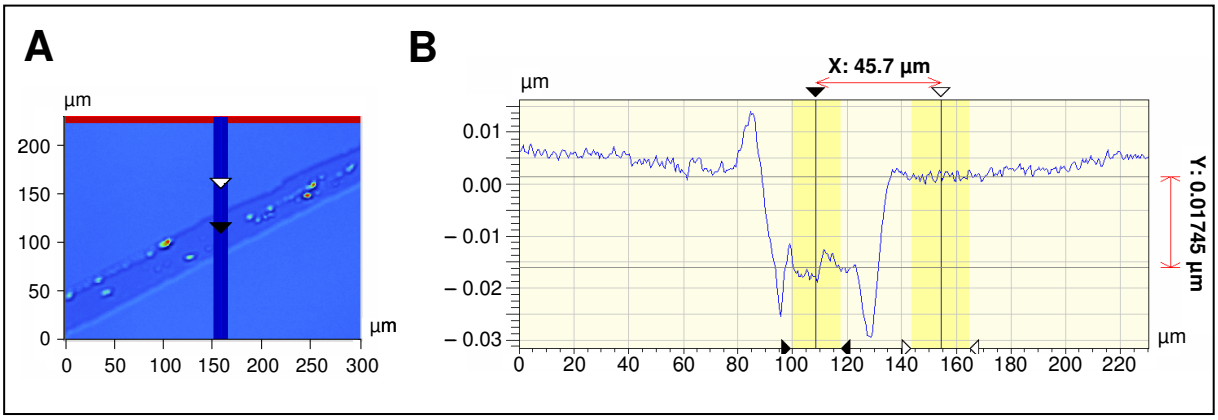

Fig. 4.11 Film thickness determination of spin coated PMMA. **A** 2D height image of PMMA with an experimental step within the polymer film (diagonal line). **B** Height profile taken over the step along the blue line in A. The two arrow heads mark the region which was used for thickness determination.

Film Thickness of Poly(dimethyl siloxane)

The film thickness determination of spin coated PDMS is presented in Fig. 4.12. In contrast to the previously described polymer films, spin coated PDMS does not exhibit a smooth surface. The 2D height image (Fig. 4.12 A) shows a rough and inhomogeneous surface topography.

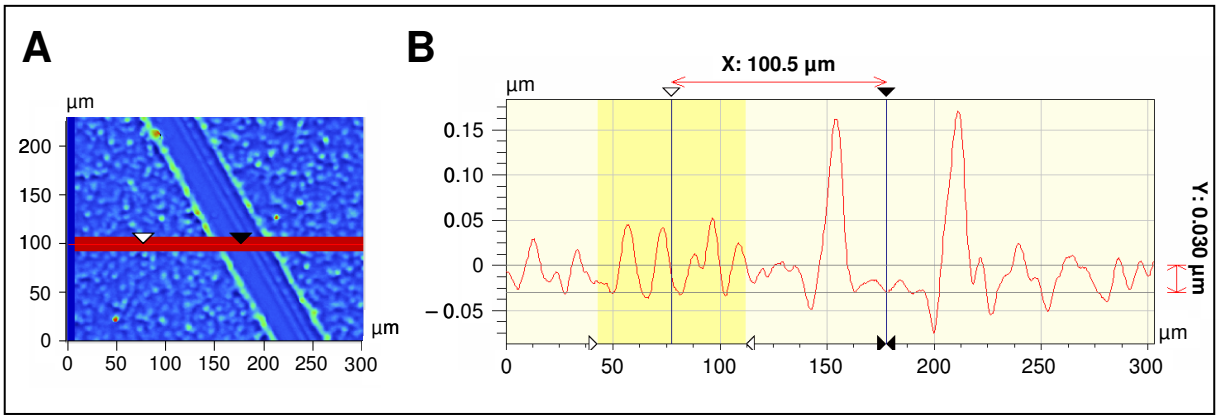

Fig. 4.12 Film thickness determination of spin coated PDMS. **A** 2D height image of PDMS with an experimental step within the polymer film (diagonal line). **B** Height profile taken over the step along the red line in A. The two arrow heads mark the region which was used for thickness determination.

Phase contrast images taken from the surface of spin coated PDMS (appendix A, Fig. A.1 C) reveal an inhomogeneous and rough polymer surface as well, indicated as dark spots in the polymer film (granular appearance). The height profile (Fig. 4.12 B) confirms this optical impression. Following the red profile line over the PDMS surface, almost periodic undulations of the layer thickness can be found. Compared to the uncoated region of the glass substrate, the thickness of the PDMS layer increases by approximately 30 nm and decreases to the value of the uncoated glass substrate, thereafter. This course recurs several times, leading to repeating undulations. In order to determine the film thickness of PDMS, the periodic height profile was averaged over a certain region showing regular undulations

(marked in yellow) and compared to the value for the uncoated region. Thus, an averaged thickness of (30 ± 2) nm was obtained for PDMS spin coated from hexane (1 % (w/v)) at 5000 rpm for 30 s on the substrate surface (n = 8, with two measurements per sample). A similar value is measured by Shahal et al. (2008), who determined a thickness of (18 ± 2) nm for PDMS spin coated on 1-hexadecanthiol-activated gold coated glass slides. However, the spin coating parameters used by Shahal et al. vary slightly (rotation speed: 4000 rpm, rotation time: 40 s and organic solvent: *n*-octane).
As concluded from VSI measurements, the dot like structures within the PDMS film revealed by phase contrast microscopy originate from film thickness inhomogeneities, since the polymer is *per se* a homogeneous substance.

Film Thickness of Photopolymer

In contrast to the previously described polymers, the step in the PhoP film could be generated by means of photolithography using the inherent properties of PhoP. Thus, a more well-defined step could be obtained for the subsequent film thickness determination of PhoP (Fig. 4.13).

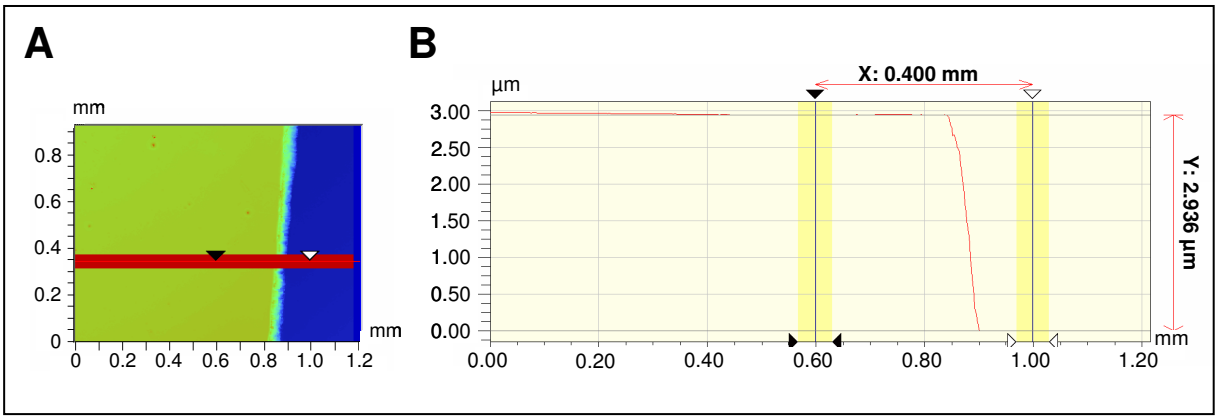

Fig. 4.13 Film thickness determination of spin coated PhoP. **A** 2D height image of PhoP with an experimental step (green: PhoP; blue: glass substrate). **B** Height profile taken over the step along the red line in A. The two arrow heads mark the region which was used for thickness determination.

The 2D height image (Fig. 4.13 A) in accordance with a representative phase contrast micrograph of a spin coated PhoP film (appendix A, Fig. A.1 D) shows that the PhoP film exhibits a homogeneous and regular surface of uniform film thickness. This is supported by the even course of the height profile in Fig. 4.13 B. The height profile taken along the red line in Fig. 4.13 A indicates an average film thickness of (2972 ± 11) nm for PhoP which was spin coated on the substrate surface at 3500 rpm for 1 min (n = 18, with two measurements per sample). No thickness data were available for the spin coated positive photoresist *Microposit® SC® 1827* in the literature.

The following table 4.1 summarizes the thickness data of the polymer films. The values for each polymer film were averaged from $n \geq 6$ individual measurements using at least two individually prepared films per polymer.

Tab. 4.1 Thickness of the spin coated polymer films (mean ± SDM; n ≥ 6).

Polymer	Thickness [nm]
PS	40 ± 1
PMMA	19 ± 1
PDMS	30 ± 2
PhoP	2972 ± 11

4.1.3 Quantification of the Polymer Thickness from QCM Readings

After addressing completeness and thickness of the polymer coating, the amount of polymer deposited by spin coating was quantified using the QCM technique. As previously described (chapter 3.5) the QCM technique is a surface-analytical tool which reports on any mass deposition on the crystal's surface by changes of its resonant oscillation. Thus, it is possible to calculate the deposited mass – hence the polymer film thickness – from the parameters of the resonant oscillation. Besides providing information about the deposited mass and film thickness, the QCM measurement should additionally indicate whether the deposited mass exhibits elastic behavior and whether it is free of entrapped solvent, which is important for further measurements under liquid loading.
In order to quantify the mass of the deposited polymer on the resonator surface, quartz resonators were characterized in their unloaded, empty state and after polymer film deposition using impedance analysis of the shear oscillation (chapter 3.5.3.3). All measurements were performed in air in order to exclude possible interactions of the spin coated polymer films with fluids, like for instance, polymer swelling.

Deposited Mass of Polystyrene

Figure 4.14 shows the impedance magnitude (A) and the phase shift (B) as a function of frequency for a 5 MHz quartz resonator near its fundamental frequency. The data for a resonator covered with a thin and homogeneous PS film are presented in comparison to the data for the same resonator in its unloaded, empty state.
Loading the quartz resonator with a PS film translates the impedance and phase spectra along the frequency axis to slightly lower frequencies. The internal structure of both spectra remains unchanged. This indicates an increase in the motional inductance L as it is observed when a resonator is loaded with a rigid and homogeneous mass layer. Thus, the spin coated PS film – investigations of PMMA, PDMS and PhoP indicate a similar behavior – can be regarded as a

thin and homogeneous mass layer which is rigidly coupled to the resonator surface. Any viscoelastic energy losses can be disregarded. The polymer layer follows the oscillation synchronously and loss-free.

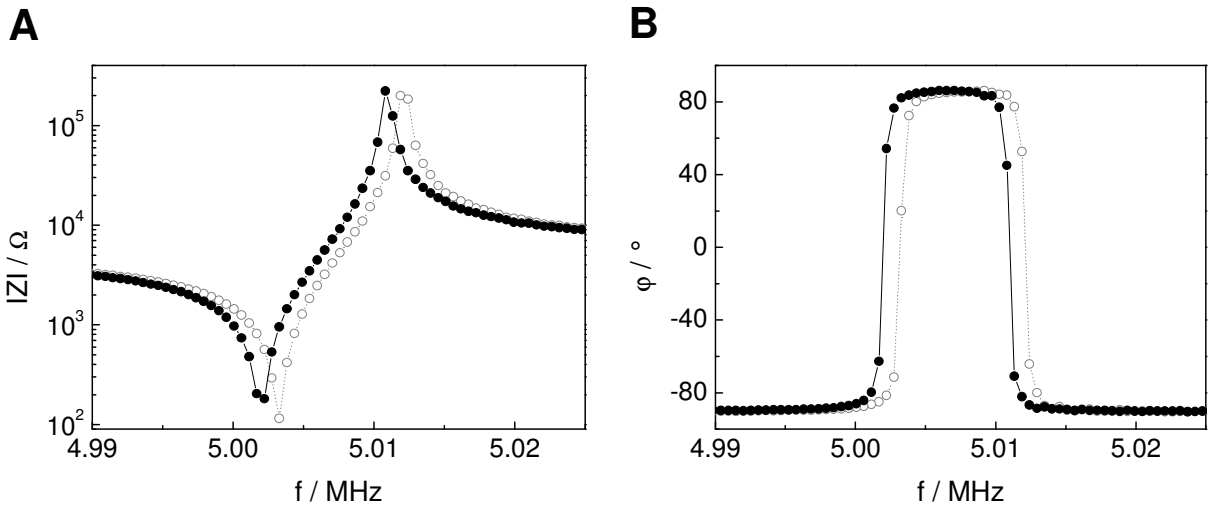

Fig. 4.14 A Impedance magnitude and **B** phase spectra near resonance of a quartz resonator, before (○) and after (●) deposition of a PS film.

From measurements of the resonator's total inductance before and after mass deposition it is possible to quantify the mass of the deposited polymer. In order to quantify the inductance change, the impedance data were analyzed by fitting the transfer function of the BVD equivalent circuit to the recorded phase spectrum of the unloaded and the polymer coated quartz resonator.

For two individual quartz resonators coated with PS, an average value of $L_m = (11.7 \pm 6.0)$ µH is obtained for the additional inductance due to the polymer film deposition while the other electrical parameters remain almost unaffected. The deposited mass can be calculated following Eq. 3.22 (chapter 3.5.2.2):

$$L_m = S_l \cdot \frac{m}{A}.$$

The integral mass sensitivity S_l for the 5 MHz quartz resonators used in this study had been determined by electrodeposition of rigid copper films on the resonator's surface by Wegener (1998) and amounts to $S_l = (0.62 \pm 0.01)$ H·cm^2/g. With a piezoelectric active area of 0.28 cm^2, the amount of PS spin coated on the resonator surface can be quantified as:

$$m = \frac{L_m \cdot A}{S_l} = \frac{(11.7 \pm 6.0)\,\mu H \cdot 0.28\,cm^2}{0.62\,\mu H \cdot cm^2 / \mu g} = (5.3 \pm 2.7)\,\mu g\ .$$

The calculation returns a value of $m = (5.3 \pm 2.7)$ µg for the amount of PS deposited on the resonator surface via spin coating.

Deposited Mass of Poly(methyl methacrylate)

Figure 4.15 compares the impedance magnitude (A) and phase spectra (B) for the same resonator with and without a PMMA film on the resonator surface. The presence of PMMA on the resonator surface has a slight impact on both quantities, $|Z|(f)$ and $\varphi(f)$, expressed in a minor shift of both spectra towards lower frequencies. The internal structure of both spectra remains unchanged, indicating the absence of any viscoelastic energy losses. The PMMA film can be regarded as a thin and homogeneously mass layer which is rigidly coupled to the resonator surface.

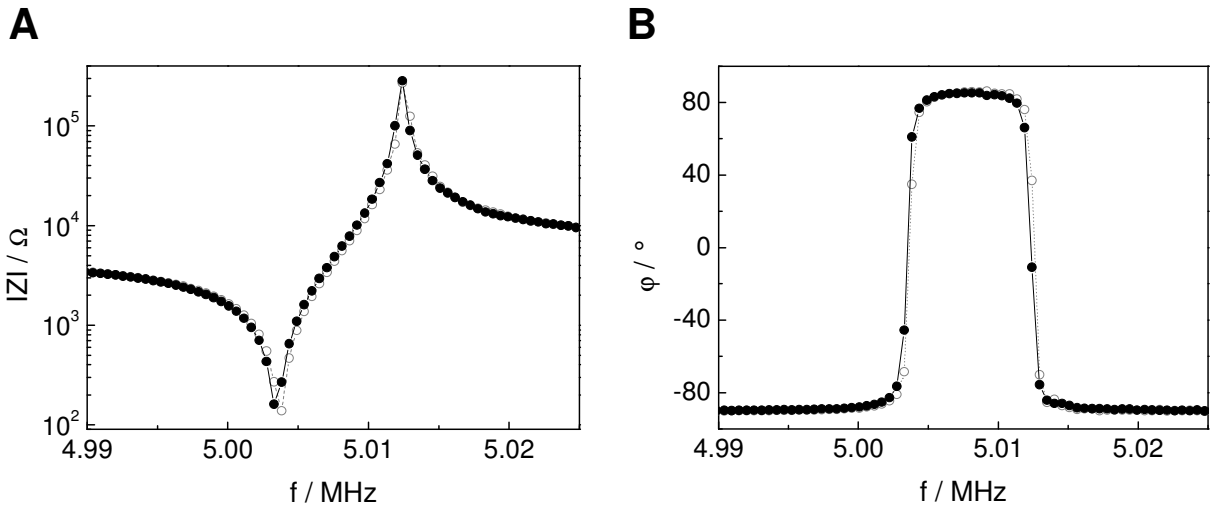

Fig. 4.15 A Impedance magnitude and **B** phase spectra near resonance of a quartz resonator, before (○) and after (●) deposition of a PMMA film.

When analyzing the impedance raw data of the uncoated and the PMMA coated resonator using the BVD equivalent circuit, an inductance change of $L_m = (5.54 \pm 0.99)$ µH is obtained for two resonators individually coated with PMMA, resulting in a value of $m = (2.50 \pm 0.45)$ µg for the deposited mass of PMMA.

Deposited Mass of Poly(dimethyl siloxane)

The shift in resonance frequency for a PDMS coated resonator compared to the same resonator in its unloaded state is exemplarily shown in Fig. 4.16 for the impedance magnitude (A) and phase spectra (B).

Deposition of PDMS on the resonator surface results in a minor shift of both spectra to lower frequencies to a similar extent as described for PMMA. Any viscoelastic energy losses can be disregarded. The polymer layer exhibits purely elastic behavior, following the oscillation synchronously and loss-free.

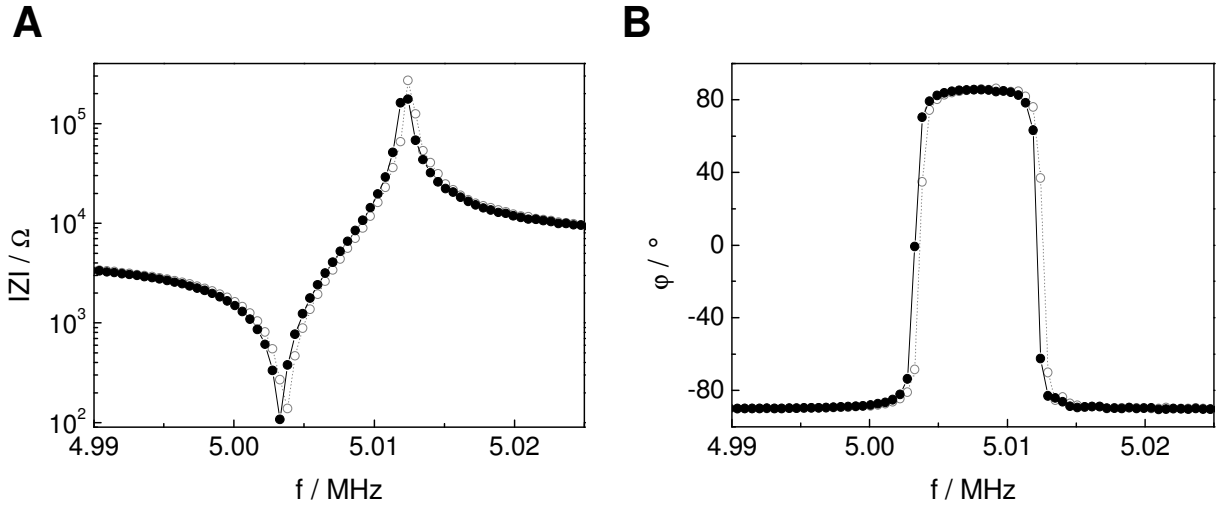

Fig. 4.16 A Impedance magnitude and **B** phase spectra near resonance of a quartz resonator, before (○) and after (●) deposition of a PDMS film.

Quantitative analysis of the impedance raw data recorded with and without PDMS provides an average additional inductance of $L_m = (9.24 \pm 1.31)$ µH for two resonators individually coated with PDMS. The calculation of the deposited mass m using Eq. 3.22 returns a value of $m = (4.17 \pm 0.59)$ µg for the amount of PDMS on the resonator surface.

Deposited Mass of Photopolymer

As shown in Fig. 4.17, the presence of the PhoP film on the resonator surface has a strong impact on both quantities, $|Z|(f)$ and $\varphi(f)$. Spin coated PhoP induces a much bigger shift of the impedance and phase spectra towards lower frequencies as it could be anticipated from the thickness data.

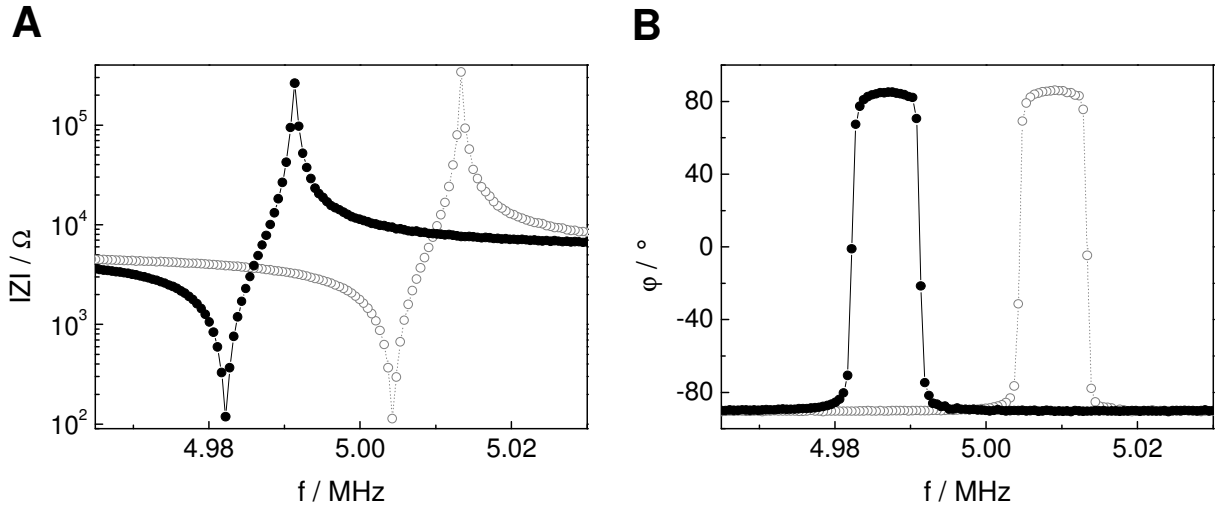

Fig. 4.17 A Impedance magnitude and **B** phase spectra near resonance of a quartz resonator, before (○) and after (●) deposition of a PhoP film.

The unchanged internal structure of both spectra after polymer film deposition indicates the absence of any viscoelastic energy losses. Thus, the PhoP film can be regarded as a rigid and homogeneous mass layer which follows the resonator's oscillation synchronously and loss-free. When analyzing the impedance raw data of the uncoated and the PhoP coated resonator, an average additional inductance of $L_m = (419.0 \pm 4.0)$ µH is obtained for two individually prepared resonators. This results in an amount of mass of $m = (189.2 \pm 1.8)$ µg for spin coated PhoP.

As an alternative to VSI measurements, the film thickness can be calculated from the quantified mass of the spin coated polymer films on the resonator surface. The following paragraph details the calculation of these film thickness values as well as their correlation to the optical film thickness data obtained from VSI measurements (chapter 4.1.2).
For film thickness calculations, two assumptions need to be made: (i) the spin coated polymer film is assumed to homogeneously cover the complete resonator, thereby exhibiting the same thickness at any place on the surface and (ii) the density ρ of the spin coated polymer film is regarded to be equal to the density of the original solid state polymer.
Using the mass data for the spin coated polymer films from QCM measurements, the volume of the deposited polymer films can be calculated as:

$$V = \frac{m}{\rho}. \tag{4.1}$$

The theoretical thickness of the deposited polymer films on the resonator surface can be calculated as:

$$h = \frac{V}{\pi \cdot r^2}, \tag{4.2}$$

with $\pi \cdot r^2$ (= 0.28 cm^2) being the piezoelectrically active area of the quartz resonator and h the film thickness.

For a PS coated resonator, the calculation of the polymer film thickness is demonstrated. PS exhibits a density of $\rho = 1.047$ g/cm^3 and its mass after being spin coated on the resonator surface was determined to be (5.3 ± 2.7) µg.

$$V = \frac{(5.3 \pm 2.7) \cdot 10^{-6}\, g}{1.047\, g / cm^3} = (5.1 \pm 2.6) \cdot 10^{-6}\, cm^3$$

$$h = \frac{(5.1 \pm 2.6) \cdot 10^{-6}\, cm^3}{0.28\, cm^2} = (18.1 \pm 9.2) \cdot 10^{-6}\, cm = (181 \pm 92)\, nm$$

For PS a film thickness of $h = (181 \pm 92)$ nm is calculated.

The same calculation for the spin coated PMMA film, using a density of $\rho = 1.188$ g/cm^3 and a mass deposition of (2.50 ± 0.45) µg returns a value of $h = (75 \pm 14)$ nm. The film thickness of PDMS with a density of $\rho = 1.03$ g/cm^3 and a mass deposition of (4.17 ± 0.59) µg is calculated to $h = (145 \pm 21)$ nm. A precise theoretical film thickness for the spin coated PhoP could not be determined, since no density data was available for the polymer in its cured state. Assuming a density for PhoP similar to the other polymers, like, for instance, $\rho = 1.09$ g/cm^3 returns for the thickness of PhoP deposited on the resonator surface $h = (6200 \pm 59)$ nm.

Table 4.2 compares the theoretical film thickness as calculated from QCM mass data and the optical film thickness obtained from VSI measurements of the spin coated polymers.

Tab. 4.2 Polymer film thickness calculated from QCM derived mass data and determined by optical VSI measurements (mean ± SDM; n = 2; * data is based on a hypothetical density of PhoP).

Polymer	QCM mass [µg]	Density [g/cm^3]	QCM Thickness [nm]	VSI Thickness [nm]
PS	5.3 ± 2.7	1.047	181 ± 92	40 ± 1
PMMA	2.50 ± 0.45	1.188	75 ± 14	19 ± 1
PDMS	4.17 ± 0.59	1.03	145 ± 21	30 ± 2
PhoP	189.2 ± 1.8	1.09*	6200 ± 59*	2972 ± 11

All film thickness data obtained from the QCM measurements are 4 – 4.8 fold higher than the data obtained from VSI measurements. The thickness data for PhoP are excluded from this consideration since its theoretical thickness calculation is based on a hypothetical PhoP density. The disagreement of the thickness data may be due to non appropriate assumptions which were made for the theoretical thickness calculation. An underestimation of the polymer film density after spin coating, which was assumed to be equal to the density of the original solid state polymer, can account for the higher values for the calculated polymer film thickness.

4.1.4 Wettability of the Polymer Surface

Contact angle measurements were performed in order to quantify the surface wettability of the spin coated polymer films of PS, PMMA, PDMS and PhoP. The respective polymers were spin coated from organic solution on microscopic coverslips and the dynamic water contact angles of the different surfaces were measured with a video-based drop shape analysis system using the sessile drop method (chapter 3.3.3). Advancing and receding water contact angles were obtained by keeping a thin syringe needle in the water droplet after positioning it on the sample surface while carefully injecting and withdrawing water. During this process, a digital camera mounted in plane with the sample surface continuously captured images of the water droplet. These images were used to calculate the left and right contact angles from the shape of the drop using image analysis.

For the calculation of the dynamic contact angle, the drop volume was altered during the measurement. Water droplets of an initial volume of 3-5 µL were extended to a maximal volume of 10 µL during a time frame of approximately 19 s. Subsequently, the drop was continuously reduced in volume till the starting volume was obtained or the drop separated from the syringe needle. Since the drop volume can not be exactly determined during this process, the time, i.e. the age of the drop, is used instead against which the dynamic contact angle is plotted. This leads to a so-called hysteresis diagram (Fig. 4.18).

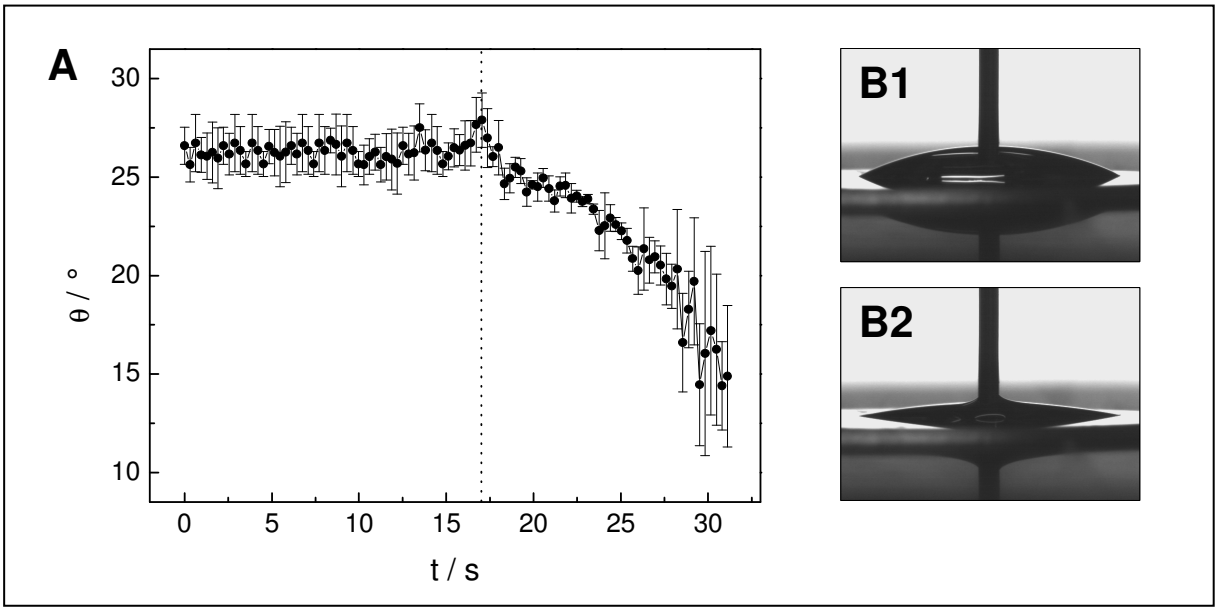

Fig. 4.18 Dynamic contact angle for water measured on glass at (22 ± 1) °C during the increase and decrease in drop volume. **A** Since the drop volume can not be determined precisely, the contact angle is plotted against the time. The first 17 seconds display the advancing angle, followed by the receding angle (mean ± SDM; n = 4 with 2 measurements per sample). **B** Representative photographic images of the drop at maximal volume during wetting (**B1**) and at minimal volume during dewetting (**B2**).

The dynamic contact angle measured on glass during the increase and decrease in drop volume versus time is shown in Fig. 4.18. Unmodified and cleaned glass substrates (uncoated microscopic coverslips) served as a reference for the polymer coated substrates. A total of four contact angle measurements were performed with two measurements per substrate. The mean values of the contact angle measured at both sides of the droplet were averaged for the four individual measurements. They are shown as average contact angle with their respective standard deviation of the mean in the diagram above (Fig. 4.18).

On the basis of this measurement the general course of the dynamic contact angle, which will recur in a similar way for all successive measurements, can be explained as follows: During the initial increase to a maximal drop volume, which comprises the first 17 seconds of the measurement, the contact angle remains almost constant. An advancing contact angle of $\theta_A = (25.8 \pm 1.2)°$, averaged over this time frame of 17 s, is obtained. During the process of dewetting, where the drop volume is reduced by withdrawal of water, the contact angle decreases continuously. If the drop does not separate from the needle, a constant final receding value for θ_R will be obtained. However, this is rarely the case when dealing with highly hydrophilic surfaces ($\theta = 0° – 30°$), since a strong affinity (hydrophilic interactions) of the sample surface for the water droplet often causes the droplet to detach early from the needle rather than being taken back into the syringe. In this case, θ_R is taken from the last seconds of the measurement and accounts for $(14.9 \pm 3.6)°$ for the glass substrate. The measured contact angles are characteristic for glass, being in good agreement with previously reported values (Kanan et al., 2002; Saneinejad and Shoichet, 1998).
The difference between the two constant values for θ_A and θ_R is calculated to obtain the contact angle hysteresis $\Delta\theta$, allowing for certain correlations with surface roughness and homogeneity (Jung and Bhushan, 2006). For a glass substrate, $\Delta\theta$ is determined to yield $(10.9 \pm 4.8)°$. Hysteresis can arise from molecular interactions between the liquid and the solid support as well as from surface anomalies such as roughness or heterogeneities. Among these factors, none is capable of exerting a greater influence on apparent contact angles than roughness (Extrand, 2003). For a homogeneous interface, increasing roughness leads to an increase in the contact angle hysteresis.

The polymer coated substrates were analyzed in a more sophisticated way. Since cell attachment and spreading upon a polymer film were studied with various surface modifications in this study, like the impact of argon plasma exposure and/or fluid pre-incubation of the polymer film, it was interesting to analyze whether and to which extent the contact angle and thus the wettability of the polymer surfaces are modified by these pretreatments.

The dynamic contact angle data should give certain hints to explain protein adsorption and cell adhesion to these surfaces or even allow for a correlation between polymer surface properties and the cellular response. As used throughout all further experiments, the polymer surface was investigated under the following processing conditions:

(i) Unmodified
(ii) Unmodified + PBS^{--} or SFM pre-incubation (20 h, 37 °C)
(iii) Argon plasma modified (1 min)
(iv) Argon plasma modified (1 min) + PBS^{--} or SFM pre-incubation (20 h, 37 °C)

In the following paragraph, the dynamic water contact angle measured during the increase and decrease in volume is presented for each polymer film and its various processing conditions in a hysteresis diagram. At least two identically prepared polymer surfaces were studied onto which droplets of water were placed at one (plasma treated surface) to three (unmodified surface) different regions on each sample surface. For the sake of clarity, only one representative curve for each processing condition is shown. Advancing angles were obtained by averaging the values over the constant region of the contact angle during the increase in drop volume for all individual measurements of the same processing condition. The averaged contact angle value of the individual measurements for minimal drop volume at the end of each measurement was assigned as the receding contact angle. Photographs of the water droplet deposited on an unmodified and a plasma modified polymer surface illustrate the experimental data. The images were taken at the time point of constant θ_A and θ_R, i.e. at maximal and minimal drop volume, respectively, and display the drop shape on the various polymer films.

Wettability of PS Coated Surfaces

The results for the dynamic contact angle measured on a PS surface exposed to various processing conditions are summarized in Fig. 4.19. PS was studied in its unmodified form, after the incubation in PBS^{--} or SFM over a period of 20 h at 37 °C, in its argon plasma modified form as well as after an argon plasma treatment followed by a PBS^{--} or SFM incubation (20 h, 37 °C). The reported contact angles are mean values ± standard deviation of the mean based on n = 4 measurements.
Spin coated films of PS exhibit an advancing angle of (91.7 ± 0.8)° and a receding angle of (82.2 ± 0.7)°. Incubating the PS film in PBS^{--} over a period of 20 h results in contact angles of θ_A = (92.1 ± 1.2)° and θ_R = (64.3 ± 1.0)°. Using SFM instead of PBS^{--} for incubation, the advancing contact angle decreases slightly to a value of (84.6 ± 1.8)° when compared to the PBS^{--} incubation while the receding angle differs greatly, showing a value of (34.1 ± 1.6)°. When the PS film is subjected to an argon plasma for 1 min, the advancing and the receding contact angle are significantly reduced. θ_A accounts for (25.4 ± 1.7)° and θ_R for (6.3 ± 1.2)°, indicating a substantial increase of hydrophilicity. An additional incubation in a physiological fluid does not alter the dynamic contact angle significantly.

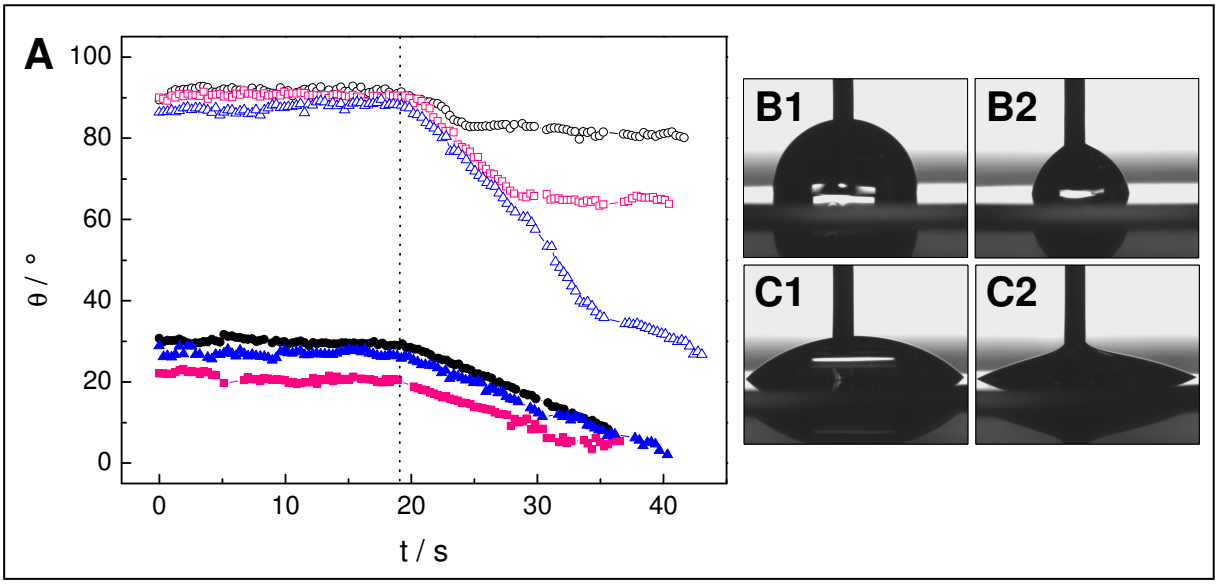

Fig. 4.19 A Representative dynamic contact angles for water measured during the process of wetting and dewetting of PS surfaces exposed to different surface modifications at (22 ± 1) °C. The preceding processing conditions of the spin coated PS film are the following: no pretreatment (○), pre-incubation with PBS^{--} (□) / SFM (Δ) over 20 h at 37 °C, argon plasma treatment for 1 min (●), argon plasma treatment for 1 min followed by a PBS^{--} (■) / SFM (▲) incubation over 20 h at 37 °C. The first 19 seconds display the advancing angle (vertical line), followed by the receding angle. **B** and **C** Photographs of a water droplet on two differently processed PS surfaces: **B** Water drop of maximal volume during the process of wetting (1) and of minimal volume during dewetting (2) of an unmodified PS surface. **C** Water drop on the surface of a PS sample previously exposed to an argon plasma for 1 min, showing maximal (1) and minimal (2) drop size.

An argon plasma treatment followed by an incubation in PBS^{--} over 20 h results in contact angles of $\theta_A = (24.0 \pm 2.3)°$ and $\theta_R = (7.0 \pm 2.9)°$. The contact angles for an argon plasma modified and additionally SFM incubated PS film are $(27.7 \pm 1.0)°$ for the advancing and $(4.9 \pm 0.8)°$ for the receding angle. Table 4.3 summarizes advancing and receding contact angles as well as the calculated hysteresis of water measured on differently treated PS surfaces.

Tab. 4.3 Contact angels and hysteresis for differently treated PS surfaces presented as mean values and standard deviation of the mean (mean ± SDM; n = 4, except for "Plasma, SFM": n = 2).

Pretreatment	θ_A [°]	θ_R [°]	$\Delta\theta$ [°]
Unmodified	91.7 ± 0.8	82.2 ± 0.7	9.5 ± 1.5
PBS^{--}	92.1 ± 1.2	64.3 ± 1.0	27.8 ± 2.2
SFM	84.6 ± 1.8	34.1 ± 1.6	50.5 ± 3.4
Plasma	25.4 ± 1.7	6.3 ± 1.2	19.1 ± 2.9
Plasma, PBS^{--}	24.0 ± 2.3	7.0 ± 2.9	17.0 ± 5.2
Plasma, SFM	27.7 ± 1.0	4.9 ± 0.8	22.8 ± 1.8

The contact angles measured for unmodified PS are in good agreement with the literature, where an advancing angle of 94° and a receding angle of 86° are reported for a pristine PS surface (Fredriksson et al., 1998). Van Oss et al. (1988) as well as Owens and Wendt (1969) obtained a water contact angle of 91° measured under static conditions. The contact angle data for plasma modified PS are similar to those Fredriksson et al. (1998) measured on a PS sample that had been subjected to UV light for 3 min, leading to a similar hydrophilization of the polymer surface. Values of $\theta_A = 29°$ and $\theta_R < 5°$ were obtained.

Wettability of PMMA Coated Surfaces

The time course of the contact angle measured on differently processed PMMA surfaces is shown in Fig. 4.20. PMMA was subjected to similar surface treatments as described for the PS surface.

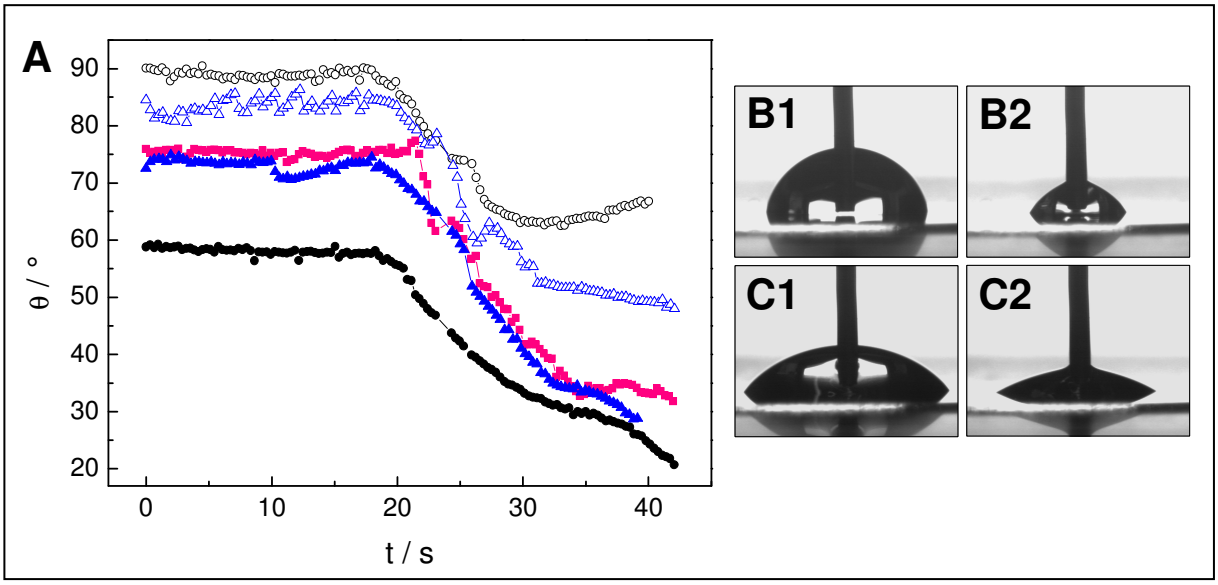

Fig. 4.20 A Representative dynamic contact angles for water measured during the process of wetting and dewetting of PMMA surfaces exposed to different surface modifications at (22 ± 1) °C: no pretreatment (○), pre-incubation with SFM (Δ) over 20 h at 37 °C, argon plasma treatment for 1 min (●), argon plasma treatment for 1 min followed by a PBS^{--} (■) / SFM incubation (▲) over 20 h at 37 °C. The first 18 seconds display the advancing angle, followed by the receding angle. **B** and **C** Photographs of a water droplet on two differently processed PMMA surfaces: **B** Water drop of maximal volume during the process of wetting (1) and of minimal volume during dewetting (2) of an unmodified PMMA surface. **C** Water drop on the surface of a PMMA sample previously exposed to an argon plasma for 1 min, showing maximal (1) and minimal (2) drop size.

PMMA was studied in its unmodified form, after the incubation in SFM (20 h), in its argon plasma modified form as well as after an argon plasma treatment followed by a PBS^{--} or SFM incubation (20 h). An unmodified PMMA surface exhibits an advancing contact angle of (88.4 ± 0.6)° and a receding angle of (62.9 ± 0.5)°. After an incubation in SFM, the advancing angle slightly decreases to (84.0 ± 0.2)° while the receding contact angle is altered more strongly, showing a value of (50.1 ± 0.2)°. The impact of a PBS^{--} incubation on the contact angle could not be measured, since the PMMA film detached from the substrate surface.

Argon plasma treatment decreases the advancing contact angle to (59.7 ± 0.9)° and the receding contact angle to (20.0 ± 0.8)°, indicating an increase of hydrophilicity. An additional incubation of the plasma modified PMMA surface in either PBS^{--} or SFM influences the dynamic contact angle to the same extent. Both physiological buffers cause an increase in the advancing angle when compared to a plasma treated surface to (74.5 ± 1.1)° for a PBS^{--} and (72.0 ± 0.8)° for a SFM incubated surface. The receding angles are increased either, accounting for (32.8 ± 1.2)° and (30.8 ± 1.6)°, respectively. All reported values are listed in Tab. 4.4.

Tab. 4.4 Contact angels and hysteresis for differently treated PMMA surfaces (mean ± SDM; n = 4, except for "SFM": n = 1).

Pretreatment	θ_A [°]	θ_R [°]	$\Delta\theta$ [°]
Unmodified	88.4 ± 0.6	62.9 ± 0.5	25.5 ± 1.1
SFM	84	50	34
Plasma	59.7 ± 0.9	20.0 ± 0.8	39.7 ± 1.7
Plasma, PBS^{--}	74.5 ± 1.1	32.8 ± 1.2	41.7 ± 2.3
Plasma, SFM	72.0 ± 0.8	30.8 ± 1.6	41.2 ± 2.4

The results obtained for unmodified and plasma modified PMMA are slightly higher than those previously reported in literature. Static contact angles measured on unmodified PMMA are reported to range between 70° and 82° (van Oss et al., 1988; Briggs et al., 1990; Jung and Bhushan, 2006; Owens and Wendt, 1969). Dynamic contact angles account for 70° and 77° for the advancing angle and 55° and 47.7° for the receding angle (Banerjee et al., 2000; Extrand and Kumugai, 1995). Chai et al. (2004) observed a decrease in the advancing contact angle of PMMA upon oxygen plasma treatment from 72.5° to 51.0° for a 50 s treatment.

Wettability of PDMS Coated Surfaces

Figure 4.21 shows the results of contact angle measurements on differently processed PDMS surfaces. PDMS was studied in its unmodified form, after the incubation in PBS^{--} or SFM at 37 °C over a period of 20 h as well as after an argon plasma treatment for 1 min.

An unmodified PDMS surface shows an advancing contact angle of (121.6 ± 0.9)°. The receding contact angle drops to a final value of θ_R = (40.2 ± 1.1)°. In literature, slightly lower values are reported for the contact angle measured on a PDMS surface under static conditions. Here, contact angles of 112.9°, 115° and 116° were found (Gillmor et al., 2002; Shahal et al., 2008; Thorslund et al., 2005). Efimenko et al. (2002) obtained an advancing contact angle of ~ 108°. The course of the contact angle measured after the PDMS surface had been incubated in PBS^{--} and SFM, respectively, at 37 °C over a period of 20 h is similar to that of an unmodified PDMS surface. For a PDMS surface incubated in PBS^{--}, an advancing angle of (118.7 ± 1.0)° and a receding angle of (32.5 ± 0.8)° are obtained. The SFM incubated PDMS surface exhibits dynamic contact angles of θ_A = (119.8 ± 1.1)° and θ_R = (35.8 ± 0.7)°.

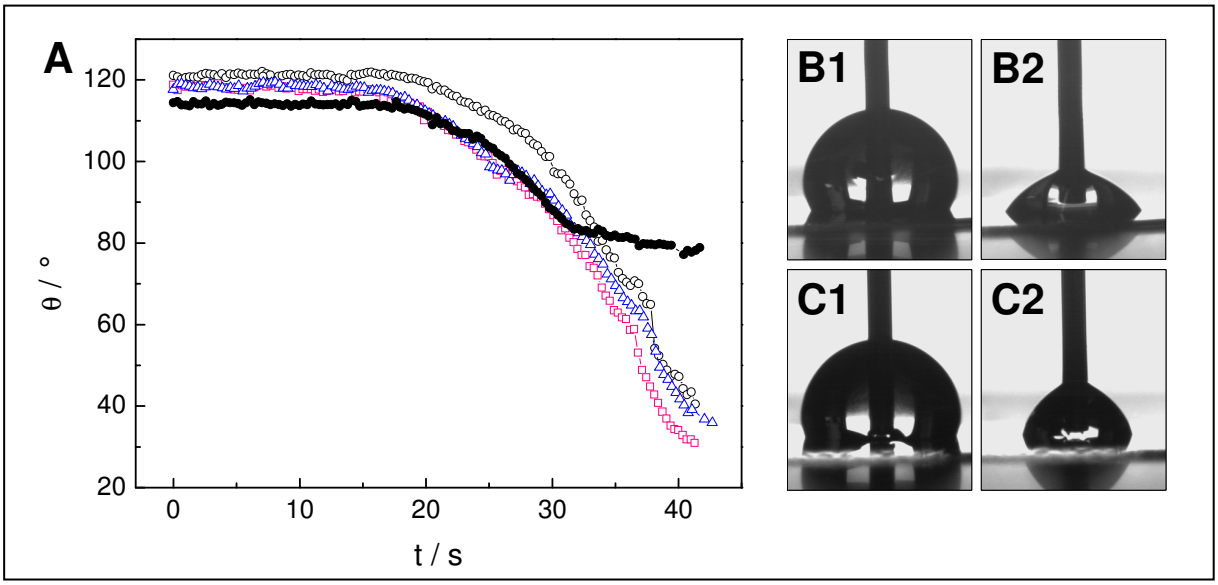

Fig. 4.21 **A** Representative dynamic contact angles for water measured during the process of wetting and dewetting of PDMS surfaces exposed to different surface modifications at (22 ± 1) °C: no pretreatment (○), pre-incubation with PBS^{--} (□) / SFM (Δ) over 20 h at 37 °C and argon plasma treatment for 1 min (●). The first 17 seconds display the advancing angle, followed by the receding angle. **B** and **C** Photographs of a water droplet on two differently processed PDMS surfaces: **B** Water drop of maximal volume during the process of wetting (1) and of minimal volume during dewetting (2) of an unmodified PDMS surface. **C** Water drop on the surface of a PDMS sample previously exposed to an argon plasma for 1 min, showing maximal (1) and minimal (2) drop size.

If PDMS is subjected to an argon plasma for 1 min, the subsequent contact angle measurement shows only a slight decrease in the advancing angle to a value of (110.4 ± 2.3)°, but a significantly different receding angle of $\theta_R = (81.0 \pm 1.2)°$, when compared to the previously described measurements. This slight increase in wettability is in agreement with the data obtained by Efimenko et al. (2002), who measured an advancing contact angle of ~ 100° after having subjected the PDMS film to UV light for 10 min, which, similar to a plasma treatment, is known to increase surface wettability. Table 4.5 presents the contact angle values and the calculated hysteresis obtained for water on variously processed PDMS surfaces.

Tab. 4.5 Contact angels and hysteresis for differently treated PDMS surfaces (mean ± SDM; n = 6, except for "Unmodified": n = 4).

Pretreatment	θ_A [°]	θ_R [°]	$\Delta\theta$ [°]
Unmodified	121.6 ± 0.9	40.2 ± 1.1	81.4 ± 2
PBS^{--}	118.7 ± 1.0	32.5 ± 0.8	86.2 ± 1.8
SFM	119.8 ± 1.1	35.8 ± 0.7	84.0 ± 1.8
Plasma	110.4 ± 2.3	81.0 ± 1.2	29.4 ± 3.5

Wettability of PhoP Coated Surfaces

The advancing and receding contact angles during the increase and decrease in drop volume as a function of time, measured on differently treated PhoP surfaces, are shown in Fig. 4.22.

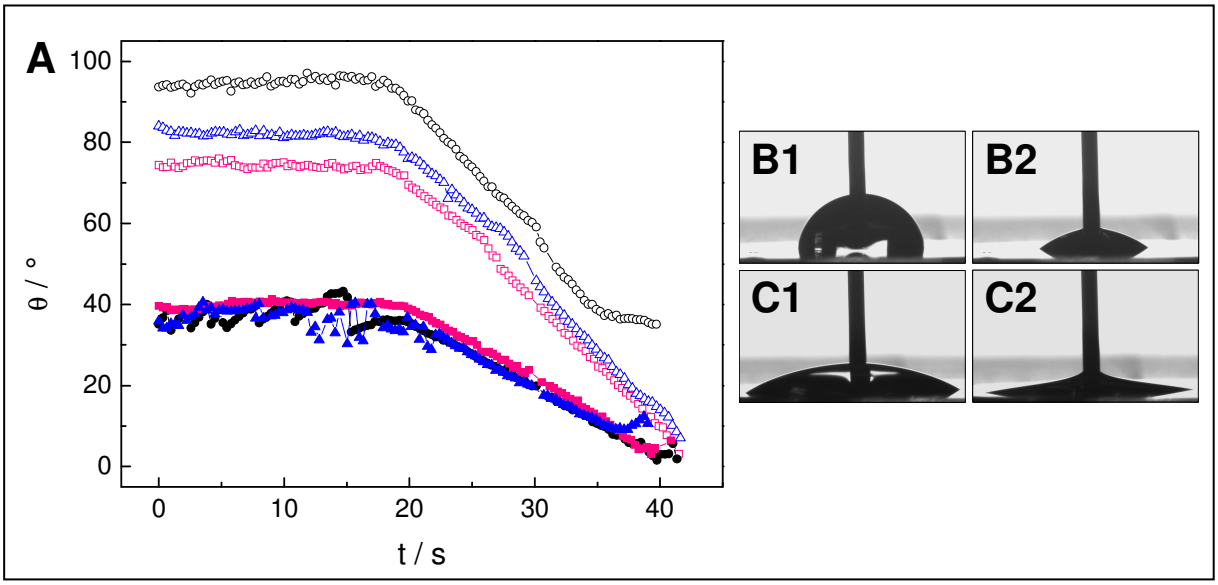

Fig. 4.22 **A** Representative dynamic contact angle for water measured during the process of wetting and dewetting of PhoP surfaces exposed to different surface modifications at (22 ± 1) °C: no pretreatment (○), pre-incubation with PBS^{--} (□) / SFM (Δ) over 20 h at 37 °C, argon plasma treatment for 1 min (●), argon plasma treatment for 1 min followed by a PBS^{--} (■) / SFM incubation (▲) over 20 h at 37 °C. The first 18 seconds display the advancing angle, followed by the receding angle. **B** and **C** Photographs of a water droplet on two differently processed PhoP surfaces: **B** Water drop of maximal volume during the process of wetting (1) and of minimal volume during dewetting (2) of an unmodified PhoP surface. **C** Water drop on the surface of a PhoP sample previously exposed to an argon plasma for 1 min, showing maximal (1) and minimal (2) drop size.

Spin coated films of PhoP exhibit an advancing angle of (92.5 ± 0.8)° and a receding angle of (35.5 ± 0.6)°. Upon incubation of this PhoP film in a physiological buffer, advancing and receding contact angles decrease nearly to the same extent. After an incubation period of 20 h in PBS^{--}, the PhoP film exhibits an advancing contact angle of (73.4 ± 0.9)° and a receding angle of (6.7 ± 0.7)°. The contact angles for a SFM incubated PhoP film are (80.0 ± 1.8)° and (9.6 ± 1.3)°. Argon plasma treatment leads to a significant decrease of the advancing angle to a value of θ_A = (35.8 ± 1.7)° and of the receding angle to θ_R = (5.3 ± 0.5)° when compared to an unmodified PhoP surface. This indicates a significant plasma-induced modification of the surface properties, indicating a hydrophilization of the surface. An additional incubation of the plasma treated PhoP film in a physiological buffer has no measurable effect on the contact angle. A plasma modified and additionally PBS^{--} incubated PhoP film exhibits values of θ_A = (39.5 ± 3.1)° and θ_R = (6.5 ± 1.4)°, while the values for the contact angles measured for a SFM incubated PhoP film are just slightly different. They account for (37.1 ± 0.3)° and (9.5 ± 0.2)°, respectively. The results of the dynamic water contact angles measured on differently processed PhoP surfaces as well as the respective hysteresis are summarized in Table 4.6.

Tab. 4.6 Contact angels and hysteresis for differently treated PhoP surfaces (mean ± SDM; n ≥ 4, except for "Plasma, SFM": n = 1).

Pretreatment	θ_A [°]	θ_R [°]	$\Delta\theta$ [°]
Unmodified	92.5 ± 0.8	35.5 ± 0.6	57.0 ± 1.4
PBS^{--}	73.4 ± 0.9	6.7 ± 0.7	66.7 ± 1.6
SFM	80.0 ± 1.8	9.6 ± 1.3	70.4 ± 3.1
Plasma	35.8 ± 1.7	5.3 ± 0.5	30.5 ± 2.2
Plasma, PBS^{--}	39.5 ± 3.1	6.5 ± 1.4	33.0 ± 4.5
Plasma, SFM	37	10	28

In summary, all applied polymers are strongly hydrophobic in their native, unmodified state. Except for PDMS, an argon plasma treatment of the polymers leads to a polymer-specific decrease of the advancing contact angle. Incubation of the unmodified polymers in a physiological fluid has a polymer-specific impact mainly on the contact angle hysteresis. Except for PMMA, incubation of plasma modified polymers in a physiological fluid has no significant impact on the advancing contact angle or the contact angle hysteresis.

4.2 Long-Term Stability of Polymer Films under Physiological Conditions

In order to analyze the biocompatibility of a polymer material, it is crucial to investigate its long-term stability in a liquid environment under physiological conditions. When technical surfaces are exposed to cellular systems, like, for instance, when they are used as culture substrates in cell culture or even as an implant integrated in human tissue, they encounter physiological fluids. With regard to the polymers in the focus of this study, fundamental questions arise concerning the long-term stability of such polymers under liquid conditions. Thus, it has to be clarified if the polymer is altered in such an environment and if so, what is the impact on cell attachment and spreading to this surface.

In literature, the swelling of polymers in a liquid environment is a well-known phenomenon (Chen and Shull, 1999; Ruzzu and Matthis, 2002; Welle, 2004). In order to address this issue, the polymers were studied with respect to their long-term stability in two different physiological fluids, PBS^{--} and serum-free culture medium (SFM) at 37 °C over a time frame of 20 h. An incubation of the polymer in a physiological fluid is also reasonable with respect to subsequent cell attachment and spreading studies, since possible changes of the polymer as they may occur during fluid exposure may overlap with the process of cell adhesion, possibly leading to distorted results when only cell attachment and spreading are in the focus of the investigations.

The polymers' long-term stability was monitored with time using double mode impedance analysis. The QCM was used as a mass-sensitive device being operated in the passive mode. Additionally, the experimental setup was extended by a low-impedance dipping electrode that served as a counter electrode for the electrochemical impedance analysis of the polymer film on the upper surface electrode of the quartz resonator (chapter 3.5.3, Fig. 3.26). In the following, the two modes of impedance analysis are referred to as **quartz mode** and **ECIS mode**. Impedance data were recorded for spin coated films of the polymers PS, PMMA, PDMS and PhoP, which were – except for PDMS – applied in their native, unmodified form as well as in their hydrophilized form.

Before presenting the results of double mode impedance measurements, some preliminary remarks are noteworthy for a better understanding and interpretation of the presented data.
The impedance raw data of the polymer coated quartz resonator recorded in the quartz mode during the incubation of the polymer film with a physiological fluid were analyzed by the BVD equivalent circuit and are presented in terms of changes of the real (load resistance R_L) and the imaginary components (load reactance X_L). Whereas R_L quantifies the energy dissipation of the surface material, X_L reflects the energy that is elastically stored in the system. Viscoelastic effects like alterations of the density and/or viscosity of the spin coated polymer close to the resonator surface can cause a change of the load resistance R_L. Changes in the load reactance X_L arise from changes of the motional inductance L due to either a simple mass deposition on the resonator surface or changes in the elastic properties close to the resonator surface.

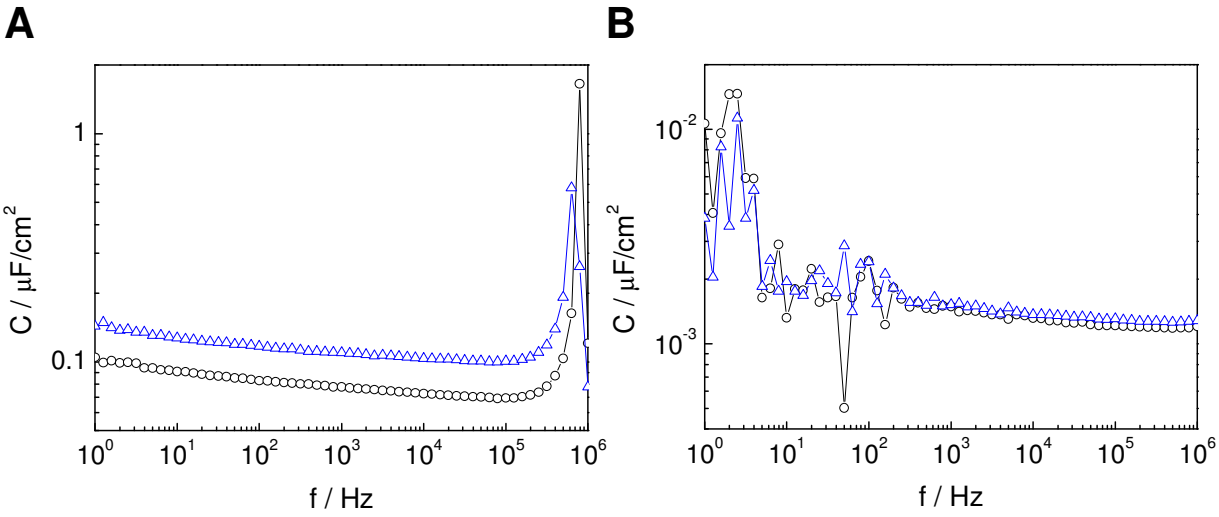

Fig. 4.23 Long-term stability of spin coated polymer films under physiological conditions. Spectra of the area normalized capacitance *C* recorded in a frequency range of 1 – 10^6 Hz for **A** a PDMS coated quartz resonator and **B** a PhoP coated quartz resonator directly after addition of SFM (○) and after incubation with the fluid over 20 h at 37 °C (Δ).

The complex impedance recorded in ECIS mode during exposure of the polymer film to a physiological fluid was separated into its real and imaginary components as well, presented by the resistance *R* and the capacitance *C* (chapter 3.6, Fig. 3.29). Figure 4.23 exemplarily compares the course of the electrochemical capacitance *C* recorded in a frequency range of $1 – 10^6$ Hz for a PDMS (A) and a PhoP (B) coated quartz resonator directly after exposure to a physiological fluid (SFM) as well as after an incubation time of 20 h.

The capacitance of the PDMS coated electrode exhibits a more or less constant value along the entire frequency range for both experimental conditions, before and after an incubation time of 20 h (Fig. 4.23 A). For high frequencies ($f > 10^5$ Hz), the capacitance shows a peak of approximately 0.6 μF/cm^2 and 1.7 μF/cm^2 for either of the surface treatments, which is mainly an artifact due to parasitic contributions of the electronic equipment and wiring. Thus, when studying the change in capacitance under liquid conditions over time, it is essential to choose a frequency below 10^5 Hz. After incubating the PDMS film in SFM over 20 h at 37 °C, the capacitance slightly increases compared to the capacitance measured directly after addition of SFM. Since the capacitance increases to the same extent along the frequency range, all frequencies – except for $f > 10^5$ Hz – are equally suited to follow the swelling behavior of the polymer over time.

By contrast, the capacitance spectrum of a PhoP coated electrode shows a completely different course (Fig. 4.23 B). For low frequencies ($f < 400$ Hz), the capacitance values are much smaller and strongly fluctuate due to technical limitations. The electrode is coated with a thick insulating PhoP film (~ 3 μm) and the amplifier is not able to resolve the signal in this low frequency range.

In order to be sure that the above mentioned phenomena do not interfere with the capacitance measurements and to allow for a comparison of the results for all polymers under study, it is reasonable to choose a frequency which is on the one hand below the high frequency peak and on the other hand beyond the capacitance fluctuations at low frequencies. Thus, a sampling frequency of 40 kHz was chosen to study the long-term stability of a polymer film in a time-dependent manner, as presented in Fig. 4.24 for a PDMS and a PhoP coated quartz resonator after SFM exposition.

The figure depicts the time course of the normalized capacitance C_{norm} of the electrode measured at a sampling frequency of 40 kHz. The first data point is taken from the spectrum recorded directly after the addition of SFM. During the first 350 min, the capacitance of the PDMS coated electrode shows a steep 1.44-fold increase to a stationary value, which is stationary for the remaining observation period of 800 min. When a PhoP coated electrode is exposed to SFM, C_{norm} shows an initial steep increase by a factor of 1.09 to a stationary value within 250 min after SFM addition.

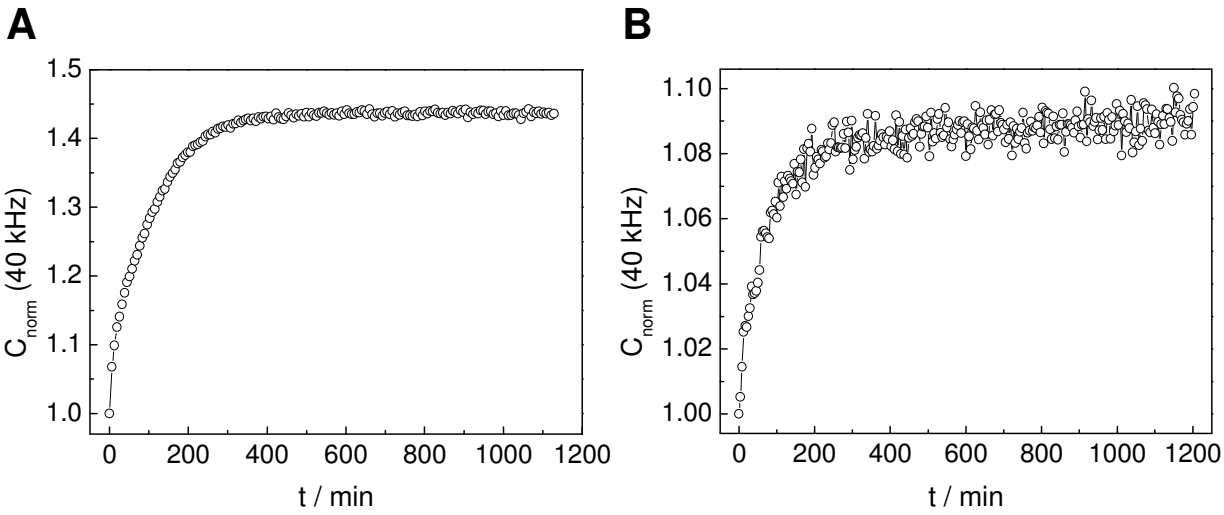

Fig. 4.24 Time course of the normalized electrochemical capacitance C_{norm} at a sampling frequency of 40 kHz during the incubation of **A** a PDMS coated quartz resonator and **B** a PhoP coated quartz resonator in SFM. The time point directly after the addition of fluid was defined as time point zero ((A) C_{start} = 0.070 µF/cm^2, (B) C_{start} = 1.234·10^{-3} µF/cm^2; T = 37 °C).

In the following, time courses of the above mentioned parameters, ΔR_L, ΔX_L (quartz mode) and C_{norm} (40 kHz) (ECIS mode) during the incubation of the different polymer films with the physiological fluids PBS^{--} and SFM are shown and compared in detail.

4.2.1 Long-Term Stability of Polystyrene

PS was studied in its unmodified and plasma modified form with respect to its long-term stability in PBS^{--} and SFM at 37 °C. The PS coated quartz resonators were exposed to both fluids in the measuring chamber over a period of 20 h.

Quantitative analysis of the impedance data recorded over a period of 20 h provides the time resolved change in the load resistance ΔR_L and the load reactance ΔX_L that are due to fluid exposure. Parameters of the polymer coated resonator directly after the addition of PBS^{--} or SFM was chosen as the basis relative to which the changes in both quantities are expressed.

Figure 4.25 shows the time courses of ΔR_L and ΔX_L during the incubation of PS with SFM at 37 °C over 20 h. Since the time courses of ΔR_L for all four processing conditions, i.e. PBS^{--} and SFM incubation of unmodified as well as plasma modified PS, are similar, only one processing condition is presented in Fig. 4.25 (see appendix C 1, Fig. C.1 A – C for the remaining processing conditions). The addition of SFM to the polymer coated resonator at time point zero induces a decrease of the load resistance ΔR_L within roughly 200 – 300 min, reaching a stationary value of – (41.2 ± 0.5) Ω (Fig. 4.25 A).

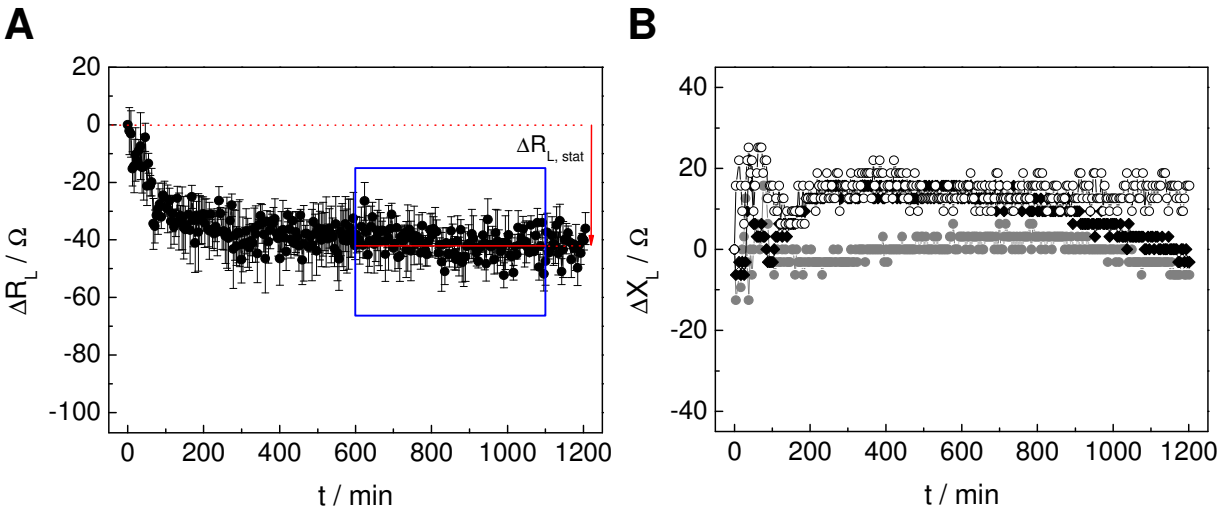

Fig. 4.25 Long-term stability of PS (quartz mode). **A** Time course of the load resistance ΔR_L and **B** the load reactance ΔX_L during the incubation of a PS coated quartz resonator with SFM at 37 °C. Changes of the load parameters are given relative to the PS coated resonator directly after addition of fluid. The blue box in A indicates the time interval used to determine $\Delta R_{L,\,stat}$. ((A) mean ± SDM, n = 3; B shows the time course of ΔX_L for three individual measurements).

In order to compare the long-term stability of PS for the different processing conditions, the ΔR_L values for the individual curves were averaged in the stationary region using the time interval between 600 min and 1100 min after fluid addition (see Fig. 4.25 A).This average decrease of the motional resistance is presented as $\Delta R_{L,\,stat}$ value below in Tab. 4.7.

Tab. 4.7 Change in the load resistance ΔR_L of PS coated quartz resonators due to incubation with a physiological fluid, averaged over an exposure time of 600 min and 1100 min. The values are presented relative to the same resonator directly after fluid addition (mean ± SDM, n ≥ 2).

Processing Condition	$\Delta R_{L,\,stat}$ [Ω]
PBS^{--}	– (49.1 ± 0.4)
SFM	– (41.2 ± 0.5)
Plasma Treatment + PBS^{--}	– (60.1 ± 1.4)
Plasma Treatment + SFM	– (42.3 ± 0.5)

The change in the motional resistance $\Delta R_{L,\,stat}$ shows very similar variations for the different processing conditions. The values range from – (41.2 ± 0.5) Ω for SFM incubated PS to a maximum decrease of – (60.1 ± 1.4) Ω for plasma modified as well as PBS^{--} incubated PS. Whereas an SFM incubation causes an identical decrease of the load resistance regardless of a preceding plasma treatment, the polymer films which are exposed to PBS^{--} reveal a bigger decrease of ΔR_L. Comparing both PBS^{--} incubated surfaces – the unmodified and the plasma modified one – PBS^{--} exposition to a plasma modified PS film leads to a 11 Ω bigger decrease of ΔR_L than for unmodified PS.

The time course of the load reactance as it is shown for an SFM incubated PS film for three individual measurements in Fig. 4.25 B does not reveal a clear tendency. Whereas for one

experiment (filled circles) ΔX_L mainly stays on a rather stationary level of approximately zero, a slight increase of roughly 15 Ω is recorded for the two remaining curves, followed by a decrease to 0 Ω for one of them (filled diamonds). As concluded from all three graphs, SFM incubation has a negligible impact on the load reactance – no increase in energy storage is observed. The same conclusion can be drawn from the time courses of ΔX_L for the remaining three processing conditions not shown here (appendix C 1, Fig. C.2 A – C). Fluid exposure to spin coated PS, either unmodified or plasma modified, has no significant impact on the load reactance.

Taken together, this part of the study reveals that the exposure of PS to a physiological fluid leads to a decrease of energy dissipation ranging in the order of approximately 41 – 60 Ω, depending on the processing condition. The contribution from elastic components and thus the impact on energy storage can be disregarded.

Using the ECIS mode, the long-term stability of PS was analyzed in terms of the electrochemical area-normalized capacitance measured at a sampling frequency of 40 kHz. The capacitance was normalized to the first data point taken from the spectrum recorded directly after the addition of fluid (Fig. 4.26).

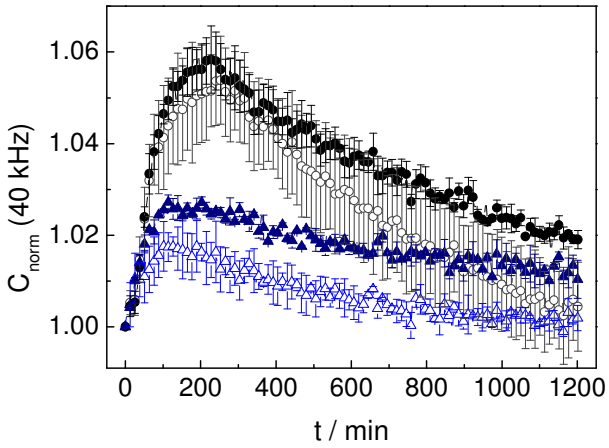

Fig. 4.26 Long-term stability of PS (ECIS mode). Time course of the normalized capacitance C_{norm} measured at 40 kHz during the incubation with PBS^{--} or SFM at 37 °C. The surface treatment of the PS film is as follows: (○) unmodified + PBS^{--}, (Δ) unmodified + SFM, (●) plasma modified + PBS^{--}, (▲) plasma modified + SFM. The measured parameters are: (○) C_{start} = (0.096 ± 0.012) µF/cm^2, (Δ) C_{start} = (0.079 ± 0.002) µF/cm^2, (●) C_{start} = (0.090 ± 0.005) µF/cm^2, (▲) C_{start} = (0.086 ± 0.003) µF/cm^2 (mean ± SDM, n ≥ 2). The number of points was reduced for reason of clarity.

The addition of fluid upon the polymer film leads to an instantaneous increase of C_{norm} for all four processing conditions independent of the surface modification. For the unmodified and the plasma modified PS coated electrodes which are exposed to PBS^{--}, the capacitance reaches a transient maximum roughly 230 min after addition of PBS^{--}, i.e. showing a 1.05 fold (unmodified) and a 1.06 fold (plasma modified) increase compared to the starting values. Subsequently, C_{norm} decreases over the remaining incubation time, with final values for the normalized capacitance of 1.005 for unmodified and 1.02 for plasma modified PS after PBS^{--}

incubation over a period of 20 h. It is noteworthy that the capacitance values recorded after an incubation period of 20 h do not have attained an equilibrium. They still continue to decrease in a moderate manner, possibly returning to their starting values.
The time courses of the capacitance for the SFM incubated PS surfaces display a similar behavior. The incubation of PS with SFM induces an increase of the capacitance by a factor of 1.019 within roughly 150 min after addition of SFM and a slight decrease thereafter along the observation time, finally reaching the starting values again after 20 h. For a hydrophilic polymer film exposure to SFM causes a maximal capacitance increase of 1.028 roughly 150 min after SFM addition compared to the starting values, followed by a slight decrease to a value of 1.012 within the remaining 1050 min.
In summary, exposure of a PS film to a physiological fluid causes mainly transient alterations in the electrode's capacitance. Although the time courses vary, the individual capacitances after the incubation process (20 h) are quite similar for all processing conditions and do not really differ from the starting values. The most obvious differences between the two fluids used for swelling, PBS^{--} and SFM, are found in the time that is needed to reach the transient maximum and the total capacitance increase at this time point. Spin coated PS films that are incubated in PBS^{--} exhibit a capacitance maximum that is significantly higher compared to the one obtained for SFM incubated PS films. Whereas PBS^{--} incubation causes a 1.05 – 1.06 capacitance increase after 230 min, SFM induces a minor increase (1.02 – 1.03 fold) already 150 min after SFM exposition.

The polymer capacitance data can be further analyzed to extract the polymer's dielectric constant. The coated gold electrode of the quartz resonator and the ions which assemble on the polymer surface form the two conducting plates of the capacitor. The polymer film in between is regarded as the dielectric. In this case, the measured capacitance can be described by:

$$C = \frac{\varepsilon_0 \cdot \varepsilon_r \cdot A}{d}, \tag{4.3}$$

with C being the capacitance of the polymer coated electrode, $\varepsilon_0 = 8.85 \times 10^{-12}\ \mathrm{Fm}^{-1}$ the permittivity of vacuum and ε_r the relative permittivity of the separation medium (= spin coated polymer). $A = 0.33\ \mathrm{cm}^2$ is the area of the electrode and d the thickness of the dielectric medium (= spin coated polymer) that separates the two conducting plates.
Following this equation, changes in capacitance during the swelling process of the polymer film can be attributed to changes in the relative permittivity ε_r of the respective polymer. In principle, changes in polymer film thickness can also alter the measured electrode capacitance as well. For the following calculation, the thickness of the spin coated polymer is regarded as a constant value.

On the basis of a PS coated resonator, which has been plasma modified prior to the addition of PBS^{--}, the calculation of the relative permittivity shall be demonstrated. Using the thickness data obtained from VSI measurements (chapter 4.1.2), the corresponding dielectric constant of the polymer film before and after swelling can be calculated. Spin coated PS exhibits a thickness of (40 ± 1) nm. The capacitance values of the PS coated electrode of the quartz resonator measured directly after the addition of the electrolyte and after the incubation period of 20 h are taken from ECIS mode measurements (Fig. 4.26) and inserted in Eq. 4.3 in order to calculate ε_r.

$$\varepsilon_r = \frac{3.14 \cdot 10^{-8}\, F \cdot 40 \cdot 10^{-9}\, m}{8.85 \cdot 10^{-12}\, Fm^{-1} \cdot 0.33 \cdot 10^{-4}\, m^2} = 4.3$$

The relative permittivity for PS directly after the addition of the electrolyte solution is calculated to be $\varepsilon_r = 4.3$. Using the value of $C = 3.21 \cdot 10^{-8}$ F for the capacitance recorded after the incubation period of 20 h, ε_r yields a value of 4.4.

In a similar manner, the relative permittivities for PS directly after addition of the physiological fluids and after an incubation interval of 20 h were calculated for the different processing conditions. The results are listed below in Tab. 4.8.

Tab. 4.8 Relative permittivity of the unmodified and the plasma modified PS film directly after addition of the physiological fluids PBS^{--} and SFM, respectively, and after an incubation time of 20 h (mean ± SDM, n ≥ 2).

Processing Condition	ε_r (0 h)	ε_r (20 h)
PBS^{--}	4.34 ± 0.54	4.36 ± 0.49
SFM	3.55 ± 0.10	3.56 ± 0.09
Plasma Treatment + PBS^{--}	4.05 ± 0.24	4.13 ± 0.27
Plasma Treatment + SFM	3.87 ± 0.15	3.91 ± 0.14

For all four processing conditions, changes in the relative permittivity due to the incubation with a physiological fluid are insignificant. Although transient changes of this quantity occur, the values recorded after an incubation time of 20 h range in the same order and do not differ significantly from the starting values.

4.2.2 Long-Term Stability of Poly(methyl methacrylate)

PMMA coated quartz resonators were exposed to PBS^{--} or SFM in the measuring chamber over 20 h at 37 °C. The long-term stability was studied for the unmodified as well as for the plasma modified form (Fig. 4.27 A, B).

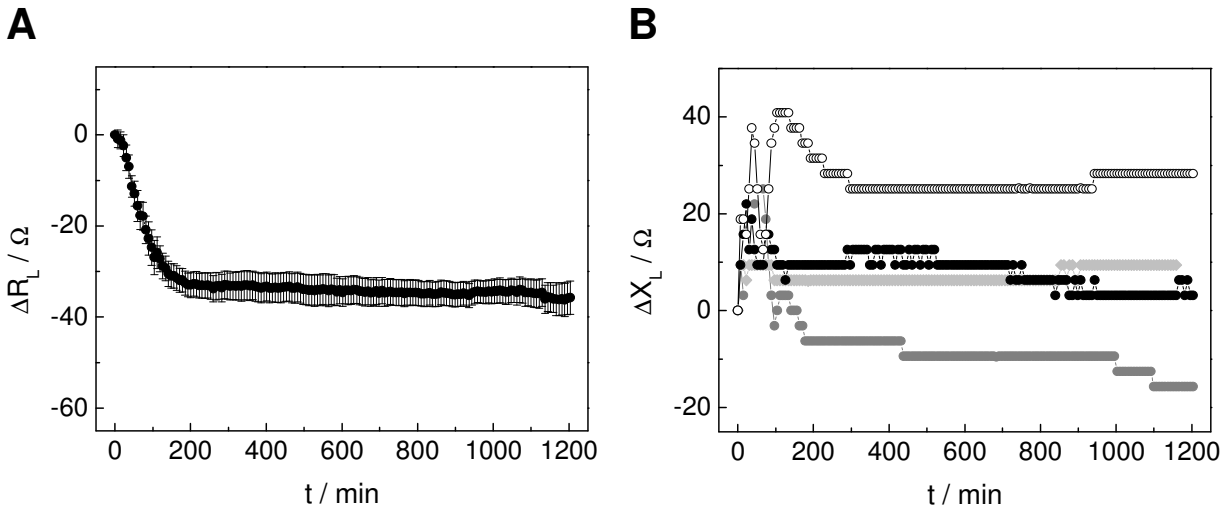

Fig. 4.27 Long-term stability of PMMA (quartz mode). **A** Time course of the load resistance ΔR_L and **B** the load reactance ΔX_L during the incubation of a PMMA coated quartz resonator with SFM at 37 °C. Changes of the load parameters are given relative to the PMMA coated resonator directly after addition of fluid ((A) mean ± SDM, n = 10; B shows the time course of ΔX_L for four individual measurements).

The incubation with SFM was chosen to exemplarily demonstrate the long-term stability of spin coated PMMA. The time courses for the remaining processing conditions can be found in the appendix C 2 (Fig. C.3 A – C).

The incubation of the PMMA coated resonator with SFM induces an instantaneous decrease of ΔR_L by $-(33.4 \pm 0.4)\ \Omega$ during a period of 200 min after the addition of SFM. For the remaining incubation period, ΔR_L stays on this stationary level (Fig. 4.27 A). The following table summarizes the stationary $\Delta R_{L,\,stat}$ values for each processing condition. Changes in the load resistance for each processing condition were averaged in a time interval between 600 min and 1100 min for all individual curves (Tab. 4.9).

Tab. 4.9 Change in the load resistance ΔR_L of PMMA coated quartz resonators due to incubation with a physiological fluid, averaged over an exposure time of 600 min and 1100 min. The values are presented relative to the same resonator directly after fluid addition (mean ± SDM, n ≥ 4).

Processing Condition	$\Delta R_{L,\,stat}$ [Ω]
PBS^{--}	$-(39.5 \pm 0.5)$
SFM	$-(33.4 \pm 0.4)$
Plasma Treatment + PBS^{--}	$-(49.3 \pm 0.4)$
Plasma Treatment + SFM	$-(45.0 \pm 0.2)$

Comparing the long-term stability of PMMA for the different processing conditions in terms of absolute changes of the load resistance reveals minor variations of this parameter. The values range from $-(33.4 \pm 0.4)\ \Omega$ for SFM incubated PMMA to $-(49.3 \pm 0.4)\ \Omega$ for plasma modified as well as PBS^{--} incubated PMMA. It is apparent that unmodified PMMA which is exposed to either of the fluids reveals a $10 - 12\ \Omega$ lower decrease of the load resistance compared to the plasma modified form.

The time course for the load reactance ΔX_L during the incubation process of a PMMA coated quartz resonator with SFM at 37 °C over 20 h presents no reproducible effects (Fig. 4.27 B). As shown on the basis of four individual measurements, ΔX_L either remains unaffected by the fluid incubation or increases or decreases in a moderate way by roughly 15 – 30 Ω. In summary, SFM incubation has a negligible impact on the load reactance – no increase in energy storage is observed. The same conclusion can be drawn from the time courses of ΔX_L for the remaining three processing conditions (appendix C 2, Fig. C.4 A – C). Fluid exposure to spin coated PMMA, either unmodified or plasma modified, has a negligible impact on the load reactance.

Taken together, PBS^{--} and SFM incubation of unmodified as well as plasma modified PMMA cause the motional resistance to decrease instantaneously after fluid addition by roughly 33 – 49 Ω, whereas the impact on energy storage can be disregarded.

In Fig. 4.28 the impedance data for PMMA recorded in the ECIS mode during the incubation with the two physiological fluids, PBS^{--} and SFM, are presented. The time course of the electrode impedance was studied in terms of the area-normalized capacitance at a sampling frequency of 40 kHz. The capacitance was normalized to the first data point taken from the spectrum recorded directly after the addition of fluid.

Similar to the measurements of the stationary $\Delta R_{L,\,stat}$ values recorded in the quartz mode, the ECIS mode impedance analysis also reveals slight differences in the course of the capacitance, depending on the polymer's wettability and the physiological fluid it had been exposed to.

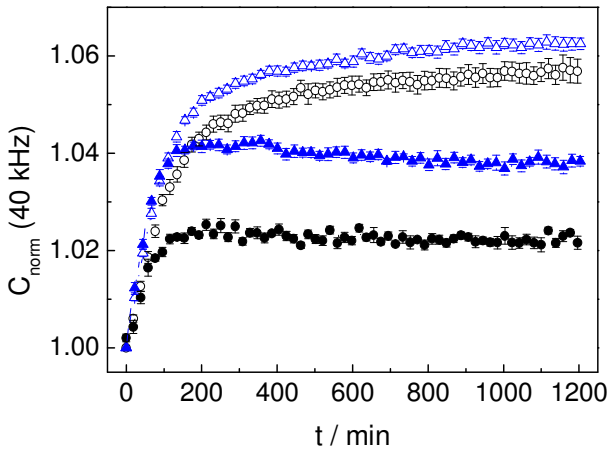

Fig. 4.28 Long-term stability of PMMA (ECIS mode). Time course of C_{norm} measured at 40 kHz during the incubation with PBS^{--} or SFM at 37 °C. The surface treatment of the PMMA film is as follows: (○) unmodified + PBS^{--}, (Δ) unmodified + SFM, (●) plasma modified + PBS^{--}, (▲) plasma modified + SFM. The measured parameters are: (○) C_{start} = (0.130 ± 0.002) µF/cm^2, (Δ) C_{start} = (0.132 ± 0.003) µF/cm^2, (●) C_{start} = (0.163 ± 0.002) µF/cm^2, (▲) C_{start} = (0.158 ± 0.002) µF/cm^2 (mean ± SDM, n ≥ 6). The number of points was reduced for reason of clarity.

The incubation of unmodified PMMA with PBS^{--} induces an increase of the capacitance by a factor of 1.057, recorded after an incubation period of 1200 min. The time course of the

capacitance is characterized by an initial steep increase during the first 200 – 300 min, which is followed by a more moderate increase along the remaining incubation time. When terminating the incubation process, C_{norm} has not reached an equilibrium. It still continues to increase slightly. An argon plasma treated polymer film shows a normalized capacitance that increases to a 1.02 fold maximum roughly 150 – 200 min after PBS^{--} addition and remains constant during the complete time frame. Spin coated PMMA films that are incubated in SFM over a period of 20 h exhibit capacitance values that are slightly higher compared to the ones obtained for PBS^{--} incubated PMMA films. The capacitance for a SFM incubated surface shows a steep increase during the first 200 – 300 min after SFM addition, and still continues to increase in a more moderate manner during the following 900 min, exhibiting a maximum increase of 1.063 when terminating the experiment. By contrast, SFM incubation of the argon plasma treated polymer causes an initial steep increase of the C_{norm} to a transient maximum roughly 200 min after SFM addition, followed by a slight decrease to a stationary value of 1.04 in the following 1000 min.

It can be concluded from the electrode impedance data during fluid exposure, that the polymer shows a measurable swelling behavior for all four different processing conditions. The capacitance increase during the incubation time of 20 h ranges in the order of 1.02 and 1.06. The time courses of the capacitance values in Fig. 4.28 show a general trend: Unmodified PMMA surfaces that are exposed to either of the fluids show a time course of the capacitance that is characterized by an initial steep increase during the first 200 – 300 min after fluid exposure, followed by a continued but slower increase during the remaining incubation time of 900 min. Additionally, the capacitance increase for SFM incubated PMMA is greater than for PBS^{--} incubated PMMA. By contrast, plasma modified PMMA reveals a capacitance that reaches a stationary level roughly 150 – 200 min after fluid exposure. Once again, the SFM incubated PMMA shows a bigger increase in C_{norm} than the PBS^{--} incubated surface. When using the same fluid but PMMA of different wettable forms, the capacitance increase is higher for an unmodified than for a plasma modified PMMA film.

As already demonstrated for PS, the recorded increase in capacitance can be explained by a possible change in the relative permittivity ε_r of the polymer. Using the formula mentioned above (Eq. 4.3), the relative permittivity for a spin coated PMMA film in its unmodified and its plasma modified form was calculated directly after the addition of PBS^{--} or SFM as well as after an incubation time of 20 h. From the respective capacitance values and the thickness of the spin coated PMMA film of (19 ± 1) nm, Eq. 4.3 returns the relative permittivities which are listed below in Tab. 4.10.

Tab. 4.10 Relative permittivity of the unmodified and the plasma modified PMMA film directly after addition of the physiological fluids PBS^{--} and SFM, respectively, and after an incubation time of 20 h (mean ± SDM, n ≥ 6).

Processing Condition	ε_r (0 h)	ε_r (20 h)
PBS^{--}	2.80 ± 0.05	2.96 ± 0.06
SFM	2.83 ± 0.06	3.01 ± 0.06
Plasma Treatment + PBS^{--}	3.50 ± 0.04	3.58 ± 0.05
Plasma Treatment + SFM	3.38 ± 0.04	3.51 ± 0.04

The relative permittivity of PMMA which had been exposed to PBS^{--} over a period of 20 h increases from (2.80 ± 0.05) to (2.96 ± 0.06). An incubation of PMMA with SFM causes a change in ε_r from (2.83 ± 0.06) to (3.01 ± 0.06). Fluid exposition to plasma modified PMMA induces even smaller changes in the relative permittivities. When plasma modified PMMA is subjected to PBS^{--}, the change in ε_r is insignificant. SFM causes ε_r to increase from (3.38 ± 0.04) to (3.51 ± 0.04). Plasma modified PMMA that is exposed to either PBS^{--} or SFM reveals relative permittivities which are higher compared to the ones obtained for unmodified PMMA.

4.2.3 Long-Term Stability of Poly(dimethyl siloxane)

The long-term stability of PDMS was only studied for the unmodified form over 20 h at 37 °C using SFM as the physiological fluid. The QCM response to the exposition of the PDMS film to SFM is shown in Fig. 4.29 A and B.

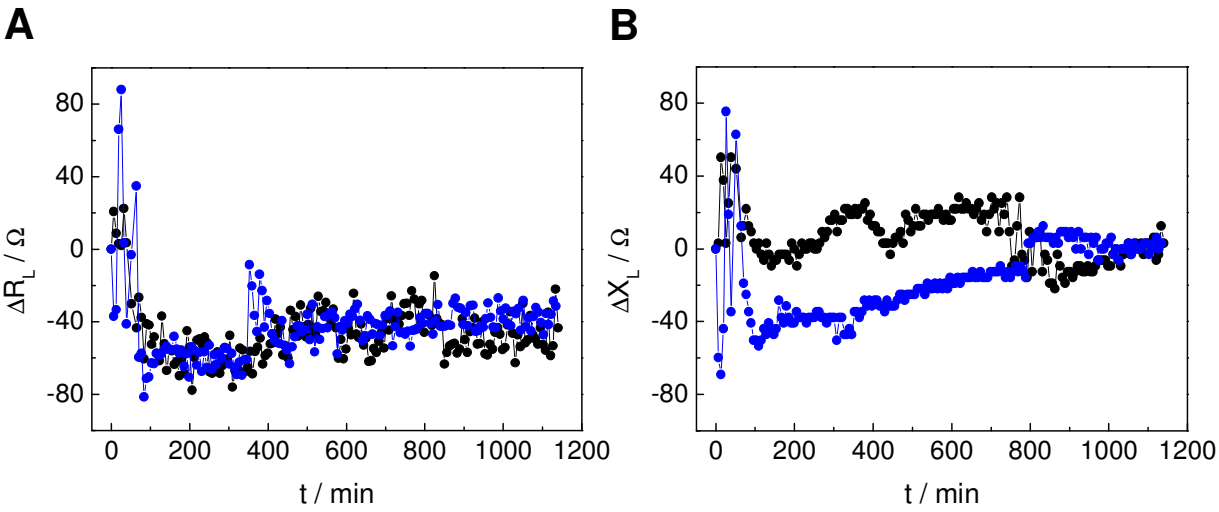

Fig. 4.29 Long-term stability of PDMS (quartz mode). **A** Time course of the load resistance ΔR_L and **B** the load reactance ΔX_L during the incubation of a PDMS coated quartz resonator with SFM at 37 °C. The time course for two individual measurements is depicted. Changes of the load parameters are given relative to the PDMS coated resonator directly after addition of SFM.

An incubation of the PDMS coated resonator with SFM gives rise to an instantaneous decrease of ΔR_L. A maximum decrease of roughly 60 Ω is obtained within about 100 min after SFM addition. After 400 min, ΔR_L reaches an equilibrium at approximately – 40 Ω for the rest of the observation period. The average value for ΔR_L during the stationary phase in the time interval between 600 min and 1100 min accounts for $\Delta R_{L,\,stat} = -(42 \pm 1)$ Ω.
The time courses of ΔX_L reveal no clear tendency (Fig. 4.29 B). Whereas one curve mainly fluctuates around 0 Ω (black circles), the other curve shows an initial decrease of ΔX_L by approximately 40 Ω which is followed by a moderate increase finally returning to 0 Ω (blue circles). At the end of the observation period, the ΔX_L values for both curves are equal.

The QCM results for the long-term stability of spin coated PDMS in SFM reveal a decrease of energy dissipation of $\Delta R_{L,\,stat} = -(42 \pm 1)$ Ω, thus ranging in the same dimension as recorded for the two previously mentioned polymers, PS and PMMA. The contribution from elastic components and thus the impact on energy storage can be disregarded – ΔX_L only fluctuates around zero.

Using the ECIS mode, the long-term stability of PDMS was analyzed in terms of the electrochemical area-normalized capacitance measured at a sampling frequency of 40 kHz. The capacitance was normalized to the first data point taken from the spectrum recorded directly after the addition of SFM (Fig. 4.30). C_{norm} shows a final increase by a factor of 1.5 for all three individual measurements. However, the individual time courses show significant differences. Whereas two measurements (open circles and filled circles) exhibit a moderate increase of C_{norm} within the first 400 min of the measurement, the third graph (open squares) reveals a steep 1.6 fold increase of C_{norm} within 250 min after SFM addition, followed by a slight decrease thereafter.

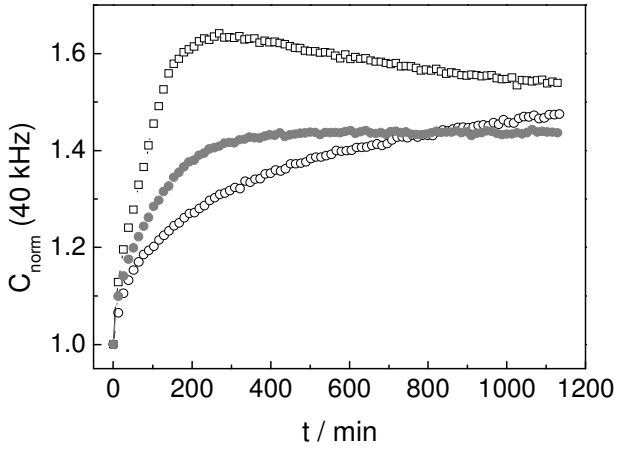

Fig. 4.30 Long-term stability of PDMS (ECIS mode). Time course of C_{norm} measured at 40 kHz during the incubation with SFM at 37 °C. The measured parameters are: (○) C_{start} = 0.100 µF/cm^2, (●) C_{start} = 0.070 µF/cm^2, (□) C_{start} = 0.082 µF/cm^2. The number of points was reduced for reason of clarity.

The increase in capacitance can be further analyzed by calculating the relative permittivity ε_r for the spin coated PDMS after the first contact with SFM and after an incubation time of 20 h. Thus, the respective capacitance values from the ECIS mode measurements and the thickness value of the spin coated PDMS of (30 ± 2) nm were inserted in Eq. 4.3, returning $\varepsilon_r = (2.8 \pm 0.3)$ for the polymer directly after the addition of SFM and $\varepsilon_r = (4.2 \pm 0.4)$ for the same polymer after an incubation period of 20 h. The relative permittivity increases by a factor of 1.5, as reflected in the course of the capacitance in Fig. 4.30.

In summary, the data obtained by QCM mode as well as ECIS mode measurements are sensitive indicators for the swelling behavior of PDMS in SFM. ΔR_L and C_{norm} show a similar time course, where the most considerable changes occur during the first 200 – 400 min after SFM exposure (Fig. 3.29 A and Fig. 4.30).

4.2.4 Long-Term Stability of Photopolymer

PhoP was only studied in its unmodified form with respect to its long-term stability in PBS^{--} and SFM at 37 °C in terms of changes of the load resistance and the load reactance during the incubation process (Fig. 4.31 A, B).

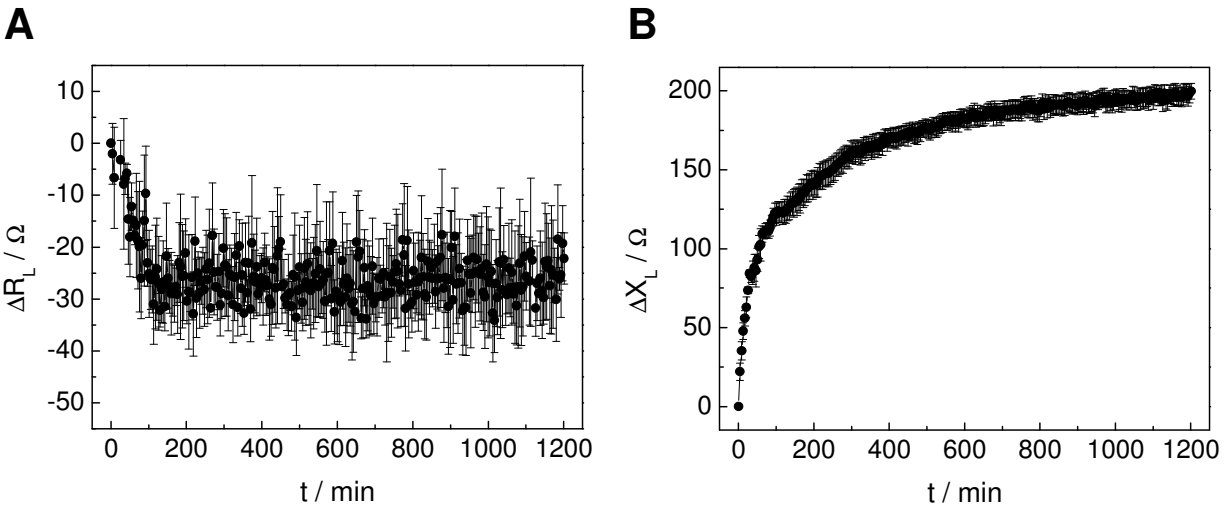

Fig. 4.31 Long-term stability of PhoP (quartz mode). **A** Time course of the load resistance ΔR_L and **B** the load reactance ΔX_L during the incubation of a PhoP coated quartz resonator with SFM at 37 °C. Changes of the load parameters are given relative to the PhoP coated resonator directly after addition of fluid (mean ± SDM, n = 4).

Figure 4.31 shows the time courses of ΔR_L and ΔX_L during the incubation of PhoP with SFM at 37 °C over 20 h. A similar graph results from the exposure of unmodified PhoP to PBS^{--} (appendix C 3, Fig. C.5 A, B). The exposition of spin coated PhoP to SFM leads to an instantaneous decrease of the load resistance ΔR_L by approximately 30 Ω during the first 120 min of fluid incubation and remains constant for another 1100 min (Fig. 4.31 A). The

average determination of $\Delta R_{L,\,stat}$ for the individual curves during the stationary phase using the time interval between 600 min and 1100 min returns a total decrease of $-(26.6 \pm 0.7)\ \Omega$ for the load resistance due to SFM exposure. The incubation with PBS^{--} causes the motional resistance to reach an equilibrium of $\Delta R_{L,\,stat} = -(33.1 \pm 0.6)\ \Omega$ (Tab. 4.11). This is similar to the $\Delta R_{L,\,stat}$ values as obtained by QCM measurements for the other polymers after a 20 h exposure to a physiological fluid.

Tab. 4.11 Change in the load resistance ΔR_L of PhoP coated quartz resonators due to incubation with a physiological fluid, averaged over an exposure time of 600 min and 1100 min. The values are presented relative to the same resonator directly after fluid addition (mean ± SDM, n ≥ 2).

Processing Condition	$\Delta R_{L,\,stat}$ [Ω]
PBS^{--}	$-(33.1 \pm 0.6)$
SFM	$-(26.6 \pm 0.7)$

The load reactance ΔX_L shows a time course that is characterized by a steep increase to a value of about 120 Ω during the first 100 min of SFM exposure. This steep increase is followed by a rather moderate increase of 80 Ω to a final value of $(199 \pm 6)\ \Omega$ in the remaining incubation period (Fig. 4.31 B). The exposure to PBS^{--} causes a similar time course of ΔX_L (appendix C 3, Fig. C.5 B).

In summary, PBS^{--} as well as SFM incubation of unmodified PhoP lead to an instantaneous increase in the load reactance by roughly 200 Ω. The change of the load resistance of roughly − 30 Ω is similar to those observed for the other polymers. For PhoP, the increase of ΔX_L is the predominant change induced by the fluid, indicating a mass increase on the resonator surface by embedded fluid in the polymer film. Fluid exposure can also alter the elasticity close to the quartz surface causing a change in L as well and being indistinguishable from a simple mass increase by embedded fluid.

The time course of the area-normalized capacitance for a PhoP coated electrode as obtained from ECIS mode measurements is presented in Fig. 4.32. The capacitance was normalized to the first data point taken from the spectrum recorded directly after fluid addition and is followed for a sampling frequency of 40 kHz.
When spin coated PhoP is exposed to a physiological fluid, either PBS^{--} or SFM, C_{norm} shows an initial steep increase by a factor of 1.09 to a stationary value within roughly 200 min after fluid addition. It is apparent that both physiological fluids reveal an identical time course of C_{norm}.

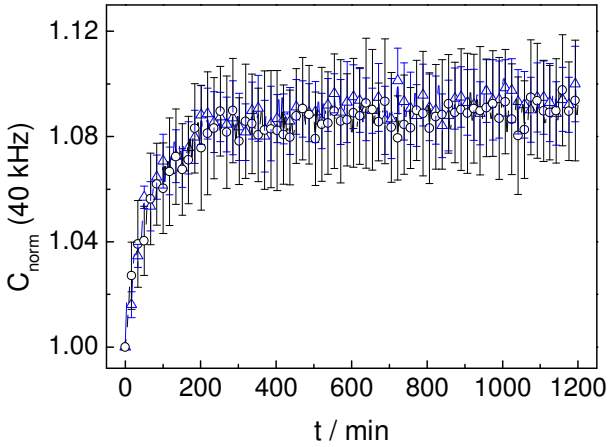

Fig. 4.32 Long-term stability of PhoP (ECIS mode). Time course of C_{norm} measured at 40 kHz during the incubation with PBS^{--} or SFM at 37 °C. The surface treatment of the PhoP film is as follows: (○) unmodified + PBS^{--}, (Δ) unmodified + SFM. The measured parameters are: (○) C_{start} = $(1.245 \pm 0.004)\cdot10^{-3}$ µF/cm^2,(Δ) C_{start} = $(1.234 \pm 0.012)\cdot10^{-3}$ µF/cm^2 (mean ± SDM, n ≥ 5).

In order to quantify the swelling process of PhoP, the relative permittivity ε_r of the polymer film directly after the addition of fluid and after an incubation time of 20 h was calculated using Eq. 4.3. The capacitance values from the ECIS mode measurements and the thickness of the spin coated PhoP of (2972 ± 11) nm were inserted in Eq. 4.3, returning the relative permittivities which are listed below in Tab. 4.12.

Tab. 4.12 Relative permittivity of the unmodified PhoP film directly after addition of the physiological fluids PBS^{--} and SFM, respectively, and after an incubation time of 20 h (mean ± SDM, n ≥ 5).

Processing Condition	ε_r (0 h)	ε_r (20 h)
PBS^{--}	4.18 ± 0.05	4.50 ± 0.01
SFM	4.14 ± 0.04	4.54 ± 0.09

The relative permittivity of PhoP which had been exposed to PBS^{--} over a period of 20 h increases from (4.18 ± 0.05) measured directly after PBS^{--} addition to (4.50 ± 0.01) after 20 h of incubation. An incubation of PhoP with SFM causes a similar change in ε_r from (4.14 ± 0.04) to (4.54 ± 0.09). Irrespective of the fluid used for the incubation of the polymer film, ε_r increases by a factor of 1.09 upon fluid exposure, as reflected in the course of the capacitance in Fig. 4.32.

4.3 Quantification of Protein Adsorption upon Polymer Surfaces

For any detailed description of the interactions of mammalian cells with the polymer surface, the adsorption of proteins upon the polymers needs to be characterized. Detailed knowledge about protein adsorption is of crucial importance when cell adhesion to a certain surface is interpreted, since cells do not interact directly with an underlying surface but anchor to adhesive proteins that pre-adsorbed to a substrate surface. Cell-protein interaction is mediated by specialized cell-surface receptors. So-called integrins are the most prominent type and are specialized to recognize and specifically bind to these adhesion-promoting proteins on the surface. Even though many non-specific electrostatic or electrodynamic interactions are involved in cell adhesion, specific ligand-receptor interactions are regarded more important for the final strength and the dynamic properties of the adhesion sites (Bongrand, 1998). Thus, protein adsorption is an essential prerequisite for cell adhesion and can be regarded as a sensitive parameter for the biocompatibility of a given surface.

The following chapter addresses the adsorption of various proteins upon polymer surfaces and the resulting surface coverage of the polymer with protein as measured by the QCM technique operated in the active oscillator mode. Protein adsorption upon polymer films of PS, PMMA, PDMS and PhoP spin coated on the resonator surface was analyzed from solution. Except for PDMS, the polymers were used in their unmodified, native form as well as in their hydrophilized form after having been exposed to an argon plasma. In order to prevent polymer swelling to interfere with protein adsorption, a preceding equilibration of each polymer film with DI-water (~ 1 h) was a prerequisite. The adsorption process of the protein from solution (DI-water) to the polymer coated quartz resonator was monitored by reading the series resonance frequency of the free oscillation over time while adding increasing protein concentrations to the supernatant at distinct time intervals, i.e. every 30 min (Fig. 4.33 A). The shift in resonance frequency Δf upon protein adsorption was plotted versus the respective protein concentration in the bulk solution for each of the proteins under study (Fig. 4.33 B). The decrease in frequency was assumed to be proportional to the adsorbed mass of protein on the resonator surface and thus its fractional coverage. In order to describe the adsorption process in a quantitative manner, a Langmuir adsorption isotherm was fitted to the experimental Δf data (Fig. 4.33 B). The equation can be applied to a large number of cases of adsorption on plane surfaces if a monolayer of adsorbates is formed (Langmuir, 1932). The model is only applicable if i) the surface is perfectly plane with no irregularities, ii) all binding sites are energetically equivalent and iii) interactions between adsorbate molecules on adjacent sites are absent. Adsorption and desorption are assumed as being elementary processes and at a dynamic equilibrium (Langmuir, 1932). The typical course of such an isotherm is a saturation curve, indicating a complete coverage of the surface with proteins for a finite concentration, following a dynamic equilibrium of adsorption and desorption. Fitting the Langmuir isotherm to the experimental data allows to extract two adsorption parameters, $-\Delta f_{max}$ and $c_{50\%}$. The maximal frequency change is related to the protein coverage upon

saturation. In this context, it has to be stressed that the entrapment of water in the protein layer as well as internal dissipative effects can have an impact on $-\Delta f_{max}$ as well. $c_{50\%}$ is the bulk protein concentration required for half-maximal surface coverage with protein.
The results obtained for different proteins on the polymer surfaces were correlated with further cell attachment and spreading studies in order to describe the material's biocompatibility on a molecular and cellular level.

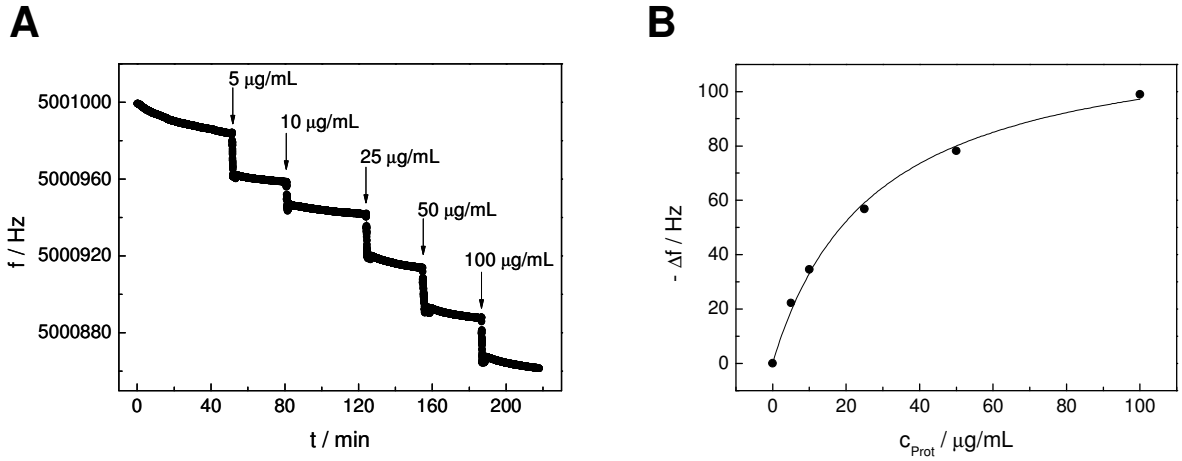

Fig. 4.33 A Time course of the resonance frequency *f* for a PDMS coated quartz resonator during the adsorption of Col IV from differently concentrated bulk solutions in water at 18 °C. The protein solution was exchanged by an increasingly higher concentrated solution every 30 min after a constant baseline was reached. The initial 50 min of the measurements show the equilibration with DI-water. **B** Frequency shift as a function of protein concentration c_{Prot} in the bulk solution. The solid line represents the fit according to the Langmuir adsorption isotherm (Δf_{max} = (123.8 ± 5.0) Hz, $c_{50\%}$ = (27.4 ± 2.9) µg/mL).

As an example, Fig. 4.33 A shows the course of the resonance frequency *f* over time during the sequential addition of Col IV solutions with increasing concentrations to a PDMS coated quartz resonator. Instantaneously after addition of the protein solution, the resonance frequency decreases and reaches a stable value. The initial addition of Col IV solution with a bulk protein concentration of 5 µg/mL causes the resonance frequency to decrease by 22 Hz. Subsequent exposures to Col IV solutions with increasing concentrations results in a step-like decrease of the resonance frequency. Plotting the respective equilibrium frequency shift against the protein concentration in the bulk solution returns a saturation curve for Col VI (Fig. 4.33 B). The frequency shift increases monotonically with the protein concentration in the bulk solution and remains constant above $-\Delta f_{max}$ = (123.8 ± 5.0) Hz, indicating complete surface coverage. The $c_{50\%}$ value obtained from the Langmuir fit for half-maximal coverage of the PDMS coated resonator is determined to (27.4 ± 2.9) µg/mL.

Protein Adsorption upon Polystyrene Coated Surfaces

The adsorption was quantified for the proteins Bovine Serum Albumin (BSA), Gelatin (Gel), Collagen G (Col G), Collagen IV (Col IV), and Laminin I (Lam I) as well as for the proteins

contained in Normal Calf Serum (NCS) on unmodified and plasma modified PS. The respective diagrams showing the shift in resonance frequency as a function of the respective protein concentration in the bulk solution as well as the fitted Langmuir isotherms are presented in the appendix B 1 (Fig. B.1 – B.6). The following table 4.13 summarizes the adsorption parameters determined by the Langmuir fit to the frequency curves in terms of the maximal frequency shift $-\Delta f_{max}$ for a completely saturated surface and the bulk protein concentration at half-maximal surface coverage, $c_{50\%}$.

Tab. 4.13 Adsorption parameters characterizing the adsorption of the proteins BSA, Gel, Col G, Col IV, and Lam I as well as the proteins contained in NCS upon an unmodified and a plasma modified PS surface, as determined from the frequency shifts and subsequent data fitting using a Langmuir adsorption isotherm. n/a means "not applicable". (Mean ± SDM, n ≥ 1; * = concentration in vol-%).

Protein	Unmodified		Plasma Modified	
	$-\Delta f_{max}$ [Hz]	$c_{50\%}$ [µg/mL]	$-\Delta f_{max}$ [Hz]	$c_{50\%}$ [µg/mL]
BSA	114 ± 20	47 ± 18	56.8 ± 2.5	5.1 ± 1.0
Gel	167.0 ± 5.0	23.8 ± 1.6	105 ± 15	32 ± 11
Col G	n/a	n/a	332.3 ± 7.4	64.1 ± 2.8
Col IV	45.6 ± 4.8	77 ± 15	76.2 ± 5.0	45.3 ± 6.5
Lam I	n/a	n/a	n/a	n/a
NCS	67.3 ± 4.4	0.055 ± 0.029*	51.2 ± 2.2	0.436 ± 0.081*

The Langmuir isotherms determined for the adsorption of BSA upon unmodified and plasma modified PS are quite different. Regarding the adsorption of BSA upon unmodified PS, the frequency shift mainly remains on a constant level of $-\Delta f \sim 25$ Hz for the low concentration range (5 – 25 µg/mL). By contrast, the addition of a 50 µg/mL BSA solution leads to an increase of $-\Delta f$ by approximately 40 Hz. On plasma modified PS, the frequency shift already reaches its maximum for a BSA concentration of 10 µg/mL and does not change significantly thereafter for the higher protein concentrations, showing a typical saturation curve in the investigated concentration range. The maximal frequency shift for BSA on unmodified PS is $-\Delta f_{max} = (114 \pm 20)$ Hz and the concentration for half-maximal surface coverage is $c_{50\%} = (47 \pm 18)$ µg/mL. $-\Delta f_{max}$ as well as $c_{50\%}$ quantifying BSA adsorption upon plasma modified PS are smaller than for the unmodified form. $-\Delta f_{max}$ is determined to be (56.8 ± 2.5) Hz and $c_{50\%}$ to be (5.1 ± 1.0) µg/mL. The $-\Delta f_{max}$ values for BSA adsorption might indicate that the amount of protein adsorbing to unmodified PS is twice as high as on plasma modified PS. However, BSA has a higher affinity to adsorb upon the plasma modified surface than upon the unmodified one, as indicated by $c_{50\%}$.

For Gel adsorption upon unmodified PS the two parameters $-\Delta f_{max} = (167.0 \pm 5.0)$ Hz and $c_{50\%} = (23.8 \pm 1.6)$ µg/mL can be found. The maximal frequency shift upon saturation for Gel adsorbing upon a plasma modified PS surface accounts for (105 ± 15) Hz. This value is 62 Hz smaller than the one determined for an unmodified PS surface, indicating that the final amount of protein adsorbing to plasma modified PS might be smaller than on an unmodified

surface. Half-maximal surface coverage can be found for a bulk protein concentration of $c_{50\%}$ = (32 ± 11) µg/mL.

When an unmodified PS surface is subjected to differently concentrated solutions of Col G, a Langmuir fit of the adsorption isotherm can not be applied. The frequency shift increases linearly with the protein concentration in the bulk solution, revealing no saturation behavior. Thus, the adsorption of Col G to unmodified PS could not be quantified by the adsorption parameters. For a plasma modified PS surface the Langmuir fit returns values of $-\Delta f_{max}$ = (332.3 ± 7.4) Hz and $c_{50\%}$ = (64.1 ± 2.8) µg/mL.

The adsorption process of Col IV upon unmodified PS is characterized by $-\Delta f_{max}$ = (45.6 ± 4.8) Hz whereas the plasma modified surface exhibits a maximal frequency shift of $-\Delta f_{max}$ = (76.2 ± 5.0) Hz, indicating that the amount of protein adsorbed upon a plasma modified surface might be higher than on an unmodified one. The values for half-maximal surface coverage are $c_{50\%}$ = (77 ± 15) µg/mL for an unmodified and $c_{50\%}$ = (45.3 ± 6.5) µg/mL for a plasma modified PS surface. Col IV has a higher affinity to plasma modified PS.

For unmodified and plasma modified PS, the frequency data for Lam I show no saturation behavior. Instead, the frequency shift increases linearly with increasing protein concentration in the bulk solution, which prevents a detailed analysis by using the Langmuir isotherm.

The adsorption of the proteins contained in NCS upon PS shows for both surface modifications typical saturation curves. Fitting the Langmuir isotherm to the experimental data results $-\Delta f_{max}$ = (67.3 ± 4.4) Hz and $c_{50\%}$ = (0.055 ± 0.029) vol-% for the unmodified PS surface and $-\Delta f_{max}$ = (51.2 ± 2.2) Hz and $c_{50\%}$ = (0.436 ± 0.081) vol-% for the plasma modified substrate.

The following bar diagram (Fig. 4.34) compares the average $c_{50\%}$ for all proteins under study to further visualize the differences in the protein adsorption behavior upon unmodified and plasma modified PS.

A general dependence of protein adsorption upon unmodified and plasma modified PS on the surface hydrophilicity can not be found. The $c_{50\%}$ values for half-maximal surface coverage differ significantly for the proteins BSA and Col IV, showing both smaller values on plasma modified PS than on the unmodified form. Gel exhibits instead similar values for half-maximal surface coverage on both modifications of PS. If the $-\Delta f_{max}$ values of the proteins BSA, Gel and NCS are compared for the two different surface modifications of PS, it is apparent that these values are 1.3 – 2 fold bigger for protein adsorption on unmodified than on plasma modified PS, which might indicate a higher amount of protein on the unmodified than on the plasma treated surface. In the case of Col IV, more protein might adsorb upon the plasma modified than upon the unmodified PS surface, indicated by a 1.7-fold higher $-\Delta f_{max}$ for the plasma modified substrate.

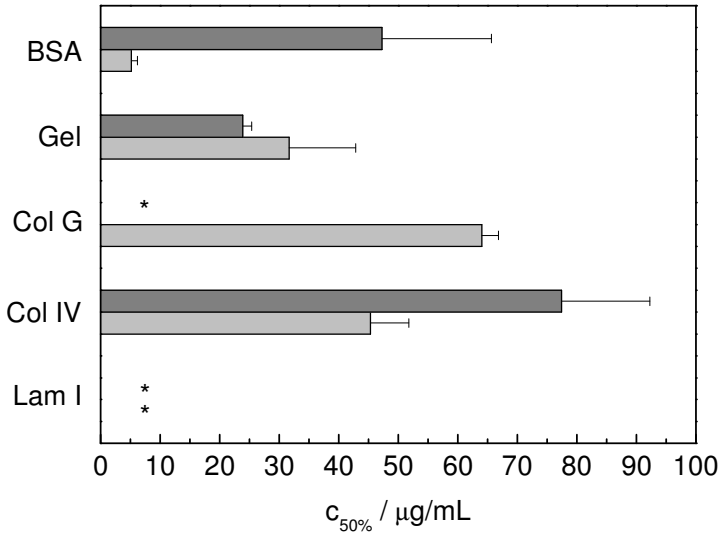

Fig. 4.34 $c_{50\%}$ values for the adsorption of selected proteins to a PS surface at 18 °C. The data was obtained from active oscillator mode QCM measurements and subsequent parameter fitting using a Langmuir adsorption isotherm. The dark grey bars represent the $c_{50\%}$ values for the unmodified PS surface while the light grey bars indicate a plasma modified PS surface (mean ± SDM[1], n ≥ 1; * = Langmuir fit not possible. The error bars show the error of the Langmuir fit).

Protein Adsorption upon Poly(methyl methacrylate) Coated Surfaces

In order to study the adsorption of selected proteins on PMMA, the polymer was used in its unmodified state as well as in its hydrophilized form after argon plasma treatment. The adsorption of the proteins BSA, Gel, Col G, Col IV, Lam I and NCS was studied. The individual diagrams showing the shift in resonance frequency upon the adsorption of protein from solution are displayed in the appendix B 2 (Fig. B.7 – B.12). The following table 4.14 gives an overview about the adsorption parameters – Δf_{max} and $c_{50\%}$, which were determined by parameter fitting using the Langmuir adsorption isotherm.

Tab. 4.14 Adsorption parameters characterizing the adsorption of the proteins BSA, Gel, Col G, Col IV, and Lam I as well as the proteins contained in NCS upon an unmodified and a plasma modified PMMA surface, as determined from the frequency shifts and subsequent data fitting using a Langmuir adsorption isotherm (mean ± SDM, n ≥ 2; * = concentration in vol-%).

Protein	Unmodified		Plasma Modified	
	$-\Delta f_{max}$ [Hz]	$c_{50\%}$ [µg/mL]	$-\Delta f_{max}$ [Hz]	$c_{50\%}$ [µg/mL]
BSA	37.5 ± 1.4	17.0 ± 2.0	42.2 ± 1.0	33.0 ± 1.9
Gel	11.6 ± 0.6	4.2 ± 1.1	55.3 ± 8.1	37 ± 13
Col G	117 ± 13	125 ± 22	201.2 ± 7.8	67.2 ± 5.0
Col IV	55.6 ± 1.3	12.1 ± 1.0	113.5 ± 8.1	36.9 ± 6.3
Lam I	111 ± 12	28.0 ± 6.6	218 ± 51	60 ± 23
NCS	70.6 ± 3.7	0.146 ± 0.044*	67.4 ± 3.2	0.195 ± 0.050*

The maximal frequency shift measured for the adsorption process of BSA is similar for an unmodified and a plasma modified PMMA surface. The values account for $-\Delta f_{max} = (37.5 \pm 1.4)$ Hz and $-\Delta f_{max} = (42.2 \pm 1.0)$ Hz, respectively. However, the concentration which is necessary to reach half-maximal coverage on both surfaces is different: (17.0 ± 2.0) µg/mL for BSA adsorbing upon an unmodified and (33.0 ± 1.9) µg/mL for a plasma modified PMMA surface. This might indicate different adsorption kinetics, revealing a higher affinity of BSA for the unmodified PMMA surface than for the plasma modified one.

The adsorption of Gel upon the two differently treated PMMA surfaces depends on the wettability of the polymer as well. Fitting the Langmuir isotherm to the experimental frequency data obtained for the adsorption process of Gel upon unmodified PMMA returns values of $-\Delta f_{max} = (11.6 \pm 0.6)$ Hz and $c_{50\%} = (4.2 \pm 1.1)$ µg/mL. The maximal frequency shift for the adsorption of Gel upon plasma modified PMMA is significantly higher, accounting for $-\Delta f_{max} = (55.3 \pm 8.1)$ Hz. Half-maximal surface coverage is attained for $c_{50\%} = (37 \pm 13)$ µg/mL.

Col G displays quite high values for $-\Delta f_{max}$ and $c_{50\%}$ when compared to the adsorption parameters for the other proteins. The Langmuir isotherm for Col G adsorbed upon an unmodified PMMA surface exhibits a value of (117 ± 13) Hz for $-\Delta f_{max}$ and (125 ± 22) µg/mL for $c_{50\%}$. The maximal frequency shift for a plasma modified PMMA surface completely covered with Col G is $-\Delta f_{max} = (201.2 \pm 7.8)$ Hz and $c_{50\%}$ accounts for (67.2 ± 5.0) µg/mL.

The amount of Col IV adsorbing upon plasma modified PMMA might be larger than upon unmodified PMMA. This is reflected in the adsorption parameter $-\Delta f_{max}$. Col IV adsorption upon unmodified PMMA is characterized by $-\Delta f_{max} = (55.6 \pm 1.3)$ Hz and $c_{50\%} = (12.1 \pm 1.0)$ µg/mL. Higher values are obtained for the adsorption upon plasma modified PMMA ($-\Delta f_{max} = (113.5 \pm 8.1)$ Hz and $c_{50\%} = (36.9 \pm 6.3)$ µg/mL).

The course of $-\Delta f$ as a function of Lam I concentration in the bulk solution returns as the maximal frequency shift for a completely saturated and unmodified PMMA surface $-\Delta f_{max} = (111 \pm 12)$ Hz. Half-maximal surface coverage can be found for a bulk protein concentration of $c_{50\%} = (28.0 \pm 6.6)$ µg/mL. Higher values are obtained for the parameters after analyzing the adsorption process of Lam I on plasma modified PMMA. $-\Delta f_{max}$ accounts for (218 ± 51) Hz and $c_{50\%}$ for (60 ± 23) µg/mL.

NCS shows similar adsorption curves upon unmodified and plasma modified PMMA. The maximal frequency shift upon saturation is $-\Delta f_{max} = (70.6 \pm 3.7)$ Hz and $-\Delta f_{max} = (67.4 \pm 3.2)$ Hz, respectively. The $c_{50\%}$ values indicating half-maximal surface coverage are also very similar with $c_{50\%} = (0.146 \pm 0.044)$ vol-% for the adsorption of NCS upon unmodified PMMA and $c_{50\%} = (0.195 \pm 0.050)$ vol-% upon the plasma modified surface.

Figure 4.35 compares the protein concentration needed for half-maximal surface coverage, $c_{50\%}$, for the proteins under study.

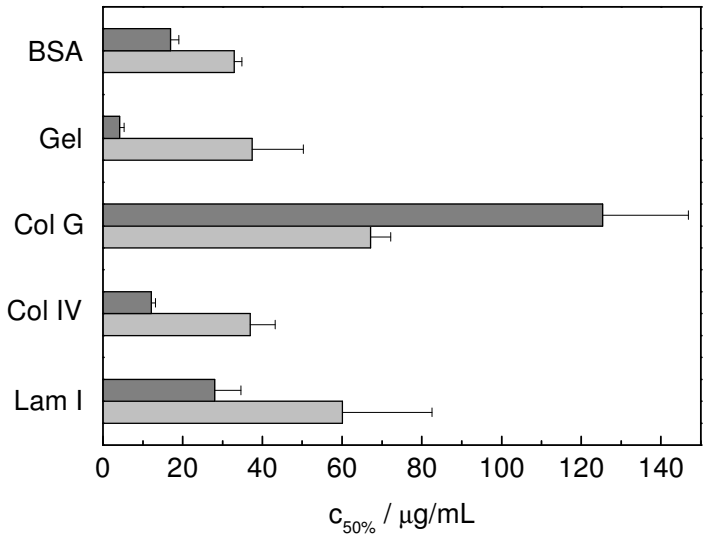

Fig. 4.35 $c_{50\%}$ values for the adsorption of selected proteins to a PMMA surface at 18 °C. The data was obtained from active oscillator mode QCM measurements and subsequent parameter fitting using a Langmuir adsorption isotherm. The dark grey bars represent the $c_{50\%}$ values for the unmodified PMMA surface while the light grey bars indicate a plasma modified PMMA surface (mean ± SDM, n ≥ 2. The error bars show the error of the Langmuir fit).

With the exception of Col G, the investigated proteins show significantly higher $c_{50\%}$ values on plasma modified than on unmodified PMMA (Fig. 4.35). A higher protein concentration in the bulk solution is necessary to cover 50 % of the polymer surface, indicating a lower affinity for protein adsorption upon plasma modified PMMA than upon the unmodified surface. Regarding the protein adsorption upon a plasma modified PMMA surface, the proteins BSA, Gel and Col IV exhibit similar $c_{50\%}$ values, ranging in the order of 33 – 37 µg/mL, whereas the $c_{50\%}$ values for the proteins Col G and Lam I are roughly twice as high (60 and 67 µg/mL). Upon unmodified PMMA, the $c_{50\%}$ values vary more significantly, with the minimal value for the protein Gel (4 µg/mL) and the highest value for Col G (125 µg/mL). $-\Delta f_{max}$ is either similar (BSA, NCS) or clearly higher for the plasma modified than the unmodified polymer.

Protein Adsorption upon Poly(dimethyl siloxane) Coated Surfaces

The adsorption of the proteins BSA, Gel, Col G, Col IV and NCS upon PDMS was investigated only for the unmodified polymer. The diagrams showing the frequency shifts as a function of protein concentration in the bulk solution as well as the fitted Langmuir isotherms can be found in the appendix B 3 (Fig. B.13 – B.15). The resulting parameter values characterizing the adsorption process, $-\Delta f_{max}$ and $c_{50\%}$, are summarized below for each protein (Tab. 4.15). Figure 4.36 additionally summarizes the average $c_{50\%}$ for the proteins under test.

Tab. 4.15 Adsorption parameters characterizing the adsorption of the proteins BSA, Gel, Col G and Col IV as well as the proteins contained in NCS upon an unmodified PDMS surface, as determined from the frequency shifts and subsequent data fitting using a Langmuir adsorption isotherm. n/a means "not applicable". (Mean ± SDM, n ≥ 2; * = concentration in vol-%).

Protein	$-\Delta f_{max}$ [Hz]	$c_{50\%}$ [µg/mL]
BSA	22.8 ± 1.6	9.0 ± 2.4
Gel	23.6 ± 2.1	22.1 ± 5.4
Col G	n/a	n/a
Col IV	107.4 ± 4.0	27.5 ± 2.7
NCS	68.8 ± 5.1	0.303 ± 0.108*

The adsorption of BSA upon PDMS shows a typical saturation behavior. Fitting the Langmuir isotherm to the experimental data returns values for $-\Delta f_{max}$ of (22.8 ± 1.6) Hz and $c_{50\%}$ of (9.0 ± 2.4) µg/mL.

For the adsorption of Gel a frequency shift for maximal surface coverage similar to the one obtained for BSA is achieved, with $-\Delta f_{max}$ = (23.6 ± 2.1) Hz. The $c_{50\%}$ value accounts for (22.1 ± 5.4) µg/mL.

The shift of the resonance frequency for a PDMS coated resonator upon the adsorption of Col G linearly increases with increasing protein concentration. No saturation behavior is detectable in the investigated concentration range, thus preventing a Langmuir fit of the raw data and a subsequent quantification of the Col G adsorption.

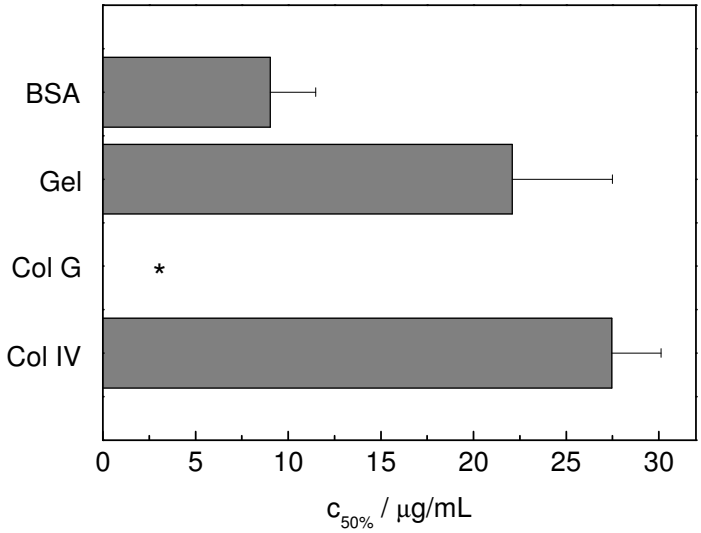

Fig. 4.36 $c_{50\%}$ values for the adsorption of selected proteins to an unmodified PDMS surface at 18 °C. The data was obtained from active oscillator mode QCM measurements and subsequent parameter fitting using a Langmuir adsorption isotherm (mean ± SDM, n ≥ 2; * = Langmuir fit not possible. The error bars show the error of the Langmuir fit).

The course of $-\Delta f$ as a function of Col IV concentration in the bulk solution shows a maximal adsorption value for a completely saturated surface of $-\Delta f_{max}$ = (107.4 ± 4.0) Hz.

Half-maximal surface coverage is obtained for a bulk protein concentration of $c_{50\%}$ = (27.5 ± 2.7) µg/mL.
For NCS adsorption upon unmodified PDMS, a typical saturation curve is obtained. The adsorption parameters are determined to be $-\Delta f_{max}$ = (68.8 ± 5.1) Hz and $c_{50\%}$ = (0.303 ± 0.108) vol-%.

Protein Adsorption upon Photopolymer Coated Surfaces

The adsorption process of selected proteins upon PhoP was studied for the unmodified as well as for the hydrophilized, plasma modified form of the polymer. The applied protein solutions were BSA, Gel, Col G, Col IV, Lam I and NCS.
Similar to the polymer surfaces discussed above, the diagrams documenting the frequency shift as a function of protein concentration in the bulk solution and the individual Langmuir isotherms are presented in the appendix B 4 (Fig. B.16 – B.21). Table 4.16 shows the results of the Langmuir fit for each protein.

Tab. 4.16 Adsorption parameters characterizing the adsorption of the proteins BSA, Gel, Col G, Col IV and Lam I as well as the proteins contained in NCS upon an unmodified and a plasma modified PhoP surface, as determined from the frequency shifts and subsequent data fitting using a Langmuir adsorption isotherm. n/a means "not applicable". (Mean ± SDM, n ≥ 2; * = concentration in vol-%).

Protein	Unmodified		Plasma Modified	
	$-\Delta f_{max}$ [Hz]	$c_{50\%}$ [µg/mL]	$-\Delta f_{max}$ [Hz]	$c_{50\%}$ [µg/mL]
BSA	19.4 ± 2.0	16.1 ± 5.1	21.6 ± 1.5	31.2 ± 5.3
Gel	19.2 ± 0.6	10.10 ± 0.95	–	–
Col G	323 ± 149	336 ± 191	265 ± 18	63.1 ± 8.2
Col IV	98.6 ± 3.7	28.9 ± 2.8	93.5 ± 1.7	30.3 ± 1.4
Lam I	n/a	n/a	n/a	n/a
NCS	58.7 ± 3.6	0.109 ± 0.042*	71.5 ± 4.6	0.130 ± 0.051*

The adsorption of BSA upon an unmodified and a plasma modified PhoP surface shows similar values for the maximal frequency shift upon saturation: $-\Delta f_{max}$ = (19.4 ± 2.0) Hz and $-\Delta f_{max}$ = (21.6 ± 1.5) Hz. Since the two curves exhibit a different slope, the $c_{50\%}$ values are quite different as indicated by (16.1 ± 5.1) µg/mL for BSA adsorption upon an unmodified and (31.2 ± 5.3) µg/mL upon a plasma modified PhoP surface. Although the overall amount of BSA might be the same for both surface modifications of PhoP, the unmodified surface is a better substrate for BSA adsorption.
The adsorption of Gel was only quantified upon the unmodified polymer. The Langmuir fit to the frequency data returns the adsorption parameters $-\Delta f_{max}$ = (19.2 ± 0.6) Hz and $c_{50\%}$ = (10.1 ± 0.95) µg/mL.
For Col G adsorption upon the PhoP surface, the highest adsorption parameters are obtained. For unmodified PhoP, the adsorption of Col G can be described by the parameters $-\Delta f_{max}$ = (322 ± 149) Hz and $c_{50\%}$ = (336 ± 191) µg/mL. Parameter fitting for Col G

adsorption upon the plasma modified surface results in values for $-\Delta f_{max} = (265 \pm 18)$ Hz and $c_{50\%} = (63.1 \pm 8.2)$ µg/mL. The affinity of Col G to plasma modified PhoP is 5.3 fold higher than to unmodified PhoP.

Col IV adsorption upon a PhoP surface does not seem to depend on the surface hydrophilicity. The maximal frequency shift upon saturation is $-\Delta f_{max} = (98.6 \pm 3.7)$ Hz and $-\Delta f_{max} = (93.5 \pm 1.7)$ Hz, respectively. The $c_{50\%}$ values amount to (28.9 ± 2.8) µg/mL for unmodified and (30.3 ± 1.4) µg/mL for plasma modified PhoP.

The adsorption of Lam I to the two differently treated PhoP surfaces gives rise to a frequency shift which increases linearly with rising protein concentration in the bulk solution. Thus, parameter fitting using the Langmuir adsorption isotherm was not possible for both modifications of PhoP.

NCS shows – as described before for the other polymer surfaces – two nearly identical saturation curves, characterized by the adsorption parameters $-\Delta f_{max} = (58.7 \pm 3.6)$ Hz and $c_{50\%} = (0.109 \pm 0.042)$ vol-% for the unmodified PhoP surface and $-\Delta f_{max} = (71.5 \pm 4.6)$ Hz and $c_{50\%} = (0.130 \pm 0.051)$ vol-% for the plasma modified surface.

A comparison of the $c_{50\%}$ values for the different proteins is given in Fig. 4.37. A general preference for protein adsorption upon a PhoP surface of a distinct hydrophilicity, either the unmodified or the plasma modified form, can not be detected.

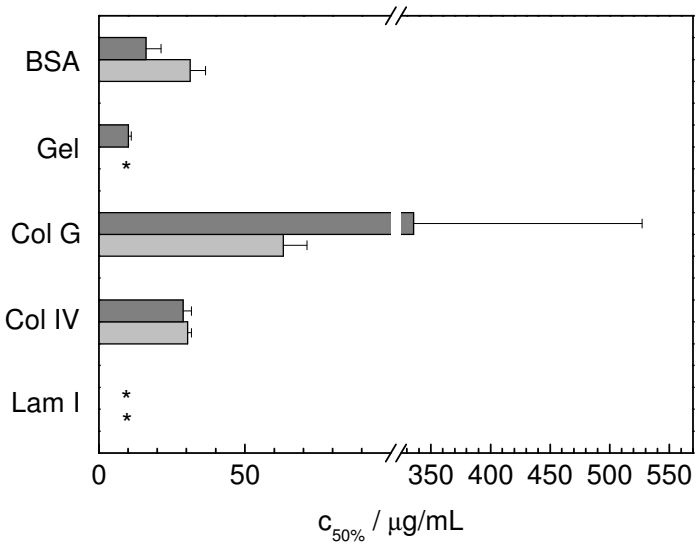

Fig. 4.37 $c_{50\%}$ values for the adsorption of selected proteins to a PhoP surface at 18 °C. The data was obtained from active oscillator mode QCM measurements and subsequent parameter fitting using a Langmuir adsorption isotherm. The dark grey bars represent the $c_{50\%}$ values for the unmodified PhoP surface while the light grey bars indicate a plasma modified PhoP surface (mean ± SDM, $n \geq 2$; * = Langmuir fit not possible. The error bars show the error of the Langmuir fit).

The $c_{50\%}$ value for half-maximal surface coverage with Col G differs significantly for both surface modifications, as indicated by a 5.3 fold higher value for unmodified than for plasma modified PhoP. Whereas half-maximal surface coverage of PhoP with Col IV is almost

similar on both polymer modifications, BSA exhibits a higher $c_{50\%}$ value on plasma modified PhoP than on the unmodified form. As already observed for plasma modified PMMA (see Tab. 4.14), BSA and Col IV have similar $c_{50\%}$ values (31 and 30 µg/mL) for the adsorption upon plasma modified PhoP, whereas $c_{50\%}$ for Col G adsorption is nearly twice as high. Upon unmodified PhoP, the $c_{50\%}$ values range between 10 and 29 µg/mL for the proteins BSA, Gel and Col IV, whereas Col G shows the highest value for half-maximal surface coverage with $c_{50\%}$ = 336 µg/mL. The maximal amount of protein which adsorbs to PhoP of both modifications might be similar for BSA, Col IV and NCS. Only Col G shows a higher $-\Delta f_{max}$ for the unmodified than for the plasma modified polymer.

4.4 Cell Attachment and Spreading upon Polymer Surfaces Monitored by Piezo-Resonators

A common technique to analyze the biocompatibility of certain materials is to study the attachment and spreading behavior of initially suspended cells upon a certain surface using microscopic and/or staining methods. The number of attached cells after a certain time interval as well as their spreading characteristics can be used to evaluate the cell-material interactions. In order to analyze the interactions of cells with polymer surfaces in a quantitative way and with a high time resolution, the QCM technique was used in this study. Two mammalian cell lines, MDCK-II as well as NRK cells, were studied with respect to their individual attachment and spreading characteristics on different polymer films by impedance analysis of the shear oscillation.
But before presenting the quantitative parameters to describe the cytocompatibility of the respective surfaces, some experimental details are summarized briefly.

For QCM measurements, initially suspended cells were seeded to confluence into the measuring chamber using serum containing medium as culture fluid. After attachment and spreading the cells form a confluent monolayer on the sensor surface without any need of further cell division. Since serum naturally contains the adhesive proteins vitronectin and fibronectin which instantaneously adsorb from solution to the surface, there is no need to precoat the resonators with any other adhesive protein before cell inoculation. The QCM device was placed into a cell culture incubator at 37 °C. Immediately after cell inoculation, attachment and spreading of the cells was followed with time by continuously recording impedance data of the shear oscillation in a frequency range close to the fundamental resonance frequency of the quartz, usually from 4.97 MHz to 5.05 MHz, and a non-invasive AC potential of 150 mV amplitude.

4.4.1 Attachment and Spreading of NRK Cells upon Uncoated Quartz Resonators

The attachment and spreading characteristics of NRK cells upon an uncoated quartz resonator are exemplarily quantified as demonstrated below. Before presenting the quantities which were used to characterize cell adhesion in a time-resolved manner, typical Bode diagrams of the impedance magnitude $|Z|$ and the phase shift φ for a medium-loaded resonator compared to the same resonator covered with a confluent monolayer of NRK cells are shown (Fig. 4.38). The presence of cells on the resonator surface gives rise to a strong impact on both spectra, $Z(f)$ and $\varphi(f)$, and is most obviously expressed in a significant damping of the shear oscillation as indicated by alterations of the minimal $|Z_{min}|$ and the maximal impedance $|Z_{max}|$ (Fig. 4.38 A) as well as in the phase maximum (Fig. 4.38 B). Attachment of the cells to the resonator induces only a minor shift of the impedance and phase spectra along the frequency axis towards lower frequencies. This indicates that the cell monolayer induces primarily dissipation of motional energy and only a negligible storage of elastic energy.

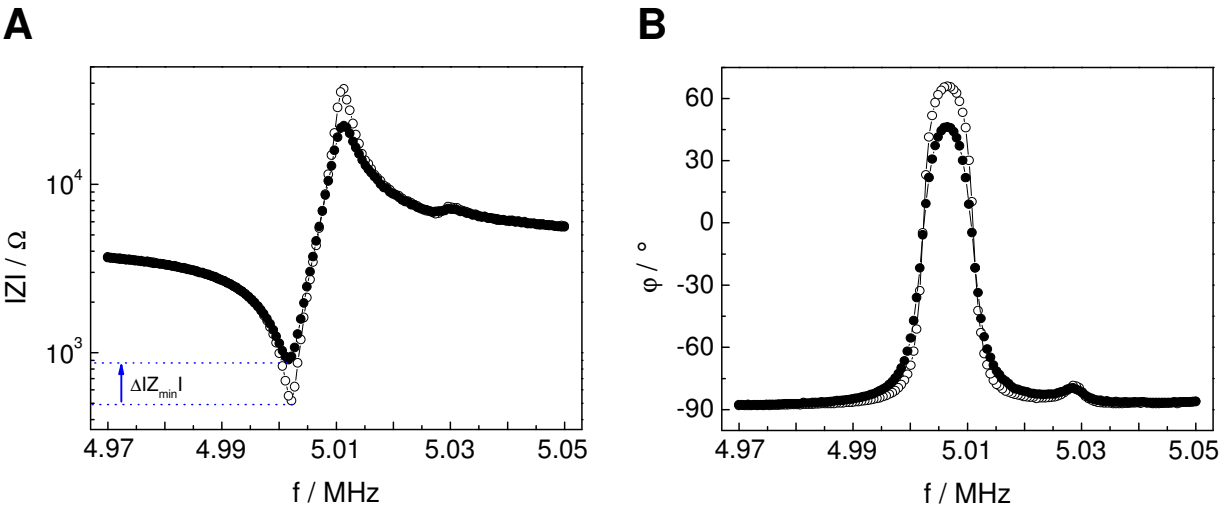

Fig. 4.38 Bode presentation of the experimental raw data of the shear oscillation as recorded by impedance spectroscopy. **A** Impedance magnitude $|Z|$ and **B** phase shift φ of a cell-free (○) and a cell-covered (●) 5 MHz quartz resonator near its fundamental resonance as a function of frequency. The arrow marks the change of the minimal impedance $\Delta|Z_{min}|$, which was used to follow cell attachment and spreading upon the resonator surface (T = 37 °C).

The impact of cell adhesion on the shear oscillation can be demonstrated in a time-resolved manner when the attachment and spreading of initially suspended cells to the resonator surface is followed with time by continuously recording impedance spectra as the one shown in Fig. 4.38. Cells in contact with a resonator surface can be described by the complex load impedance Z_L, which is obtained by fitting the BVD equivalent circuit (chapter 3.5.2.2) to the raw data (Fig. 4.39 A). The change of the load impedance ΔZ_L and can be decomposed in its real and imaginary components (Fig. 4.39 B).

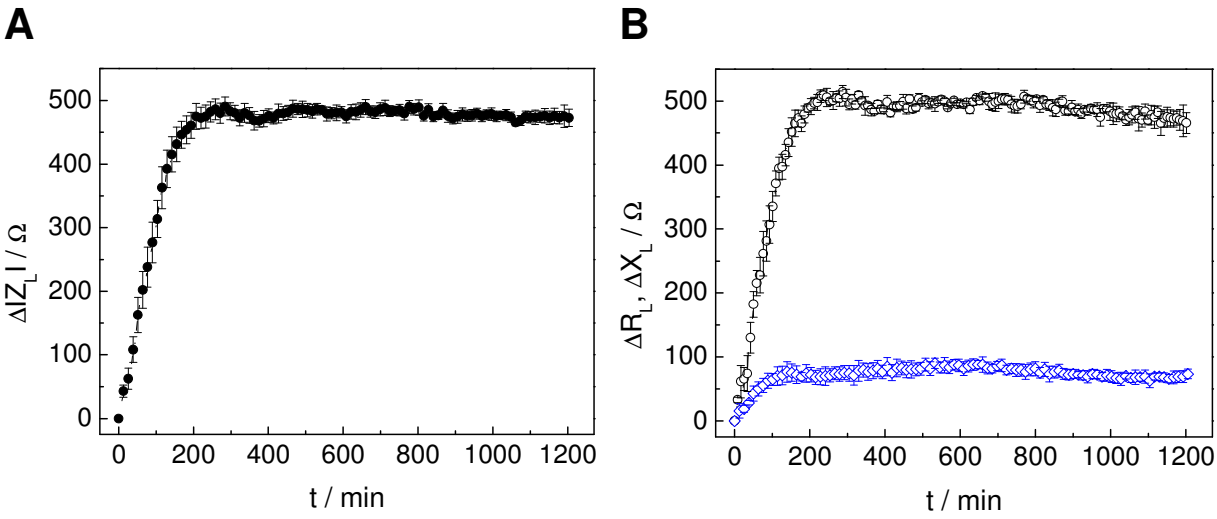

Fig. 4.39 A Time course of the load impedance magnitude $\Delta|Z_L|$ and **B** time course of the load resistance ΔR_L (○) and the load reactance ΔX_L (◊) during the attachment and spreading of NRK cells upon the quartz resonator. B depicts the decomposition of the complex load impedance ΔZ_L into its real and imaginary components. The cell density was adjusted to 4.5 x 10^5 cm^{-2}. Changes of the load parameters are given relative to a cell-free but medium-loaded resonator. The number of points was reduced for reason of clarity (mean ± SDM, n = 5; T = 37 °C).

Fig. 4.39 shows the time courses of $\Delta|Z_L|$, ΔR_L and ΔX_L during the attachment and spreading of NRK cells upon the resonator surface. All quantities are expressed relative to the values for the medium-loaded resonator, which was always the beginning of any QCM experiment. Instantaneously after cell inoculation, the load impedance $\Delta|Z_L|$ shows a characteristic steep increase within 250 – 300 min, reaching a stationary value of roughly 480 Ω once spreading is complete. Since the cells were seeded to confluence into the measuring chamber, i.e. they cover the entire quartz surface already after sedimentation and adhesion without any need for further cell proliferation, the final change in $\Delta|Z_L|$ corresponds to a confluent monolayer of cells on the surface. With respect to the time courses of ΔR_L and ΔX_L (Fig. 4.39 B), it is apparent that the observed changes in $\Delta|Z_L|$ primarily originate from frictional energy dissipation (ΔR_L) with minor contribution from elastic components (ΔX_L). For different mammalian cell types it could be demonstrated that the dissipated energy is many times larger than the stored energy, showing a ratio between 3 and 20, dependent on the cell type (Reiß, 2004).

Besides using the BVD equivalent circuit to analyze the impedance raw data of the quartz resonator recorded during the adhesion of suspended cells, it is possible to follow cell attachment and spreading using the minimal impedance magnitude $\Delta|Z_{min}|$. This quantity can be directly extracted from the raw data without using any equivalent circuit model and fitting routine. In Fig. 4.38 A, the minimal impedance for a medium-loaded and a cell-covered quartz resonator is marked by a blue horizontal line.

In order to become more familiar with this quantity, the course of the minimal impedance $|Z_{min}|$ is compared to the course of the commonly applied load impedance $\Delta|Z_L|$ of a quartz resonator when either the motional inductance L or the motional resistance R are discretely varied while keeping the other parameters at a constant value (Fig. 4.40 A, B).

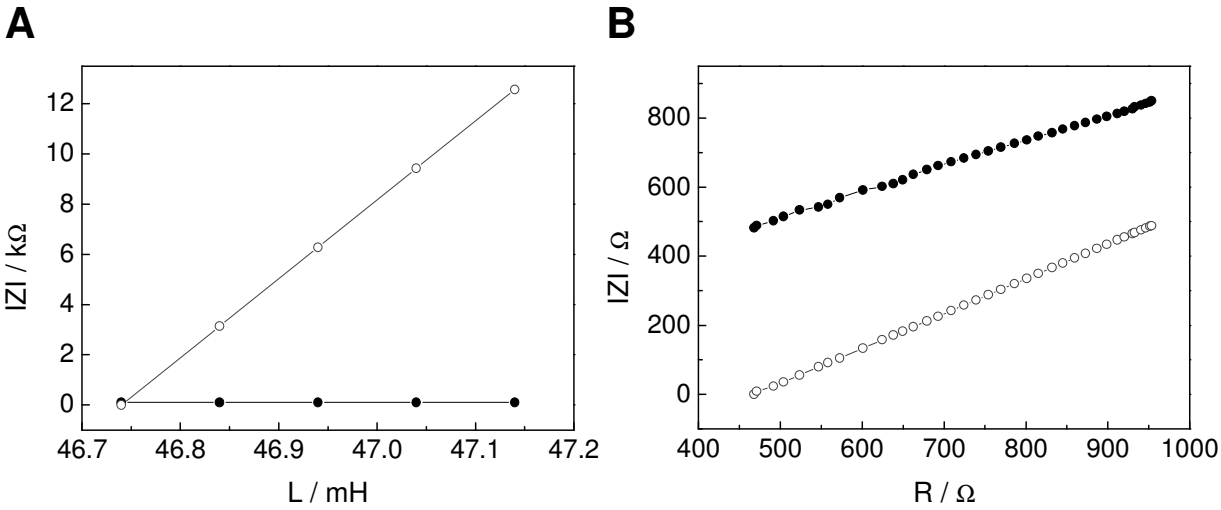

Fig. 4.40 Simulated diagrams for the minimal impedance $|Z_{min}|$ (●) and the load impedance $\Delta|Z_L|$ (○) when **A** the inductance L (R = 100 Ω) and **B** the resistance R (L = 46.77 mH) are discretely varied. The remaining parameters are kept constant (C = 21.655 fF, C_0 = 7 pF).

Discrete variations of the BVD parameters L and R induce characteristic changes in the course of $|Z_{min}|$ and $\Delta|Z_L|$ of a quartz resonator. Discrete variation of the motional inductance L as induced by a pure deposition of a rigid mass layer on the resonator surface, results in a linear increase in $\Delta|Z_L|$ with increasing L while $|Z_{min}|$ remains unchanged (Fig. 4.40 A). An increase of the motional resistance R results in a linear increase of both quantities, $|Z_{min}|$ and $\Delta|Z_L|$ (Fig. 4.40 B). It is noteworthy that changes of Z_{min} are proportional to changes of R, while $\Delta|Z_L|$ is affected by both parameters, R and L. Thus, when following pure mass deposition on the resonator surface, the parameter $\Delta|Z_L|$ is most suitable while $|Z_{min}|$ and $\Delta|Z_L|$ can be equally used to characterize changes in R.

As aforementioned, cells that attach and spread upon a resonator surface mainly give rise to changes in the motional resistance ΔR_L while the motional inductance ΔX_L is a minor contributor to the complex load impedance. Since the motional resistance linearly scales with the minimal impedance, the quantity $|Z_{min}|$ is equally well-suited to follow attachment and spreading of mammalian cells. An advantage of using the minimal impedance over the motional resistance or the load impedance is that it can be directly extracted from the impedance spectrum without applying any fitting routine. Moreover, an exact viscoelastic model which describes the mechanical properties of cells in contact with the resonator surface does not exist to date.

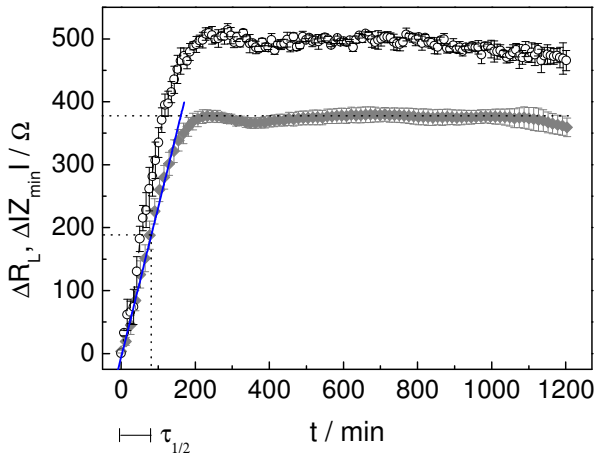

Fig. 4.41 Time course of the load resistance ΔR_L (○) and the minimal impedance $\Delta|Z_{min}|$ (♦) during the attachment and spreading of NRK cells upon the quartz resonator. The cell density was adjusted to 4.5 x 10^5 cm^{-2}. Changes of the load parameters are given relative to a cell-free but medium-loaded resonator. The blue line was used to determine the slope of the attachment curve. $\tau_{1/2}$ is the required time after cell inoculation to reach half-maximal $\Delta|Z_{min}|$. The number of points was reduced for reason of clarity (Mean ± SDM, n = 5; T = 37 °C).

Figure 4.41 compares the time course of the load resistance ΔR_L to the time course of the minimal impedance $\Delta|Z_{min}|$ during the attachment and spreading of initially suspended NRK cells upon the resonator surface. Both quantities are expressed relative to their values for the medium-loaded resonator. As aforementioned, it is apparent that $\Delta|Z_{min}|$ reflects changes in R_L induced by the load material on top of the quartz resonator. The final values differ by roughly 120 Ω, but the time courses are similar. Thus, all further QCM experiments on attachment and spreading of initially suspended mammalian cells are presented by the time course of $\Delta|Z_{min}|$. For NRK cells which are seeded at time point zero on the resonator surface, $\Delta|Z_{min}|$ instantaneously increases to a stationary value of (380 ± 11) Ω within roughly 240 min after cell inoculation, which is maintained for the complete measuring period.

The initial increase of $\Delta|Z_{min}|$ with time mirrors the kinetics of cell attachment and spreading. In order to quantify the kinetics of cell adhesion properly, two parameters were chosen. The first one is the slope m of the attachment curve in the time regime of linear increase until a stationary value of $\Delta|Z_{min}|$ is reached, i.e. the first 200 min after cell inoculation for the above mentioned measurement (see blue line in Fig. 4.41). The second parameter is $\tau_{1/2}$. This quantity describes the time that is needed to reach half-maximal $\Delta|Z_{min}|$, or in other words, to reach half-maximal surface coverage (see also Fig. 4.41). The slope of $\Delta|Z_{min}|$ during the adhesion of NRK cells upon an uncoated quartz resonator yields (2.38 ± 0.05) Ω/min. $\tau_{1/2}$ can be determined to (77 ± 8) min.

4.4.2 Attachment and Spreading of MDCK-II Cells upon Uncoated Quartz Resonators

MDCK-II cells were also investigated with respect to their attachment and spreading behavior upon an uncoated resonator by plotting $\Delta|Z_{min}|$ as a function of time beginning at point zero, when a MDCK-II cell suspension prepared in serum-containing medium was seeded on the resonator surface (Fig. 4.42).

The time course of $\Delta|Z_{min}|$ is characterized by an immediate increase to a first, transient maximum of (376 ± 7) Ω roughly 135 min after cell inoculation, giving rise to a slope of (4.52 ± 0.14) Ω/min. After roughly 300 min, the steep increase is followed by a rather moderate increase leading to a second maximum of (458 ± 9) Ω about (520 ± 15) min after cell inoculation. $\Delta|Z_{min}|$ decreases after having passed this second maximum by approximately 50 Ω and finally stabilizes at (410 ± 15) Ω. The time that is needed to reach half-maximal surface coverage, $\tau_{1/2}$, is determined to (46 ± 3) min.

$\Delta|Z_{min}|$ shows a time course which is characteristic for MDCK-II cells. Whereas the first increase of the curve (t < 135 min) leading to the transient plateau phase can be correlated with the formation of cell-substrate adhesion sites and a continuous progress in cell attachment and spreading, the second increase of $\Delta|Z_{min}|$ can not be explained by a change in surface coverage.

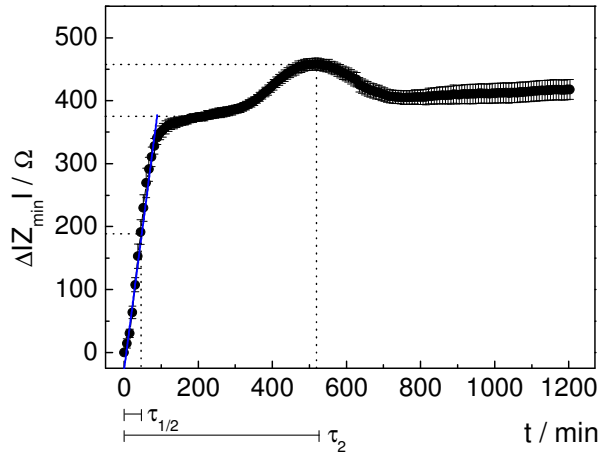

Fig. 4.42 Time course of the minimal impedance $\Delta|Z_{min}|$ during the attachment and spreading of initially suspended MDCK-II cells upon the quartz resonator. The cell density was adjusted to 4.5 x 10^5 cm^{-2}. Changes of the load parameter are given relative to a cell-free but medium-loaded resonator. τ_2 describes the time that is needed to reach the second maximum. (Mean ± SDM, n = 10; T = 37 °C).

The additional impedance arises from acoustic changes within the cell bodies anchored to the quartz surface. Shaping up of the actin cytoskeleton, as indicated by visual structural changes is reported to be the cause of the second increase in impedance (Wegener, 1998).

Besides the two parameters which are used to describe the adhesion kinetics of NRK cells, the slope m as well as $\tau_{1/2}$, a third parameter shall be introduced to characterize the attachment and

spreading behavior of MDCK-II cells – the τ_2 value. τ_2 describes the time that is needed to reach the second maximum (Fig. 4.42) and thus reports on the dynamics of actin reorganization of MDCK-II cells. For MDCK-II cells which have been seeded on an uncoated quartz resonator, τ_2 is determined to (520 ± 15) min.

The following table 4.17 summarizes the different parameters that were used to characterize the adhesion kinetics of the two cell types, NRK and MDCK-II cells, for an uncoated quartz resonator.

Tab. 4.17 Summary of parameters used to characterize the adhesion kinetics of NRK and MDCK-II cells on an uncoated quartz resonator. The slope m of the attachment curve till it reaches the (first) plateau phase expresses the spreading rate and $\tau_{1/2}$ the time to reach half-maximal $\Delta|Z_{min}|$. τ_2 is the time that is needed to reach the second maximum (MDCK-II cells) (mean ± SDM, n ≥ 5; T = 37 °C).

Adhesion Parameter	NRK Cells	MDCK-II Cells
$\Delta\|Z_{min}\|$ [Ω]	380 ± 11	410 ± 15
m [Ω/min]	2.38 ± 0.05	4.52 ± 0.14
$\tau_{1/2}$ [min]	77 ± 8	46 ± 3
τ_2 [min]	–	520 ± 15

It is apparent that different cell types induce individual changes in the minimal impedance when they adhere to the quartz surface. The maximal increase in $\Delta|Z_{min}|$ as well as the time courses differ significantly for the two cell types. NRK cells reach a $\Delta|Z_{min}|$ of (380 ± 11) Ω, whereas MDCK-II cells exhibit a higher $\Delta|Z_{min}|$ of (410 ± 15) Ω. As already reported for the parameter $\Delta|Z_L|$, the impact of cells on energy dissipation is dependent on the cell type, reflecting the individual micromechanical properties of the various cell types (Reiß, 2004).
These cell-type specific parameters as obtained for the adhesion process of NRK and MDCK-II cells upon an uncoated quartz resonator shall be used as a reference for the evaluation of the adhesion parameters for the two cell types on different polymers.

The attachment and spreading characteristics of mammalian cells upon different polymer surfaces were studied and quantified for the polymers PS, PMMA, PDMS and PhoP under a variety of processing conditions:

i) unmodified polymer
ii) unmodified polymer + PBS^{--}/SFM pre-incubation over 20 h at 37 °C
iii) plasma modified polymer
iv) plasma modified polymer + PBS^{--}/SFM pre-incubation over 20 h at 37 °C

Whereas PS and PMMA were analyzed with respect to all processing conditions, PDMS was only analyzed in the categories i) and ii) and PhoP in the categories ii) and iv).
These modifications of the polymer surfaces and their impact on subsequent attachment and spreading of mammalian cells should clarify relevant issues, like: How does a preceding

incubation in a physiological fluid over a period of 20 h affect cell attachment and spreading? How can the influence of argon plasma treatment be quantified?
After the quartz resonator coated with the polymer of interest had been exposed to one of the above mentioned processing conditions, MDCK-II or NRK cell suspensions, prepared in serum-containing culture medium, were transferred into the measuring chamber. Impedance data were continuously recorded in a frequency range from 4.97 MHz to 5.05 MHz and a non-invasive AC voltage of 150 mV amplitude. Cell attachment and spreading was followed over a period of 20 h using the change of the magnitude of the minimal impedance $\Delta|Z_{min}|$ with respect to the values for the same, polymer-coated but only medium-loaded resonator which was the beginning of any QCM experiment.

4.4.3 Cytocompatibility Testing of Polystyrene Surfaces

The cytocompatibility of PS was studied by following cell attachment and spreading of initially suspended MDCK-II and NRK cells upon PS coated quartz resonators. Polymer films prepared according to all four processing conditions mentioned above were included in these experiments.

Attachment and Spreading of MDCK-II Cells

The following figure 4.43 compares the time courses of the minimal impedance $\Delta|Z_{min}|$ as recorded by the QCM technique after seeding of initially suspended MDCK-II cells upon PS coated quartz resonators which had been pre-treated according to the four different protocols.
Figure 4.43 A presents $\Delta|Z_{min}|$ as a function of time when a suspension of MDCK-II cells is seeded on a PS coated quartz resonator which had been previously exposed to two different physiological fluids, i.e. PBS^{--} and SFM, for 20 h at 37°C. An immediate increase of $\Delta|Z_{min}|$ can be detected in both cases, giving rise to a slope of (6.04 ± 0.22) Ω/min in the case of the PBS^{--} pre-incubation and (3.11 ± 0.20) Ω/min for the SFM pre-incubated PS film. Whereas the time course of $\Delta|Z_{min}|$ leads to the first plateau phase of (465 ± 8) Ω roughly 200 min after cell inoculation for the cells seeded upon the PBS^{--} pre-incubated PS surface, no real plateau phase is observed when MDCK-II cells are seeded upon an SFM pre-incubated surface. After roughly 130 min the slope of the curve is reduced, leading to a maximum value of (450 ± 19) Ω about (980 ± 74) min after cell inoculation. The maximum value for the PBS^{--} pre-incubated surface of $\Delta|Z_{min}| = (540 \pm 19)$ Ω is already attained after (860 ± 15) min. In both cases, $\Delta|Z_{min}|$ decreases after having passed the maximum by approximately 141 Ω (PBS^{--}) and 107 Ω (SFM). The $\tau_{1/2}$ values for MDCK-II cell attachment and spreading on these two fluid pre-incubated PS surfaces are (50 ± 3) min in the case of PBS^{--} and (64 ± 5) min in the case of SFM, whereas for the latter it has to be considered that $\Delta|Z_{min}|$ reaches only about one half of the value which is obtained for the PBS^{--} pre-incubated surface in the first transient plateau phase.

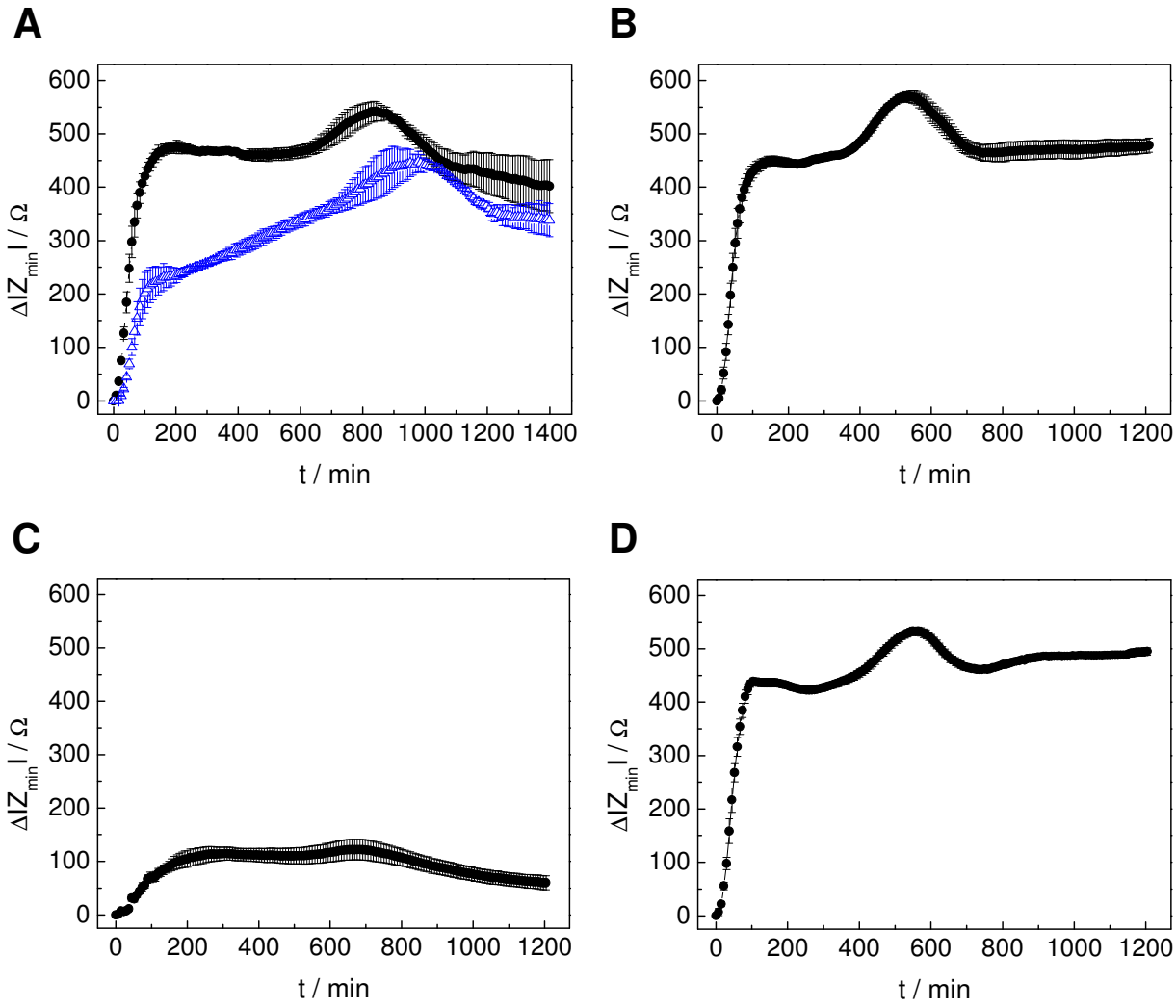

Fig. 4.43 Time course of $\Delta|Z_{min}|$ after seeding equal amounts of initially suspended MDCK-II cells on a PS coated quartz resonator at time point zero. The cell density was adjusted to 4.5 x 10^5 cm^{-2}. The PS coated resonator had been pre-treated as follows: **A** Incubation with PBS^{--} (●) / SFM (Δ) for 20 h at 37 °C, **B** argon plasma treatment for 1 min followed by a SFM incubation for 20 h at 37 °C, **C** no pretreatment and **D** argon plasma treatment for 1 min. The value of $|Z_{min}|$ at the beginning of the experiment was set to zero. (Mean ± SDM, n ≥ 4, except for graph A: n = 2; T = 37 °C).

Similar to a PBS^{--} pre-incubated PS surface, the time course of $\Delta|Z_{min}|$ recorded for a plasma modified, SFM pre-incubated surface (Fig. 4.43 B) is characterized by an immediate rise directly after seeding the cells. In contrast to the PS surface which had only been exposed to PBS^{--} or SFM without a preceding plasma treatment (Fig. 4.43 A), here, the cells do not discriminate between the two physiological fluids, PBS^{--} or SFM, the hydrophilized polymer had been exposed to. The time courses are similar and thus, cell attachment and spreading is presented only on plasma-modified, SFM pre-incubated PS – the series of experiments for PBS^{--} pre-incubation is summarized in the appendix E (Fig. E.1). The slope of the attachment curve of MDCK-II cells during the first 130 min is (6.66 ± 0.28) Ω/min. After having passed the first transient maximum of (446 ± 7) Ω, $\Delta|Z_{min}|$ increases again to a second maximum at (570 ± 11) Ω roughly (540 ± 9) min after cell inoculation. $\Delta|Z_{min}|$ finally reaches an

equilibrium at (480 ± 13) Ω. The time that is needed to attain half-maximal surface coverage is determined to (42 ± 3) min.

Figure 4.43 C shows the time course of $\Delta|Z_{min}|$ for a completely unmodified PS surface. MDCK-II cells are not able to attach and spread properly on this surface, reflected in a minor increase of $\Delta|Z_{min}|$ to a transient value of (110 ± 12) Ω roughly 260 min after cell seeding, followed by a decrease to (60 ± 13) Ω roughly 700 min after cell inoculation. The slope of the initial increase of $\Delta|Z_{min}|$ is (0.78 ± 0.05) Ω/min. When compared to the three remaining graphs, the shape of the curve is completely different. Since the $\Delta|Z_{min}|$ value of the first plateau phase is only about one forth of the value for the other surface conditions, $\tau_{1/2}$ was not determined.

An argon plasma induced hydrophilization of the PS surface (Fig. 4.43 D) leads to an attachment and spreading curve similar to the curve observed for a plasma modified, pre-incubated surface (compare Fig. 4.43 B). The graph shows an initial slope of (6.16 ± 0.14) Ω/min. The first transient maximum is reached 100 min after cell inoculation, ranging in the order of (431 ± 6) Ω. The second maximum of $\Delta|Z_{min}|$ = (533 ± 7) Ω is attained 554 min after cell inoculation. $\tau_{1/2}$ for MDCK-II cell attachment and spreading is determined to (46 ± 3) min.

Table 4.18 summarizes the QCM based data for the adhesion kinetics of MDCK-II cells upon spin coated PS, which had been pre-treated according to the four different protocols, on the basis of the kinetic parameters m, $\tau_{1/2}$ and τ_2.

Tab. 4.18 Summary of parameters used to characterize the adhesion kinetics of MDCK-II cells on PS. The slope m of the attachment curve till it reaches the first plateau phase expresses the spreading rate and $\tau_{1/2}$ the time to reach half-maximal $\Delta|Z_{min}|$. τ_2 is the time that is needed to reach the second maximum. (Mean ± SDM, n ≥ 2; T = 37 °C).

Kinetic Parameter	No Plasma, Swelling		Plasma, PBS⁻⁻/SFM	No Plasma, No Swelling	Plasma, No Swelling
	PBS⁻⁻	SFM			
m [Ω/min]	6.04 ± 0.22	3.11 ± 0.20	6.66 ± 0.28	0.78 ± 0.05	6.16 ± 0.14
$\tau_{1/2}$ [min]	50 ± 3	64 ± 5	42 ± 3	n/a	46 ± 3
τ_2 [min]	860 ± 15	980 ± 74	540 ± 9	n/a	554 ± 5

In order to correlate the QCM-based spreading data with a microscopic study addressing the adhesion kinetics of MDCK-II cells upon PS surfaces, phase contrast images of initially suspended MDCK-II cells seeded upon spin coated PS were taken at regular time intervals after cell inoculation. As the optical qualities of the quartz plate covered with gold electrodes on opposite sides of the quartz do not allow to document cell growth onto the quartz surface by phase contrast microscopy, microscopic glass coverslips spin coated with PS were used as culture substrates instead. The PS coated substrates were pre-treated in a similar way as described above for the PS coated quartz resonators. Phase contrast images were acquired 2, 4, 6, 8, 10, 24 and 48 h after cell inoculation in order to document the adhesion kinetics and the degree of confluence.

Phase contrast micrographs of MDCK-II cells seeded upon PBS^{--} pre-treated PS are shown in Fig. 4.44 A – G.

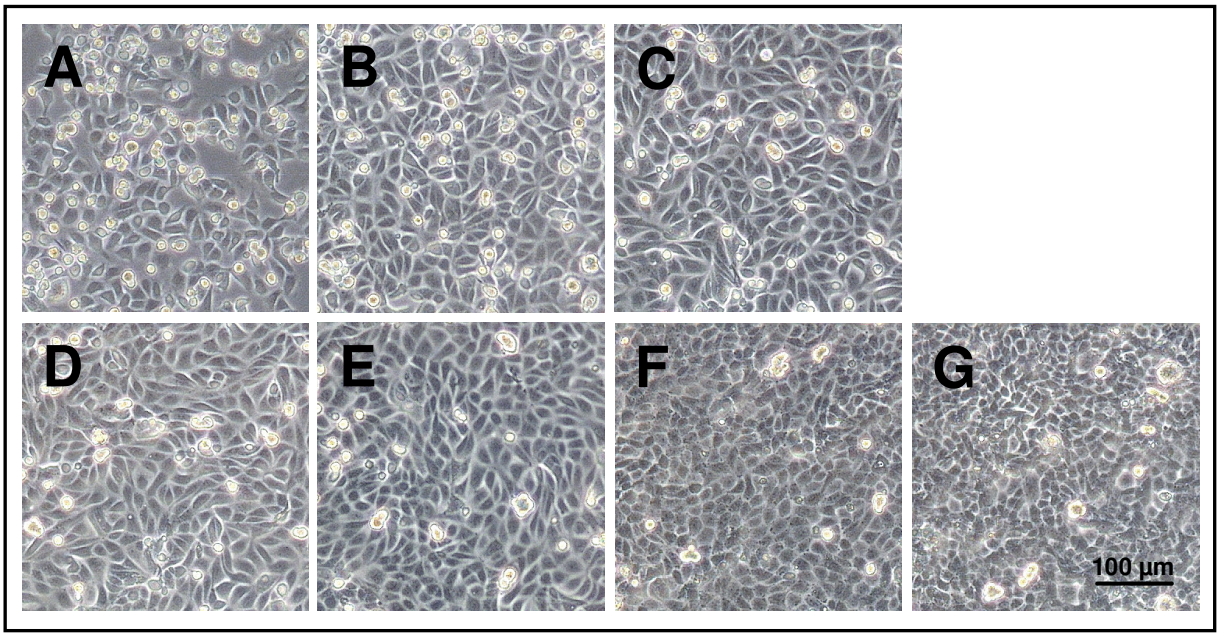

Fig. 4.44 Phase contrast micrographs of MDCK-II cells at various time points after inoculation, documenting attachment and spreading upon PS coated coverslips that were exposed to PBS^{--} for 20 h at 37 °C prior to cell inoculation. The cells were suspended in serum-containing medium with a cell density of 4.5 x 10^5 cm^{-2}. The pictures were taken **A** 2 h, **B** 4 h, **C** 6 h, **D** 8 h, **E** 10 h, **F** 24 h and **G** 48 h after cell inoculation.

Two hours after seeding a suspension of MDCK-II cells on PBS^{--} pre-incubated PS, the major fraction of the cells is spread upon the surface (Fig. 4.44 A). Approximately 80 % of the surface is covered with spread cells, while the remaining fraction of the cells is still spherically shaped and/or suspended in the culture medium. Four hours after seeding, the cells cover the whole surface (Fig. 4.44 B). In the following hours after cell inoculation, the cells become more regular and smaller. This is mainly due to cell migration or cell division processes, leading to a reduced space for each single cell, as can be taken from Fig. 4.44 C – G. A documentation of the cell morphology beyond the observation time of the QCM-based assay of 20 h reveals that MDCK-II cells do not exhibit their typical cobblestone morphology 48 h after cell inoculation – they look rather irregular in shape and size, with less clearly defined cell boundaries (Fig. 4.44 G).

The following figure presents phase contrast micrographs which were taken at regular time intervals after the inoculation of initially suspended MDCK-II cells upon SFM pre-treated PS (Fig. 4.45 A – G). Following cell attachment and spreading upon a SFM pre-incubated PS surface, the phase contrast image taken 2 h after cell inoculation shows that MDCK-II cells attach and spread on this surface, leading to a surface coverage of approximately 75 % (Fig. 4.45 A). Four hours after cell inoculation, only minor parts of the PS surface are still uncovered (Fig. 4.45 B) whereas the PS surface is completely covered with spread cells after

6 h (Fig. 4.45 C). Similar to the PBS^{--} pre-incubated surface, the cells exhibit irregularities concerning their size and shape 48 h after inoculation (Fig. 4.45 G).

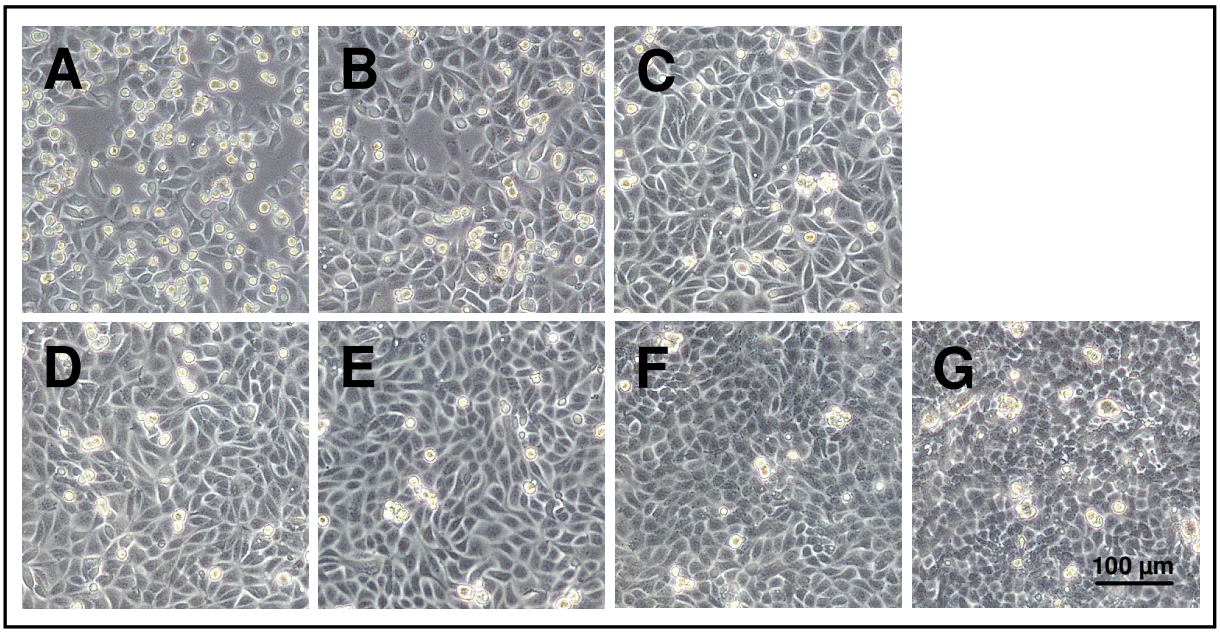

Fig. 4.45 Phase contrast micrographs of MDCK-II cells at various time points after inoculation, documenting attachment and spreading upon PS coated coverslips that were exposed to SFM for 20 h at 37 °C prior to cell inoculation. The cells were suspended in serum-containing medium with a cell density of 4.5×10^5 cm^{-2}. The pictures were taken **A** 2 h, **B** 4 h, **C** 6 h, **D** 8 h, **E** 10 h, **F** 24 h and **G** 48 h after cell inoculation.

Initially suspended MDCK-II cells spread upon an argon plasma modified, pre-incubated surface at a similar rate, regardless of which fluid – PBS^{--} or SFM – was used to pre-incubate the PS surface with. Thus, MDCK-II cell attachment and spreading is exemplarily shown for a plasma modified, SFM pre-incubated surface (Fig. 4.46), while phase contrast micrographs for cell adhesion upon a PBS^{--} pre-incubated PS surface are presented only in the appendix D 1 (Fig. D.1). While most of the cells have attached and spread on the surface after an incubation time of 2 h, leaving only small fractions of surface area uncovered (Fig. 4.46 A), the micrographs taken after an incubation time of 4 h show a surface which is confluently covered with MDCK-II cells. In contrast to the cells which have been seeded upon only fluid pre-incubated PS, the cells are more regular in size and shape and exhibit their typical cobblestone morphology already 8 – 10 h after cell inoculation (Fig. 4.46 D, E). The cell boundaries are clearly defined (Fig. 4.46 G).

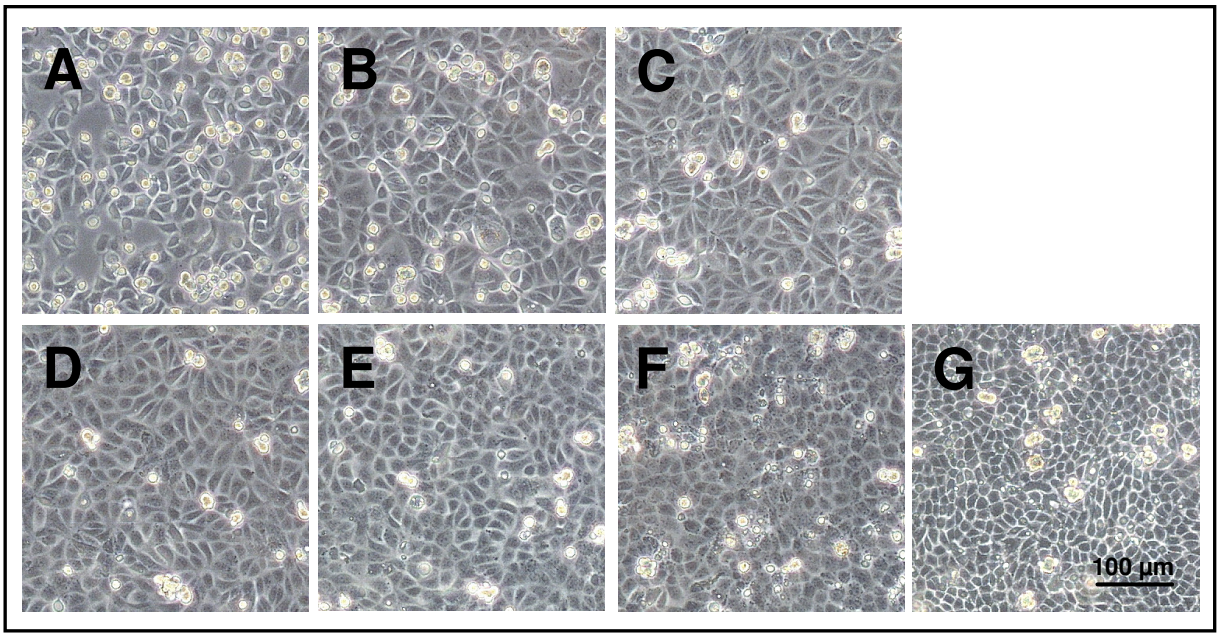

Fig. 4.46 Phase contrast micrographs of MDCK-II cells at various time points after inoculation, documenting attachment and spreading upon PS coated coverslips that were argon plasma modified for 1 min followed by an exposure to SFM for 20 h at 37 °C prior to cell inoculation. The cells were suspended in serum-containing medium with a cell density of 4.5 x 10^5 cm^{-2}. The pictures were taken **A** 2 h, **B** 4 h, **C** 6 h, **D** 8 h, **E** 10 h, **F** 24 h and **G** 48 h after cell inoculation.

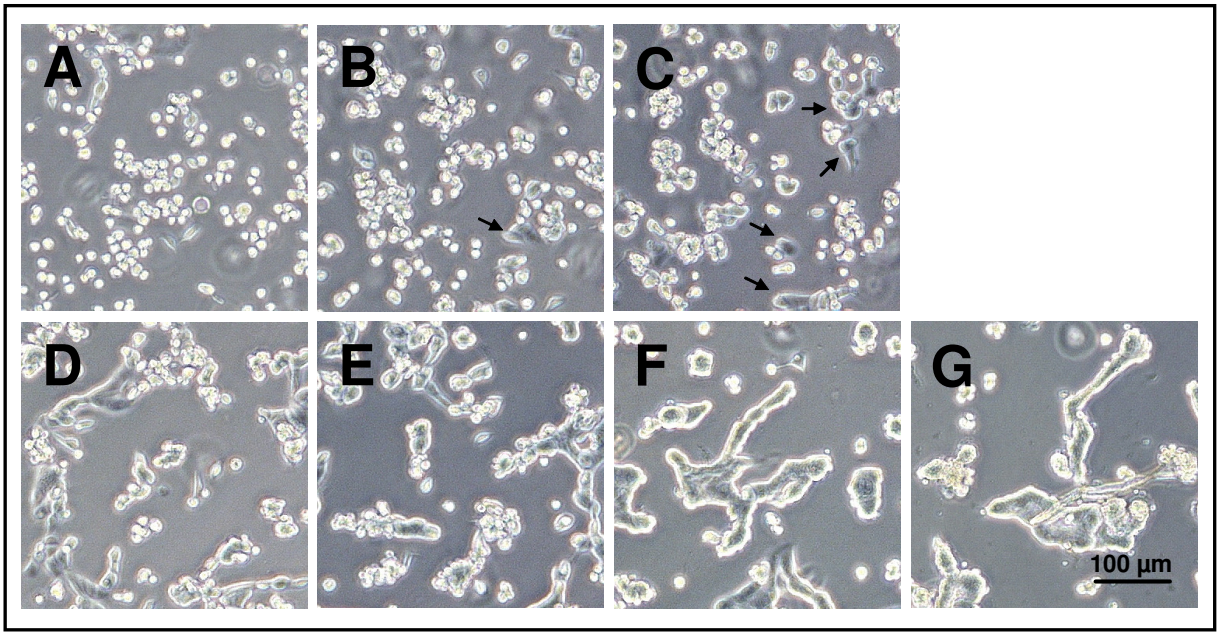

Fig. 4.47 Phase contrast micrographs of MDCK-II cells at various time points after inoculation, documenting attachment and spreading upon unmodified PS coated coverslips. The cells were suspended in serum-containing medium with a cell density of 4.5 x 10^5 cm^{-2}. The pictures were taken **A** 2 h, **B** 4 h, **C** 6 h, **D** 8 h, **E** 10 h, **F** 24 h and **G** 48 h after cell inoculation.

Initially suspended MDCK-II cells do not attach and spread upon an unmodified PS surface (Fig. 4.47 A – G). Four to six hours after cell inoculation, only a few single cells have spread on the surface (Fig. 4.47 B and C, arrows). After a longer incubation time, a few cell islets are

visible consisting of cells which have completely lost their typical morphology. It is hard to detect single cells since the cell borders are not clearly visible. The predominant fraction of the cells remains spherically shaped and forms clump-like aggregates, floating around in the culture medium (Fig. 4.47 E – G).

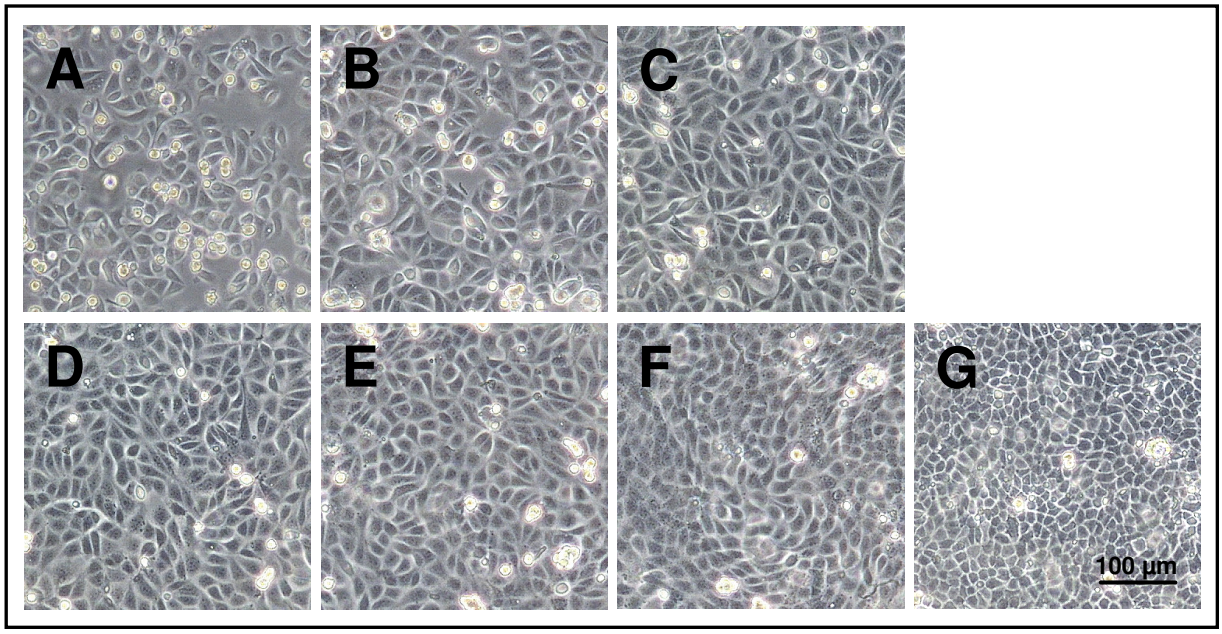

Fig. 4.48 Phase contrast micrographs of MDCK-II cells at various time points after inoculation, documenting attachment and spreading upon PS coated coverslips that were argon plasma modified for 1 min prior to cell inoculation. The cells were suspended in serum-containing medium with a cell density of 4.5 x 10^5 cm^{-2}. The pictures were taken **A** 2 h, **B** 4 h, **C** 6 h, **D** 8 h, **E** 10 h, **F** 24 h and **G** 48 h after cell inoculation.

An argon plasma induced surface modification of PS leads to an improved attachment and spreading behavior of MDCK-II cells upon the polymer, as can be seen in Fig. 4.48 A – G. Six hours after cell inoculation, the surface is completely covered with spread cells (Fig. 4.48 C). In contrast to the plasma modified, pre-incubated PS film, the cells seem to be more irregular in size and shape (compare Fig. 4.46 and 4.48, F). After an incubation time of 48 h, the micrographs of MDCK-II cells on plasma modified PS regardless of fluid pre-incubation look alike, presenting cells with cobblestone morphology (Fig. 4.46 and 4.48, G).

Attachment and Spreading of NRK Cells

Attachment and spreading studies of NRK cells on PS coated surfaces were performed along the same protocols as aforementioned for MDCK-II cells. Figure 4.49 summarizes the time courses of $\Delta|Z_{min}|$ obtained for NRK cells seeded to confluence upon differently pre-treated PS coated quartz resonators.

Figure 4.49 A shows the time course of $\Delta|Z_{min}|$ for the attachment and spreading of initially suspended NRK cells upon a fluid pre-incubated PS coated quartz resonator. Since the cellular response to the PS surfaces pre-incubated for 20 h with either PBS^{--} or SFM are

almost identical, only SFM pre-incubation is presented in Fig. 4.49 A – the series of experiments for PBS^{--} pre-incubation is summarized in the appendix E (Fig. E.2 A). For SFM pre-incubation, the time course of $\Delta|Z_{min}|$ is characterized by an immediate increase to a transient maximum of (410 ± 10) Ω roughly 275 min after cell inoculation, followed by a slight decrease to (340 ± 20) Ω during the remaining 900 min. The slope within the initial period of linear $\Delta|Z_{min}|$ increase is determined to be (2.78 ± 0.05) Ω/min and $\tau_{1/2}$ is calculated to (53 ± 3) min (Tab. 4.19).

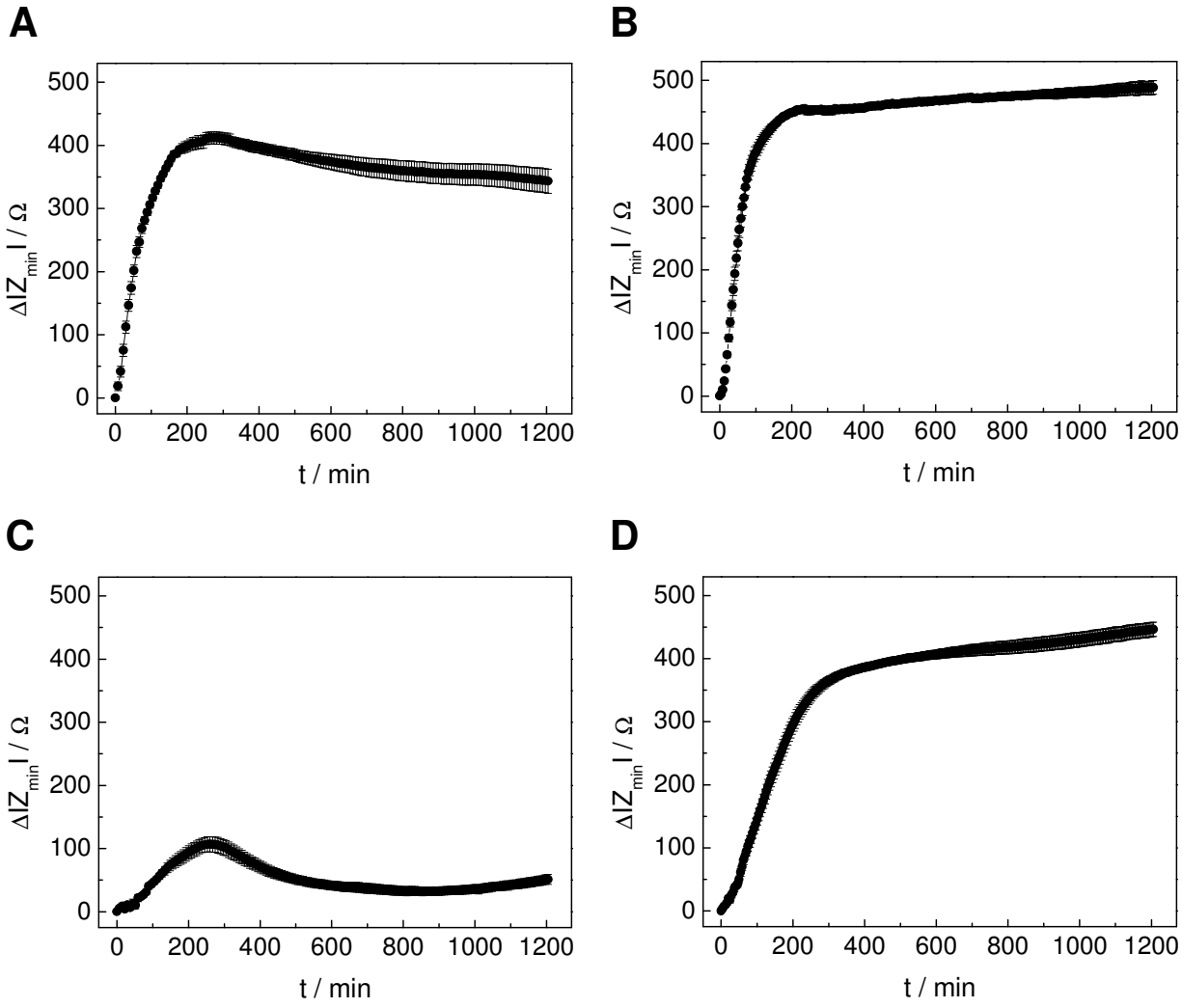

Fig. 4.49 Time course of $\Delta|Z_{min}|$ after seeding equal amounts of initially suspended NRK cells on a PS coated quartz resonator at time point zero. The cell density was adjusted to 4.5 x 10^5 cm^{-2}. The PS coated resonator had been pre-treated as follows: **A** Incubation with SFM for 20 h at 37 °C, **B** argon plasma treatment for 1 min followed by a SFM incubation for 20 h at 37 °C, **C** no pre-treatment and **D** argon plasma treatment for 1 min. The value of $|Z_{min}|$ at the beginning of the experiment was set to zero. (Mean ± SDM, n ≥ 5; T = 37 °C).

NRK cells seeded upon plasma modified, pre-incubated PS reveal a similar attachment and spreading behavior independent of the fluid used for pre-incubation. Thus, only one condition is presented in Fig. 4.49 B (see appendix E, Fig. E.2 B for the remaining condition). Cells seeded upon a PS surface that has been exposed to an argon plasma for 1 min followed by a

SFM incubation for 20 h reveal an increase in their attachment and spreading rate, as can be taken from the initial slope of the attachment curve ((4.53 ± 0.05) Ω/min) and the smaller $\tau_{1/2}$ value of (48 ± 2) min (Fig. 4.49 B). $\Delta|Z_{min}|$ shows a steep rise to a value of (452 ± 6) Ω within 240 min after cell inoculation, which still continues to increase moderately to a maximum of (490 ± 11) Ω during the period of observation. The similar time course of $\Delta|Z_{min}|$ obtained for a plasma treatment, pre-incubated PS surface indicates that the buffer composition does not have an impact on NRK cell attachment and spreading.

The time course of $\Delta|Z_{min}|$ for NRK cells seeded upon unmodified PS does not indicate any significant cell adhesion onto the polymer surface (Fig. 4.49 C). $\Delta|Z_{min}|$ shows a moderate increase to (110 ± 12) Ω within 260 min after cell inoculation. The subsequent time course is marked by a continuous decrease to 50 Ω during the observation time. Since NRK cells only give rise to a rather marginal increase of $\Delta|Z_{min}|$ on this surface, $\tau_{1/2}$ could not be determined. Only a slight transient increase of $\Delta|Z_{min}|$ can be measured, indicating that specific interactions between cells and the underlying surface are not allowed to form.

A simple argon plasma treatment for 1 min as presented in Fig. 4.49 D clearly demonstrates that NRK cell attachment and spreading takes place on this surface. Similar to the graph recorded for a plasma modified and fluid incubated surface (Fig. 4.49 B), $\Delta|Z_{min}|$ increases instantaneously to a transient maximum of (378 ± 6) Ω within 350 min after cell inoculation and continues to increase to a final maximum of (450 ± 12) Ω. However, cell attachment and spreading is slower on a simple plasma modified surface – the slope of the curve is calculated to (1.52 ± 0.02) Ω/min and the time needed to cover half of the polymer surface is $\tau_{1/2}$ = (128 ± 8) min.

Tab. 4.19 Summary of parameters used to characterize the adhesion kinetics of NRK cells on PS. The slope *m* of the attachment curve till it reaches the plateau phase expresses the spreading rate and $\tau_{1/2}$ the time to reach half-maximal $\Delta|Z_{min}|$. n/a means "not applicable". (Mean ± SDM, n ≥ 5, T = 37 °C).

Kinetic Parameter	No Plasma, PBS^{--}/SFM	Plasma, PBS^{--}/SFM	No Plasma, No Swelling	Plasma, No Swelling
m [Ω/min]	2.78 ± 0.05	4.53 ±0.05	0.53 ± 0.02	1.52 ± 0.02
$\tau_{1/2}$ [min]	53 ± 3	48 ± 2	n/a	128 ± 8

Phase contrast images taken at 2, 4, 6, 8, 10, 24 and 48 h after seeding of NRK cells upon differently modified spin coated PS films (Fig. 4.50 – 4.54) visualize the adhesion kinetics of NRK cells and support the QCM results. Initially suspended NRK cells were seeded upon PS coated glass coverslips which were pre-treated as described above for the PS coated quartz resonators.

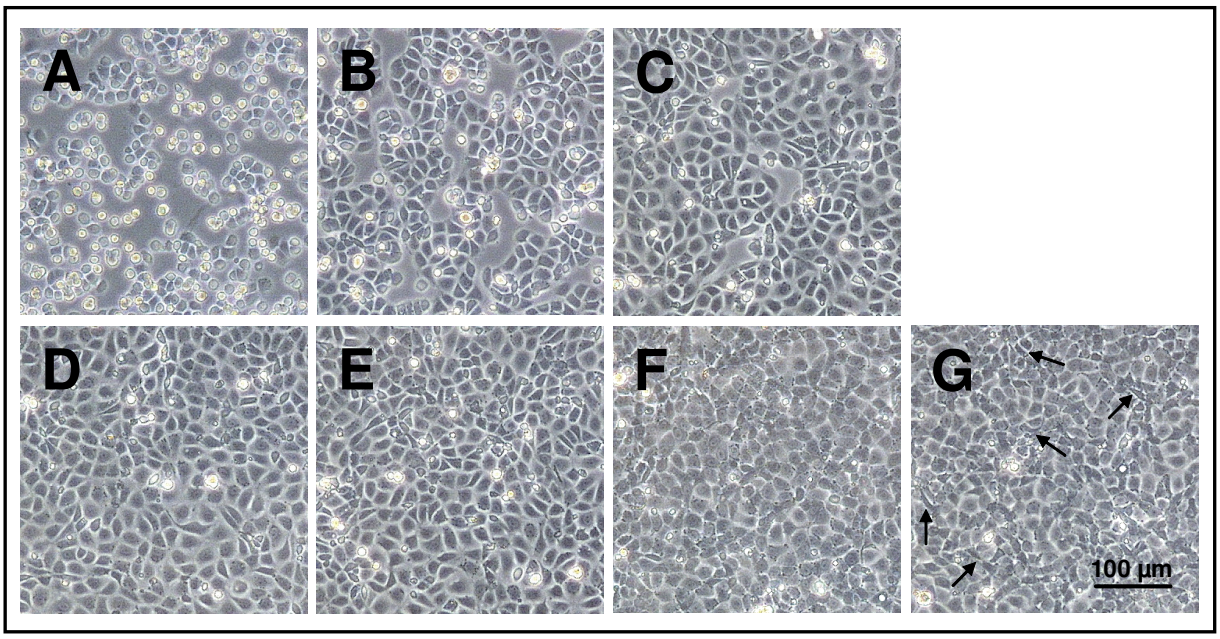

Fig. 4.50 Phase contrast micrographs of NRK cells at various time points after inoculation, documenting attachment and spreading upon PS coated coverslips that were exposed to PBS^{--} for 20 h at 37 °C prior to cell inoculation. The cells were suspended in serum-containing medium with a cell density of 4.5 x 10^5 cm^{-2}. The pictures were taken **A** 2 h, **B** 4 h, **C** 6 h, **D** 8 h, **E** 10 h, **F** 24 h and **G** 48 h after cell inoculation.

Two hours after seeding a suspension of NRK cells on PBS^{--} pre-incubated PS, a small fraction of the cells has already spread upon the surface, although their degree of spreading is still low (Fig. 4.50 A). Approximately 55 % of the surface is covered with cells, while the remaining fraction of the cells is still spherically shaped and suspended in the culture medium. After four hours of incubation, further cells have spread upon the surface, covering a surface area of roughly 78 % (Fig. 4.50 B). A complete surface coverage is attained after an incubation time of 8 h (Fig. 4.50 D). 48 h after cell inoculation adherent NRK cells are rather irregular in shape and size (Fig. 4.50 G). Some cells appear to have an elongated, spindle-like shape and filopodia-like extensions, respectively (Fig. 4.50 G, arrows).

Cell attachment and spreading of initially suspended NRK cells upon SFM pre-incubated PS (Fig. 4.51) proceeds slightly slower compared to a PBS^{--} pre-incubated surface (compare Fig. 4.50). After 10 h of incubation, the cells form a confluent monolayer on the PS surface (Fig. 4.51 E). In contrast to the PBS^{--} pre-incubated surface, cells seeded on a SFM pre-incubated surface are not only rather inhomogeneous in size and shape and thus uncommon for NRK cells, some cells also seem to grow on top of each other, forming overlapping domains (Fig. 4.51 G, arrows).

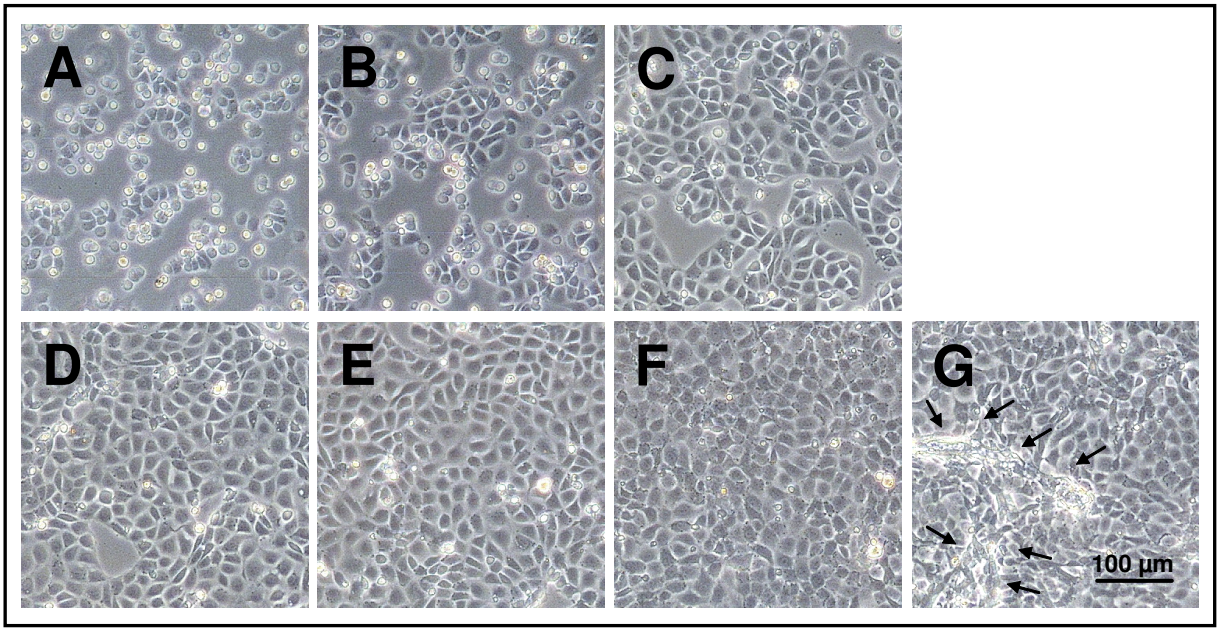

Fig. 4.51 Phase contrast micrographs of NRK cells at various time points after inoculation, documenting attachment and spreading upon PS coated coverslips that were exposed to SFM for 20 h at 37 °C prior to cell inoculation. The cells were suspended in serum-containing medium with a cell density of 4.5 x 10^5 cm^{-2}. The pictures were taken **A** 2 h, **B** 4 h, **C** 6 h, **D** 8 h, **E** 10 h, **F** 24 h and **G** 48 h after cell inoculation.

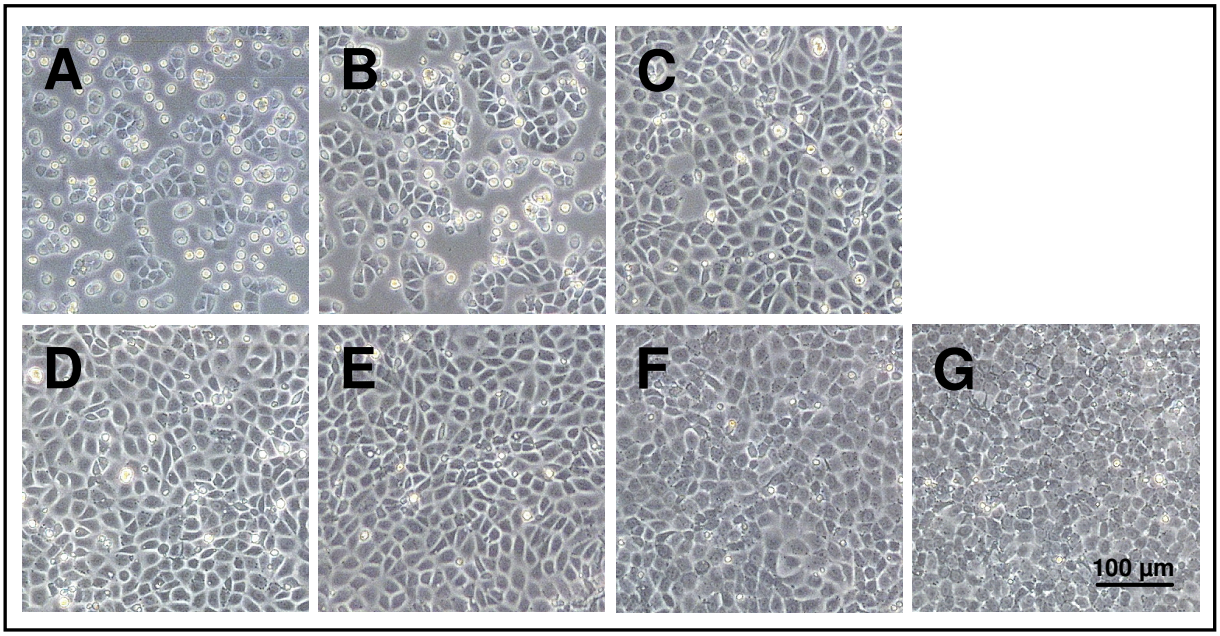

Fig. 4.52 Phase contrast micrographs of NRK cells at various time points after inoculation, documenting attachment and spreading upon PS coated coverslips that were argon plasma modified for 1 min followed by an exposure to SFM for 20 h at 37 °C prior to cell inoculation. The cells were suspended in serum-containing medium with a cell density of 4.5 x 10^5 cm^{-2}. The pictures were taken **A** 2 h, **B** 4 h, **C** 6 h, **D** 8 h, **E** 10 h, **F** 24 h and **G** 48 h after cell inoculation.

The rate of NRK cell attachment and spreading on a plasma modified, pre-incubated PS surface is similarly independent of the fluid, PBS^{--} or SFM, the surface had been exposed to prior to cell inoculation. Figure 4.52 exemplarily presents the cell attachment and spreading

behavior on a plasma modified, SFM pre-incubated surface while phase contrast micrographs for a plasma modified, PBS^{--} pre-incubated surface are shown in the appendix D 1 (Fig. D.2). After an incubation time of 6 h, the surface is almost completely covered with NRK cells, leaving only very small regions cell free (Fig. 4.52 C). During the subsequent period of observation, the cells exhibit their typical cobblestone morphology of uniform size.

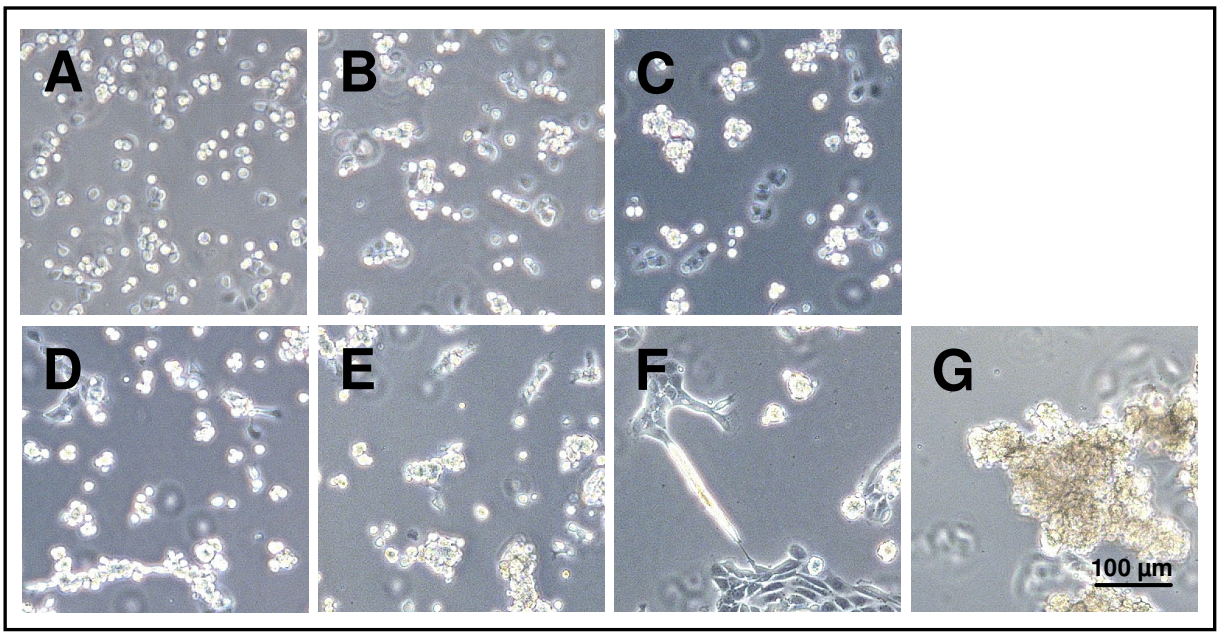

Fig. 4.53 Phase contrast micrographs of NRK cells at various time points after inoculation, documenting attachment and spreading upon unmodified PS coated coverslips. The cells were suspended in serum-containing medium with a cell density of 4.5 x 10^5 cm^{-2}. The pictures were taken **A** 2 h, **B** 4 h, **C** 6 h, **D** 8 h, **E** 10 h, **F** 24 h and **G** 48 h after cell inoculation.

Using an unmodified PS surface as a culture substrate, only a minor fraction of the seeded cells has spread on the surface after 6 h (Fig. 4.53 C). The predominant fraction of the seeded cells remains spherically shaped and forms clump-like aggregates, floating in the culture medium. 24 h after cell inoculation, small cell islets have formed (Fig. 4.53 F). The cell morphology is quite untypical, presenting rather elongated, spindle-like cells. 48 h after cell inoculation, no adherent cells can be observed on the PS surface. The PS surface is cell-free, while big aggregates of cell fragments and apoptotic cells are floating in the culture medium (Fig. 4.53 G).

Argon plasma treatment of the spin coated PS film is sufficient to convert the initially non-cytocompatible surface into a cytocompatible one. After an incubation time of 2 h, single cells have spread on the surface, showing a low degree of spreading (Fig. 4.54 A). More cells spread on the surface during the next 8 h, till after 10 h, the predominant fraction of the surface is covered, leaving only small regions cell-free (Fig. 4.54 E). Similar to a plasma modified, pre-incubated surface, the confluent cell layer consists of individual cells which are uniform in size and shape, exhibiting cobblestone morphology. When compared to the other

differently pre-treated surfaces, attachment and spreading on plasma modified PS takes the most time – even longer than on an only fluid pre-incubated surface. This difference might also be attributed to a lower seeding density. However, the cells stay vital and exhibit their typical morphology like on a plasma modified, fluid incubated surface.

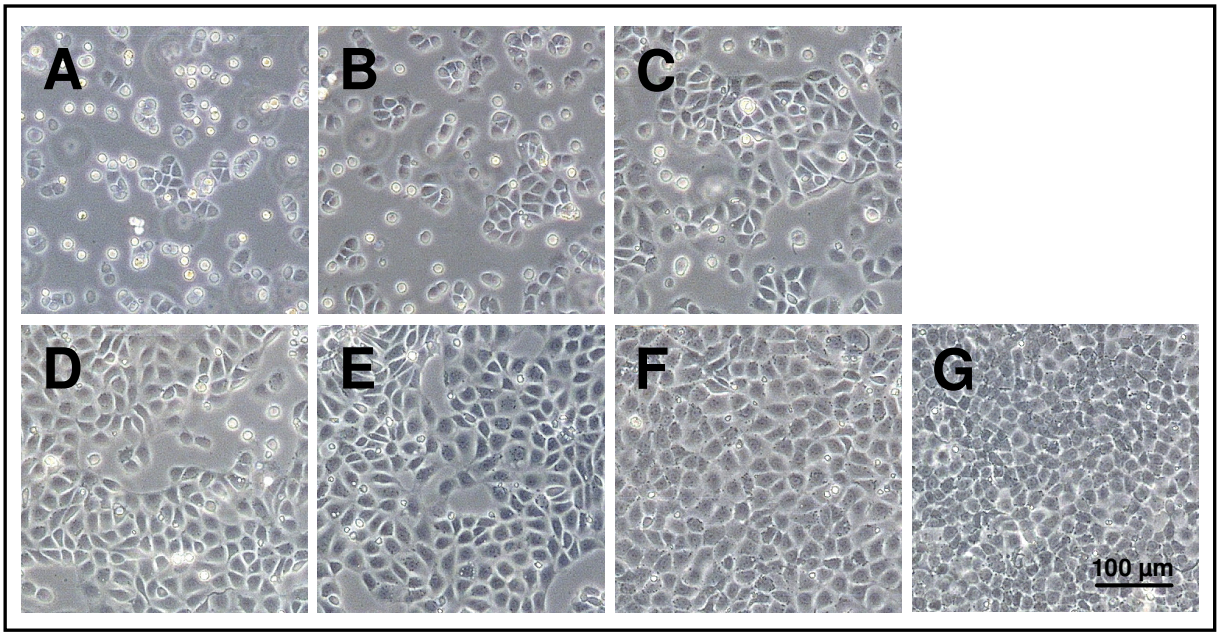

Fig. 4.54 Phase contrast micrographs of NRK cells at various time points after inoculation, documenting attachment and spreading upon PS coated coverslips that were argon plasma modified for 1 min prior to cell inoculation. The cells were suspended in serum-containing medium with a cell density of 4.5 x 10^5 cm^{-2}. The pictures were taken **A** 2 h, **B** 4 h, **C** 6 h, **D** 8 h, **E** 10 h, **F** 24 h and **G** 48 h after cell inoculation.

4.4.4 Cytocompatibility Testing of Poly(methyl methacrylate) Surfaces

The cytocompatibility of PMMA was studied by following cell attachment and spreading of initially suspended MDCK-II and NRK cells upon PMMA coated quartz resonators. Similar to PS, the impact of plasma treatment and/ or a pre-incubation with a physiological buffer was studied with respect to the time course of cell attachment and spreading and quantified by measurements of $\Delta|Z_{min}|$. Furthermore, the QCM results were supported by a microscopic study documenting the cell adhesion kinetics on the PMMA surfaces.

Attachment and Spreading of MDCK-II Cells

The time courses of $\Delta|Z_{min}|$ after MDCK-II cells have been seeded onto PMMA surfaces are presented in Fig. 4.55.

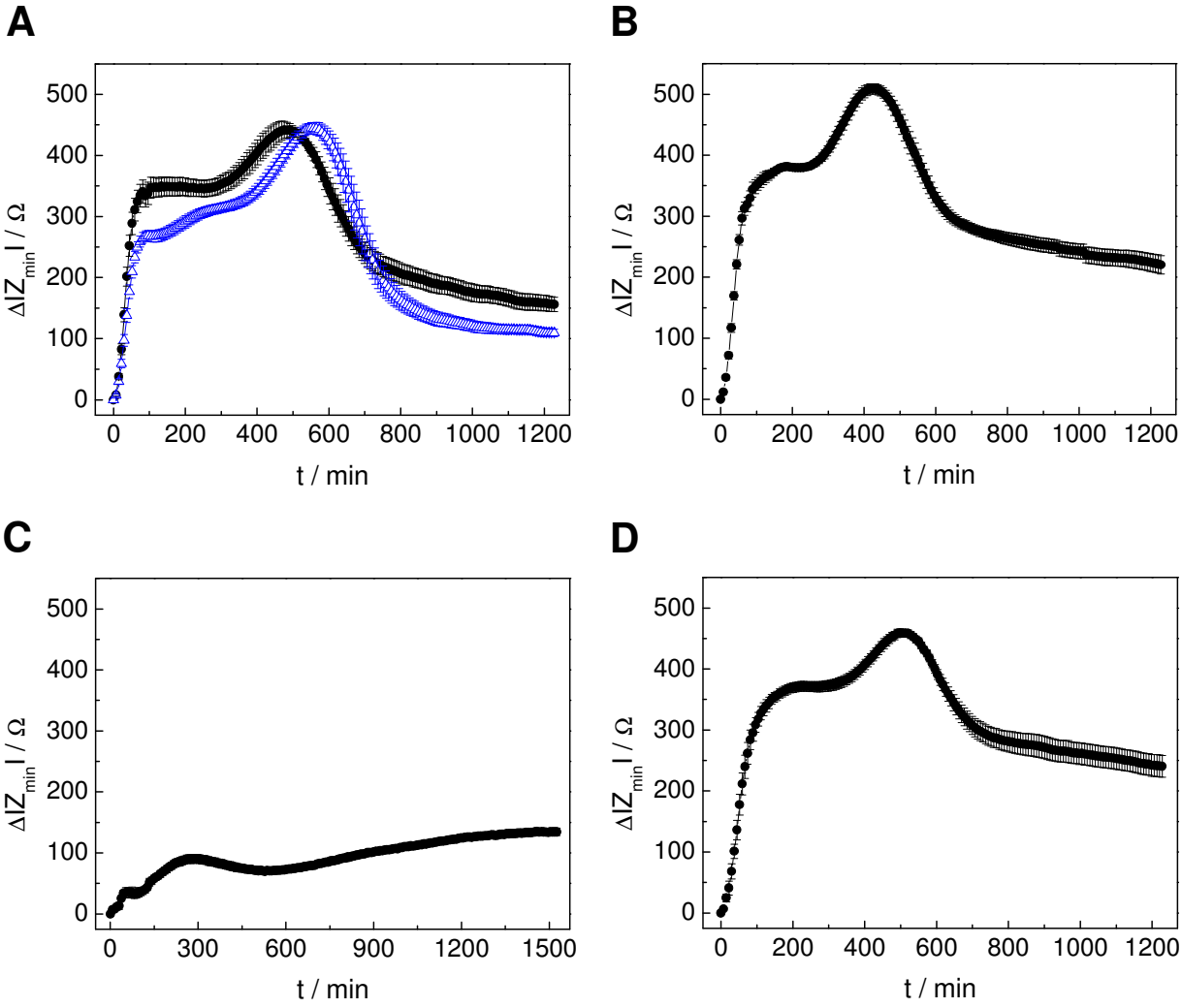

Fig. 4.55 Time course of $\Delta|Z_{min}|$ after seeding equal amounts of initially suspended MDCK-II cells on a PMMA coated quartz resonator at time point zero. The cell density was adjusted to 4.5 x 10^5 cm^{-2}. The PMMA coated resonator had been pre-treated as follows: **A** Incubation with PBS^{--} (●) / SFM (Δ) for 20 h at 37 °C, **B** argon plasma treatment for 1 min followed by a PBS^{--} incubation for 20 h at 37 °C, **C** no pre-treatment and **D** argon plasma treatment for 1 min. The value of $|Z_{min}|$ at the beginning of the experiment was set to zero. (Mean ± SDM, n ≥ 6; T = 37 °C).

Figure 4.55 A presents $\Delta|Z_{min}|$ as a function of time when a suspension of MDCK-II cells is seeded on a PMMA coated quartz resonator which had been previously exposed to PBS^{--} or SFM for 20 h at 37 °C. An immediate increase of $\Delta|Z_{min}|$ can be detected due to cell adhesion upon the polymer pre-incubated with either of the fluids, giving rise to an initial slope of (6.00 ± 0.19) Ω/min in the case of the PBS^{--} pre-incubation and (4.37 ± 0.13) Ω/min for the SFM pre-incubation. Apart from the similar course of the attachment curve in the very beginning (~ 90 min) of the experiment, the further course differs to some extent. Whereas for the cells seeded upon a PBS^{--} pre-incubated PMMA surface, the increase of $\Delta|Z_{min}|$ leads to the first plateau phase of (350 ± 15) Ω within 120 min after cell inoculation, no real plateau phase is observed when MDCK-II cells are seeded upon a SFM pre-incubated surface. Instead, a monotonic rise of $\Delta|Z_{min}|$ can be detected. After roughly 90 min the values shortly stabilize on the level of (269 ± 9) Ω before they increase in a biphasic manner – a rather

moderate increase is followed by a steep increase – to a transient maximum of (445 ± 9) Ω roughly (570 ± 13) min after cell inoculation. The maximum value for the PBS^{--} pre-incubated surface with $\Delta|Z_{min}| = (440 \pm 13)\ \Omega$ is reached slightly earlier within (500 ± 16) min. Both $\Delta|Z_{min}|$ values decrease after having passed their respective maxima by approximately 290 Ω (PBS^{--}) and 340 Ω (SFM). The $\tau_{1/2}$ values for MDCK-II cell attachment and spreading on these two fluid incubated PMMA surfaces are calculated to (35 ± 2) min in case of the PBS^{--} and (37 ± 2) min in case of the SFM treated surface.

MDCK-II cells seeded upon plasma modified, pre-incubated PMMA provide a similar time course of $\Delta|Z_{min}|$ independent of the fluid used for pre-incubation. Thus, only one condition is presented in Fig. 4.55 B while the series of experiments for the remaining condition is summarized in the appendix E (Fig. E.3). The initial 190 min of the time course of $\Delta|Z_{min}|$ recorded for a plasma modified, PBS^{--} pre-incubated surface (Fig. 4.55 B) is characterized by a slope of (5.50 ± 0.12) Ω/min. After having passed the transient plateau phase at (380 ± 5) Ω, $\Delta|Z_{min}|$ continues to increase to a second maximum at (509 ± 8) Ω within (425 ± 9) min after cell inoculation. The values finally stabilize at (220 ± 15) Ω after about 900 min. The $\tau_{1/2}$ values for cell attachment and spreading on this plasma modified, pre-incubated surface is determined to (41 ± 1) min.

Figure 4.55 C shows $\Delta|Z_{min}|$ for a completely unmodified PMMA surface. MDCK-II cells do not attach and spread properly on this surface, as indicated by a moderate increase of $\Delta|Z_{min}|$ to a transient maximum of only (90 ± 7) Ω within 280 min after cell seeding, followed by a slight increase to a value of (130 ± 6) Ω which is maintained along the remaining observation period. The initial slope of $\Delta|Z_{min}|$ is determined to (0.38 ± 0.03) Ω/min. When compared to the three remaining graphs, the typical biphasic shape of the curve is completely lost. Since the $\Delta|Z_{min}|$ value of the first maximum is only about a quarter of the value for the other surface conditions, determination of $\tau_{1/2}$ was not meaningful.

An argon plasma induced hydrophilization of the PMMA surface (Fig. 4.55 D) leads to an attachment and spreading curve similar to those observed in Fig. 4.55 A and B for fluid pre-incubated surfaces. The initial slope determined for the graph amounts to (3.45 ± 0.07) Ω/min. The first transient maximum is reached 200 min after cell inoculation, ranging in the order of (370 ± 8) Ω. The second maximum of $\Delta|Z_{min}| = (460 \pm 6)\ \Omega$ is attained roughly 510 min after cell inoculation. $\tau_{1/2}$ for MDCK-II cell attachment and spreading was determined to (56 ± 4) min.

Table 4.20 summarizes the QCM based data for the adhesion kinetics of MDCK-II cells on variously pre-treated PMMA surfaces on the basis of the initial slope of $\Delta|Z_{min}|$, $\tau_{1/2}$ and τ_2.

Tab. 4.20 Summary of parameters used to characterize the adhesion kinetics of MDCK-II cells on PMMA. The slope m of the attachment curve till it reaches the first plateau phase expresses the spreading rate and $\tau_{1/2}$ the time to reach half-maximal $\Delta|Z_{min}|$. τ_2 is the time that is needed to reach the second maximum. n/a means "not applicable". (Mean ± SDM, n ≥ 6; T = 37 °C).

Kinetic Parameter	No Plasma, Swelling		Plasma, PBS^{--}/SFM	No Plasma, No Swelling	Plasma, No Swelling
	PBS^{--}	SFM			
m [Ω/min]	6.00 ± 0.19	4.37 ± 0.13	5.50 ± 0.12	0.38 ± 0.03	3.45 ± 0.07
$\tau_{1/2}$ [min]	35 ± 2	37 ± 2	41 ± 1	n/a	56 ± 4
τ_2 [min]	500 ± 16	570 ± 13	425 ± 9	n/a	510 ± 6

The corresponding microscopic study of MDCK-II cells at regular time intervals after inoculation on differently pre-treated PMMA films are summarized in the following figures (Fig. 4.56 – 4.60).

A comparison of MDCK-II cell attachment and spreading upon the PBS^{--} pre-incubated PMMA surface (Fig. 4.56) and the SFM pre-incubated PMMA surface (Fig. 4.57) reveals that this process proceeds faster on the PBS^{--} pre-incubated surface. After an incubation time of 6 – 8 h the PBS^{--} pre-incubated PMMA surface is almost entirely covered with cells (Fig. 4.56 C, D), whereas the SFM pre-incubated surface shows a surface coverage of only approximately 50 % (Fig. 4.57 C, D).

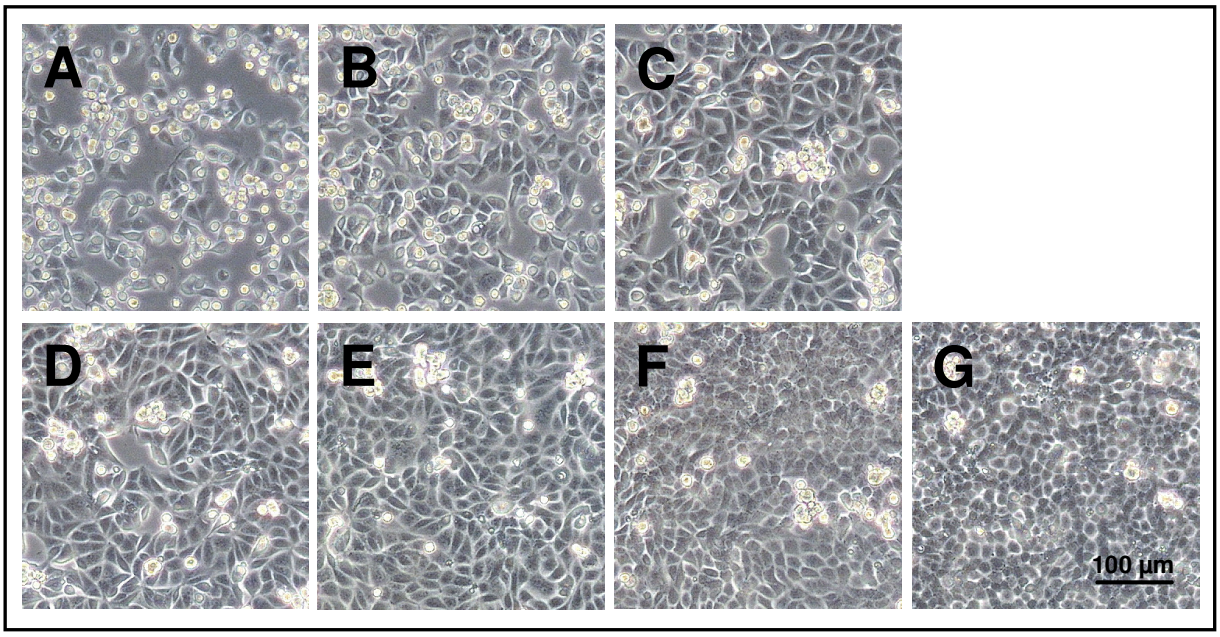

Fig. 4.56 Phase contrast micrographs of MDCK-II cells at various time points after inoculation, documenting attachment and spreading upon PMMA coated coverslips that were exposed to PBS^{--} for 20 h at 37 °C prior to cell inoculation. The cells were suspended in serum-containing medium with a cell density of 4.5 x 10^5 cm^{-2}. The pictures were taken **A** 2 h, **B** 4 h, **C** 6 h, **D** 8 h, **E** 10 h, **F** 24 h and **G** 48 h after cell inoculation.

Besides this difference in adhesion kinetics, further significant differences concerning the cell morphology can also be observed. Cells that were seeded upon a PBS^{--} pre-incubated surface appear to be more regular in size and shape, whereas those that were cultivated upon SFM pre-incubated PMMA are rather elongated with an irregular shape (Fig. 4.56 and 4.57, F, G).

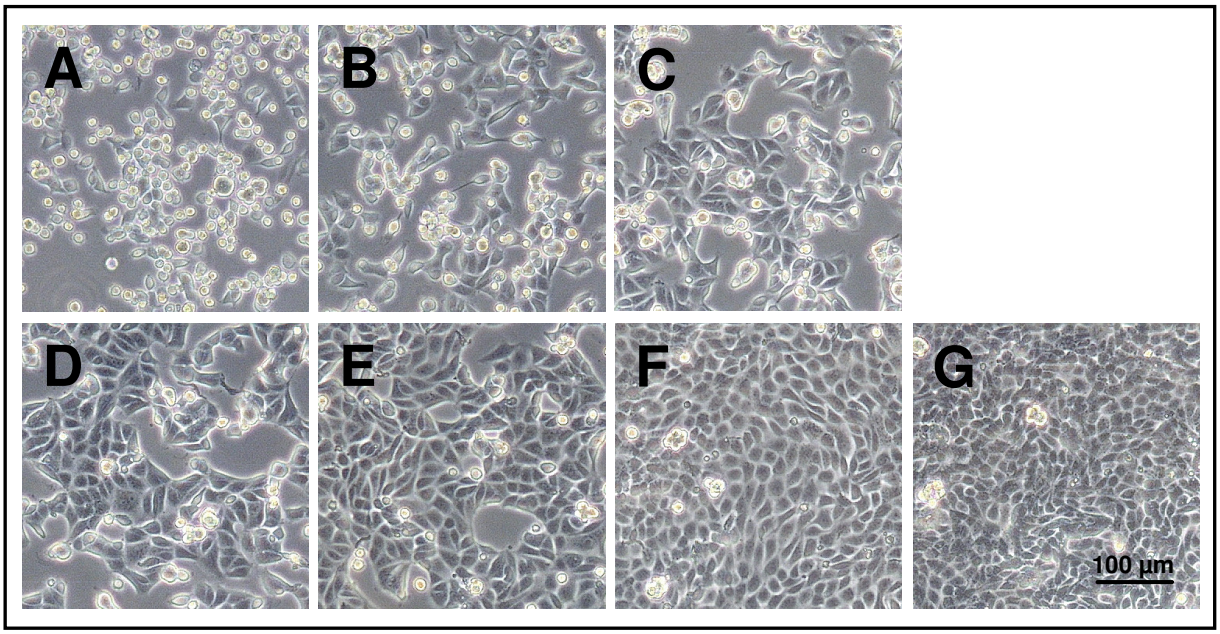

Fig. 4.57 Phase contrast micrographs of MDCK-II cells at various time points after inoculation, documenting attachment and spreading upon PMMA coated coverslips that were exposed to SFM for 20 h at 37 °C prior to cell inoculation. The cells were suspended in serum-containing medium with a cell density of 4.5×10^5 cm^{-2}. The pictures were taken **A** 2 h, **B** 4 h, **C** 6 h, **D** 8 h, **E** 10 h, **F** 24 h and **G** 48 h after cell inoculation.

The adhesion kinetics of MDCK-II cells on plasma modified PMMA are identical regardless of the fluid, PBS^{--} or SFM, the polymer had been incubated in. Thus, only MDCK-II attachment and spreading upon plasma modified, PBS^{--} pre-incubated PMMA are presented here (Fig. 4.58), while cell attachment and spreading upon the plasma modified, SFM pre-incubated surface are shown in the appendix D 2 (Fig. D.3).

In the initial hours after cell inoculation, the cells attach and spread upon the surface till they form an almost confluent cell layer 8 h after cell inoculation (Fig. 4.58 D). The spreading characteristics are similar to those of MDCK-II cells on a non plasma treated, PBS^{--} pre-incubated surface. The phase contrast micrograph showing the confluent monolayer of MDCK-II cells 48 h after cell inoculation reveals individual cells which are regular in size and shape (Fig. 4.58 G).

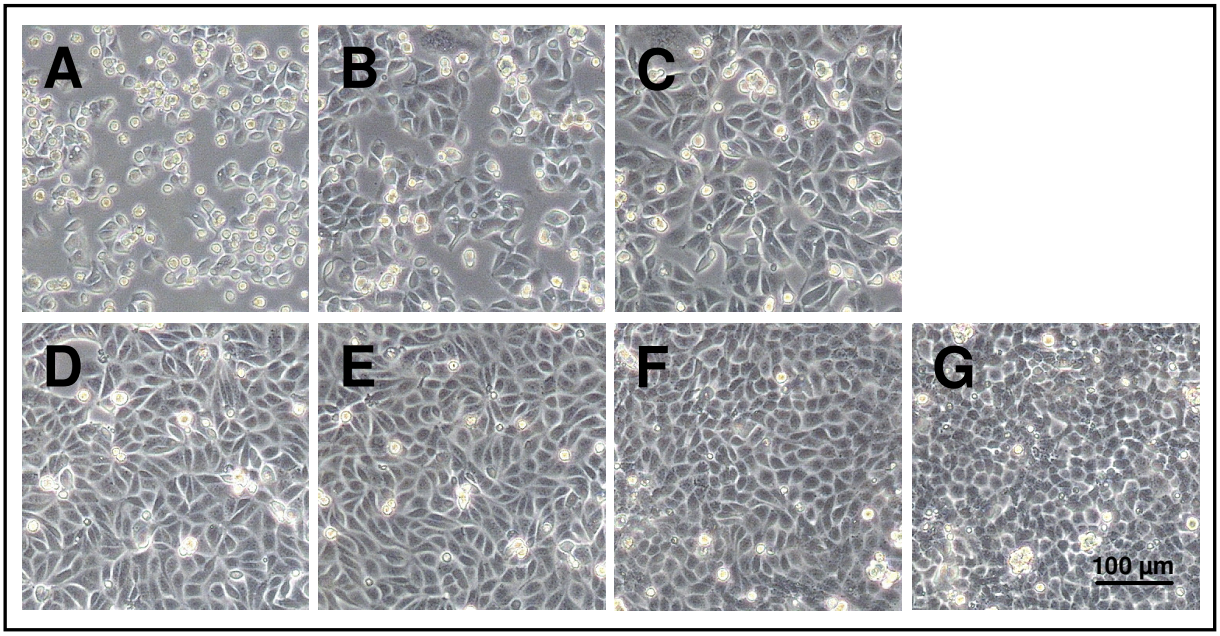

Fig. 4.58 Phase contrast micrographs of MDCK-II cells at various time points after inoculation, documenting attachment and spreading upon PMMA coated coverslips that were argon plasma modified for 1 min followed by an exposure to PBS^{--} for 20 h at 37 °C prior to cell inoculation. The cells were suspended in serum-containing medium with a cell density of 4.5 x 10^5 cm^{-2}. The pictures were taken **A** 2 h, **B** 4 h, **C** 6 h, **D** 8 h, **E** 10 h, **F** 24 h and **G** 48 h after cell inoculation.

Following cell attachment and spreading upon unmodified PMMA in the initial hours after cell inoculation, mainly spherical cells which are floating in the culture medium are present (Fig. 4.59 A, B).

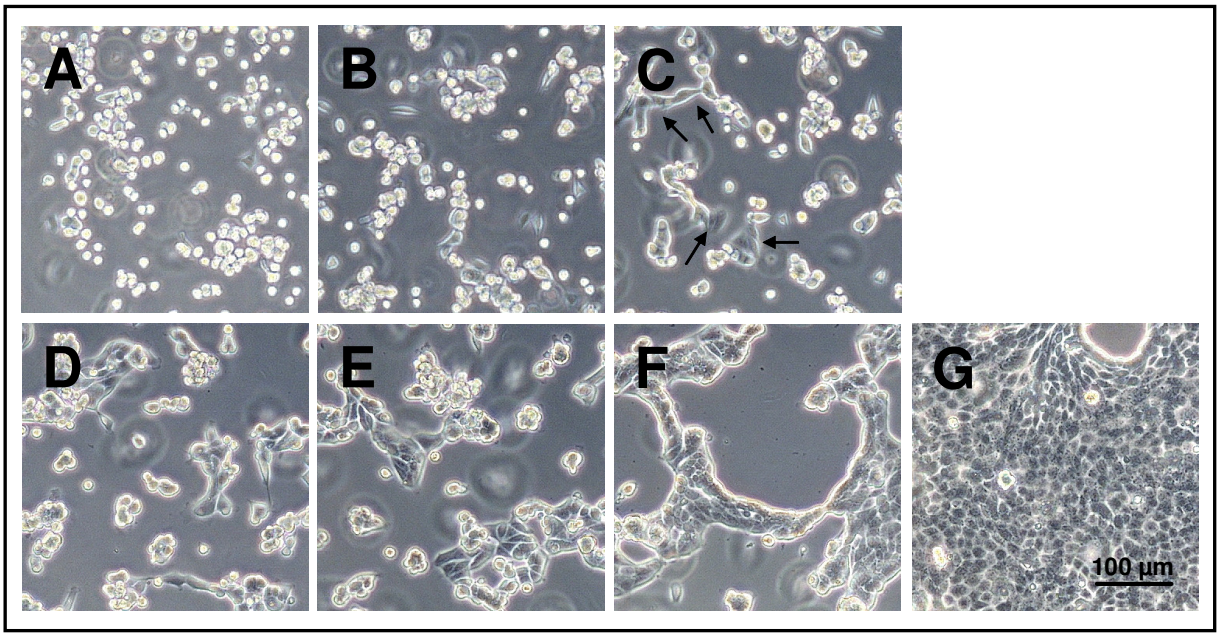

Fig. 4.59 Phase contrast micrographs of MDCK-II cells at various time points after inoculation, documenting attachment and spreading upon unmodified PMMA coated coverslips. The cells were suspended in serum-containing medium with a cell density of 4.5 x 10^5 cm^{-2}. The pictures were taken **A** 2 h, **B** 4 h, **C** 6 h, **D** 8 h, **E** 10 h, **F** 24 h and **G** 48 h after cell inoculation.

After an incubation time of 6 h, only a few single cells have spread upon the surface (Fig. 4.59 C, arrows). During the following incubation time, small cell islets are visible. Whereas 24 h after cell inoculation, a fraction of about 40 % of the surface is covered with cells, the image taken after 48 h reveals an almost confluent monolayer of MDCK-II cells whose cells boundaries appear hardly defined (Fig. 4.59 G).

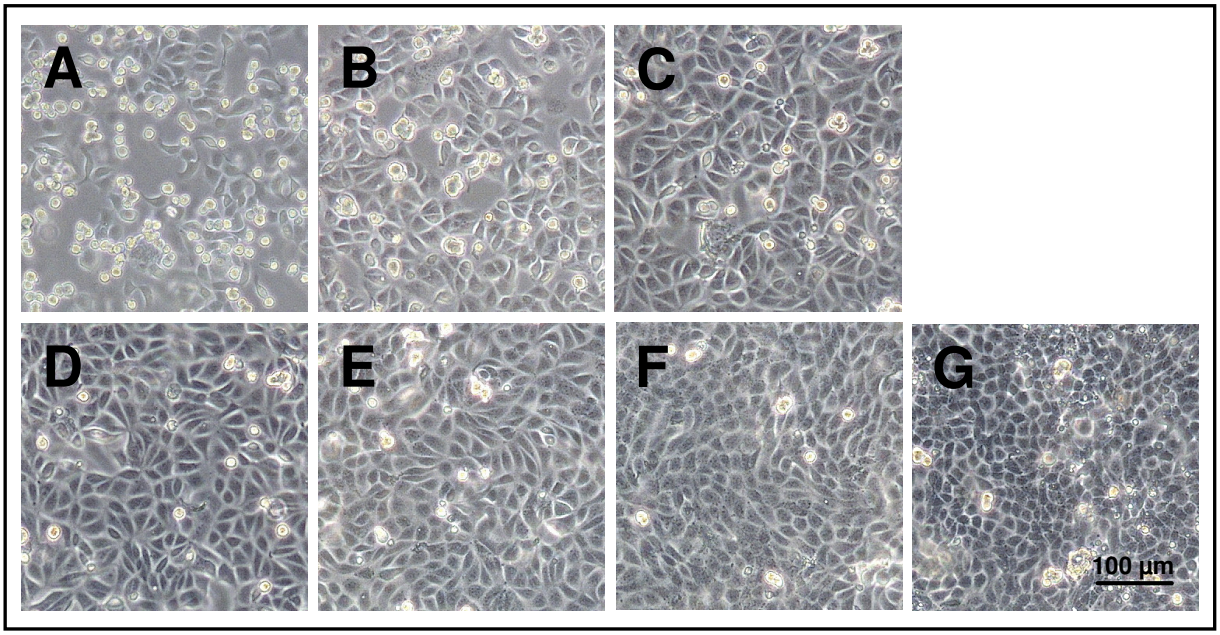

Fig. 4.60 Phase contrast micrographs of MDCK-II cells at various time points after inoculation, documenting attachment and spreading upon PMMA coated coverslips that were argon plasma modified for 1 min prior to cell inoculation. The cells were suspended in serum-containing medium with a cell density of 4.5 x 10^5 cm^{-2}. The pictures were taken **A** 2 h, **B** 4 h, **C** 6 h, **D** 8 h, **E** 10 h, **F** 24 h and **G** 48 h after cell inoculation.

An argon plasma treatment of PMMA promotes cell attachment and spreading to a similar degree as observed for a plasma modified, fluid pre-incubated surface. After 6 – 8 h, the surface is completely covered with a confluent monolayer of MDCK-II cells (Fig. 4.60 C, D). The cells exhibit their typical cobblestone morphology characterized by a polygonal shape.

Attachment and Spreading of NRK Cells

Attachment and spreading studies on PMMA were also performed for NRK cells. Figure 4.61 summarizes the time courses of $\Delta|Z_{min}|$ as obtained for NRK cells seeded upon differently pre-treated PMMA surfaces.

The attachment and spreading curves of NRK cells seeded upon the differently pre-treated PMMA surfaces mainly differ in their initial slope – except for the unmodified surface in Fig. 4.61 C. Since cell adhesion kinetics on the PMMA surface pre-incubated with either PBS^{--} or SFM are almost identical, only the cellular response on SFM pre-incubated PMMA is presented in Fig. 4.61 A (see appendix E, Fig. E.4 A for PBS^{--} pre-incubation). For NRK cells seeded upon SFM pre-incubated PMMA, an immediate increase in $\Delta|Z_{min}|$ to a stationary

value of $(380 \pm 14)\ \Omega$ is recorded within roughly 335 min after cell inoculation, as demonstrated in Fig. 4.61 A. The initial slope of $\Delta|Z_{min}|$ for both conditions is $(1.96 \pm 0.03)\ \Omega$/min and $\tau_{1/2}$ is determined to (61 ± 3) min.

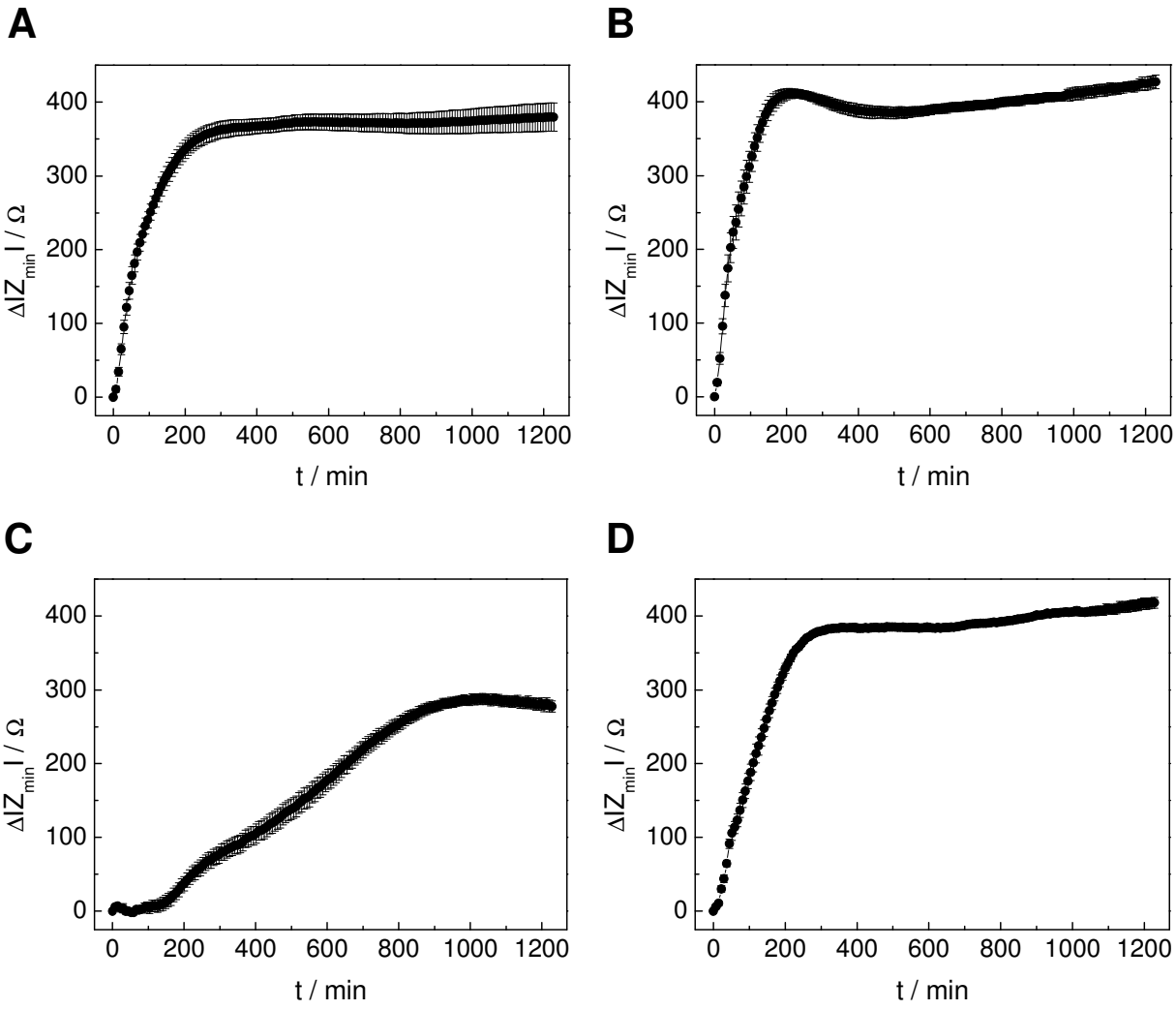

Fig. 4.61 Time course of $\Delta|Z_{min}|$ after seeding equal amounts of initially suspended NRK cells on a PMMA coated quartz resonator at time point zero. The cell density was adjusted to 4.5 x 10^5 cm^{-2}. The PMMA coated resonator had been pre-treated as follows: **A** Incubation with SFM for 20 h at 37 °C, **B** argon plasma treatment for 1 min followed by a SFM incubation for 20 h at 37 °C, **C** no pre-treatment and **D** argon plasma treatment for 1 min. The value of $|Z_{min}|$ at the beginning of the experiment was set to zero. (Mean ± SDM, n ≥ 7; T = 37 °C).

Similar to only pre-incubated PMMA, the cellular response to plasma modified, pre-incubated PMMA does not differ with respect to the physiological buffer, either PBS^{--} or SFM, used for pre-incubation. Figure 4.61 B shows the time course of $\Delta|Z_{min}|$ after cell inoculation on plasma modified, SFM pre-incubated PMMA whereas the time course for plasma modified, PBS^{--} pre-incubated PMMA is shown in the appendix E (Fig. E.4 B). An argon plasma treatment followed by an SFM pre-incubation causes an increase of the cell attachment and spreading rate, as concluded from the increase of the slope to $(2.94 \pm 0.06)\ \Omega$/min as well as the drop of the $\tau_{1/2}$ value to (53 ± 8) min (Fig. 4.61 B).

NRK cells that are seeded upon an unmodified PMMA surface show a significantly different attachment and spreading behavior (Fig. 4.61 C). After an initial lag phase of 140 min, during which $\Delta|Z_{min}|$ does not change significantly, it increases slightly to a constant value of $\Delta|Z_{min}| = (283 \pm 7)\ \Omega$ within 975 min after cell inoculation. The time that is needed to cover half of the polymer surface is $\tau_{1/2} = (500 \pm 35)$ min.
A 1 min argon plasma treatment (Fig. 4.61 D) induces an instantaneous increase of $\Delta|Z_{min}|$ to a constant value of $(385 \pm 5)\ \Omega$ within 350 min after cell inoculation – similar to the value observed for a fluid pre-incubated surface. The initial slope of the curve is determined to $(1.64 \pm 0.02)\ \Omega$/min and $\tau_{1/2}$ is (108 ± 6) min.

The analytical parameters characterizing the adhesion kinetics of NRK cells upon the variously pre-treated PMMA surfaces are summarized in Tab. 4.21.

Tab. 4.21 Summary of parameters used to characterize the adhesion kinetics of NRK cells on PMMA. The slope m of the attachment curve till it reaches the plateau phase expresses the spreading rate and $\tau_{1/2}$ the time to reach half-maximal $\Delta|Z_{min}|$. (Mean ± SDM, n ≥ 7; T = 37 °C).

Kinetic Parameter	No Plasma, PBS^{--}/SFM	Plasma, PBS^{--}/SFM	No Plasma, No Swelling	Plasma, No Swelling
m [Ω/min]	1.96 ± 0.03	2.94 ±0.06	0.36 ± 0.01	1.64 ± 0.02
$\tau_{1/2}$ [min]	61 ± 4	53 ± 8	500 ± 35	108 ± 6

The following figures (Fig. 4.62 – 4.65) show phase contrast images that were acquired at regular time intervals after seeding initially suspended NRK cells upon differently pre-treated PMMA substrates.

NRK cells which are seeded on PMMA pre-incubated with either PBS^{--} or SFM attach and spread upon this surface within 4 h after cell inoculation. Since it makes no difference to which of the fluids the polymer has been exposed to before seeding, the NRK adhesion kinetics shall be exemplarily documented for a SFM pre-incubated surface (Fig. 4.62) whereas cell adhesion upon the PBS^{--} pre-incubated surface is presented in the appendix D 2 (Fig. D.4). After an incubation period of 10 h, the surface is almost entirely covered with spread cells (Fig. 4.62 E). The documentation of the NRK cell monolayer 24 h and 48 h after cell inoculation reveals a cell morphology which is untypical for NRK cells (Fig. 4.62 F, G). The cells are irregular in size and the shape of single cells is rather spindle-like. There are areas in the cell layer where the cells seem to grow on top of each other (Fig. 4.62 G, arrows).

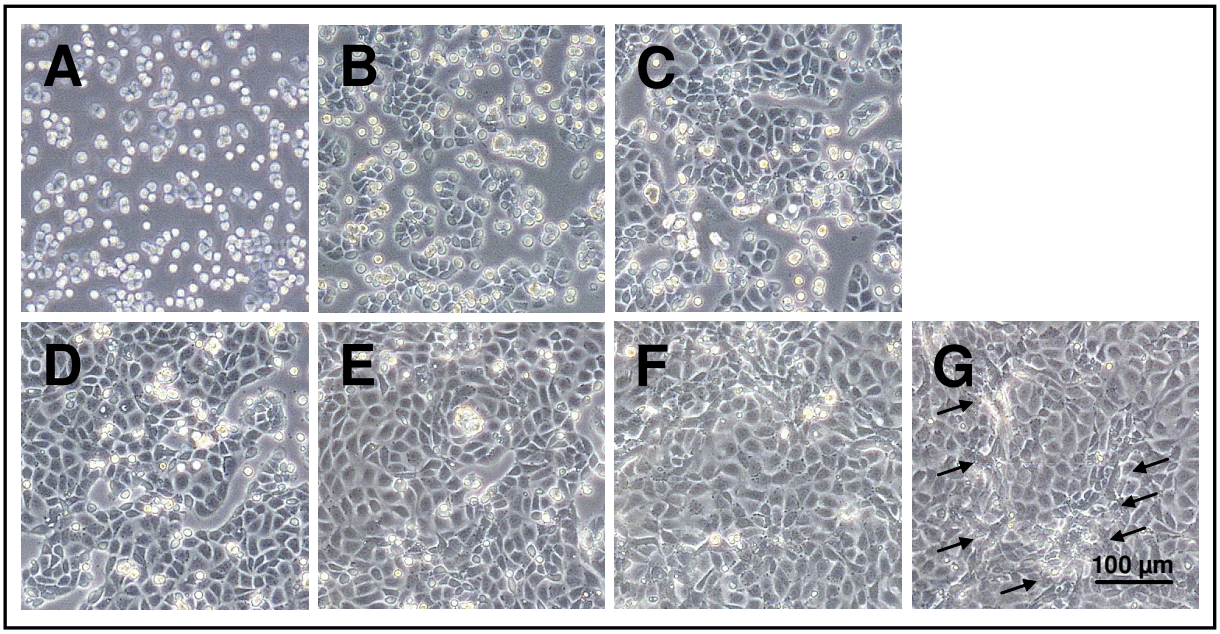

Fig. 4.62 Phase contrast micrographs of NRK cells at various time points after inoculation, documenting attachment and spreading upon PMMA coated coverslips that were exposed to SFM for 20 h at 37 °C prior to cell inoculation. The cells were suspended in serum-containing medium with a cell density of 4.5 x 10^5 cm^{-2}. The pictures were taken **A** 2 h, **B** 4 h, **C** 6 h, **D** 8 h, **E** 10 h, **F** 24 h and **G** 48 h after cell inoculation.

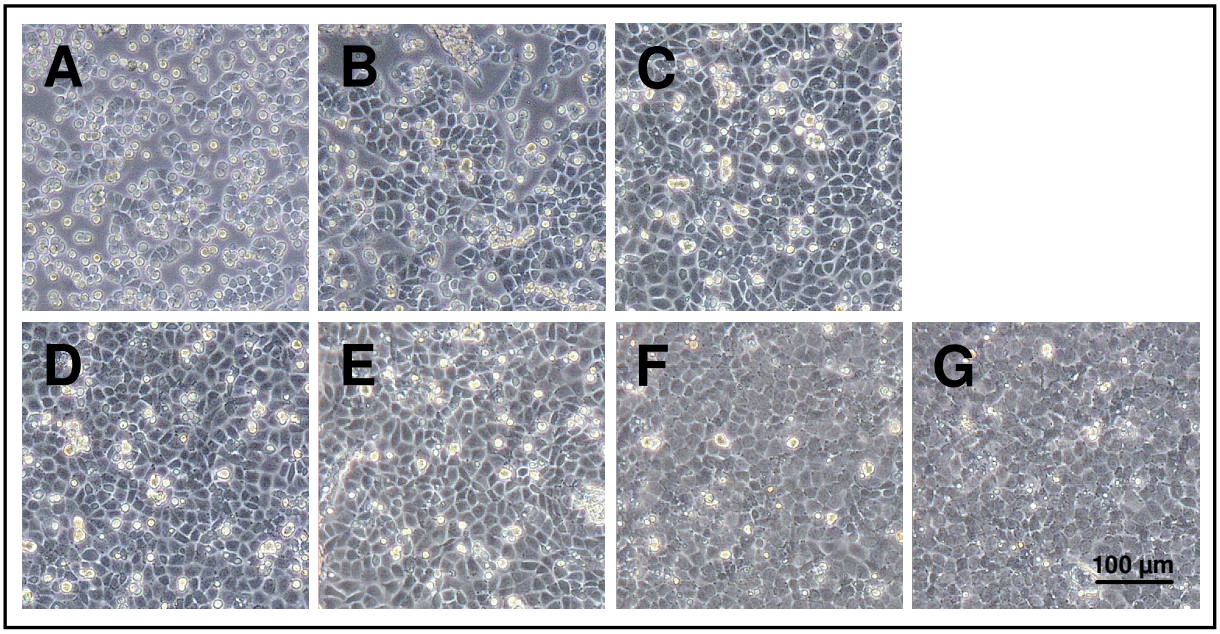

Fig. 4.63 Phase contrast micrographs of NRK cells at various time points after inoculation, documenting attachment and spreading upon PMMA coated coverslips that were argon plasma modified for 1 min followed by an exposure to SFM for 20 h at 37 °C prior to cell inoculation. The cells were suspended in serum-containing medium with a cell density of 4.5 x 10^5 cm^{-2}. The pictures were taken **A** 2 h, **B** 4 h, **C** 6 h, **D** 8 h, **E** 10 h, **F** 24 h and **G** 48 h after cell inoculation.

The attachment and spreading behavior of NRK cells upon plasma modified, pre-incubated PMMA is similar for both physiological buffers, PBS^{--} and SFM. Thus, the phase contrast

images for a plasma modified, SFM pre-incubated surface are shown in Fig. 4.63 whereas the ones for the PBS^{--} pre-incubated surface are presented in the appendix D 2 (Fig. D.5). The attachment and spreading kinetics seem to be faster on a plasma modified, pre-incubated surface than on a simple pre-incubated surface. Already 2 h after cell seeding, the cells start to spread upon the surface till they finally form a confluent cell monolayer after an incubation period of 6 – 8 h (Fig. 4.63 A – D). The cells exhibit their typical cobblestone morphology and are uniform in size and shape (Fig. 4.63 E – G).

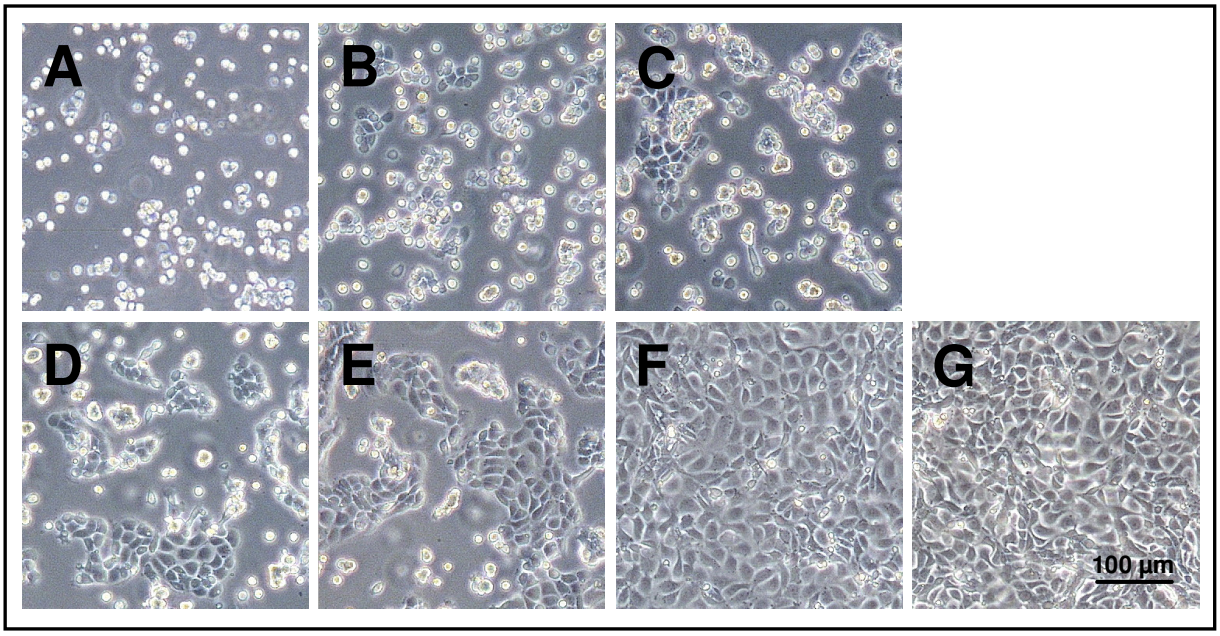

Fig. 4.64 Phase contrast micrographs of NRK cells at various time points after inoculation, documenting attachment and spreading upon unmodified PMMA coated coverslips. The cells were suspended in serum-containing medium with a cell density of 4.5 x 10^5 cm^{-2}. The pictures were taken **A** 2 h, **B** 4 h, **C** 6 h, **D** 8 h, **E** 10 h, **F** 24 h and **G** 48 h after cell inoculation.

Two hours after cell inoculation on unmodified PMMA, all NRK cells are still spherical (Fig. 4.64 A). After four hours, single cells start to spread upon the surface, with the major fraction of the cells still being spherical and floating in the culture medium (Fig. 4.64 B, C). Small cell islets start to form until the cells establish a confluent monolayer 24 h after cell seeding (Fig. 4.64 F). Within the cell monolayer, the individual cells exhibit a morphology which differs from their typical cobblestone morphology. The cells appear irregular in size and shape, with some cells showing elongated extensions (Fig. 4.64 F, G).

Attachment and spreading of NRK cells upon a plasma modified PMMA surface proceeds with similar kinetics as observed for a simply fluid pre-incubated PMMA surface. Approximately 8 – 10 h after cell inoculation, the surface is covered with a confluent cell monolayer (Fig. 4.65 D, E). Compared to a simple fluid pre-incubated surface covered with irregular spindle-like cells, the morphology of NRK cells seeded upon a plasma modified

surface is more regular. The cells are uniform in size and shape, revealing their typical cobblestone morphology which is marked by a polygonal cell shape (Fig. 4.65 F, G).

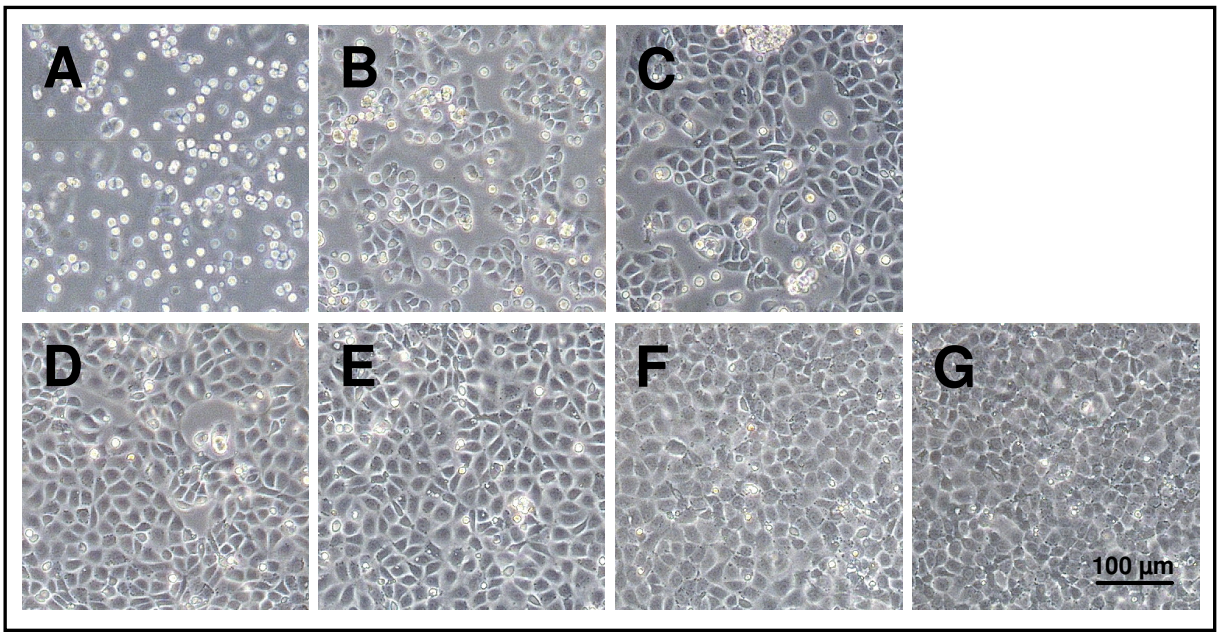

Fig. 4.65 Phase contrast micrographs of NRK cells at various time points after inoculation, documenting attachment and spreading upon PMMA coated coverslips that were argon plasma modified for 1 min prior to cell inoculation. The cells were suspended in serum-containing medium with a cell density of 4.5 x 10^5 cm^{-2}. The pictures were taken **A** 2 h, **B** 4 h, **C** 6 h, **D** 8 h, **E** 10 h, **F** 24 h and **G** 48 h after cell inoculation.

4.4.5 Cytocompatibility Testing of Poly(dimethyl siloxane) Surfaces

The QCM response to the attachment and spreading of initially suspended MDCK-II and NRK cells upon differently pre-treated PDMS surfaces is presented in the following figures (Fig. 4.66 and 4.69). The PDMS coated quartz resonators were either left unmodified or exposed to SFM in the measuring chamber for 20 h at 37 °C prior to the seeding of cells. A microscopic study documenting the cell adhesion kinetics on the different PDMS surfaces was performed in order to support the QCM results.

Attachment and Spreading of MDCK-II Cells

The QCM response to the adhesion of MDCK-II cells in serum-containing medium on the two polymer surfaces – the SFM pre-incubated and the unmodified surface – is shown in Fig. 4.66.

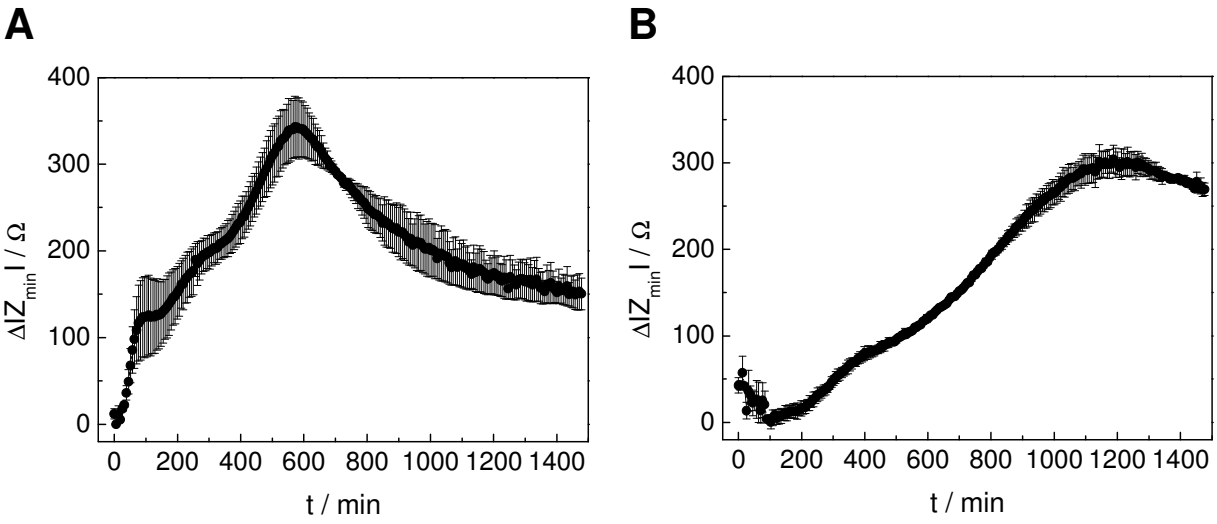

Fig. 4.66 Time course of $\Delta|Z_{min}|$ after seeding equal amounts of initially suspended MDCK-II cells on a PDMS coated quartz resonator at time point zero. The cell density was adjusted to 4.5 x 10^5 cm^{-2}. The PDMS coated resonator had been pre-treated as follows: **A** Incubation with SFM for 20 h at 37 °C, **B** no pre-treatment. The value of $|Z_{min}|$ at the beginning of the experiment was set to zero. (Mean ± SDM, n = 2; T = 37 °C).

Figure 4.66 A shows the time course of $\Delta|Z_{min}|$ after seeding of suspended MDCK-II cells onto a SFM pre-incubated PDMS coated quartz resonator at time point zero. $\Delta|Z_{min}|$ shows an instantaneous steep increase after cell inoculation and reaches a first transient maximum at (130 ± 44) Ω after 103 min. The slope in this initial regime of the plot is (1.63 ± 0.17) Ω/min. The plateau phase is followed by a second steep increase of $\Delta|Z_{min}|$ to a maximal value of (340 ± 35) Ω within 575 min after cell inoculation. After passing this maximum, $\Delta|Z_{min}|$ continuously decreases till the end of the measurement. The last recorded value for $\Delta|Z_{min}|$ after a time period of 1480 min is $\Delta|Z_{min}|$ = (150 ± 18) Ω.

MDCK-II cells which are seeded onto a PDMS coated resonator that has not been pre-incubated with SFM give rise to a different time course of $\Delta|Z_{min}|$ (Fig. 4.66 B). $\Delta|Z_{min}|$ moderately increases to a maximal value of (300 ± 15) Ω within 1188 min after cell inoculation and slightly decreases thereafter by approximately 30 Ω. The slope of the attachment curve is determined to be (0.29 ± 0.002) Ω/min. Since the course of both attachment and spreading curves looks quite different when compared to the typical biphasic behavior found for MDCK-II cells on cytocompatible substrates before (compare Fig. 4.42 in chapter 4.4.2), a determination of the $\tau_{1/2}$ value was omitted. Whereas Fig. 4.66 A reveals a slight indication of two maxima, the biphasic character of the curve in Fig. 4.66 B is completely lost. For both substrates on which the cells are seeded, $\Delta|Z_{min}|$ reaches a similar maximum value, 340 Ω and 300 Ω, respectively, while the time needed to reach this maximum differs. When compared to final $\Delta|Z_{min}|$ values for an uncoated cytocompatible quartz surface ((410 ± 15) Ω), lower absolute $\Delta|Z_{min}|$ values are obtained for MDCK-II cell adhesion upon PDMS. In summary, both PDMS surfaces do not seem to be cytocompatible, since $\Delta|Z_{min}|$ either decreases again to a small value after having passed its maximum

indicating an instable cell adhesion as in the case of a SFM pre-incubated PDMS film (Fig. 4.66 A) or it takes rather long to reach this maximum (Fig. 4.66 B).

In order to support the QCM results, phase contrast images of MDCK-II cells seeded onto the same two PDMS surfaces were taken at regular time intervals after cell inoculation.

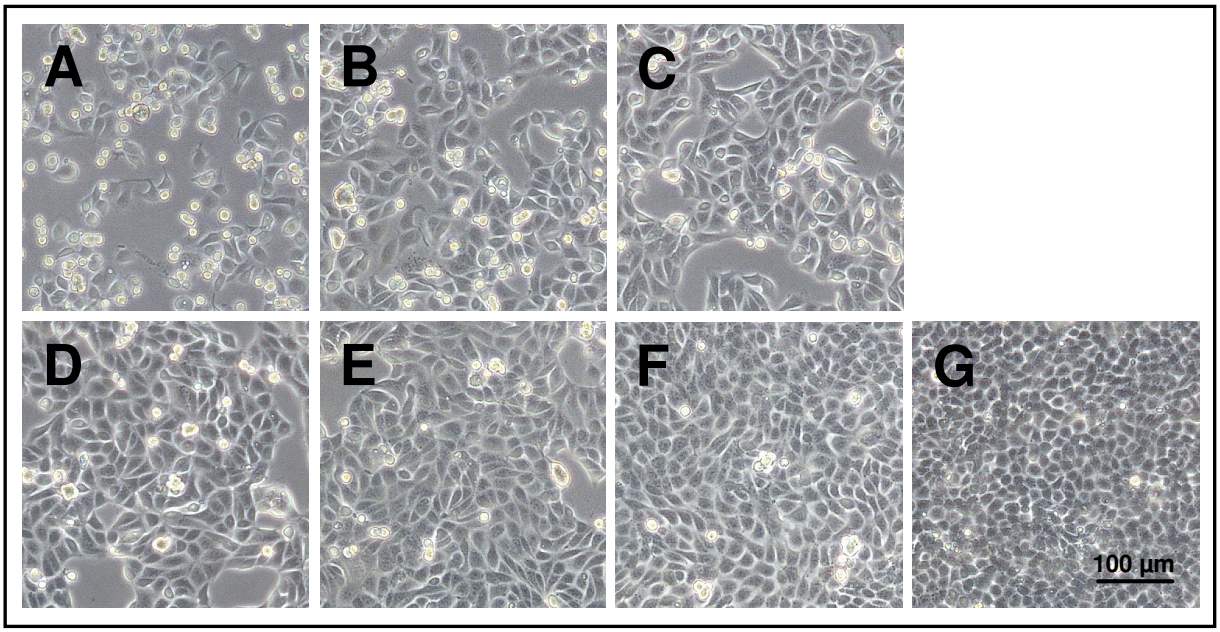

Fig. 4.67 Phase contrast micrographs of MDCK-II cells at various time points after inoculation, documenting attachment and spreading upon PDMS coated coverslips that were exposed to SFM for 20 h at 37 °C prior to cell inoculation. The cells were suspended in serum-containing medium with a cell density of 4.5 x 10^5 cm^{-2}. The pictures were taken **A** 2 h, **B** 4 h, **C** 6 h, **D** 8 h, **E** 10 h, **F** 24 h and **G** 48 h after cell inoculation.

Following attachment and spreading of MDCK-II cells upon SFM pre-incubated PDMS reveals that the cells start to spread upon this surface already 2 h after cell seeding (Fig. 4.67 A). After an incubation period of roughly 10 h, the surface is almost entirely covered with cells (Fig. 4.67 E). Cells in a confluent monolayer show their typical cobblestone morphology (Fig. 4.67 G).

MDCK-II cells which are seeded upon unmodified PDMS remain spherically shaped during the initial 4 h after cell inoculation (Fig. 4.68 A, B). After an incubation period of 6 h, only very few cells have spread upon the surface (~ 10 %), whereas the major fraction of the cells remains spherically shaped (Fig. 4.68 C). The phase contrast image taken after 24 h reveals a PDMS surface with 60 % cell coverage (Fig. 4.68 F). 48 h after cell inoculation, the cells cover the complete surface, as shown in Fig. 4.68 G. Their morphology appears to be quite irregular in size and shape, showing an undulated growth pattern.

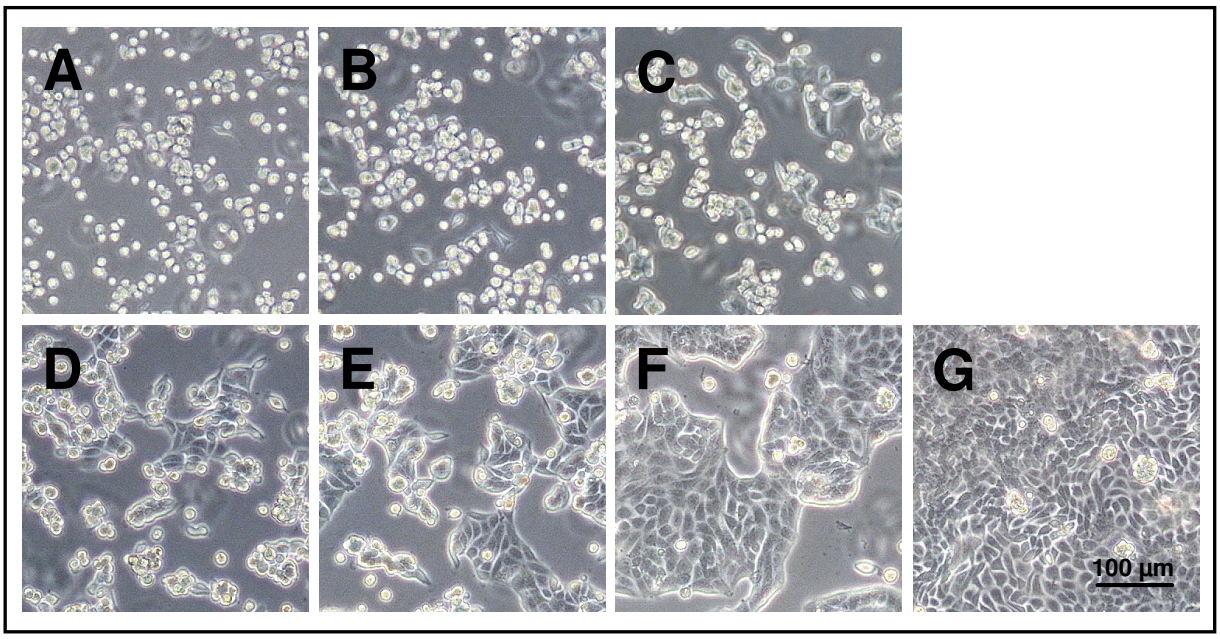

Fig. 4.68 Phase contrast micrographs of MDCK-II cells at various time points after inoculation, documenting attachment and spreading upon unmodified PDMS coated coverslips. The cells were suspended in serum-containing medium with a cell density of 4.5 x 10^5 cm^{-2}. The pictures were taken **A** 2 h, **B** 4 h, **C** 6 h, **D** 8 h, **E** 10 h, **F** 24 h and **G** 48 h after cell inoculation.

The documentation of the attachment and spreading behavior of MDCK-II cells upon the remaining conditions not shown here since they were not studied by the QCM technique can be found in the appendix D 3 (Fig. D.6 – D.13).

Attachment and Spreading of NRK Cells

Similar to the measurements described for MDCK-II cells, NRK cells were studied with respect to their adhesion kinetics upon PDMS coated quartz resonators which were either pre-incubated in SFM or left unmodified.

When NRK cells are seeded upon a PDMS coated resonator pre-incubated with SFM at 37 °C for 20 h, $\Delta|Z_{min}|$ increases to a value of 256 Ω within 250 min, followed by a slight increase to $\Delta|Z_{min}| = (282.7 \pm 0.3)$ Ω during the next 700 min (Fig. 4.69 A). Using linear regression, the slope was determined to be (1.56 ± 0.09) Ω/min and $\tau_{1/2}$ was calculated to yield 55 min.
Figure 4.69 B presents the time course of $\Delta|Z_{min}|$ when NRK cells are seeded upon an unmodified PDMS surface. After an initial increase, $\Delta|Z_{min}|$ reaches a transient plateau at $\Delta|Z_{min}| = 96$ Ω about 200 min after cell seeding. After remaining 170 min in the plateau phase, $\Delta|Z_{min}|$ continues to increase slowly to maximum of 212 Ω within 1073 min. NRK cells adhering on an unmodified PDMS surface give rise to a slope of (0.18 ± 0.002) Ω/min.

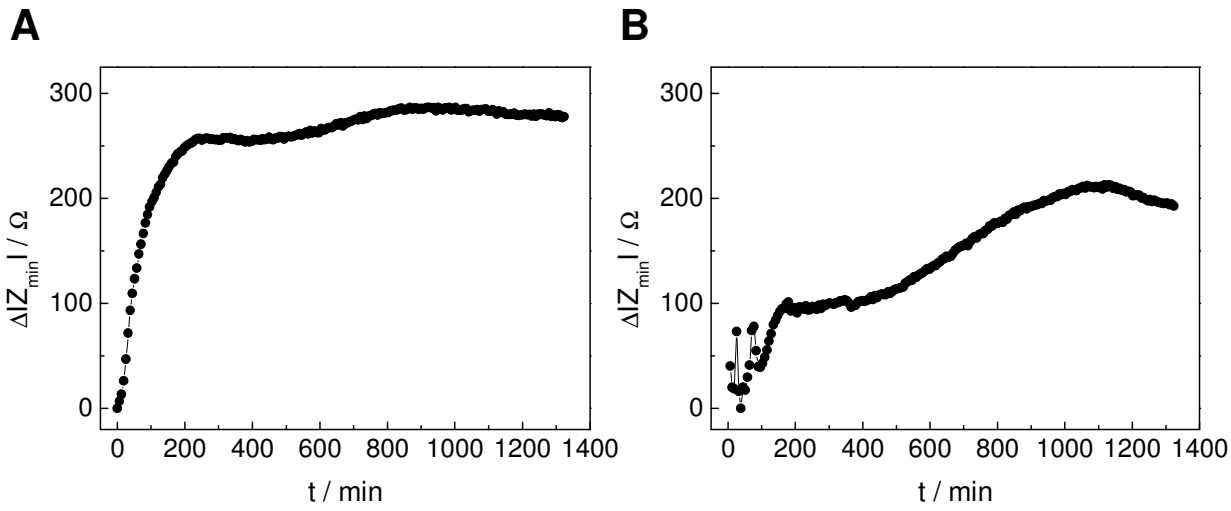

Fig. 4.69 Time course of $\Delta|Z_{min}|$ after seeding equal amounts of initially suspended NRK cells on a PDMS coated quartz resonator at time point zero. The cell density was adjusted to 4.5 x 10^5 cm^{-2}. The PDMS coated resonator had been pre-treated as follows: **A** Incubation with SFM for 20 h at 37 °C, **B** no pre-treatment. The value of $|Z_{min}|$ at the beginning of the experiment was set to zero (n = 1; T = 37 °C).

The microscopic documentation of the attachment and spreading characteristics of NRK cells upon the two above mentioned PDMS substrates is shown below (Fig. 4.70 and 4.71).

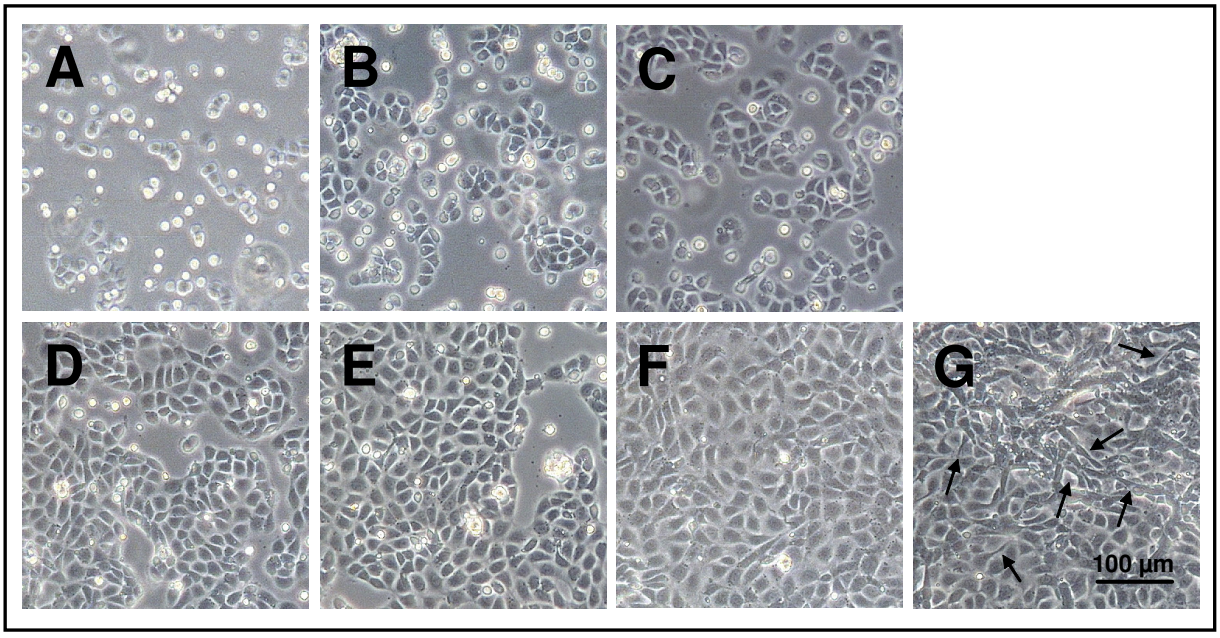

Fig. 4.70 Phase contrast micrographs of NRK cells at various time points after inoculation, documenting attachment and spreading upon PDMS coated coverslips that were exposed to SFM for 20 h at 37 °C prior to cell inoculation. The cells were suspended in serum-containing medium with a cell density of 4.5 x 10^5 cm^{-2}. The pictures were taken **A** 2 h, **B** 4 h, **C** 6 h, **D** 8 h, **E** 10 h, **F** 24 h and **G** 48 h after cell inoculation.

Two hours after cell inoculation on SFM pre-incubated PDMS, single cells start to spread upon the surface, while the predominant fraction of the cells is still spherically shaped (Fig.

4.70 A). The PDMS surface is covered by roughly 80 % after an incubation period of 8 – 10 h (Fig. 4.70 D, E). Whereas the microscopic image taken after 24 h shows a confluent monolayer of NRK cells which appear rather homogeneous in size and shape, the micrograph after 48 h reveals that the substrate does not seem to be long-term cytocompatible. Cells are not uniform in size and shape, showing some cells having elongated extensions (Fig. 4.70 G, arrows).

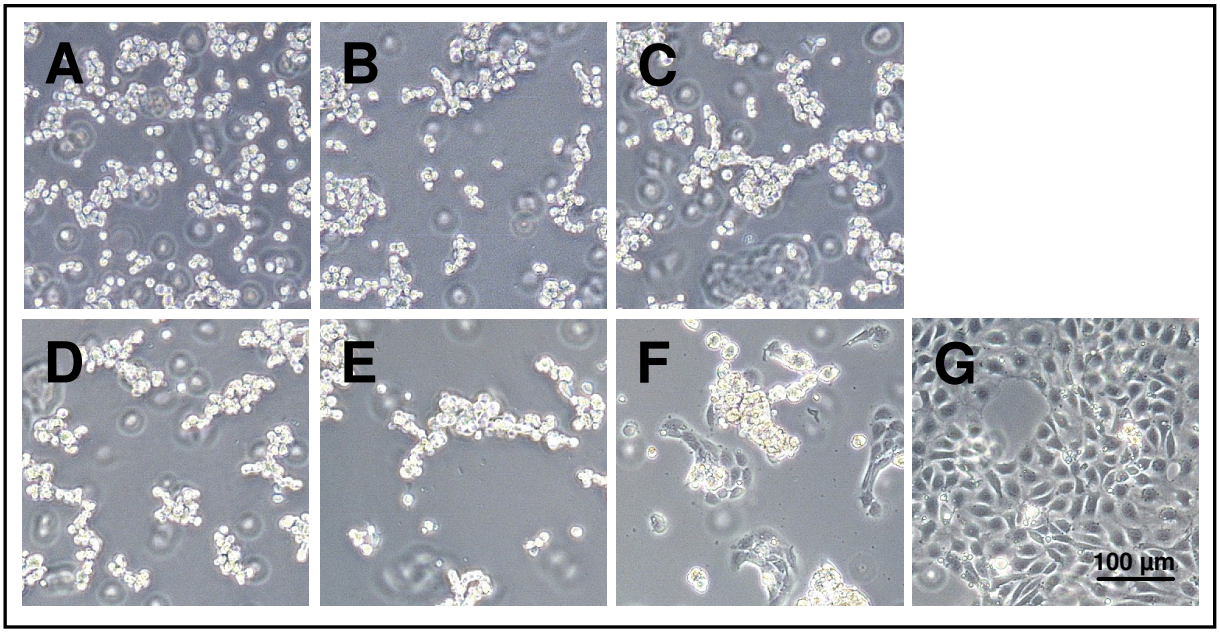

Fig. 4.71 Phase contrast micrographs of NRK cells at various time points after inoculation, documenting attachment and spreading upon unmodified PDMS coated coverslips. The cells were suspended in serum-containing medium with a cell density of 4.5 x 10^5 cm^{-2}. The pictures were taken **A** 2 h, **B** 4 h, **C** 6 h, **D** 8 h, **E** 10 h, **F** 24 h and **G** 48 h after cell inoculation.

By contrast, an unmodified PDMS surface interferes with cell adhesion even in early stages. During the initial 10 h after cell inoculation no adherent cells can be identified on the PDMS surface (Fig. 4.71 A – E). The cells are spherically shaped and are floating in the culture medium. With proceeding incubation time, the initially isolated cells form big aggregates of non adherent cells. After 24 h, a few cells have attached and spread upon the surface, forming small cell islets (Fig. 4.71 F). The predominant fraction of the cells remains spherically shaped in suspension. The image acquired 48 h after cell inoculation presents a PDMS surface which is almost entirely covered with cells. The cell morphology is quite untypical, presenting rather big and elongated cells of irregular size (Fig. 4.71 G).

4.4.6 Cytocompatibility Testing of Photopolymer Surfaces

The QCM response to the attachment and spreading of initially suspended MDCK-II and NRK cells upon differently pre-treated PhoP is presented in Fig. 4.72 and Fig. 4.75. PhoP was

applied in its unmodified and its plasma modified form followed by an additional incubation in either PBS^{--} or SFM. The QCM data were further supported by a microscopic study.

Attachment and Spreading of MDCK-II Cells

Figure 4.72 shows the results of the experiments, in which initially suspended MDCK-II cells were seeded upon PhoP coated quartz resonators which were either left unmodified or treated by an argon plasma for 1 min. Both surfaces were exposed to PBS^{--} or SFM for 20 h at 37 °C prior to cell inoculation.

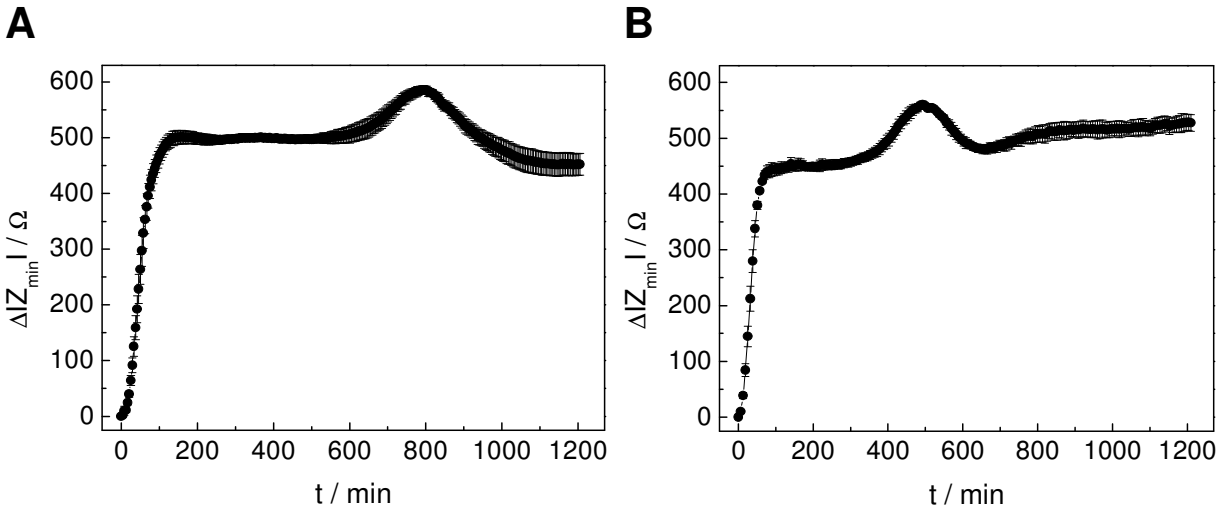

Fig. 4.72 Time course of $\Delta|Z_{min}|$ after seeding equal amounts of initially suspended MDCK-II cells on a PhoP coated quartz resonator at time point zero. The cell density was adjusted to 4.5 x 10^5 cm^{-2}. The PhoP coated resonator had been pre-treated as follows: **A** Incubation with SFM for 20 h at 37 °C, **B** argon plasma treatment for 1 min followed by a SFM incubation for 20 h at 37 °C. The value of $|Z_{min}|$ at the beginning of the experiment was set to zero. (Mean ± SDM, n ≥ 2; T = 37 °C).

Since the cellular response does not differ with respect to which physiological fluid, PBS^{--} or SFM, was used to pre-incubate the polymer with, Fig. 4.72 A presents the time course of $\Delta|Z_{min}|$ for SFM pre-incubation – the series of experiments for PBS^{--} pre-incubation is summarized in the appendix E (Fig. E.5 A). MDCK-II cells which are seeded at time point zero on a PhoP coated quartz resonator that has been pre-incubated with either PBS^{--} or SFM for 20 h at 37 °C give rise to an instantaneous increase of $\Delta|Z_{min}|$ with a slope of (6.89 ± 0.20) Ω/min (Fig. 4.72 A). This steep increase is followed by a transient plateau phase of (498.4 ± 0.2) Ω within 140 min after cell inoculation. After 560 min $\Delta|Z_{min}|$ continues to increase to a second transient maximum of (587 ± 8) Ω at (793 ± 6) min after cell inoculation. The $\Delta|Z_{min}|$ values finally stabilize at the level of (450 ± 19) Ω. $\tau_{1/2}$ for MDCK-II cell attachment and spreading is determined to be (49 ± 3) min.

The time course of $\Delta|Z_{min}|$ recorded for a plasma modified, SFM pre-incubated surface (Fig. 4.72 B) is characterized by an immediate rise directly after seeding of the cells to (450.9 ± 0.6) Ω within 102 min. The curve shows an initial slope of (7.87 ± 0.07) Ω/min. After roughly 300 min, the values increase again in a rather moderate manner, peaking at a

transient maximum of (561 ± 6) Ω within (496 ± 3) min after cell inoculation. Subsequently, $\Delta|Z_{min}|$ decreases by approximately 33 Ω within 160 min. The $\tau_{1/2}$ value for MDCK-II cell attachment and spreading on this plasma modified, SFM pre-incubated PhoP surface is determined to $\tau_{1/2}$ = (34 ± 2) min.

Table 4.22 summarizes the kinetic parameters for the attachment and spreading of MDCK-II cells upon spin coated PhoP.

Tab. 4.22 Summary of parameters used to characterize of the adhesion kinetics of MDCK-II cells on PhoP. The slope *m* of the attachment curve till it reaches the first plateau phase expresses the spreading rate and $\tau_{1/2}$ the time to reach half-maximal $\Delta|Z_{min}|$. τ_2 is the time that is needed to reach the second maximum. (Mean ± SDM, n ≥ 2; *T* = 37 °C).

Kinetic Parameter	No Plasma, PBS^{--}/SFM	Plasma, SFM
m [Ω/min]	6.89 ± 0.20	7.87 ± 0.07
$\tau_{1/2}$ [min]	49 ± 3	34 ± 2
τ_2 [min]	793 ± 6	496 ± 3

The following phase contrast micrographs visualize the adhesion kinetics of MDCK-II cells on the above mentioned PhoP surfaces during an observation period of 48 h (Fig. 4.73 and 4.74).

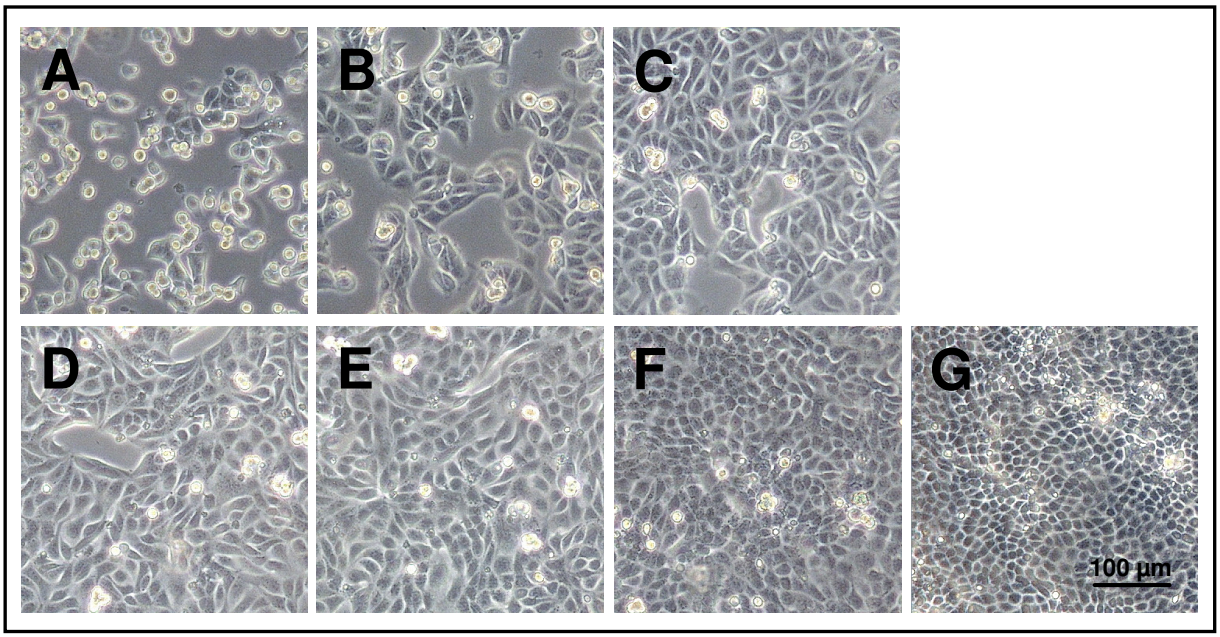

Fig. 4.73 Phase contrast micrographs of MDCK-II cells at various time points after inoculation, documenting attachment and spreading upon PhoP coated coverslips that were exposed to SFM for 20 h at 37 °C prior to cell inoculation. The cells were suspended in serum-containing medium with a cell density of 4.5 x 10^5 cm^{-2}. The pictures were taken **A** 2 h, **B** 4 h, **C** 6 h, **D** 8 h, **E** 10 h, **F** 24 h and **G** 48 h after cell inoculation.

The attachment and spreading behavior of MDCK-II cells upon fluid pre-incubated PhoP is similar for both physiological buffers, PBS^{--} and SFM, used to pre-incubate the PhoP surface. Thus, Fig. 4.73 presents the adhesion process upon SFM pre-incubated PhoP whereas the PBS^{--} incubated one is included in the appendix D 4 (Fig. D.14). Already 2 h after cell inoculation, a major fraction of the cells has spread upon the surface (Fig. 4.73 A). After 8 – 10 h, the surface is almost completely covered with cells, leaving only small regions uncovered (Fig. 4.73 D, E). The micrograph of the cell layer taken 24 h and 48 h after cell inoculation reveals a confluent cell monolayer consisting of MDCK-II cells of uniform size and shape, which exhibit their typical cobblestone morphology (Fig. 4.73 F, G).

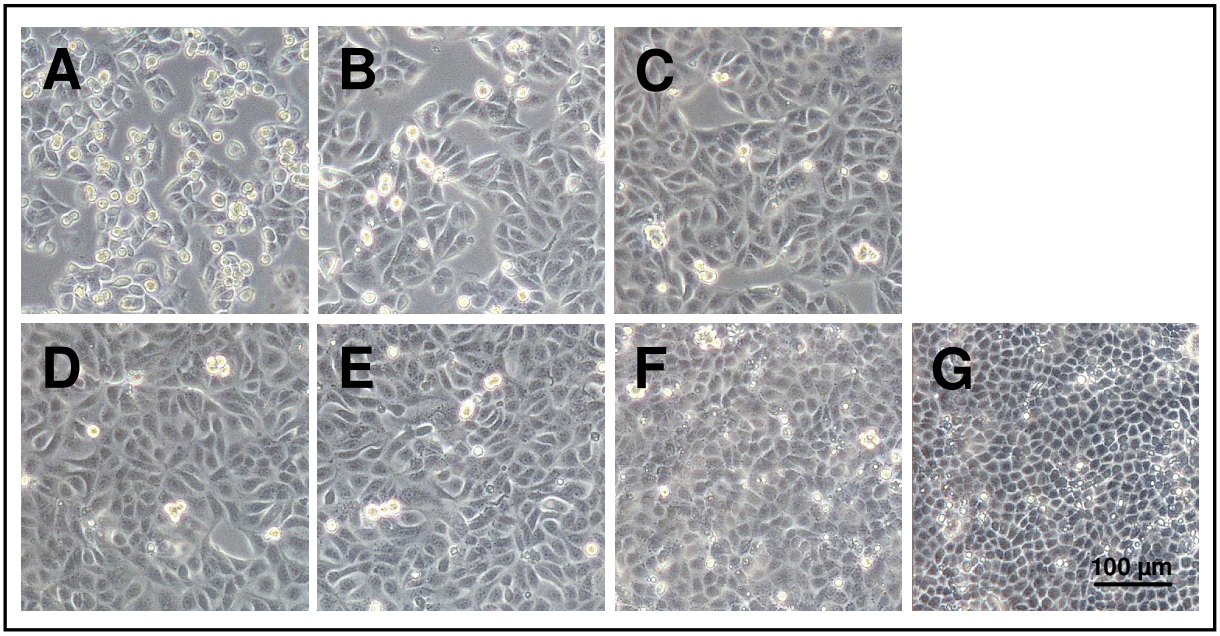

Fig. 4.74 Phase contrast micrographs of MDCK-II cells at various time points after inoculation, documenting attachment and spreading upon PhoP coated coverslips that were argon plasma modified for 1 min followed by an exposure to SFM for 20 h at 37 °C prior to cell inoculation. The cells were suspended in serum-containing medium with a cell density of 4.5×10^5 cm^{-2}. The pictures were taken **A** 2 h, **B** 4 h, **C** 6 h, **D** 8 h, **E** 10 h, **F** 24 h and **G** 48 h after cell inoculation.

The adhesion kinetics on plasma modified, SFM pre-incubated PhoP (Fig. 4.74) is similar to the adhesion kinetics on an only fluid pre-incubated surface. The cells cover the whole surface 8 – 10 h after seeding and exhibit their typical morphology (Fig. 4.74 D – G).

Attachment and Spreading of NRK Cells

Attachment and spreading of NRK cells was studied on PhoP coated quartz resonators that were exposed to either PBS^{--} or SFM for 20 h at 37 °C prior to cell inoculation. None of the other processing conditions was addressed for technical reasons.

Since the time course of $\Delta|Z_{min}|$ for NRK cells seeded upon PhoP surfaces either pre-incubated with PBS^{--} or SFM are almost identical, only one condition is shown in Fig. 4.75 while the remaining one (PBS^{--}) is included in the appendix E (Fig. E.5 B). Immediately after

cell seeding on SFM pre-incubated PhoP, $\Delta|Z_{min}|$ increases and reaches a temporary constant value of (445 ± 0.4) Ω after approximately 460 min. During the remaining observation period, $\Delta|Z_{min}|$ continues to increase to a maximal value of (480 ± 20) Ω. The initial slope of the attachment curve is calculated to (4.06 ± 0.04) Ω/min and the time of half-maximal surface coverage $\tau_{1/2}$ is (58 ± 1) min.

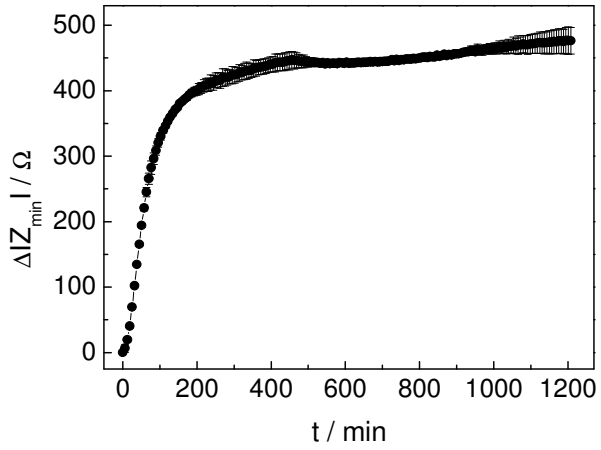

Fig. 4.75 Time course of $\Delta|Z_{min}|$ after seeding initially suspended NRK cells on a PhoP coated quartz resonator at time point zero. The cell density was adjusted to 4.5 x 10^5 cm^{-2}. The PhoP coated resonator was incubated with SFM for 20 h at 37 °C before cell inoculation. The value of $|Z_{min}|$ at the beginning of the experiment was set to zero. (Mean ± SDM, n = 3; T = 37 °C).

The following phase contrast micrographs (Fig. 4.76) were taken at regular time intervals after the inoculation of NRK cells upon SFM pre-incubated PhoP. Since the adhesion kinetics are similar on a SFM and a PBS^{--} pre-incubated PhoP surface, the images for the latter one are only presented in the appendix D 4 (Fig. D.18).

Following NRK cell attachment and spreading during the initial hours after cell inoculation reveals that already after 2 h, a fraction of cells has spread upon the surface, whereas some cells are still spherically shaped and in suspension (Fig. 4.76 A). After 4 h of incubation, the surface is covered with cells by roughly 70 % (Fig. 4.76 B). The cells show a confluent monolayer 8 – 10 h after cell inoculation. Whereas the morphology of the NRK cells is uniform in size and shape after 24 h, the image acquired after 48 h reveals cells that appear rather irregular in size and shape (Fig. 4.76 F, G).

Documentation of the attachment and spreading behavior of NRK cells upon the remaining conditions not shown here since they were not studied by the QCM technique can be found in the appendix D 4 (D.19 – D.22).

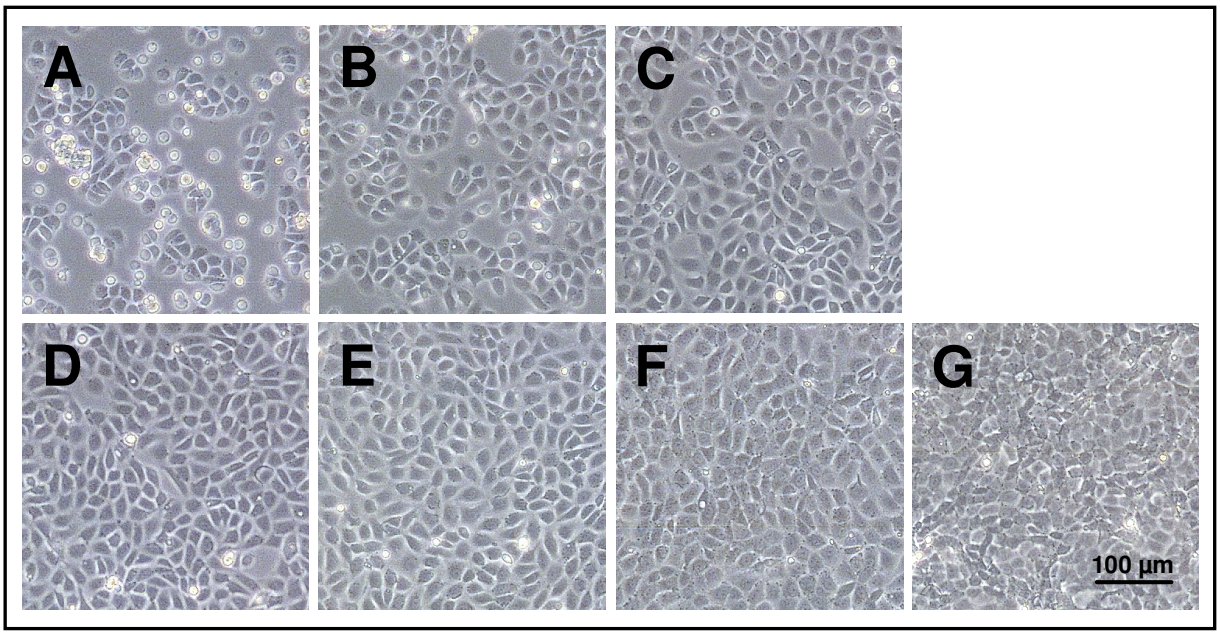

Fig. 4.76 Phase contrast micrographs of NRK cells at various time points after inoculation, documenting attachment and spreading upon PhoP coated coverslips that were exposed to SFM for 20 h at 37 °C prior to cell inoculation. The cells were suspended in serum-containing medium with a cell density of 4.5 x 10^5 cm^{-2}. The pictures were taken **A** 2 h, **B** 4 h, **C** 6 h, **D** 8 h, **E** 10 h, **F** 24 h and **G** 48 h after cell inoculation.

4.5 Discussion

QCM measurements are used to follow a multitude of biological adsorption processes to a quartz surface or surface-decorating entities. During the last two decades, the QCM has become a valuable analytical tool to monitor the mechanical interactions between mammalian cells and their growth substrate *in vitro*. With shear wave resonators used as growth substrates, it is possible to follow the *de novo* formation of cell substrate-contacts, as in cell attachment and spreading, or the modulation of established cell-substrate contacts under the influence of biological, chemical or physical stimuli from readings of the characteristic shear wave parameters non-invasively and in real time (Wegener et al., 2001).
The formation, modulation and strength of cell-substrate contacts are important in many areas of the life sciences. In the development and optimization of biomaterials, the interactions between the material surface and mammalian cells are a highly important indicator of the cytocompatibility of a material brought in contact with a biological system. In order to ensure that a material of interest exhibits the desired long-term biocompatibility, it is indispensable to get a detailed and validated understanding of the interactions between a material surface and the components of a biological system.

Taking this into account, one aim of this thesis was to develop and evaluate a biosensor based on the QCM technique that is capable of analyzing the biocompatibility of different polymer surfaces with respect to their molecular and cellular interactions with a biological system in quantitative terms. Thus, model thin films of different polymers were deposited on the resonator surface and investigated regarding their long-term stability in a physiological fluid, protein adsorption as well as cell attachment and spreading. Various experimental approaches to selectively modify the polymer surface were studied in detail, such as an argon plasma treatment and/or pre-incubation in a physiological fluid. The QCM measurements were accompanied by some general physicochemical characterizations of the polymer surface as well as a microscopic study of cell adhesion upon the polymers, providing a detailed correlation with the QCM data and, thus, a validation of the polymer coated sensor system. The technical polymers used in this comprehensive biocompatibility study were the polymers PS, PMMA, PDMS and PhoP.

4.5.1 Physicochemical Surface Characterization of Spin Coated Polymer Films

The preparation and characterization of polymer films was of paramount importance to ensure a reproducible polymer surface free of defects, like areas of incomplete coverage, pin holes or cracks. The challenge in polymer film preparation was to produce a homogenous film that covered the entire sensor surface evenly. In parallel, this film should be both, rigid in nature and thin enough not to cause any significant acoustic losses as this would reduce the inherent sensitivity of the resonator for the subsequent cell adhesion studies. For the biocompatibility study of technical polymers using the QCM technique, thin films of the respective polymers were spin coated from organic solution on the surface of quartz resonators. In order to interpret subsequently recorded data of protein adsorption or cell adhesion upon these particular surfaces, a preceding physicochemical surface analysis of the deposited polymer films was a crucial requirement. Since interactions between the biological environment and the technical material take place on the outermost atomic layers (~ 1 nm) of the material's surface (Kasemo and Lausmaa, 1986), it is the chemical and physical surface properties which influence many biological reactions occurring in response to the material. These surface properties include chemical composition, wettability, charge, rigidity and topography.
Different surface-analytical techniques were applied to address polymer surface properties, characterizing the completeness of the surface coverage, the polymer film thickness as well as the polymer surface wettability.
In the following subchapters, the results of the physicochemical surface analysis of the different polymer films deposited on the resonator surface via spin coating are discussed.

Confirmation of the Completeness of Surface Coverage by ToF-SIMS

ToF-SIMS experiments should address two fundamental issues. The first main concern was to verify a complete surface coverage since areas of incomplete coverage could interfere with subsequent measurements or provide artificial data. If parts of the resonator surface are uncovered like in the case of pin holes or cracks in the polymer film, the secondary ion mass spectra recorded for the polymer samples should show a characteristic gold signal due to the exposed gold electrode of the quartz resonator. Such a signal could not be observed in any spectrum (chapter 4.1.1), confirming a complete coverage of the entire sensor surface with a polymer film free of any noticeable surface defects for all polymers under study.
The second main concern was to check for contaminations of the surface. As ToF-SIMS provides detailed atomic and molecular information about the chemical composition of the uppermost molecular monolayer of a material surface, it is capable of identifying possible surface contaminations which might interfere with the overall biocompatibility of the polymer surfaces. Typical contaminants would be mainly polysiloxanes and salts, the latter being represented by alkali cations such as sodium, potassium or lithium, which are often enriched at the polymer surface. A sample contamination can have various origins: it can arise during

the preparation and spin coating procedure or even during the subsequent drying or storage of the polymer films. For instance, siloxanes may originate from silicon oils used to lubricate the spin coater. Salts can be possibly contained in the organic solvent or can be introduced by impure film preparation conditions and poor sample handling. However, these assumptions could be excluded for all polymer films, since the ToF-SIMS spectra indicated no contaminants to be present on the polymer surface. The confirmation of a contaminant-free polymer surface is also important with respect to the surface modification obtained by an argon plasma treatment of the polymer films. The absence of surface contaminants provides experimental support that the wettability increase (hydrophilization) typically observed for argon plasma treated polymers does not result from simple cleaning of the polymer surface from adsorbates or weakly bound contaminant layers, but rather is a consequence of the introduction of oxygen functionalities into the polymer surface (France and Short, 1997 and 1998). Furthermore, the detected peaks in the secondary ion mass spectra did not only prove the absence of surface contaminants, they also represented the respective fragmentation pattern of the polymers, thereby confirming the expected chemical composition. This verified a proper film deposition procedure creating polymer films with the typical polymer characteristics.

In summary, the existence of a clean polymer surface with no surface defects or contaminations could be confirmed by ToF-SIMS measurements, ensuring a pure polymer surface for the following experiments using the polymer coated microgravimetric biosensor.

Determination of the Polymer Film Thickness by Vertical Scanning Interferometry (VSI)

VSI measurements were performed in order to determine the thickness of the spin coated polymer films. The film thickness is a crucial parameter, since the polymer films must be compatible with the sensor's functionality. In the case of very thick polymer films, the entire energy can not be transferred from the oscillating crystal to the outermost surface of the polymer, leading to a high loss of sensitivity and thus to an incomplete quantification of all further adsorption processes.

The VSI measurements returned very similar values for the thickness of PS, PMMA and PDMS films ranging between (40 ± 1) nm for PS, (19 ± 1) nm for PMMA and (30 ± 2) nm for PDMS, whereas the average PhoP film thickness was significantly higher ((2972 ± 11) nm) (chapter 4.1.2, Tab. 4.1). This difference may be caused by the polymer film preparation procedure itself. For PS, PMMA and PDMS film preparation, the organic polymer solutions used for spin coating were home-made with a defined polymer concentration of 1 % (w/v), whereas for PhoP film preparation, a commercially available PhoP solution was applied as purchased, which is a rather viscous fluid with a concentration of 10 – 30 % (w/v).

Film thickness measurements in the center and at the edge of the spin coated polymer films revealed a uniform film thickness (data not shown), independent of the radial distance from the center, where the solution was initially applied during the spin coating process. Thus,

local differences in sensitivity due to film thickness inhomogeneities from the center to the edge of the resonator can be excluded.
Since the VSI technique monitors the microscopic surface topography in 3D, it can provide additional information about surface roughness or possible discontinuities of the coating, like steps or cavities. All polymer films under study revealed a complete surface coating without any pin holes or other surface defects, in accordance with the results of the ToF-SIMS measurements. Except for PDMS, the polymer surfaces were rather smooth, exhibiting a surface roughness that ranged in the order of only a few – below ten – nanometers (chapter 4.1.2). In contrast, spin coated PDMS exhibited a rough and inhomogeneous surface topography, showing periodic undulations of approximately 30 nm in the film thickness (chapter 4.1.2, Fig. 4.12). These thickness inhomogeneities may only originate from the film preparation procedure, since the polymer *per se* is a homogeneous substance. As PDMS films were prepared *in situ* from two components, a base and a curing agent, it could possibly happen that the two components of the polymer, which were diluted in hexane to 1 % (w/v) for spin coating, were not completely and homogeneously dissolved in their solvent, leading to variations in the degree of interchain crosslinking. The observed inhomogeneities in the PDMS film thickness might also arise due to air bubbles which were included in the polymer solution, preventing the formation of a homogeneous surface coverage during spin coating and polymerization. However, as the resonator surface was completely covered with a polymer film (see ToF-SIMS measurements chapter 4.1.1, Fig. 4.5 and 4.6), the PDMS coated quartz resonators were used for the following protein adsorption and cell adhesion studies.

Quantification of the Polymer Thickness from QCM Readings

Impedance analysis of the shear oscillation of polymer coated quartz resonators was performed in air and compared to the unloaded resonator in order to quantify the amount of polymer deposited by spin coating on the sensor surface (chapter 4.1.3). Consistent with film thickness measurements of the spin coated polymer films, the amount of mass as deduced from QCM measurements in the passive mode was very similar for the polymers PS ((5.3 ± 2.7) µg), PMMA ((2.50 ± 0.45) µg) and PDMS ((4.17 ± 0.59) µg). As it could be already anticipated from the thickness data for PhoP, the mass of PhoP deposited on the sensor surface was significantly higher, accounting for (189.2 ± 1.8) µg.
The calculation of the polymer film thickness from the mass data of the deposited polymer films revealed a film thickness of (181 ± 92) nm for PS, (75 ± 14) nm for PMMA, (145 ± 20) nm for PDMS and (6199 ± 59) nm for PhoP. These QCM-based thickness values were 4 – 4.8 fold higher than the optical thickness values obtained from VSI measurements (chapter 4.1.2). This disagreement in the thickness data may partly be due to non appropriate assumptions which were made for the calculation of the polymer film thickness from QCM measurements. One assumption was that the density of the spin coated polymer film is regarded to be equal to the density of the original solid state polymer. An underestimation of the polymer film density after spin coating could account for the higher values for the

calculated thickness. However, a fivefold higher film density for the spin coated polymer films can not be assumed and further aspects need to be considered. A possible reason for the discrepancy between QCM-based and VSI-based thickness values might be attributed to the integral mass sensitivity S_I. $S_I = (0.62 \pm 0.01)$ H·cm^2/g as determined by Wegener (1998) for 5 MHz resonators was used for the calculation of the mass of the polymer deposited on the resonator surface. However, the author used a different measuring chamber for the calibration of the QCM, so that the integral mass sensitivity for the measuring chamber used in this study might be different. In order to clarify this issue, it would be necessary to determine S_I for the experimental setup used in this study.

Besides mass quantification and film thickness determination, the most important result demonstrated by the QCM measurements is that loading the resonator with the different polymer films only translated the recorded impedance and phase spectra along the frequency axis towards lower frequencies, while the internal structure of both spectra remained unchanged (chapter 4.1.3, Fig. 4.14 – 4.17). This indicated an increase only in the motional inductance L as it is observed when a resonator is loaded with a rigid and homogeneous mass layer. No viscoelastic energy losses were observed. Thus, the spin coated polymer films can be regarded as an ideal rigid and homogeneous mass coupled to the resonator surface which follows the resonator's oscillation synchronously and loss-free. This purely elastic behavior of the polymer films further confirms the absence of possibly entrapped solvent, which would cause energy dissipation. Consequently, the polymer coated biosensor fulfilled all prerequisites to be applicable for further adhesion studies.

Wettability of the Polymer Surface probed by Contact Angle Measurements

Surface wettability is regarded as one of the most important surface characteristics governing the response of a biological system to a technical material (Lee et al., 1998). The most common method for evaluating surface wettability are contact angle measurements, as performed in this thesis (chapter 4.1.4) in order to explain and understand the molecular and cellular responses to the polymer surfaces monitored by QCM measurements. Spin coated polymer films of PS, PMMA, PDMS and PhoP were subjected to different processing conditions and probed for their surface wettability by dynamic water contact angle measurements using the sessile drop method (chapter 3.3.3).

For the following analysis and evaluation of the surface wettability of the different polymer films, a theoretical consideration regarding two important parameters, the advancing contact angle and the contact angle hysteresis, deduced from dynamic contact angle measurements shall be given upfront:

i) The advancing contact angle θ_A was used to characterize the wettability of polymer surfaces. Since the expanding drop always wets a fresh surface, measurements of θ_A are the most reproducible way of measuring contact angles. Receding contact angles are regarded less reproducible, since they are measured on an already wetted surface, where swelling events could have taken place, and they are usually smaller than advancing angles.

ii) The second important parameter to characterize the polymer surfaces is the contact angle hysteresis $\Delta\theta$, which is the difference between the two values for the advancing θ_A and the receding θ_R contact angle. Thermodynamically, the advancing and receding contact angles should be equal. In real systems, they often differ due to deviations from the ideal behavior (de Gennes, 1985). The origin of this difference can be attributed to surface inhomogeneities – real surfaces do not exhibit perfect smoothness, rigidity or chemical homogeneity, thus they usually show a contact angle hysteresis different from zero (Jung and Bhushan, 2006; Extrand, 2003). Among these factors, none is capable of exerting a greater influence on apparent contact angles than roughness (Extrand, 2003). Even though there is no direct relation between the contact angle hysteresis and roughness, certain conclusions can be drawn. For a homogeneous surface, increasing roughness has been observed to lead to an increase in the contact angle hysteresis (Jung and Bhushan, 2006). By analyzing $\Delta\theta$, it is possible to obtain information on surface roughness but also chemical contaminations or chemical inhomogeneities (de Gennes, 1985).
One of the first theoretical treatments of rough surfaces was given by Wenzel (1936), who used thermodynamic arguments to modify the Young equation, introducing a roughness factor (σ) which relates the apparent (θ_i) to the true contact angle ($\theta_{i,0}$). When considering a rough solid surface with a typical size of roughness details smaller than the size of the droplet, and the droplet in contact with the rough surface does not form air pockets – a so-called homogeneous interface – the contact angle is given as

$$\cos\theta_i = \sigma \cos\theta_{i,0}\,, \tag{4.4}$$

where i = A for advancing angles, i = R for receding angles. θ_i is the contact angle for a rough surface and θ_0 the one for a smooth surface. σ is a roughness factor defined as the ratio between the actual solid/liquid area (A) and its projection on a flat plane (A_0),

$$\sigma = A / A_0 \geq 1. \tag{4.5}$$

This model as well as more elaborate models often do not accurately predict contact angles on rough surfaces. As the wetting behavior is generally determined by interaction at the gas/liquid/solid triple line and not only by the liquid/solid interfacial area, it is not surprising that this and other area based concepts have not always been successful (Jung and Bhushan, 2006). However, the rationale for the dependence of the contact angle on the roughness factor is the following: the model predicts that roughness enhances hydrophobicity as it increases the contact angle if θ_0 is greater than 90°. If θ_0 is less than 90°, then the contact angle for the rough surface will decrease with increasing roughness factor. This relation has also been experimentally confirmed by Jung and Bhushan (2006).

In this thesis, surface wettability of polymers was characterized by means of the advancing contact angle θ_A for a set of different surface modifications that were studied throughout all

further experiments. The change in the contact angle hysteresis $\Delta\theta$ was utilized for statements on surface roughness.

Polystyrene

Unmodified PS is strongly hydrophobic and exhibits an advancing contact angle of $(91.7 \pm 0.8)°$ and a low hysteresis of $(9.5 \pm 1.5)°$, which is in good agreement with the literature, where an advancing angle of 94° is reported for unmodified PS (Fredriksson et al., 1998). Van Oss et al. (1988) as well as Owens and Wendt (1969) obtained a water contact angle of 91° measured under static conditions.

Argon plasma treatment led to a significant increase in hydrophilicity, which is indicated by a substantial decrease of the advancing contact angle for the plasma treated PS surface to $(25.4 \pm 1.7)°$. Thus, argon plasma treatment of PS has been shown to be similarly applicable as UV light exposure to generate a hydrophilic PS surface. Fredriksson et al. (1998) obtained an advancing contact angle of 29° for a PS sample that had been subjected to UV light. The increase in surface hydrophilicity of PS upon argon plasma treatment can be explained by the introduction of new oxygen-based functionalities on the polymer surface, as determined by France and Short (1997 and 1998) from XPS (X-ray photoelectron spectroscopy) measurements of argon plasma treated samples of PS and other polymers. The introduction of oxygen is thought to occur mainly by the reaction of surface free radicals created during plasma exposure with atmospheric oxygen when the sample is exposed to air (chapter 1.4.5). Besides the increase in surface wettability, the contact angle hysteresis slightly increased by 9.6°, indicating a minor increase in surface roughness induced by the plasma treatment.

Incubation of the PS film with a physiological fluid had a different influence on these parameters, depending on a preceding argon plasma treatment. Fluid incubation of an unmodified PS sample had no significant impact on the advancing contact angle, but influenced the contact angle hysteresis. Whereas an unmodified PS film exhibits a hysteresis of $\Delta\theta = (9.5 \pm 1.5)°$, a PS film pre-incubated in PBS^{--} shows a contact angle hysteresis of $(27.8 \pm 2.2)°$, and SFM incubation resulted in an even more significant hysteresis increase ($\Delta\theta = (50.5 \pm 3.4)°$). A hypothesis for the observed behavior might be that fluid exposure leads to a reorganization of the polymer surface structure accompanied by an increase in surface roughness. PBS^{--} and SFM seem to have an individual impact on $\Delta\theta$ – however, the reason for this fluid-specific behavior of unmodified PS is still unclear. Besides possible changes in surface roughness, chemical inhomogeneities arising on the polymer surface due to an orientation of surface-near polymer chains in response to the fluid might also be a contributor to the increase in $\Delta\theta$. Furthermore, an individual and specific adsorption of ions from the two differently composed buffers might be possible as well.

In contrast, fluid incubation of plasma modified PS had neither an impact on the advancing contact angle nor on the contact angle hysteresis when compared to plasma modified PS without pre-incubation. θ_A for argon plasma modified as well as argon plasma modified pre-

incubated PS ranges between 24 – 28° and $\Delta\theta$ between 17 – 23°. Thus, surface wettability and surface roughness remained unchanged when plasma modified PS was exposed to a fluid.

Poly(methyl methacrylate)

Similar to unmodified PS, unmodified PMMA is hydrophobic with a typical advancing contact angle of (88.4 ± 0.6)° while the contact angle hysteresis is of (25.5 ± 1.1)° and thus bigger than for PS. Extrand and Kumagai (1995) determined a slightly lower advancing contact angle of (77.0 ± 1.1)° for PMMA but a similar contact angle hysteresis ((29.3 ± 2.3)°). In this special case, the relative big $\Delta\theta$ value is not an indication for a rough surface, since the authors could confirm a rather smooth PMMA surface via AFM measurements. Instead, the inherent chemical nature (chemical heterogeneity) of the PMMA surface was found to be responsible for this hysteresis (Extrand and Kumagai, 1995). Confirmed by VSI measurements (chapter 4.1.2), the PMMA surface studied in this thesis can be regarded a smooth surface as well.

Argon plasma treatment of PMMA resulted in a hydrophilization of the polymer surface, indicated by the decrease of θ_A to (59.7 ± 0.9)°. A similar θ_A value of 51.0° is reported by Chai et al. (2004) for an oxygen plasma treated PMMA surface. Comparing the advancing contact angles for plasma modified PS and plasma modified PMMA, it is obvious that the extent of surface hydrophilization is significantly smaller for PMMA than for PS. France and Short (1997) showed that oxygen incorporation into the polymer surface and thus the degree of surface hydrophilization induced by argon plasma treatment is polymer-specific. Thus, it might be concluded that the smaller surface hydrophilization of PMMA in comparison to PS is possibly related to the fact that plasma activation generates less free radicals on the PMMA surface, leading to a reduced incorporation of oxygen functionalities compared to PS. Another reason for the smaller wettability increase may be attributed to hydrophobic recovery, a phenomenon strongly observed for PDMS (chapter 1.4.5). It describes the thermodynamically driven rearrangements of the polymer chains, bringing new hydrophobic groups to the surface to lower the surface free energy, thus increasing the contact angle. Additionally, argon plasma treatment led to a ~ 14° increase of $\Delta\theta$ compared to an unmodified PMMA surface, which can be a result of an increase in surface roughness induced by minimal microetching of the argon plasma or chemical inhomogeneities within the polymer surface after oxygen incorporation.

SFM exposure of unmodified PMMA had only a minor impact on the advancing contact angle as well as the contact angle hysteresis. $\Delta\theta$ increased by about 8°, indicating a minimal rise in surface roughness or chemical inhomogeneity. In contrast, fluid incubation (PBS^{--} or SFM) of plasma modified PMMA resulted in an increase of θ_A by roughly 12 – 15° compared to a simply plasma modified PMMA surface, while the contact angle hysteresis remained unchanged. The decrease in surface wettability due to fluid exposure after an argon plasma treatment can not entirely be explained at this point. The reorientation of surface-near polymer chains might be a possible explanation; however, it is unclear why contact with polar fluids should support hydrophobic recovery.

Poly(dimethyl siloxane)

Unmodified PDMS is highly hydrophobic, exhibiting an advancing contact angle of $(121.6 \pm 0.9)°$, which agrees well with data previously reported by Gillmor et al. (2002), Thorslund et al. (2005) and Shahal et al. (2008). Here, contact angles of 112.9°, 115° and 116° were found. The contact angle hysteresis is quite high compared to the one for unmodified PS and PMMA, amounting to $\Delta\theta = (81.4 \pm 2.0)°$. This might indicate that the surface is significantly rougher than PS or PMMA, which is in accordance with the results obtained by VSI measurements, revealing a rough and inhomogeneous surface topography with periodic undulations of the film thickness (chapter 4.1.2, Fig. 4.12). Fluid incubation using either PBS^{--} or SFM had no significant impact on the surface wettability or the surface roughness. Advancing contact angles as well as the contact angle hysteresis remained unchanged compared to unmodified PDMS. This finding confirms the well-known inert character of PDMS, which should not be susceptible to swelling in hydrophilic fluids. Consistent with these results, Mata et al. (2005) showed that exposure of PDMS to water did not affect the surface wettability of PDMS. The static contact angles were $(113.5 \pm 2.0)°$ before and $(115.1 \pm 2.8)°$ after 30 min water exposure.

Argon plasma treatment of PDMS led to a small decrease of 11° for the advancing contact angle, indicating that an argon plasma treatment does not improve surface wettability significantly. However, the surface of PDMS can be rendered hydrophilic by plasma exposure, as demonstrated in various studies (Lai et al., (1996); Ginn and Steinbock, 2003). Ginn and Steinbock (2003) reported a significant reduction in the contact angle from $(112 \pm 2)°$ for unmodified PDMS to $(15 \pm 2)°$ directly after oxygen plasma treatment.

The moderate increase in surface wettability observed for PDMS after argon plasma treatment might be related to hydrophobic recovery, well-known for PDMS. It has been reported that plasma treated PDMS regains its hydrophobicity within less than one hour when left in contact with air (Morra et al., 1990; Lai et al., 1996; Sia and Whitesides, 2003). During hydrophobic recovery, thermodynamically driven rearrangement processes take place: hydrophilic groups generated at the polymer surface are supposed to reorient away from the surface into the bulk of the polymer. Additionally, unpolar low-molecular-weight polymer chains generated in the sub-surface during plasma exposure or preexisting in the bulk polymer diffuse to the surface (Hillborg et al., 2000; Kim et al., 2000 and 2001; Fritz and Owen, 1995). Since the time between the argon plasma treatment of the sample and the contact angle measurements ranged in the order of at least one hour, the small wettability and thus the high value of the advancing contact angle might originate from hydrophobic recovery after argon plasma treatment.

However, the contact angle hysteresis decreased substantially after argon plasma treatment compared to unmodified PDMS, accounting for $\Delta\theta = (29.4 \pm 3.5)°$. The decrease by 52° might indicate that the surface roughness was reduced to a great extent by the argon plasma treatment. This observation is in accordance with the results of Vasilets et al. (2006), who reported a significant, threefold decrease in the average surface roughness of PDMS during

the exposure to UV light under ambient conditions and under vacuum. The authors attributed the decrease in roughness to the creation of additional crosslinks in the polymer surface.

Photopolymer

PhoP exhibits a hydrophobic surface in its unmodified form, as indicated by an advancing contact angle of (92.5 ± 0.8)°. The contact angle hysteresis amounts to (57.0 ± 1.4)°, and could either indicate a rough surface or might be attributed to an inherent chemical heterogeneity of the polymer, as in the case of PMMA. However, neither of the assumptions could be fully supported, since this type of polymer was not addressed by other groups in the literature and the VSI measurements did not provide information on nanometer surface roughness since the PhoP film thickness was in the order of several micrometers (~ 3 µm) (chapter 4.1.2, Fig. 4.13). Incubation in a physiological fluid significantly decreased the advancing contact angle by 19° for PBS^{--} and 13° for SFM exposure. The contact angle hysteresis slightly increased by 10 – 13°. These results indicate that both fluids led to an increase in surface wettability as well as in surface roughness, which might be due to polymer swelling and conformational rearrangements of surface-near polymer chains in response to the fluid.
Argon plasma treatment of PhoP caused a significant surface hydrophilization due to the incorporation of oxygen functionalities into the polymer surface to a similar extent as observed for PS – the advancing contact angle decreased to (35.8 ± 1.7)°. The contact angle hysteresis decreased by roughly 27° compared to an unmodified PhoP surface and amounts to (30.5 ± 2.2)°. In addition to surface hydrophilization, argon plasma treatment possibly caused a smoother surface, similar to the results obtained for argon plasma treated PDMS.
Fluid incubation (PBS^{--} or SFM) of a plasma modified PhoP film did neither influence the surface hydrophilicity nor the surface roughness, as evident from the unchanged advancing contact angle as well as the contact angle hysteresis.

In summary, all applied polymers are strongly hydrophobic in their native, unmodified state. Hydrophobic polymers present a poor wettability for aqueous solutions, enhance unspecific protein adsorption and limit cell attachment and spreading. An argon plasma treatment is known to increase the surface wettability of various polymers by introducing oxygen-based functionalities into the polymer surface (France and Short, 1997 and 1998). This argon plasma-induced surface modification could be verified with contact angle measurements for the polymer samples under study. The degree of surface hydrophilization was polymer-specific and in the case of PDMS completely masked by hydrophobic recovery. Incubation of unmodified polymers in a physiological fluid had a polymer-specific impact on the contact angle hysteresis, which might be mainly attributed to an increase in surface roughness or chemical inhomogeneities occurring in the polymer film due to conformational rearrangements of surface-near polymer chains in response to the fluid. Only PhoP showed a significant increase in surface wettability upon fluid incubation, which might be an indication

for water uptake and thus for polymer swelling. The incubation of the plasma modified polymers in a physiological fluid had no significant impact on surface wettability or surface roughness. Only PMMA behaves differently, since fluid incubation of plasma modified PMMA led to a decrease in surface wettability while the surface roughness remained unchanged.
In order to clarify whether the changes in contact angle hysteresis observed for the polymers upon fluid incubation or argon plasma treatment are due to changes in polymer surface roughness, additional AFM measurements could help to confirm the polymer surface structure (topography).
These polymer-specific contact angle data as well as their change upon an argon plasma treatment and/or fluid incubation of the polymer films will be of special interest when interpreting protein adsorption and cell adhesion to the polymer surfaces later in the text.

The physicochemical surface characterization of spin coated polymer films has shown that the spin coating technique is well-suited to obtain a complete surface coverage of the quartz resonator in a designated thickness. These spin coated polymer films show purely elastic behavior, following the resonator's oscillation synchronously and loss-free. Except for PDMS, they exhibit a relative smooth and homogeneous surface with hardly any surface irregularities and are hydrophobic in their native state. Surface modifications using an argon plasma treatment or exposure to a physiological fluid are capable of changing surface wettability and surface roughness in a polymer-type specific manner.

4.5.2 Long-Term Stability of Polymer Films in a Physiological Fluid

One aspect of the biocompatibility analysis of spin coated polymer films addresses their long-term stability in a physiological fluid. Technical materials that are exposed to a biological system inevitably encounter physiological fluids. Since swelling in a liquid environment is a well-known phenomenon for many polymers (Chen and Shull, 1999; Ruzzu and Matthis, 2002; Welle, 2004) and can influence the biocompatibility or biofunctionality of these materials significantly, the four polymers under study were exposed to two different physiological fluids, PBS^{--} and SFM, at 37 °C over a time span of 20 h. During exposure their long-term stability was probed by the QCM technique in double mode analysis (chapter 4.2). Monitoring the behavior of the polymers upon fluid exposure does not only provide information about the long-term stability of the spin coated films, it also helps to separate swelling-induced changes of the QCM shear wave parameters from changes caused by cell attachment and spreading. PDMS and PhoP were only investigated in their unmodified form, whereas PS and PMMA were additionally studied in their argon plasma modified form.
The data recorded in quartz mode were analyzed in terms of changes of the load resistance ΔR_L and the load reactance ΔX_L upon fluid exposure. Changes in the mass of the polymer are

directly related to ΔX_L, while ΔR_L reports on viscoelastic loss due to the deposited polymer film. A complex viscoelastic behavior of the polymer would affect both ΔX_L and ΔR_L. The normalized electrochemical capacitance C_{norm} (40 kHz) of the resonator's electrode deduced from ECIS mode measurements provides information about the stability of the polymer film during fluid incubation. In the following, the results obtained for each polymer film spin coated on top of a quartz resonator are shortly summarized (see chapter 4.2 for more details) and discussed in a comparative manner, especially with respect to a possible correlation with the contact angle data.

Polystyrene

Upon fluid exposure of either unmodified or plasma modified PS films, the load resistance ΔR_L decreased within 200 – 300 min to a stationary value. The decrease of ΔR_L showed only minor variations for the different processing conditions, revealing values between $-(41.2\pm 0.5)\,\Omega$ and $-(60.1 \pm 1.4)\,\Omega$ (chapter 4.2.1, Tab. 4.7). Fluid exposure had no significant impact on the load reactance ΔX_L. The capacitance C_{norm} (40 kHz) of the PS coated electrode revealed mainly transient alterations upon fluid incubation (chapter 4.2.1, Fig. 4.26). Although the time courses varied for the different processing conditions, the individual capacitances determined after the incubation period were quite similar and did not significantly differ from the starting values.

Poly(methyl methacrylate)

Similar to the data recorded for PS upon fluid incubation, ΔR_L of the PMMA coated resonator decreased within about 200 min to a stationary value between $-(33.4\pm 0.4)\,\Omega$ and $-(49.3 \pm 0.4)\,\Omega$, thus showing only minor variations of this parameter for the different processing conditions (chapter 4.2.2, Tab. 4.9). Fluid exposure to spin coated PMMA had no measurable impact on ΔX_L. The ECIS mode impedance analysis revealed only minor differences in the courses of the electrode capacitance, depending on the polymer's wettability and the physiological fluid it had been exposed to. The capacitance increase during the incubation time of 20 h ranged in the order between 2 % and 6 % for the different processing conditions (chapter 4.2.2, Fig. 4.28).

Poly(dimethyl siloxane)

The QCM results for the long-term stability of PDMS, which was only tested in its unmodified form in SFM, revealed a decrease of ΔR_L of roughly $-(42 \pm 1)\,\Omega$ within 200 min. No significant impact on ΔX_L could be detected (chapter 4.2.3, Fig. 4.29). C_{norm} (40 kHz) showed a final increase by a factor of 1.5 upon SFM incubation (chapter 4.2.3, Fig. 4.30).

Photopolymer

The long-term stability of PhoP in PBS^{--} or SFM was only probed for the unmodified polymer. ΔR_L decreased by $-(33.1 \pm 0.6)\,\Omega$ for PBS^{--} and $-(26.6 \pm 0.7)\,\Omega$ for SFM incubation within the first 120 min after fluid addition. However, there is a major difference to the other polymers under study: the load reactance was altered significantly for the PhoP coated resonator during fluid incubation independent of the applied fluid. PBS^{--} or SFM incubation of unmodified PhoP led to an increase in ΔX_L by $(199 \pm 6)\,\Omega$ (chapter 4.2.4, Fig. 4.31 B). The capacitance increase was similar for both fluids and showed a maximal increase of 9 % (chapter 4.2.4, Fig. 4.32).

In summary, a decrease in the load resistance ΔR_L could be observed for all polymers upon fluid incubation. This decrease ranged between $-27\,\Omega$ and $-60\,\Omega$ and was attained in a similar time interval after fluid exposure was started. Since the change in ΔR_L occurred for all polymers to a similar extent independent of a preceding plasma treatment or the nature of the applied fluid (PBS^{--}/SFM), it can be concluded that this phenomenon is a general and not an individual polymer response and thus independent of polymer surface chemistry or wettability.

The load resistance ΔR_L mirrors the energy that is dissipated in the system and is affected by changes in the viscoelastic properties, like density and/or viscosity of the polymer film. The uptake of fluid into the polymer film during swelling is thought to cause the material to change from the original ideal rigid to a more viscoelastic behavior, since the increasing water content changes the polymer's density and viscosity. Consequently, the polymer film – assumed to be a highly viscous load material after swelling – would no longer follow the oscillation of the resonator synchronously and loss-free but it would dissipate energy. Such a scenario predicts a significant increase in ΔR_L. However, a decrease in ΔR_L was observed for all four spin coated polymer films upon fluid exposure. A possible explanation for this decrease could be a modification of the polymer surface by the fluid during incubation. This surface modification can lead to an altered coupling of the fluid to the polymer film. Usually, a liquid load adsorbs with its first molecular layer tightly to the resonator surface – here, the polymer film which is rigidly coupled to the resonator surface – and moves synchronously with the oscillating surface, showing no slip behavior. In the case of polymer surface modification upon fluid exposure, the polymer surface/fluid interface may be altered in a manner that the "no slip" condition is not fulfilled anymore. This change in the polymer surface/fluid interface seems to be independent of the polymer surface chemistry, the surface wettability and the applied fluid, since ΔR_L changed to the same extent in a similar time interval for all polymers and processing conditions. Furthermore, there is also no dependence of the time course of ΔR_L decrease on the polymer film thickness. Spin coated PhoP, which exhibits a thickness that is two orders of magnitude higher than the thickness of the other polymers, revealed a similar ΔR_L decrease in a similar time interval during fluid exposure.

The independence of the ΔR_L decrease on the polymer film thickness emphasizes the assumption that a surface modification is responsible for the change in the load resistance.

The load reactance ΔX_L reflects the energy that is elastically stored in the system and can provide further hints with respect to polymer swelling. Generally, polymer swelling and thus water uptake by the polymer film should result in a mass increase and thus in an increase of ΔX_L. A significant increase in the load reactance upon fluid exposure was only observed for PhoP. Since ΔX_L is proportional to mass changes on the resonator surface, the increase of this parameter by roughly 200 Ω is a clear indication of fluid uptake in the PhoP film. The time course of ΔX_L is typical for a swelling isotherm (Schott, 1992). ΔX_L showed a steep initial increase and leveled off asymptotically to the equilibrium swelling limit (chapter 4.2.4, Fig. 4.31 B). Whereas the first steep increase of ΔX_L can be interpreted as diffusion-limited water uptake (swelling), the further moderate asymptotical increase may represent mechanical relaxations of the polymer chains in response to the swelling stress, which allows additional fluid to be incorporated into the polymer film. Water uptake by PhoP did only lead to an increase in ΔX_L while ΔR_L decreased by roughly 30 Ω presumably due to the reasons mentioned above. Since water uptake would be expected to cause also a significant increase in ΔR_L, the absence of this increase allows the assumption that water uptake into the PhoP film obviously does not alter the polymer's dissipative properties.
For the polymer films of PS, PMMA and PDMS, no significant change in ΔX_L was observed during fluid incubation. This indicates that the mass deposited on the resonator surface remained unchanged and excludes significant water uptake for these polymers.

The capacitance of the polymer coated gold electrode as deduced from ECIS mode measurements revealed only slight increases for all investigated polymers upon fluid exposure. First, this verifies that the spin coated polymer films are stable in a physiological fluid. No indication of polymer loss from the surface exists, which would otherwise cause a significant increase in the measured electrode capacitance. According to equation 4.3 (chapter 4.2), a decrease in polymer film thickness due to solvation of organic material would cause a significant increase in capacitance.
The relative small capacitance increase during fluid incubation might be interpreted as a slight decrease in film thickness. However, thinning of the polymer film during fluid exposure is unlikely, since the load reactance remained unchanged, indicating no mass loss. Another possible reason for this capacitance increase might be changes in the relative permittivity ε_r of the polymer during fluid incubation (Eq. 4.3). For the calculation of this parameter, the gold electrode of the quartz resonator and ions which assemble on the polymer surface from the bulk phase form the two conducting plates of the capacitor while the polymer film in between is regarded as the dielectric. Assuming a modification of the polymer surface upon fluid exposure, as it has been suggested above, changes at the polymer surface/fluid interface will occur and the assembly of ions from the bulk phase to the polymer surface will be altered. Consequently, changes in ε_r and thus in C_{norm} may be attributed to changes at the polymer surface/fluid interface. The assumption that fluid-induced modifications at the polymer

surface are the reason for the slight capacitance increase is further supported by the similar time courses of both quantities C_{norm} (40 kHz) and ΔR_L.

In summary, the polymers under study were long-term stable in a physiological fluid and did not dissolve. For all polymer films, fluid incubation changed the polymer surface/fluid interface and thus the coupling of the fluid to the polymer surface. This phenomenon seems to be a general one, since it was independent of polymer surface chemistry, wettability and the applied fluid. Additionally, only the PhoP film revealed a significant water uptake (swelling). This water uptake did not affect the elastic properties of the polymer film.

When comparing the results obtained from the double mode QCM measurements with the results obtained from contact angle measurements, one thing is obvious: PhoP, the only polymer which was shown to significantly swell in a physiological fluid in its unmodified state, is the only polymer which revealed a significant reduction of its advancing contact angle (θ_A) after fluid incubation. θ_A decreased by about 19° (PBS^{--}) or 13° (SFM), respectively. This decrease, accompanied by an increase in contact angle hysteresis by 10° (PBS^{--}) and 13° (SFM), agrees well with the uptake of fluid into the polymer film, leading to an increase in surface wettability as well as an increase in surface roughness. According to this, the swelling effect of unmodified PhoP is mirrored in the increase of the load reactance ΔX_L as well as in the decrease of the advancing contact angle θ_A. The decrease of both, advancing and receding contact angles as observed for PhoP (chapter 4.1.4, Tab. 4.6) is typical for swelling of a polymer surface. Sedev et al. (1996) studied the modification of a fluoropolymer during its contact with organic solvents via dynamic contact angle measurements and observed a decrease in both advancing and receding contact angles with the time of fluid contact, which was interpreted as the result of polymer swelling. The observed increase in contact angle hysteresis was thought to be due to loosening of the polymer chains during swelling.
A mechanistic hypothesis for the molecular rearrangements during PhoP swelling might be that the water molecules penetrate between the polymer chains, weakening their interaction and allowing some hydroxyl groups of the novolak resin, having higher tendencies than their methyl groups, to become exposed to the liquid. At the same time, the penetrating fluid increases the interchain distances and the surface pores or cavities filled by the liquid become larger. This reorientation of PhoP hydroxyl groups from the bulk polymer to the polymer surface would manifest itself as a decrease of the advancing contact angle, thus causing a better wettability.
The polymers PS, PMMA and PDMS showed no mass change and thus fluid uptake during fluid exposure in QCM measurements. This fits to the observations that no significant changes in the advancing contact angles upon fluid incubation could be observed for unmodified and plasma modified polymers. The only exception is plasma modified PMMA, showing an increase in θ_A by 12 – 15°, which can not be explained at the moment.

All polymers revealed a slight decrease in the load resistance which was attributed to molecular rearrangements at the polymer surface/fluid interface. This surface modification is possibly mirrored in the increased contact angle hysteresis observed for unmodified polymers of PS, PMMA and PhoP after fluid incubation. However, the ΔR_L values are not correlated to the $\Delta\theta$ values as for PDMS no increase in $\Delta\theta$ was observed despite the observed decrease in ΔR_L. To plasma modified polymers, this correlation does not seem to apply either: although ΔR_L decreased upon fluid exposure, the contact angle hysteresis remained unaffected. This might be due to the fact that contact angle measurements are possibly not sensitive enough on hydrophilic surfaces.

QCM measurements performed in the double mode have shown that the sensor system is sensitive enough to quantify the swelling of polymer films and to differentiate between fluid-induced swelling (water uptake) and fluid-induced modifications of the polymer surface, which affects the coupling of the fluid to the surface (surface roughness).

4.5.3 Protein Adsorption upon Polymer Surfaces

It was another important aspect of the QCM-based biocompatibility sensor to quantify protein adsorption upon the polymer surfaces. Knowledge about protein adsorption from aqueous solutions upon technical surfaces is of great relevance when determining a material's biocompatibility, especially with respect to an interpretation of subsequent cell adhesion. It has to be remembered that cells do not interact directly with the material surface, but specifically bind via cell-surface receptors, namely integrins, to specific peptide regions within adhesive proteins that have been pre-adsorbed to the substrate surface. These preadsorbed proteins originate in *in vitro* experiments either from serum-containing culture fluid or are synthesized and secreted by the cells themselves. Accordingly, protein adsorption is always the initial step of cell adhesion and the adsorbed proteins – their orientation, conformation and amount – determine the surface biocompatibility for the arriving cells, either allowing or avoiding cell attachment and spreading. Proteins do not only mediate cell attachment and spreading to the substrate surface, they also serve as signals that direct subsequent cellular responses, including proliferation and differentiation. Consequently, analysis of protein adsorption to various biomaterials is of major interest for the fundamental understanding of mechanisms controlling cell-surface interactions.

In this thesis, the adsorption of a range of proteins from aqueous solution upon different polymer surfaces was studied using the QCM technique operated in the active oscillator mode. The proteins in the focus of interest were different ECM-derived proteins such as Col G, Col IV and Lam I as well as the serum protein BSA, gelatin and proteins contained in newborn calf serum. Polymer films of PS, PMMA and PhoP, deposited by spin coating upon quartz resonators, were used with two different surface characteristics: a native hydrophobic

form and an argon plasma modified form (see chapter 4.3) PDMS was applied only in its unmodified, hydrophobic form. Before starting protein adsorption measurements, the polymer coated quartz resonators were equilibrated in DI-water (~ 1 h) in order to prevent polymer swelling to interfere with protein adsorption. The shift in resonance frequency Δf upon protein adsorption was plotted against the respective protein concentration in the bulk solution for each of the proteins under study. Data analysis was performed by fitting a Langmuir isotherm to the experimental Δf data, returning two adsorption parameters, $-\Delta f_{max}$ and $c_{50\%}$. Δf_{max} indicates the maximum frequency shift that is related to the amount of protein on the surface when the surface is saturated with the protein from solution. $c_{50\%}$ denotes the protein concentration in the bulk solution required for half-maximal surface coverage with protein and it mirrors the equilibrium of adsorbing and desorbing protein species. This parameter estimates the affinity of a protein to adsorb to a certain surface.

Before analyzing protein adsorption upon the different polymer substrates, a general introduction to protein adsorption is given. Theoretically, it is still a major challenge to understand the mechanisms behind protein adsorption to solid surfaces. It is a complex process involving van der Waals, hydrophobic and electrostatic interactions and hydrogen bonding. Proteins can adsorb in differing quantities, packing densities, conformations and orientations. Thus, protein-substrate interactions are quite diverse and depend on the properties of the protein, in particular its structural stability, as well as on the chemical and physical properties of the substrate surface. Regarding the role of substrate surface properties, both surface wettability and surface roughness have been shown to exert a significant influence on the adsorption of proteins, governing their quantity as well as their orientation and conformation on the surface (Taborelli et al., 1995; Denis et al., 2002). A general observation is that hydrophobic surfaces tend to bind more protein and they tend to bind it more strongly than hydrophilic surfaces. A soluble protein in an aqueous environment will adopt a conformation with its hydrophilic polar and charged amino acids generally pointing to the periphery of the protein molecule whereas the hydrophobic residues are buried in the interior, where they are shielded from contact with water.

For a hydrophilic surface, it is more likely that protein adsorption occurs through polar and ionic interactions. If this is the case, the hydrophilic amino acids on the surface of the protein molecule are readily available for interaction and no conformational changes are necessary for the adsorption on hydrophilic surfaces. Thus, protein conformation will be similar to that expected whilst in solution (Fig. 4.77 A). It has been suggested that proteins can adsorb to hydrophilic surfaces through the entrapment within bound water layer (Vogler, 1998). This leads to a relatively weak, reversible protein adsorption.

On a hydrophobic surface, proteins are thought to become irreversibly bound through dehydration of the interface and significant rearrangement of the protein conformation (conformational changes), leading to denaturation or unfolding of the protein: the hydrophobic regions of the protein core are exposed to the substrate surface to allow for interaction with the hydrophobic surface (Haynes and Norde, 1995) and the hydrophilic

regions are oriented towards the aqueous solution (Fig. 4.77 B). Dehydration of both the substrate and the protein surface provides an entropic driving force for the adsorption on hydrophobic surfaces. However, the degree of this conformational change is highly dependent on the balance between the strength of protein-surface interactions and the internal bonding strength holding the protein in its particular conformation (structural stability of the protein) (Roach et al., 2005). Protein structural changes occurring upon adsorption on hydrophobic surfaces may have a strong impact on cell adhesion, as specific recognition sequences within the proteins may not be accessible for the cell-surface receptors, leading to the loss of cell-adhesive properties of the proteins.

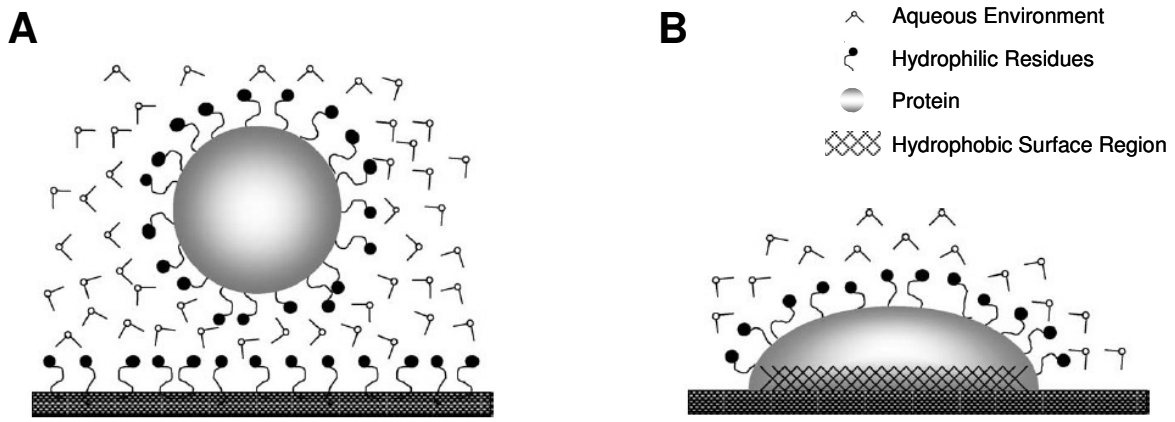

Fig. 4.77 Schematic representation of protein adsorption to a hydrophilic (**A**) and a hydrophobic (**B**) surface showing the distribution of polar functional groups (adapted from Browne et al., 2004).

Another factor known to play an important role in controlling protein adsorption characteristics is surface roughness (Denis et al., 2002). A rough surface can provide a greater surface area and thus more anchoring sites for the protein molecules compared to a smooth surface.

The following discussion concentrates on the comparison of the adsorption characteristics of the different proteins upon the unmodified and the plasma modified form of each polymer under study. In particular, the amount of protein and the affinity of the protein for a polymer substrate of a distinct wettability are compared. In this context, it has to be stressed that the interpretation of $-\Delta f_{max}$, as an indicator for the amount of protein adsorbed to the sensor surface, is difficult. Besides adsorbed protein mass, the entrapment of water in the protein layer as well as internal dissipative effects can have an impact on this parameter, leading to an increase in $-\Delta f_{max}$ as well. For the following considerations, the effect of entrapped water on the maximal frequency shift is disregarded and the decrease in frequency is assumed to be proportional to the adsorbed protein mass. The protein adsorption studies should give an experimental basis for a better understanding of cell attachment and spreading to polymer surfaces addressed later in the discussion.

Polystyrene

For most of the proteins under study, their adsorption to the unmodified as well as the plasma modified PS surface showed a Langmuir-type behavior. Only for Col G, adsorbing upon unmodified PS and for Lam I, adsorbing upon both forms of PS, no saturation behavior was obtained in the concentration range studied here, making a quantification using the Langmuir parameters impossible. It has to be mentioned that the highest concentration range for Lam I was set to 50 µg/mL whereas 100 µg/mL were used for all other protein studies.

The comparison of the absolute frequency shifts upon saturation, $-\Delta f_{max}$, obtained for the proteins under study revealed that the final amount of protein adsorbed to the PS surface is significantly higher on the unmodified than on the plasma modified surface (chapter 4.3, Tab. 4.13). This observation is in good agreement with previous studies that have generally found greater amounts of protein on hydrophobic surfaces than on hydrophilic surfaces (Sigal et al., 1998; Denis et al., 2002). The only exception is Col IV, with a higher amount of protein adsorbed upon the plasma modified surface. In this context it is noteworthy that most correlations between surface wettability and protein adsorption originate from model surfaces exhibiting a well-defined surface chemistry and are, thus, hard to transfer to real and complex polymer surfaces. Using the QCM technique, Browne et al. (2004) investigated human serum albumin (HSA) adsorption from solution upon unmodified and UV/ozone oxidized PS substrates with the same mean roughness (0.2 – 0.5 nm). The authors determined higher amounts of adsorbed HSA on unmodified than on oxidized PS surfaces. The AFM images revealed an 8 nm thicker protein layer with a "peak and ridge" topography on unmodified PS compared to the layer on oxidized PS, showing a "grainy" type structure. This indicated a substrate driven change in adsorption mechanism from hydrophobic to hydrophilic surfaces which was accompanied by a change in HSA conformation.

The affinity of the proteins for either of the wettable polymer forms does not follow a clear trend. A small $c_{50\%}$ value corresponds to a high binding affinity of the respective protein, since the equilibrium favors the adsorbed protein. Conversely, a high $c_{50\%}$ value represents a lower affinity for protein adsorption and the equilibrium favors the protein in solution. The proteins BSA and Col IV revealed a higher affinity for the plasma modified surface ($c_{50\%}$ (BSA) = (5.1 ± 1.0) µg/mL; $c_{50\%}$ (Col IV) = (45.3 ± 6.5) µg/mL) compared to the unmodified polymer ($c_{50\%}$ (BSA) = (47 ± 18) µg/mL; $c_{50\%}$ (Col IV) = (77 ± 15) µg/mL). Gel and the proteins contained in NCS exhibited a higher affinity for the hydrophobic PS surface (chapter 4.3, Tab. 4.13). The absence of a clear dependence of protein binding affinity on surface wettability may be surprising, especially when considering the advancing contact angles for the PS surface before argon plasma treatment ((92.1 ± 1.2)° after PBS^{--} incubation) and thereafter ((24.0 ± 2.3)°after PBS^{--} incubation), differing by 68° (chapter 4.1.4, Tab. 4.3). A possible reason for the lack of correlation between surface wettability and protein binding affinity can arise from surface roughness, which is another factor known to strongly influence protein adsorption (Denis et al., 2002). As indicated by the contact angle hysteresis measured for the unmodified and the plasma modified PS surface after fluid incubation, surface

roughness is in the measurable range and differs for the two wettable forms of PS. PBS^{--} incubation of unmodified PS led to a contact angle hysteresis of (27.8 ± 2.2)°, whereas PBS^{--} incubation of plasma modified PS induced a $\Delta\theta$ of (17.0 ± 5.2)° (chapter 4.1.4, Tab. 4.3). Thus, both surfaces do not exhibit the same surface roughness after fluid exposure and protein adsorption might be influenced by a combination of surface wettability and surface roughness. For example, the proteins Gel and NCS may not necessarily exhibit a higher binding affinity for the hydrophobic PS surface, but could also have a higher affinity for the rougher surface, which is the hydrophobic one in this case. Since both, surface wettability as well as surface roughness, which are known to profoundly influence protein adsorption, change, a clear correlation between surface wettability and protein adsorption might be masked. Experimental work by Denis et al. (2002) has revealed the influence of surface wettability and surface roughness separately in terms of both, adsorbed amount and supramolecular organization of Col I. The authors used model substrates with a controlled topography (smooth surface vs. nanoscale (~ 5 nm roughness) protrusions) and surface chemistry (CH_3- vs. OH-terminated self-assembled monolayers (SAMs)). In accordance with other studies, they determined much larger amounts of Col I on hydrophobic surfaces (θ = 109.5°) compared to hydrophilic ones (θ = 24°). For smooth substrates, the adsorbed films were thinner (~ 6 nm thick) and more homogeneous on hydrophilic surfaces compared to hydrophobic surfaces (~ 20 nm thick), that showed a protein layer with elongated suprastructural Col I aggregates. These aggregates were not observed on rough hydrophobic substrates, indicating that the supramolecular organization of adsorbed Col I was strongly affected by both surface wettability and surface roughness. However, the adsorbed amounts of Col I on smooth and rough substrates were similar.

Poly(methyl methacrylate)

Protein adsorption curves for PMMA showed a saturation behavior for all proteins under study, allowing for the quantification of the adsorption parameters using a Langmuir isotherm.

The maximal amount of protein adsorbed to PMMA in equilibrium was either similar (BSA, NCS) or significantly higher (Gel, Col G, Col IV, Lam I) for the plasma modified PMMA surface compared to the unmodified one (chapter 4.3, Tab. 4.14). These results do not fit to the more general rule that a higher amount of protein adsorbs upon hydrophobic surfaces. A further clarification of the results might be achieved when considering the contact angles for the two forms of PMMA – the unmodified and the plasma modified. Unmodified PMMA exhibits an advancing contact angle of 84° after fluid incubation whereas plasma modified PMMA shows an angle of (72.0 ± 0.8)°. This difference in the advancing contact angles is rather small and obviously further surface characteristics, such as surface roughness, might be responsible for the observed protein adsorption behavior. However, the contact angle hysteresis between the two wettable forms of PMMA differs only by 7° (chapter 4.1.4, Tab.

4.4), a rather small difference that makes a direct correlation between protein adsorption and surface roughness alone questionable.
The $c_{50\%}$ values were – with the exception of the protein Col G – significantly higher on plasma modified than on the unmodified PMMA surface (chapter 4.3, Tab. 4.14). Regarding the protein adsorption upon the plasma modified surface, the proteins BSA, Gel and Col IV exhibited similar $c_{50\%}$ values, ranging in the order of (33.0 ± 1.9) µg/mL and (37 ± 13) µg/mL, whereas the $c_{50\%}$ values for the proteins Col G and Lam I were with (60 ± 23) µg/mL and (67.2 ± 5.0) µg/mL roughly twice as high. Upon unmodified PMMA, the $c_{50\%}$ values varied more significantly, with the smallest value for the protein Gel ((4.2 ± 1.1) µg/mL) and the highest value for Col G ((125 ± 22) µg/mL. The significantly higher $c_{50\%}$ values obtained on plasma modified PMMA indicate a lower affinity of the proteins for this surface than for the unmodified surface.

Poly(dimethyl siloxane)

Protein adsorption upon PDMS was only studied for the unmodified polymer (chapter 4.3, Tab. 4.15). Thus, correlations between two forms of different surface wettability can not be made. Furthermore, studying protein adsorption on plasma modified PDMS would not have been promising, since contact angle measurements have revealed no significant change in the dynamic contact angles of PDMS upon argon plasma treatment (chapter 4.1.4, Tab. 4.5). Except for Col G, all proteins returned a Langmuir-type saturation curve for their adsorption upon PDMS. The $c_{50\%}$ values for Gel and Col IV were similar on PDMS ((22.1 ± 5.4) µg/mL and (27.5 ± 2.7) µg/mL), whereas for BSA, a significantly smaller value was obtained ((9.0 ± 2.4) µg/mL). PDMS is a strongly hydrophobic polymer with an advancing contact angle of (118.7 ± 1.0)° and a contact angle hysteresis of (86.2 ± 1.8)°. Correlations with protein adsorption to the other polymers which exhibit completely different surface properties are therefore difficult. Regarding the high contact angle hysteresis, surface roughness effects will certainly contribute to a great extent to protein adsorption.

Photopolymer

On both wettable forms of PhoP, adsorption of all proteins followed a Langmuir-type behavior in the investigated concentration range. Lam I was an exception as surface adsorption did not saturate for concentrations up to 50 µg/mL.
The maximal amount of adsorbed protein was almost similar for both wettable forms of PhoP. Simply the proteins contained in NCS exhibited a significantly higher mass on the plasma modified polymer. Regarding the affinity of the proteins for the two distinct surface wettabilities, the proteins Col IV and NCS did not discriminate between the two surfaces, whereas BSA showed a higher and Col G a lower affinity for the hydrophobic surface (chapter 4.3, Tab. 4.16). Thus, a general preference for protein adsorption upon a PhoP surface of a distinct wettability is not expressed in the data. As already observed for plasma modified PMMA, BSA and Col IV had similar $c_{50\%}$ values ((31.2 ± 5.3) µg/mL and

(30.3 ± 1.4) µg/mL) for the adsorption upon plasma modified PhoP, whereas $c_{50\%}$ for Col G adsorption was nearly twice as high. Upon unmodified PhoP, the $c_{50\%}$ values ranged between (10.10 ± 0.95) µg/mL and (28.9 ± 2.8) µg/mL for the proteins BSA, Gel and Col IV, whereas Col G showed the highest value for half-maximal surface coverage with $c_{50\%}$ = (336 ± 191) µg/mL. Considering the contact angle data for PhoP, the unmodified form and the plasma modified form vary significantly in their advancing contact angle ((73.4 ± 0.9)° unmodified + PBS^{--}; (39.5 ± 3.1)° plasma modified + PBS^{--}) as well as in their contact angle hysteresis, (66.7 ± 1.6)° and (33.0 ± 4.5)°, respectively (chapter 4.1.4, Tab. 4.6). Obviously, both surface properties, i.e. surface wettability and surface roughness, differ significantly for the two wettable forms of the polymer and seem to influence protein adsorption in a distinct way.

The proteins studied for their adsorption upon the different polymer surfaces reveal individual characteristics and some remarkable points of their adsorption behavior shall be addressed. In this context, it has to be remembered that the proteins Col G, Col IV and Lam I are known to self-assemble into supramolecular structures, which do not simply form monolayers but are anisotropic and may also grow in the third dimension.

As a general observation it turned out that the concentration range applied for Lam I adsorption studies was chosen to low to obtain a saturation curve upon the polymers PS and PhoP. Modeling Lam I adsorption upon PMMA using the Langmuir model provided high standard deviations of the mean, in particular on the plasma modified polymer, which indicates that the use of the Langmuir model is inappropriate. Lam I is a network-forming protein and assembles into suprastructural aggregates. If such an interaction between adsorbed protein molecules takes place, one essential assumption inherent in the classical Langmuir adsorption model is not fulfilled. In order to completely characterize Lam I upon the surfaces of PS and PhoP data for protein concentrations higher than 50 µg/mL would have to be collected.

It was another observation that a maximal concentration of 100 µg/mL does not saturate Col G adsorption upon unmodified surfaces of PS and PDMS. These two surfaces are the most hydrophobic ones, revealing advancing contact angles of (92.1 ± 1.2)° and (118.7 ± 1.0)°, respectively, after PBS^{--} incubation. Col G, which is a fibril-forming protein, will certainly interact with neighboring protein molecules in the adsorbed protein layer, a fact which is excluded in the assumptions within the Langmuir model. This interaction may not lead to a protein monolayer but more to a multilayer on the polymer surface, necessitating higher protein concentrations than the ones applied in this thesis to achieve saturation of the surface with Col G. On less hydrophobic surfaces of the unmodified polymers PMMA and PhoP with contact angles of 84° and (73.4 ± 0.9)°, a Langmuir isotherm could be fitted to the experimental Δf data, but the standard deviations of the mean were quite high, revealing that the Langmuir isotherm is not applicable to interpret the adsorption data. Additionally, the relatively high Δf and $c_{50\%}$ values compared to proteins of even higher size further underline the above proposed multilayer adsorption of Col G on hydrophobic polymer surfaces. Thus,

the analysis of Col G adsorption to hydrophobic polymer surfaces using the Langmuir model can only be a rough approximation, since there are interactions between the adsorbed protein molecules for which the Langmuir theory does not account.
The adsorption of Col IV, which is also a network-forming protein, could be described by the Langmuir model showing only small standard deviations of the mean. This indicates that the assumptions for the model are fulfilled and the adsorbed Col IV protein molecules either do not interact with each other on the polymer surfaces or the formation of a 2D network, in contrast to a fibril, does not interfere with the Langmuir model.

The difficulty to establish a unique correlation between surface wettability and protein adsorption for polymer surfaces has also been confirmed by various groups in the literature. Thus, model surfaces with well-controlled surface properties have often been used for protein adsorption studies instead of using real and complex polymer surfaces, reducing the complexity of real systems and allowing for better correlations between surface wettability and protein adsorption. A useful model system are self-assembled monolayers (SAMs) of functionalized alkanethiols on gold substrates. Using alkanethiols terminated with different functional end groups, the surface wettability can be tailored without altering other surface properties such as surface roughness. Sigal et al. (1998) showed that more protein is adsorbed upon hydrophobic model surfaces, such as SAM-CH_3 with an advancing contact angle of 112°, than upon hydrophilic surfaces, such as SAM-OH with an advancing contact angle of < 15°. Keselowsky et al. (2003) confirmed for fibronectin a 3.3 fold higher amount of protein on SAM-CH_3 than on SAM-OH, with a twofold higher affinity for the SAM-OH surface. While the general observation that hydrophobic surfaces adsorb greater amounts of proteins than hydrophilic surfaces may be true for model systems, the polymer surfaces applied in this study have revealed that the knowledge on protein adsorption gained from hydrophobic and hydrophilic model surfaces has only limited applicability to real surfaces. Real polymer surfaces are different from model surfaces, since a change in surface wettability usually comes along with a change in surface roughness. The influence of both parameters can not be separated, thus obscuring unique correlations. The proteins used in this study gave an individual response to these polymer surface properties, following no clear trend and preventing the establishment of a general theory. Other authors do not even believe in a general correlation between macroscopic surface properties such as wettability and protein adsorption. Ostuni et al. (2003) pointed out, that although it is true that strongly hydrophobic surfaces adsorb proteins, it is not true, in general, that hydrophilic surfaces do not. In particular, charged surfaces which are strongly hydrophilic adsorb proteins of the opposite charge strongly. Furthermore, surfaces which are most resistant to adsorption of proteins, like those presenting oligo(ethylene glycol) groups, are intermediate in hydrophilicity (Chapman et al., 2000; Ostuni et al., 2001).

The studies on protein adsorption conducted in this thesis provided the amount of adsorbed protein as well as the protein binding affinity for the polymer surfaces. However, in order to

be able to explain cell attachment and spreading to these surfaces, further investigations would be necessary. It is well accepted that the properties of surfaces will govern both, the degree of conformational change and orientation of proteins. Conformational rearrangements and orientational changes in the adsorbing protein molecules are a major factor in determining whether or not a cell recognizes a certain peptide sequence within a protein, and thus, if and to which degree cell attachment and spreading can be established (adhesion strength). Consequently, it would certainly be helpful to investigate the protein conformation and orientation within the adsorbed protein layer on the polymer surfaces. A valuable method to image the topography of adsorbed protein layers is the atomic force microscopy (AFM) technique in the tapping mode, which is able to analyze protein monolayer packaging or monolayer thickness.

Additional information on the spatial access of receptor binding sites and, thus, protein functionality after adsorption on the polymer surfaces might be gained by performing a study similar to Keselowsky et al. (2003). The authors quantified integrin binding to fibronectin adsorbed on CH_3-terminated ($\theta_A = 107°$) and OH-terminated ($\theta_A = 25°$) SAMs. After crosslinking integrins to their bound ligands using a water-soluble, cell-membrane-impermeable, homobifunctional crosslinker, the cell bodies were removed. The proteins adsorbed on the surface with the bound integrins were left behind. Bound integrins were further quantified via ELISA using an alkaline phosphatase-conjugated antibody specific for the integrin subunit or visualized by immunofluorescence staining. This way, the authors could show that the integrin binding affinity was significantly higher on the OH-functionalized than on the CH_3-functionalized surface.

In addition to the study of protein adsorption from solutions of purified proteins, it is also interesting to analyze the adsorption from multicomponent solutions, as done in the case of NCS in this study, since this scenario is most relevant to the cell-substrate interface. The culture medium is supplemented with FCS which contains numerous types of proteins, in particular fibronectin and vitronectin but also different albumins and globulins and also the cells synthesize and secrete a mixture of ECM proteins adsorbing to the polymer surface. Several proteins compete for surface binding sites, resulting in a series of collision, adsorption and exchange processes on the polymer surface. For NCS, it would be important to know which types of proteins accumulate on the polymer surface, their distribution and how this relates to the bulk composition of the solution. Furthermore, other multicomponent solutions could be applied to elucidate the competitive adsorption of proteins, such as physiological fluids (blood, tear fluid, saliva), providing a greater insight into the nature of the protein interactions on polymer surfaces.

4.5.4 Cell Attachment and Spreading upon Polymer Surfaces

Studying cell attachment and spreading upon the polymer surfaces has been the final step in the sequence of experiments aiming to characterize the biocompatibility of different polymers. Characterizing and understanding the mechanisms of cell attachment and spreading to synthetic polymers are of crucial importance for their applicability as biomaterials in a variety of important biomedical and bioanalytical applications, such as biosensors or implants. Furthermore, these kind of studies also provide an insight into the surface properties that will govern cell-substrate interactions.

The cytocompatibility of the polymers PS, PMMA, PDMS and PhoP was analyzed by following the attachment and spreading kinetics of epithelial MDCK-II cells and epithelial-like NRK cells upon the polymer surfaces using the QCM technique in the passive mode (impedance analysis of the shear oscillation). Quartz resonators were spin coated with the polymer of interest and processed in different ways in order to study the impact of a selective polymer surface modification on cell attachment and spreading. For most polymers, the cellular response was investigated for the following process conditions:

i) unmodified polymer
ii) unmodified polymer + PBS^{--}/SFM pre-incubation over 20 h at 37 °C
iii) plasma modified polymer
iv) plasma modified polymer + PBS^{--}/SFM pre-incubation over 20 h at 37 °C

Cell attachment and spreading upon polymer coated quartz resonators was followed over a period of 20 h using the change in the magnitude of the minimal impedance $\Delta|Z_{min}|$, which has been proven to mirror the mechanical properties of cells during their specific interaction with the resonator surface relative to the same polymer-coated but only medium-loaded quartz resonator. The cell adhesion kinetics were quantified from the time course of $\Delta|Z_{min}|$ using the slope of the attachment curve in the time regime of linear increase as well as $\tau_{1/2}$, describing the time to reach half-maximal surface coverage. Complete description of the attachment and spreading behavior of MDCK-II cells required another parameter – τ_2 – describing the time that is needed to reach the second maximum (cell differentiation).
Prior to a comprehensive discussion with respect to the information obtained from contact angle measurements, the long-term stability in a physiological fluid and protein adsorption, a short summary of the attachment and spreading characteristics on the differently pretreated polymer films is given (see chapter 4.4.3 – 4.4.6 for more details).

Polystyrene

The time courses of $\Delta|Z_{min}|$ after seeding of initially suspended MDCK-II or NRK cells on PS coated quartz resonators which had been differently pretreated are compared in Fig. 4.78.

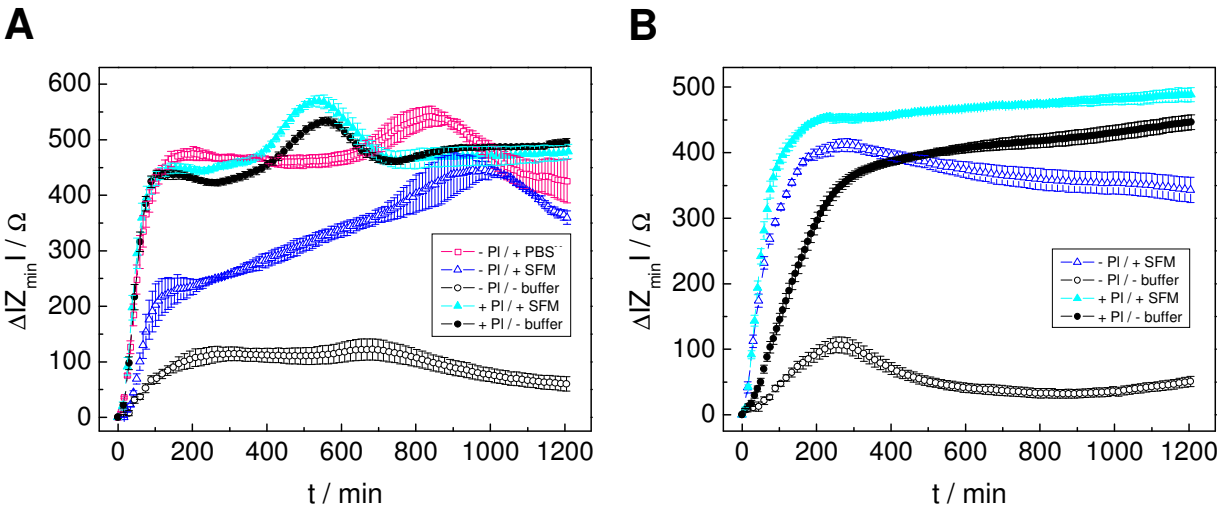

Fig. 4.78 Time course of $\Delta|Z_{min}|$ after seeding equal amounts of initially suspended MDCK-II (**A**) and NRK (**B**) cells on a PS coated quartz resonator at time point zero. The PS coated resonator had been pretreated as described in the legend. The number of points was reduced for reason of clarity.

MDCK-II Cell Attachment and Spreading

MDCK-II cells that were seeded on a PBS^{--} pre-incubated, on a plasma modified pre-incubated as well as on an only plasma modified surface revealed a similar attachment and spreading behavior, as reflected in the initial slopes of the graphs all ranging in the same order of (6.04 ± 0.22) Ω/min and (6.66 ± 0.28) Ω/min and the $\tau_{1/2}$ values which did not differ significantly (chapter 4.4.3, Tab. 4.18). For these processing conditions, a first transient plateau phase of 431 – 465 Ω was reached in a similar period after cell inoculation (100 – 200 min). However, great differences were obvious when regarding the times the cells stayed in the transient plateau phase and thus the times that were needed to reach the second plateau. Whereas cells that were seeded upon plasma modified pre-incubated PS were marginally faster in reaching the maximum ($\tau_2 = (540 \pm 9)$) min than cells on only plasma modified PS ($\tau_2 = (554 \pm 5)$ min), the maximum was attained not until (860 ± 15) min after cell inoculation for a PBS^{--} pre-incubated surface. The cells were not only the fastest in reaching the maximum on plasma modified pre-incubated PS, they also revealed the highest maximum value, which was 30 – 40 Ω higher than for the plasma modified or PBS^{--} pre-incubated PS surfaces. MDCK-II cells did need more time to attach and spread on an SFM pre-incubated PS surface, as can be taken from the $\tau_{1/2}$ value which was (64 ± 5) min. No real plateau phase was reached and the biphasic time course of $\Delta|Z_{min}|$ which is typical for the attachment and spreading behavior of MDCK-II cells appeared modified. However, the cells were able to attach and spread on this surface, giving rise to a maximum value of (450 ± 19) Ω, and thus only about 100 Ω lower than those values obtained for the previously mentioned surfaces. This maximum value was attained roughly (980 ± 74) min after cell inoculation. MDCK-II cells were not able to attach and spread on an unmodified PS surface. They only induced an impedance increase of roughly 110 Ω, followed by a decrease to 60 Ω during the complete period of observation.

NRK Cell Attachment and Spreading

Except for NRK cells which had been seeded upon unmodified PS, where hardly any cell adhesion took place, the courses of $\Delta|Z_{min}|$ recorded during cell attachment and spreading upon the remaining PS surfaces mainly differed in their initial slope (chapter 4.4.3, Tab. 4.19). NRK cells attached and spread upon plasma modified pre-incubated PS with the highest rate as indicated by $\tau_{1/2} = (48 \pm 2)$ min. In comparison to the other PS surfaces, cells seeded upon this surface also exhibited the highest absolute values for $\Delta|Z_{min}|$ ((490 ± 11) Ω), which even continued to increase during the time of the measurement. A PBS^{--} or SFM pre-incubated PS surface gave rise to a slight slowdown of the cell attachment and spreading rate, exhibiting a $\tau_{1/2}$ value of (53 ± 3) min. In contrast to the plasma modified, pre-incubated surface, $\Delta|Z_{min}|$ showed a temporary maximum and decreased thereafter by roughly 70 Ω when the surface was only pre-incubated, indicating that this surface may not be long-term cytocompatible. Cell attachment and spreading took significantly longer on a simply plasma modified PS surface ($\tau_{1/2} = (128 \pm 8)$ min) compared to the ones previously mentioned. The $\Delta|Z_{min}|$ values continued to increase slightly during the time period of 1200 min, finally reaching a similar $\Delta|Z_{min}|$ value as observed for the plasma modified pre-incubated surface.

Both cell lines have revealed that unmodified PS prevented a proper cell attachment and spreading, meaning that the surface is not cytocompatible. Hardly any cell adhesion took place, as indicated by the marginal increase in $\Delta|Z_{min}|$ (Fig. 4.78 A, B). This finding is in good agreement with the literature. Mitchell et al. (2004 and 2005) showed that almost all CHO (Chinese hamster ovary) cells seeded upon unmodified PS stayed rounded. The cells were only loosely associated with the surface, since they could be easily washed off. Welle and Gottwald (2002) also demonstrated that unmodified PS is non-adhesive for cells. Hepatocytes formed floating multicellular aggregates and fibroblasts remained round. Only 2 % of the seeded fibroblasts and 6 % of the hepatocytes adhered to unmodified PS.
The inability of cells to attach and spread upon unmodified PS might be related to the pre-adsorbed protein layer, which influences the behavior of cells approaching the surface. Cell attachment and spreading are mediated by interactions of cellular integrins with specific peptide sequences present in proteins bound to the substrate surface. The key determinants of cell attachment and spreading are the protein adsorption profiles, i.e. which proteins are adsorbed in what quantities (composition and concentration), and the protein cell-binding activity as determined by conformation and/or orientation of the surface-bound proteins. In this *in vitro* study, the adhesive proteins originated from the serum-supplemented cell culture medium and spontaneously adsorbed upon the surface before the first cells made contact. As it was mentioned above (chapter 4.5.3) surface wettability and surface roughness are known to have an impact on the sort and quantity of adsorbed proteins as well as on their orientation and conformation. Consequently, cell attachment and spreading on material surfaces are strongly influenced by these two surface parameters as well. It is widely observed that cells usually spread poorly on hydrophobic surfaces and attach and spread more extensively, rapid

and firmly on hydrophilic substrates (Steele et al., 1993; Teare et al., 2000; Wilson et al., 2005).

The reduced cellular adhesion to unmodified PS might indicate that on the one hand mainly the wrong sort of proteins was adsorbed from serum. For example, non-adhesive proteins like albumin might have a high surface density on unmodified PS. Albumin is known to irreversibly adsorb on hydrophobic substrates and to inhibit the adsorption of other adhesive proteins (Baszkin and Biossonnade, 1993). On the other hand, the pre-adsorbed proteins might provide only a few binding sites for the cellular integrins. Since unmodified PS was shown to be strongly hydrophobic ($\theta_A \sim 92°$) (chapter 4.1.4, Tab. 4.3), the proteins may experience conformational changes upon adsorption. Surface-induced changes in the protein conformation upon adsorption might modify the accessibility of the integrin binding sites within the adsorbed proteins for the cells, complicating or preventing specific recognition and thus attachment and spreading of most cells. For example, fibronectin adsorbed to hydrophobic PS surfaces ($\theta = 88°$) showed a marked reduction in its adhesiveness for cells compared to fibronectin adsorbed to hydrophilic PS ($\theta = 31°$) (Grinnell and Feld, 1982; Steele et al., 1993), suggesting that the adsorbed protein adopts different conformations, with the more biologically active conformation on the hydrophilic surface. Analyses comparing the binding of fibronectin on either hydrophobic or hydrophilic surfaces have shown that conformational changes were greater on the hydrophobic surface (Andrade et al., 1984). Consequently, specific cell-substrate contacts can not be established and cell adhesion is almost completely inhibited. But cells do not only attach and spread upon proteins deposited from serum-containing culture medium, they are also able to attach and spread to endogenous ECM proteins. The cells synthesize and secrete ECM proteins, which may replace proteins pre-adsorbed to the substrate surface, thus remodeling the adsorbed protein layer. However, this modulation of the adsorbed protein layer by the cells will not be possible on hydrophobic surfaces, since protein adsorption is known to be irreversible here. This very strong binding of proteins such as albumin to the surface may resist competitive replacement by other ECM proteins which cells would subsequently recognize and attach to, preventing a belated cell adhesion.

A preceding argon plasma treatment of PS, leading to a significant surface hydrophilization as indicated by an advancing contact angle of ~ 25° (chapter 4.1.4, Tab. 4.3), allowed the formation of specific cell-substrate contacts. This was indicated by an instantaneous increase of $\Delta|Z_{min}|$ showing absolute values even roughly 75 Ω higher than the values obtained for a cytocompatible gold surface (chapter 4.4.2, Tab. 4.17). In general, surfaces containing hydrophilic or polar functional groups have been found to be superior to hydrophobic surfaces with respect to their ability to promote a rapid cell attachment and spreading (Teare et al., 2000; Wilson et al., 2005). The introduction of oxygen functionalities into the PS surface upon argon plasma treatment leads to a hydrophilic surface, which can easily interact with the proteins present in the serum-supplemented culture medium without inducing structural rearrangements. Thus, the integrin binding sites within the adsorbed proteins should be

accessible for the cell-surface receptors of the arriving cells. In summary, modification of the PS surface using an argon plasma was successful in rendering the non-cytocompatible PS surface cytocompatible, supporting cell attachment and spreading. The ability of cells to adhere to a hydrophilic PS surface has also been demonstrated by several authors. Mitchell et al. (2004 and 2005) exposed PS to an UV/ozone treatment, leading to a hydrophilic PS surface with a contact angle of ~ 60° (15 min exposure time). Most of the CHO cells on oxidized PS showed a flat morphology indicating extensive spreading, whereas those on untreated PS remained rounded and were easily washed off. Using a PS surface locally modified by oxidation, the authors could achieve a spatially selective attachment of CHO cells, showing cells which adhered preferentially on the UV/ozone treated regions. An improved growth on PS surfaces with increasing wettability was demonstrated by van Kooten et al. (2004). The authors deposited HUVEC cells on PS surfaces of different wettability, using unmodified PS (θ_A = 86°) and PS after different argon plasma treatment times, resulting in surfaces with gradually decreasing contact angles between 59° and 27°. The cells attached on all plasma treated surfaces, but not on the untreated PS surface. However, the appearance of the cell layer was affected by the treatment duration. PS5 (5 s plasma, θ_A = 59°) and PS10 (10 s plasma, θ_A = 54°) yielded a cell layer with patches of cells interspersed with open areas. Furthermore, cell debris was floating in the medium and detaching cells were observed 48 h after cell inoculation. The overall appearance resembled a restless cell population which was gradually detaching. For PS30 (30 s plasma, θ_A = 29°) and PS60 (60 s plasma, θ_A = 30°) the cell population appeared much more homogeneous. Cell coverage was clearly increased on both surfaces and detaching cells were less frequently observed. Elucidating the cellular response to hydrophobic and hydrophilic PS, Underwood et al. (1993) identified a difference in fibronectin's biological activity to be due to different fibronectin conformations on the two wettable surfaces. The authors used monoclonal antibodies directed to cell adhesion sites of fibronectin and could show that they were more accessible on hydrophilic PS than on the hydrophobic surface.
Since the argon plasma treatment performed in this thesis did not result in significant changes in surface roughness, as shown by the contact angle hysteresis (chapter 4.1.4, Tab. 4.3), the observations regarding cell attachment and spreading can be ascribed to PS surface wettability rather than to surface roughness.

Not only plasma treatment was capable of rendering a PS surface cytocompatible. A pre-incubation in either PBS^{--} or SFM also supported cell attachment and spreading on the PS surface. Contact angle measurements indicated that fluid incubation did not change the surface wettability but caused a significant increase in the contact angle hysteresis, and thus in surface roughness (chapter 4.1.4, Tab. 4.3). Presumably this surface property allowed NRK cells to attach and spread upon the pre-incubated surface, showing even a higher spreading rate compared to a plasma modified surface. Thus, the NRK cells are able to establish specific cell-substrate contacts even on a hydrophobic surface when the surface roughness is appropriate. For NRK cells, surface roughness seems to outweigh the cell-resistant effect of a

hydrophobic surface. The fluids (PBS^{--} or SFM) used for pre-incubation induced a similar response of the NRK cells. By contrast, MDCK-II cells were sensitive to the kind of fluid used to pre-incubate the PS surface. Whereas the adhesion kinetics were similar to the plasma modified surface for PBS^{--} pre-incubated PS, it was significantly lower for SFM pre-incubated PS. The curve even lost its typical biphasic shape. The reason for this fluid-specific response may be found in the significantly increased surface roughness for SFM pre-incubated PS compared to the PBS^{--} pre-incubated surface, as revealed by the contact angle hysteresis of $\Delta\theta(PBS^{--}) \sim 28°$ and $\Delta\theta(SFM) \sim 51°$ (chapter 4.1.4, Tab. 4.3). Proteins might adsorb differently with variations in surface roughness. Apart from increasing the surface area and providing more anchoring sites for the interaction with proteins, topographic features (surface roughness) may also create confined spaces. These might permit multiple adsorption mechanisms, leading to a protein layer with a distribution of protein orientations, hampering the recognition of adhesive peptide sequences by the integrins of the MDCK-II cells. For the SFM pre-incubated surface, the first steep increase to only $(220 \pm 30)\ \Omega$ might indicate that only a fraction of the suspended MDCK-II cells can recognize the integrin binding sites whereas the conformation and/or orientation of most proteins bound to this surface does not allow accessibility of the binding sites for the cellular integrins. Consequently, the formation of specific cell-substrate contacts is restricted. Thus, synthesis and secretion of endogenous ECM proteins is necessary to allow further cell-substrate contacts. When cells have to synthesize their own ECM attachment and spreading are often much slower. The subsequent moderate increase of $\Delta|Z_{min}|$ over 600 min might be governed by this process of ECM self-synthesis, i.e. synthesis and secretion of ECM proteins, their competitive adsorption on the PS surface, thereby possibly replacing a fraction of the proteins adsorbed from the culture medium, finally allowing the formation of specific cell-substrate contacts. The second maximum for MDCK-II cells seeded upon pre-incubated PS was reached significantly later than on plasma modified PS. This indicates that the reorganization of the actin cytoskeleton, which is the main contributor for this increase, begins later on this surface than on plasma modified PS. However, this significantly different response of NRK and MDCK-II cells to SFM pre-incubated PS might also indicate that further aspects – besides surface wettability and surface roughness – might be involved, governing the kinetics of cell attachment and spreading.

Plasma treatment and subsequent fluid incubation led to an acceleration of cell adhesion kinetics for both cell lines. NRK cell attachment and spreading were the fastest on this pretreated surface and additionally revealed the highest $\Delta|Z_{min}|$ values. For MDCK-II cells, this pretreatment induced the fastest differentiation kinetics with the highest $\Delta|Z_{min}|$ for the second maximum. This processing condition – plasma treatment followed by fluid incubation – obviously caused the most cytocompatible surface. Unlike for MDCK-II cell inoculation on only pre-incubated PS, the fluid used to pre-incubate the plasma modified PS surface induced a similar cellular response. These results are also supported by the contact angle data, revealing a similar surface wettability and surface roughness for plasma modified PBS^{--} pre-

incubated and plasma modified SFM pre-incubated PS (chapter 4.1.4, Tab. 4.3). But it was also obvious that the contact angle data for plasma modified PS and plasma modified pre-incubated PS were similar, making an interpretation of the increased adhesion kinetics difficult. However, the QCM measurements concerning the long-term stability of plasma modified PS in PBS^{--} and SFM revealed a modification of the polymer surface (chapter 4.2.1, Tab. 4.7), which might lead to an adsorbed protein layer exhibiting an orientation and conformation allowing NRK cells to attach and spread faster and MDCK-II cells to differentiate slightly faster than on only plasma modified PS.

The protein adsorption data generally support the attachment and spreading characteristics of MDCK-II and NRK cells on PS. Protein adsorption upon unmodified and plasma modified PS, which had been pre-incubated with DI-water, showed no clear trend for protein binding affinity upon both surfaces (chapter 4.3, Tab.4.13). This result is also mirrored in the fact that MDCK-II and NRK cells were able to establish specific cell-substrate contacts on both pretreated PS surfaces. Except for MDCK-II cell adhesion upon SFM pre-incubated PS, the time course of $\Delta|Z_{min}|$ even revealed a similar slope and thus similar attachment and spreading kinetics for MDCK-II and NRK cells on pre-incubated and on plasma modified pre-incubated PS (Fig. 4.78 A, B).

Poly(methyl methacrylate)

Figure 4.79 summarizes the time courses of $\Delta|Z_{min}|$ recorded during adhesion of MDCK-II and NRK cells upon PMMA coated quartz resonators which were subjected to different processing conditions.

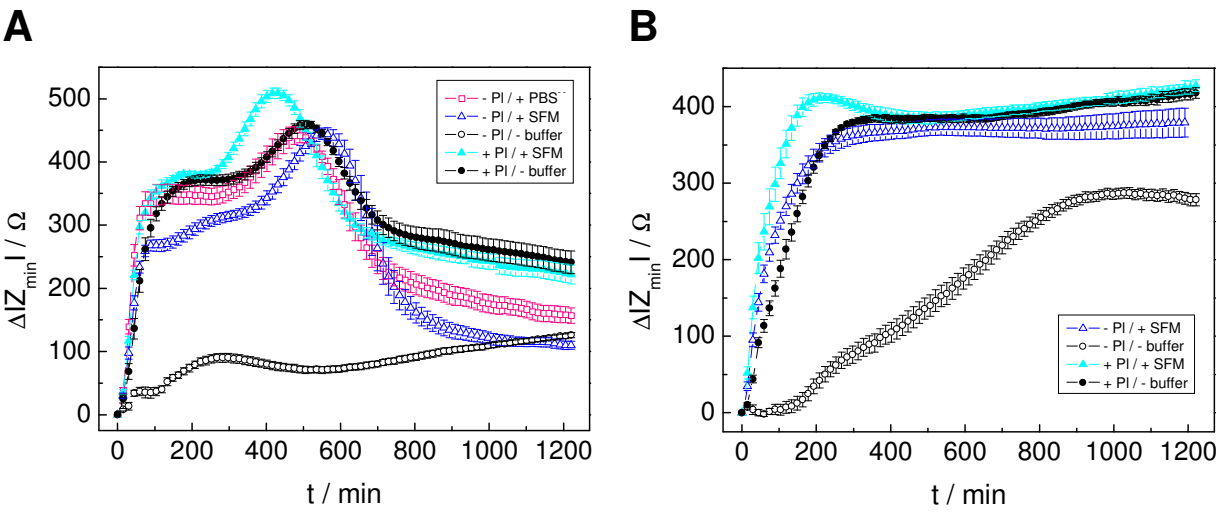

Fig. 4.79 Time course of $\Delta|Z_{min}|$ after seeding equal amounts of initially suspended MDCK-II (**A**) and NRK (**B**) cells on a PMMA coated quartz resonator at time point zero. The PMMA coated resonator had been pretreated as described in the legend. The number of points was reduced for reason of clarity.

MDCK-II Cell Attachment and Spreading

MDCK-II cells did not attach and spread properly on an unmodified PMMA surface. Their adhesion only gave rise to an impedance increase of roughly 130 Ω during the complete period of observation. For the other processing conditions of PMMA, $\Delta|Z_{min}|$ showed a biphasic time course, which is typical for the attachment and spreading behavior of MDCK-II cells on cytocompatible surfaces. The initial slope of these attachment curves was quite similar for all processing conditions (chapter 4.4.4, Tab. 4.20). A first transient plateau of 350 – 380 Ω was reached in a similar period of time after inoculation (120 – 200 min), except for the SFM pre-incubated surface. The latter surface revealed a significantly lower plateau value of $\Delta|Z_{min}| = (269 \pm 9)\ \Omega$ which only shortly remained on this level and continued to increase in a biphasic manner. Further differences could be noted in the time needed for reaching the second maximum. Whereas for three PMMA pre-treatment conditions, i.e. PBS^{--} pre-incubation, SFM pre-incubation and plasma treatment, the second maximum ranged in a similar dimension of 440 – 460 Ω and was attained within 500 – 570 min, the plasma modified, pre-incubated surface exhibited a roughly 50 Ω higher $\Delta|Z_{min}|$ value already at $\tau_2 = (425 \pm 9)$ min after cell inoculation. For all processing conditions except for unmodified PMMA, $\Delta|Z_{min}|$ decreased significantly after having passed the maximum. Whereas the plasma modified surfaces – irrespective of pre-incubation – revealed a similar value at the end of the measurement of roughly 230 Ω, $\Delta|Z_{min}|$ for the PBS^{--} and SFM pre-incubated PMMA surfaces even decreased to a value of 110 Ω and 160 Ω, respectively, similar to $\Delta|Z_{min}|$ observed for an unmodified surface.

NRK Cell Attachment and Spreading

The attachment and spreading curves of NRK cells seeded upon PMMA that had been pre-processed by pre-incubation (PBS^{--} or SFM), plasma treatment and pre-incubation or plasma treatment only differed in their initial slope whereas the final $\Delta|Z_{min}|$ values attained in equilibrium were similar, ranging between 380 Ω and 430 Ω. The attachment and spreading kinetics were the fastest on plasma modified, pre-incubated PMMA, as revealed by a $\tau_{1/2}$ value of (53 ± 8) min. For pre-incubated or only plasma modified PMMA, cell adhesion was slowed down, requiring (61 ± 4) min and (108 ± 6) min, respectively, to cover half of the surface area. On unmodified PMMA, NRK cells were only able to attach and spread with a significantly reduced rate, as indicated by $\tau_{1/2} = (500 \pm 35)$ min (chapter 4.4.4, Tab. 4.21). Furthermore, the stationary $\Delta|Z_{min}|$ was roughly 100 – 150 Ω lower than the values observed for the other surface conditions.

MDCK-II and NRK cells responded differently to unmodified PMMA (Fig. 4.79 A, B). Unmodified PMMA is a hydrophobic polymer with an advancing contact angle of ~ 88° (chapter 4.1.4, Tab. 4.4). Proteins which adsorb from serum-containing culture medium upon the PMMA surface are thought to undergo significant structural alterations which might lead to the inaccessibility of binding sites for the cellular integrins. This scenario may be true for

MDCK-II cells, which were able to establish only a few cell-substrate contacts, as indicated by the slight increase in $\Delta|Z_{min}|$. Whereas adhesion of MDCK-II cells was strongly hindered on unmodified PMMA, NRK cells did attach and spread upon unmodified PMMA, although it took significantly longer than on all other surfaces. The reason for this unexpected behavior may be the fact that the integrins expressed by NRK cells are able to detect binding sites in the adsorbed proteins which exhibit the optimal orientation and/or conformation for interaction with the integrins of NRK cells only. Since many proteins presumably have a non-optimal orientation, this recognition process took quite long. Studies in the literature confirm this finding that cell attachment and spreading upon unmodified PMMA strongly depend on the cell type. Risbud et al. (2002) observed no significant attachment and spreading for endothelial cells (CPA-47 cells) seeded upon spin coated films of PMMA ($\theta = 80°$). Phase contrast micrographs taken two days after inoculation showed only a few spread cells on the PMMA surface. Similar results were obtained by D'Sa et al. (2010) for lens epithelial cells seeded upon unmodified PMMA ($\theta = 84°$). After 24 h culture the surface showed only a few cells, with those present displaying a contracted morphology. Actin fibres were either contracted in shape or ran along the long axis of the cells with few of these fibres extending into the cell interior, suggesting poor spreading. By contrast, fibroblasts (WT NR6) did attach and spread on unmodified PMMA, as indicated by phase contrast micrographs taken 24 h after seeding (Banerjee et al., 2000).

Argon plasma treatment of PMMA allowed MDCK-II as well as NRK cells to attach and spread upon PMMA in a time interval and with $\Delta|Z_{min}|$ values similar to those for a cytocompatible gold surface (chapter 4.4.2, Tab. 4.17). The increased attachment and spreading on the argon plasma modified PMMA surface can be clearly related to the increased hydrophilicity after plasma treatment as demonstrated by the advancing contact angle of roughly 60° (chapter 4.1.4, Tab. 4.4). The proteins adsorbing from serum-supplemented culture medium should not be denatured just much as those adsorbing on unmodified PMMA, so that the integrin binding sites are accessible for the arriving cells. Whereas NRK cells exhibited constant $\Delta|Z_{min}|$ values after attachment and spreading throughout the remaining measurement, MDCK-II cells revealed a significant decrease of $\Delta|Z_{min}|$ after having passed the second maximum. This decrease was roughly 170 Ω higher compared to that on a cytocompatible gold surface (chapter 4.4.2, Tab. 4.17). The reasons for this behavior can not be clarified by this study. One possible scenario might be that the MDCK-II cells detached from the surface or revealed shrinkage. This might be explained by the transmission of growth-inhibitory signals. Additionally, the cells might be expected to become less mechanically stiff, leading to a decrease of $\Delta|Z_{min}|$ as well. The results observed for MDCK-II cells might be correlated to the observations made by van Kooten et al. (2003). The authors seeded HUVEC cells on argon plasma modified PS surfaces, exhibiting an advancing contact angle of 59° and thus similar to the angle measured for plasma modified PMMA. From phase contrast micrographs taken 24 h after inoculation, they found that the cells were able to adhere to the surfaces, forming a cell layer with confluent patches of cells

interspersed with cell-free areas. But the cell populations were not able to maintain themselves on this surface after 48 h of incubation. Individual cells rounded up and detached over time one by one, while others kept their spread morphology.
D'Sa et al. (2010) studied lens epithelial cell attachment and spreading on unmodified and plasma modified PMMA. Whereas only a few cells attached on unmodified PMMA ($\theta = 84°$), displaying poor spreading (contracted morphology) 24 h after inoculation, the cells did attach and spread upon the plasma treated surface ($\theta = 62°$), exhibiting their typical polygonal morphology with well spread actin stress fibres. This cellular behavior validates the results observed for NRK cells on plasma modified PMMA.

Pre-incubation of PMMA in a physiological buffer resulted in MDCK-II and NRK cell adhesion kinetics similar to that observed for a plasma treated surface. Irrespective of the fluid used for pre-incubation, NRK cells revealed a similar attachment and spreading rate, which was even slightly higher than for only plasma modified PMMA. MDCK-II cells showed slight differences in the shape of the time course for the two different fluids, regarding the first plateau values and the time to reach the second maximum. Reorganization of the actin cytoskeleton took slightly longer on SFM compared to PBS^{--} pre-incubated PMMA. Since contact angle data for PBS^{--} pre-incubated PMMA are not available, these two fluids can not be compared with respect to fluid-induced differences in surface wettability or surface roughness. Both cell lines were able to establish specific cell-substrate contacts on pre-incubated PMMA. This indicates that the surface bound proteins exposed their specific binding sites to the cellular integrins so that the recognition could proceed fast. The contact angle data for SFM pre-incubated PMMA revealed an advancing contact angle of 84° and a contact angle hysteresis of 34° (chapter 4.1.4, Tab. 4.4). Although pre-incubated PMMA is not significantly more hydrophilic than unmodified PMMA, it did support cell attachment and spreading. Obviously surface roughness results in a protein orientation which is optimal for the recognition by the cells. Whereas $\Delta|Z_{min}|$ for NRK cells remained constant during the measurement, $\Delta|Z_{min}|$ for MDCK-II cells seeded upon pre-incubated PMMA showed a significant decrease after having passed the maximum. The value even reached that for an unmodified PMMA surface. This might indicate that MDCK-II cell adhesion on pre-incubated PMMA could not be sustained, revealing that this surface might not be long-term cytocompatible. Whereas MDCK-II cell attachment and spreading proceeded similar to that on a gold substrate, $\Delta|Z_{min}|$ was 250 – 300 Ω lower than on a gold surface at the end of the measurement. The adsorbed proteins may have reoriented so that established cell-substrate contacts loosen. Since this phenomenon was only observed for MDCK-II cells, it can be expected that only the proteins containing the integrin binding sites for MDCK-II cells may reorient or that MDCK-II cell-substrate contacts are not as firm as those for NRK cells. Another possible explanation for this lower stationary $\Delta|Z_{min}|$ value obtained on PS in comparison to a gold surface might reflect a cell-type specific rearrangement of the actin cytoskeleton.

Argon plasma treatment and pre-incubation (PBS^{--} or SFM) of PMMA provoked mainly the same adhesion kinetics of MDCK-II cells as on pre-incubated or plasma modified PMMA. The only difference is the second maximum which was reached significantly earlier, indicating that reorganization of the actin cytoskeleton proceeded much faster on plasma modified, pre-incubated PMMA. NRK cells revealed the fastest cell attachment and spreading kinetics on this surface type with only marginal differences to the further processing conditions. At first sight, this surface condition represents the most cytocompatible surface for both cell lines. However, MDCK-II cells again showed a significant decrease of $\Delta|Z_{min}|$ after having passed the second maximum, reaching a value similar to the one for a plasma treated surface. PMMA, irrespective of the pre-treatment, does not seem to be long-term compatible for MDCK-II cells. The reason for this observation might be the reorientation of selective proteins, inhibiting the proteins' ability to bind the integrins of MDCK-II cells in the length of time. The fluid used to pre-incubate plasma modified PMMA, either PBS^{--} or SFM, provoked a similar cellular response, further confirmed by the contact angle data for both plasma modified pre-incubated surfaces which did not differ significantly (chapter 4.1.4, Tab. 4.4).

The observed protein adsorption is in accordance with the cell attachment and spreading characteristics of MDCK-II and NRK cells on PMMA. Regarding the proteins contained in NCS, the Langmuir parameter $c_{50\%}$ describing the protein binding affinity of the pre-incubated and plasma modified, pre-incubated PMMA, was similar (chapter 4.3, Tab. 4.14). This is also mirrored in the fact that MDCK-II and NRK cells did establish specific cell-substrate contacts on both pretreated PMMA surfaces. The time course of $\Delta|Z_{min}|$ even revealed a similar slope and thus similar attachment and spreading kinetics for MDCK-II and NRK cells on pre-incubated and on plasma modified pre-incubated PMMA. The significant decrease of $\Delta|Z_{min}|$ only observed for MDCK-II cells can not be explained from the protein adsorption data.

Poly(dimethyl siloxane)

Attachment and spreading of MDCK-II and NRK cells was investigated for PDMS surfaces that were either unmodified or pre-incubated with SFM. Adhesion characteristics are compared in Fig. 4.80.

MDCK-II Cell Attachment and Spreading

$\Delta|Z_{min}|$ recorded after inoculation of MDCK-II cells on unmodified and on SFM pre-incubated PDMS revealed a time course which differed significantly to the typical biphasic adhesion behavior found for MDCK-II cells on cytocompatible substrates (chapter 4.4.2, Fig. 4.42). For the SFM pre-incubated surface, a strongly modified, but still biphasic course could be observed. $\Delta|Z_{min}|$ reached a plateau value of $(130 \pm 44)\ \Omega$ which was maintained for only 30 min, followed by a steep increase to the second maximum of $(340 \pm 35)\ \Omega$. Having passed the maximum, $\Delta|Z_{min}|$ continuously decreased to a value of $(150 \pm 18)\ \Omega$. For cell attachment

and spreading on unmodified PDMS, the biphasic character of the curve was completely lost. $\Delta|Z_{min}|$ moderately increased to a maximal value of (300 ± 15) Ω within 1200 min after cell inoculation.

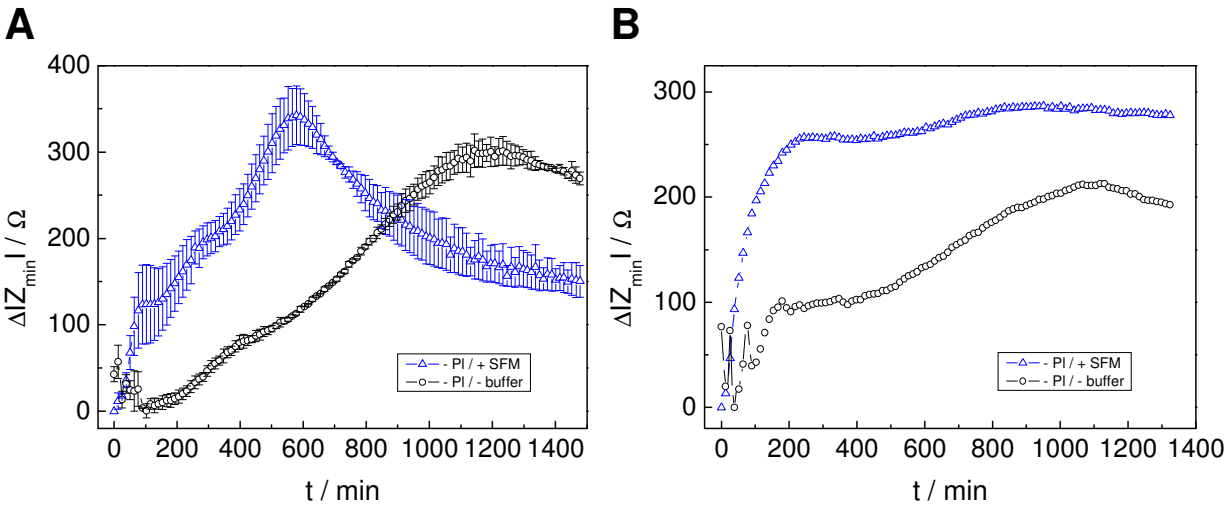

Fig. 4.80 Time course of $\Delta|Z_{min}|$ after seeding equal amounts of initially suspended MDCK-II (**A**) and NRK (**B**) cells on a PDMS coated quartz resonator at time point zero. The PDMS coated resonator had been pretreated as described in the legend. The number of points was reduced for reason of clarity.

NRK Cell Attachment and Spreading

The attachment and spreading kinetics for NRK cells seeded upon SFM pre-incubated PDMS were characterized by a stationary $\Delta|Z_{min}|$ value of roughly 280 Ω and a $\tau_{1/2}$ value of 55 min. The time course of $\Delta|Z_{min}|$ after inoculation of NRK cells upon unmodified PDMS revealed significantly altered adhesion kinetics, reaching a maximum of $\Delta|Z_{min}| = 212$ Ω after roughly 1100 min.

MDCK-II and NRK cell attachment and spreading was significantly retarded on unmodified PDMS as expected for this highly hydrophobic polymer with an advancing contact angle of ~ 122° (chapter 4.1.4, Tab. 4.5). This can be explained by the inability of the hydrophobic polymer to adsorb proteins in a functional conformation. The proteins adsorbed to such a hydrophobic surface supposedly undergo strong structural alterations so that the integrin binding sites might be inaccessible for the cells. However, a few cell-substrate contacts could be established, although it took a quite long time when compared to cell attachment and spreading on a cytocompatible gold substrate (chapter 4.4, Tab. 4.17). The final $\Delta|Z_{min}|$ values were roughly 140 Ω (MDCK-II) and 170 Ω (NRK) lower than the values for an uncoated cytocompatible quartz surface. Since a decrease of $\Delta|Z_{min}|$ is already indicated for these substrates, it would be interesting to analyze the ongoing time course of $\Delta|Z_{min}|$, providing information whether the attached cells would remain on the surface. In the literature, unmodified PDMS is often described as a cell-resistant surface. Rat retinal cells remained rounded on unmodified PDMS (Reyes et al., 2004). Faid et al. (2005) found the attachment of

cortical cells on unmodified PDMS to be very weak, as reported for the culture of porcine kidney epithelial (LLC-PK1) cells or HUVEC cells (De Silva et al., 2004). The poor cell adhesion properties of unmodified PDMS have also been confirmed by Nakazawa et al. (2009). Rat hepatocytes seeded in serum-containing medium upon unmodified PDMS revealed a cell adhesion ratio of $< 15\ \%$ within 24 h after cell inoculation. The cells predominantly formed floating cell aggregates which were easily removed from the PDMS surface by washing with PBS solution.
The yet considerable attachment and spreading of MDCK-II and NRK cells observed on this highly hydrophobic surface might be attributed to the high surface roughness of PDMS, as indicated by the contact angle hysteresis of $\Delta\theta \sim 81°$ and the undulated surface topography in VSI measurements (chapter 4.1.2, Fig. 4.12). Protein adsorption and thus cellular interactions would certainly not remain unaffected from this surface property. Surface roughness may contribute to a random adsorption and orientation of proteins, with some of them having a favorable orientation and/or conformation, exposing integrin binding sites for the cells.

Pre-incubation of PDMS using SFM as the physiological fluid led to an increase of attachment and spreading kinetics for both cell lines. The cells were able to establish specific cell-substrate contacts with proteins decorating this pre-incubated surface. However, the time course was different from the time course of $\Delta|Z_{min}|$ for a cytocompatible gold surface. The strongly modified biphasic time course of $\Delta|Z_{min}|$ for MDCK-II cells might be explained by initial cell attachment and spreading on pre-adsorbed proteins followed by endogenous synthesis and secretion of ECM proteins, remodeling the protein layer and allowing for additional attachment sites for the cells. The significant decrease of $\Delta|Z_{min}|$ to roughly 150 Ω after having passed the maximum might indicate the dissociation of established cell-substrate contacts and the detachment of MDCK-II cells due to reasons mentioned above for the PMMA substrate. For NRK cells seeded upon SFM pre-incubated PDMS, the slope of the attachment curve was even similar to the slope of the curve for NRK attachment and spreading on gold. However, the stationary $\Delta|Z_{min}|$ values were roughly 100 Ω lower on pre-incubated PDMS than on gold.

Regarding the contact angle data for unmodified PDMS and PDMS pre-incubated with SFM, a different attachment and spreading behavior of the cells on both surfaces would not be expected at first sight, since the contact angle data indicate a similar surface wettability and surface roughness (chapter 4.1.4, Tab. 4.5). However, the QCM data obtained for the long-term stability of PDMS in SFM have to be considered, as they revealed a distinct surface modification possibly not accessible by the contact angle measurements (chapter 4.2.3). This change of surface properties might be responsible for the observed cellular response.

Photopolymer

Figure 4.81 shows the time course of $\Delta|Z_{min}|$ for the attachment and spreading of MDCK-II cells upon PhoP coated quartz resonators, analyzed in the unmodified pre-incubated and the plasma modified pre-incubated form.

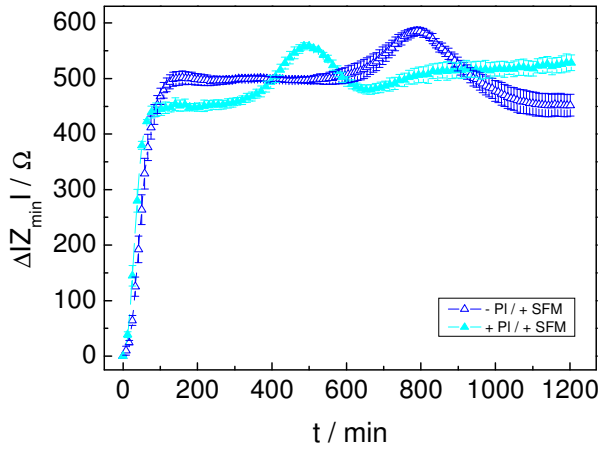

Fig. 4.81 Time course of $\Delta|Z_{min}|$ after seeding equal amounts of initially suspended MDCK-II cells on a PhoP coated quartz resonator at time point zero. The PhoP coated resonator had been pretreated as described in the legend. The number of points was reduced for reason of clarity.

MDCK-II Cell Attachment and Spreading

MDCK-II cells which were seeded on a plasma modified, pre-incubated (PBS^{--} or SFM) PhoP surface attached and spread slightly faster than upon PhoP that was only pre-incubated. This is obvious from the initial slope of the attachment curves, (6.89 ± 0.20) Ω/min and (7.87 ± 0.07) Ω/min, as well as the $\tau_{1/2}$ values (chapter 4.4.6, Tab. 4.22). For both processing conditions, a first transient plateau phase was reached within a similar time after cell inoculation (100 min and 140 min), although the plateau value for plasma modified pre-incubated PhoP was roughly 50 Ω lower than that for the pre-incubated polymer. The most apparent difference was the time the cells stayed in the transient plateau phase and thus the time needed to reach the second maximum. Whereas MDCK-II cells seeded upon plasma modified, pre-incubated PhoP needed (496 ± 3) min to reach the second maximum, this process took significantly longer on a pre-incubated PhoP surface, i.e. (793 ± 6) min.

NRK Cell Attachment and Spreading

Attachment and spreading of NRK cells was only analyzed on pre-incubated PhoP (chapter 4.4.6, Fig. 4.75) for technical reasons and thus can not be compared for different surface treatments.

MDCK-II cells were able to establish specific cell-substrate contacts on pre-incubated PhoP. The attachment and spreading kinetics were only slightly different compared to those recorded for an uncoated quartz resonator (chapter 4.4.2, Tab. 4.17). Both pre-incubation fluids provided surfaces with almost identical adhesion kinetics, in contrast to the fluid-specific attachment and spreading behavior of MDCK-II cells observed on the polymers PS and PMMA. The contact angle data further support this finding, since surface wettability as well as surface roughness were similar after incubation with either of the fluids (chapter 4.1.4, Tab. 4.6). More importantly, the contact angle data revealed that PBS^{--} as well as SFM incubation caused a significant increase in surface wettability, as indicated by the advancing contact angle of ~ 73° for PBS^{--} and ~ 80° for SFM pre-incubation, compared to unmodified PhoP (θ_A ~ 93°). Although pre-incubated PhoP can not be regarded as a hydrophilic polymer, it did support cell attachment and spreading. The reason for this phenomenon could be the high surface roughness of pre-incubated PhoP. The contact angle hysteresis of $\Delta\theta_A(PBS^{--})$ ~ 67° and $\Delta\theta_A(SFM)$ ~ 70° indicates a rough surface. Obviously, this combination of surface parameters led to a protein layer with an optimal orientational and conformational status of adsorbed proteins, providing MDCK-II and NRK cells easy access to the integrin binding sites and to attach and spread upon the pre-incubated surface.

For plasma modified PBS^{--} or SFM pre-incubated PhoP, the rate of MDCK-II cell adhesion was slightly increased compared to only pre-incubated PhoP. The main difference was the time to reach the second maximum und thus the time that was needed for actin cytoskeleton reorganization. This took significantly longer on only pre-incubated PhoP, whereas the time was similar to that on a gold surface (chapter 4.4.2, Tab. 4.17) when the cells were seeded on plasma modified, pre-incubated PhoP. The fluid used to pre-incubate plasma modified PhoP provoked a similar cellular response, as confirmed by the contact angle data for both pre-incubated surfaces which did not differ significantly (chapter 4.1.4, Tab. 4.6). Contact angle measurements revealed a surface which was much more hydrophilic (θ_A ~ 40° (PBS^{--}) and ~ 37° (SFM)) but less rough ($\Delta\theta$ ~ 33° (PBS^{--}) and ~ 28° (SFM)) than compared to PhoP that was only pre-incubated. These surface characteristics caused a cellular response similar to that on pre-incubated PhoP with the exception of the time needed to reorganize the cytoskeleton. Cell-substrate contacts on this surface could be established to a similar extent and with similar kinetics compared to an only pre-incubated surface.
In summary, both differently pre-treated PhoP surfaces can be regarded as long-term cytocompatible. Nicolau et al. (1996) analyzed neuronal cell attachment on spin coated films of a diazonaphthoquinone/novolak photoresist with a similar composition as the PhoP used in this study. They utilized unmodified and UV light exposed photoresist films and observed cell attachment on both surfaces, with a slightly increased number of cells on the UV treated polymer.

The protein adsorption data support the attachment and spreading characteristics of MDCK-II cells on both surface types. Protein adsorption upon unmodified and plasma modified PhoP, which had been pre-incubated with DI-water, showed no significant differences with respect

to protein binding affinity (chapter 4.3, Tab. 4.16). For Col IV and the proteins contained in NCS, the affinity to adsorb to either of the pre-treated polymer surfaces was similar. This result is mirrored in the fact that MDCK-II cells were able to establish specific cell-substrate contacts on both pre-treated PhoP surfaces to a similar extent and at a similar rate.

Microscopic Analysis of Cell Attachment and Spreading upon Polymer Surfaces and Comparison with the QCM Data

In addition to QCM measurements, attachment and spreading of MDCK-II and NRK cells to the different polymer surfaces was also studied microscopically, taking phase contrast images at regular time intervals after cell inoculation upon the spin coated polymer films. Below, the observed cell morphology is related to the QCM results for each cell line on the differently pretreated polymers.

Attachment and Spreading of MDCK-II Cells on Polystyrene

The QCM data and the phase contrast micrographs revealed that MDCK-II cells were in general not able to attach and spread upon unmodified PS. The microscopic images showed only a few cell islets as well as spherically shaped cells on the surface 24 h after cell inoculation, which is in accordance with the slight increase of $\Delta|Z_{min}|$ by roughly 60 Ω (chapter 4.4.3, Fig. 4.43 C and Fig. 4.47). The phase contrast micrographs taken 120 min after cell inoculation on PBS^{--} or SFM pre-incubated PS revealed completely spread cells. No significant difference in the degree of spreading could be observed for MDCK-II cells on both types of surfaces, in contrast to the QCM data which clearly indicated that cell attachment and spreading proceeded faster on a PBS^{--} than on a SFM pre-incubated surface (chapter 4.4.3, Fig. 4.43 A and Fig. 4.44 and 4.45). The fact that the second plateau phase was reached only after a quite long period of 860 min and 980 min, respectively, could not be probed by phase contrast micrographs either, since this maximum mirrors the reorganization of the actin cytoskeleton. However, irregularities in size and shape of the cellular bodies as well as less clearly defined cell boundaries 48 h after cell inoculation were apparent in comparison to cells on a plasma modified, pre-incubated surface. This observation might be relatable to the dynamics of actin cytoskeleton reorganization. For a plasma modified, pre-incubated surface, the cells did not discriminate whether the surface had been exposed to PBS^{--} or SFM before cell inoculation, as confirmed by both techniques (chapter 4.4.3, Fig. 4.43 B and Fig. 4.46). It was obvious for both surfaces that the cells appeared more regular in size and shape than on only pre-incubated PS, exhibiting their typical cobblestone morphology under these conditions. This finding might be correlated with the second maximum in the QCM measurements, which was attained already 540 min after cell inoculation. A plasma induced hydrophilization of the PS film allowed for MDCK-II cell attachment and spreading similar to

that observed for plasma treated pre-incubated PS, as indicated by the QCM data as well as the phase contrast micrographs.

Summarizing the results obtained by phase contrast microscopy, it can be concluded that the microscopic observations in general confirm the QCM studies. Significant differences in cellular adhesion such as cell spreading upon plasma modified PS and the inability of cells to spread upon unmodified PS could be easily detected by phase contrast microscopy. However, substrate-dependent differences in the attachment and spreading kinetics of MDCK-II cells for surfaces usually supporting cell adhesion could not be detected microscopically. This is mainly due to the fact that it is possible to microscopically differentiate between spherical cells and completely spread cells, but the different degrees of spreading are hard to detect. For the differently processed PS surfaces, a further important characteristic was the time needed to reach the second maximum, which did significantly differ for the pre-treatments PBS^{--} pre-incubation and plasma exposure, although MDCK-II cells exhibited similar attachment and spreading kinetics on these surfaces. Since this second maximum can be attributed to the dynamics of actin cytoskeleton reorganization, it could not be observed in the phase contrast micrographs. Simply the cell morphology 48 h after cell inoculation differed for both surfaces, but this time was considerably longer than the time for the appearance of the second maximum. Immunocytochemical staining of actin might reveal differences in the actin cytoskeleton, but only the QCM is capable of quantifying these changes as well as following their dynamics due to the technique's sensitivity for cellular micromechanics.

Attachment and Spreading of NRK Cells on Polystyrene

Both techniques revealed that no significant cell attachment and spreading took place on unmodified PS. The phase contrast micrographs showed only a few spread cells on the surface which is in accordance with the slight increase of $\Delta|Z_{min}|$ by roughly 50 Ω. 48 h after cell inoculation, no adherent cells were detected but cell aggregates floating in the culture medium, indicating that the few spread cells did not remain on the surface (chapter 4.4.3, Fig, 4.49 C and Fig. 4.53). The visual examination of the NRK cell morphology after inoculation on pre-incubated and on plasma modified, pre-incubated PS revealed no significant differences with respect to the incubation fluid, PBS^{--} or SFM. Moreover, the spreading kinetics seemed to be similar on both, pre-incubated PS and plasma modified, pre-incubated PS. The rather marginal differences in the NRK cell adhesion kinetics on these two surfaces as recorded with the QCM could not be detected microscopically for reasons mentioned above. The decrease of $\Delta|Z_{min}|$ of roughly 70 Ω recorded for NRK cells on pre-incubated PS and the resulting conclusion that pre-incubated PS may not be long-term cytocompatible is possibly mirrored in the phase contrast micrographs taken 24 h and especially 48 h after seeding: the cells formed a confluent monolayer on the surface, but they did not exhibit their typical cobblestone morphology. The cells were irregular in size and shape with partially overlapping cell domains. For plasma modified PS, the QCM data in accordance with the phase contrast micrographs revealed that cell attachment and spreading was supported on this

surface. However, the rate of cell attachment and spreading was significantly slowed down in comparison to a pre-incubated or a plasma modified, pre-incubated surface.
In summary, the microscopic study of NRK cell attachment and spreading could be correlated with the QCM results, mainly confirming the QCM-based spreading data for the respective surface condition. For slight differences in cell adhesion kinetics, as observed for pre-incubated and plasma modified, pre-incubated PS, only the QCM technique has the required sensitivity to monitor marginal differences in cellular micromechanics during spreading. Another fact that was obvious is that the time courses obtained for the QCM based adhesion kinetics were different from that extracted from phase contrast micrographs. Whereas the QCM measurements indicated a confluent monolayer on the resonator surface already 240 min after cell inoculation on pre-incubated PS and on plasma modified, pre-incubated PS, the visual examination gave a confluent monolayer only after 360 – 480 min. This discrepancy between the microscopic and the QCM data might arise from the regular disturbances of the adhesion process by removal of the substrates from the incubator and their transport to the microscope. This might lead to a significant delay in the process of cell attachment and spreading. By contrast, the QCM allowed monitoring of the cell attachment and spreading without intervention, presenting the undisturbed cellular response in real time.

Attachment and Spreading of MDCK-II Cells on Poly(methyl methacrylate)

The microscopic data mainly reflected the general trend of the QCM measurements. Both methods showed that only a fraction of the inoculated cells spread on unmodified PMMA during the incubation period of 20 h. A longer period of incubation, as seen in the phase contrast micrograph taken 48 h after cell inoculation, allowed the cells to spread and almost entirely cover the substrate surface (chapter 4.4.4, Fig. 4.59). This might be indicated by the increase in $\Delta|Z_{min}|$ recorded in the QCM experiment in the time interval of 600 – 1200 min after inoculation (chapter 4.4.4, Fig. 4.55). The minor differences in the cell attachment and spreading kinetics as returned from QCM measurements for MDCK-II cells seeded upon PBS^{--} pre-incubated, on plasma modified or on plasma modified, pre-incubated PMMA were all observed in a time frame of 120 – 200 min, and thus could not be resolved by phase contrast images due to the technique's inability to visualize minor variations in the degree of cell spreading. The microscopic documentation for these surfaces 120 min after cell inoculation did not only reveal a rather similar picture, they also showed mainly spherical cells and a minor fraction of spread cells on the surface. This indicates a slowdown of the cell attachment and spreading rate in the microscopic study in comparison to the QCM analysis where a confluent MDCK-II monolayer was attained already 120 – 200 min after inoculation for PBS^{--} pre-incubated PMMA, plasma modified PMMA and plasma modified pre-incubated PMMA. By contrast, the phase contrast micrographs did not show a confluent monolayer before 360 – 480 min. This difference in the adhesion kinetics is due to the reasons mentioned above for PS. The significant decrease of $\Delta|Z_{min}|$ by 220 – 340 Ω after having passed the second maximum recorded for all surface conditions except for unmodified

PMMA might be mirrored in the phase contrast micrographs. 48 h after inoculation, MDCK-II cells grown in a confluent monolayer did not reveal clearly visible cell boundaries as they are usually observed on cytocompatible substrates (compare chapter 4.4.4, Fig. 4.56, and appendix D.5, Fig. D.23). Moreover, several cells exhibited a shriveled morphology or were rounded, possibly indicating apoptotic and/or detaching cells.

Attachment and Spreading of NRK Cells on Poly(methyl methacrylate)

The microscopic study in accordance with the QCM measurements showed that attachment and spreading of NRK cells upon unmodified PMMA was possible, but it took significantly longer than for the other surface conditions. The phase contrast micrograph taken 24 h after inoculation revealed a confluent cell monolayer, which was in good agreement with the QCM data (chapter 4.4.4, Fig. 4.61 C and 4.64). The roughly 100 – 150 Ω lower $\Delta|Z_{min}|$ value for unmodified PMMA compared to the values for the other PMMA surfaces might be correlated to the irregularities in cell morphology observed microscopically, showing some cells with elongated extensions. In contrast to the QCM-based spreading data, the microscopic study did not detect differences in the spreading kinetics for NRK cells seeded upon pre-incubated PMMA as well as plasma modified PMMA. As indicated by the similar slope of the attachment curve for both surface conditions (chapter 4.4.4, Tab. 4.21), this difference is too small as it could be resolved by the microscopic observation of the degree of spreading. 120 min after inoculation, almost all cells on both surfaces exhibited a spherical morphology whereas after 240 min, a significant fraction of the cells had spread (chapter 4.4.4, Fig. 4.62 and 4.65). Only for cells seeded upon plasma modified pre-incubated PMMA, an increase in the spreading rate could be observed as indicated by the phase contrast micrograph taken after 120 min, showing a small fraction of spread cells. This finding is in accordance with the QCM data, which identified cell attachment and spreading to be the fastest on plasma modified pre-incubated PMMA (chapter 4.4.4, Fig. 4.61 B and 4.63). However, the QCM measurements gave no hints regarding the irregularities in the cell size and shape for the confluent NRK cell layer grown on pre-incubated PMMA (chapter 4.4.4, Fig. 4.62). This might be due to the fact that the cells obviously grew on top of each other and this multilayer was not accessible to the QCM technique. Analogous to the observations made before, the cell attachment and spreading kinetics in the microscopic study were slowed down when compared to the QCM measurements for reasons mentioned above. Although the adhesion kinetics differed for both studies, the general trend for the adhesion kinetics observed microscopically is consistent with the QCM data. Thus, the phase contrast micrographs confirm the results obtained by the QCM measurements.

Attachment and Spreading of MDCK-II Cells on Poly(dimethyl siloxane)

The phase contrast micrographs as well as the QCM data revealed that MDCK-II cell attachment and spreading took place on both, the unmodified and the SFM pre-incubated PDMS surfaces. The rate of cell attachment and spreading was slowed down on the

unmodified PDMS surface compared to the SFM pre-incubated one. The phase contrast micrographs showed the onset of cell spreading on unmodified PDMS only 360 – 480 min after inoculation whereas on pre-incubated PDMS, a fraction of the cells was already spread 120 min after inoculation (chapter 4.4.5, Fig. 4.67 and 4.68). This trend could also be confirmed by QCM measurements (chapter 4.4.5, Fig. 4.66). Cell attachment and spreading upon unmodified PDMS took quite long and after completion of this process the cells did not exhibit their typical morphology. A hint in the QCM data for this observation could be the fact that $\Delta|Z_{min}|$ was roughly 140 Ω lower than that obtained for a cytocompatible gold surface. For MDCK-II cells seeded upon the SFM pre-incubated PDMS surface, only the QCM data revealed that the surface was not long-term cytocompatible, as indicated by the significant decrease of $\Delta|Z_{min}|$ of roughly 190 Ω after having passed the second maximum. By contrast, the microscopic study showed MDCK-II cells with their typical cobblestone morphology. Again, the microscopic data indicated a slowdown of the spreading rate compared to the QCM measurements possibly due to intervention in the system during the microscopic examination.

Attachment and Spreading of NRK Cells on Poly(dimethyl siloxane)

The microscopic data supported the QCM results although both techniques did not show the same adhesion kinetics, the overall trend was similar. NRK cells attached and spread upon SFM pre-incubated PDMS and formed a confluent monolayer (chapter 4.4.5, Fig. 4.69 A and 4.70). The phase contrast micrograph taken after 48 h revealed that this surface was not long-term cytocompatible, since the cells looked not uniform in size and shape and exhibited elongated extensions. This finding might be correlated to the fact that the stationary $\Delta|Z_{min}|$ value was roughly 90 Ω lower than that for a cytocompatible gold surface. The unmodified PDMS surface was not cytocompatible either. As revealed by the QCM experiments, it took about 1100 min to reach the stationary $|Z_{min}|$ value which was approximately 170 Ω lower than the one for the gold surface. The phase micrographs revealed a surface coverage of only 20 % after 24 h and even after 48 h, the cells had not built a confluent monolayer (chapter 4.4.5, Fig. 4.71).

Attachment and Spreading of MDCK-II Cells on Photopolymer

The QCM technique as well as the microscopic observation revealed similar attachment and spreading kinetics for MDCK-II cells seeded upon pre-incubated PhoP and plasma modified pre-incubated PhoP (chapter 4.4.6, Tab. 4.22 and Fig. 4.73 and 4.74). Again, the spreading rate was decreased in the microscopic study. Whereas the QCM data indicated the formation of a confluent cell layer within 100 – 140 min, the phase contrast micrographs showed a confluent cell layer only after 480 – 600 min. The cells were of uniform size and shape and exhibited their typical cobblestone morphology on both surfaces. The QCM data mainly revealed significant differences in the time needed to reach the second maximum and thus to

reorganize the actin cytoskeleton. This process could not be detected or even quantified by simple phase contrast microscopy.

In summary, the comparison of the QCM-based spreading data with the visual examination of the cell morphology (phase contrast micrographs) has revealed that the microscopic study basically confirmed the cellular response detected via QCM measurements. The inconsistency in the attachment and spreading kinetics as recorded by these two methods – a significant slowdown of the spreading rate was observed in the microscopic study – might be attributed to the interference in the adhesion process during the microscopic examination. For instance, the removal of the culture substrates from the incubator and their exposure to room temperature as well as motion of the culture substrates due to the microscopic documentation might manipulate and thus reduce the attachment and spreading rate.
The microscopic study could differentiate between surfaces which generally supported or retarded/inhibited cell attachment and spreading via the number of spread cells on the surface. But only the QCM technique could reveal the degree of surface cytocompatibility, analyzing and quantifying even subtle differences in the kinetics of cell attachment and spreading due to the technique's high time resolution and sensitivity to cellular micromechanics. Moreover, the microscopic evaluation of the cell morphology, in particular the degree of spreading, was subjective dependent on the operator whereas the QCM provided quantitative data of cell attachment and spreading. The fully automated approach of QCM measurements carried out under computer control avoided any handling of the surfaces to perform the measurement as it was necessary for microscopic evaluation of cell behavior. Furthermore, the QCM technique also provided quantitative data concerning cell-type specific characteristics, such as the dynamics of actin cytoskeleton reorganization of MDCK-II cells, which could not be detected or even quantified microscopically.
Thus, the developed QCM-based biosensor proved to be capable of quantifying the attachment and spreading characteristics of MDCK-II and NRK cells on the different polymer films with a high time resolution, providing a useful means to evaluate the cytocompatibility of the spin coated polymer films.

The experimental QCM data in this work studying the cytocompatibility of different polymer surfaces from various perspectives revealed that hydrophobic, unmodified polymers prevent cell adhesion only when they exhibit a smooth surface topography, as shown at the example of PS. Here, the proteins are thought to adsorb under conformational rearrangement on the polymer surface, avoiding the accessibility of the integrin binding sites. In the case of hydrophobic polymers with a rough surface topography, cell attachment and spreading is possible, as shown at the example of PDMS. This might be attributed to the fact that the surface-immobilized proteins exhibit the appropriate orientation on such surfaces and can be recognized by the cellular integrins. The assumption that surface topography can mask the negative effect of a hydrophobic surface might also be confirmed by the finding that pre-incubation of the hydrophobic polymer films in a physiological fluid promoted cell

attachment and spreading upon most of the polymer surfaces. As revealed by contact angle measurements, fluid pre-incubation of the polymer films mainly resulted in an increase in surface roughness without altering surface wettability. Hydrophilic polymer surfaces, as generated by exposure of the polymer films to an argon plasma, promoted cell attachment and spreading. The argon plasma treatment mainly led to a polymer-specific increase in surface wettability (hydrophilization), allowing the proteins to adsorb without unfolding, thus rendering the surface cytocompatible. The results of this study indicate that polymer surface properties have a complex and individual impact on cell attachment and spreading, mainly because two influencing parameters – surface wettability and surface roughness – are involved, which govern the molecular and the cellular response. No simple rule can be deduced from these measurements to predict the biocompatibility of a polymer surface.

So far, the QCM could be successfully established as a biosensor to probe the biocompatibility of different polymers. Cell attachment and spreading upon the polymer films was quantified by means of different kinetic parameters. Furthermore, it would be interesting to extend the cytocompatibility study by quantifying the strength of cell adhesion, i.e. the mechanical stability of cell-substrate contacts, on the different polymer surfaces. Following the experimental rationale described by Heitmann (2008), the QCM might be used in the actuator mode, where the resonator is used at elevated lateral shear amplitudes which can be controlled by the applied voltage. Shear oscillations of gradually increasing amplitudes might be applied to the established confluent cell layer on the different polymers and studied for a possible threshold shear amplitude to disrupt established cell-substrate contacts and displace the attached cells from the polymer surface. Another possible approach would be to apply shear stress at distinct time points during cell attachment and spreading to probe the quality of the cell-substrate interactions in a time resolved manner. This could give access to the time point after cell seeding where the cell-substrate contacts will be strong enough to resist the shear stress.

The results reported here indicate that the QCM-based biosensor is highly sensitive and well-adapted to analyze and quantify the biocompatibility of different polymer films from various perspectives. In addition, this biocompatibility study may also contribute to a fundamental understanding of the decisive material surface properties, like wettability and roughness, and how these govern the response of the contacting biological system (proteins and cells).
Furthermore, this approach may be particularly useful in biomaterials research. The applicability of this sensor to other polymers or a variety of other materials like metals or ceramics will facilitate the identification of new biomaterials that are tailored to the requirements of a specific biotechnological or biomedical application. In addition, surface modifications of biomaterials can be easily studied for their success or failure in achieving the demanded surface biocompatibility. This makes the QCM an extremely useful tool to evaluate the biocompatibility of diverse biomaterials as well as to find correlations between material surface properties and the response of a biological system.

5 An Impedimetric Biosensor to Study the Impact of Surface Topography on Cell-Surface Interactions

This part of the thesis focuses on the development and evaluation of an impedimetric biosensor capable of characterizing cell-surface interactions on substrates with different surface topographies. The topographies were modeled by mesoporous silicon substrates. The impact of surface topography on cell-surface interactions was analyzed with respect to cell attachment and spreading, cell differentiation as well as cellular micromotion. In addition, the electrical properties of the cell layer after differentiation on these different surface topographies were quantified by analyzing frequency-resolved impedance data with an established physical model for adherent cells.

5.1 Microscopic Characterization of Mesoporous Silicon Substrates

The mesoporous silicon substrates were kindly provided by Dr. Petra Göring (MPI für Mikrostrukturphysik, Halle, Germany) from the research group of Prof. Dr. Gösele. These substrates are based on silicon wafers with pores on one side of the wafer. Two different types of mesoporous substrates were used in this study, which are presented in Fig. 5.1 and Fig. 5.3. Regardless of the individual surface topography, all mesoporous silicon substrates are coated with a ~ 100 nm thick layer of silicon dioxide in order to insulate the silicon substrate surface for electrochemical measurements. This was performed at the MPI in Halle by thermal oxidation at 900 °C in air, providing a homogeneous oxide layer on the surface and the inner walls of the pores.

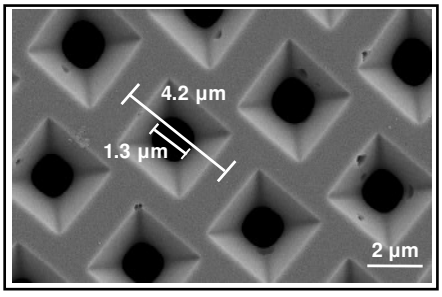

Fig. 5.1 SEM micrograph (nanoAnalytics GmbH, Münster, Germany) of the surface topography of a mesoporous silicon substrate type I (top view). The pyramidal pre-etched areas form a pit which tapers into a pore. The lattice constant is 4.2 µm and the pore diameter amounts to 1.3 µm.

The SEM micrograph (Fig. 5.1) shows the surface topography of a mesoporous silicon substrate, which is termed type I from now on. Mesoporous silicon substrates type I contain pores that are arranged in a hexagonal lattice with a pore diameter of 1.3 µm, a pore depth of 10 µm and an interpore distance of 4.2 µm (lattice constant). Additionally, this substrate type exhibits inverted pyramidal pre-etched areas that taper into a pore, so-called KOH-pits. They arise during a pre-structuring process of the silicon substrate that involves alkaline etching and is used to define nucleation spots of the pores at the silicon surface. Figure 5.2 shows a schematic side view and top view of the silicon substrate type I.

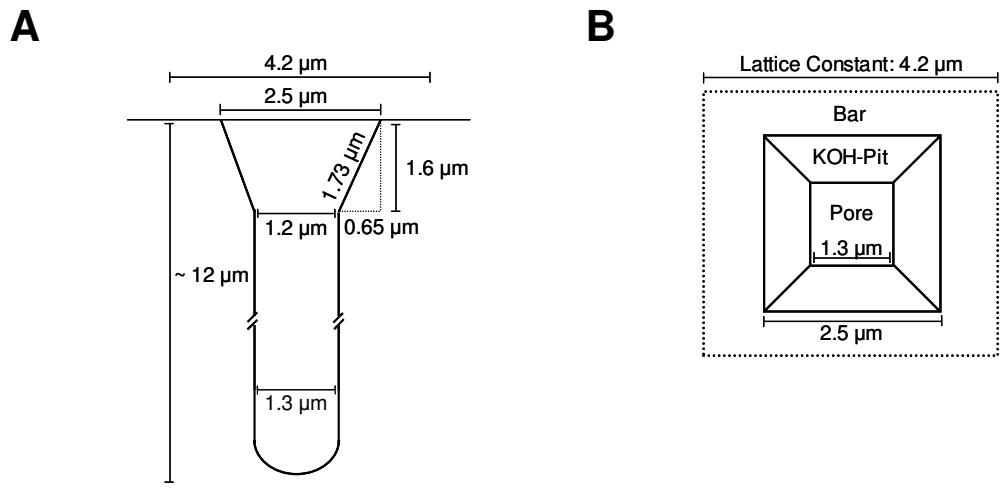

Fig. 5.2 Schematic presentation of a single pore from the hexagonal lattice of a mesoporous silicon substrate (type I). **A** Side view of a pore and the corresponding pre-etched area. **B** Top view on a single pore of the hexagonal lattice (pore diameter: 1.3 µm, pore depth: 10 µm, lattice constant: 4.2 µm, width of the ridges: 1.7 µm).

Based on the parameters presented in Fig. 5.2, the fraction of the surface with no topographic elements relative to an entirely flat reference surface can be calculated. The mesoporous silicon surface provides a fraction of 65 % of unstructured growth surface presumably available for the attachment of cells – given that the basal cell membrane does not follow the surface topography – whereas the remaining fraction is covered by pores and the KOH-pits. The KOH-pits have an inclination angle of approximately 68° and are located by as much as 1.6 µm underneath the planar surface.

The other substrate type used in this study is termed silicon substrate type II. This type comprises a group of three different mesoporous silicon substrates on whose surface the KOH-pits have been almost entirely removed. Type II substrates exhibit a similar lattice constant of 2 µm and a pore depth of 10 µm. They differ in pore diameter and width of the ridges, resulting in individual surface topographies (Fig. 5.3), and are therefore further devided into the categories 1 – 3. The parameters for all substrates are summarized in chapter 3.6.4.1 (Tab. 3.4).

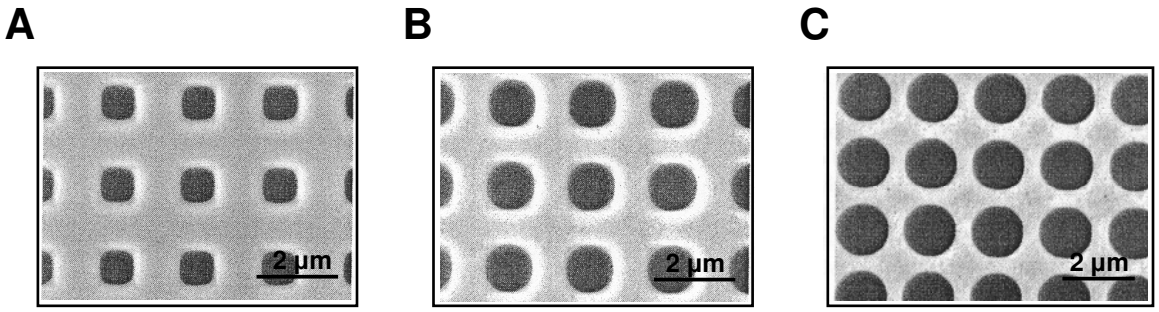

Fig. 5.3 SEM micrographs (MPI für Mikrostrukturphysik, Halle, Germany) of the surface topography of mesoporous silicon substrates type II (top view). The lattice constant is 2 µm and the pore depth amounts to 10 µm. The substrates exhibit different pore diameters (Ø) and widths of the ridges (b). **A** Ø = 700 –750 nm, b = 1000 nm; **B** Ø = 1000 nm, b = 750 nm; **C** Ø = 1350 – 1400 nm, b = 360 – 400 nm. The KOH-pits have been almost completely removed.

The fraction of the unstructured growth surface available for cell adhesion relative to an entirely flat reference surface decreases with increasing pore size as follows: ~ 89 % (type II 1, Ø = 700 – 750 nm), 80 % (type II 2, Ø = 1000 nm) and ~ 63 % (type II 3, Ø = 1350 –1400 nm).

In order to analyze the cellular response upon growth substrates with different topographies via the ECIS technique, the mesoporous silicon substrates were first sputter coated with a 100 nm thin gold film, that should serve as a measuring electrode without changing surface structures. By means of photolithography (chapter 3.6.4.2) a well-defined electrode layout was established on the substrate surface. After electric insulation of the gold contact line (gold path), a working electrode with a surface area of $A \sim 0.03$ cm^2 was obtained.
Figure 5.4 shows SEM micrographs of a gold coated mesoporous silicon substrate type I. Directly after sputter deposition of gold, the gold film covers the ridges as well as the KOH-pits of the silicon substrate homogeneously (Fig. 5.4 A). The electrode layout is sharply confined (Fig. 5.4 B). However, the gold film was affected by the photolithographic process as indicated by cracks within the gold film (Fig. 5.4 B and C). This surface roughness might contribute to a surface enlargement. Figure 5.4 D shows a gold layer which partly delaminates from the silicon surface, verifying that the KOH-pits are completely coated with a gold film during sputter deposition. Additionally, the uppermost region of the pores seems to be coated with gold as well, but the extent to which the inner walls of the pores may also be coated with gold and, thus, are electrically active can not be deduced from these SEM micrographs.

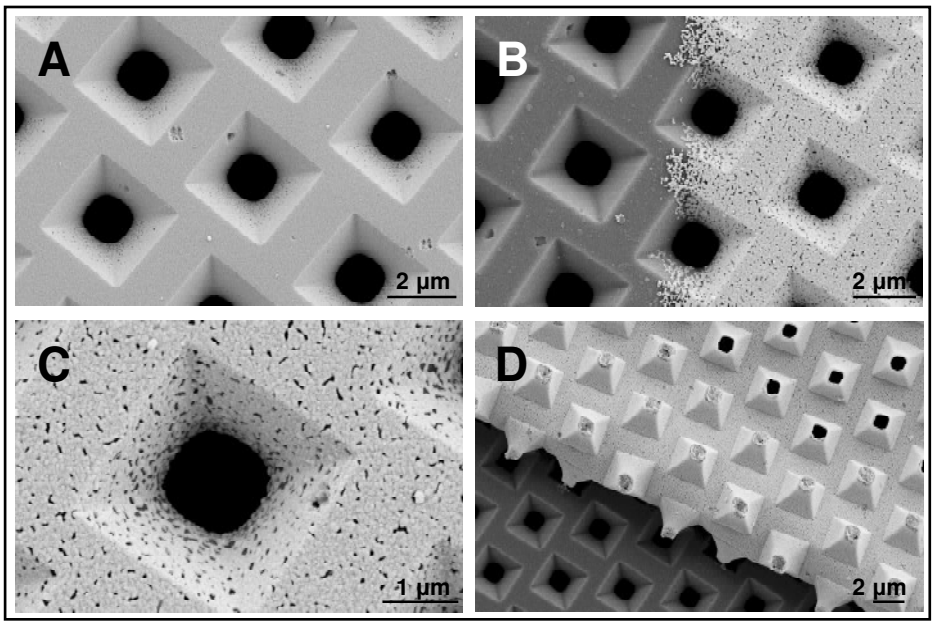

Fig. 5.4 SEM micrographs (nanoAnalytics GmbH, Münster, Germany) of a gold coated mesoporous silicon substrate (type I). **A** Complete surface coverage with gold directly after sputter deposition. **B** Gold film after photolithographic processing. A sharp border between silicon dioxide and the gold film is visible. The gold film exhibits a rough surface structure and cracks within the coating. **C** Magnification of B showing one gold coated pore. **D** Delaminating gold film, confirming a complete coating of the pyramidal KOH-pits with gold.

In summary, the SEM micrographs reveal that after sputter deposition of gold and photolithography, the gold film completely covers the ridges as well as the KOH-pits. The porous structure of the substrate is maintained. With respect to subsequent impedimetric measurements, the planar ridges as well as the pyramidal KOH-pits can be regarded to be electrically accessible.

Based on these findings and the parameters of the mesoporous substrate presented in Fig. 5.2, the electrically active area, comprising the planar ridges as well as the pyramidal KOH-pits, is 37 % larger than an entirely flat reference surface. A possible change of the surface area due to the rough topography of the sputtered gold film or gold coated parts of the inner walls of the pores is disregarded. This calculated enlargement of the electrically active area will be important when comparing the results of impedimetric measurements using flat and mesoporous gold film electrodes of similar geometrical surface area.

Since no precise data concerning the KOH-pits in the surface of type II silicon substrates were available and to which extent they have been removed, the enlargement of the electrically active area after sputter deposition of gold and subsequent photolithography is not calculated for this substrate type.

5.2 Applicability of Mesoporous Silicon Substrates as Growth Substrates for Mammalian Cells

MDCK-II cells were used as a model epithelial cell line of adherently growing barrier-forming cells in order to quantify the impact of surface topography on cell-surface interactions. The applicability of the mesoporous silicon substrates as growth substrates for mammalian cells is a crucial prerequisite for subsequent impedimetric measurements and has been validated in a previous study (Michaelis, 2005). The basic results are shortly summarized below. It was shown that the substrates were easily wettable with culture medium and pore filling occured instantaneously after fluid exposure. MDCK-II cells were able to attach and spread upon the mesoporous substrates and formed a confluent monolayer revealing their typical cobblestone morphology. For a qualitative evaluation of the state of cell differentiation on mesoporous silicon substrates, the cells were stained for their actin cytoskeleton as well as the tight junction associated protein ZO-1 (*zonula occludens*) and analyzed microscopically in direct comparison to cells cultured on planar glass substrates.

The staining of the actin cytoskeleton of MDCK-II cells cultured on type I mesoporous silicon substrates using TRITC-phalloidin correctly revealed three prominent actin structures in the fluorescence micrographs: the microvilli, the actin belt and the actin stress fibres. The microvilli, finger-like protrusions of the apical cell membrane, could be identified as blurred, spot like fluorescence signals in the region of the apical cell membrane. The junctional actin belt following the cell periphery and stabilizing cell-cell junctions was detected in the fluorescence micrograph as well. The actin stress fibres, parallel bundles of microfilaments that run along the lower membrane interconnecting different sites of cell-substrate adhesion, were present as well. The three components of the actin cytoskeleton were expressed to a similar extend as by MDCK-II cells cultured on planar glass substrates. Only the expression of actin stress fibres seemed to be slightly reduced for cells cultured on mesoporous silicon substrates.

The immuncytochemical staining of the tight junction associated protein ZO-1 of MDCK-II cells cultured on mesoporous substrates revealed a sharply localized fluorescence along the cell perimeter where the tight junctions are located. ZO-1 expression and localization was similar for MDCK-II cells cultured on both mesoporous silicon and planar glass substrates.

In summary, the degree of MDCK-II cell differentiation was found to be similar for planar and mesoporous growth substrates. Thus, the mesoporous silicon substrates can be regarded as a cytocompatible surface providing all requirements for cell attachment and spreading. Cell-cell contacts (tight junctions) are formed and MDCK-II cells are completely differentiated on mesoporous silicon substrates.

5.3 Adhesion and Differentiation of MDCK-II Cells on Mesoporous Silicon Substrates (Type I)

In order to quantify the impact of surface topography on cellular parameters by means of impedimetric ECIS measurements, the mesoporous silicon substrates were coated with a gold film in a well-defined electrode layout. Since the ECIS technique uses planar gold film electrodes, a preceding impedimetric characterization of the cell-free mesoporous gold film electrodes in comparison to planar ones should reveal the influence of the porous surface topography on the impedance spectra. This should contribute to an understanding of the impedance data obtained after the deposition of cells on the porous electrode surface. Lexan substrates served as a flat reference surface on which the electrode layout was established in a similar manner as on the mesoporous silicon substrates.

5.3.1 Impedimetric Characterization of Cell-Free Mesoporous and Planar Gold Film Electrodes

Sputter deposition of a gold film on the mesoporous silicon substrate has been shown to result in a complete surface coverage (chapter 5.1). The SEM micrographs demonstrated the coverage of the ridges as well as the KOH-pits with gold, which should lead to a theoretical surface enlargement of the electrically active area of 37 % compared to a planar reference surface of the same geometrical size[1]. However, the SEM micrographs could not clarify if the gold coated KOH-pits are electrically connected with the gold coated ridges. Thus, impedance spectra of a mesoporous and a planar cell-free gold film electrode were recorded and compared to each other.

The process of the electrode production on the mesoporous silicon substrates and the planar Lexan substrates was identical (chapter 3.6.4.2), so that both mesoporous and planar gold film electrodes exhibit a similar geometrical surface area of $A \sim 0.03$ cm^2. The precise surface area of the electrode was determined by taking microscopic reflection images using the confocal laser scanning microscope.

Figure 5.5 A depicts a typical impedance spectrum for a cell-free porous gold film electrode in comparison to a planar gold film electrode of similar geometrical size measured in culture medium. For high frequencies ($f > 10^4$ Hz), the course of the impedance for both gold film electrodes is almost frequency-independent. The total impedance of the system is dominated by the bulk resistance of the electrolyte. At lower frequencies ($f < 400$ Hz) the capacitance of the electrode-electrolyte interface dominates the impedance spectrum. Comparison of the impedance spectra for the cell-free electrodes of planar and mesoporous topography reveals a similar impedance spectrum for both electrodes but the impedance spectrum for the porous gold film electrode is shifted to lower frequencies. This indicates that the electrically active

[1] The geometrical size depends on the microscopic reflection image (CLSM) and does not consider any three dimensional topographical features of the surface.

area is significantly bigger for the porous gold film electrode even though the geometrical surface area for both electrodes is similar. This can be pinpointed to the coating of the KOH-pits with gold, which leads to a significant surface enlargement of the porous gold film electrode (see chapter 5.1).

The complex impedance of the system was separated into its real and imaginary components, presented by the resistance R and the capacitance C, in order to allow for a more detailed analysis. For the same electrode material the electrode capacitance only depends on the surface area when assuming identical experimental conditions for both substrates. Thus, the capacitance can be used to determine the electrically active area of the electrode. As shown in Fig. 5.5 A, the capacitance of the electrode-electrolyte interface dominates the impedance spectrum in the frequency range of $f < 400$ Hz. Thus, the capacitive component of the total impedance in this frequency range mirrors the capacitance of the gold film electrode.
Figure 5.5 B exemplarily compares the course of the capacitance C recorded in a frequency range of $10^{-1} - 10^{5}$ Hz for a mesoporous and a planar gold film electrode exposed to culture medium. Along the frequency range of 1 – 400 Hz, the capacitance exhibits a more or less constant value. For high frequencies ($f > 10^{3}$ Hz), the capacitance shows a significant decrease, which is mainly an artifact due to parasitic contributions of the electronic equipment and wiring. In the impedance spectrum (Fig. 5.5 A), this capacitance decrease at high frequencies is masked by the bulk resistance of the electrolyte. Thus, when determining and comparing the electrode capacitance for both substrate topographies, it is essential to choose a frequency below 400 Hz.

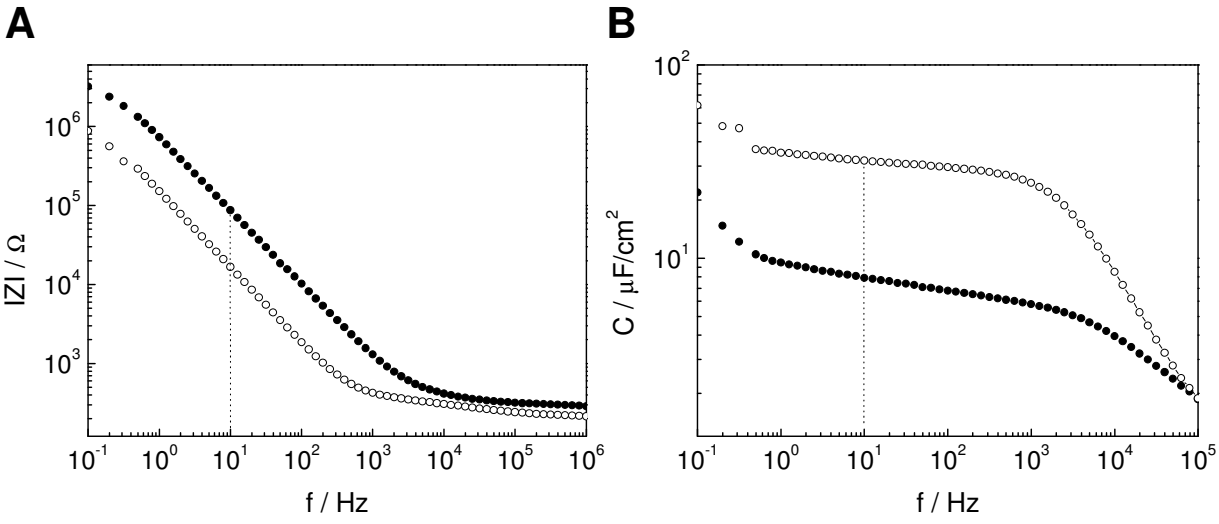

Fig. 5.5 ECIS data of a flat (Lexan substrate) (●) and a mesoporous (silicon substrate type I) (○) gold film electrode of similar geometrical surface area ((●) $A = 0.023$ cm^2 and (○) $A = 0.030$ cm^2). **A** Impedance spectra and **B** spectra of the area normalized capacitance C recorded in a frequency range of $10^{-1} - 10^{6}$ Hz. The horizontal line indicates the capacitance values at 10 Hz used for the calculation of the surface enlargement.

A sampling frequency of 10 Hz was used to compare the capacitance values of the mesoporous and the planar gold film electrodes, providing electrochemical information on a possible enlargement of the electrically active area due to the porous surface topography. Determination of the electrode capacitance at 10 Hz and division by the geometrical surface area of the electrode returns the area normalized capacitance. Planar gold film electrodes prepared on Lexan substrates reveal an area normalized capacitance of (9.16 ± 0.98) μF/cm^2 (n = 5, mean ± SDM). For mesoporous electrodes on type I silicon substrates a value of (32.93 ± 0.60) μF/cm^2 (n = 7, mean ± SDM) is obtained. This increase of the area normalized capacitance for mesoporous gold film electrodes corresponds to an increase in the electrically active area. However, an increase by a factor of 3.6 is considerably higher than the theoretically calculated surface enlargement, so that in addition to gold coated ridges and KOH-pits further factors such as coating of the inner walls of the pores with gold as well as surface roughness of the gold film obviously play an important role.

5.3.2 Adhesion and Differentiation Kinetics of MDCK-II Cells on Mesoporous and Planar Gold Film Electrodes

Using the ECIS technique, the adhesion and differentiation characteristics of MDCK-II cells on mesoporous substrates were studied in a time-resolved manner. In order to quantify the impact of surface topography on these fundamental biological processes, comparative impedimetric measurements using a planar reference surface, i.e. planar gold film electrodes prepared on Lexan substrates of similar geometrical surface area, were performed.
Initially suspended MDCK-II cells were seeded to confluence onto the mesoporous and planar substrates with the established electrode layouts (A ~ 0.03 cm^2) using serum-containing medium as culture fluid. ECIS measurements were performed with the experimental setup and the self-made measuring chamber introduced in chapter 3.6.4.3 (Fig. 3.35 and 3.36). Immediately after cell inoculation, data acquisition was started by continuously recording impedance spectra in a frequency range between 10^{-1} Hz and 10^5 Hz using a sinusoidal AC voltage of 10 mV.

Figure 5.6 exemplarily shows the course of the impedance |Z|, the resistance R and the capacitance C recorded in the frequency range of 10^{-1} – 10^5 Hz for a medium-loaded mesoporous gold film electrode and the same electrode with an additional monolayer of MDCK-II cells present on its surface (A = 0.030 cm^2).
The presence of cells on the electrode surface primarily affects the impedance spectrum at intermediate frequencies between 15 Hz and 10^4 Hz (Fig. 5.6 A). At the highest frequencies ($f > 10^4$ Hz), the two plots merge to a horizontal plateau that represents the ohmic solution resistance between the working electrode and the counter electrode (gold dipping electrode).

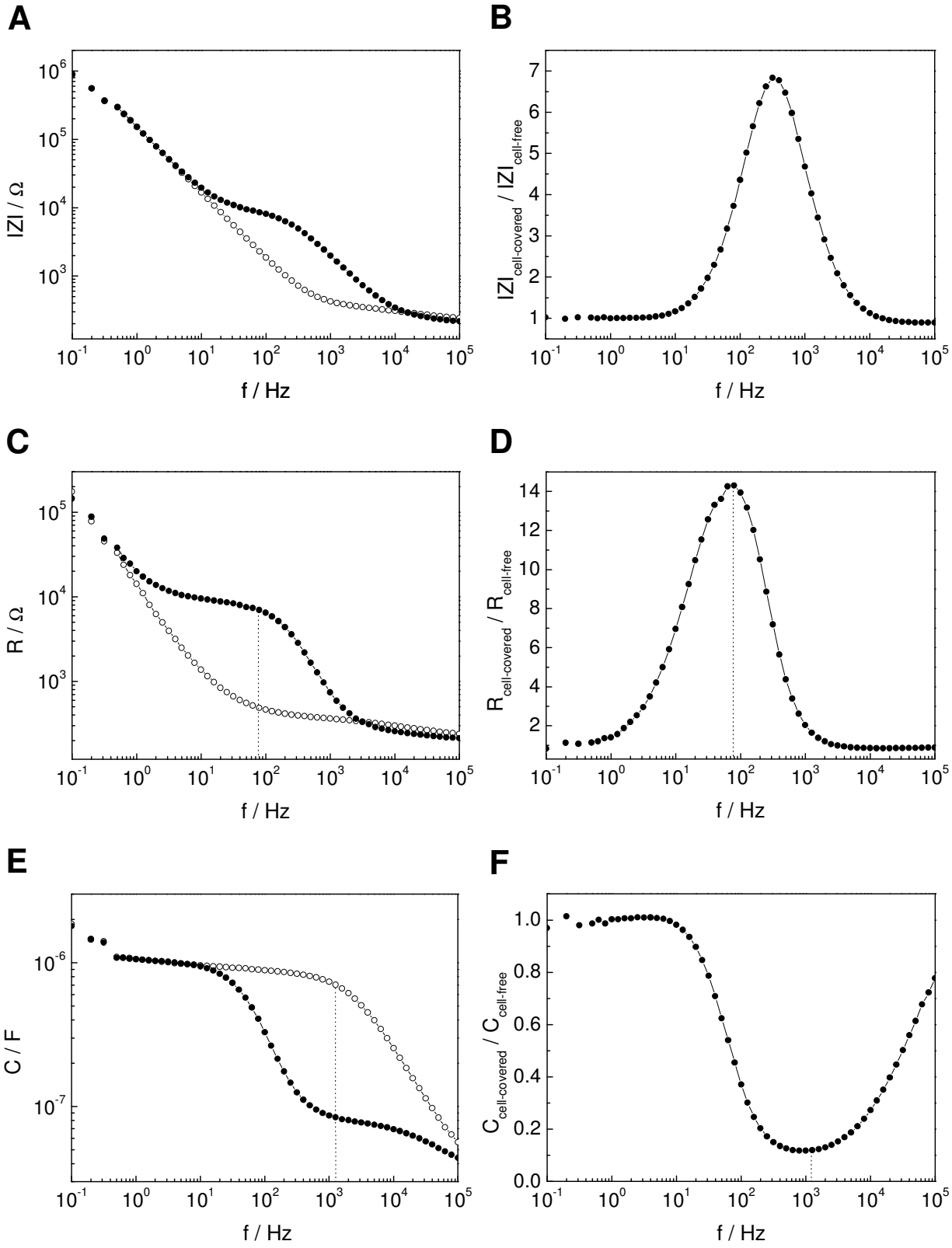

Fig. 5.6 Data of a typical ECIS experiment using a mesoporous gold film electrode ($A = 0.030$ cm^2) with (●) and without (○) a confluent monolayer of MDCK-II cells grown on the electrode surface. **A** The impedance spectrum of a mesoporous gold film electrode, **C** the resistive portion of the impedance and **E** the capacitance of the system in a frequency range between $10^{-1} - 10^5$ Hz. **B**, **D** and **F** show the normalized values of the respective quantities ($|X|_{cell-covered}/|X|_{cell-free}$) plotted against the frequency. The vertical lines in C, D and E, F indicate the sampling frequency used for time-resolved resistance or capacitance measurements.

The best sampling frequency with the contribution of the cell layer dominating the total impedance of the system is determined by dividing the impedance spectrum of the cell-covered electrode by the spectrum of the same cell-free, only medium-covered electrode (Fig. 5.6 B). In doing so, the most sensitive frequency for time-resolved impedance measurements can be found for a frequency of 300 Hz, which is indicated by a maximum in the ratio $|Z|_{\text{cell-covered}}(f)/|Z|_{\text{cell-free}}(f)$.

The resistance spectrum is affected by the presence of cells on the electrode surface in a frequency range of 1 – 2000 Hz (Fig. 5.6 C). Time-resolved resistance measurements to follow cell differentiation are most sensitive when using a sampling frequency of 80 Hz, as indicated by the peak of the normalized resistance $R_{\text{cell-covered}}(f)/R_{\text{cell-free}}(f)$ (Fig. 5.6 D). It is noteworthy that the most sensitive frequency may change with the electrode size and the individual electrical properties of the cells under study. For planar gold film electrodes of similar geometrical size, the contribution of the cell layer to the total resistance of the system is most pronounced at a frequency of 200 Hz (data not shown). Thus, a frequency of 80 Hz was selected in order to guarantee highly sensitive resistance measurements on mesoporous gold film electrodes and a frequency of 200 Hz was applied to follow the time course of R for MDCK-II cells seeded upon planar gold film electrodes.

Figure 5.6 E compares the capacitance spectrum of a cell-covered mesoporous electrode to the spectrum of a cell-free, medium-covered electrode. At low frequencies ($f < 10$ Hz), the capacitance spectrum for a cell-covered electrode is equal to the spectrum measured for a cell-free electrode, showing a horizontal plateau. For $f > 10$ Hz, the capacitance decreases due to the attachment and spreading of dielectric cell bodies on the electrode surface. The normalized capacitance spectrum reveals the most sensitive frequency to be 2 kHz where the contribution of the cell layer dominates the total capacitance of the system (Fig. 5.6 F). Thus, time-resolved capacitance measurements were performed at a frequency of 2 kHz, reflecting the formation of close cell-electrode contacts and reporting on the time course of cell attachment and spreading.

In the following, the time courses of the quantities C_{norm} measured at 2 kHz and R_{norm} measured at either 80 Hz (for mesoporous electrodes) or 200 Hz (for planar electrodes) are shown and compared for MDCK-II cells during their adhesion and differentiation on mesoporous and planar gold film electrodes.

Figure 5.7 traces the time course of the normalized capacitance C_{norm} at a sampling frequency of 2 kHz during attachment and spreading of initially suspended MDCK-II cells upon mesoporous and planar gold film electrodes, starting directly after seeding a suspension of MDCK-II cells to confluence onto the substrate surfaces.

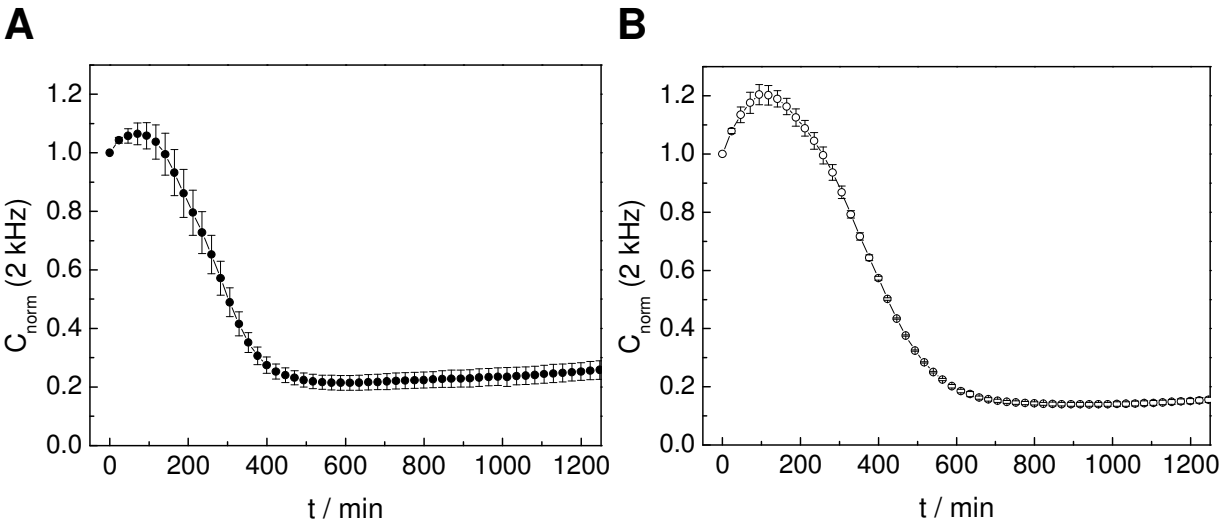

Fig. 5.7 Time course of the normalized electrode capacitance C_{norm} at 2 kHz during attachment and spreading of initially suspended MDCK-II cells on planar (**A**) and mesoporous (**B**) gold film electrodes. The cells were seeded in a density of 1 x 10^6 cm^{-2} on the substrate surface at time point zero. The values of C were normalized to the first C value of the measurement. ((●) C_{start} = (6.61 ± 0.77) µF/cm^2, (○) C_{start} = (17.83 ± 1.16) µF/cm^2; mean ± SDM, n = 4; T = 37 °C).

When MDCK-II cells attach and spread on the planar electrode surface, C_{norm} decreases within 500 min to a stationary value, accounting for one fifths of the initial capacitance value (Fig. 5.7 A). This final value of C_{norm} corresponds to a confluent monolayer of cells on the substrate surface and the decrease in C_{norm} with time mirrors the kinetics of cell spreading. The time that is needed to attain half-maximal capacitance decrease and thus half-maximal surface coverage is measured to be $\tau_{1/2}$ = (259 ± 12) min. For a mesoporous gold film electrode, C_{norm} shows a decrease to a stationary value of 0.14 of the starting value within 700 min after cell inoculation (Fig. 5.7 B). The $\tau_{1/2}$ value amounts to (351 ± 7) min.

In order to characterize MDCK-II cell differentiation on planar and mesoporous gold film electrodes, the time course of the normalized resistance R_{norm} was followed for a sampling frequency of either 200 Hz (planar electrodes) or 80 Hz (mesoporous electrodes) starting directly after cell inoculation (Fig. 5.8). The resistance at 80 Hz/200 Hz directly mirrors the establishment of barrier-forming cell-cell contacts between MDCK-II cells on the respective surface topography.

The normalized resistance R_{norm} recorded for MDCK-II cell differentiation on a planar gold film electrode at 200 Hz is characterized by a steep increase starting 200 min after cell inoculation (Fig. 5.8 A). An 11-fold increase of R_{norm} is attained after 640 min, indicating full establishment of cell-cell contacts and thus complete cell differentiation. Following cell differentiation on a mesoporous gold film electrode at 80 Hz, R_{norm} starts to increase about 350 min after cell inoculation, rising to a 15-fold resistance increase after 1040 min, followed by a slight decrease in R_{norm} (Fig. 5.8 B).

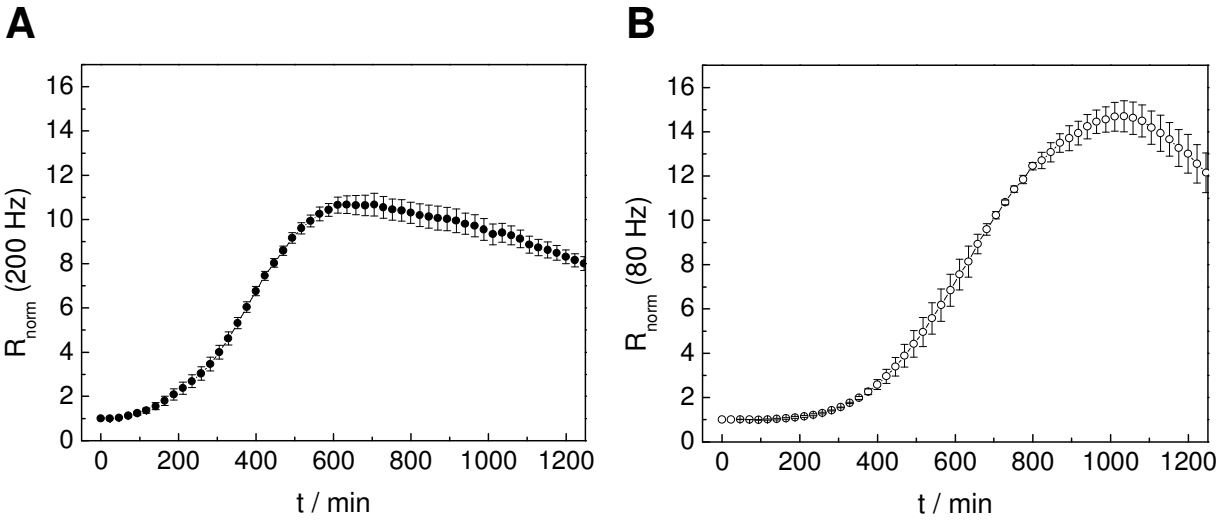

Fig. 5.8 Time course of the normalized resistance R_{norm} measured at 200 Hz (planar electrodes) or 80 Hz (mesoporous electrodes) during the adhesion and differentiation of initially suspended MDCK-II cells on planar (**A**) and mesoporous (**B**) gold film electrodes. The cells were seeded in a density of 1 x 10^6 cm^{-2} on the substrate surface at time point zero. The values of R were normalized to the first resistance value of the measurement ((●) R_{start} = (840 ± 46) Ω, (○) R_{start} = (580 ± 32) Ω; mean ± SDM, n = 4; T = 37 °C).

Table 5.1 summarizes the kinetic parameters for the attachment and spreading of MDCK-II cells upon planar and mesoporous gold film electrodes.

Tab. 5.1 Parameters used to characterize MDCK-II cell adhesion and differentiation kinetics upon planar and mesoporous gold film electrodes. $\tau_{1/2}$ is the time to reach half-maximal capacitance decrease and τ_3 the time to reach the maximal resistance value. (Mean ± SDM, n = 4; T = 37 °C).

Kinetic Parameter	Planar	Mesoporous Type I
$\tau_{1/2}$ [min]	(259 ± 12)	(351 ± 7)
τ_3 [min]	(640 ± 23)	(1040 ± 15)

5.3.3 Passive Electrical Properties of MDCK-II Cell on Mesoporous and Planar Gold Film Electrodes

In addition to analyzing the kinetics of MDCK-II cell adhesion and differentiation on mesoporous gold film electrodes in comparison to planar ones, the electrical properties of the cells after formation of a confluent monolayer and full differentiation on the substrate surface were quantified by analyzing frequency-resolved impedance data with an established physical model for adherent cells.

Figure 5.9 A compares the impedance spectra for a cell-free (open symbols) and a cell-covered (filled symbols) mesoporous gold film electrode to the spectra for a planar gold film electrode of similar geometrical surface area. Both cell-free gold film electrodes reveal a similar characteristic frequency dependence of the impedance, but the impedance spectrum

for the mesoporous electrode is shifted to lower frequencies relative to the planar electrode. This shift to lower frequencies indicates an increase in capacitance due to an enlargement of the electrically active surface area for the mesoporous gold film electrode in consequence of coating of the KOH-pits and the inner walls of the pores with gold and the surface roughness of the gold film.

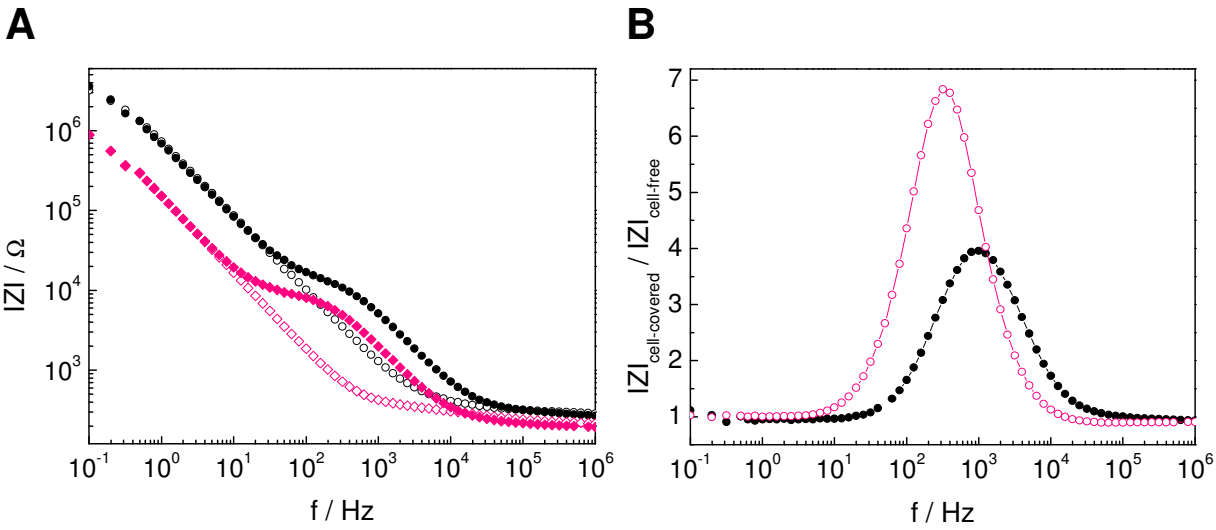

Fig. 5.9 A Typical impedance spectra of a cell-free (open symbols) and a MDCK-II cell-covered (filled symbols) planar (●, ○) and mesoporous (■, □) gold film electrode of similar geometrical surface area ((○) $A = 0.023$ cm^2, (□) $A = 0.030$ cm^2). **B** Normalized impedance ($|Z|_{\text{cell-covered}}/|Z|_{\text{cell-free}}$) for MDCK-II cells grown to confluence on a planar (●) and a mesoporous (○) gold film electrode plotted against the frequency. (T = 37 °C).

The impedance spectrum for the cell-covered mesoporous electrode is shifted to lower frequencies as well. The presence of cells on the planar electrode ($A = 0.023$ cm^2) contributes to the impedance spectrum at intermediate frequencies between 50 Hz and $3 \cdot 10^4$ Hz (Fig. 5.9 A, ●). For a mesoporous gold film electrode ($A = 0.030$ cm^2), cellular contributions stretch along the frequency range from 15 Hz to 10^4 Hz (Fig. 5.9 A, ■). Furthermore, the plateau is more prominent and borader with respect to the frequency axis.

The normalized impedance $|Z|_{\text{cell-covered}}/|Z|_{\text{cell-free}}$ plotted as a function of frequency for both cell-covered electrodes is presented in Fig. 5.9 B. For the planar electrode, the normalized impedance shows a maximum at 1000 Hz. The normalized impedance for the mesoporous electrode peaks at 300 Hz. Besides the shift to lower frequencies, also the maximal value of the normalized impedance increases, indicating an increase in sensitivity for ECIS measurements using mesoporous gold film electrodes.

In order to describe the morphological properties of the cells on the different surface topographies, the cell-covered impedance spectra (Fig. 5.9 A) were analyzed using the *ECIS model*. The transfer function of the ECIS model (chapter 3.6.1, Fig. 3.30) was fitted to the impedance spectra based on a method described by Wegener et al. (2000), returning the cell-specific parameters α, R_b and C_m as well as the parameters A and n that are the adjustable

parameters of a constant phase element (CPE). The CPE is a well-defined, non-ideal impedance element that accurately describes the interface impedance between the electrode and the electrolyte. All electrical parameters obtained for MDCK-II cells grown to confluence on mesoporous as well as planar gold film electrodes are summarized in Tab. 5.2. Since the cell-specific parameters as well as the electrode parameters were normalized to the exact geometrical electrode surface area, a comparison for both surface topographies is valid.

The parameter α quantifies the impedance contributions from the subcellular region and provides an electrical characterization of the adhesion contact between cells and substrate surface. For MDCK-II cells cultured on mesoporous gold film electrodes α amounts to $(25.5 \pm 1.1)\ \Omega^{0.5}$cm. On the planar growth surface, α is significantly higher and amounts to $(32.6 \pm 4.4)\ \Omega^{0.5}$cm.

R_b, which mirrors the specific barrier resistance originating from cell-cell contacts, shows a value of $(146.4 \pm 7.8)\ \Omega\text{cm}^2$ on a mesoporous gold film electrode. On the planar growth surface, R_b is higher and amounts to $(175.2 \pm 6.1)\ \Omega\text{cm}^2$.

The specific cell membrane capacitance C_m providing information on the topography of the cell surface such as membrane protrusions or folding is significantly higher for MDCK-II cells cultured on mesoporous gold film electrodes and accounts for $(4.90 \pm 0.29)\ \mu\text{Fcm}^{-2}$. On planar gold film electrodes C_m is $(3.05 \pm 0.13)\ \mu\text{Fcm}^{-2}$. This increase in C_m for the mesoporous growth surface corresponds to an enlargement of the cell membrane surface.

Tab. 5.2 Model parameters for mesoporous and planar gold film electrodes covered with a confluent monolayer of MDCK-II cells.

	ECIS Parameters			**CPE Parameters**	
Substrate	α [$\Omega^{0.5}$cm]	R_b [Ωcm^2]	C_m [μFcm^{-2}]	A [μFs^{n-1}cm^{-2}]	n
Porous	21.2	146.7	4.94	41.8	0.97
	28.7	153.7	5.23	37.6	0.96
	27.4	185.3	5.29	46.4	0.93
	27.4	142.0	5.80	42.5	0.93
	26.4	135.6	5.35	34.5	0.93
	28.2	155.3	5.28	36.7	0.90
	23.7	127.7	3.36	37.3	0.96
	21.2	125.5	3.93	50.8	0.93
	25.5 ± 1.1	**146.4 ± 7.8**	**4.90 ± 0.29**	**41.0 ± 2.0**	**0.94 ± 0.01**
Planar	37.5	172.7	3.01	10.4	0.89
	42.1	173.0	3.40	14.4	0.92
	28.3	192.1	2.97	24.6	0.82
	22.4	162.9	2.81	11.2	0.93
	32.6 ± 4.4	**175.2 ± 6.1**	**3.05 ± 0.13**	**15.2 ± 3.3**	**0.89 ± 0.02**

The electrical properties of the CPE, as characterized by the parameters A and n, were analyzed as well in order to obtain information on the electrode-electrolyte interface. The parameter n has been linked to the degree of surface roughness – it is thought to decrease with increasing surface roughness (McAdams et al., 1995; Kurtyka and de Levie, 1992). For $n = 1$ the CPE can be described as an ideal capacitor and A corresponds to the capacitance of the electrode. On mesoporous gold film electrodes A is determined to be $(41.0 \pm 2.0)\ \mu Fs^{n-1}cm^{-2}$ and n to be (0.94 ± 0.01). Values of $A = (15.2 \pm 3.3)\ \mu Fs^{n-1}cm^{-2}$ and $n = (0.89 \pm 0.02)$ are obtained on planar gold film electrodes. Since the CPE has resistive as well as capacitive properties, a direct correlation with the electrode capacitance is not valid. However, the increase of the parameters A and n for the mesoporous electrodes in comparison to the planar ones is in accordance with the total capacitance of the system measured at 10 Hz (chapter 5.3.1, Fig. 5.5), indicating an enlargement of the electrically active surface area for mesoporous gold film electrodes.

5.4 Motility of MDCK-II Cells on Mesoporous and Planar Gold Film Electrodes

Living adherent cells in a confluent monolayer do not behave completely static, but they exhibit motility, performing continuous movements, altering the distance between the basal cell membrane and the substrate as well as cellular shape. These so-called micromotion are a major characteristic of living cells and were analyzed for MDCK-II cells cultured on mesoporous and planar gold film electrodes. The motility of MDCK-II cells was followed by tracking the impedance of one electrode at a constant frequency of 500 Hz as a function of time. ECIS measurements in micromotion mode were performed after cell attachment and spreading was completed, i.e. after establishment of a confluent monolayer with stable electrical properties. The micromotion on mesoporous gold film electrodes was compared to that on planar gold film electrodes.

Figure 5.10 shows a typical time course of the normalized impedance at 500 Hz for a porous gold film electrode confluently covered with MDCK-II cells in comparison to the same cell-free and only medium-covered electrode. The impedance fluctuations recorded for the cell-covered electrode are a measure for the motility of MDCK-II cells on the substrate surface and can be correlated with their metabolic activity (Lo et al., 1993). An empty electrode does not show significant impedance fluctuations.

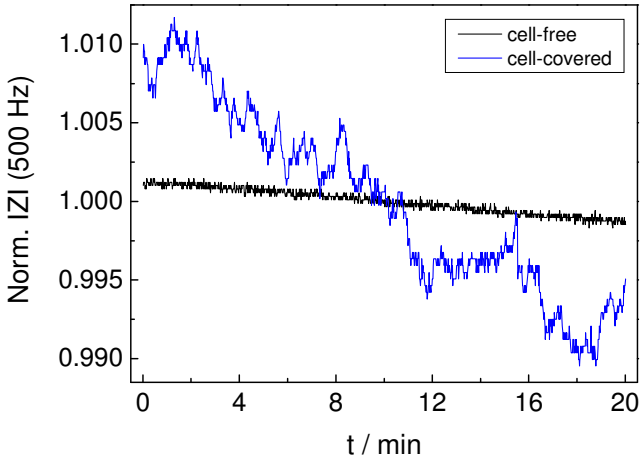

Fig. 5.10 Normalized impedance of a mesoporous gold film electrode either confluently covered with MDCK-II cells (blue) or cell-free (black) as a function of time measured at 500 Hz each second (A = 0.030 cm^2, T = 37 °C).

In order to compare the motility of MDCK-II cells on substrates with different surface topographies in quantitative terms, the micromotion data were analyzed using the standard deviation of the increments (SDI) for a time resolution of 64 s (see chapter 3.6.2). This sampling interval turned out to be the most sensitive one to quantify cellular micromotion. The SDI value was used as a measure to describe the impedance fluctuations: strong impedance fluctuations indicative for a high motility of cells on the electrode surface result in a high SDI value. In addition to cell-covered gold film electrodes, cell-free electrodes were also analyzed to clearly differentiate between the cellular signal and the technical noise.

The motility of MDCK-II cells on mesoporous and planar gold film electrodes is compared in Fig. 5.11 in terms of the averaged SDI (64 s) values of the normalized impedance measured at 500 Hz.

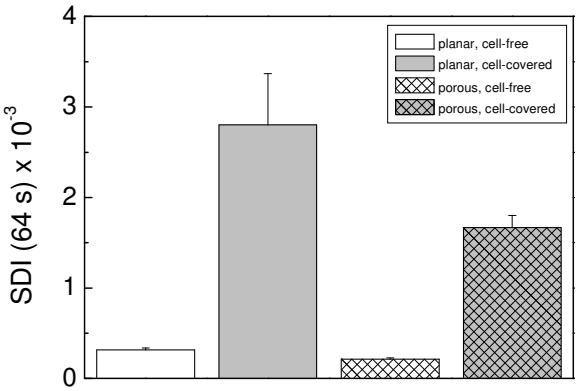

Fig. 5.11 Analysis of MDCK-II cell motility on planar and mesoporous gold film electrodes (A ~ 0.03 cm^2). The standard deviation of the increments (SDI) of the normalized impedance measured at 500 Hz (time resolution 64 s) is shown for planar and mesoporous gold film electrodes covered with a confluent monolayer of MDCK-II cells and cell-free (mean ± SDM, n ≥ 3; T = 37 °C).

As shown in previous studies, the cell-covered electrodes reveal significant higher impedance fluctuations than the cell-free electrodes covered with culture medium only. The biological motion is significantly higher than the technical noise.
MDCK-II cells on a planar gold film electrode reveal an SDI (64 s) value of $(2.80 \pm 0.57)\cdot10^{-3}$, and an SDI (64 s) value of $(1.67 \pm 0.13)\cdot10^{-3}$ on a mesoporous electrode. An empty planar or mesoporous gold film electrode shows values of $(0.32 \pm 0.02)\cdot10^{-3}$ and $(0.21 \pm 0.02)\cdot10^{-3}$, respectively. When dividing the SDI (64 s) value of the cell-covered electrode by the SDI (64 s) value of the cell-free electrode, an 8.8-fold increase is obtained for the planar and an 8-fold increase for the mesoporous electrode due to the presence of cells.
Thus, micromotion measurements can be performed on mesoporous gold film electrodes and can be used to quantify cell vitality on these surfaces. The porous structure of the growth surface and concomitant changes in the cell-adhesion contact zone do not limit the detection of cell motility.

5.5 Adhesion and Differentiation of MDCK-II Cells on Mesoporous Silicon Substrates (Type II)

Type II mesoporous silicon substrates were also investigated with respect to MDCK-II cell adhesion and differentiation. This group of substrates comprises mesoporous silicon substrates which differ in pore diameter (Ø) and width of the ridges (*b*) (see chapter 5.1, Fig. 5.3) and are denominated as follows:

Type II 1: Ø = 700 – 750 nm, *b* = 1000 nm
Type II 2: Ø = 1000 nm, *b* = 750 nm
Type II 3: Ø = 1350 – 1400 nm, *b* = 360 – 400 nm

In contrast to mesoporous silicon substrates type I, the KOH-pits on the surface of type II substrates have been almost entirely removed.
In order to allow for impedimetric ECIS measurements, the electrode layout on the substrates' surfaces was established via sputter deposition of gold and photolithography as previously described (chapter 3.6.4.2). With the complete absence of KOH-pits the electrically active surface area comprises only the gold coated planar ridges and, thus, it should decrease with increasing pore size for a similar geometrical surface area. Impedance spectra of cell-free mesoporous gold film electrodes exposed to culture medium were recorded to quantify the electrically active surface area of the electrodes. The area normalized electrode capacitance at 10 Hz reveals values of (30.28 ± 1.80) µF/cm^2 for substrate type II 1, (29.34 ± 0.83) µF/cm^2 for substrate type II 2 and (37.18 ± 3.15) µF/cm^2 for substrate type II 3 ($n \geq 4$, mean ± SDM). For a planar gold film electrode established on Lexan substrates, C (10 Hz) amounts to (9.16 ± 0.98) µF/cm^2.

All three different mesoporous gold film electrodes exhibit significantly higher capacitance values than the planar gold film electrode although their planar gold coated fraction of the surface is only ~ 89 % (type II 1), 80 % (type II 2) and ~ 63 % (type II 3), assuming that gold coverage does not extend into the inner walls of the pores. Moreover, the *C* (10 Hz) values for type II 1 and type II 2 mesoporous gold film electrodes do not differ significantly despite of different fractions of the surface are coated with gold. The type II 3 mesoporous gold film electrode even shows a significantly higher *C* (10 Hz) value – the decreased fraction of the surface that is coated with gold would indicate the opposite. The increase of the area normalized capacitance by a factor of 3.2 – 4.1 for the mesoporous gold film electrodes compared to a planar electrode corresponds to an increase in the electrically active area. Obviously, further gold coated parts than only the planar ridges do contribute to the electrically active surface. These might be due to fractions of the inner walls of the pores coated with gold or due to the surface roughness of the gold film.

The adhesion and differentiation kinetics of MDCK-II cells on type II mesoporous silicon substrates was monitored in a quantitative manner by continuously recording impedance spectra in a frequency range between 10^{-1} Hz and 10^{6} Hz. Initially suspended MDCK-II cells were seeded to confluence onto the mesoporous substrate surface modified with the established electrode layout (working electrode: A ~ 0.03 cm^2) and data acquisition was started subsequently. The complex impedance was separated into *C* and *R* to allow for a detailed analysis of cell adhesion and differentiation.

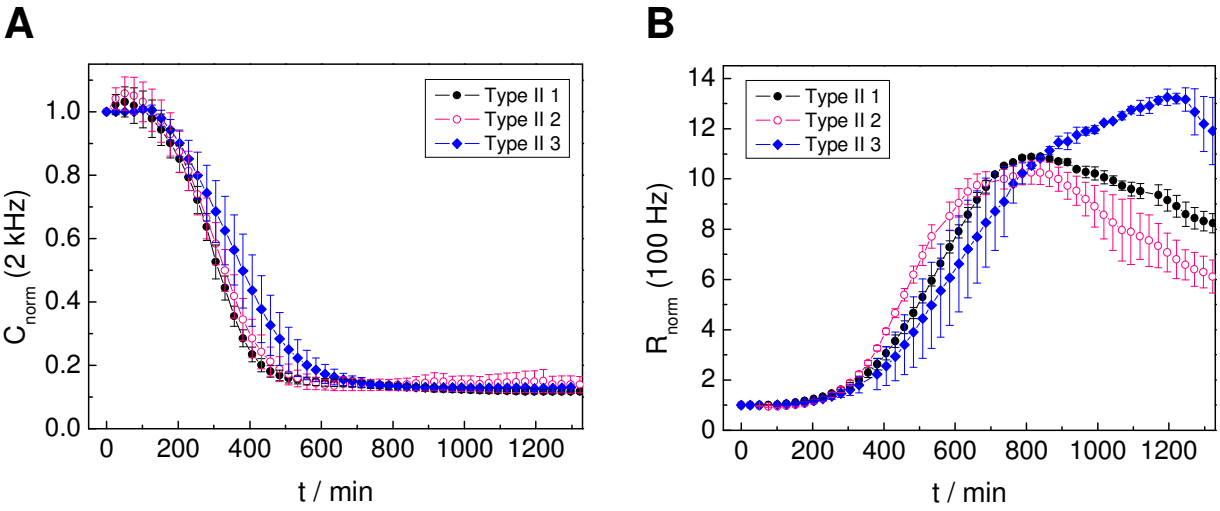

Fig. 5.12 Adhesion and differentiation of MDCK-II cells on type II mesoporous silicon substrates. Time courses of the normalized electrode capacitance C_{norm} at 2 kHz (**A**) and the normalized resistance R_{norm} at 100 Hz (**B**) during adhesion and differentiation of initially suspended MDCK-II cells. The cells were seeded in a density of 1 x 10^6 cm^{-2} at time point zero on the substrate surface. The values of *C* and *R* were normalized to the first *C* and *R* values of the measurement. ((●) C_{start} = (20.32 ± 2.54) µF/cm^2, R_{start} = (650 ± 24) Ω, (○) C_{start}= (21.37 ± 0.91) µF/cm^2, R_{start} = (515 ± 21) Ω, (♦) C_{start} = (28.70 ± 1.42) µF/cm^2, R_{start} = (466 ± 4) Ω; mean ± SDM, n ≥ 2; *T* = 37 °C).

Figure 5.12 A compares the time courses of the normalized electrode capacitance C_{norm} at a sampling frequency of 2 kHz after seeding a suspension of MDCK-II cells to confluence upon the different mesoporous substrates. A frequency of 2 kHz turned out to be most sensitive to follow cell attachment and spreading on the substrate surface. Figure 5.12 B traces the time courses of R_{norm} measured at 100 Hz starting directly after cell inoculation on the different surface topographies. The resistance at 100 Hz directly mirrors the formation of cell-cell contacts (cell differentiation).

For MDCK-II cells which are seeded at time point zero into the measuring chamber, C_{norm} instantaneously decreases to a stationary value of 0.13 for all three substrate types (Fig. 5.12 A). For type II 1 and type II 2 mesoporous silicon substrates, the stationary value is reached in a similar time interval of 600 min after inoculation. For type II 3 substrates, the stationary value is attained within 750 min. When comparing the kinetics of cell attachment and spreading on the different substrate topographies, it is obvious that the individual time courses are quite similar. The time that is needed to reach half-maximal capacitance decrease, or in other words, half-maximal surface coverage amounts to $\tau_{1/2} = (306 \pm 19)$ min and (305 ± 10) min on type II 1 and type II 2 mesoporous silicon substrates, respectively, whereas on a type II 3 silicon substrate, this process takes slightly longer ((350 ± 45) min).

The time course of R_{norm} measured at a sampling frequency of 100 Hz undergoes a steep increase within the first 300 min after cell inoculation for all three substrate types (Fig. 5.12 B). Following cell differentiation on a type II 1 mesoporous gold film electrode, R_{norm} rises to 11 within about 820 min. For a type II 2 mesoporous gold film electrode, the maximum of R_{norm} is attained after 820 min. MDCK-II cells that are seeded upon a type II 3 mesoporous gold film electrode give rise to a maximum, normalized resistance of 13 after 1200 min. All time courses of R_{norm} show a slight decrease after having passed the maximum resistance values.

Table 5.3 summarizes the kinetic parameters for the attachment and spreading of MDCK-II cells upon planar and different mesoporous gold film electrodes.

Tab. 5.3 Parameters used to characterize MDCK-II cell adhesion and differentiation kinetics upon planar and different mesoporous gold film electrodes. $\tau_{1/2}$ is the time to reach half-maximal capacitance decrease and τ_3 the time to reach the maximal resistance value. (Mean ± SDM, n ≥ 2; T = 37 °C).

Kinetic Parameter	Planar	Mesoporous Type II 1	Mesoporous Type II 2	Mesoporous Type II 3
$\tau_{1/2}$ [min]	(259 ± 12)	(306 ± 19)	(305 ± 10)	(350 ± 45)
τ_3 [min]	(640 ± 23)	(827 ± 12)	(823 ± 6)	(1200 ± 2)

Electrical Properties of MDCK-II Cells on Mesoporous Gold Film Electrodes

Figure 5.13 A exemplarily shows the frequency spectra of the impedance magnitude |Z| for a cell-free (open symbols) and a MDCK-II cell covered (filled symbols) mesoporous gold film electrode (type II 2) in comparison to a planar gold film electrode of similar geometrical surface area. Since the impedance spectra of all three different mesoporous gold film electrodes are almost identical, the impedance spectrum of only one substrate type is shown for reason of clarity.

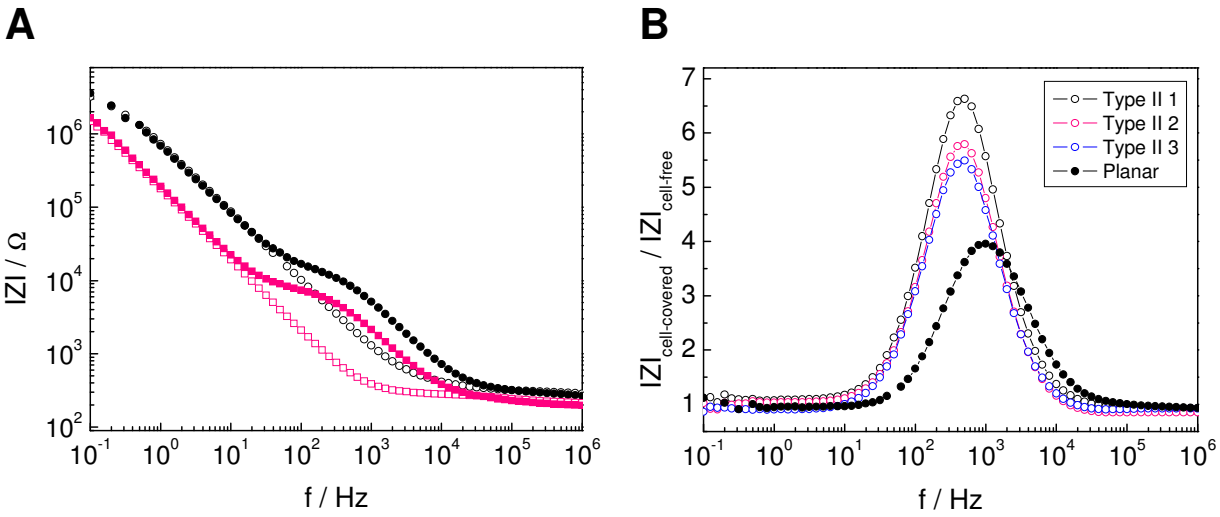

Fig. 5.13 A Typical impedance spectra of a cell-free (open symbols) and an MDCK-II cell-covered (filled symbols) planar (●, ○) and type II 2 mesoporous (■, □) gold film electrode of similar geometrical surface area ((○) A = 0.023 cm^2, (□) A = 0.026 cm^2). **B** Normalized impedance ($|Z|_{\text{cell-covered}}/|Z|_{\text{cell-free}}$) for MDCK-II cells grown to confluence on a planar (●) and different mesoporous (○, ○, ○) gold film electrodes plotted against the frequency ((○) A = 0.026 cm^2, (○) A = 0.026 cm^2, (○) A = 0.025 cm^2).

The impedance spectrum for the cell-free mesoporous gold film electrode is shifted to lower frequencies compared to the cell-free planar electrode. As already shown by means of the C (10 Hz) values, the electrically active area is significantly bigger for the porous gold film electrode. The impedance spectrum for the cell-covered mesoporous electrode is shifted to lower frequencies as well. The presence of cells on the electrode surface primarily affects the impedance spectrum at intermediate frequencies between 20 Hz and $2 \cdot 10^4$ Hz. For the planar gold film electrode, cellular contributions stretch along the frequency range from 50 Hz to $3 \cdot 10^4$ Hz.

The normalized impedance spectra $|Z|_{\text{cell-covered}}(f)/|Z|_{\text{cell-free}}(f)$ for the different cell-covered electrodes are presented in Fig. 5.13 B. For the planar electrode, the normalized impedance shows a maximum at 1000 Hz (Fig. 5.13 B). The normalized impedance for the mesoporous electrodes peaks at 500 Hz irrespective of the individual surface topography. Besides the shift to lower frequencies, also the maximal value of the normalized impedance increases, indicating an increase in sensitivity for ECIS measurements when using mesoporous gold film electrodes. For the type II 1 mesoporous gold film electrode, the normalized impedance

reveals a maximal value of 6.6 whereas for type II 2 and type II 3 mesoporous gold film electrodes, the maxima amount to 5.8 and 5.5, respectively.

The electrical properties of MDCK-II cells after formation of a confluent monolayer and full differentiation on the different surface topographies were quantified by fitting the transfer function of the ECIS model (chapter 3.6.1, Fig. 3.30) to the impedance spectra based on a method described by Wegener et al. (2000). This analysis returned the cell-specific parameters α, R_b, C_m as well as the parameters A and n which describe the electrical properties of the CPE. All model parameters are summarized in Tab. 5.4. The cell-specific parameters as well as the CPE parameters were normalized to the geometrical surface area of the electrode.

For MDCK-II cells which are cultured on type II 1 mesoporous gold film electrodes, an α value of $(26.3 \pm 0.9)\ \Omega^{0.5}$cm is obtained. On type II 2 and type II 3 mesoporous silicon substrates, α is slightly lower and is determined to be $(22.7 \pm 1.0)\ \Omega^{0.5}$cm and $(23.3 \pm 1.7)\ \Omega^{0.5}$cm, respectively.

The R_b values also decrease with decreasing fraction of planar substrate surface, i.e. with increasing pore diameter. Whereas for planar gold film electrodes, R_b is calculated to be $(175.2 \pm 6.1)\ \Omega\text{cm}^2$, the value for type II 1 mesoporous gold film electrodes is $(130 \pm 11)\ \Omega\text{cm}^2$. For type II 2 and type II 3 mesoporous substrates similar R_b values of $(86.4 \pm 4.7)\ \Omega\text{cm}^2$ and $(88.0 \pm 8.7)\ \Omega\text{cm}^2$ are obtained.

The specific cell membrane capacitance C_m for MDCK-II cells cultured on the different surface topographies increases with increasing porosity. On planar gold film electrodes, C_m accounts for $(3.05 \pm 0.13)\ \mu\text{Fcm}^{-2}$. C_m on mesoporous gold film electrodes type II 1 – 3 is significantly higher and show values of $(4.80 \pm 0.20)\ \mu\text{Fcm}^{-2}$, $(5.70 \pm 0.14)\ \mu\text{Fcm}^{-2}$ and $(6.39 \pm 0.33)\ \mu\text{Fcm}^{-2}$.

Tab. 5.4 Model parameters for planar and different mesoporous gold film electrodes covered with a confluent monolayer of MDCK-II cells. (Mean ± SDM, n ≥ 4).

	ECIS Parameters			**CPE Parameters**	
Substrate	α [$\Omega^{0.5}$cm]	R_b [Ωcm^2]	C_m [μFcm^{-2}]	A [$\mu\text{Fs}^{n-1}\text{cm}^{-2}$]	n
Planar	32.6 ± 4.4	175.2 ± 6.1	3.05 ± 0.13	15.2 ± 3.3	0.89 ± 0.02
Type II 1	26.3 ± 0.9	130 ± 11	4.80 ± 0.20	32.7 ± 2.6	0.95 ± 0.01
Type II 2	22.7 ± 1.0	86.4 ± 4.7	5.70 ± 0.14	38.8 ± 1.2	0.94 ± 0.01
Type II 3	23.3 ± 1.7	88.0 ± 8.7	6.39 ± 0.33	50.3 ± 5.4	0.94 ± 0.01

The parameters A and n describe the electrical properties of the electrode-electrolyte interface. For planar gold film electrodes, A is determined to be $(15.2 \pm 3.3)\ \mu\text{Fs}^{n-1}\text{cm}^{-2}$ and n to be (0.89 ± 0.02). For mesoporous gold film electrodes, higher values for both parameters are obtained. The parameter n does not differ significantly for the individual mesoporous gold

film electrodes. However, the parameter *A* shows significant differences between the surface topographies. For type II 1 and type II 2 mesoporous substrates, *A* is similar and amounts to (32.7 ± 2.6) $\mu Fs^{n-1}cm^{-2}$ and (38.8 ± 1.2) $\mu Fs^{n-1}cm^{-2}$, respectively. For type II 3 mesoporous substrates, *A* is considerably higher and amounts to (50.3 ± 5.4) $\mu Fs^{n-1}cm^{-2}$. Since the CPE has resistive as well as capacitive properties, a direct correlation with the electrode capacitance is not valid. However, the increase of the parameters *A* and *n* for the different mesoporous gold film electrodes in comparison to the planar electrode is in accordance with the total capacitance of the system measured at 10 Hz.

5.6 Motility of MDCK-II Cells on Mesoporous Gold Film Electrodes (Type II)

In addition to analyzing the kinetics of MDCK-II cell adhesion and differentiation on type II mesoporous substrates, the cellular micromotion on the different surface topographies was quantified. The motility of MDCK-II cells was followed by tracking the impedance of the electrode at a constant frequency of 500 Hz. ECIS measurements in micromotion mode were performed after formation of a confluent cell monolayer with stable electrical properties. The micromotion data were analyzed using the standard deviation of the increments (SDI) for a time resolution of 64 s (see chapter 3.6.2). A high SDI (64 s) value indicates strong impedance fluctuations and, thus, a high motility of MDCK-II cells on the electrode surface. Figure 5.14 compares the SDI (64 s) values for MDCK-II cells cultured on the different mesoporous gold film electrodes with the values obtained on a planar gold film electrode.

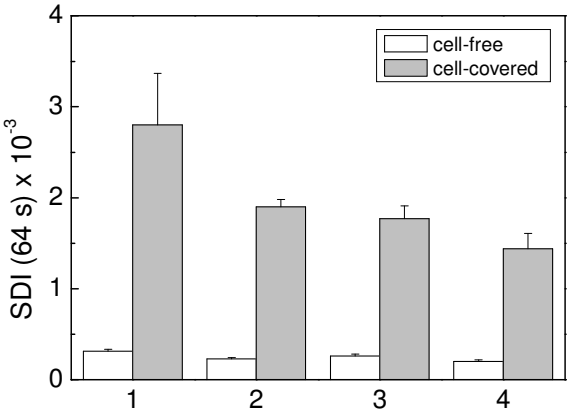

Fig. 5.14 Analysis of MDCK-II cell motility on planar and mesoporous gold film electrodes (A ~ 0.03 cm^2). The standard deviation of the increments (SDI) of the normalized impedance measured at 500 Hz (time resolution 64 s) is shown for planar (**1**) and mesoporous gold film electrodes (**2** = type II 1, **3** = type II 2, **4** = type II 3) covered with a confluent monolayer of MDCK-II cells and cell-free (mean ± SDM, n ≥ 3; T = 37 °C).

The cell-covered electrodes reveal significantly higher impedance fluctuations than the cell-free electrodes covered only with culture medium. The SDI (64 s) values for the empty electrodes are all in a similar range between $0.20 \cdot 10^{-3}$ and $0.32 \cdot 10^{-3}$ irrespective of the individual surface topography. The SDI (64 s) value for a planar cell-covered gold film electrode is significantly higher than the values obtained for mesoporous gold film electrodes and amounts to $(2.80 \pm 0.57) \cdot 10^{-3}$. MDCK-II cells cultured on type II 1 and type II 2 mesoporous gold film electrodes reveal SDI (64 s) values of $(1.90 \pm 0.08) \cdot 10^{-3}$ and $(1.77 \pm 0.14) \cdot 10^{-3}$ which do not differ significantly. On type II 3 mesoporous gold film electrodes, a slightly lower SDI (64 s) value of $(1.44 \pm 0.17) \cdot 10^{-3}$ is obtained.

The micromotion measurements reveal that the porous structure of the growth surface still allows the performance of cellular micromotion but it is significantly reduced in comparison to a planar growth surface.

5.7 Discussion

The ECIS technique was established more than 25 years ago as a non-invasive means to monitor morphological changes in adherent cells (Giaever and Keese, 1984, 1991 and 1993). In this approach, mammalian cells are cultured directly on the surface of planar gold film electrodes which serve as a growth substrate for the cells and as a sensory surface for the electrochemical measurement at the same time. The close proximity between cells and the underlying electrode is decisive for the high sensitivity of this technique. The principle of ECIS is based on measuring changes in the AC impedance of the small gold film electrodes, upon which cells are deposited, as a function of AC frequency used for excitation. ECIS readings can be used to follow the *de novo* formation or the modulation of established cell-substrate contacts and cell-cell contacts non-invasively and in real time.

Surface topography with feature sizes at the micrometer scale is known to influence cell behavior in many ways, including cell adhesion and spreading, morphology, orientation, motility and proliferation (Britland et al., 1996; Damji et al., 1996; Kaiser et al., 2006; Curtis and Wilkinson, 1997 and 1998; Van Kooten et al., 1998; Wilkinson et al., 2002). Topographically structured growth substrates have various applications in the life sciences, ranging from cellular biosensor technology to implant materials and tissue engineering. For some implants to be effective, parts of the device need to be porous. In some cases, the porosity is at the surface of the implant to allow tissue ingrowth for anchorage of the device. Certain devices contain membranes as cell supports and the porosity of these membranes enables flux of hormones or blood components between the cells and blood. Topographical surface structures can be applied to manipulate cell shape, as illustrated by cells becoming polarized and elongated in the direction of the grooves on grooved substrates. This so-called contact guidance can be induced by various topographical features and was observed with different cell types. The width, depth and spacing of the grooves all influence the orientation and have been studied intensely (Clark et al., 1990 and 1992; Oakley and Brunette, 1993; Walboomers et al., 1999; Alaerts et al., 2001). Surface topography is also used to control and spatially dictate the adhesion of cells ("cell traps"), e.g. for the arrangement of neurons on the surface of sensor devices, like microelectrode arrays (Miller et al., 2001; Tatic-Lucic et al., 1997; Maher et al., 1999). All these examples demonstrate that extensive knowledge about the interactions of cells *with* and the cell response *to* topographically structured growth surfaces is important.

Taking this into account, one aim of this thesis was to develop and evaluate a biosensor based on the ECIS technique and capable of investigating the impact of surface topography on cell behavior in quantitative terms. The different surface topographies were modeled by mesoporous silicon substrates. In order to apply ECIS to mesoporous substrates, a thin gold film was deposited on the substrate surface and a well-defined electrode layout was

established by means of photolithography. The impact of surface topography on cell-surface interactions was analyzed with respect to cell attachment and spreading, cell differentiation as well as cellular micromotion using the epithelial MDCK-II cell line. The high time resolution of the ECIS technique provided valuable insights into the formation of cell-substrate and cell-cell contacts with respect to pore diameter and width of the ridges within the mesoporous substrate. In addition to the kinetic measurements of cell adhesion and differentiation, the electrical properties of the cell layer after differentiation on the topographically structured growth substrates were quantified by analyzing frequency-resolved impedance data with an established physical model for adherent cells, providing valuable information on cell morphology.

5.7.1 Characterization of Mesoporous Gold Film Electrodes

The mesoporous silicon substrates which were studied in this thesis exhibit a similar surface topography and were divided into two groups. Mesoporous silicon substrates type I exhibit pyramidal pre-etched areas (KOH-pits) which taper into a pore of $\varnothing = 1.3$ µm. For mesoporous silicon substrates type II, the KOH-pits have been almost entirely removed. These substrates differ in pore diameter and width of the ridges, resulting in individual surface topographies.
The mesoporous structure leads to a reduction of the planar growth surface with respect to an entirely planar reference to 65 % for type I and ~ 89 % (type II 1), 80 % (type II 2) and ~ 63 % (type II 3) for type II mesoporous silicon substrates. When coating type I mesoporous substrates with a gold film, the gold does not only cover the planar ridges but also the KOH-pits which have an inclination angle of 68° (chapter 5.1, Fig. 5.4). Adding the surface area of the planar ridges and the KOH-pits, the resulting electrically active area is 37 % bigger compared to a planar surface of similar geometrical size. A coating of the inner walls of the pores with gold as well as the surface roughness of the gold film which may also lead to a surface enlargement are disregarded. For a calculation of the electrically active area for type II mesoporous substrates, the gold film can be assumed to cover only the planar ridges, so that the resulting electrically active area should correspond to the planar growth surface mentioned above.

In order to allow an impedimetric characterization of cells on the mesoporous growth substrates, the substrates were coated with a 100 nm thin gold film and a well-defined electrode layout was established on the substrate surface by means of photolithography (chapter 3.6.4.2). The characterization of the established mesoporous gold film electrodes without cells but exposed to culture medium was a crucial requirement for the development of this sensor system in contact with cells. Thus, the impedance spectrum of a cell-free mesoporous gold film electrode was compared to the impedance spectrum of an entirely planar gold film electrode of similar geometrical surface area established on Lexan substrates.

For the application of the ECIS model, it is crucial to know about the frequency-dependent impedance of the electrode-electrolyte interface, which can be described using empirical impedance elements. For planar gold film electrodes immersed in culture medium, the corresponding equivalent circuit comprises an ohmic resistor (R_{bulk}), representing the specific electrolyte resistivity of the bulk and the geometrical characteristics of the measurement cell, and a constant phase element (CPE), which describes the electrode-electrolyte interface. At high frequencies ($f > 10^4$ Hz) the impedance spectrum is determined by the bulk resistance R_{bulk} of the electrolyte. The electrode-electrolyte interface has capacitive as well as resistive properties, resulting in a linear increase of the impedance with decreasing frequency. This frequency-dependent behavior of the impedance described for planar gold film electrodes could also be found for the mesoporous gold film electrodes type I (chapter 5.3.1, Fig. 5.5) as well as type II (chapter 5.5, Fig. 5.13). Thus, the mesoporous gold film electrodes were found to behave similar to flat electrodes and can be used for the impedimetric characterization of mammalian cells during adhesion and differentiation.

The comparison of the impedance spectra for cell-free planar and mesoporous gold film electrodes of similar geometrical surface area revealed a shift of the impedance spectrum to lower frequencies for both mesoporous electrode types (I and II). The frequency shift is of peculiar interest, since it might result in an increase in sensitivity for the impedimetric characterization of cells.

The observed frequency shift in comparison to a planar electrode of similar geometrical size indicates an enlargement of the electrically active electrode surface for the mesoporous substrates and was analyzed in more detail as follows: for similar experimental conditions, the electrode capacitance is linear dependent on the electrode surface area. However, the electrode-electrolyte interface is not accurately described by a capacitor, since resistive properties need to be taken into account as well. For this reason, an empirical impedance element, the CPE, is applied. The electrode-electrolyte interface dominates the impedance spectrum for $f < 400$ Hz. This is also valid for the total capacitance of the system. Thus, determination of the total capacitance at 10 Hz allows for a comparison of the electrically active electrode surface for the different surface topographies. With respect to a planar gold film electrode, the capacitance normalized to the projected area showed an increase by a factor of 3.6 for mesoporous substrates type I and an increase by a factor of 3.3 (type II 1), 3.2 (type II 2) and 4.1 (type II 3) for mesoporous substrates type II.

This increase in the electrically active surface area for type I mesoporous gold film electrodes might be attributed to a surface enlargement due to gold coated KOH-pits as well as gold coated inner walls of the pores. The observed increase of the electrically active area for type II mesoporous gold film electrodes can not be attributed to a surface enlargement due to gold coated KOH-pits, since these should be almost entirely removed. Assuming only a coating of the planar ridges with gold, the capacitance for type II mesoporous electrodes should be smaller than the one for planar gold film electrodes of similar geometrical surface area and should decrease with decreasing fraction of planar surface (decreasing width of the ridges).

This was not the case. By contrast, type II 3 mesoporous gold film electrodes revealed a capacitance value which was even higher than the values for type II 1 and type II 2 electrodes. These findings might be explained by the assuming that a significant fraction of the inner walls of the pores is coated with gold, contributing to the electrically active electrode surface. Besides surface topography of the silicon substrate, also the surface roughness of the gold film, as prevalent after photolithographic processing (chapter 5.1, Fig. 5.4 B and C) might contribute to a surface enlargement.

For an impedimetric characterization of the electrode surface, the parameters A and n of the constant phase element (CPE) describing the interface impedance of the electrode were compared for the different surface topographies. The parameter n reveals to which extent the properties of the electrode-electrolyte interface deviate from the properties of an ideal capacitor ($n = 1$). n has been linked to the degree of surface nano-roughness – it decreases with increasing surface roughness (McAdams, 1995, Kurtyka and de Levie, 1992). The values of n for all electrodes under study were in the same range, indicating a similar surface roughness of the gold film (chapter 5.3.3 Tab. 5.2, chapter 5.5, Tab. 5.4). The similarity of n values allows for a direct comparison of the parameter A for the different electrodes. Since $0 < n < 1$, the CPE exhibits capacitive as well as resistive properties, which prohibits a simple physical interpretation of the values of A. The calculated values for A can be found in chapter 5.3.3 (Tab. 5.2) and chapter 5.5 (Tab. 5.4). The parameter A is an area normalized parameter – it was normalized to the geometrical surface area of the electrode. A change in the surface topography as in the case of mesoporous gold film electrodes would result in a change of the parameter A.

For type I mesoporous gold film electrodes A amounts to (41.0 ± 2.0) $\mu Fs^{n-1}cm^{-2}$ whereas on planar gold film electrodes, a value of $A = (15.2 \pm 3.3)$ $\mu Fs^{n-1}cm^{-2}$ was obtained. For type I mesoporous gold film electrodes, the parameter A indicates an extra surface due to gold-coated KOH-pits and inner walls of the pores of 170 %. Assuming the planar ridges as well as the KOH-pits to be completely coated with a gold film, the electrically active electrode surface is only 37 % bigger than a planar surface of similar geometrical size. Thus, a significant fraction of the inner walls of the pores is obviously coated with a gold film. A complete coating of the inner walls of the pores with gold would lead to an extra electrically active electrode surface of 276 %. Another possible source for surface enlargement might be related to the surface roughness of the deposited gold film.

For type II mesoporous gold film electrodes, the parameter A was determined to be (32.7 ± 2.6) $\mu Fs^{n-1}cm^{-2}$ (type II 1), (38.8 ± 1.2) $\mu Fs^{n-1}cm^{-2}$ (type II 2) and (50.3 ± 5.4) $\mu Fs^{n-1}cm^{-2}$ (type II 3). With respect to a planar surface, an extra surface of 115 %, 155 % and 230 % is obtained. For these substrates the KOH-pits have been almost entirely removed so that they can not contribute significantly to a surface enlargement. Assuming a complete coating of the inner walls of the pores with gold, an extra surface of 578 % (type II 1), 766 % (type II 2) or 1061 % (type II 3) might be obtained. Thus, either gold-coated parts of the pores or the surface roughness of the gold film contribute to the enlargement of the electrically active area.

5.7.2 Impact of Surface Topography on Cell Adhesion and Differentiation

The kinetics of cell adhesion and cell differentiation of MDCK-II cells, which were used as a model epithelial cell line for barrier-forming cells, were studied on different surface topographies using the ECIS technique. Cellular properties on mesoporous silicon substrates were compared to those on a planar Lexan surface used as a reference. Characterizing the kinetics of cell attachment and spreading to topographically structured growth substrates is of crucial importance for their applicability as biomaterials in a variety of important biomedical and bioanalytical applications, such as biosensors or implants. Furthermore, this kind of studies also provides insights into the surface properties that will govern cell-substrate interactions.

After establishment of the electrode layout on the mesoporous and planar substrates (working electrode: A ~ 0.03 cm^2), MDCK-II cell suspensions prepared in serum containing medium were seeded on the substrate surface and data acquisition was started subsequently. The cellular response was investigated for the following surface topographies:

i)	Planar			
ii)	Mesoporous type I:	Ø = 1300 nm	b = 1700 nm	KOH-pits
iii)	Mesoporous type II 1:	Ø = 700 – 750 nm	b = 1000 nm	no KOH-pits
iv)	Mesoporous type II 2:	Ø = 1000 nm	b = 750 nm	no KOH-pits
v)	Mesoporous type II 3:	Ø = 1350 – 1400 nm	b = 360 – 400 nm	no KOH-pits

The recorded impedance data were analyzed in terms of the normalized capacitance C_{norm} at 2 kHz and the normalized resistance R_{norm} at the most sensitive frequency for either substrate type (80, 100 or 200 Hz). Changes in the surface coverage of the electrode are directly related to the decrease in C_{norm} while the formation of cell-cell contacts (cell differentiation) is mirrored in the time course of R_{norm}. Table 5.5 summarizes the results obtained for cell adhesion and differentiation on planar and different mesoporous surfaces. Cell attachment and spreading kinetics were quantified from the time course of C_{norm} using the parameter $\tau_{1/2}$, describing the time necessary to reach half-maximal surface coverage. The parameter τ_3 describes the time that is needed to reach the maximal R_{norm} value.

Tab. 5.5 Parameters characterizing MDCK-II cell adhesion and differentiation upon planar and mesoporous gold film electrodes. (Mean ± SDM, n ≥ 2)

	Planar	Porous Type I	Porous Type II 1	Porous Type II 2	Porous Type II 3
$\tau_{1/2}$ [min]	259 ± 12	351 ± 7	306 ± 19	305 ± 10	350 ± 45
τ_3 [min]	640 ± 23	1040 ± 15	827 ± 12	823 ± 6	1200 ± 2

MDCK-II cells attached and spread on planar gold film electrodes with the highest rate, as indicated by $\tau_{1/2} = (259 \pm 12)$ min. The cells did need more time to attach and spread on all mesoporous gold film electrodes under study. On a type I mesoporous gold film electrode, half-maximal surface coverage was reached in $\tau_{1/2} = (351 \pm 7)$ min. Despite of differences in pore diameter and width of the ridges for type II mesoporous substrates, MDCK-II cell attachment and spreading on these surfaces was almost similar. For MDCK-II cells that were seeded on type II 1 and on type II 2 mesoporous gold film electrodes, the time needed to reach half-maximal surface coverage accounted for (306 ± 19) min and (305 ± 10) min, respectively. On a type II 3 mesoporous gold film electrode, cells attached and spread with a slightly lower rate, as indicated by $\tau_{1/2} = (350 \pm 45)$ min.

For MDCK-II cell differentiation on the different surface topographies, the ECIS measurements showed greater differences than for cell attachment and spreading. MDCK-II cell differentiation on planar gold film electrodes showed the highest kinetics compared to cells on the porous substrates – MDCK-II cells were fully differentiated within $\tau_3 = (640 \pm 23)$ min. For a type I mesoporous gold film electrode, full establishment of barrier-forming cell-cell contacts was attained within $\tau_3 = (1040 \pm 15)$ min after cell inoculation. On type II 1 and type II 2 mesoporous gold film electrodes, MDCK-II cell differentiation was similar and was completed within roughly 820 min after cell inoculation. MDCK-II cells did need more time to differentiate upon a type II 3 mesoporous gold film electrode ($\tau_3 = (1200 \pm 2)$ min).

In summary, the ECIS measurements revealed that MDCK-II cells were able to attach and spread on the different mesoporous growth substrates and they formed a confluent monolayer. Furthermore, this process took only slightly longer on mesoporous substrates than on planar ones. Thus, the mesoporous surface topography did not prevent or hinder cell attachment and spreading. Specific cell-substrate contacts could be established on these surfaces. The measurements also revealed that the rate of cell attachment and spreading was reduced with decreasing fraction of planar growth surface. Mesoporous silicon substrates type II 1 and type II 2 exhibit a planar growth surface of ~ 89 % and 80 %, respectively, resulting in $\tau_{1/2}$ values which are slightly higher (~ 47 min) than the ones for a planar growth surface. Type I and type II 3 mesoporous gold film electrodes exhibit a planar growth surface of 65 % and ~ 63 %, respectively. For both substrates, similar $\tau_{1/2}$ values were obtained which are higher than the values for the mesoporous substrates type II 1 and type II 2 with a greater fraction of the surface being planar and available for cell attachment. With decreasing fraction of planar growth surface, the adhesion sites for the cells on the surface are reduced, resulting in reduced cell attachment and spreading kinetics.

The mesoporous substrates also allowed a proper cell differentiation. The time to reach full establishment of barrier-forming cell-cell contacts also increased with decreasing fraction of planar growth surface. Whereas on a planar growth substrate 640 min were necessary to reach the maximum R_{norm}, this process took significantly longer (820 min) on substrates type II 1

and type II 2. On mesoporous silicon substrates type I and type II 3 with a planar growth surface of 65 % and ~ 63 %, the time for complete cell differentiation was determined to be 1040 min and 1200 min, respectively. Thus, the porous surface topography has a stronger impact on cell differentiation than on cell attachment and spreading.

The great majority of studies addressing the interactions of cells with topographically structured surfaces have been performed with groove/ridge patterns. In the literature, only a few studies can be found describing the impact of an ordered, porous microscale topography on cell behavior. Richter et al. (1996) cultured mouse fibroblasts (NIH 3T3 and L929) on porous silicon substrates containing square pores of different sizes (edge length: 5, 10 and 20 µm). In the case of small pores (5 µm × 5 µm) the cells were able to spread over them and to cover them completely. The cells were distributed uniformly on the substrate surface and formed a confluent cell layer, indicating that the small pores did not notably disturb cell attachment and spreading. With pores of 10 µm edge length, cell spreading mainly occurred on the planar ridges between the pores, but single cells could bridge the pores. The 20 µm × 20 µm pores were larger than the cells and cells attached and spread mainly on the ridges or moved into the pores.
Berry et al. (2004) studied the interaction of fibroblasts with a micro-pit patterned quartz surface, consisting of a regular array of pits with diameters of 7, 15 and 25 µm and spacings between the pits of either 20 µm or 40 µm (depth: 4.8 µm). They demonstrated that fibroblasts are sensitive to a pitted topography, in particular to the diameter of the pits. The 25 µm pits combined with both spacings allowed cells to completely enter the pits. Conversely, the 7 µm pitted surface allowed the majority of cells to move over and cover the pits completely. The 15 µm pits were in between the two extremes. This cellular reaction was ascribed to the fact that cells may sense differences in radius of curvature.
The porous substrates applied in both literature studies have a significantly higher fraction of planar growth surface and a higher pore diameter compared to the mesoporous silicon substrates used in this thesis. However, the MDCK-II cells show an average radius of (8.6 ± 0.2) µm and are only half the size of the fibroblasts which exhibit an average radius of (16 ± 2) µm (Reiß, 2004), so that certain correlations between the results are valid.

5.7.3 Impact of Surface Topography on the Electrical Properties of the Cell Layer

Besides the kinetic measurements of cell adhesion and differentiation, the electrical properties of the confluent cell layers after full differentiation were studied in order to evaluate the impact of surface topography on cell morphology and the state of cell differentiation. Data modeling of the recorded impedance spectra following a method described by Wegener et al. (2000) returned the cell-specific electrical parameters α, R_b and C_m which can be used to describe the morphological properties of MDCK-II cells on the different surface topographies

in a quantitative manner (Wegener et al., 2000). However, the method is based on planar gold film electrodes and has not been applied to mesoporous gold film electrodes so far.

The specific barrier resistance R_b describes the impedance contribution arising from the intercellular cleft and is a measure for the strength of the cell-cell contacts and in particular the tight junctions between adjacent cells when dealing with barrier-forming cells.
For MDCK-II cells cultured on planar gold film electrodes, R_b was calculated to be $(175.2 \pm 6.1)\ \Omega cm^2$. This value is significantly higher than those reported in the literature. Lo et al. (1999) found an R_b value of $(60 \pm 4)\ \Omega cm^2$ and Reiß (2004) determined a value of $(88 \pm 4)\ \Omega cm^2$ for MDCK-II cells cultured on planar gold film electrodes. On type I mesoporous gold film electrodes, R_b is reduced and amounts to $(146.4 \pm 7.8)\ \Omega cm^2$. For MDCK-II cells cultured on type II mesoporous gold film electrodes, R_b decreases with increasing pore diameter. Whereas R_b accounts for $(130 \pm 11)\ \Omega cm^2$ on type II 1 mesoporous gold film electrodes, considerably lower R_b values of $(86.4 \pm 4.7)\ \Omega cm^2$ and $(88.0 \pm 8.7)\ \Omega cm^2$ were obtained on type II 2 and type II 3 mesoporous gold film electrodes.
A direct comparison of R_b and further conclusions concerning the expression of tight junctions and thus the cellular barrier function are only valid when the cells exhibit similar average cell diameters on the different surfaces. For barrier-forming cells, the main contribution to R_b arises from the cell-cell contacts, in particular the tight junctions between adjacent cells (Wegener et al., 2000). Besides the geometry of the cleft the cell size und thus the cell diameter have a significant impact on R_b as well. Treating the cells like circular disks the sum of all cell perimeters for a similar geometrical surface area is higher for small cells than for big cells. A high sum of cell perimeters provides a high number of cell-cell contacts and thus the number of resistors combined in parallel is higher per unit area. According to Kirchhoff's laws, the reciprocals of the individual resistances are added to give the total resistance R_b. Thus, the R_b value for small cells is smaller than the value for bigger cells, although the quality of the tight junctions is similar. For this reason it is crucial to determine the cell radius and, thus, the cell perimeter on the different surface topographies in order to evaluate the observed changes of R_b. Rommel (2007) found significantly bigger cell radii for spread MDCK-II cells cultured on type I mesoporous gold film electrodes ($(10.5 \pm 0.2)\ \mu m$) than for MDCK-II cells cultured on planar gold film electrodes ($(7.9 \pm 0.3)\ \mu m$). This 1.3-fold bigger cell radius should lead to a higher R_b value for MDCK-II cells on mesoporous gold film electrodes in comparison to cells cultured on planar electrodes. However, an increase in R_b could not be observed. Thus, the decrease in R_b can be assumed to mirror a significant weakening of the barrier function (lower expression of tight junctions) due to the porous substrate topography.
For MDCK-II cells cultured on type II mesoporous gold film electrodes no microscopic studies addressing the cell size were available. Thus, the impact of the cell radius on the value of R_b could not be quantified. Assuming a similar cell size as on type I mesoporous substrates, the decreased R_b value for cells on type II mesoporous substrates indicates weaker cell-cell

contacts on mesoporous in comparison to planar substrates. Moreover, the strength of cell-cell contacts decreases with increasing pore diameter.

The parameter α describes the impedance contribution from the cleft underneath the cells and thus electrically characterizes the cell-substrate adhesion zone. On planar gold film electrodes α was calculated to be (32.6 ± 4.4) $\Omega^{0.5}$cm. This value is significantly higher than the values determined in the literature. Lo et al. (1999) found a value of (18 ± 2.0) $\Omega^{0.5}$cm for MDCK-II cells cultured on planar gold film electrodes, Reiß (2004) determined α to be (16.0 ± 0.6) $\Omega^{0.5}$cm. On type I mesoporous gold film electrodes α was found to be significantly lower ((25.5 ± 1.1) $\Omega^{0.5}$cm) than on planar surfaces. MDCK-II cells which were cultured on type II mesoporous gold film electrodes revealed a decrease of α with increasing pore diameter. For type II 1 substrates, α amounts to (26.3 ± 0.9) $\Omega^{0.5}$cm, whereas similar values for α of (22.7 ± 1.0) $\Omega^{0.5}$cm and (23.3 ± 1.7) $\Omega^{0.5}$cm were obtained on type II 2 and type II 3 substrates.
The parameter α is defined by:

$$\alpha = r_c \cdot \sqrt{\frac{\rho_{sub}}{d}}$$

α itself depends on three parameters, allowing for different interpretations of these observed changes. According to its definition, changes in α can be caused either by a corresponding change of the radius of the spread cell (r_c), the average distance between basal cell membrane and substrate surface (d), the specific resistivity (ρ_{sub}) of the electrolyte in the adhesion cleft underneath the cells or any combination of these.
When MDCK-II cells are seeded upon type I mesoporous substrates, the cells experience two different areas where they can adhere to: i) planar ridges which comprise 65 % of the growth surface where the cell-substrate contact is supposed to be similar to a planar growth substrate and ii) the KOH-pits which have an inclination angle of 68° and lie by as much as 1.6 µm underneath the planar surface. However, it is unclear if and to which extent the KOH-pits are actually used for cell adhesion. Moreover, the SEM micrographs (chapter 5.1, Fig. 5.4 C, D) did not reveal to which extent the inner walls of the pores were coated with a conducting gold film. The capacitance values for type I and especially for type II mesoporous gold film electrodes, which should not exhibit significant KOH-pits, indicated a coating of parts of the inner walls of the pores with gold. Although it could not be clarified if and to which extent the basal cell membrane follows the porous surface topography, it is hard to envision that the complete electrically active surface of the mesoporous electrode is covered with cells and/or that a constant distance between cells and substrate surface is obtained. In particular in the region of the KOH-pits and the pores a higher distance might result between electrode and basal cell membrane compared to the planar ridges. This higher average cell-substrate distance (d) for MDCK-II cells cultured on mesoporous gold film electrodes would result in a smaller α value, as observed for mesoporous gold film electrodes. However, this trend can

also be superposed by a concomitant change of the specific resistivity in the adhesion cleft. The 1.3 fold increase in the cell radius as observed for MDCK-II cells cultured on type I mesoporous substrates in comparison to planar substrates (Rommel, 2007) provides an increase in α and thus complicates unique correlations concerning the cell-substrate separation distance. In order to estimate the contribution of the cell radius to the value of α for cells cultured on type II mesoporous substrates, further microscopic studies are needed.

The parameter C_m describes the specific cell membrane capacitance of a single cell membrane. It contains information about the true not the projected area of the cell surface, as it may be folded by microvilli and membrane protrusions, allowing insights into the membrane surface topography.

The capacitance of the cell membrane is determined by the dielectric properties of the membrane constituents and the topography of the cell membrane. For an ideally smooth lipid bilayer ($\varepsilon_r \approx 2$, $d \approx 4$ nm) a value of 0.44 μFcm^{-2} is obtained (Adam et al., 2009). For the specific cell membrane capacitance of an ideally smooth cell membrane a value of 1 μFcm^{-2} is reported independent of the cell type. This difference has been attributed to the water and protein content of a cell membrane in comparison to a protein-free lipid bilayer. Since the specific membrane capacitance is normalized to the size of the cells and not the actual membrane surface, processes which lead to an enlargement of the cell surface such as membrane folding or protrusions result in an increase of the area-specific membrane capacitance. Thus, morphological changes of the cell membrane such as a surface enlargement due to the formation of microvilli can be identified by means of the parameter C_m.

The C_m value of (3.05 ± 0.13) μFcm^{-2} for MDCK-II cells cultured on planar gold film electrodes indicates an increased membrane surface in comparison to an ideally smooth cell membrane ($C_m = 1$ μFcm^{-2}). This increased value of C_m is typical for epithelial cells exhibiting microvilli and membrane folding and is in good agreement with $C_m = (3.03 \pm 0.03)$ μFcm^{-2} determined by Reiß (2004) for MDCK-II cells cultured on planar gold film electrodes. When cells are grown on planar, impermeable substrates, the possibility for a surface enlargement of the basal cell membrane is strongly limited. However, this is not true for mesoporous growth substrates. For MDCK-II cells cultured on type I mesoporous gold film electrodes C_m was calculated to be (4.90 ± 0.29) μFcm^{-2}. For type II mesoporous substrates the specific cell membrane capacitance increases with increasing pore diameter. MDCK-II cells which are seeded upon type II 1 mesoporous gold film electrodes show a C_m value of (4.80 ± 0.20) μFcm^{-2}. For type II 2 and type II 3 electrodes even higher C_m values were obtained, i.e. (5.70 ± 0.14) μFcm^{-2} and (6.39 ± 0.33) μFcm^{-2}.

From these C_m data, it might be concluded that the basal cell membrane follows the surface topography, resulting in a surface enlargement of the cell membrane. This assumption is also supported by the course of the impedance spectrum for cell-covered mesoporous gold film electrodes (chapter 5.3.2, Fig. 5.9, chapter 5.5, Fig. 5.13) which showed a shift to lower frequencies as observed for the cell-free electrode. Rommel (2007) found a completely

different cell behavior on mesoporous substrates with a pore diameter of 900 nm. The impedance spectrum for the cell-covered electrode was not shifted to lower frequencies, which led to the conclusion that the cells simply bridged the pores. The ability of cells to bridge the pores and follow the surface topography has also been reported in other studies. Petronis et al. (2003) showed that fibroblasts are able to bridge channels with a width of 1.8 µm, and that the basal cell membrane penetrates the channels to a depth of 2 – 3 µm. Butor and Davoust (1992) demonstrated by means of SEM micrographs that MDCK-II cells significantly penetrate 3 µm diameter pores of a polycarbonate membrane. In the basal membrane extrusions, cytoplasmic organelles like mitochondria were found. Based on these studies, a penetration of the basal cell membrane in the KOH-pits (type I) and the pores (type I and II) is not unlikely (Fig. 5.16). The increase in C_m for type II mesoporous substrates with increasing pore size confirms this assumption. The bigger the pore size and the smaller the fraction of planar growth surface, the more can the basal cell membrane extend in the pores and increase its surface area. Besides extension of the basal cell membrane into the pores, the cells might also use the porous topography for additional folding of their basal cell membrane.

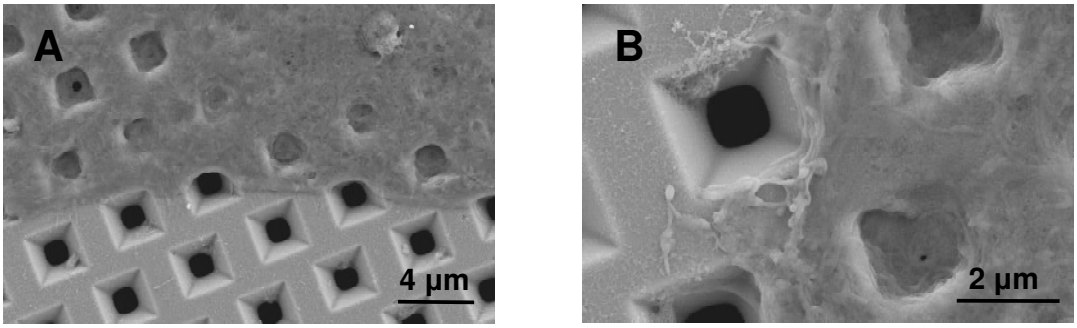

Fig. 5.15 SEM micrographs of MDCK-II cells seeded to sub-confluence on type I mesoporous silicon substrates.

The SEM micrographs (Fig. 5.15) might indicate that the increase in C_m for a mesoporous substrate originates from the enlargement of the basal cell membrane. Figure 5.15 shows MDCK-II cells which have been seeded to sub-confluence upon type I mesoporous substrates. For microscopic analysis of their morphology the cells were fixed with glutaraldehyde. Both micrographs show the boundary between the cell-covered and the cell-free substrate surface. For some pores, the whole cell membrane extends in the pores and follows the surface topography, while for other pores, the apical cell membrane covers the pores. If and to what extent the basal cell membrane follows the surface topography can not be learned from the SEM micrographs. The SEM micrographs might also be an artifact caused by cell shrinking during dehydration or by drying of the specimen. An extension of the apical cell membrane inside the pores is not expected.

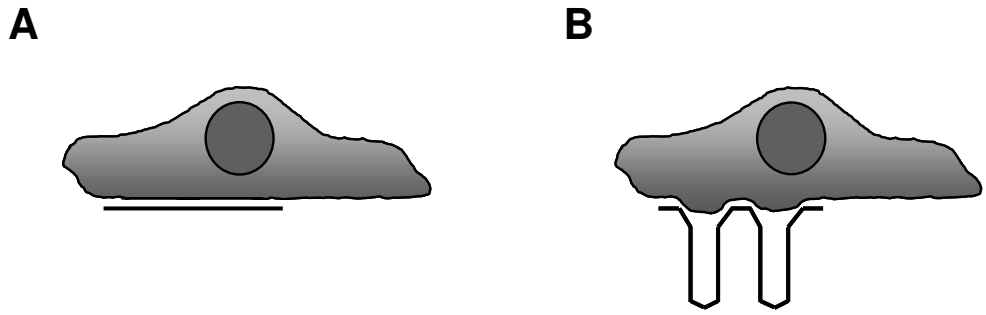

Fig. 5.16 Schematic illustration of the assumed interaction of MDCK-II cells with **A** planar and **B** mesoporous substrates.

Since the parameter C_m is a measure for the average membrane capacitance across the cellular body, a change in the surface topography of the apical cell membrane, such as an increase in the number and size of microvilli in response to the porous surface structure, can not be excluded.

5.7.4 Impact of Surface Topography on Cell Motility

A further aspect of this study was to quantify cell motility on the different surface topographies. Cell motility arises due to the continuous assembly and disassembly of cell-substrate and cell-cell contacts and was termed micromotion (Giaever and Keese, 1991). Micromotion have been electrically recorded as small and rapid fluctuations of the impedance signal of cell-covered gold film electrodes, when the impedance is tracked as a function of time at a single frequency sensitive for these movements. Micromotion was observed to be a fundamental property of living cells and could be correlated with their vitality and metabolic activity (Giaever and Keese, 1991; Lo et al., 1993).

After formation of a confluent cell layer with stable electrical properties on the different surface topographies, the cell motility was followed by recording the impedance of the electrode at 500 Hz as a function of time. The micromotion of MDCK-II cells on different topographically structured surfaces in comparison to planar surfaces was analyzed using the averaged standard deviation of the increments for a sampling interval of 64 s. A high SDI (64 s) value corresponds to high impedance fluctuations and indicates a high cellular motility.

Cell motility on planar substrates was shown to be significantly higher than on the mesoporous substrates (chapter 5.4, Fig. 5.11 and chapter 5.6, Fig. 5.14). For MDCK-II cells cultured on planar gold film electrodes, an SDI (64 s) value of $(2.80 \pm 0.57)\cdot10^{-3}$ was obtained. On type I mesoporous gold film electrodes the SDI (64 s) value amounts to $(1.67 \pm 0.13)\cdot10^{-3}$. On type II mesoporous gold film electrodes, the SDI value decreases with increasing pore diameter. MDCK-II cells cultured on type II 1 and type II 2 mesoporous gold film electrodes reveal SDI (64 s) values of $(1.90 \pm 0.08)\cdot10^{-3}$ and $(1.77 \pm 0.14)\cdot10^{-3}$ which do not differ significantly. On type II 3 mesoporous gold film electrodes, a slightly lower SDI

(64 s) value of $(1.44 \pm 0.17) \cdot 10^{-3}$ was recorded. In summary, the micromotion measurements revealed that MDCK-II cells which were cultured on mesoporous gold film electrodes seemed to be less motile than those cultured on planar gold film electrodes.
A possible explanation for the reduced motility of MDCK-II cells cultured on mesoporous substrates might be the fact that the basal cell membrane seems to follow the surface topography and penetrate the pores, which might hinder the cells to perform micromotion. Moreover, less cell-substrate contacts can be formed on a mesoporous surface than on a planar surface. In order to further elucidate cell motility on mesoporous substrates, it would be interesting to investigate the organization of the cytoskeleton in a cell spreading over a pore, especially in that part of the cell body which is not in contact with the surface of the substrate.

In addition to the experiments reported in this study, this impedimetric approach may have considerable potential to be used in biomaterials research. By varying the substrate material and the surface topographical parameters, such as pore size, depth and pore distribution independently, the influence of surface topography on the cellular properties can be investigated and quantified systematically. This will facilitate the design of biomaterials that are optimally matched to the requirements of a specific biotechnological or biomedical application.

6 Double Mode Impedance Analysis to Probe Cell-Cell and Cell-Surface Interactions

The preceding chapters have demonstrated the applicability and the potential of two different electrical biosensors to analyze the biocompatibility of technical surfaces. In chapter 4 the QCM technique was used as a bioanalytical tool to study the bio- and cytocompatibility of different polymers. Chapter 5 has introduced a biosensor based on the ECIS technique with the potential to analyze the cytocompatibility of a surface containing different topographical features. Both biophysical techniques are based on impedance analysis. The present paragraph deals with the combination of both impedimetric techniques in one experimental setup, which is also referred to as electrochemical QCM or *double mode impedance analysis*. This opens up the possibility to follow and analyze the electrical and viscoelastic properties of the load material on the resonator surface simultaneously. The combined approach was applied to study the adhesion and differentiation characteristics of mammalian cells.
Besides using the *double mode* impedance technique to follow the adhesion and differentiation kinetics of mammalian cells, it was also applied for basic methodological studies addressing several technical details important for data interpretation. For instance, the size and position of the electrochemical electrode were varied systematically or in another approach a partial removal of the cell layer served as an assay to probe the local sensitivity of the mechanical oscillation.

6.1 Cell Adhesion and Differentiation Kinetics of Mammalian Cells Using Double Mode Impedance Analysis

When using uncoated quartz resonators, mass-sensitive QCM readings can be combined with electrochemical studies in one experimental setup, providing additional information about the electrical properties of the surface electrode of the quartz resonator that is facing the liquid. This approach is also known as *double mode impedance analysis* or electrochemical QCM (Wegener et al., 2001). In order to perform *double mode impedance analysis*, the QCM setup (passive mode) was extended by an additional low-impedance dipping electrode, which was introduced into the culture medium from the top of the chamber (chapter 3.5.3.3, Fig. 3.26). This dipping electrode served as a counter electrode for the gold electrode (= working electrode) on the quartz surface. In the following, impedance analysis of the shear oscillation is referred to as "quartz mode" and electrochemical impedance analysis of the upper gold surface electrode as "ECIS mode".

When cells are analyzed with this approach, quartz mode data provide information about cell spreading and cellular micromechanics. ECIS readings on the other hand can be used to follow both, changes in the contact area to the conducting electrode surface, i.e. cell attachment and spreading, as well as changes in cell-cell contacts (cell differentiation). Analysis of cell differentiation is an extension of the analytical options of simple microgravimetric QCM measurements. By selecting the sampling frequency in ECIS mode properly, either the cell-cell contacts or cell-substrate contacts dominate the overall impedance signal such that the frequency can be used to tune in on a certain portion of the cell bodies.
In summary, the combined ECIS-QCM approach provides the experimental options to follow attachment, spreading, cytoskeletal reorientation and cellular differentiation of barrier-forming cell types in a single experimental setup. Since the data are recorded simultaneously from one and the same cell population, the individual time courses of the independent parameters provide a deeper insight into the adhesion and differentiation characteristics of the investigated cells.

Using *double mode impedance analysis*, the adhesion and differentiation characteristics of MDCK-II and NRK cells were studied in a time-resolved manner over a period of 20 h. The experimental setup is shown in chapter 3.5.3.3 (Fig. 3.26). Initially suspended cells were seeded to confluence onto the quartz resonator using serum-containing medium as culture fluid. The QCM measuring chamber was placed in an incubator at 37 °C. Immediately after cell inoculation data acquisition was started by continuously recording double mode impedance spectra. Quartz mode impedance spectra were recorded in the vicinity of the fundamental resonance frequency of 5 MHz, usually from 4.97 MHz to 5.05 MHz, using a non-invasive AC potential of 150 mV amplitude. ECIS mode impedance spectra were acquired in the frequency range between 1 Hz and 10^5 Hz, using a sinusoidal AC voltage of 10 mV.
For a time-resolved representation of cell attachment and spreading, the *quartz mode* data are presented in terms of $\Delta|Z_{min}|$ as a function of time (compare chapter 4.4) normalized to the value for the same, only medium-loaded resonator. In *ECIS mode* the complex impedance Z is converted to resistance and capacitance in order to allow for a more detailed analysis. Cell attachment and spreading are followed using the normalized capacitance C_{norm} at a sampling frequency of 40 kHz. For the analysis of cell differentiation, the normalized electrical resistance R_{norm} at a frequency of 100 Hz (for MDCK-II cells) or 4 kHz (for NRK cells) was followed with time. The resistance at 100 Hz directly mirrors the establishment of cell-cell contacts between epithelial MDCK-II cells. The selection of these two sensitive sampling frequencies is explained below.
Figure 6.1 exemplarily shows the course of the electrochemical impedance $|Z|$, the resistance R and the capacitance C recorded in the frequency range of $1 – 10^5$ Hz for a medium-loaded quartz resonator and the same resonator with an additional layer of MDCK-II cells present on its surface (electrode surface area: 0.33 cm^2).

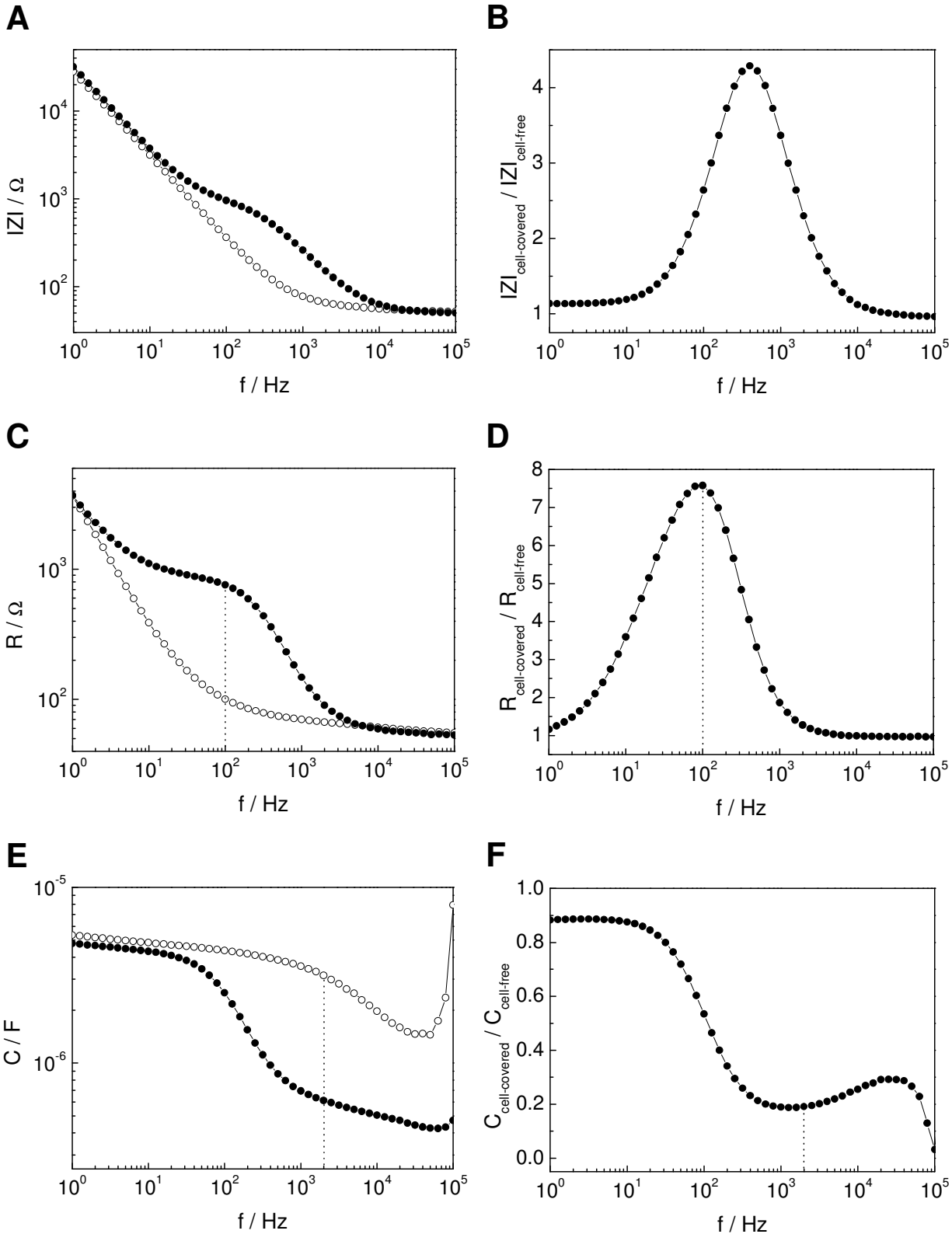

Fig. 6.1 ECIS data of a quartz electrode (0.33 cm^2) with (●) and without (○) a confluent monolayer of MDCK-II cells grown on the resonator surface. **A** The impedance spectrum of the quartz electrode is shown. **C** The resistive portion of the impedance and **E** the capacitance of the system in a frequency range between 1 Hz and 10^5 Hz are depicted. **B**, **D** and **F** show the normalized values of the respective quantities ($|X|_{cell\text{-}covered}/|X|_{cell\text{-}free}$) plotted against the frequency. The vertical lines in C, D indicate the sampling frequency used for time-resolved resistance or capacitance measurements.

The presence of cells on top of the electrode surface primarily affects the impedance spectrum at intermediate frequencies between 20 Hz and 10^4 Hz (Fig. 6.1 A). At the highest frequencies ($f > 10^4$ Hz), the two plots merge to a horizontal plateau that represents the ohmic solution resistance between the working electrode (quartz surface electrode) and the counter electrode (Pt dipping electrode). The best sampling frequency with the contribution of the cell layer dominating the total impedance of the system is determined by dividing the impedance spectrum of the cell-covered electrode by the spectrum of the same empty, only medium-covered electrode (Fig. 6.1 B). In doing so, the most sensitive frequency for time-resolved impedance measurements can be found at a frequency of 400 Hz, which is indicated by a maximum in the ratio $|Z|_{\text{cell-covered}}(f)/|Z|_{\text{cell-free}}(f)$.
The resistance spectrum is affected by the presence of cells on the electrode surface for a frequency range of $10 - 10^4$ Hz (Fig. 6.1 C). Time-resolved resistance measurements to follow cell differentiation are most sensitive when using a sampling frequency of 100 Hz, as indicated by the peak of the normalized resistance $R_{\text{cell-covered}}(f)/R_{\text{cell-free}}(f)$ (Fig. 6.1 D). It is noteworthy that the most sensitive frequency may change with the electrode size and the individual electrical properties of the cells under study. With respect to further resistance studies using surface electrodes of different size, the most sensitive frequency was determined separately for each electrode size in order to guarantee tailored resistance measurements (chapter 6.2.1, Fig. 6.16). A frequency of 100 Hz was selected to follow MDCK-II cell differentiation only on electrodes with a surface area of 0.33 cm^2. For NRK cells, a frequency of 4 kHz was most sensitive for time-resolved resistance measurements during the establishment of a cell monolayer on the 0.33 cm^2 electrode (data not shown).
Figure 6.1 E compares the capacitance spectrum of a cell-covered electrode to the spectrum of a cell-free, only medium-covered electrode. At low frequencies ($f < 20$ Hz), the capacitance spectrum for a cell-covered electrode is equal to the spectrum measured for a cell-free electrode, showing a horizontal plateau. For $f > 20$ Hz, the capacitance decreases due to the attachment and spreading of dielectric cell bodies on the electrode surface. The normalized capacitance spectrum reveals a frequency of 2 kHz where the contribution of the cell layer dominates the total capacitance of the system (Fig. 6.1 F). However, time-resolved capacitance measurements were not performed at 2 kHz, as explained below in Fig. 6.2.

Figure 6.2 traces the capacitance spectrum at different time points after inoculation of MDCK-II cells on the resonator surface. Following the capacitance at a sampling frequency of 2 kHz over time reveals that this frequency is not sensitive for low coverage of the electrode surface with cells. Only high frequencies are suitable to follow the decrease of the electrode capacitance, thus reflecting the formation of close cell-electrode contacts. For this reason, a sampling frequency of 40 kHz was selected for time-resolved capacitance measurements reporting on the time course of cell attachment and spreading even though it holds obvious contributions from parasitic elements like cables or electronics.

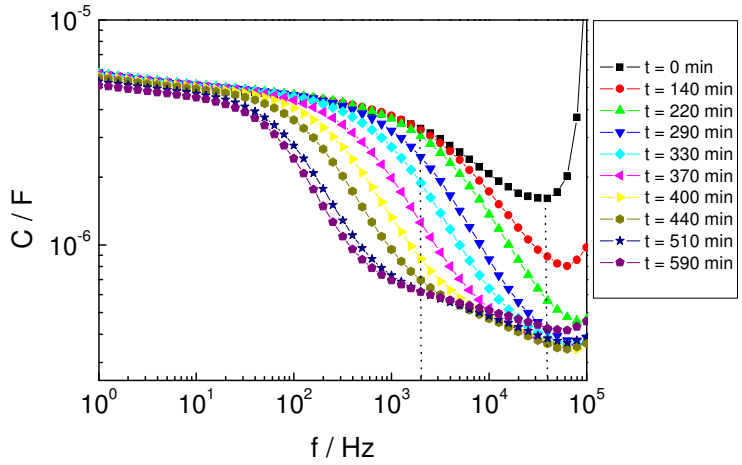

Fig. 6.2 Capacitance *C* of a quartz electrode (0.33 cm^2) at different time points after inoculation of MDCK-II cells plotted against the frequency (see legend). A sampling frequency of 40 kHz was selected for time-resolved capacitance measurements.

In the following, the time courses of the quantities $\Delta|Z_{min}|$ (quartz mode) as well as R_{norm} (100 Hz for MDCK-II cells and 4 kHz for NRK cells) and C_{norm} (40 kHz) (ECIS mode) are shown and compared in detail for the cell lines NRK and MDCK-II during their adhesion and differentiation.

6.1.1 Monitoring NRK Cell Attachment and Spreading Kinetics

The time course of NRK cell attachment and spreading on the surface of an uncoated quartz resonator was investigated by *double mode impedance analysis*. Figure 6.3 compares the time course of the minimal impedance $\Delta|Z_{min}|$ (*quartz mode*) to the time course of the normalized capacitance C_{norm} at a sampling frequency of 40 kHz (*ECIS mode*), starting directly after seeding a suspension of NRK cells to confluence onto the quartz surface.

As already shown in chapter 4.4.1, the time course of $\Delta|Z_{min}|$ is characterized by an immediate increase, leading to a stationary value of (380 ± 11) Ω within 240 min after cell inoculation. The time that is needed to reach half-maximal $\Delta|Z_{min}|$ accounts for $\tau_{1/2}$ = (77 ± 8) min.

When NRK cells attach and spread on the electrode surface, C_{norm} decreases within 350 min to an almost stationary value of 0.15. This final value of C_{norm} corresponds to a confluent monolayer of cells on the surface. The time that is needed to attain half-maximal capacitance decrease and thus half-maximal surface coverage is measured to be (141 ± 6) min.

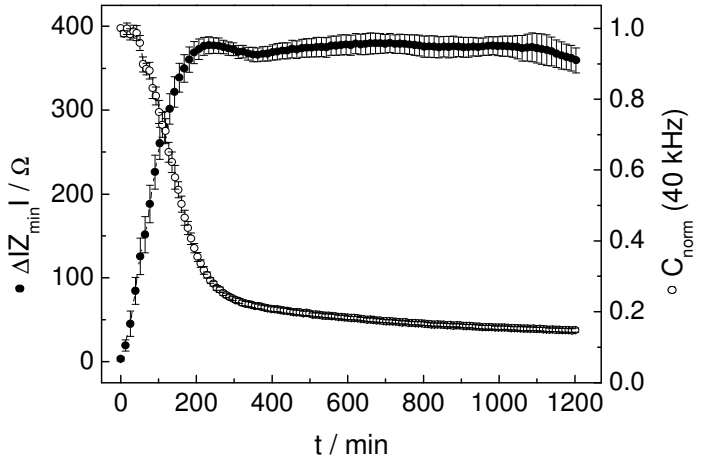

Fig. 6.3 Attachment and spreading of NRK cells followed by *double mode impedance analysis*. The time courses of the minimal impedance $\Delta|Z_{min}|$ (●) and the normalized electrode capacitance C_{norm} at 40 kHz (○) during the adhesion of initially suspended NRK cells are shown. The cells were seeded in a density of 4.5 x 10^5 cm^{-2} at time point zero on the resonator surface. Changes of $|Z_{min}|$ are given relative to a cell-free but medium-loaded resonator. The values of C were normalized to the first capacitance value of the measurement. (C_{start} = (9.17 ± 0.46) μF/cm^2; mean ± SDM, n = 5; T = 37 °C).

Figure 6.4 depicts the time course of the normalized resistance R_{norm} (4 kHz) as deduced from *ECIS mode* measurements as well as the time course of $\Delta|Z_{min}|$ (*quartz mode*) starting directly after cell inoculation.

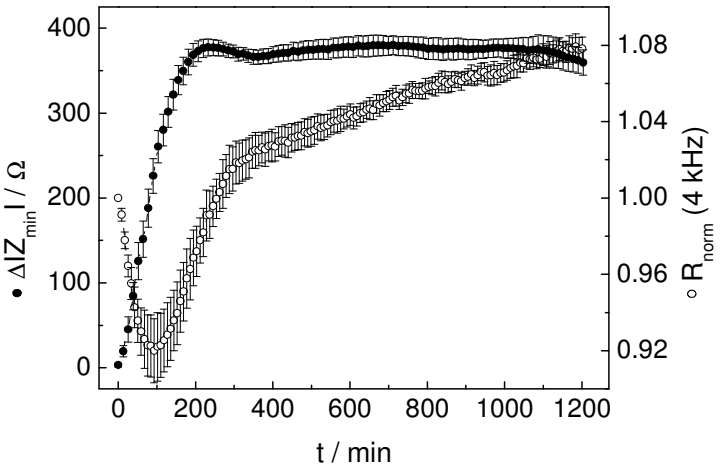

Fig. 6.4 Differentiation of NRK cells recorded in *double mode*. The time courses of the minimal impedance $\Delta|Z_{min}|$ (●) and the normalized resistance R_{norm} measured at 4 kHz (○) during the adhesion and differentiation of initially suspended NRK cells are shown. The cells were seeded in a density of 4.5 x 10^5 cm^{-2} at time point zero on the resonator surface. Changes of $|Z_{min}|$ are given relative to a cell-free but medium-loaded resonator. The values of R were normalized to the first resistance value of the measurement (R_{start} = (74 ± 6) Ω; mean ± SDM, n = 5; T = 37 °C).

The normalized resistance R_{norm} measured at a sampling frequency of 4 kHz passes a minimum at 0.92 within 100 min after cell inoculation which is followed by an increase of R_{norm} to 1.08 during the following experimental time of 1100 min.

Since the double mode impedance data is recorded simultaneously from identical cell populations, the averaged time courses of all three quantities, $\Delta|Z_{min}|$, C_{norm} (40 kHz) as well as R_{norm} (4 kHz) can be directly correlated. Immediately after cell inoculation there is a continuous increase in $\Delta|Z_{min}|$ and a concomitant decrease in C_{norm}, both reflecting primarily the formation of cell-substrate adhesion sites and a continuous progress in cell attachment and spreading to the resonator surface. Whereas $\Delta|Z_{min}|$ reaches a stationary value already after 240 min, it takes 350 min for C_{norm} to reach the steady state. The $\tau_{1/2}$ value deduced from *ECIS mode* measurements is calculated to (141 ± 6) min and hence is almost twice as high as $\tau_{1/2}$ obtained by *quartz mode* measurements, which is (77 ± 8) min. Since NRK cells are leaky epithelial-like cells which do not form a strong diffusion barrier, the parameter R_{norm} does not show a significant increase.

A deeper insight into this correlation of the two quantities $\Delta|Z_{min}|$ and C_{norm} can be gained by plotting the normalized capacitance C_{norm} as obtained from *ECIS mode* measurements as a function of the normalized minimal impedance $|Z_{min}|_{norm}$ acquired by *quartz mode* measurements during cell attachment and spreading (Fig. 6.5).

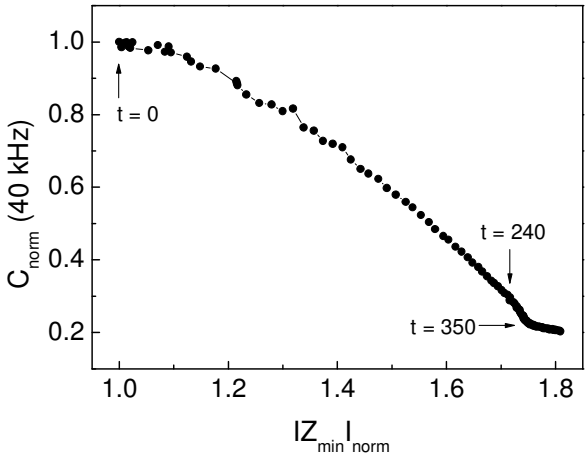

Fig. 6.5 Normalized capacitance C_{norm} (40 kHz) as a function of the normalized minimal impedance $|Z_{min}|_{norm}$ during attachment and spreading of NRK cells for a typical data set. Cells were seeded in a density of 4.5 x 10^5 cm^{-2} into the measuring chamber at $t = 0$ ($\Delta t = 4.2$ min; n = 1; $T = 37$ °C).

Starting at the arrow labeled $t = 0$, the cells were seeded onto the quartz resonator. Each data point marks an increase of the experimental time by 4.2 min. The C_{norm} versus $|Z_{min}|_{norm}$ plot returns a descending line indicating a close-to-linear correlation of both parameters during the time frame of $t = 0$ and $t = 240$ min. This linear range of the curve where both parameters rapidly change indicates the time period during which cell attachment and spreading upon the surface take place. Since the decrease in ΔC_{norm} is proportional to an increase in surface coverage, a linear relation between the quantities C_{norm} and $|Z_{min}|_{norm}$ reveals a linear correlation between surface coverage and $|Z_{min}|_{norm}$. Thus, the initial increase in $|Z_{min}|_{norm}$ can also be regarded as a means to determine the fractional surface coverage.

6.1.2 Monitoring MDCK-II Cell Adhesion and Differentiation Kinetics

As another test cell line MDCK-II cells were investigated with respect to their adhesion and differentiation characteristics on an uncoated resonator using the *double mode* technique. MDCK-II cells exhibit different cell biological, micromechanical and electrical properties. Figure 6.6 compares the time course of the minimal impedance $\Delta|Z_{min}|$ as recorded in *quartz mode* to the time course of the normalized electrode capacitance C_{norm} at a sampling frequency of 40 kHz, acquired in *ECIS mode*, after seeding a MDCK-II cell suspension to confluence on the resonator surface.

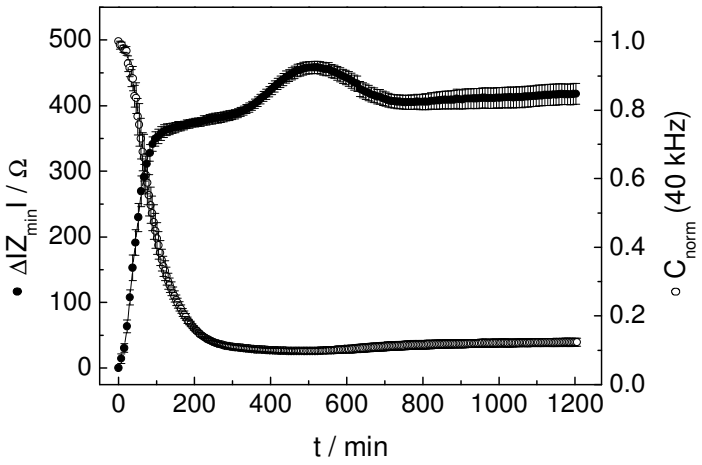

Fig. 6.6 Attachment and spreading of MDCK-II cells followed by *double mode impedance analysis*. The time courses of the minimal impedance $\Delta|Z_{min}|$ (•) and the normalized electrode capacitance C_{norm} at 40 kHz (○) during the adhesion of initially suspended MDCK-II cells are shown. The cells were seeded in a density of 4.5 x 10^5 cm^{-2} at time point zero on the resonator surface. Changes of $|Z_{min}|$ are given relative to a cell-free but medium-loaded resonator. The values of C were normalized to the first capacitance value of the measurement. (C_{start} = (9.32 ± 0.54) µF/cm^2; mean ± SDM, n = 7; T = 37 °C).

For MDCK-II cells which are seeded at time point zero into the measuring chamber, $\Delta|Z_{min}|$ instantaneously increases to a first plateau phase at (376 ± 7) Ω within 135 min. After about 300 min the plateau phase is followed by a second moderate increase to a maximum value of (458 ± 9) Ω at (520 ± 15) min after cell inoculation. After having passed the maximum, $\Delta|Z_{min}|$ decreases by approximately 50 Ω to a constant value. The time that is needed to reach half-maximal $\Delta|Z_{min}|$ increase, $\tau_{1/2}$, is determined to be (46 ± 3) min.

The time course of C_{norm} at 40 kHz undergoes a steep decrease directly after cell inoculation, reaching a stationary value after about 300 min. This final value of C_{norm} accounts for one tenth of the initial capacitance value and corresponds to a confluent monolayer of cells on the surface. The time needed to reach half-maximal capacitance decrease is determined to (80 ± 7.5) min.

Figure 6.7 depicts the time course of the normalized resistance R_{norm} (100 Hz) as deduced from ECIS mode measurements in direct comparison to the time course of $\Delta|Z_{min}|$ (quartz mode), starting directly after cell inoculation.

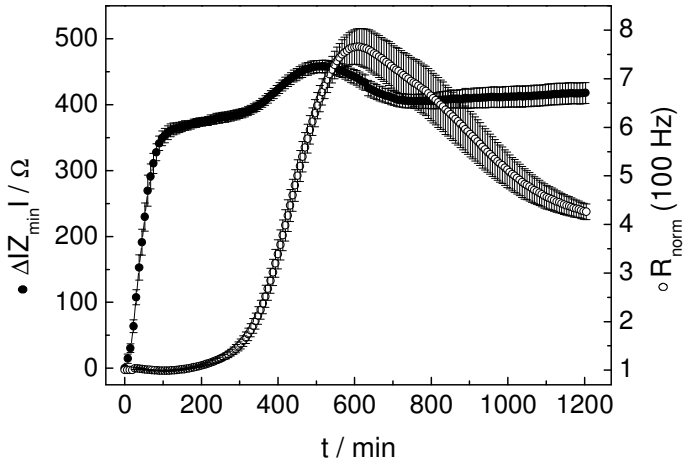

Fig. 6.7 Differentiation of MDCK-II cells recorded in *double mode*. The time courses of the minimal impedance $\Delta|Z_{min}|$ (●) and the normalized resistance R_{norm} measured at 100 Hz (○) during the adhesion and differentiation of initially suspended MDCK-II cells are shown. The cells were seeded in a density of 4.5 x 10^5 cm^{-2} at time point zero on the resonator surface. Changes of $|Z_{min}|$ are given relative to a cell-free but medium-loaded resonator. The values of R were normalized to the first resistance value of the measurement (R_{start} = (98 ± 2) Ω; mean ± SDM, n = 7; T = 37 °C).

The normalized resistance R_{norm} measured at a sampling frequency of 100 Hz undergoes a steep increase starting 250 min after cell inoculation. The maximum which corresponds to an almost eightfold increase of R_{norm} is attained after (600 ± 12) min, followed by a decrease in R_{norm}.

Both independent quantities $\Delta|Z_{min}|$ as well as C_{norm} (40 kHz) recorded simultaneously for the same sample primarily report on the kinetics of cell attachment and spreading to the resonator surface. Thus, their individual time courses are similar. Whereas $\Delta|Z_{min}|$ reaches a stationary value already after 135 min, C_{norm} takes 300 min. Exact at this time point (300 min), $\Delta|Z_{min}|$ continues to increase to the second maximum which is attained after (520 ± 15) min. The second increase of $\Delta|Z_{min}|$ arises from acoustic changes within the cell bodies anchored to the surface, due to shaping up of the actin cytoskeleton. The barrier properties of the MDCK-II cell layer, characterized by the parameter R_{norm}, do not establish before $\Delta|Z_{min}|$ has reached the first transient plateau phase and C_{norm} its respective steady state. The maximum of $\Delta|Z_{min}|$ is attained within (520 ± 15) min after cell inoculation, while it takes longer for R_{norm} to reach its maximum value ((600 ± 12) min).

The following Fig. 6.8 traces C_{norm} versus $|Z_{min}|_{norm}$, illustrating the correlation of both adhesion parameters for MDCK-II cell adhesion and differentiation. When MDCK-II cells are seeded on the quartz resonator at t = 0, they give rise to an instantaneous decrease in C_{norm} and a concomitant increase in $|Z_{min}|_{norm}$. In contrast to the C_{norm} versus $|Z_{min}|_{norm}$ plot for NRK cells, this plot shows a close-to-linear type relation of both parameters only in a short time interval

between $t = 42$ and $t = 100$ min. At $t = 135$ min, the slope of the plot increases in magnitude, indicating that C_{norm} still continues to decrease while $|Z_{min}|_{norm}$ does not change significantly anymore.

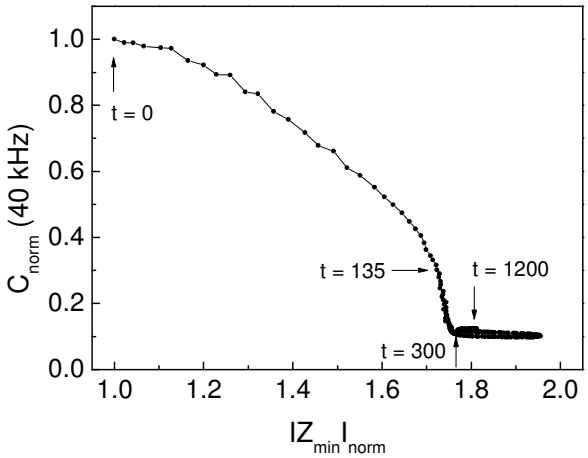

Fig. 6.8 Normalized capacitance C_{norm} (40 kHz) as a function of the normalized minimal impedance $|Z_{min}|_{norm}$ during attachment and spreading of MDCK-II cells for a typical data set. Cells were seeded in a density of 4.5 x 10^5 cm^{-2} into the measuring chamber at $t = 0$ ($\Delta t = 4.2$ min; n = 1; $T = 37$ °C).

300 min after cell inoculation, the capacitance reaches a stationary value, while $|Z_{min}|_{norm}$ still changes. This latter increase and the final decrease in $|Z_{min}|_{norm}$ describes the transient second maximum (compare Fig. 6.6) and can be ascribed to changes (reorganization) of the actin cytoskeleton. Since MDCK-II cells reveal more features which mask cell spreading, a linear type correlation between C_{norm} and $|Z_{min}|_{norm}$ is only obtained for a short period of time.

6.2 Monitoring Cell Adhesion and Differentiation Kinetics upon Resonators with Partly Covered Surface Electrode

Quartz resonators as used in this study are interfaced to the experimental electronics via gold electrodes with a surface area of 0.33 cm^2. This is much larger (factor 660) than the surface area of working electrodes usually applied in ECIS experiments, leading to a reduced sensitivity of the recorded ECIS mode impedance signal. As this interferes with the detection of non barrier-forming leaky epithelia, an experimental setup was established which should provide an increased sensitivity in the impedance data of *ECIS mode* measurements. This increase in sensitivity can be achieved by reducing the surface area of the resonator's top electrode in contact to the electrolyte for the electrochemical experiment whereas the electrode to excite the shear oscillation should be unchanged. The applicability of the combined experimental setup with increased sensitivity in the *ECIS mode* should be validated by seeding MDCK-II or NRK cells on these modified quartz resonators and monitoring their adhesion and spreading with time using *double mode impedance analysis*.

In order to attain and study the sensitivity increase of *ECIS mode* measurements, the size of the exposed gold electrode on the quartz resonator had to be reduced. This was achieved by coating the complete quartz resonator surface with photopolymer (PhoP) in order to insulate the gold electrode. By means of photolithography (chapter 3.2.2) well defined circular holes were introduced into the insulating PhoP film in order to expose only a fraction of the total surface electrode area to the bulk. Thus, an individual working electrode with a surface area of either 0.083 cm^2 (Ø ~ 3 mm) or 0.0022 cm^2 (Ø ~ 0.5 mm) could be established on the resonator surface. The electrodes of either size were located in the center on the quartz surface. Figure 6.9 presents stereomicroscopic pictures of the two established gold electrode designs.

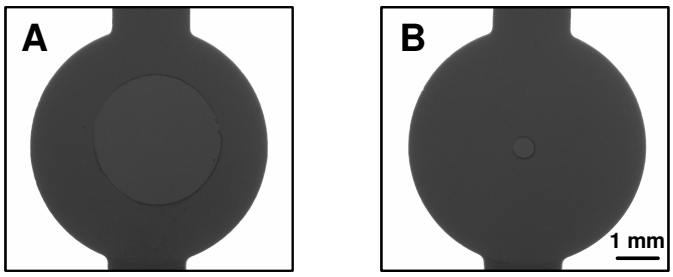

Fig. 6.9 Stereomicroscopic pictures documenting the electrode layout established on top of the upper surface electrode of the quartz resonator. The electrodes with a surface area of **A** 0.083 cm^2 (Ø ~ 3mm) and **B** 0.0022 cm^2 (Ø ~ 0.5 mm) cm^2 using diascopic (transmitted) illumination are shown.

Film Thickness Determination

Vertical scanning interferometry (VSI) measurements were performed for quality control of the photolithographic process and to determine the PhoP film thickness. Figure 6.10 presents a 3D height map of a typical PhoP film with a circular opening of 0.0022 cm^2 introduced by photolithography, showing the polymer-free substrate surface (glass) in the middle as well as the surrounding intact polymer.

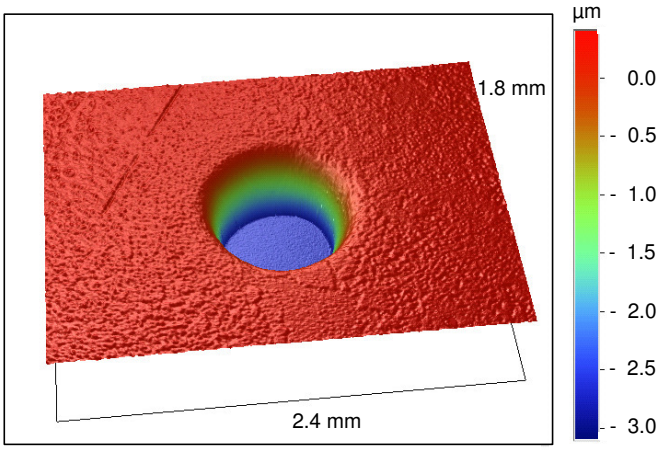

Fig. 6.10 3D VSI image of a typical spin coated PhoP surface with a circular opening (0.0022 cm^2) within the polymer film. Height profiles provide the film thickness.

The PhoP surface appears to be rough, which might be a possible consequence of the photolithographic procedure. From the 3D height map the thickness of the PhoP film was determined by choosing a line profile which crosses the circular hole in the polymer film. Thus, the depth of this area relative to the surrounding polymer was measured. The height profile (Fig. 6.11 B) taken along the red line in Fig. 6.11 A indicates an average film thickness of (2972 ± 11) nm, identical to the thickness previously determined for spin coated PhoP (see chapter 4.1.2).

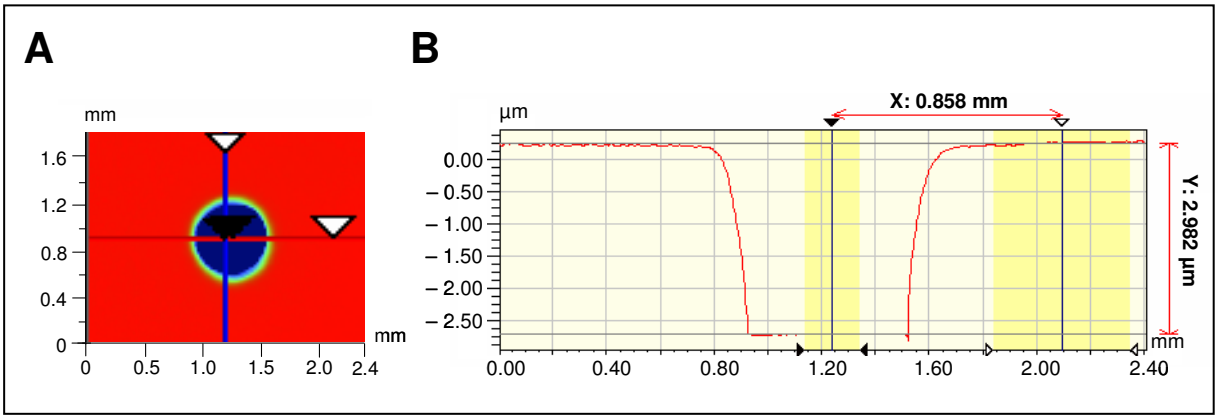

Fig. 6.11 Film thickness determination of spin coated PhoP. **A** 2D height image of PhoP with the circular opening introduced into the polymer film (red: PhoP; blue: glass substrate). **B** Height profile taken across the circular area along the red line in A. The two arrow heads mark the region which was used for thickness determination.

Besides film thickness or surface roughness, additional information can be extracted from the height profile: the slope of the PhoP at the edge to the substrate surface. It is apparent from Fig. 6.11 B that photolithography does not generate a sharp edge. For seven individual electrodes, an average inclination angle between PhoP and the substrate surface of (1.5 ± 0.1)° is obtained. It is noteworthy that a small inclination angle as the one obtained for PhoP is a prerequisite when studying cell attachment and spreading upon these surfaces, since a small angle should allow the cells to bridge between the different areas, i.e. the gold electrode and the PhoP, without any loss of their cell-cell contacts.

Monitoring the Photolithographic Process by QCM

The amount of PhoP remaining on the resonator surface after photolithographic introduction of the electrode openings was quantified by performing QCM measurements in the *passive mode*. The resonator was characterized in its empty unloaded state, after PhoP film deposition and after photolithographic introduction of circular openings of 0.0022 cm^2 as well as 0.083 cm^2. The measurement was performed in air in order to exclude possible interactions of the spin coated polymer film with fluids like polymer swelling. The results are presented in terms of the phase shift as a function of frequency for a 5 MHz quartz resonator near its fundamental frequency (Fig. 6.12).

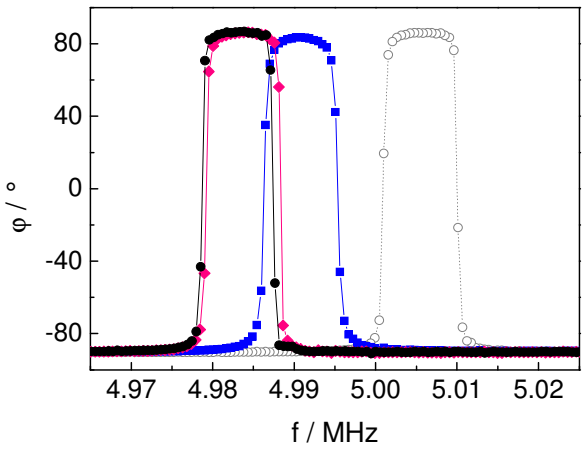

Fig. 6.12 Phase spectra near resonance of a quartz resonator, before (○) and after (●) spin coating a PhoP film. A circular opening of 0.0022 cm^2 (♦) or 0.083 cm^2 (■) was introduced at the center of the original surface electrode by means of photolithography.

Loading the quartz resonator with a PhoP film translates the phase spectrum along the frequency axis to lower frequencies. The internal structure of the spectra remains unchanged. The magnitude of the frequency shift depends on the surface area of the quartz resonator that is covered with PhoP. A circular opening of 0.083 cm^2 (■) induces a significant frequency shift when compared to the unloaded resonator. The phase spectrum for a quartz resonator with a circular opening of 0.0022 cm^2 (♦) in the PhoP overlayer is shifted to even lower frequencies and gets close to the spectrum for a completely covered quartz resonator.

From measurements of the resonator's total inductance before and after mass deposition as well as after having introduced the circular openings of different diameters into the insulating PhoP film, it is possible to quantify the deposited mass of PhoP. The value for the inductance change can be obtained by fitting the transfer function of the BVD equivalent circuit to the recorded phase spectrum of the unloaded and PhoP coated quartz resonators (see chapter 4.1.3).

Table 6.1 compares the amount of mass deposited on the sensor surface for a complete coverage, coverage with a circular opening of 0.0022 cm^2 as well as 0.083 cm^2.

Tab. 6.1 Deposited mass on the resonator surface (0.28 cm^2) quantified by QCM. (Mean ± SDM; n ≥ 2).

PhoP Coverage	QCM mass [µg]	Mass Fraction [%]	Surface Coverage [%]
Complete	189.2 ± 1.8	100	100
0.0022 cm^2 opening	179.8 ± 1.2	95	99.2
0.083 cm^2 opening	120.8 ± 3.4	64	70.4

For the PhoP coated quartz resonator with a circular opening of 0.083 cm^2 within the PhoP layer, an average value of $L_m = (267.5 \pm 7.5)$ µH is obtained for the inductance due to polymer film deposition (n = 2). Using Eq. 3.22 (chapter 3.5.2.2), the deposited mass is

calculated to (120.8 ± 3.4) µg. When analyzing the impedance raw data of the PhoP coated resonator with a circular opening of 0.0022 cm^2, an average inductance of L_m = (398.1 ± 2.7) µH is obtained for three individually prepared resonators. This results in an amount of mass of m = (179.8 ± 1.2) µg. The mass fraction of PhoP on the resonator surface determined by QCM measurements and the PhoP surface coverage obtained from microscopic pictures (CLSM) are in reasonable agreement. The QCM data indicate a slightly lower surface coverage than the microscopic data, which is most likely due to the non-uniform lateral mass sensitivity of the resonator which is highest in the center and falls off to the edges.

Attachment and Spreading of Mammalian Cells

Polymer deposition and subsequent photolithography constitutes an inclination angle of (1.5 ± 0.1)° with the substrate surface. This rather smooth transition from the substrate surface to the PhoP surface does not hinder or interfere with cell attachment and spreading.

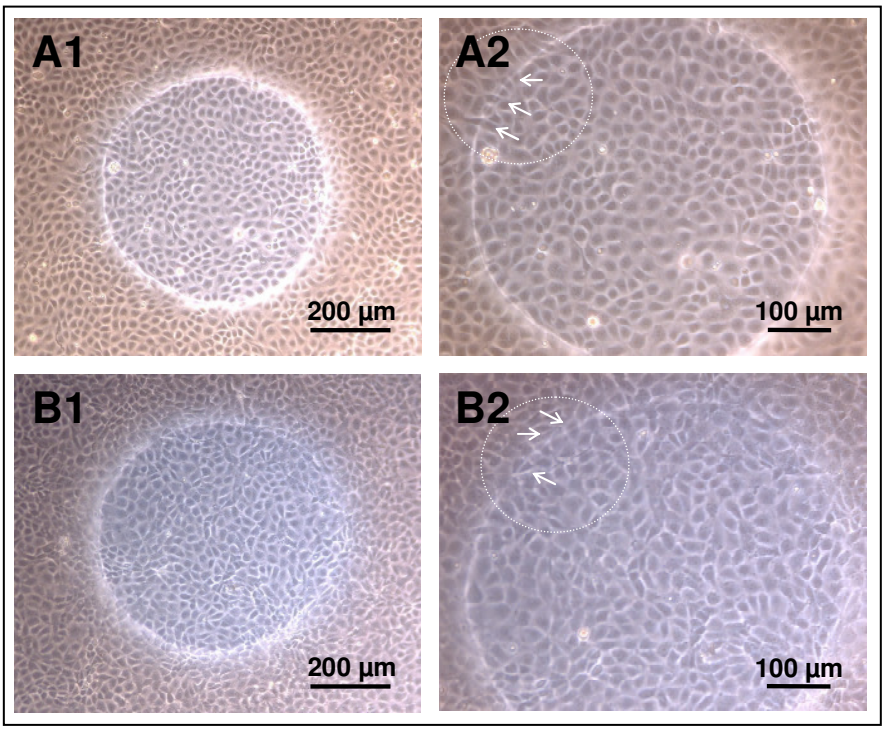

Fig. 6.13 Phase contrast micrographs of **A** MDCK-II and **B** NRK cells 24 h after seeding to confluence on PhoP with a circular opening of 0.0022 cm^2. The images document the ability of cells to bridge the height difference between the substrate and the PhoP surface (arrows).

Mammalian cells are able to bridge such a height difference between substrate surface and PhoP as confirmed by the phase contrast micrographs, showing MDCK-II and NRK cells 24 h after seeding to confluence on a PhoP coated substrate with a circular opening of 0.0022 cm^2 (Fig. 6.13 A, B). MDCK-II as well as NRK cells do not differentiate between the glass substrate surface and the PhoP surface they adhere to, indicated by the formation of a

confluent monolayer regardless of the underlying substrate. Thus, the slight height difference between the two substrate surfaces does not seem to influence cell growth. The cells easily bridge the border between substrate surface and PhoP surface, justifying this approach as a suitable means for studying cell attachment and spreading.

The applicability of these modified resonators with smaller working electrodes provided by circular openings in a PhoP overlayer were tested in cell attachment and spreading assays. The main focus was on the sensitivity increase in *ECIS mode* measurements. MDCK-II or NRK cells were seeded to confluence on the modified quartz resonators and their adhesion and spreading was monitored with time by *double mode impedance analysis*. In order to prevent polymer swelling to interfere with the adhesion signal, the PhoP coated resonators were exposed to a physiological fluid (SFM) over a period of 20 h (37 °C) prior to cell inoculation.

6.2.1 Adhesion and Differentiation of MDCK-II Cells

The following two figures (Fig. 6.14 and 6.15) present the raw data as they were recorded in either measuring modes (*quartz mode* and *ECIS mode*) for electrodes of different sizes before MDCK-II cells were seeded and after the cell layer was fully established. Besides showing the spectra for surface electrodes with an area of 0.083 cm^2 and 0.0022 cm^2, the raw data for an uncoated (0.33 cm^2) and a completely coated quartz resonator are also presented in order to allow for a full comparison of results. *Quartz mode* raw data was chosen to be presented in the form of phase spectra and *ECIS mode* data in the form of impedance spectra.
The surface load of the quartz resonator with PhoP increases when following Fig. 6.14 A till D. Fig. 6.14 A presents an empty, uncoated quartz resonator before and after the formation of a confluent MDCK-II cell layer. The presence of a confluent cell layer on the uncoated resonator surface causes the phase maximum to decrease by approximately 27.4° compared to a cell-free resonator covered with medium only. On a quartz resonator completely coated with PhoP, MDCK-II cells induce a decrease in the phase angle by 26.7° (Fig. 6.14 D). Thus, the existence of an underlying PhoP layer does not change the acoustic load of the resonator significantly. The cells damp the quartz oscillation to the same extent, i.e. the impact of the cells on the mechanical oscillation remains unchanged. For a quartz resonator wearing a PhoP coating with a circular opening of either 0.083 cm^2 or 0.0022 cm^2, the phase spectra are very similar with no extra resonance (Fig. 6.14 B, C). This finding is surprising, since the resonator is not uniform in thickness. Due to the circular electrode, the center of the sensor surface is uncoated while the surrounding region is coated by a PhoP film, increasing the resonator's thickness by approximately 3 µm and thereby changing the resonance condition of the crystal in these areas. Thus, the quartz resonator might exhibit two resonance conditions, as presented by one resonance frequency for the uncoated region and another lower resonance frequency

for the PhoP coated region. At least, a change in the resonance curve is expected. However, such a change in the resonance frequency is not observed.

MDCK-II cells which are cultured on a quartz resonator with a 0.083 cm^2 working electrode decrease the phase maximum by 34.5° (Fig. 6.14 B), whereas a confluent MDCK-II cell monolayer on a quartz resonator with an active electrode of 0.0022 cm^2 causes a 32.3° decrease of φ_{max} (Fig. 6.14 C). This similar decrease of the phase maximum for both electrode sizes indicates that the impact of cells on the mechanical oscillation is similar and does not depend on the surface area of the working electrode exposed to the bulk. The whole cell layer attached to the gold electrode as well as to the PhoP film seems to contribute to the damping of the quartz oscillation.

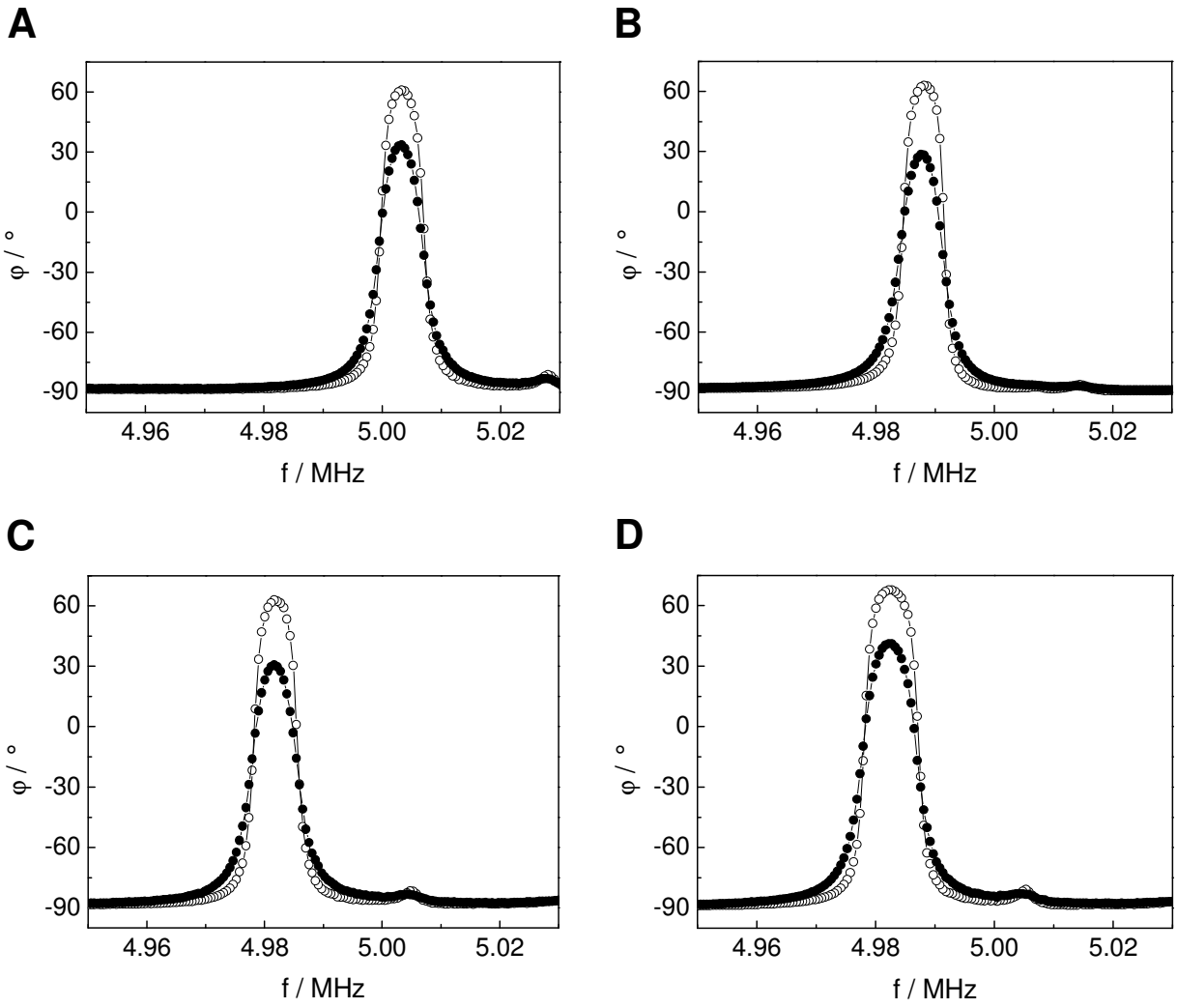

Fig. 6.14 Phase shift φ of a 5 MHz quartz resonator as a function of frequency with (●) and without (○) a confluent monolayer of MDCK-II cells directly grown on its surface (*quartz mode*). Different fractions of the total electrode area on the resonator surface are coated with PhoP: **A** Uncoated (0.33 cm^2 gold electrode), **B**, **C** coated with PhoP except for a circular opening of 0.083 cm^2 (B) and 0.0022 cm^2 (C) in the center, **D** completely coated with PhoP. (T = 37 °C).

The corresponding *ECIS mode* measurements performed in parallel are presented in the following. Figure 6.15 compares the frequency spectra of the impedance magnitude |*Z*| for gold working electrodes of different diameter established on the resonator surface with and without a confluent monolayer of MDCK-II cells.

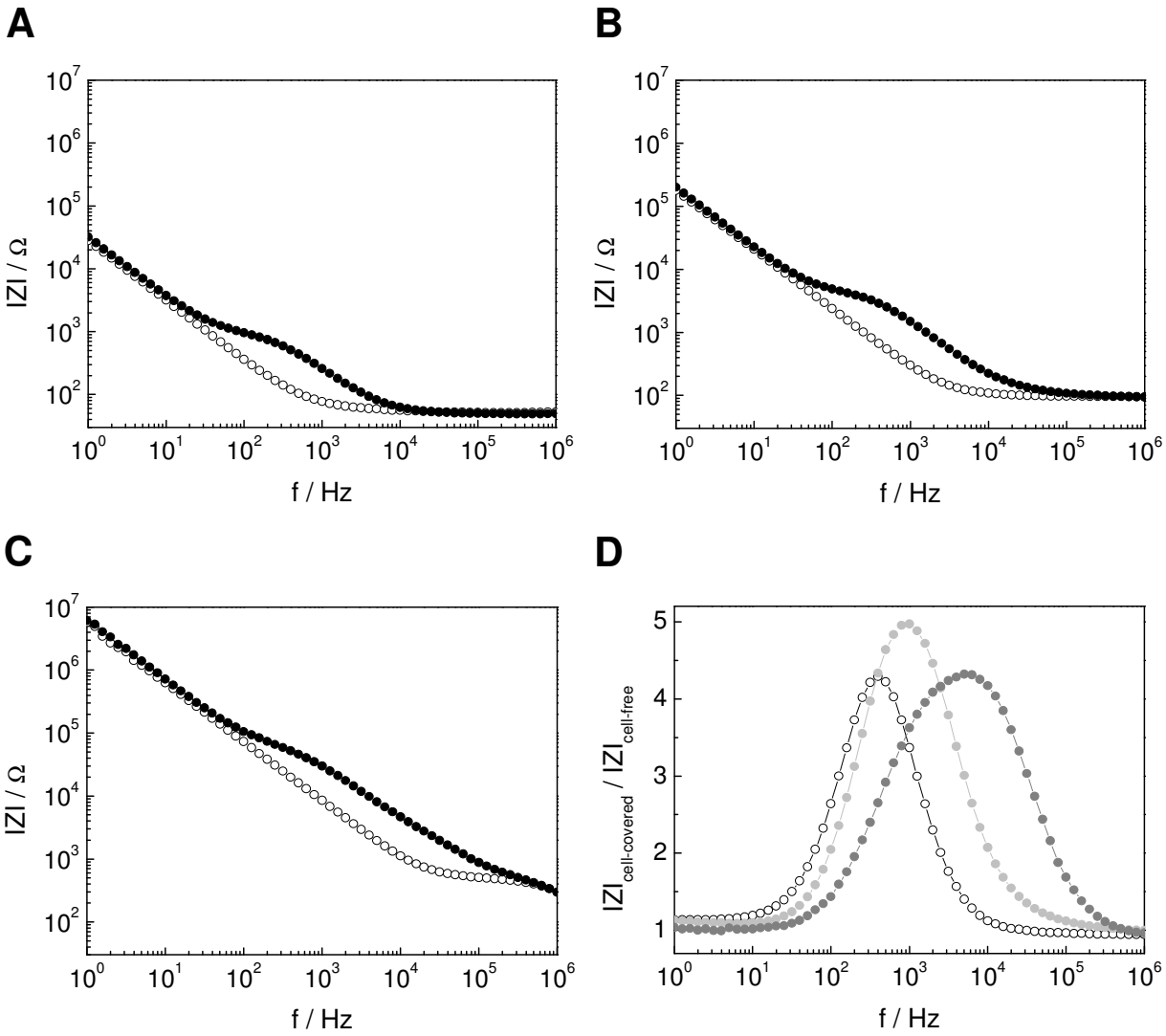

Fig. 6.15 Frequency-dependent impedance magnitude |*Z*| for gold electrodes with (●) and without (○) a confluent monolayer of MDCK-II cells directly grown on the resonator surface (*ECIS mode*). Different fractions of the surface electrode on the resonator are coated with PhoP, giving rise to the following surface areas of the active working electrodes in ECIS mode: **A** 0.33 cm^2 (Ø = 6 mm), **B** 0.083 cm^2 (Ø = 3mm), **C** 0.0022 cm^2 (Ø = 0.5mm). **D** Normalized impedance $|Z|_{cell\text{-}covered}/|Z|_{cell\text{-}free}$ plotted against the frequency for the electrodes of different area (○) 0.33 cm^2, (◉) 0.083 cm^2 and (●) 0.0022 cm^2.

A comparison of the impedance spectra for the cell-free electrodes reveals that a reduction of the surface area of the working electrode from 0.33 cm^2 (Fig. 6.15 A) to 0.0022 cm^2 (Fig. 6.15 C) causes an increase of the overall system impedance and a resulting shift of the spectrum to higher frequencies. The presence of cells on the standard electrode setup with a 0.33 cm^2 working electrode contributes to the impedance spectrum for intermediate frequencies between 20 Hz and 10^4 Hz (Fig. 6.15 A). For an electrode area of 0.083 cm^2,

cellular contributions stretch along the frequency range from 30 Hz to $5 \cdot 10^4$ Hz (Fig. 6.15 B). A confluent cell layer on the electrode with a surface area of 0.0022 cm^2 influences the total impedance of the system in the frequency range between 80 Hz and $3 \cdot 10^5$ Hz (Fig. 6.15 C). The sensitive frequency range where the contribution of cells to the impedance of the system is significant broadens with decreasing surface area of the working electrode. Fig. 6.15 D compares the normalized impedance spectra $|Z|_{cell\text{-}covered}(f)/|Z|_{cell\text{-}free}(f)$ for the electrodes of different surface area. For the 0.33 cm^2 working electrode (○), the normalized impedance shows a maximum at 400 Hz. The normalized impedance for the 0.083 cm^2 working electrode (●) peaks at 1000 Hz and for the 0.0022 cm^2 electrode (●) at 5000 Hz. Besides the shift of the normalized impedance to higher frequencies with decreasing electrode size, the area under the curve also increases, indicating an increase in sensitivity for *ECIS mode* measurements when using smaller working electrodes.

In order to quantify cell adhesion and differentiation in a time-resolved manner by ECIS measurements, the normalized capacitance C_{norm} at 40 kHz and the normalized resistance R_{norm} at the most sensitive frequency for each surface area of the working electrodes were followed with time after cell inoculation. The most sensitive frequency for time-resolved resistance measurements was obtained by determining the frequency where the ratio $R_{cell\text{-}covered}(f)/R_{cell\text{-}free}(f)$ shows an absolute maximum (Fig. 6.16).

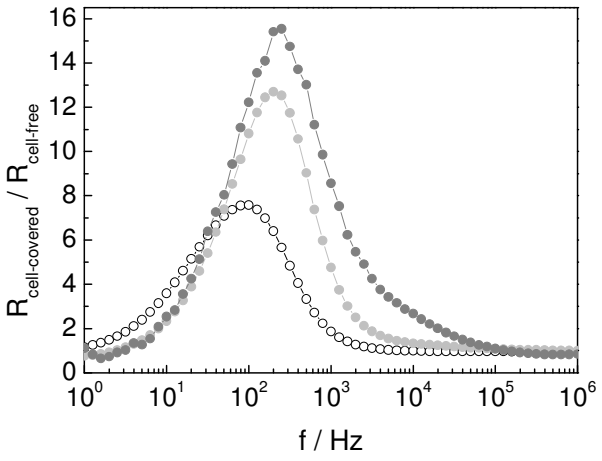

Fig. 6.16 Normalized resistance $R_{cell\text{-}covered}/R_{cell\text{-}free}$ for MDCK-II cells grown to confluence on electrodes of different area (○) 0.33 cm^2, (●) 0.083 cm^2 and (●) 0.0022 cm^2. The measured resistance of the electrode with confluent MDCK-II cells was divided by the corresponding values of the cell-free electrode and plotted as a function of frequency.

It is apparent that the most sensitive frequency to follow cell differentiation changes with the electrode size. For an uncoated quartz resonator with a working electrode of 0.33 cm^2, the contribution of the cell layer to the total resistance of the system is most pronounced at a frequency of 100 Hz. The most sensitive sampling frequency for a 0.083 cm^2 electrode is shifted to slightly higher frequencies and is 200 Hz. For the smallest electrode (0.0022 cm^2) the plot shows a maximum at 250 Hz. Thus, time-resolved resistance measurements after

inoculation of MDCK-II cells on the different electrodes were performed at the most sensitive frequency individually determined for each electrode size, i.e. at 100 Hz for 0.33 cm^2 working electrodes, at 200 Hz for 0.083 cm^2 working electrodes and at 250 Hz for 0.0022 cm^2 working electrodes. Besides the minor shift to higher frequencies with decreasing electrode size, also the maximal values of the normalized resistance increase, indicating an increase in sensitivity of resistance measurements with smaller electrode sizes.

The following figures (Fig. 6.17 – 6.19) show the time course of $\Delta|Z_{min}|$ as extracted from *quartz mode* measurements as well as C_{norm} (40 kHz) and R_{norm} (100 Hz, 200 Hz or 250 Hz) as extracted from *ECIS mode* measurements during the adhesion and differentiation of MDCK-II cells.

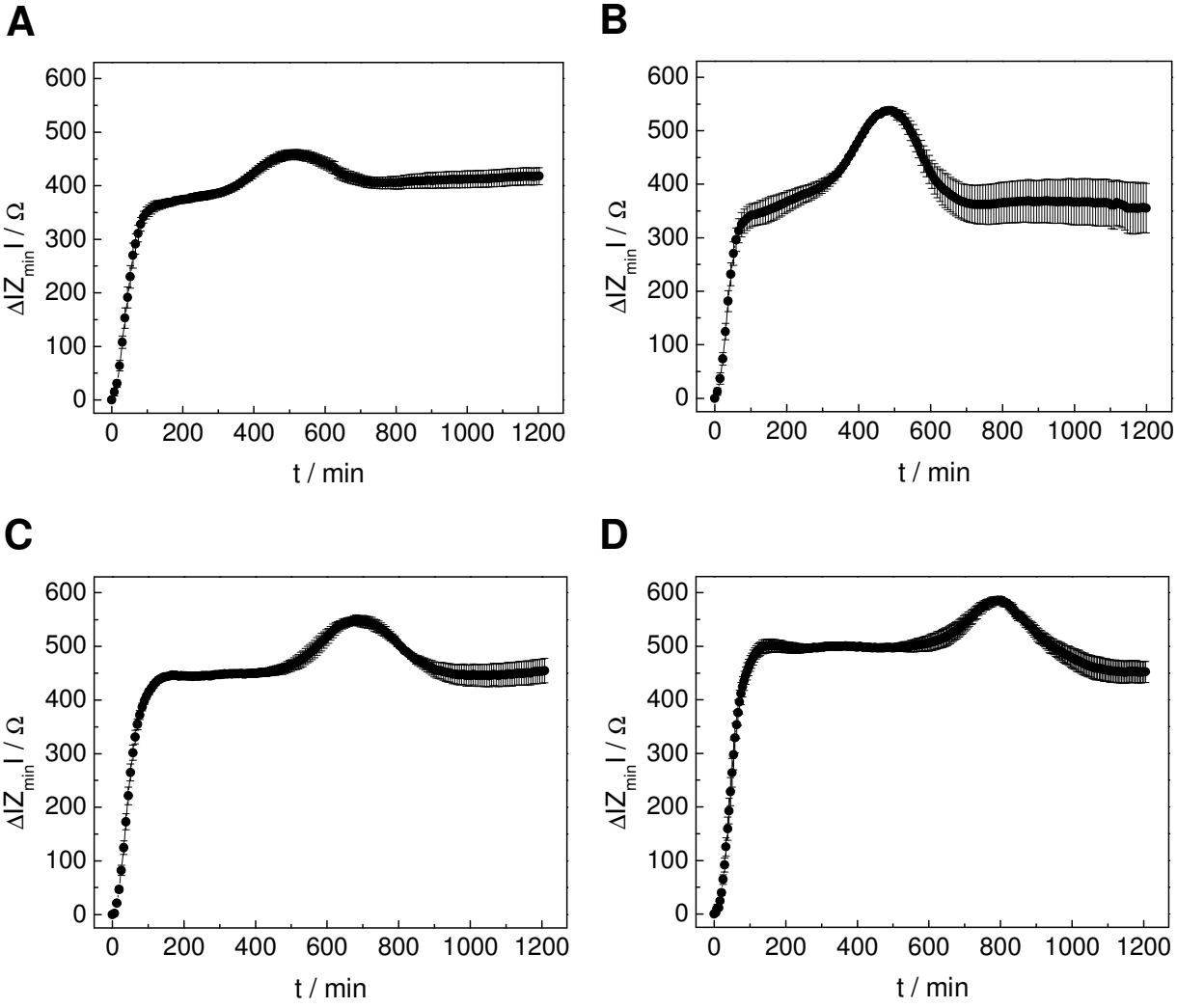

Fig. 6.17 Time course of $\Delta|Z_{min}|$ when equal amounts of initially suspended MDCK-II cells are seeded at time point zero on quartz resonators whose surface electrode is gradually covered by PhoP films: The sensor surface is **A** uncoated, **B**, **C** coated with PhoP except for a circular opening of 0.083 cm^2 (B) or 0.0022 cm^2 (C), **D** completely coated with PhoP. The cell density was adjusted to 4.5×10^5 cm^{-2}. The value of $|Z_{min}|$ at the beginning of the experiment was set to zero. (Mean ± SDM, $n \geq 3$; $T = 37$ °C).

The comparison of the time course of MDCK-II cell attachment and spreading upon an uncoated resonator (Fig. 6.17 A), which has been described in detail before (chapter 4.4.2), with the course of $\Delta|Z_{min}|$ for a quartz resonator covered with PhoP except for a circular opening of 0.083 cm^2 (Fig. 6.15 B) reveals similarities regarding the time that is needed to reach the transient plateau phase, the absolute $\Delta|Z_{min}|$ values in this plateau phase and its duration (Tab. 6.2). However, a difference can be found in the recorded $\Delta|Z_{min}|$ values for the second plateau. Whereas cells seeded upon an uncoated resonator give rise to a maximum of (458 ± 9) Ω, a value of (538 ± 6) Ω is obtained for the resonator with the 0.083 cm^2 circular opening.

Figure 6.15 C presents $\Delta|Z_{min}|$ as a function of time when a suspension of MDCK-II cells is seeded onto a PhoP coated quartz resonator with a circular opening of 0.0022 cm^2. The curve shows only similarities in the very beginning of the experiment, whereas the further course differs to some extent from the previously mentioned curves (Tab. 6.2). Having reached the first plateau phase, it is maintained for as long as 300 min. The second plateau of (549 ± 10) Ω is attained only 684 min after cell inoculation. A second difference is the absolute $\Delta|Z_{min}|$ values, which are in general 70 – 90 Ω higher than the respective values on the uncoated resonator surface.

For a quartz resonator completely covered with PhoP, a similar behavior can be found (Fig. 6.15 D). $\Delta|Z_{min}|$ increases to a first plateau phase of (498 ± 6) Ω before it continues to rise reaching a second plateau of (586 ± 7) Ω about 793 min after cell inoculation.

In summary, all four attachment and spreading curves recorded for MDCK-II cells seeded onto quartz resonators with different fractions of its surface electrode being covered with PhoP are similar with respect to their initial slope. Depending on the fractional coverage of the resonator surface with PhoP, the length of the first plateau phase as well as the time that is needed to reach the second plateau differ (Tab. 6.2). With increasing coverage of the resonator surface with PhoP, starting with an uncoated resonator and ending up with a completely coated one, the length of the first plateau phase is gradually extended from 200 min to finally 440 min. In a similar manner the τ_2 values rise with increasing PhoP surface coverage. Here, the τ_2 value for the resonator with the 0.083 cm^2 circular opening seems to be an exception. Moreover, the absolute $\Delta|Z_{min}|$ values for the first plateau phase as well as the second plateau also increase with increasing PhoP surface coverage.

Tab. 6.2 Parameters characterizing MDCK-II cell adhesion and differentiation upon quartz resonators with a different fractional PhoP coverage of the sensor surface. (Mean ± SDM, n ≥ 3).

PhoP Coverage	**$\Delta\|Z_{min}\|_{stat}$ [Ω]** 1st plateau	**Length [min]** 1st plateau	**$\Delta\|Z_{min}\|_{max}$ [Ω]** 2nd plateau	**τ_2 [min]**
Uncoated	376 ± 7	200	458 ± 9	520 ± 15
0.083 cm^2 opening	368 ± 18	200	538 ± 6	484 ± 9
0.0022 cm^2 opening	447 ± 6	300	549 ± 10	684 ± 17
Complete	498 ± 6	440	586 ± 7	793 ± 6

The applicability of the resonators with small *ECIS mode* electrodes to follow cell attachment and spreading in a time-resolved manner was also studied. The attachment and spreading behavior of MDCK-II cells upon quartz resonators with different fractions of its upper surface electrode being covered with PhoP and thus revealing working electrodes with a surface area of either 0.33 cm^2, 0.083 cm^2 or 0.0022 cm^2 was followed in terms of the time course of the normalized capacitance C_{norm} measured at a sampling frequency of 40 kHz (Fig. 6.18).

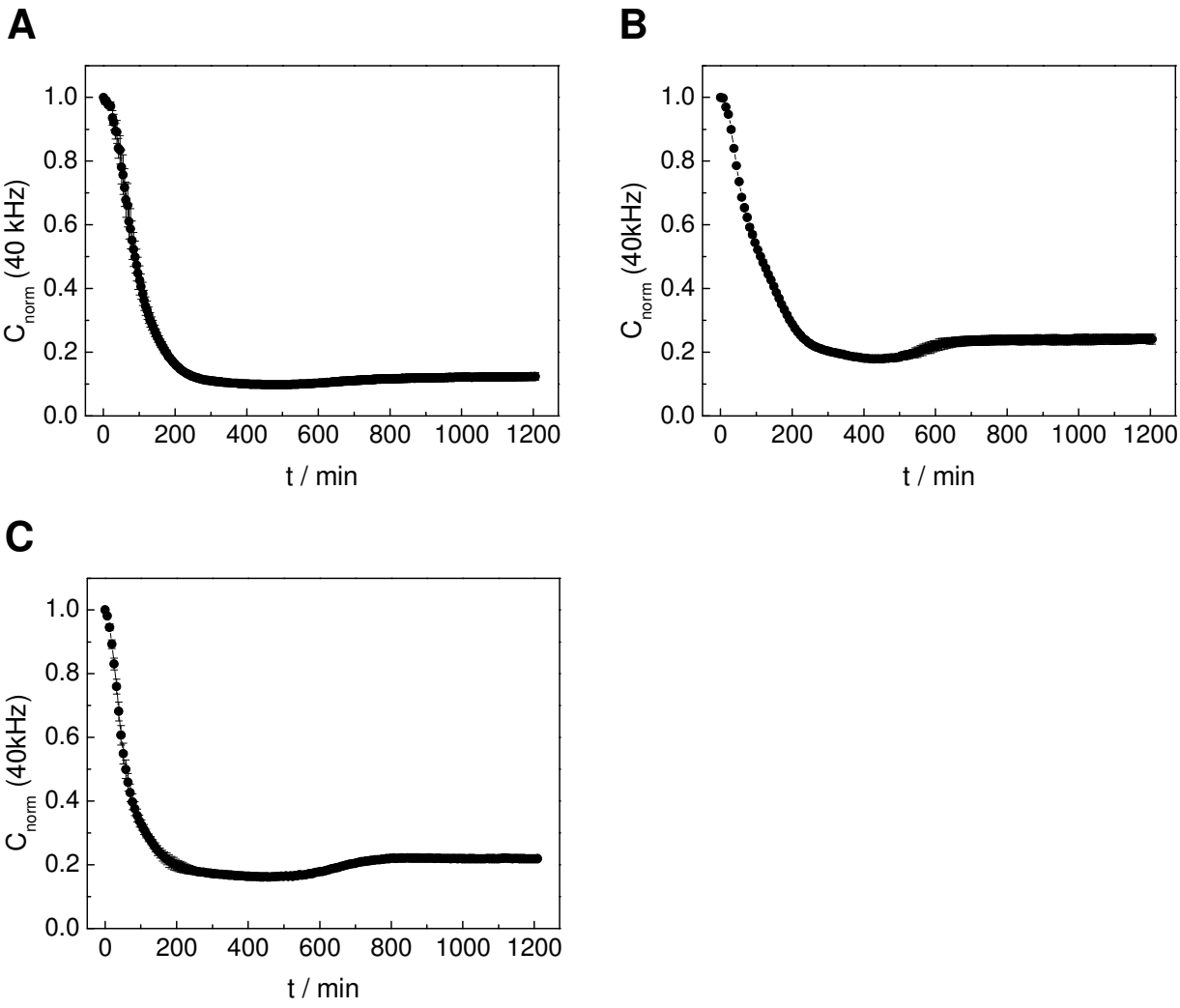

Fig. 6.18 Time course of C_{norm} measured at 40 kHz when equal amounts of initially suspended MDCK-II cells are seeded at time point zero on a quartz resonator with different fractions of its total surface electrode being coated with PhoP, giving rise to working electrodes for ECIS mode measurements with the following surface area: **A** 0.33 cm^2 (Ø = 6 mm), **B** 0.083 cm^2 (Ø = 3 mm), **C** 0.0022 cm^2 (Ø = 0.5 mm). The cell density was adjusted to 4.5 x 10^5 cm^{-2}. The values of *C* were normalized to the first *C* value of the measurement in order to allow for a direct comparison of the different experimental setups. ((A) C_{start} = (9.32 ± 0.54) µF/cm^2, (B) C_{start} = (4.44 ± 0.14) µF/cm^2, (C) C_{start} = (7.20 ± 0.14) µF/cm^2; mean ± SDM, n ≥ 3; *T* = 37 °C).

The time course of C_{norm} for the attachment and spreading of MDCK-II cells upon an uncoated quartz resonator with a gold electrode of 0.33 cm^2 shows a characteristic shape which starts with an immediate decrease, leading to a stationary value of one tenth of the initial capacitance value about 300 min after cell inoculation (Fig. 6.18 A). When MDCK-II

cells attach and spread on a resonator surface with a 0.083 cm^2 gold electrode, C_{norm} decreases within approximately 400 min to a temporary minimum, followed by a slight increase to a stationary value of 0.23 after 600 min (Fig. 6.18 B). For an electrode with a surface area of 0.0022 cm^2, C_{norm} shows a steep decrease to a transient value 300 min after cell inoculation. After 550 min, C_{norm} starts to increase slightly till it finally reaches the stationary value of 0.22 (800 min) (Fig. 6.18 C).

In order to characterize MDCK-II cell differentiation on these ECIS electrodes with different electrode area, the time course of the normalized resistance R_{norm} was followed for a sampling frequency of 100 Hz (0.33 cm^2), 200 Hz (0.083 cm^2) and 250 Hz (0.0022 cm^2), starting directly after cell inoculation (Fig. 6.19).

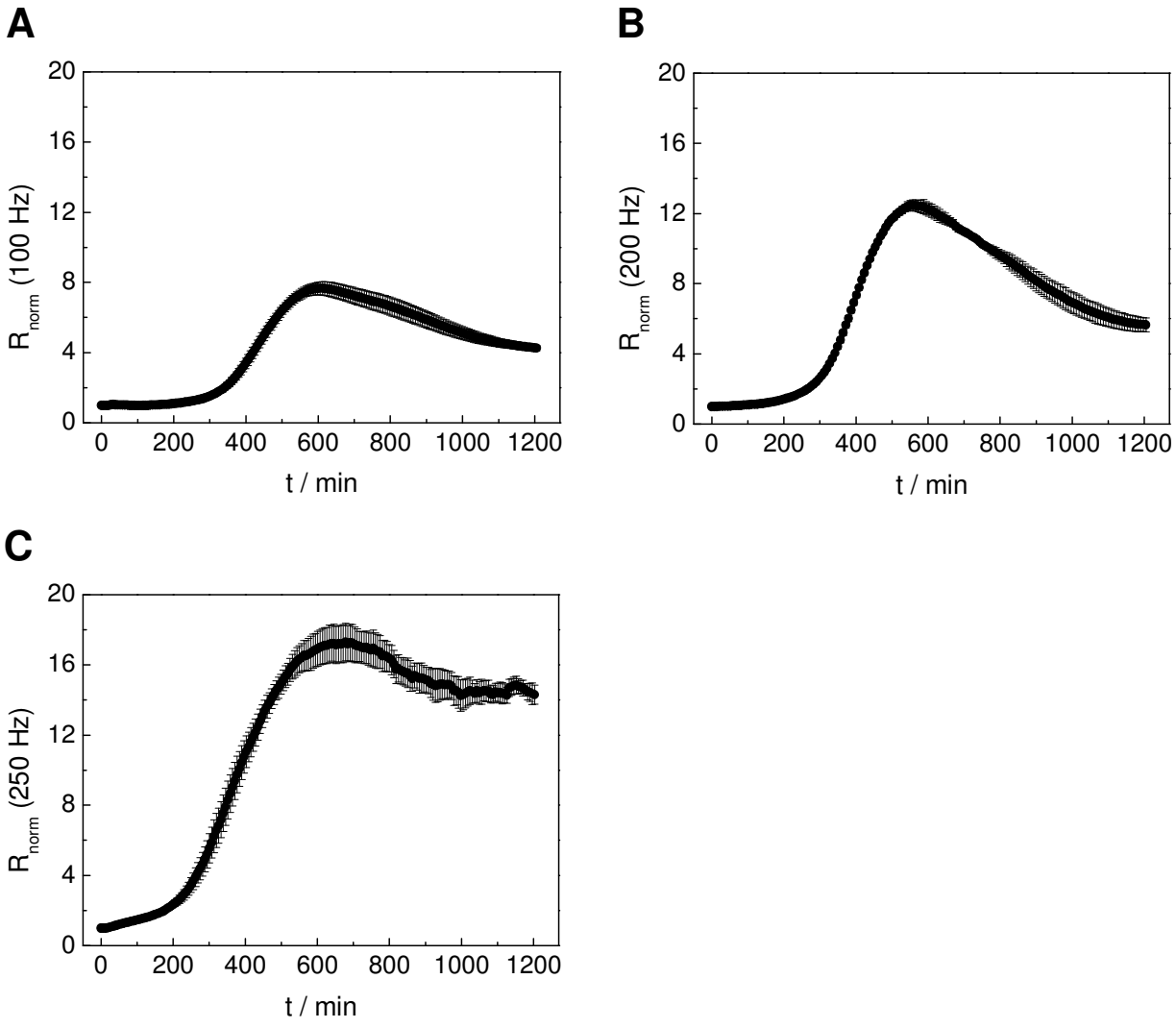

Fig. 6.19 Time course of R_{norm} measured at 100 Hz (A), 200 Hz (B) or 250 Hz (C) when equal amounts of initially suspended MDCK-II cells are seeded at time point zero on a quartz resonator with different fractions of its total surface electrode being coated with PhoP, giving rise to working electrodes for ECIS mode measurements with the following surface area: **A** 0.33 cm^2 (Ø = 6 mm), **B** 0.083 cm^2 (Ø = 3 mm), **C** 0.0022 cm^2 (Ø = 0.5 mm). The cell density was adjusted to 4.5 x 10^5 cm^{-2}. The values of R were normalized to the first R value of the measurement. ((A) R_{start} = (98 ± 2) Ω, (B) R_{start} = (205 ± 14) Ω, (C) R_{start} = (2970 ± 60) Ω; mean ± SDM, n ≥ 3; T = 37 °C).

R_{norm} recorded for MDCK-II cell differentiation on an electrode with a surface area of 0.33 cm^2 is characterized by an increase starting 250 min after cell inoculation (Fig. 6.19 A). An almost eightfold increase of R_{norm} is attained after (600 ± 12) min. Following cell differentiation on a 0.083 cm^2 electrode, R_{norm} starts to increase 250 min after cell inoculation, rising to 12.5-fold resistance increase after (569 ± 10) min (Fig. 6.19 B). For a 0.0022 cm^2 electrode, R_{norm} starts to rise after 150 min and reaches a plateau value after (646 ± 12) min (Fig. 6.19 C). The increase in R_{norm} accounts for a factor of 17 compared to the starting values. The time courses for MDCK-II cell differentiation on these three working electrodes with different surface areas are consistent in the sense that the steady state values for R_{norm} are reached in a similar time frame after cell inoculation. However, the three curves differ in the absolute values for R_{norm}, showing an increase in the steady state values with decreasing electrode surface area. This indicates an increase in sensitivity of the resistance measurements with decreasing electrode surface area.

6.2.2 Adhesion and Differentiation of NRK Cells

The applicability of the *double mode* setup with a working electrode of 0.0022 cm^2 (Ø ~ 0.5 mm) for *ECIS mode* measurements located in the center of the resonator was also tested in an NRK cell attachment and spreading assay. NRK cell attachment and spreading was monitored by recording impedance spectra in *double mode*.

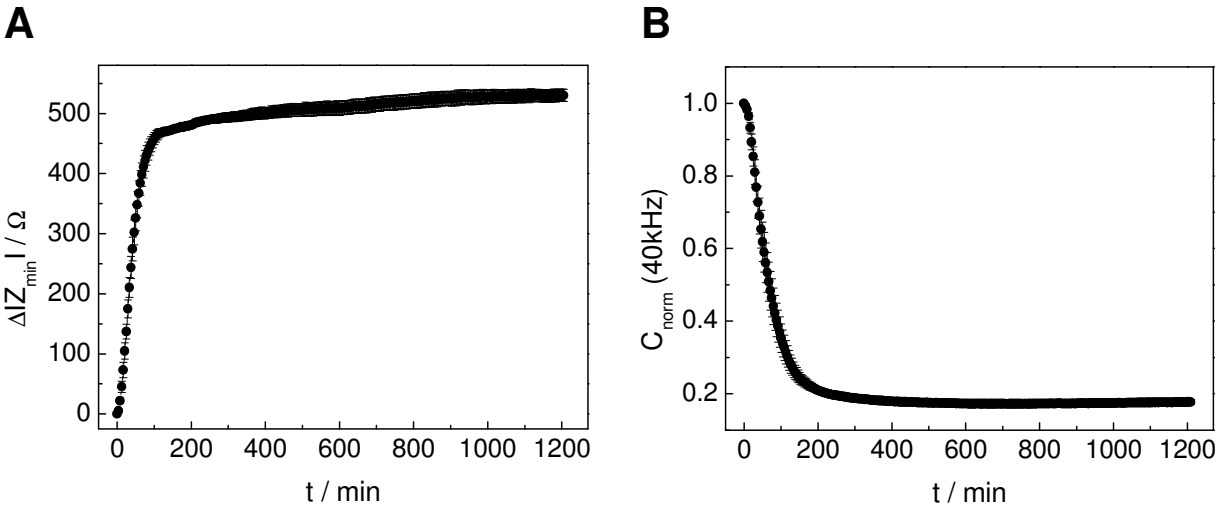

Fig. 6.20 Attachment and spreading of NRK cells characterized by *double mode* impedance analysis. **A** Time course of $\Delta|Z_{min}|$ and **B** time course of C_{norm} at 40 kHz during the adhesion of initially suspended NRK cells upon a PhoP coated quartz resonator containing a circular opening of 0.0022 cm^2 in the center of the resonator. The cell density was adjusted to 4.5 x 10^5 cm^{-2}. Changes of $|Z_{min}|$ are given relative to a cell-free but medium-loaded resonator. The values of C were normalized to the first C value of the measurement. ((B) C_{start} = (6.77 ± 0.26) μF/cm^2; mean ± SDM, n = 5; T = 37 °C).

Figure 6.20 displays the time course of $\Delta|Z_{min}|$ as recorded in *quartz mode* as well as the time course of C_{norm} at a sampling frequency of 40 kHz, acquired in *ECIS mode*. The measurement was started directly after seeding a suspension of NRK cells upon the resonator surface.
Instantaneously after cell inoculation $\Delta|Z_{min}|$ increases and reaches a stationary value of (515 ± 11) Ω within about 120 – 200 min, which slightly increases to a final value of $\Delta|Z_{min}|$ = (530 ± 10) Ω during the remaining measuring period (Fig. 6.20 A). The time that is needed to reach the half-maximal $\Delta|Z_{min}|$ value is determined to $\tau_{1/2}$ = (38 ± 2) min.
The normalized capacitance at 40 kHz (Fig. 6.20 B), C_{norm}, undergoes a steep decrease directly after cell inoculation, reaching a stationary value of 0.17-fold of the initial capacitance value after about 300 – 350 min, corresponding to a confluent monolayer of cells on the sensor surface. The time that is needed to attain half-maximal capacitance decrease is determined to (58 ± 7) min.

The microgravimetric parameter $\Delta|Z_{min}|$ as well as the electrical parameter C_{norm} (40 kHz), recorded simultaneously in *double mode*, report primarily on the kinetics of cell attachment and spreading on the resonator surface. Using the entire surface electrode of the resonator (0.33 cm^2) for *ECIS mode* measurements (chapter 6.1.1, Fig. 6.4), it was not possible to follow the resistive portion of the measured impedance as it was masked by the electrolyte resistance of the bulk solution. The modified microelectrode setup with a reduced surface area of the working electrode of 0.0022 cm^2 provides the time course of R_{norm} in a sensitive way (Fig. 6.21).

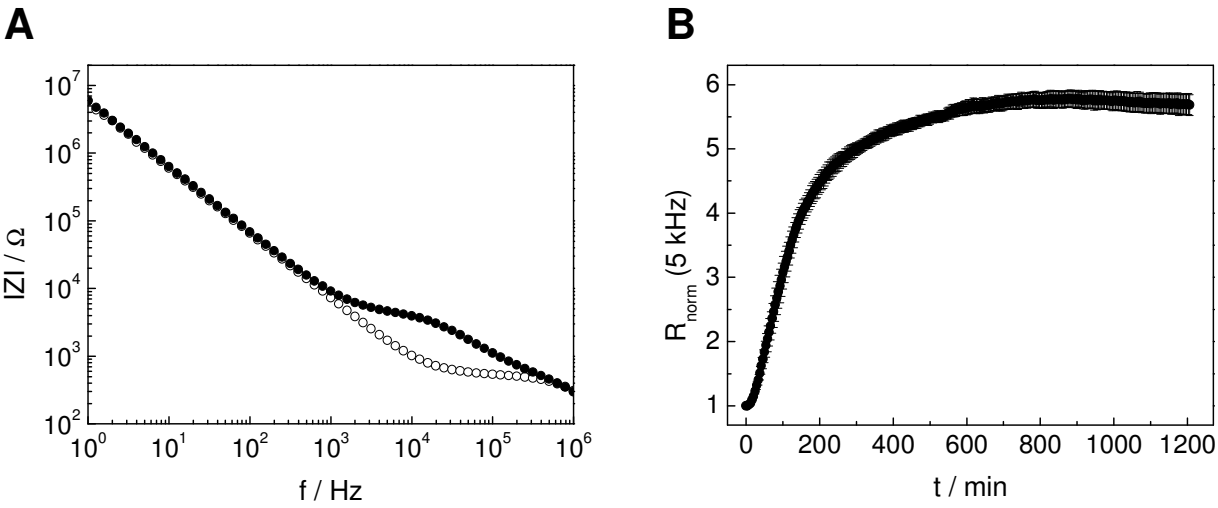

Fig. 6.21 A Impedance spectrum for a 0.0022 cm^2 working electrode established in the center of the upper surface electrode of a quartz resonator with (●) and without (○) a confluent monolayer of NRK cells. **B** Time course of R_{norm} measured at 5 kHz when initially suspended NRK cells are seeded at time point zero on this resonator. The cell density was adjusted to 4.5 x 10^5 cm^{-2}. The values of R were normalized to the first R value of the measurement. ((B) R_{start} = (644 ± 13) Ω; mean ± SDM, n = 5; T = 37 °C).

The spectrum of the electrochemical impedance magnitude |Z| recorded in the frequency range of 1 – 10^6 Hz for a medium-loaded resonator is compared to the spectrum of an NRK

cell-covered electrode in Fig. 6.21 A. The presence of NRK cells on the electrode surface primarily affects the impedance spectrum in a frequency range between 10^3 Hz and $3 \cdot 10^5$ Hz. The most sensitive frequency for time-resolved resistance measurements during the establishment of an NRK cell monolayer was determined from the resistive portion of the impedance and amounts to $f = 5$ kHz.

The time course of R_{norm} measured at a sampling frequency of 5 kHz is characterized by an immediate increase after cell inoculation and reaches a stationary, almost sixfold resistance increase after about 700 min (Fig. 6.21 B).

6.3 Monitoring MDCK-II Cell Adhesion and Differentiation Kinetics upon Resonators with Partly Covered Surface Electrodes at Two Different Positions

In order to address the local sensitivity of the mechanical oscillation to a given surface load, a circular opening of 0.0022 cm^2 (Ø ~ 0.5mm) was introduced into the PhoP layer at two different positions of the original surface electrode, which were expected to show a different surface sensitivity: it was introduced i) in the center or ii) at the edge of the underlying gold surface electrode (Fig. 6.22). After exposure of the PhoP coated resonator to a physiological fluid (SFM) for 20 h at 37 °C, MDCK-II cells were seeded on quartz resonators of either kind. Cell attachment and spreading was monitored with time by *double mode impedance analysis*.

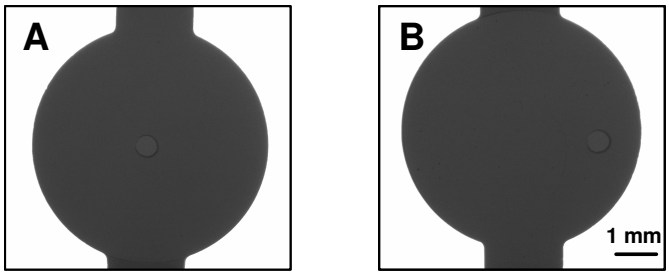

Fig. 6.22 Stereomicroscopic pictures documenting the electrode layout established on top of the upper surface electrode of the quartz resonator (diascopic illumination). The circular opening with a surface area of 0.0022 cm^2 is either **A** located in the center or **B** resides at the edge of the original gold surface electrode.

Figure 6.23 traces the time course of $\Delta|Z_{min}|$ as recorded in *quartz mode* after seeding a suspension of MDCK-II cells upon the resonator surface with a circular opening of 0.0022 cm^2 in the PhoP film either in the center or at the edge of the original surface electrode.

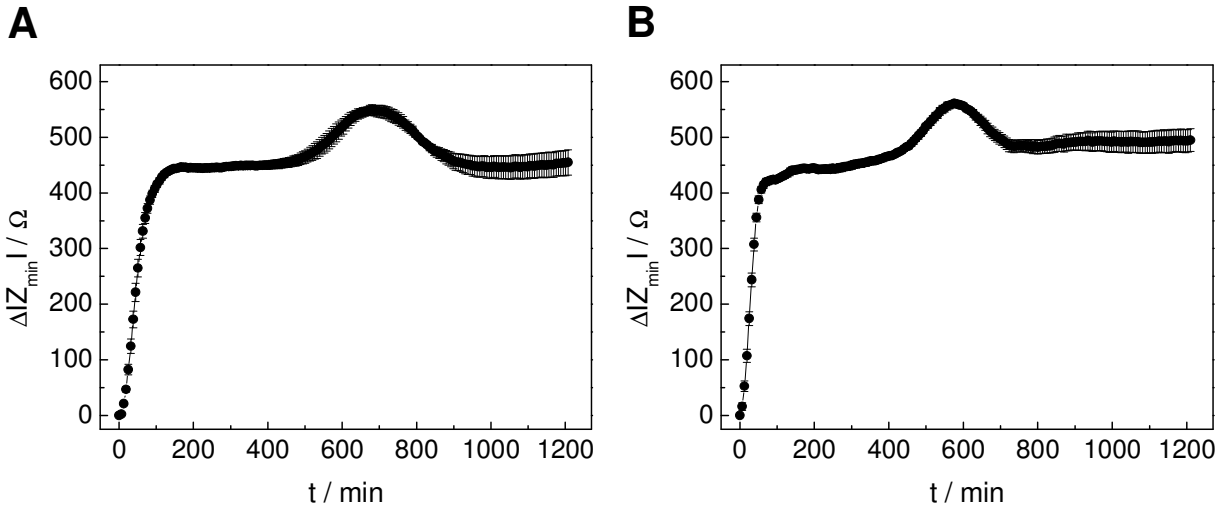

Fig. 6.23 Time course of $\Delta|Z_{min}|$ when equal amounts of initially suspended MDCK-II cells are seeded on a PhoP coated quartz resonator at time point zero (*quartz mode*). A circular opening of 0.0022 cm^2 was introduced **A** in the center and **B** at the edge of the original surface electrode of the resonator. The cell density was adjusted to 4.5 x 10^5 cm^{-2}. The value of $|Z_{min}|$ at the beginning of the experiment was set to zero. (Mean ± SDM, n ≥ 4; T = 37 °C).

The time courses observed for $\Delta|Z_{min}|$ are similar and obviously independent of the lateral position of the circular opening. The time course of $\Delta|Z_{min}|$ is characterized by an initial steep increase directly after cell inoculation, reaching a similar plateau value of roughly 450 Ω for both surfaces. The time needed to reach the plateau phase is also similar for both electrode layouts, i.e. 160 min for cells seeded onto the resonator with the central opening and 150 min for cells seeded upon the resonator with the peripheral opening. At first sight, actin rearrangement seems to progress faster on the PhoP coated resonator with the peripheral opening at the edge of the electrode. The second plateau of (561 ± 6) Ω is attained already 580 min after cell inoculation (Fig. 6.23 B), whereas on the PhoP coated resonator with the opening in the center, it takes about 680 min to reach the maximum value of (549 ± 10) Ω (Fig. 6.23 A). This difference in the time that is needed to reach the second transient maximum mainly originates from different time points when these experiments were carried out and is not caused by the position of the electrode. Thus, the *quartz mode* measurements do not indicate any differences with respect to the location of the circular opening in the PhoP film covering the sensor surface.

The time courses of C_{norm} measured at 40 kHz and R_{norm} measured at 250 Hz as extracted from *ECIS mode* measurements performed in parallel are presented in Fig. 6.24 A – D.
MDCK-II cells reveal a similar attachment and spreading behavior on both electrodes independent of the electrode position, central on the original quartz electrode or at its edge. C_{norm} decreases instantaneously after cell inoculation and reaches a transient minimum after about 300 min. After 600 min, C_{norm} continues to increase to a stationary value accounting for the 0.22-fold of the initial capacitance value (Fig. 6.24 A, B).

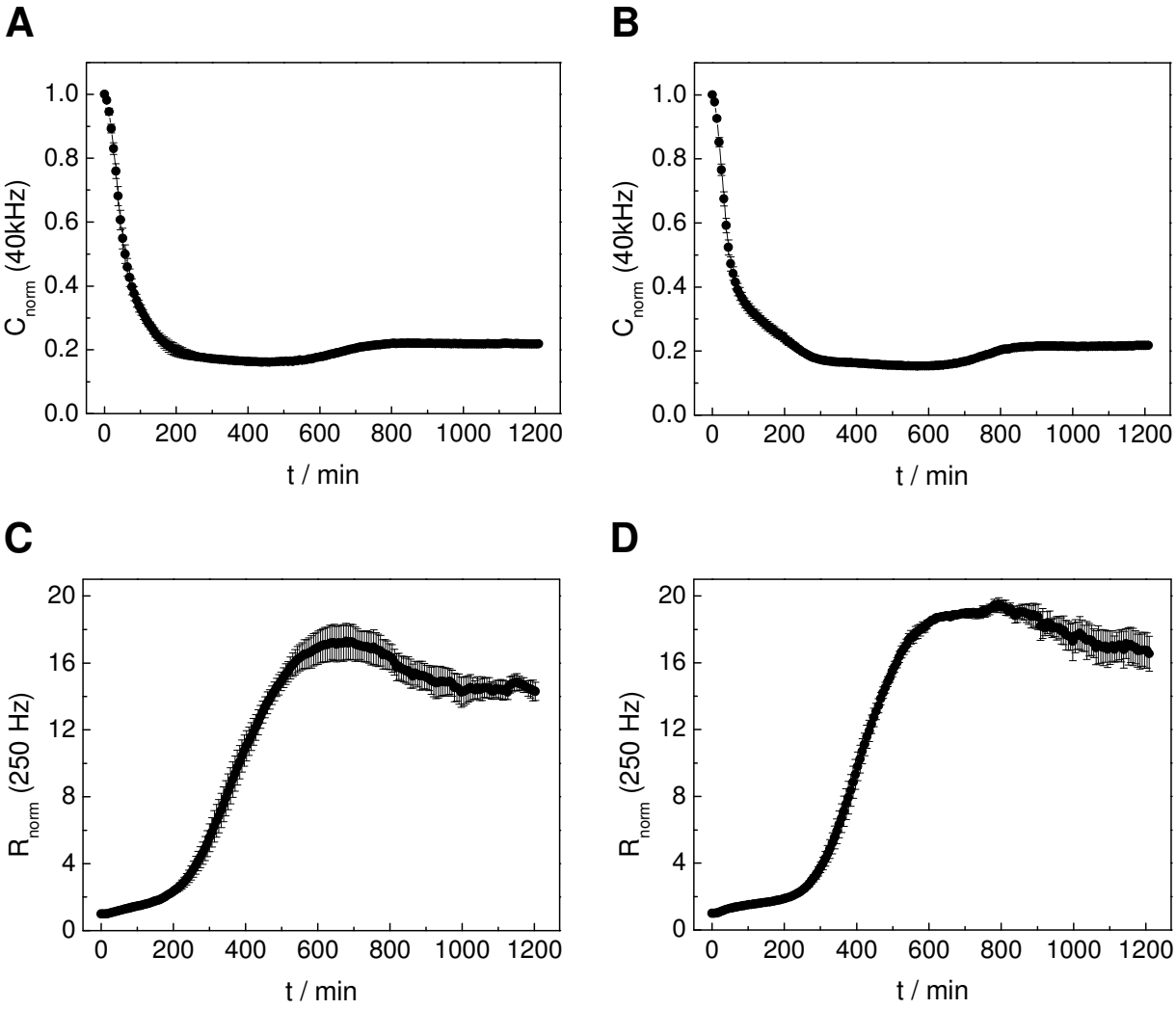

Fig. 6.24 Time course of C_{norm} measured at 40 kHz (**A**, **B**) and R_{norm} measured at 250 Hz (**C**, **D**) when equal amounts of initially suspended MDCK-II cells are seeded at time point zero on PhoP coated quartz resonators containing a circular opening (= working electrode) of 0.0022 cm^2 either at the center (A, C) or at the edge (B, D) of the original surface electrode of the resonator (*ECIS mode*). The cell density was adjusted to 4.5 x 10^5 cm^{-2}. The values of C and R were normalized to the first values of the measurement. ((A) C_{start} = (7.20 ± 0.14) µF/cm^2, (B) C_{start} = (7.81 ± 0.33) µF/cm^2, (C) R_{start} = (2970 ± 60) Ω, (D) R_{start} = (2360 ± 43) Ω; mean ± SDM, n ≥ 4; T = 37 °C).

The time courses of R_{norm} measured at 250 Hz for MDCK-II cell differentiation are also independent of the electrode position. Approximately 200 min after cell inoculation, R_{norm} increases to a plateau phase which is reached after 660 min. The increase in R_{norm} is 17-fold for the electrode in the center and 19-fold for the electrode located at the edge (Fig. 6.24 C, D). These differences are not considered as being significant.

The *ECIS mode* measurements show consistence in the time courses and the absolute values of the adhesion and differentiation parameters C_{norm} and R_{norm}, which are obtained for MDCK-II cell adhesion and differentiation for two different lateral electrode positions. Thus, the location of the working electrode on the original quartz electrode has no influence on the ECIS results.

6.4 Partial Cell Layer Removal to Probe the Local Sensitivity of the Mechanical Oscillation

In order to support the findings from chapters 6.2 and 6.3 regarding the local sensitivity of the mechanical oscillation, the problem was tackled with a complementary approach: parts of an initially confluent MDCK-II cell monolayer grown on the resonator surface were sequentially removed, beginning with a small circular wound introduced in the cell layer at the center of the electrode. The wounded area was gradually extended to the edge of the surface electrode using stamps of different diameters (chapter 3.5.3.3). The load situation on the resonator surface was documented after each step of cell layer removal using stereomicroscopy (Fig. 6.25) and *double mode impedance analysis* (Fig. 6.26).

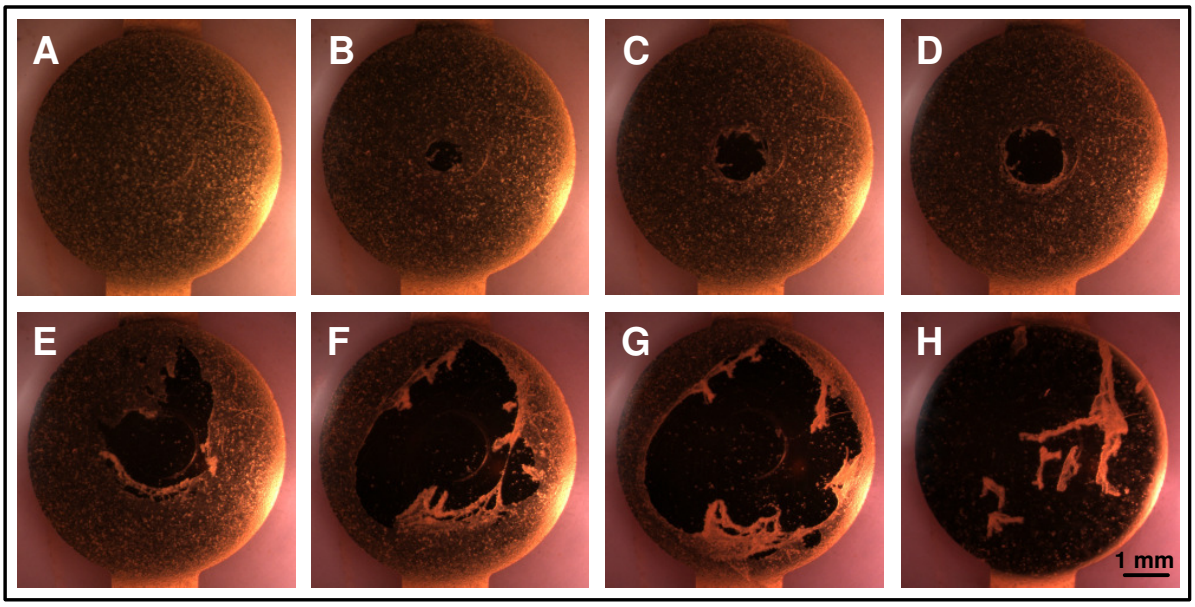

Fig. 6.25 Stereomicroscopic pictures documenting the size of the artificial wound introduced in an initially confluent MDCK-II cell monolayer grown on a quartz resonator using episcopic illumination. **A** Confluent monolayer, **B** – **G** increasing size of the center wound and **H** complete cell layer removal.

Figure 6.25 presents stereomicroscopic images acquired immediately after introducing an artificial wound in the cell layer. The wound was extended stepwise (Fig. 6.25 B – G). The images document the size of the artificial wound and thus the load situation on the quartz resonator. The estimated surface coverage of the gold electrode with MDCK-II cells for the single steps is given in Tab. 6.3.

The impact of cell layer removal on the shear oscillation of the quartz resonator was documented using *double mode impedance analysis*. Figure 6.26 shows the data recorded in *quartz mode* and *ECIS mode* for a quartz resonator completely covered with an MDCK-II cell monolayer after each step of cell layer removal. The *quartz mode* data are presented in terms of $\Delta|Z_{min}|$ referenced to the value for the same resonator loaded with medium only, as a

function of fractional surface coverage (Fig. 6.26 A). The ECIS mode data are presented in terms of the electrode capacitance *C* at a sampling frequency of 2 kHz as a function of fractional surface coverage (Fig. 6.26 B).

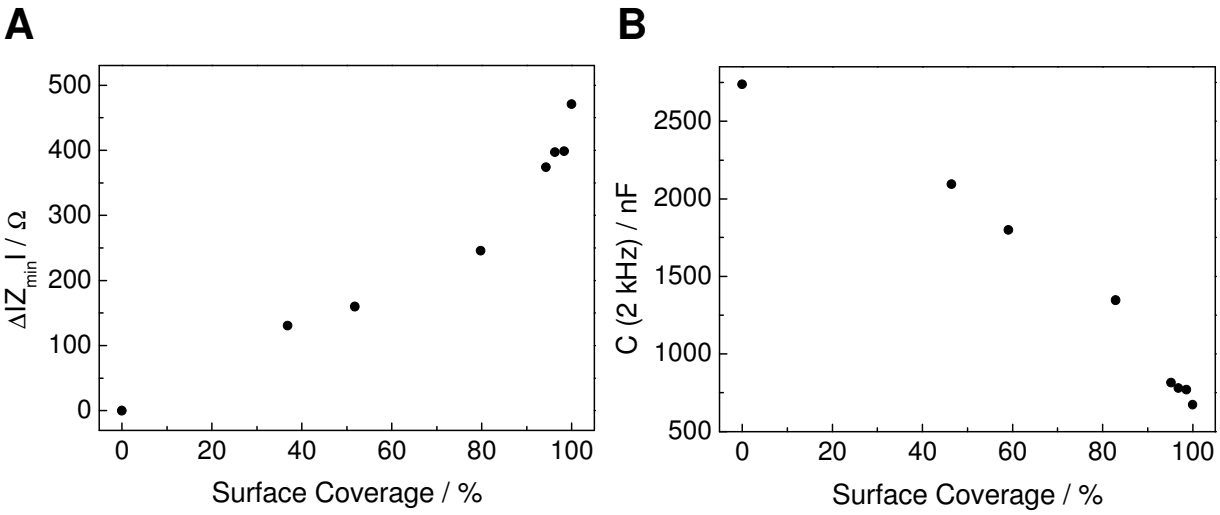

Fig. 6.26 Typical *double mode* data for a confluent MDCK-II cell monolayer and after each step of cell layer removal from the quartz resonator. **A** Minimal impedance magnitude $\Delta|Z_{min}|$ (*quartz mode*) and **B** electrode capacitance at 2 kHz (*ECIS mode*) plotted against the fractional surface coverage of the resonator with cells.

The introduction of relative small wounds in the center of the resonator, reducing the surface coverage to 98.3 – 94.3 % (Fig. 6.25 B – D), leads to a significant decrease of $\Delta|Z_{min}|$ to 84.6 – 79.4 % of the total cell-induced change in $\Delta|Z_{min}|$ (Fig. 6.26 A, Tab. 6.3). A larger wound, reducing the surface coverage to 79.8 %, leads to a significant decrease of $\Delta|Z_{min}|$ to 52.2 % compared to the cell-covered resonator. The further steps of cell layer removal provide a decrease of $\Delta|Z_{min}|$ to 34 % for an optical surface coverage of 51.8 % and to 27.8 % for an optical surface coverage of 36.9 %, respectively.

Figure 6.26 B reveals a close-to-linear type relation between the decrease of the electrode capacitance at 2 kHz and the optical surface coverage of the quartz resonator. Reducing the surface coverage to 98.6 – 95.2 % results in an increase of *C* (2 kHz) by 96 – 142 nF (Tab. 6.3), indicating a surface coverage of 95.3 – 93.1 %. The reduction of the surface coverage to 82.9 % leads to an increase in $C_{2\,kHz}$ by roughly 672 nF compared to a completely cell-covered electrode (67.4 % surface coverage). The further steps of cell layer removal cause the electrode capacitance to adapt the capacitance of the cell-free electrode.

Tab. 6.3 Reduction of the electrode surface coverage by partial removal of the adherent MDCK-II cell layer and the individual impact on the parameters $\Delta|Z_{min}|$ (*quartz mode*) and *C* (2 kHz) (*ECIS mode*).

	Quartz Mode			ECIS Mode		
Stereo-micro-graph	**Optical Coverage [%]**	**$\Delta\|Z_{min}\|$ [Ω]**	**Change of $\Delta\|Z_{min}\|$ [%]**	**Optical Coverage [%]**	**C (2 kHz) [nF]**	**Change of C (2 kHz) [%]**
A	100	470.9	100	100	673.7	100
B	98.3	398.5	84.6	98.6	770.1	95.3
C	96.3	397.1	84.3	96.8	780.0	94.8
D	94.3	374.1	79.4	95.2	815.7	93.1
E	79.8	245.8	52.2	82.9	1346	67.4
F	51.8	159.9	34.0	59.1	1798	45.5
G	36.9	130.9	27.8	46.5	2094	31.2
H	0	0	0	0	2737	0

Whereas the decrease of the capacitance and the electrode surface coverage reveal a close-to-linear type of correlation (Fig. 6.25 B), the increase of $\Delta|Z_{min}|$ is linear only for a surface coverage of the resonator between 0 % and 80 % (Fig. 6.25 A). Moreover, both *double mode* parameters reveal a higher decrease of the signal compared to the surface coverage determined by stereomicroscopy.

6.5 Wound Healing of NRK Cells on Quartz Resonators

The microelectrode preparation on quartz resonators (0.0022 cm^2 working electrode) opens up the possibility to analyze the migratory properties of mammalian cells on the small gold electrode using an electrical wound healing assay as established for small ECIS electrodes ($5 \cdot 10^{-4}$ cm^2) by Keese et al. (2004). By applying an invasive AC field for a short time of several seconds, the cells directly bound to the small gold electrode are electrically wounded, i.e. their cell membranes are permeabilized and irreversibly damaged. After wounding, the migration of intact cells from the electrode periphery to the center of the electrode can be monitored with time in a quantitative manner by recording the electrode impedance via ECIS measurements. The *quartz mode* measurements performed in parallel allow to investigate the micromechanical properties of the complete cell layer during wound healing.

After the formation of a confluent cell monolayer with stable electrical properties, the cells on the small active electrode were wounded by applying an invasive electric field across the cell layer (see chapter 3.6.5.5). In order to achieve a complete, homogeneous and reproducible wounding of all cells residing on the small active electrode, it is necessary to find the wounding frequency where the contribution of the cell layer to the total impedance of the

system is most pronounced. This ensures that the major part of the voltage drops across the cell layer and not across the electrode interface or the electrolyte. The most sensitive frequency is determined by dividing the impedance spectrum of a cell-covered electrode by the spectrum of the respective cell-free electrode. The resulting spectrum of the normalized impedance is characterized by a single peak, indicating the frequency which shows the biggest difference between the impedances for a cell-covered and a cell-free electrode and is therefore supposed to be most effective for the electrical wounding. The normalized impedance revealed a maximum at $f = 40$ kHz. Thus, the wounding frequency of the applied voltage was set to 40 kHz, which is in accordance with established wound healing assays of NRK cells on small ECIS electrodes ($5 \cdot 10^{-4}$ cm^2). Further parameters that were chosen are a 5 V pulse and a pulse duration of 30 s.

The suitability of the microelectrode on the resonator (0.0022 cm^2) to be used in wound healing assays was validated by performing a live/dead assay after application of the wounding pulse. The assay is based on double staining of the wounded cell layer with the DNA-intercalating dye ethidium homodimer-1 (EthD-1; red fluorescence) as a marker for the loss of membrane integrity, and calcein acetoxymethylester (CaAM) as a means to detect esterases only active in living cells. Intracellular esterases hydrolyze the cell-permeable CaAM to the membrane-impermeable calcein, which emits a green fluorescence.

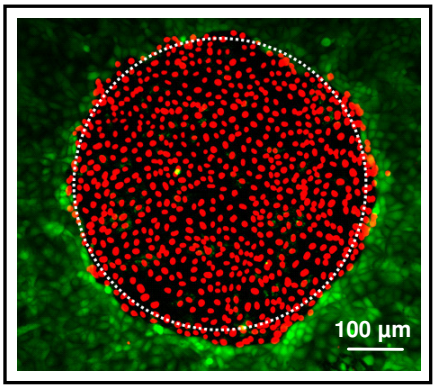

Fig. 6.27 Live/Dead assay of electrically wounded NRK cells on a resonator's small gold electrode (0.0022 cm^2) directly after wounding (wounding parameters: 5 V, 30 s, 40 kHz). The fluorescent micrograph shows the CaAM staining (green) of vital cells surrounding the active electrode surface and EthD stained (red) dead cells on the electrode itself.

The viability staining shows that electrically induced cell death is restricted to only those cells attached to the small active electrode. The surrounding vital cells exhibit a green, cytoplasmic fluorescence (Fig. 6.27). Thus, the chosen wounding parameters – a 5 V pulse at 40 kHz for 30 s – were appropriate to selectively wound the cells residing on the small active electrode without damaging the gold electrode. Thus, these wounding parameters were used in all other wound healing experiments with the microelectrode setup and NRK cells.

The following Fig. 6.28 documents the wound healing process of NRK cells that repopulate the 0.0022 cm^2 gold electrode. After the wounding pulse was applied, the migration of intact cells from the electrode periphery onto the electrode was followed by ECIS mode measurements with time. C_{norm} measured at a sampling frequency of 40 kHz was used in order to quantify surface coverage.

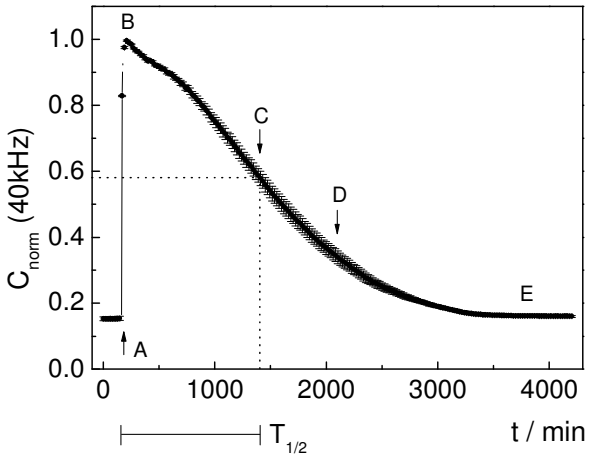

Fig. 6.28 Time course of C_{norm} measured at 40 kHz during a complete wound healing experiment with NRK cells on the small electrode (arrow A). The arrows A – E indicate the time points at which a viability staining of the cells on the electrode was performed in parallel. $T_{1/2}$ is the time that is needed to reach half-maximal repopulation of the electrode. The values of C were normalized to the C value after wounding (cell-free electrode). (C_{start} = (1.20 ± 0.05) µF/cm^2; mean ± SDM, n = 5; T = 37 °C).

Position A marks the time point when the invasive electric field was applied to the cells, wounding the cells on the small active electrode. Upon permeabilization of the cell layer, the capacitance increases from its minimum value indicative for a confluent cell layer (0.17) to a typical reading for an open, cell-free electrode (1.0). The permeabilization of the cell membranes allows the electrical current to flow freely across the dead cells without a measurable capacitance contribution from the cell membranes. Over time, C_{norm} continuously decreases as the electrode is repopulated. The healthy NRK cells in the periphery of the small gold electrode migrate inward and repopulate the wounded area, thereby replacing the dead cell bodies. After about 3300 min, the capacitance has reached the stationary level of a cell-covered electrode, indicating that the healing process is completed (closure of the wound). In order to quantify the wound healing process, the parameter $T_{1/2}$ is introduced. $T_{1/2}$ describes the time needed to attain half-maximal capacitance decrease and thus half-maximal repopulation of the electrode (= wound healing) and is determined to be (1241 ± 35) min.

In order to support the impedance measurements, the migration of intact NRK cells from the electrode periphery onto the gold electrode was followed by performing a live/dead assay at different time points of the healing process (Fig. 6.29). Microscopic images of the cells on the small electrode were taken directly before and immediately after application of the elevated field pulse as well as several hours later after capacitance measurements indicated the

continuous progression of the healing process. The arrows in Fig. 6.28 indicate the corresponding time points of microscopic analysis. The fluorescence micrographs taken after the viability staining of control and electrically wounded NRK cells are shown in Fig. 6.29.

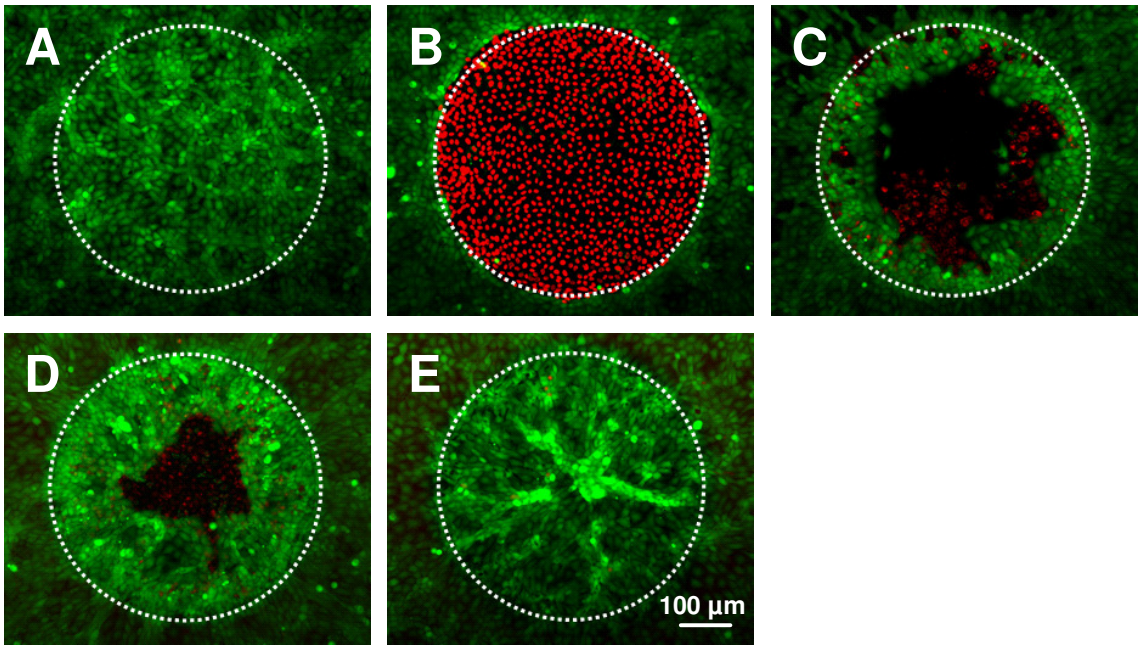

Fig. 6.29 Fluorescence micrographs of NRK cells taken before and after wounding. Electrode size is 0.0022 cm^2. The cells were stained using a live/dead assay at different time points after the wounding pulse to document the healing process. Viability staining of NRK cells on the electrode **A** before and **B** immediately after the wounding pulse, **C** after 50 % wound healing, **D** after 80 % wound healing and **E** after complete wound healing is shown. The wounding pulse was 5 V at 40 kHz applied for 30 s. The white circles denote the location of the small active surface electrode.

Figure 6.29 A shows a fluorescence image of the confluent layer of NRK cells attached to the working electrode before the high-field application. All cells exhibit a green cytoplasmic fluorescence, indicating that all cells are vital. By applying the elevated field, all cells attached to the gold electrode are selectively wounded due to severe irreversible damage of their plasma membranes. All cells on the electrode show a red fluorescence while the cells in the periphery fluoresce green (Fig. 6.29 B). The cell-impermeable dye EthD-1 is able to enter the wounded cells and intercalates into the DNA, leading to a red fluorescence of the cell nuclei. The neighboring cells not in contact to the electrode remain intact, as indicated by a green cytoplasmic fluorescence. Figure 6.29 C shows a fluorescence image of an electrode covered with NRK cells 1241 min after the elevated field wounding took place, i.e. about after half-maximal wound healing. A radial like growth pattern in the cell layer near the electrode periphery can be observed as the cells have migrated inward, suggesting an alignment of cells during the migration process. This radial like growth pattern is even more pronounced for the image showing an 80 % reclosure of the wound (Fig. 6.29 D). Figure 6.29 E presents a fluorescence micrograph of NRK cells after wound closure. The radial like growth pattern in the cell layer which has repopulated the electrode is still visible.

Capacitance measurements at 40 kHz are in good agreement with the microscopic data. The fluorescence micrographs confirm that the decrease in capacitance is a result of the migration of cells from the periphery into the wounded area, thereby replacing the dead cellular bodies.

In addition to *ECIS mode* measurements, the wound healing process of NRK cells that repopulate the 0.0022 cm^2 gold electrode was also monitored in *quartz mode*. Figure 6.30 presents the time course of $\Delta|Z_{min}|$ during wound healing of NRK cells. After application of the wounding pulse (arrow A), $\Delta|Z_{min}|$ shows a continuous decrease by approximately 150 Ω over the complete experimental time.

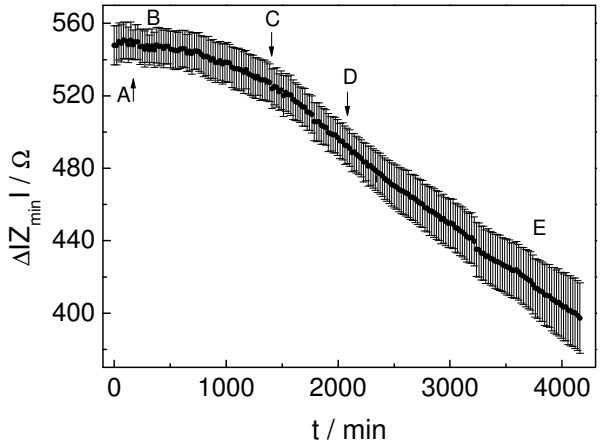

Fig. 6.30 Time course of $\Delta|Z_{min}|$ during a complete wound healing experiment with NRK cells on the small electrode. The arrows A – E indicate the time points at which a viability staining of the cells on the electrode was performed in parallel. The values of $|Z_{min}|$ were normalized to the value for a cell-free, only medium-covered electrode (Mean ± SDM, n = 5; T = 37 °C).

In summary, the electrode layout established on the surface electrode of quartz resonators opens up the possibility to selectively wound cells attached to the small active gold electrode and to monitor their migratory potential in a time-resolved manner using an ECIS based wound healing assay. However, the time course of $\Delta|Z_{min}|$ does not allow for a correlation of *quartz mode* data to the healing process measured in *ECIS mode* and observed microscopically. *Quartz mode* measurements reveal the micromechanical response of the complete cell layer upon wounding and wound healing.

6.6 Discussion

It has been the objective of this part of the thesis to follow and analyze simultaneously the electrical and viscoelastic properties of mammalian cells during their adhesion and differentiation. This was achieved by combining the QCM technique and the ECIS technique in one experimental setup, which is also known as *double mode impedance analysis* (Wegener et al., 2001). Furthermore, the double mode impedance technique was used for basic methodological studies addressing several technical details important for data interpretation. For instance, the size and lateral position of the electrochemical electrode were systematically varied and partial removal of the cell layer served as an assay to probe the local sensitivity of the mechanical oscillation.

6.6.1 Cell Adhesion and Differentiation Kinetics on Quartz Resonators monitored in Double Mode

In order to perform double mode impedance analysis, the QCM setup (passive mode) was extended by an additional low-impedance Pt dipping electrode, which was immersed in the culture medium from the top of the chamber. This dipping electrode served as a counter electrode for the upper surface electrode of the quartz resonator. Using the double mode technique, the kinetics of cell adhesion and differentiation on the surface of an uncoated quartz resonator were studied in a time-resolved manner for the epithelial MDCK-II cells and the epithelial-like NRK cells. Cell suspensions prepared in serum-containing culture medium were seeded on the resonator surface and data acquisition was started subsequently. The quartz mode data have been presented in terms of $\Delta|Z_{min}|$ referenced to the value for the same, only medium-loaded resonator as a function of time. $\Delta|Z_{min}|$ has been proven to mirror the mechanical properties of cells during their specific interaction with the resonator surface. The ECIS mode data were analyzed in terms of the normalized capacitance C_{norm} at 40 kHz and the normalized resistance R_{norm} at either 4 kHz (NRK) or 100 Hz (MDCK-II). Since the time courses of both quantities $\Delta|Z_{min}|$ and C_{norm} primarily mirror the formation of cell-substrate adhesion sites, the cell attachment and spreading kinetics were quantified from the individual time courses of both quantities using the parameter $\tau_{1/2}$. This parameter describes the time necessary to reach half-maximal $\Delta|Z_{min}|$ increase or half-maximal C_{norm} decrease, or in other words, half-maximal surface coverage. In order to characterize the differentiation behavior of MDCK-II cells, two additional parameters – τ_2 and τ_3 – were used. In quartz mode measurements τ_2 describes the time needed to reach the second maximum, which has been attributed to actin reorganization. In ECIS mode measurements τ_3 is the time needed to attain the maximal R_{norm} value indicating full establishment of barrier-forming cell-cell contacts

(cell differentiation). Table 6.4 summarizes all results obtained for NRK and MDCK-II cell adhesion and differentiation kinetics on an uncoated quartz resonator.

Tab. 6.4 Parameters characterizing NRK and MDCK-II cell adhesion and differentiation upon uncoated quartz resonators. (Mean ± SDM, n ≥ 5)

	$\tau_{1/2}$ [min] Quartz Mode	$\tau_{1/2}$ [min] ECIS Mode	τ_2 [min] Quartz Mode	τ_3 [min] ECIS Mode
NRK	77 ± 8	141 ± 6	–	–
MDCK-II	46 ± 3	80 ± 7.5	520 ± 15	600 ± 12

According to the quartz mode data, attachment and spreading of NRK cells was completed within 240 min after seeding, as indicated by a stationary value of $\Delta|Z_{min}|$. The time that was needed to reach half-maximal $\Delta|Z_{min}|$ was determined to be $\tau_{1/2} = (77 \pm 8)$ min. Regarding the time course of C_{norm}, it took 350 min to reach the stationary value and thus a confluent cell layer. The time to attain half-maximal capacitance decrease accounted for $\tau_{1/2} = (141 \pm 6)$ min (chapter 6.1.1, Fig. 6.3). Although the microgravimetric parameter $\Delta|Z_{min}|$ as well as the electrical parameter C_{norm} are supposed to report primarily on the kinetics of cell attachment and spreading on the resonator surface, the individual time courses of both independent quantities differ, as it is obvious from the $\tau_{1/2}$ values differing by a factor of almost two. This poses the question whether both quantities truly mirror similar processes. The quartz mode measurements indicated cell attachment and spreading to progress significantly faster than reported by the ECIS mode measurements. Apparently, the micromechanical properties of the cells were already stationary while the time course of C_{norm} still indicated an ongoing progress of cell attachment and spreading. Although the cells are not yet completely spread on the resonator surface, the viscoelastic properties of the cells (cellular micromechanics) were already stationary. As all experiments were performed under exactly the same conditions and even with the identical cell population, the observed differences between QCM-based and ECIS-based cell attachment and spreading kinetics might be attributed to the origin of both signals: capacitance readings in ECIS mode report on changes in the contact area to the conducting electrode. When the dielectric cell bodies attach and spread on the electrode surface, they decrease the equivalent capacitance of the electrode proportional to the fraction of the area they cover. The QCM reads the overall viscoelastic load on the resonator, which is governed by the space between basal cell membrane and gold electrode but also by changes in cell volume and viscoelasticity. These individual signal sources and their inherent dynamics during adhesion might account for the difference in the time course between the quantities $\Delta|Z_{min}|$ and C_{norm}.

For NRK cells it was not possible to follow the time course of R_{norm} during establishment of a cell monolayer on the resonator surface. The application of the big quartz electrode (0.33 cm^2) in combination with NRK cells which do not form a tight diffusion barrier caused the electrolyte resistance of the bulk solution to mask the resistive portion of the impedance, so that no significant increase of R_{norm} could be observed (chapter 6.1.1, Fig. 6.4).

When comparing the time courses of $\Delta|Z_{min}|$ and C_{norm} for MDCK-II cell attachment and spreading on the resonator surface, the inconsistency in the time courses of both quantities is apparent as well. Whereas $\Delta|Z_{min}|$ increased to a transient first plateau phase within 135 min after cell inoculation, C_{norm} took 300 min to reach the stationary value. The $\tau_{1/2}$ value amounts to (46 ± 3) min for the time course of $\Delta|Z_{min}|$ and (80 ± 7.5) min for the time course of C_{norm}. Both characteristic times differ by a factor of almost two (chapter 6.1.2, Fig. 6.6). These results indicate that the inconsistency in the time courses of $\Delta|Z_{min}|$ and C_{norm} is not a peculiarity of the cell type but a general phenomenon. In addition, double mode impedance analysis using quartz resonators with a reduced electrochemical electrode revealed the same time discrepancies, proving that this phenomenon does not depend on the size of the working electrode either (chapter 6.2.1 and 6.2.2). After 300 min, i.e. after C_{norm} had reached its stationary value, $\Delta|Z_{min}|$ continued to increase to the second plateau within (520 ± 15) min after cell inoculation. The increase of $\Delta|Z_{min}|$ to the second plateau value has been attributed to acoustic changes within the cell bodies anchored to the surface, due to the formation of a mature and polarized actin cytoskeleton (Wegener, 1998). The barrier properties of the MDCK-II cell layer, characterized by the time course of R_{norm}, did not establish before $\Delta|Z_{min}|$ had reached the first transient plateau phase and C_{norm} its respective steady state. This indicates that the expression of barrier-forming cell-cell contacts (tight junctions) between MDCK-II cells cannot start before the cells have completely attached and spread on the resonator surface. The second maximum of $\Delta|Z_{min}|$ was attained within (520 ± 15) min after cell inoculation, while it took (600 ± 12) min for R_{norm} to reach its maximum value. This finding strongly supports the understanding that two adjacent cells have to form mechanically stable adherens junctions before they can establish barrier-forming tight junctions that occlude the intercellular shunt. Adherens junctions are characterized by the thick actin belt that follows the cell periphery close to the apical pole and has been shown to be most prominent at the time point of maximal $\Delta|Z_{min}|$ (Heitmann et al., 2007).

6.6.2 Double Mode Impedance Analysis with Increased Sensitivity in ECIS Mode

The relative big surface area of the quartz electrode (0.33 cm^2) provides only a reduced sensitivity of the ECIS mode impedance signal, which is, however, in particular crucial when monitoring leaky epithelia and cells that do not form tight junctions, as it has been shown for NRK cells seeded on an uncoated quartz resonator (chapter 6.1.1, Fig. 6.4). In order to achieve a sensitivity increase in the impedance data of ECIS mode measurements, the surface area of the resonator's top electrode available for the electrochemical experiment was reduced. However, the electrode to excite the shear oscillation should be unchanged. This was achieved by coating the complete quartz resonator surface with PhoP and introducing well-defined circular holes into the insulating polymer film by means of photolithography. Thus, working electrodes with a surface area of either 0.083 cm^2 or 0.0022 cm^2 located in the center

of the quartz surface were obtained (chapter 6.2, Fig. 6.9). In order to use this modified resonator in contact with cells, it was important to guarantee that the electrode layout did not interfere with cell attachment and spreading. By means of VSI measurements, the PhoP film was shown to have a thickness of ~ 3 µm and to constitute an inclination angle of (1.5 ± 0.1)° with the substrate surface. This rather smooth transition from the substrate surface to the PhoP surface did not hinder or interfere with attachment and spreading of MDCK-II cells and NRK cells, as confirmed by phase contrast micrographs (chapter 6.2, Fig. 6.13). The cells were able to bridge between the substrate surface and the PhoP film, justifying this approach as a suitable means for studying cell attachment and spreading.
Before monitoring cell attachment and spreading with this modified double mode setup, the characterization of these modified quartz resonators in the cell-free state but exposed to culture medium was a crucial prerequisite for cellular experiments.
The phase spectra recorded in *quartz mode* for a cell-free, medium-loaded quartz resonator with a circular opening of either 0.083 cm^2 or 0.0022 cm^2 in the PhoP film in comparison to an uncoated resonator revealed a pronounced shift along the frequency axis to lower frequencies with increasing fraction of the surface covered by PhoP. The phase maximum as well as the internal shape of the resonance curve were not influenced by the PhoP coverage (chapter 6.2.1, Fig. 6.14). These results led to the following conclusions concerning the quartz resonators with the different circular openings in the PhoP film:

i) Assuming the acoustic wave to be confined to the small electrochemical working electrode, it would be expected that this significant decrease of the piezoelectrically active area from 0.28 cm^2 for an uncoated resonator to 0.083 cm^2 and finally 0.0022 cm^2 would result in a significant damping of the mechanical shear oscillation[1]. A damping of the quartz oscillation was not observed for quartz resonators with smaller electrodes, indicating that the complete surface electrode of the quartz resonator, i.e. the uncoated circular area as well as the PhoP coated area, seems to contribute to the quartz signal.

ii) When a foreign mass layer, in this case PhoP, is deposited rigidly and uniformly on the resonator surface, the additional mass film increases the resonator's thickness, and the resonance frequency of the quartz crystal is diminished, as indicated by the shift of the phase spectrum to lower frequencies. When introducing a circular hole in the PhoP overlayer on the quartz resonator, the resonator is not uniform in thickness anymore: it is ~ 3 µm thicker in areas covered with PhoP than it is in the circular area without. The resonance frequency is diminished in the PhoP covered area compared to the uncoated region, which might result in a modified resonance curve due to two different resonance conditions. However, the internal shape of the resonance curve remained unaffected by the existence of a circular opening of either size within the PhoP film. Thus, it can be assumed that the recorded QCM signal is an integral signal originating from both surface areas, the uncoated and the PhoP coated one.

[1] Quartz resonators with a mm-diameter electrode are damped to such an extent that they do not perform mechanical shear oscillations (personal communication from A. Janshoff, Göttingen)

The impedance spectra recorded in *ECIS mode* for the three different sizes of electrodes established on the resonator surface and only exposed to culture medium revealed a shift to higher frequencies and an increase in the total impedance of the system as expected when reducing the electrode surface area from 0.33 cm^2 to 0.083 cm^2 and finally 0.0022 cm^2.

After having characterized the modified quartz resonators in the cell-free state, the raw data recorded in double mode for quartz resonators covered with a confluent monolayer of MDCK-II cells were compared for an uncoated, a completely PhoP coated and partly PhoP coated resonators with circular holes in the polymer film.
The presence of a confluent MDCK-II cell monolayer grown on these quartz resonators decreased the phase maximum to a similar extent regardless of the fraction of the quartz surface being coated with PhoP (chapter 6.2, Fig. 6.14). This similar impact of cells on the mechanical oscillation might indicate that the whole cell layer – the cells that are attached to the uncoated gold electrode and the cells that are attached to the PhoP film – seems to contribute to the damping of the quartz oscillation.
The impedance spectra recorded in ECIS mode for a confluent monolayer of MDCK-II cells grown on the three working electrodes with different size revealed that the sensitive frequency range, where the contribution of cells to the impedance of the system is significant, broadened with decreasing surface area of the working electrode (chapter 6.2.1, Fig. 6.15). The normalized resistance spectra $R_{\text{cell-covered}}(f)/R_{\text{cell-free}}(f)$ for the different cell-covered electrodes showed an increase in the maximal values of the normalized resistance with decreasing electrode size (chapter 6.2.1, Fig. 6.16). This indicates an increase in sensitivity for ECIS mode measurements when using smaller working electrodes.
In the following the attachment and spreading characteristics of MDCK-II cells on the differently prepared quartz resonators as deduced from double mode measurements are shortly summarized (see chapter 6.2 for more details).

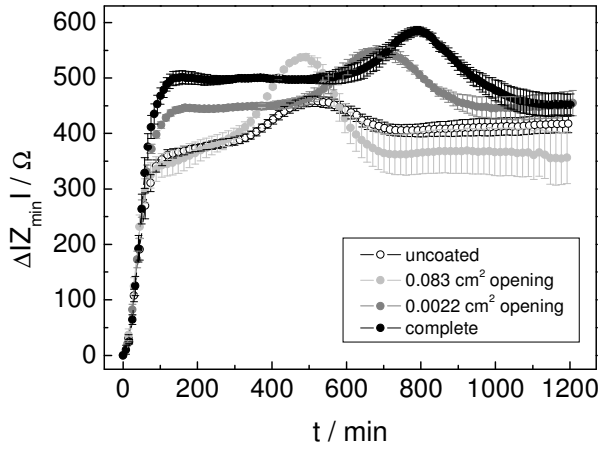

Fig. 6.31 Time course of $\Delta|Z_{min}|$ when equal amounts of initially suspended MDCK-II cells are seeded at time point zero on quartz resonators whose surface electrode is gradually covered by PhoP films. The sensor surface is (○) uncoated, coated with PhoP except for a circular opening of (●) 0.083 cm^2 and (●) 0.0022 cm^2 and (●) completely coated with PhoP. The number of points was reduced for reason of clarity.

Figure 6.31 compares the time courses of $\Delta|Z_{min}|$ when a suspension of MDCK-II cells was seeded on quartz resonators with different fractions of its upper surface electrode being coated with PhoP. The time course of $\Delta|Z_{min}|$ mirrored the fractional PhoP coverage of the quartz resonator. Whereas the transient plateau phase was reached in a similar period of time for all quartz resonators, the time needed to reach the second plateau phase increased with increasing coverage of the resonator with PhoP. MDCK-II cells that were seeded upon an uncoated quartz resonator and a PhoP coated resonator with a circular opening of 0.083 cm^2 reached the maximum in a similar time interval of (520 ± 15) min and (484 ± 9) min), respectively. On a PhoP coated resonator with a 0.0022 cm^2 circular opening, MDCK-II cells were significantly slower in reaching the second plateau ((684 ± 17) min) and for a completely PhoP coated resonator the maximum was attained not until (793 ± 6) min after cell inoculation. Additionally, the absolute $\Delta|Z_{min}|$ values which were attained in the first as well as in the second plateau phase increased with increasing PhoP surface coverage. These values mirror the individual micromechanical properties of the cell layer on the respective growth surface. Thus, the stepwise increase of the absolute $\Delta|Z_{min}|$ values attained in the first transient maximum and in the second maximum with increasing PhoP coverage leads to the conclusion that the measured cellular response to the fractionally PhoP covered quartz resonators encompasses the contribution from cells attached to the electrochemical working electrode as well as the contribution from cells attached to the surrounding PhoP film.

The time courses of C_{norm} (40 kHz), providing cell attachment and spreading kinetics in ECIS mode for the different working electrodes, were similar. C_{norm} reached a minimal value within 300 – 400 min after cell inoculation. Whereas the minimum remained stationary for the 0.33 cm^2 working electrode, C_{norm} slightly increased for the 0.083 cm^2 and the 0.0022 cm^2 working electrode after a certain time interval to a stationary value. This increase can not be explained at the moment, but it seemed to be characteristic for the small working electrodes. In summary, cell attachment and spreading was almost independent of the size of the electrochemical electrode.

The time courses of R_{norm} that report on MDCK-II cell differentiation on these ECIS electrodes with different electrode surface area are compared in Fig. 6.32. R_{norm} was followed at the most sensitive frequency for each electrode size, i.e. at 100 Hz for the 0.33 cm^2 working electrode, at 200 Hz for the 0.083 cm^2 working electrode and at 250 Hz for the 0.0022 cm^2 working electrode. The time course of R_{norm} was similar for the three different working electrode sizes, i.e. the steady state values for R_{norm} were reached in a similar time frame after cell inoculation. However, the absolute R_{norm} values differed with respect to the surface area of the working electrode, showing an increase in the steady state values of R_{norm} with decreasing electrode surface area. This clearly indicates an increase in sensitivity for resistance measurements with decreasing electrode surface area.

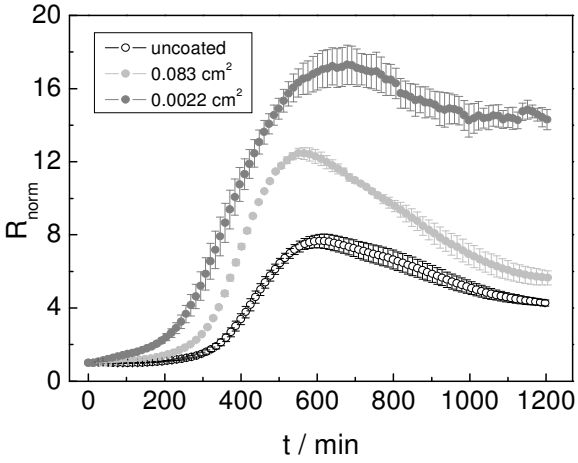

Fig. 6.32 Time course of R_{norm} when equal amounts of MDCK-II cells are seeded at time point zero on quartz resonators with different fractions of its total surface electrode being coated with PhoP, giving rise to working electrodes for ECIS mode measurements with the following surface area: (○) 0.33 cm^2, (●) 0.083 cm^2 and (●) 0.0022 cm^2. The number of points was reduced for reason of clarity.

The increase in sensitivity for ECIS mode measurements using the *double mode* setup with smaller electrochemical electrodes was also confirmed by following attachment and spreading of NRK cells. Whereas the *double mode* setup using the uncoated quartz resonator with a 0.33 cm^2 working electrode for ECIS mode measurements did not allow to follow the resistive portion of the measured impedance as it was masked by the electrolyte resistance of the bulk solution (chapter 6.1.1, Fig. 6.4), the modified microelectrode setup with a reduced surface area of the working electrode of 0.0022 cm^2 provided the time course of R_{norm} during establishment of a NRK cell layer in a sensitive way (chapter 6.2.2, Fig. 6.21). In summary, this setup with a smaller electrochemical electrode for ECIS mode measurements is well-adapted to detect even non barrier-forming leaky epithelia, as shown for NRK cells.

Coating the quartz resonator with a PhoP film and introducing a circular hole of either 0.083 cm^2 or 0.0022 cm^2 in the PhoP overlayer, exposing the quartz electrode only with a fraction of its total surface area to the electrolyte, led to the establishment of small working electrodes for ECIS mode measurements. Using these modified quartz resonators, the sensitivity of resistance measurements in ECIS mode could be significantly increased. It was possible to follow the resistive portion of the measured impedance during establishment of a leaky NRK cell monolayer on the electrode surface. The quartz mode measurements were not affected by the presence of a circular hole within the PhoP film on the quartz resonator and thus the presence of a small electrochemical electrode. The data indicate that the quartz signal originates from the uncoated as well as from the PhoP coated area of the quartz electrode, meaning that it encompasses the contribution from cells attached to the electrochemical working electrode and the contribution from cells attached to the PhoP film.

6.6.3 Probing the Local Sensitivity of the Mechanical Quartz Oscillation

The local sensitivity of the mechanical quartz oscillation to a given surface load was addressed by introducing a small circular opening of 0.0022 cm^2 into the PhoP overlayer either at the center or at the edge of the original quartz surface electrode. These two positions are expected to show a different surface sensitivity. The oscillation of a quartz resonator is confined to the area of the quartz disk that is sandwiched between the evaporated surface electrodes. But even within the electrode-covered, piezoelectrically active area of the quartz resonator there is no uniform shear amplitude along the crystal surface, but it is radially symmetric (Martin and Hager, 1989 a and b). The amplitude of particle displacement is maximum where the distance to the non-moving particles of the crystal is maximum, i.e. in the center of the surface electrode. With increasing distance from the center, the amplitude decreases monotonically in a Gaussian manner and almost vanishes at the electrode edges. The shear amplitude at the electrode edges has been determined to be ~ 13.5 % of the maximum amplitude in the center of the resonator (Heitmann and Wegener, 2007). In consequence, the quartz resonator is not uniformly sensitive over its entire area to the adsorption of cells, and sensitivity peaks in the center. For a driving voltage of 150 mV as applied in this study, the maximum shear amplitude in the center of a medium-loaded quartz resonator has been calculated to be 0.5 nm (Heitmann, 2008).

Following $\Delta|Z_{min}|$ after seeding MDCK-II cells on the quartz resonator with the circular opening located either in the center or at the edge of the surface electrode, the time courses for $\Delta|Z_{min}|$ as well as the stationary $\Delta|Z_{min}|$ values were similar regardless of the lateral position of the working electrode (circular opening). The only difference was the time needed to reach the second plateau, but this time discrepancy of 100 min can be most likely ascribed to the different time points when the experiments were carried out and was not caused by the electrode position. The quartz mode results obtained with the working electrodes located in the center or at the edge confirm the results obtained with working electrodes of different sizes: apparently, the cells grown on the uncoated (0.0022 cm^2 working electrode) and the PhoP coated area of the quartz electrode contributed to the recorded quartz signal. Since the cellular impact on the shear oscillation was averaged over the complete area of the quartz electrode (0.28 cm^2), the local sensitivity of the mechanical oscillation can not be addressed with this kind of approach. Since the surface area of the quartz resonator coated with PhoP is identical for the circular and the peripheral working electrode having both a surface area of 0.0022 cm^2, the absolute values of $\Delta|Z_{min}|$ are identical as well. The mechanical interactions of the cells with the PhoP film and the uncoated gold electrode, respectively, are averaged and result in the same overall load situation for both electrode positions.

For ECIS mode measurements the location of the working electrode should have no influence on the outcome of the measurements. Since the electrode surface area for both electrode positions is identical, ECIS mode measurements should not depend on the position of the working electrode and give the same results for cell adhesion and differentiation. The ECIS mode measurements provided consistent time courses and the absolute values of the adhesion and differentiation parameters C_{norm} and R_{norm}, which were obtained for MDCK-II cells seeded upon either of the electrodes, have been similar. The lateral position of the working electrode on the original quartz electrode had no influence on the ECIS results.

Since the establishment of a small working electrode at two lateral positions on the quartz electrode was not successful in probing the local sensitivity of the mechanical oscillation to adhering cells, the problem was tackled with another approach: parts of a confluent MDCK-II cell monolayer grown on the surface of an uncoated quartz resonator were sequentially removed. Beginning with a small circular wound introduced in the cell layer at the center of the electrode, the wounded area was gradually extended to the edge of the surface electrode. The load situation on the resonator surface was documented using double mode impedance analysis and stereomicroscopy.

Only for small wound sizes, reducing the surface coverage to 98.6 – 95.2 %, the increase in capacitance was proportional to the decrease in surface coverage (chapter 6.4, Fig. 6.26 B). For larger wounds reducing the surface coverage to more than 83 % (chapter 6.4, Fig. 6.25 E – G), the capacitance readings indicated a larger wounded area than the stereomicroscopic pictures did, suggesting a deviation from the linear-type relation. This might be attributed to the fact that the size of the wound possibly was not correctly determined by the stereomicroscopic pictures. Although a cell layer was visible, the cells might have loosened their cell-substrate contacts and only lie on the electrode surface. These cells can not be distinguished from strongly attached cells. Moreover, the strong cell-cell contacts between MDCK-II cells may lead to the detachment of cells from the resonator surface as intact sheets, what complicates the differentiation between a firmly attached and a loosely associated cell layer.

The course of $\Delta|Z_{min}|$ plotted against the fractional surface coverage with cells as deduced from stereomicroscopic pictures revealed a close-to-exponential relation. Since the mass sensitivity of the mechanical oscillation is maximum in the center of the quartz resonator, removal of cells in the center of the electrode should have a greater impact on the QCM response than cells in the periphery. The introduction of relative small wounds in the center of the resonator, reducing the coverage of the cell layer to 98.3 – 94.3 %, provided a decrease of $\Delta|Z_{min}|$ by 72 – 97 Ω, which accounts for 84.6 – 79.4 % of the value recorded for a confluent cell layer (chapter 6.4, Tab. 6.3). Besides the spatial distribution of the differential mass sensitivity of the mechanical oscillation, an overestimation of the surface coverage from the microscopic pictures might also account for the differences observed between the $\Delta|Z_{min}|$ readings and the microscopic data.

6.6.4 A Novel Wound Healing Assay Established on Quartz Resonators

Using the microelectrode layout (0.0022 cm^2), an electrical wound healing assay on quartz resonators was established, opening up the possibility to analyze the migratory properties of NRK cells during wound healing in *double mode*. By applying an invasive electric field for 30 s across the confluent NRK cell layer, all cells attached to the small active gold electrode were electrically wounded. Upon permeabilization of the cell layer, the capacitance increased from its minimum value indicative for a confluent cell layer to a typical reading for an open, cell-free electrode. The wound healing process of NRK cells that repopulate the electrode from the periphery could be followed by means of the capacitance at 40 kHz in a time-resolved manner. C_{norm} showed a continuous decrease over time as the cells from the electrode periphery migrated onto the electrode to repopulate the wounded area. The decrease of the capacitance was proportional to the increase in surface coverage, as documented by a live/dead assay performed in parallel at different time points of the healing process (chapter 6.5, Fig. 6.28 and 6.29). The time course of $\Delta|Z_{min}|$ as deduced from quartz mode measurements could not be correlated to the reclosure of the wound measured in ECIS mode and observed microscopically. Wounding of cells on the 0.0022 cm^2 working electrode had no significant impact on the $\Delta|Z_{min}|$ value. During wound healing, $\Delta|Z_{min}|$ showed a continuous decrease by approximately 150 Ω over the complete experimental time (chapter 6.5, Fig. 6.30). These results indicate consistent to what has been described before, that $\Delta|Z_{min}|$ encompasses the average signal obtained from cells cultured on the established small gold electrode as well as on the PhoP film. Assuming the complete cell layer to contribute to the $\Delta|Z_{min}|$ value, removal of 0.8 % of the cell layer had no significant impact on $\Delta|Z_{min}|$. This is consistent to the mechanical wounding experiments, where a small wound reducing 1.7 % of the surface coverage showed a decrease of $\Delta|Z_{min}|$ by only 72 Ω. The continuous decrease of $\Delta|Z_{min}|$ might reflect changes in the acoustic properties of the complete cell layer due to migration-induced rearrangements in the actin cytoskeleton. Cell migration during wound healing is the result of a series of coordinated cellular events, mainly determined by the static and dynamic properties of the actin network. Controlled polymerization of actin is a prerequisite for any cell movement. In order to optimize migration the cell shape restructures, as demonstrated in the fluorescence micrographs recorded during wound healing, showing elongated cells which have aligned during the migration process (chapter 6.5, Fig. 6.29 C – E). Wegener et al. (2000 and 2001) have shown that the QCM is capable of monitoring functional changes in the actin cytoskeleton of adherent cells quantitatively. The actin cytoskeleton was determined to be an important contributor to the acoustic load on the resonator surface. Disruption of the actin cytoskeleton of MDCK-II cells using cytochalasin D, which is known to inhibit the polymerization of actin monomers and thus results in shortening and finally disappearance of actin filaments, had a considerable impact on the shear wave parameters. The signal decreased by more than 40 % of the signal for a confluent cell layer. Energy dissipation as well as energy storage was affected.

Assuming rearrangements in the actin cytoskeleton to be responsible for the decrease in $\Delta|Z_{min}|$ during wound healing, it could be shown that rearrangement processes of the actin cytoskeleton still continued although the wound healing process was already completed.
In addition to these studies, it would be further interesting to stain the actin cytoskeleton of the migrating cells during wound healing as well as to reveal possible changes in membrane stiffness by scanning force microscopy.

In summary, ECIS mode data reported on the migration properties of NRK cells that repopulate the small electrode from the periphery while quartz mode data reported on the micromechanical response of the complete cell layer residing on the PhoP film upon wounding and during wound healing. These findings have to be regarded as evidence that it is possible to monitor the micromechanical properties of adherent cells during migration using the electrical wound healing assay on quartz resonators. These experiments demonstrate that the wound healing assay on quartz resonators provides a novel means to monitor the dynamics in the cytoskeleton of migrating cells quantitatively and in real time.

7 Summary

The biocompatibility of both existing and new materials is a central and crucial issue considered in a wide field of applications within the life sciences, ranging from fundamental cell biology research and cell-based biosensors to tissue engineering and medical applications *in vivo*. A general understanding of the interactions which take place between a material surface and the components of a biological system is an important requirement for the systematic design of suitable biomaterials. This motivates the development of reliable measurement techniques to monitor these complex and dynamic processes.
It was the objective of the present study to develop and evaluate biosensors based on two well-established impedimetric techniques – the QCM technique and the ECIS technique – in order to analyze the biocompatibility of different biomaterials with respect to their interactions with a biological system on a molecular and a cellular level in quantitative terms.

In the first part of the project a biosensor based on the QCM technique was established in order to obtain fundamental information on the biocompatibility of different polymer surfaces. The QCM was used as the key transducer element after the surfaces of the quartz resonators had been coated with the different polymers (PS, PMMA, PDMS and PhoP) by means of thin-film technology. Using the QCM technique the polymer surfaces were analyzed with respect to their long-term stability in a physiological environment, protein adsorption as well as cell attachment and spreading. Furthermore, surface modifications of the polymer films induced by an argon plasma treatment and/or fluid pre-incubation were quantitatively characterized and evaluated with respect to their impact on cell adhesion.
The polymers under study were shown to be long-term stable and did not dissolve in a physiological fluid. Fluid incubation changed the polymer surface/fluid interface and, thus, the coupling of the fluid to the polymer surface. However, only the commercial photopolymer PhoP showed a significant water uptake (swelling).
Protein adsorption experiments were performed to elucidate the amount of protein adsorbing to the surface under test in quantitative terms. Protein decoration of the different polymer surfaces showed no clear dependence on surface wettability probably due to the impact of surface roughness on the immobilization of proteins.
The kinetics of cell attachment and spreading of MDCK-II and NRK cells on the different polymer surfaces revealed that the hydrophobic, unmodified polymer surfaces interfered or even prevented cell adhesion. This can be attributed to a possible unfolding of the surface-immobilized proteins into denatured conformations, making the binding sites within the adsorbed proteins inaccessible for the cell-surface receptors. However, surface modifications

of the polymer films introduced by an argon plasma treatment or pre-incubation in a physiological fluid (PBS^{--} or SFM) promoted cell attachment and spreading upon most of the polymer surfaces. The argon plasma treatment mainly resulted in a polymer-specific increase in surface wettability (hydrophilization), whereas pre-incubation of the polymer films in a physiological fluid mainly led to an increase in surface roughness as revealed by contact angle measurements. Pretreated, wettable surfaces apparently allowed the proteins to adsorb without unfolding rendering the surface cytocompatible. Supplementary microscopic data addressing the cell attachment and spreading characteristics on the different polymer surfaces confirmed the QCM results, validating the polymer coated sensor system.
Taken together, the results reported here indicate that the QCM-based biosensor is a highly sensitive and well-suited research tool to analyze the biocompatibility of biomaterials on different levels in quantitative terms.

The second part of the study was focused on the development and evaluation of a biosensor based on the ECIS technique in order to investigate the impact of surface topography on cell behavior systematically and in a quantitative manner. Topographical features were modeled by mesoporous silicon substrates which differed in pore diameter and width of the ridges. The highly ordered pores were only opened to one side of the wafer. In order to study cell adhesion on these mesoporous substrates by ECIS, a thin gold film was deposited on the substrate surface and a well-defined electrode layout was established by means of photolithography. The porous topography of the substrates remained unchanged by the gold film, thus providing mesoporous gold film electrodes. The impact of surface topography was analyzed with respect to the kinetics of cell attachment and spreading, cell differentiation as well as cellular micromotion using the epithelial MDCK-II cell line.
As determined from ECIS readings, MDCK-II cells were able to form a confluent monolayer of fully differentiated cells on the mesoporous surfaces independent of the topographical features. Cell attachment and spreading on mesoporous substrates took only slightly longer than on planar substrates. The spreading rate was reduced with decreasing fraction of planar growth surface available for the formation of cell-substrate interactions (increasing pore diameter). Cell differentiation as reported by the formation of epithelial barrier function was significantly slowed down on the mesoporous substrates in comparison to planar ones. The differentiation rate decreased with increasing pore diameter. In addition to the kinetic measurements of cell adhesion and differentiation, impedance spectra of the confluent cell layers were analyzed quantitatively, providing detailed information on cell morphology and the state of cell differentiation for the different substrates. On mesoporous substrates the specific junctional resistance R_b – a measure for the strength of barrier-forming cell junctions – was lower than on planar substrates and decreased with increasing pore diameter. The specific cell membrane capacitance C_m, reporting on the membrane topography, was found to be significantly higher on mesoporous substrates and C_m increased with increasing pore diameter. The impedance arising from the cell-substrate adhesion sites was considerably lowered on mesoporous surfaces compared to planar ones.

ECIS-based cell motility studies showed a reduced motility for MDCK-II cells cultured on mesoporous gold film electrodes. The cell motility slightly decreased with increasing pore diameter.
Taken together, the results reported here indicate that impedimetric monitoring is highly sensitive and well-suited to analyze and quantify the impact of surface topography on cellular properties from various perspectives.

The third part of this study addressed the combination of both impedimetric techniques – QCM and ECIS – in one experimental setup in order to simultaneously follow and analyze the electrochemical and the viscoelastic properties of MDCK-II and NRK cells during their adhesion and differentiation on the resonator surface (double mode impedance analysis). Stepwise coverage of the resonator's top electrode with an insulating polymer reduced the electrically active size of the electrode for electrochemical measurements while leaving the electrode to excite the shear oscillation unchanged. This approach led to an improved sensitivity of ECIS mode measurements such that the resistive portion of the measured impedance became measurable even for cell types with low barrier functions, like NRK cells. The reduced access of the electrochemical electrode to the bulk electrolyte did neither affect the resonator's resonance curve nor the quartz mode data during attachment and spreading of mammalian cells. In addition, the lateral position of the small electrochemical electrode was varied to probe the local sensitivity of the mechanical quartz oscillation which had, however, no influence on the double mode results.
The double mode impedance technique was also used to establish an electrical wound healing assay performed on quartz resonators. NRK cells grown to confluence upon the gold microelectrode were electrically wounded and their migratory potential during wound healing was monitored in a time-resolved manner by *double mode* recordings. While the migration of intact NRK cells to repopulate the small electrode could be followed in ECIS mode, quartz mode measurements revealed the micromechanical response of the complete cell layer upon wounding and during wound healing.

In summary, both impedimetric biosensors were successfully established to evaluate the biocompatibility of different biomaterial surfaces in a quantitative and non-invasive manner. This biocompatibility study performed with these sensors contributes to a fundamental understanding of the most relevant material surface properties, such as surface wettability and surface topography, and how these govern the molecular and cellular interactions with a biological system. The sensor device can be applied to a wide range of other biomaterials in order to analyze their performance in contact to biological entities.

8 Zusammenfassung

Die Biokompatibilität verfügbarer wie auch neuartiger Materialien ist ein zentraler und grundlegender Gesichtspunkt in einer Vielzahl biowissenschaftlicher Anwendungsfelder, angefangen bei der zellbiologischen Grundlagenforschung und zellbasierten Biosensoren bis hin zu *Tissue Engineering* und biomedizinischen Anwendungen *in vivo*. Ein grundlegendes Verständnis der Interaktionen zwischen der Oberfläche eines Materials und den Komponenten der biologischen Umgebung ist dabei eine notwendige Voraussetzung für die gezielte Entwicklung geeigneter Biomaterialien. Vor diesem Hintergrund tritt die Entwicklung und Etablierung leistungsfähiger physikalischer Analyseverfahren zunehmend in den Fokus, die diese komplexen und dynamischen Interaktionen zeitaufgelöst detektieren können.
Ziel der vorliegenden Arbeit war die Entwicklung und Validierung von Biosensoren auf Basis zweier etablierter impedimetrischer Techniken – der QCM- und der ECIS-Technik – zur quantitativen Charakterisierung der Biokompatibilität verschiedener Substrate im Hinblick auf deren molekulare und zelluläre Interaktionen mit der biologischen Umgebung.

Im ersten Teil der Arbeit wurde die Entwicklung eines Biosensors auf Basis der QCM-Technik zur Untersuchung der Biokompatibilität unterschiedlicher Polymerfilme vorgestellt. Die QCM diente als physikalisches Messsystem, nachdem die Oberfläche der Quarzresonatoren mit den unterschiedlichen Polymerfilmen beschichtet worden war (PS, PMMA, PDMS und PhoP). Mit Hilfe der QCM-Technik wurden die Polymeroberflächen im Hinblick auf ihre Langzeitstabilität in physiologischer Umgebung, Proteinadsorption sowie Adhäsion und Spreiten tierischer Zellen untersucht. Des Weiteren konnten Modifikationen der Polymeroberfläche wie durch eine Behandlung im Argonplasma und/oder Präinkubation in einer physiologischen Flüssigkeit quantitativ charakterisiert und bezüglich des Einflusses auf die zellulären Eigenschaften beurteilt werden.
Die untersuchten Polymere zeigten sich stabil in physiologischer Flüssigkeit und wiesen keine Anzeichen von Löslichkeit auf. Die Inkubation in Flüssigkeit bewirkte eine Änderung der Grenzflächeneigenschaften zwischen Polymeroberfläche und Flüssigkeit und somit der Ankopplung der Flüssigkeit an die Polymeroberfläche. Lediglich das kommerzielle Photopolymer PhoP zeigte eine deutliche Flüssigkeitsaufnahme (Quellen).
Die Proteinadsorption zeigte weder hinsichtlich der adsorbierten Proteinmenge noch der Adsorptionsaffinität auf den verschiedenen Polymeroberflächen eine klare Abhängigkeit von der Benetzbarkeit der Oberfläche, was möglicherweise durch eine unterschiedliche Oberflächenrauhigkeit erklärbar wird.

Adhäsion und Spreiten von MDCK-II und NRK Zellen auf den unterschiedlichen Polymeroberflächen war im Allgemeinen auf hydrophoben, unmodifizierten Polymeren deutlich erschwert bzw. komplett unterbunden. Dies lässt sich auf eine eventuelle Entfaltung der oberflächenimmobilisierten Proteine zurückführen, wodurch die Bindungsstellen in den adsorbierten Proteinen für die Integrine der Zellen unzugänglich oder deformiert worden sind. Modifikationen der Polymeroberflächen wie durch eine Behandlung im Argonplasma oder eine Inkubation in physiologischer Flüssigkeit (PBS^{--} oder SFM) verbessert die Adhäsion und das Spreiten der Zellen auf den meisten Polymeroberflächen. Wie anhand von Kontaktwinkelmessungen gezeigt, bewirkte eine Behandlung im Argonplasma vornehmlich eine verbesserte Benetzbarkeit der Oberfläche (Hydrophilisierung), während eine Inkubation in physiologischer Flüssigkeit überwiegend eine Zunahme der Oberflächenrauhigkeit zur Folge hatte. Die auf den unterschiedlich vorbehandelten Polymerfilmen adsorbierten Proteine wiesen anscheinend die passende Konformation und/oder Orientierung auf, so dass eine spezifische Erkennung zwischen den adhäsiven Peptidsequenzen und den Integrinen und damit die Bildung spezifischer Zell-Substrat-Kontakte gegeben war. Somit konnten sowohl die Benetzbarkeit der Oberfläche als auch die Rauhigkeit derselben als essentielle Parameter identifiziert werden, die einen signifikanten Einfluss auf die Proteinadsorption sowie die Adhäsion und das Spreiten tierischer Zellen auf den Polymeroberflächen besitzen. Ergänzende mikroskopische Untersuchungen zur zellulären Adhäsions- und Spreitkinetik auf den Polymeroberflächen konnten die QCM-Ergebnisse untermauern und somit das QCM-basierte Sensorsystem zur Untersuchung der Biokompatibilität validieren.
Die vorgestellten Ergebnisse zeigen, dass der entwickelte mikrogravimetrische Biosensor äußerst sensitiv und in hohem Maße geeignet ist, um die Biokompatibilität unterschiedlicher Polymerfilme in umfassender Weise zu analysieren und zu quantifizieren.

Im Zentrum des zweiten Teils der Arbeit stand die Entwicklung und Validierung eines ECIS-basierten Biosensors zur systematischen Quantifizierung des Einflusses der Substrattopographie auf das Zellverhalten. Dazu kamen strukturierte Siliziumsubstrate unterschiedlicher Topographie als Kultursubstrate zum Einsatz, die mit einem hochgeordneten *Array* von halbseitig geöffneten Poren versehen waren. Durch Verwendung mesoporöser Substrate unterschiedlicher Porendurchmesser und Stegbreiten konnte so der Einfluss der Substrattopographie systematisch ermittelt werden. Zur messtechnischen Realisierung wurden die Substrate mit einem 100 nm dicken Goldfilm belegt und das Elektrodenlayout photolithografisch etabliert. Somit wurde die topographische Struktur der Oberfläche übernommen und es wurden poröse Goldfilmelektroden erzeugt. Der Einfluss der Substrattopographie auf Adhäsion und Spreiten, Differenzierung sowie Motilität von epithelialen MDCK-II Zellen wurde durch ECIS-Untersuchungen in verschiedenen Messmodi untersucht.
Durch zeitaufgelöste ECIS-Messungen an mesoporösen im Vergleich zu planaren Goldfilmelektroden konnten neue Aspekte über den Einfluss der Substrattopographie auf die Ausbildung von Zell-Substrat- und Zell-Zell-Kontakten dargelegt werden. Ungeachtet der

Substrattopographie waren MDCK-II Zellen in der Lage, einen konfluenten, vollständig ausdifferenzierten Zelllayer auf der mesoporösen Oberfläche zu bilden. In vergleichenden Adhäsions- und Differenzierungsstudien konnte auf Basis zeitaufgelöster ECIS-Messungen gezeigt werden, dass Zelladhäsion und -spreiten auf mesoporösen Substraten etwas mehr Zeit benötigen als auf planaren. Dieser Effekt wird mit zunehmendem Porendurchmesser und damit einer relativen Abnahme der Breite der zur Adhäsion zur Verfügung stehenden Stege deutlicher. Im Hinblick auf den Zeitbedarf der Zelldifferenzierung ergab sich ein wesentlich stärkerer Einfluss der Substrattopographie. Die Ausbildung der zellulären Barrierefunktion war auf mesoporösen Substraten deutlich verlangsamt und zeigte zudem einen höheren Zeitbedarf mit zunehmendem Porendurchmesser. Die parallel zu den kinetischen Adhäsions- und Differenzierungsstudien durchgeführte Analyse der Impedanzspektren nach dem ECIS-Modell erlaubte einen Vergleich der stationären elektrischen Eigenschaften der vollständig etablierten, konfluenten Zellschichten auf den jeweiligen Substrattopographien und damit Aussagen über die Zellmorphologie und den Differenzierungszustand der Zellen. Für den parazellulären Widerstand R_b ergaben sich niedrigere Werte auf mesoporösen Substraten im Vergleich zu planaren Substraten sowie eine verstärkte Abnahme von R_b mit zunehmendem Porendurchmesser. Dieser erniedrigte R_b-Wert ließ sich auf eine möglicherweise durch die mesoporöse Topographie induzierte Schwächung der Zell-Zell-Kontakte (*tight junctions*) zurückführen. Die flächennormierte spezifische Membrankapazität C_m zeigte deutlich erhöhte Werte für Zellen auf mesoporösen Substraten im Vergleich zu planaren sowie einen Anstieg des Wertes mit zunehmendem Porendurchmesser. Dies deutet möglicherweise auf eine veränderte Topographie (zusätzliche Membranausstülpungen) der basalen Zellmembran hin. Eine Beurteilung des Einflusses der Substrattopographie auf den Parameter α, der den Zell-Substrat-Kontakt elektrisch charakterisiert, gestaltete sich schwierig, da aufgrund der porösen Substratoberfläche kein einheitlicher Zell-Substrat-Abstand vorausgesetzt werden konnte.
ECIS-basierte Untersuchungen der Zellmotilität ergaben, dass MDCK-II Zellen auf den mesoporösen Substraten weniger motil waren und demnach kleinere Formfluktuationen aufwiesen. Hierbei zeigte sich auch eine reduzierte Motilität mit zunehmendem Porendurchmesser.
Die vorgestellten Ergebnisse belegen die erfolgreiche Etablierung dieses impedimetrischen Biosensors zur Untersuchung von Substrattopographien. Durch die hohe Sensitivität dieses Biosensors bei gleichzeitiger hoher Zeitauflösung konnten so neue Erkenntnisse über den Einfluss der Substrattopographie auf Zelladhäsion, -differenzierung sowie Motilität gewonnen werden.

Gegenstand von Teil drei dieser Arbeit war die Kombination beider impedimetrischer Techniken – QCM und ECIS – in einem experimentellen Aufbau. Dieser Aufbau ermöglicht die simultane Untersuchung von elektrochemischen und viskoelastischen Eigenschaften von MDCK-II und NRK Zellen während der Adhäsion und Differenzierung auf Quarzresonatoren. Dieser auch unter dem Begriff "*double mode*" bekannte Aufbau wurde dahingehend modifiziert, dass der Zugang der Oberflächenelektrode des Quarzes zum Elektrolyten durch

partielle Bedeckung mit einem isolierenden Polymer für elektrochemische Messungen systematisch reduziert wurde, während die Elektrode zur Anregung der Scherschwingung unverändert zur Verfügung steht. Dies führte zu einem Sensitivitätsgewinn für die Messungen im ECIS-Modus und ermöglichte sogar die Detektion des Zellschichtwiderstandes während der Etablierung von NRK Zellschichten mit geringen Barriereeigenschaften. Das Vorhandensein einer partiell abgedeckten elektrochemischen Elektrode auf dem Quarzresonator hatte weder Einfluss auf dessen Resonanzkurve noch auf die im Quarz-Modus aufgezeichneten Daten zur Zelladhäsion. Des Weiteren wurde die Position der kleinen elektrochemischen Elektrode auf dem Quarz variiert, um die lokale Sensitivität der mechanischen Quarzschwingung zu untersuchen. Die Position der elektrochemischen Elektrode – im Zentrum oder am Rand der Elektrode des Quarzresonators – hatte keinen Einfluss auf die Ergebnisse der *double mode* Messungen.
Der *double mode* Aufbau wurde zudem genutzt, um einen elektrischen Wundheilungsassay auf Quarzresonatoren zu etablieren. Mit Hilfe der generierten kleinen Elektrode auf dem Quarzresonator konnten NRK Zellen auf dieser Elektrode elektrisch verwundet werden und ihr Migrationspotential während der sich anschließenden Wundheilung zeitaufgelöst in *beiden Messmodi* verfolgt werden. Während die Migration intakter NRK Zellen zur Repopulation der Elektrode im ECIS-Modus verfolgt werden konnte, zeigten Messungen im Quarz-Modus die mikromechanische Antwort des gesamten Zelllayers während der Wundheilung.

Beide impedimetrischen Biosensoren konnten im Verlauf dieser Arbeit erfolgreich etabliert werden, um die Biokompatibilität verschiedener Substrate in quantitativer und nicht-invasiver Weise zu beurteilen. Diese Biokompatibilitätsstudie konnte zu einem grundlegenden Verständnis der entscheidenden Oberflächenparameter, wie Benetzbarkeit und Topographie der Oberfläche, sowie deren Einfluss auf die molekularen und zellulären Interaktionen mit einem umgebenden biologischen System beitragen. Die hier entwickelten Sensoren können auf eine Vielzahl anderer Biomaterialien übertragen werden, um diese hinsichtlich ihrer Biokompatibilität zu evaluieren.

9 References

A

Adam G, Läuger P, Stark G. 2009. Physikalische Chemie und Biophysik. Berlin, Heidelberg: Springer Verlag.

Adams JC, Watt FM. 1993. Regulation of development and differentiation by the extracellular matrix. Development 117(4):1183-1198.

Alaerts JA, De Cupere VM, Moser S, Van den Bosh de Aguilar P, Rouxhet PG. 2001. Surface characterization of poly(methyl methacrylate) microgrooved for contact guidance of mammalian cells. Biomaterials 22(12):1635-1642.

Anderson JM, Van Itallie CM. 1995. Tight junctions and the molecular basis for regulation of paracellular permeability. Am J Physiol 269(4 Pt 1):G467-475.

Andrade JD, Hlady VL, Vanwagenen RA. 1984. Effects of plasma-protein adsorption on protein conformation and activity. Pure Appl Chem 56(10):1345-1350.

Arnaout MA, Mahalingam B, Xiong J-P. 2005. Integrin structure, allostery, and bidirectional signalling. Annu Rev Cell Dev Biol 21:381-410.

Arndt S, Seebach J, Psathaki K, Galla HJ, Wegener J. 2004. Bioelectrical impedance assay to monitor changes in cell shape during apoptosis. Biosensors & Bioelectronics 19(6):583-594.

Aumailley M, Smyth N. 1998. The role of laminins in basement membrane function. J Anat 193:1-21.

B

Babel W. 1996. Gelatine - Ein vielseitiges Biopolymer. Chemie in unserer Zeit 30(86-95).

Banerjee P, Irvine DJ, Mayes AM, Griffith LG. 2000. Polymer latexes for cell-resistant and cell-interactive surfaces. Journal of Biomedical Materials Research 50(3):331-339.

Barczyk M, Carracedo S, Gullberg D. 2010. Integrins. Cell Tissue Res 339(1):269-280.

Bashir R. 2004. BioMEMS: State-of-the-art in detection, opportunities and prospects. Adv Drug Deliv Rev 56(11):1565-1586.

Baszkin A, Boissonnade MM. 1993. Competitive adsorption of albumin against collagen at solution air and solution polyethylene interfaces. Journal of Biomedical Materials Research 27(2):145-152.

Beake BD, Ling JSG, Leggett GJ. 1998. Correlation of friction, adhesion, wettability and surface chemistry after argon plasma treatment of poly(ethylene terephthalate). Abstr Pap Am Chem S 215:U440-U440.

Benninghoven A. 1994. Chemical analysis of inorganic and organic surfaces and thin films by Static Time-of-Flight Secondary-Ion Mass-Spectrometry (ToF-SIMS). Angew Chem Int Edit 33(10):1023-1043.

Berry CC, Campbell G, Spadiccino A, Robertson M, Curtis AS. 2004. The influence of microscale topography on fibroblast attachment and motility. Biomaterials 25(26):5781-5788.

Bigi A, Panzavolta S, Rubini K. 2004. Relationship between triple-helix content and mechanical properties of gelatin films. Biomaterials 25(25):5675-5680.

Bokel C, Brown NH. 2002. Integrins in development: Moving on, responding to, and sticking to the extracellular matrix. Dev Cell 3(3):311-321.

Bongrand P. 1998. Specific and nonspecific interactions in cell biology. J Disper Sci Technol 19(6-7):963-978.

Bosman FT, Stamenkovic I. 2003. Functional structure and composition of the extracellular matrix. J Pathol 200(4):423-428.

Bottom VE. 1982. Introduction to quartz crystal unit design. New York: van Nostrand Reinhold Company.

Braun D, Fromherz P. 1997. Fluorescence interference-contrast microscopy of cell adhesion on oxidized silicon. Appl Phys a-Mater 65(4-5):341-348.

Briggs D, Chan H, Hearn MJ, Mcbriar DI, Munro HS. 1990. The contact angle of poly(methyl methacrylate) cast against glass. Langmuir 6(2):420-424.

Brinen JS, Greenhouse S, Pinatti L. 1991. ESCA and SIMS studies of plasma treatments of intraocular lenses. Surf Interface Anal 17(2):63-70.

Britland S, Morgan H, WojiakStodart B, Riehle M, Curtis A, Wilkinson C. 1996. Synergistic and hierarchical adhesive and topographic guidance of BHK cells. Exp Cell Res 228(2):313-325.

Brodsky B, Ramshaw JA. 1997. The collagen triple-helix structure. Matrix Biol 15(8-9):545-554.

Brown A, Vickerman JC. 1986. A comparison of positive and negative ion static SIMS spectra of polymer surfaces. Surf Interface Anal 8(2):75-81.

Browne MM, Lubarsky GV, Davidson MR, Bradley RH. 2004. Protein adsorption onto polystyrene surfaces studied by XPS and AFM. Surf Sci 553(1-3):155-167.

Butor C, Davoust J. 1992. Apical to basolateral surface area ratio and polarity of MDCK cells grown on different supports. Exp Cell Res 203(1):115-127.

Buttry DA, Ward MD. 1992. Measurement of interfacial processes at electrode surfaces with the electrochemical quartz crystal microbalance. Chemical Reviews 92(6):1355-1379.

C

Campbell DJ, Beckman KJ, Calderon CE, Doolan PW, Ottosen RM, Ellis AB, Lisensky GC. 1999. Replication and compression of bulk and surface structures with polydimethylsiloxane elastomer. J Chem Educ 76(4):537-541.

Cao H, Tegenfeldt JO, Austin RH, Chou SY. 2002. Gradient nanostructures for interfacing microfluidics and nanofluidics. Appl Phys Lett 81(16):3058-3060.

Carter DC, He XM, Munson SH, Twigg PD, Gernert KM, Broom MB, Miller TY. 1989. Three-dimensional structure of human serum albumin. Science 244(4909):1195-1198.

Cereijido M, Meza I, Martinezpalomo A. 1981. Occluding junctions in cultured epithelial monolayers. American Journal of Physiology 240(3):C96-C102.

Chai J, Lu F, Li B, Kwok DY. 2004. Wettability interpretation of oxygen plasma modified poly(methyl methacrylate). Langmuir 20(25):10919-10927.

Chapman RG, Ostuni E, Takayama S, Holmlin RE, Yan L, Whitesides GM. 2000. Surveying for surfaces that resist the adsorption of proteins. Journal of the American Chemical Society 122(34):8303-8304.

Chen CS, Mrksich M, Huang S, Whitesides GM, Ingber DE. 1998. Micropatterned surfaces for control of cell shape, position, and function. Biotechnol Prog 14(3):356-363.

Chen WL, Shull KR, Papatheodorou T, Styrkas DA, Keddie JL. 1999. Equilibrium swelling of hydrophilic polyacrylates in humid environments. Macromolecules 32(1):136-144.

Cheng YS, Champliaud MF, Burgeson RE, Marinkovich MP, Yurchenco PD. 1997. Self-assembly of laminin isoforms. J Biol Chem 272(50):31525-31532.

Chiu DT, Jeon NL, Huang S, Kane RS, Wargo CJ, Choi IS, Ingber DE, Whitesides GM. 2000. Patterned deposition of cells and proteins onto surfaces by using three-dimensional microfluidic systems. Proc Natl Acad Sci USA 97(6):2408-2413.

Chou LS, Firth JD, Uitto VJ, Brunette DM. 1995. Substratum surface topography alters cell shape and regulates fibronectin messenger-RNA level, messenger-RNA stability, secretion and assembly in human fibroblasts. J Cell Sci 108:1563-1573.

Chrisey LA, OFerrall CE, Spargo BJ, Dulcey CS, Calvert JM. 1996. Fabrication of patterned DNA surfaces. Nucleic Acids Res 24(15):3040-3047.

Chu PK, Chen JY, Wang LP, Huang N. 2002. Plasma-surface modification of biomaterials. Mat Sci Eng R 36(5-6):143-206.

Clark P, Connolly P, Curtis AS, Dow JA, Wilkinson CD. 1990. Topographical control of cell behaviour: II. Multiple grooved substrata. Development 108(4):635-644.

Clark P, Connolly P, Curtis AS, Dow JA, Wilkinson CD. 1991. Cell guidance by ultrafine topography in vitro. J Cell Sci 99 (Pt 1):73-77.

Clark P, Connolly P, Moores GR. 1992. Cell guidance by micropatterned adhesiveness in vitro. J Cell Sci 103 (Pt 1):287-292.

Clouet F, Shi MK. 1992. Interactions of polymer model surfaces with cold plasmas - Hexatriacontane as a model molecule of high-density polyethylene and octadecyl octadecanoate as a model of polyester. 1. Degradation rate versus time and power. J Appl Polym Sci 46(11):1955-1966.

Colognato H, Yurchenco PD. 2000. Form and function: the laminin family of heterotrimers. Dev Dyn 218(2):213-234.

Coopes IH, Gifkins KJ. 1982. Gas plasma treatment of polymer surfaces. J Macromol Sci Chem A17(2):217-226.

Cox EA, Huttenlocher A. 1998. Regulation of integrin-mediated adhesion during cell migration. Microsc Res Tech 43(5):412-419.

Curtis A, Wilkinson C. 1997. Topographical control of cells. Biomaterials 18(24):1573-1583.

Curtis ASG. 1964. Mechanism of adhesion of cells to glass - Study by interference reflection microscopy. Journal of Cell Biology 20(2):199-215.

Curtis ASG, Wilkinson CD. 1998. Reactions of cells to topography. J Biomat Sci-Polym E 9(12):1313-1329.

D

Damji A, Weston L, Brunette DM. 1996. Directed confrontations between fibroblasts and epithelial cells on micromachined grooved substrata. Exp Cell Res 228(1):114-124.

Dammel R. 1993. Diazonaphthoquinone-based resists. Bellingham: SPIE - The International Society of Optical Engineering.

Davies J, Nunnerley CS, Brisley AC, Sunderland RF, Edwards JC, Kruger P, Knes R, Paul AJ, Hibbert S. 2000. Argon plasma treatment of polystyrene microtiter wells. Chemical and physical characterisation by contact angle, ToF-SIMS, XPS and STM. Colloid Surface A 174(3):287-295.

Davies JA. 2001. Extracellular Matrix. Encyclopedia of Life Sciences Chichester: John Wiley & Sons, www.els.net.

Davis A, Tran T. 1991. Gold dissolution in iodide electrolytes. Hydrometallurgy 26(2):163-177.

de Larco JE, Todaro GJ. 1978. Epithelioid and fibroblastic rat kidney cell clones: Epidermal growth factor (EGF) receptors and the effect of mouse sarcoma virus transformation. J Cell Physiol 94(3):335-342.

De Silva MN, Desai R, Odde DJ. 2004. Micro-patterning of animal cells on PDMS substrates in the presence of serum without use of adhesion inhibitors. Biomed Microdevices 6(3):219-222.

De Gennes PG. 1985. Wetting - Statics and Dynamics. Rev Mod Phys 57(3):827-863.

den Braber ET, de Ruijter JE, Ginsel LA, von Recum AF, Jansen JA. 1998. Orientation of ECM protein deposition, fibroblast cytoskeleton, and attachment complex components on silicon microgrooved surfaces. Research Part A:291-300.

Denis FA, Hanarp P, Sutherland DS, Gold J, Mustin C, Rouxhet PG, Dufrene YF. 2002. Protein adsorption on model surfaces with controlled nanotopography and chemistry. Langmuir 18(3):819-828.

DePaola N, Phelps JE, Florez L, Keese CR, Minnear FL, Giaever I, Vincent P. 2001. Electrical impedance of cultured endothelium under fluid flow. Ann Biomed Eng 29(8):648-656.

Dong X, Proctor A, Hercules DM. 1997. Characterization of poly(dimethylsiloxane)s by time-of-flight secondary ion mass spectrometry. Macromolecules 30(1):63-70.

Dörfler HD. 2002. Grenzflächen und kolloid-disperse Systeme. Berlin, Heidelberg, New York: Springer Verlag.

Dow Corning 2009. Product data sheet for PDMS. www.dowcorning.com.

Dragsten PR, Blumenthal R, Handler JS. 1981. Membrane asymmetry in epithelia - Is the tight junction a barrier to diffusion in the plasma membrane. Nature 294(5843):718-722.

D'Sa RA, Burke GA, Meenan BJ. 2010. Protein adhesion and cell response on atmospheric pressure dielectric barrier discharge-modified polymer surfaces. Acta Biomater 6(7):2609-2620.

Duffy DC, McDonald JC, Schueller OJA, Whitesides GM. 1998. Rapid prototyping of microfluidic systems in poly(dimethylsiloxane). Analytical Chemistry 70(23):4974-4984.

Durbeej M. 2010. Laminins. Cell Tissue Res 339(1):259-268.

E

Ebato H, Herron JN, Müller W, Okahata Y, Ringsdorf H, Suci P. 1992. Spezifische Bindung einer funktionellen Proteinschicht an eine tägerfixierte Streptavidinmatrix. Angew Chem 104(8):1064-1066.

Effenhauser CS, Bruin GJM, Paulus A, Ehrat M. 1997. Integrated capillary electrophoresis on flexible silicone microdevices: Analysis of DNA restriction fragments and detection of single DNA molecules on microchips. Analytical Chemistry 69(17):3451-3457.

Efimenko K, Wallace WE, Genzer J. 2002. Surface modification of Sylgard-184 poly(dimethyl siloxane) networks by ultraviolet and ultraviolet/ozone treatment. J Colloid Interf Sci 254(2):306-315.

Ende D, Mangold KM (1993). Impedance Spectroscopy. Chemie in userer Zeit 27(3):134-140

Engvall E. 1995. Structure and function of basement membranes. Int J Dev Biol 39:781-787.

Extrand CW. 2003. Contact angles and hysteresis on surfaces with chemically heterogeneous islands. Langmuir 19(9):3793-3796.

Extrand CW, Kumagai Y. 1995. Liquid drops on an inclined plane - The relation between contact angles, drop shape and retentive force. J Colloid Interf Sci 170(2):515-521.

Eynde XV, Bertrand P. 1997. ToF-SIMS quantification of polystyrene spectra based on principal component analysis (PCA). Surf Interface Anal 25(11):878-888.

Eynde XV, Bertrand P, Jerome R. 1997. Molecular weight effects on polystyrene fingerprint time-of-flight secondary ion mass spectrometry (ToF-SIMS) spectra. Macromolecules 30(21):6407-6416.

F

Faid K, Voicu R, Bani-Yaghoub M, Tremblay R, Mealing G, Py C, Barjovanu R. 2005. Rapid fabrication and chemical patterning of polymer microstructures and their applications as a platform for cell cultures. Biomed Microdevices 7(3):179-184.

Feng J, Weng L-T, Chan CM, Xhie J, Li L. 2001. Imaging of sub-surface nano particles by tapping-mode atomic force microscopy. Polymer 42:2259-2262.

Ferguson GS, Chaudhury MK, Biebuyck HA, Whitesides GM. 1993. Monolayers on disordered substrates - Self-assembly of alkyltrichlorosilanes on surface-modified polyethylene and poly(dimethylsiloxane). Macromolecules 26(22):5870-5875.

Folch A, Toner M. 2000. Microengineering of cellular interactions. Annu Rev Biomed Eng 2:227-256.

France RM, Short RD. 1997. Plasma treatment of polymers - Effects of energy transfer from an argon plasma on the surface chemistry of poly(styrene), low density poly(ethylene), poly(propylene) and poly(ethylene terephthalate). J Chem Soc Faraday T 93(17):3173-3178.

France RM, Short RD. 1998. Plasma treatment of polymers: The effects of energy transfer from an argon plasma on the surface chemistry of polystyrene, and polypropylene. A high-energy resolution X-ray photoelectron spectroscopy study. Langmuir 14(17):4827-4835.

Fredriksson C, Khilman S, Kasemo B, Steel DM. 1998a. In vitro real-time characterization of cell attachment and spreading. J Mater Sci Mater Med 9(12):785-788.

Fredriksson C, Kihlman S, Rodahl M, Kasemo B. 1998b. The piezoelectric quartz crystal mass and dissipation sensor: A means of studying cell adhesion. Langmuir 14(2):248-251.

Freiesleben de Blasio B, Wegener J. 2006. Impedance spectroscopy. In: Webster JG, editor. Encyclopedia of Medical Devices and Instrumentation: John Wiley & Sons, Inc. p 132-144.

Friedrich J, Kühn G, Gähde J. 1979. Untersuchung zur Plasmaätzung von Polymeren, Teil I: Strukturänderungen von Polymeren nach Plasmaätzung. Acta Polymerica 30(8):470-477.

Fritz JL, Owen MJ. 1995. Hydrophobic recovery of plasma-treated polydimethylsiloxane. J Adhesion 54(1-2):33-45.

Fuller S, von Bonsdorff CH, Simons K. 1984. Vesicular stomatitis virus infects and matures only through the basolateral surface of the polarized epithelial cell line, MDCK. Cell 38(1):65-77.

G

Gao LC, McCarthy TJ. 2006. Contact angle hysteresis explained. Langmuir 22(14):6234-6237.

Gelse K, Poschl E, Aigner T. 2003. Collagens - structure, function, and biosynthesis. Adv Drug Deliver Rev 55(12):1531-1546.

Giaever I, Keese CR. 1984. Monitoring fibroblast behavior in tissue culture with an applied electric field. P Natl Acad Sci-Biol 81(12):3761-3764.

Giaever I, Keese CR. 1991. Micromotion of Mammalian-Cells Measured Electrically. P Natl Acad Sci USA 88(17):7896-7900.

Gillmor SD, Larson BJ, Braun JM, Mason CE, Cruz-Barba LE, Denes F, Lagally MG. 2003. Low-contact-angle polydimethyl siloxane (PDMS) membranes for fabricating micro-bioarrays. Proc 2nd Annu Int Con: 1-6

Ginn BT, Steinbock O. 2003. Polymer surface modification using microwave-oven-generated plasma. Langmuir 19(19):8117-8118.

Glasmacher B. 2006. Materialkunde - Biokompatibilität. Feindt P, F. H, Weyand M, editors: Steinkopff. 109-126 p.

Glube N, Giessl A, Wolfrum U, Langguth P. 2007. Caki-1 cells represent an in vitro model system for studying the human proximal tubule epithelium. Nephron Exp Nephrol 107(2):E47-E56.

Gordon MK, Hahn RA. 2010. Collagens. Cell and Tissue Research 339(1):247-257.

Grace JM, Gerenser LJ. 2003. Plasma treatment of polymers. J Disper Sci Technol 24(3-4):305-341.

Grinnell F, Feld MK. 1982. Fibronectin adsorption on hydrophilic and hydrophobic surfaces detected by antibody binding and analyzed during cell adhesion in serum-containing medium. Journal of Biological Chemistry 257(9):4888-4893.

Grosse A, Grewe M, Fouckhardt H. 2001. Deep wet etching of fused silica glass for hollow capillary optical leaky waveguides in microfluidic devices. J Micromech Microeng 11(3):257-262.

Gryte DM, Ward MD, Hu WS. 1993. Real-time measurement of anchorage-dependent cell adhesion using a quartz crystal microbalance. Biotechnol Progr 9(1):105-108.

Guerquin-Kern JL, Wu TD, Quintana C, Croisy A. 2005. Progress in analytical imaging of the cell by dynamic secondary ion mass spectrometry (SIMS microscopy). Bba-Gen Subjects 1724(3):228-238.

H

Hagenhoff B. 2000. High resolution surface analysis by TOF-SIMS. Mikrochim Acta 132(2-4):259-271.

Hall DB, Underhill P, Torkelson JM. 1998. Spin coating of thin and ultrathin polymer films. Polymer Engineering and Science 38(12):2039-2045.

Hansson GC, Simons K, van Meer G. 1986. Two strains of the Madin-Darby canine kidney (MDCK) cell line have distinct glycosphingolipid compositions. Embo J 5(3):483-489.

Harasaki A, Schmit J, Wyant JC. 2000. Improved vertical-scanning interferometry. Appl Optics 39(13):2107-2115.

Harsanyi G. 1996. Polymeric sensing films: new horizons in sensorics? Materials Chemistry and Physics 43:199-203.

Haug M, Schierbaum KD, Gauglitz G, Gopel W. 1993. Chemical sensors based upon polysiloxanes - Comparison between optical, quartz microbalance, calorimetric, and capacitance sensors. Sensor Actuat B-Chem 11(1-3):383-391.

He XM, Carter DC. 1992. Atomic structure and chemistry of human serum albumin. Nature 358(6383):209-215.

Hegemann D, Brunner H, Oehr C. 2003. Plasma treatment of polymers for surface and adhesion improvement. Nucl Instrum Meth B 208:281-286.

Hein M, Mädefessel C, Haag B, Teichmann K, Post A, Galla HJ. 1992. Implications of a non-lamellar lipid phase for the tight junction stability. Part II: Reversible modulation of transepithelial resistance in high and low resistance MDCK-cells by basic amino acids, Ca^{2+}, protamine and protons. Chem Phys Lipids 63(3):223-233.

Heitmann V. 2008. Funktionelle *in situ*-Charakterisierung des Zell-Matrix-Kontaktes. PhD Thesis, Westfälische Wilhelms-Universität, Münster.

Heitmann V, Reiß B, Wegener J. 2007. The quartz crystal microbalance in cell biology: Basics and applications. In: Wolfbeis OS, editor. Piezoelectric Sensors. Berlin, Heidelberg: Springer-Verlag. p 303-338.

Heitmann V, Wegener J. 2007. Monitoring cell adhesion by piezoresonators: Impact of increasing oscillation amplitudes. Anal Chem 79(9):3392-3400.

Henkel W, Glanville RW. 1982. Covalent crosslinking between molecules of type I and type III collagen. The involvement of the N-terminal, nonhelical regions of the alpha 1 (I) and alpha 1 (III) chains in the formation of intermolecular crosslinks. Eur J Biochem 122(1):205-213.

Hillborg H, Ankner JF, Gedde UW, Smith GD, Yasuda HK, Wikstrom K. 2000. Crosslinked polydimethylsiloxane exposed to oxygen plasma studied by neutron reflectometry and other surface specific techniques. Polymer 41(18):6851-6863.

Hirayama K, Akashi S, Furuya M, Fukuhara K. 1990. Rapid confirmation and revision of the primary structure of bovine serum albumin by ESIMS and Frit-FAB LC/MS. Biochem Bioph Res Co 173(2):639-646.

Huang BX, Kim HY, Dass C. 2004. Probing three-dimensional structure of bovine serum albumin by chemical cross-linking and mass spectrometry. J Am Soc Mass Spectr 15(8):1237-1247.

Hynes RO. 1992. Integrins: Versatility, modulation, and signaling in cell adhesion. Cell 69(1):11-25.

Hynes RO. 2002. Integrins: Bidirectional, allosteric signaling machines. Cell 110(6):673-687.

I/J

Inagaki N, Tasaka S, Kawai H. 1989. Improved adhesion of poly(tetrafluoroethylene) by NH_3 plasma treatment. J Adhes Sci Technol 3(8):637-649.

Ingber DE, Madri JA, Jamieson JD. 1986. Basement membrane as a spatial organizer of polarized epithelia - Exogenous basement membrane reorients pancreatic epithelial tumor cells *in vitro*. Am J Pathol 122(1):129-139.

Insall R, Machesky L. 2001. Cytoskeleton. Encyclopedia of Life Sciences Chichester: John Wiley & Sons, www.els.net.

Jacobson K. 2001. Fluorescence microscopy. Encyclopedia of Life Sciences Chichester: John Wiley & Sons, www.els.net.

Janshoff A, Steinem C, Sieber G, Galla H-J. 1996a. Specific binding of peanut agglutinin to GM1-doped solid supported lipid bilayers investigated by shear wave resonator measurements. Eur Biophys J 25:105-113.

Janshoff A, Wegener J, Sieber G, Galla HJ. 1996b. Double-mode impedance analysis of epithelial cell monolayers cultured on shear wave resonators. Eur Biophys J 25:93-103.

Johansson BL, Larsson A, Ocklind A, Ohrlund A. 2002. Characterization of air plasma-treated polymer surfaces by ESCA and contact angle measurements for optimization of surface stability and cell growth. J Appl Polym Sci 86(10):2618-2625.

Jung YC, Bhushan B. 2006. Contact angle, adhesion and friction properties of micro- and nanopatterned polymers for superhydrophobicity. Nanotechnology 17(19):4970-4980.

K

Kadler KE, Baldock C, Bella J, Boot-Handford RP. 2007. Collagens at a glance. J Cell Sci 120(12):1955-1958.

Kaiser JP, Reinmann A, Bruinink A. 2006. The effect of topographic characteristics on cell migration velocity. Biomaterials 27(30):5230-5241.

Kalluri R. 2003. Basement membranes: Structure, assembly and role in tumour angiogenesis. Nat Rev Cancer 3(6):422-433.

Kanan SA, Tze WTY, Tripp CP. 2002. Method to double the surface concentration and control the orientation of adsorbed (3-aminopropyl)dimethylethoxysilane on silica powders and glass slides. Langmuir 18(17):6623-6627.

Kanazawa KK, Gordon JG. 1985. Frequency of a quartz microbalance in contact with liquid. Analytical Chemistry 57(8):1770-1771.

Kasemo B. 2002. Biological surface science. Surf Sci 500(1-3):656-677.

Kasemo B, Gold J. 1999. Implant surfaces and interface processes. Adv Dent Res 13:8-20.

Kasemo B, Lausmaa J. 1986. Surface science aspects on inorganic biomaterials. Crit Rev Biocompat 2(4):335-380.

Keese CR, Bhawe K, Wegener J, Giaever I. 2002. Real-time impedance assay to follow the invasive activities of metastatic cells in culture. Biotechniques 33(4):842-850.

Keese CR, Wegener J, Walker SR, Giaever L. 2004. Electrical wound-healing assay for cells *in vitro*. P Natl Acad Sci USA 101(6):1554-1559.

Keselowsky BG, Collard DM, Garcia AJ. 2003. Surface chemistry modulates fibronectin conformation and directs integrin binding and specificity to control cell adhesion. Journal of Biomedical Materials Research Part A 66A(2):247-259.

Kim J, Chaudhury MK, Owen MJ. 2000. Hydrophobic recovery of polydimethylsiloxane elastomer exposed to partial electrical discharge. J Colloid Interf Sci 226(2):231-236.

Kim J, Chaudhury MK, Owen MJ, Orbeck T. 2001. The mechanisms of hydrophobic recovery of polydimethylsiloxane elastomers exposed to partial electrical discharges. J Colloid Interf Sci 244(1):200-207.

Kipling AL, Thompson M. 1990. Network analysis method applied to liquid-phase acoustic wave sensors. Analytical Chemistry 62(14):1514-1519.

Klee D, Hoecker H. 2000. Polymers for biomedical applications: improvement of the inter face compatibility. Advances in Polymer Science. Berlin, Heidelberg: Springer. p 1-57.

Ko JS, Yoon HC, Yang H, Pyo H-B, Chung KH, Kim SJ, Kim TK. 2003. A polymer-based microfluidic device for immunosensing biochips. Lab Chip 3:106-113.

Kragh-Hansen U. 1981. Molecular aspects of ligand binding to serum albumin. Pharmacol Rev 33(1):17-53.

Kramer J. 1999. The right filter gets the most out of a microscope. Biophotonics International 5:54-59.

Krissansen GW, Danen EH. 2006. Integrins: Signalling and disease. Encyclopedia of Life Sciences Chichester: John Wiley & Sons, www.els.net.

Krissansen GW, Danen EH. 2007. Integrin superfamily. Encyclopedia of Life Sciences Chichester: John Wiley & Sons, www.els.net.

Kühn K. 1994. Basement membrane (type IV) collagen. Matrix Biology 14:439 - 445.

Kurtyka B, Delevie R. 1992. Frequency dispersion associated with a nonhomogeneous interfacial capacitance. J Electroanal Chem 322(1-2):63-77.

Kwok DY, Gietzelt T, Grundke K, Jacobasch HJ, Neumann AW. 1997. Contact angle measurements and contact angle interpretation. 1. Contact angle measurements by axisymmetric drop shape analysis and a goniometer sessile drop technique. Langmuir 13(10):2880-2894.

L

Lai JY, Lin YY, Denq YL, Chen JK. 1996. Surface modification of silicone rubber by gas plasma treatment. J Adhes Sci Technol 10(3):231-242.

Langmuir I. 1933. Surface chemistry. Chem Rev 13(2):147-191.

Leclerc E, Sakai Y, Fujii T. 2003. Cell culture in 3-dimensional microfluidic structure of PDMS (polydimethylsiloxane). Biomed Microdevices 5(2):109-114.

Lee JH, Khang G, Lee JW, Lee HB. 1998. Interaction of different types of cells on polymer surfaces with wettability gradient. J Colloid Interface Sci 205(2):323-330.

Leeson AM, Alexander MR, Short RD, Briggs D, Hearn MJ. 1997. Secondary ion mass spectrometry of polymers: A ToF SIMS study of monodispersed PMMA standards. Surf Interface Anal 25(4):261-274.

Leighton J, Brada Z, Estes LW, Justh G. 1969. Secretory activity and oncogenicity of a cell line (MDCK) derived from canine kidney. Science 163(866):472-473.

Li J, Thielemann C, Reuning U, Johannsmann D. 2005. Monitoring of integrin-mediated adhesion of human ovarian cancer cells to model protein surfaces by quartz crystal resonators: evaluation in the impedance analysis mode (vol 20, pg 1333, 2005). Biosensors & Bioelectronics 20(11):2386-2386.

Li N, Tourovskaia A, Folch A. 2003. Biology on a chip: Microfabrication for studying the behavior of cultured cells. Critical Review in Biomedical Engineering 31(5&6):423-488.

Li RZ, Ye L, Mai YW. 1997. Application of plasma technologies in fibre-reinforced polymer composites: A review of recent developments. Compos Part a-Appl S 28(1):73-86.

Lin YC, Ho HC, Tseng CK, Hou SQ. 2001. A poly-methylmethacrylate electrophoresis microchip with sample preconcentrator. J Micromech Microeng 11(3):189-194.

Lin ZX, Ward MD. 1995. The Role of longitudinal waves in quartz crystal microbalance applications in liquids. Analytical Chemistry 67(4):685-693.

Liston E. 1989. Plasma treatment for improved bonding: A review. The Journal of Adhesion 30(1):199-218.

Lo CM, Keese CR, Giaever I. 1993. Monitoring motion of confluent cells in tissue culture. Exp Cell Res 204(1):102-109.

Lo CM, Keese CR, Giaever I. 1999. Cell-substrate contact: Another factor may influence transepithelial electrical resistance of cell layers cultured on permeable filters. Exp Cell Res 250(2):576-580.

Lord MS, Modin C, Foss M, Duch M, Simmons A, Pedersen FS, Milthorpe BK, Besenbacher F. 2006a. Monitoring cell adhesion on tantalum and oxidised polystyrene using a quartz crystal microbalance with dissipation. Biomaterials 27(26):4529-4537.

Lord MS, Stenzel MH, Simmons A, Milthorpe BK. 2006b. The effect of charged groups on protein interactions with poly(HEMA) hydrogels. Biomaterials 27(4):567-575.

Lub J, Benninghoven A. 1989. On the mechanism of secondary ion formation from poly(methylmethacrylate) under static secondary ion mass spectrometry conditions. Org Mass Spectrom 24(3):164-168.

Luo BH, Carman CV, Springer TA. 2007. Structural basis of integrin regulation and signaling. Annu Rev Immunol 25:619-647.

Luttge A, Bolton EW, Lasaga AC. 1999. An interferometric study of the dissolution kinetics of anorthite: The role of reactive surface area. Am J Sci 299(7-9):652-678.

M

Maher MP, Pine J, Wright J, Tai YC. 1999. The neurochip: a new multielectrode device for stimulating and recording from cultured neurons. J Neurosci Methods 87(1):45-56.

Martin BA, Hager HE. 1989a. Flow profile above a quartz crystal vibrating in liquid. J Appl Phys 65(7):2627-2629.

Martin BA, Hager HE. 1989b. Velocity profile on quartz crystals oscillating in liquids. J Appl Phys 65(7):2630-2635.

Martin SJ, Granstaff VE, Frye GC. 1991. Characterization of a Quartz Crystal Microbalance with Simultaneous Mass and Liquid Loading. Analytical Chemistry 63(20):2272-2281.

Massia SP, Hubbell JA. 1990a. Covalent surface immobilization of Arg-Gly-Asp- and Tyr-Ile-Gly-Ser-Arg-containing peptides to obtain well-defined cell-adhesive substrates. Anal Biochem 187(2):292-301.

Massia SP, Hubbell JA. 1990b. Covalently attached GRGD on polymer surfaces promotes biospecific adhesion of mammalian cells. Ann N Y Acad Sci 589:261-270.

Mata A, Fleischman AJ, Roy S. 2005. Characterization of polydimethylsiloxane (PDMS) properties for biomedical micro/nanosystems. Biomed Microdevices 7(4):281-293.

Matsuzawa M, Umemura K, Beyer D, Sugioka K, Knoll W. 1997. Micropatterning of neurons using organic substrates in culture. Thin Solid Films 305(1-2):74-79.

Mcadams ET, Lackermeier A, Mclaughlin JA, Macken D, Jossinet J. 1995. The linear and nonlinear electrical properties of the electrode-electrolyte interface. Biosensors & Bioelectronics 10(1-2):67-74.

McDonald JC, Duffy DC, Anderson JR, Chiu DT, Wu H, Schueller OJ, Whitesides GM. 2000. Fabrication of microfluidic systems in poly(dimethylsiloxane). Electrophoresis 21(1):27-40.

McDonald JC, Whitesides GM. 2002. Poly(dimethylsiloxane) as a material for fabricating microfluidic devices. Acc Chem Res 35(7):491-499.

Mcdonald JR. 1992. Impedance spectroscopy. Ann Biomed Eng 20:289-305.

Meredith JE, Schwartz MA. 1997. Integrins, adhesion and apoptosis. Trends Cell Biol 7(4):146-150.

Michaelis S. 2005. Nanoporöse Substrate als sensorische Oberflächen für kultivierte Zellen. Diploma Thesis, Westfälische Wilhelms-Universität Münster.

MicroChemicals. 2007. Lithografie - Theorie und Anwendung von Fotolacken, Entwicklern, Ätzchemikalien und Lösemitteln.

Miller C, Shanks H, Witt A, Rutkowski G, Mallapragada S. 2001. Oriented Schwann cell growth on micropatterned biodegradable polymer substrates. Biomaterials 22(11):1263-1269.

Mitchell SA, Poulsson AHC, Davidson MR, Bradley RH. 2005. Orientation and confinement of cells on chemically patterned polystyrene surfaces. Colloid Surface B 46(2):108-116.

Mitchell SA, Poulsson AHC, Davidson MR, Emmison N, Shard AG, Bradley RH. 2004. Cellular attachment and spatial control of cells using micro-patterned ultra-violet/ozone treatment in serum enriched media. Biomaterials 25(18):4079-4086.

Modin C, Stranne AL, Foss M, Duch M, Justesen J, Chevallier J, Andersen LK, Hemmersam AG, Pedersen FS, Besenbacher F. 2006. QCM-D studies of attachment and differential spreading of pre-osteoblastic cells on Ta and Cr surfaces. Biomaterials 27(8):1346-1354.

Morra M, Occhiello E, Marola R, Garbassi F, Humphrey P, Johnson D. 1990. On the aging of oxygen plasma-treated polydimethylsiloxane surfaces. J Colloid Interface Sci 137(1):11-24

Mott JD, Werb Z. 2004. Regulation of matrix biology by matrix metalloproteinases. Curr Opin Cell Biol 16(5):558-564.

Moy E, Lin FYH, Vogtle JW, Policova Z, Neumann AW. 1994. Contact angle studies of the surface properties of covalently bonded poly-L-lysine to surfaces treated by glow discharge. Colloid Polym Sci 272(10):1245-1251.

Mrksich M, Dike LE, Tien J, Ingber DE, Whitesides GM. 1997. Using microcontact printing to pattern the attachment of mammalian cells to self-assembled monolayers of alkanethiolates on transparent films of gold and silver. Exp Cell Res 235(2):305-313.

Mueller M, Sciarratta V, Oehr C. 2003. Plasmachemische Mikrostrukturierung von polymeren Oberflächen für Pharmazie und medizinische Diagnostik. Vakuum in Forschung und Praxis 15(1):19-22.

Muramatsu H, Dicks JM, Tamiya E, Karube I. 1987. Piezoelectric crystal biosensor modified with protein A for determination of immunoglobulins. Anal Chem 59(23):2760-2763.

N/O

Ng JMK, Gitlin I, Stroock AD, Whitesides GM. 2002. Components for integrated poly(dimethylsiloxane) microfluidic systems. Electrophoresis 23(20):3461-3473.

Nicolau DV, Taguchi T, Tanigawa H, Yoshikawa S. 1996. Control of the neuronal cell attachment by functionality manipulation of diazo-naphthoquinone/novolak photoresist surface. Biosensors & Bioelectronics 11(12):1237-1252.

Nimeri G, Fredriksson C, Elwing H, Liu L, Rodahl M, Kasemo B. 1998. Neutrophil interaction with protein-coated surfaces studied by an extended quartz crystal microbalance technique. Colloid Surface B 11(5):255-264.

Noël MAM, Topart PA. 1994. High frequency impedance analysis of quartz crystal microbalances. 1. General considerations. Analytical Chemistry 66(4):484-491.

Norde W, Haynes CA. 1995. Reversibility and the mechanism of protein adsorption. In: Horbett TA, Brash JL, editors. Proteins at interfaces II: Fundamentals and applications. Washington D.C.: American Chemical Society. p 26-40.

Nothnagle PE, Chambers W, Davidson MW. 2009. Introduction to stereomicroscopy. www.microscopyu.com.

Oakley C, Brunette DM. 1993. The sequence of alignment of microtubules, focal contacts and actin filaments in fibroblasts spreading on smooth and grooved titanium substrata. J Cell Sci 106 (Pt 1):343-354.

O'Brien J, Hughes PJ, Brunet M, O'Neill B, Alderman J, Lane B, O'Riordan A, O'Driscoll C. 2001. Advanced photoresist technologies for microsystems. J Micromech Microeng 11(4):353-358.

Ostuni E, Chapman RG, Holmlin RE, Takayama S, Whitesides GM. 2001. A survey of structure-property relationships of surfaces that resist the adsorption of protein. Langmuir 17(18):5605-5620.

Ostuni E, Grzybowski BA, Mrksich M, Roberts CS, Whitesides GM. 2003. Adsorption of proteins to hydrophobic sites on mixed self-assembled monolayers. Langmuir 19(5):1861-1872.

Owens DK, Wendt RC. 1969. Estimation of surface free energy of polymers. J Appl Polym Sci 13(8):1741-&.

P/Q

Palzer S, Hiebl C, Sommer K, Lechner H. 2001. Influence of roughness of a solid surface on the angle of contact. Chem-Ing-Tech 73(8):1032-1038.

Peppas NA, Langer R. 1994. New challenges in biomaterials. Science 263(5154):1715-1720.

Petronis S, Gretzer C, Kasemo B, Gold J. 2003. Model porous surfaces for systematic studies of material-cell interactions. Journal of Biomedical Materials Research Part A 66A(3):707-721.

Pierres A, Benoliel AM, Bongrand P. 2002. Cell fitting to adhesive surfaces: A prerequisite to firm attachment and subsequent events. Eur Cell Mater 3:31-45.

Pierschbacher MD, Ruoslahti E. 1984. Cell attachment activity of fibronectin can be duplicated by small synthetic fragments of the molecule. Nature 309(5963):30-33.

Poll H-U, Kleemann R, Meichsner J. 1981. Plasmamodifizierung von Polymeroberflächen, II. Entstehung freier Radikale durch Einwirkung einer Glimmentladung. Acta Polymerica 32(3):139-143.

Prozialeck WC, Edwards JR, Lamar PC, Smith CS. 2006. Epithelial barrier characteristics and expression of cell adhesion molecules in proximal tubule-derived cell lines commonly used for in vitro toxicity studies. Toxicol in Vitro 20(6):942-953.

Qi PH, Hiskey JB. 1991. Dissolution kinetics of gold in iodide solutions. Hydrometallurgy 27(1):47-62.

R

Raghavan S, Chen CS. 2004. Micropatterned environments in cell biology. Adv Mater 16(15):1303-1313.

Rai-Choudhury P. 1997. Handbook of microlithography, micromachining and microfabrication. Bellingham.

Ratner BD. 1993. New ideas in biomaterials science - a path to engineered biomaterials. J Biomed Mater Res 27(7):837-850.

Ratner BD. 1997. Biomaterials science. In: d'Agostino D, Favia P, Fracassi F, editors. Plasma processing of polymers. Dordrecht Boston London: Kluwer Academic Publishers. p 453-464.

Ratner BD, Castner DG. 1997. Surface modification of polymeric biomaterials. New York: Plenum Press.

Ratner BD, Hoffman AS, Schoen FJ, Lemons JE. 2004. Biomaterials science: A multidisciplinary endeavor. In: Ratner BD, editor. Biomaterials science. California London: Elsevier Academic Press.

Redepenning J, Schlesinger TK, Mechalke EJ, Puleo DA, Bizios R. 1993. Osteoblast attachment monitored with a quartz crystal microbalance. Analytical Chemistry 65(23):3378-3381.

Reiß B. 2004. Mikrogravimetrische Untersuchung des Adhäsionskontaktes tierischer Zellen : Eine biophysikalische Studie. PhD Thesis, Westfälische Wilhelms-Universität Münster.

Reiß B, Janshoff A, Steinem C, Seebach J, Wegener J. 2003. Adhesion kinetics of functionalized vesicles and mammalian cells: A comparative study. Langmuir 19(5):1816-1823.

Reyes DR, Perruccio EM, Becerra SP, Locascio LE, Gaitan M. 2004. Micropatterning neuronal cells on polyelectrolyte multilayers. Langmuir 20(20):8805-8811.

Richardson JC, Scalera V, Simmons NL. 1981a. Identification of two strains of MDCK cells which resemble separate nephron tubule segments. Biochim Biophys Acta 673(1):26-36.

Richter E, Fuhr G, Muller T, Shirley S, Rogaschewski S, Reimer K, Dell C. 1996. Growth of anchorage-dependent mammalian cells on microstructures and microperforated silicon membranes. J Mater Sci-Mater M 7(2):85-97.

Risbud MV, Dabhade R, Gangal S, Bhonde RR. 2002. Radio-frequency plasma treatment improves the growth and attachment of endothelial cells on poly(methyl methacrylate) substrates: implications in tissue engineering. J Biomater Sci Polym Ed 13(10):1067-1080.

Roach P, Farrar D, Perry CC. 2005. Interpretation of protein adsorption: Surface-induced conformational changes. J Am Chem Soc 127(22):8168-8173.

Rodahl M, Hook F, Fredriksson C, Keller CA, Krozer A, Brzezinski P, Voinova M, Kasemo B. 1997. Simultaneous frequency and dissipation factor QCM measurements of biomolecular adsorption and cell adhesion. Faraday Discuss(107):229-246.

Rodahl M, Kasemo B. 1996. A simple setup to simultaneously measure the resonant frequency and the absolute dissipation factor of a quartz crystal microbalance. Rev Sci Instrum 67(9):3238-3241.

Rommel CE. 2007. Tierische Zellen auf nanoporösen Oberflächen: Grundlagen und bioanalytische Anwendungen. PhD Thesis, Westfälische Wilhelms-Universität Münster.

Ruzzu A, Matthis B. 2002. Swelling of PMMA-structures in aqueous solutions and room temperature Ni-electroforming. Microsyst Technol 8(2-3):116-119.

S

Saito R, Ichinohe Y, Kudo M. 1999. TOF-SIMS analysis of chemical state changes in cresol-novolak photoresist surface caused by O_2 plasma downstream. Appl Surf Sci 142(1-4):460-464.

Sanderson JB. 2001. Phase Contrast Microscopy. Encyclopedia of Life Sciences Chichester: John Wiley & Sons, www.els.net.

Saneinejad S, Shoichet MS. 1998. Patterned glass surfaces direct cell adhesion and process outgrowth of primary neurons of the central nervous system. Journal of Biomedical Materials Research 42(1):13-19.

Sauerbrey G. 1959. Verwendung von Schwingquarzen zur Wägung dünner Schichten und zur Mikrowägung. Z Phys 155(2):206-222.

Schéele S, Nystrom A, Durbeej M, Talts JF, Ekblom M, Ekblom P. 2007. Laminin isoforms in development and disease. J Mol Med-Jmm 85(8):825-836.

Schindl M, Wallraff E, Deubzer B, Witke W, Gerisch G, Sackmann E. 1995. Cell-substrate interactions and locomotion of dictyostelium wild type and mutants defective in 3 cytoskeletal proteins - A study using quantitative reflection interference contrast microscopy. Biophys J 68(3):1177-1190.

Schott H. 1992. Swelling kinetics of polymers. J Macromol Sci Phys B31(1):1-9.

Schueler BW. 1992. Microscope imaging by Time-of-Flight Secondary Ion Mass-Spectrometry. Microsc Microanal M 3(2-3):119-139.

Schuhmacher R. 1990. Die Quarzmikrowaage: Eine neue Messtechnik zur *in situ*-Untersuchung des Phasengrenzbereiches fest/flüssig. Angew Chem 102:347-361.

Schwartz NB. 2009. Proteoglycans. Encyclopedia of Life Sciences Chichester: John Wiley & Sons, www.els.net.

Sedev RV, Petrov JG, Neumann AW. 1996. Effect of swelling of a polymer surface on advancing and receding contact angles. J Colloid Interf Sci 180(1):36-42.

Shahal T, Melzak KA, Lowe CR, Gizeli E. 2008. Poly(dimethylsiloxane)-coated sensor devices for the formation of supported lipid bilayers and the subsequent study of membrane interactions. Langmuir 24(19):11268-11275.

Sia SK, Whitesides GM. 2003. Microfluidic devices fabricated in poly(dimethylsiloxane) for biological studies. Electrophoresis 24(21):3563-3576.

Sigal GB, Mrksich M, Whitesides GM. 1998. Effect of surface wettability on the adsorption of proteins and detergents. Journal of the American Chemical Society 120(14):3464-3473.

Sigma-Aldrich. 2009. Product data sheet for PS and PMMA. www.sigmaaldrich.com.

Sordel T, Kermarec-Marcel F, Garnier-Raveaud S, Glade N, Sauter-Starace F, Pudda C, Borella M, Plissonnier M, Chatelain F, Bruckert F, Picollet-D'hahan N. 2007. Influence of glass and polymer coatings on CHO cell morphology and adhesion. Biomaterials 28(8):1572-1584.

Steele JG, Dalton BA, Johnson G, Underwood PA. 1993. Polystyrene chemistry affects vitronectin activity - An explanation for cell attachment to tissue culture polystyrene but not to unmodified polystyrene. Journal of Biomedical Materials Research 27(7):927-940.

Steele JG, Dalton BA, Johnson G, Underwood PA. 1995. Adsorption of fibronectin and vitronectin onto Primaria™ and tissue culture polystyrene and relationship to the mechanism of initial attachment of human vein endothelial cells and BHK-21 fibroblasts. Biomaterials 16(14):1057-1067.

Steinem C, Janshoff A, Wegener J, Ulrich WP, Willenbrink W, Sieber M, Galla HJ. 1997. Impedance and shear wave resonance analysis of ligand-receptor interactions at functionalized surfaces and of cell monolayers. Biosens Bioelectron 12(8):787-808.

Stevenson BR, Anderson JM, Goodenough DA, Mooseker MS. 1988. Tight junction structure and ZO-1 content are identical in two strains of Madin-Darby canine kidney cells which differ in transepithelial resistance. J Cell Biol 107(6 Pt 1):2401-2408.

T

Taborelli M, Eng L, Descouts P, Ranieri JP, Bellamkonda R, Aebischer P. 1995. Bovine serum albumin conformation on methyl and amine functionalized surfaces compared by scanning force microscopy. Journal of Biomedical Materials Research 29(6):707-714.

Tan JL, Liu W, Nelson CM, Raghavan S, Chen CS. 2004. Simple approach to micropattern cells on common culture substrates by tuning substrate wettability. Tissue Eng 10(5-6):865-872.

Tanaka Y, Morishima K, Shimizu T, Kikuchi A, Yamato M, Okano T, Kitamori T. 2006. Demonstration of a PDMS-based bio-microactuator using cultured cardiomyocytes to drive polymer micropillars. Lab Chip 6(2):230-235.

Tatic-Lucic S, Wright JA, Tai Y-C, Pine J. 1997. Silicon cultured-neuron prosthetic devices for *in vivo* and *in vitro* studies. Sensor Actuat B-Chem 43:105-109.

Taylor AM, Rhee SW, Tu CH, Cribbs DH, Cotman CW, Jeon NL. 2003. Microfluidic multicompartment device for neuroscience research. Langmuir 19(5):1551-1556.

Teare DOH, Emmison N, Ton-That C, Bradley RH. 2000. Cellular attachment to ultraviolet ozone modified polystyrene surfaces. Langmuir 16(6):2818-2824.

Teng R, Yasuda HK. 2002. *Ex situ* chemical determination of free radicals and peroxides on plasma treated surfaces. Plasmas and Polymers 7(1):57-69.

Thorslund S. 2006. Microfluidics in surface modified PDMS. PhD Thesis, Uppsala University.

Thorslund S, Sanchez J, Larsson R, Nikolajeff F, Bergquist J. 2005. Bioactive heparin immobilized onto microfluidic channels in poly(dimethylsiloxane) results in hydrophilic surface properties. Colloids Surf B Biointerfaces 46(4):240-247.

Tien J, Nelson CM, Chen CS. 2002. Fabrication of aligned microstructures with a single elastomeric stamp. P Natl Acad Sci USA 99(4):1758-1762.

Tourovskaia A, Barber T, Wickes BT, Hirdes D, Grin B, Castner DG, Healy KE, Folch A. 2003. Micropatterns of chemisorbed cell adhesion-repellent films using oxygen plasma etching and elastomeric masks. Langmuir 19(11):4754-4764.

Toworfe GK, Composto RJ, Adams CS, Shapiro IM, Ducheyne P. 2004. Fibronectin adsorption on surface-activated poly(dimethylsiloxane) and its effect on cellular function. J Biomed Mater Res A 71(3):449-461.

U/V

Underwood PA, Steele JG, Dalton BA. 1993. Effects of polystyrene surface chemistry on the biological activity of solid phase fibronectin and vitronectin, analysed with monoclonal antibodies. J Cell Sci 104 (Pt 3):793-803.

Urban G. 1999. Microstructuring of organic layers for microsystems. Sensor Actuat a-Phys 74(1-3):219-224.

van der Rest M, Garrone R. 1991. Collagen family of proteins. Faseb J 5(13):2814-2823.

van Kooten TG, Spijker HT, Busscher HJ. 2004. Plasma-treated polystyrene surfaces: Model surfaces for studying cell-biomaterial itneractions. Biomaterials 25:1735-1747.

van Kooten TG, Whitesides JF, von Recum A. 1998. Influence of silicone (PDMS) surface texture on human skin fibroblast proliferation as determined by cell cycle analysis. J Biomed Mater Res 43(1):1-14.

van Meer G, Simons K. 1986. The function of tight junctions in maintaining differences in lipid composition between the apical and the basolateral cell surface domains of MDCK cells. Embo J 5(7):1455-1464.

van Oss CJ, Good RJ, Chaudhury MK. 1988. Additive and nonadditive surface tension components and the interpretation of contact angles. Langmuir 4:884-891.

Vanhardeveld RM, Gunter PLJ, Vanijzendoorn LJ, Wieldraaijer W, Kuipers EW, Niemantsverdriet JW. 1995. Deposition of inorganic salts from solution on flat substrates by spin coating - Theory, quantification and application to model catalysts. Appl Surf Sci 84(4):339-346.

Vasilets VN, Kuznetsov AV, Sevast'yanov VI. 2006. Regulation of the biological properties of medical polymer materials with the use of a gas-discharge plasma and vacuum ultraviolet radiation. High Energ Chem 40(2):79-85.

Verschueren H. 1985. Interference reflection microscopy in cell biology - Methodology and applications. J Cell Sci 75(APR):279-301.

Vogler EA. 1998. Structure and reactivity of water at biomaterial surfaces. Advances in Colloid and Interface Science 74:69-117.

W

Walboomers XF, Croes HJ, Ginsel LA, Jansen JA. 1998. Growth behavior of fibroblasts on microgrooved polystyrene. Biomaterials 19(20):1861-1868.

Walboomers XF, Monaghan W, Curtis AS, Jansen JA. 1999. Attachment of fibroblasts on smooth and microgrooved polystyrene. J Biomed Mater Res 46(2):212-220.

Wang CT, Yen SC. 1995. Theoretical analysis of film uniformity in spinning processes. Chem Eng Sci 50(6):989-999.

Washo BD. 1977. Rheology and modeling of spin coating process. Ibm J Res Dev 21(2):190-198.

Wegener J. 1998. Impedanzspektroskopische und mikrogravimetrische Untersuchungen an barrierebildenden Zellen auf planaren Goldelektroden. PhD Thesis, Westfälische Wilhelms-Universität Münster.

Wegener J. 2003, June. ECIS: Ein variabel einsetzbares elektrochemisches Verfahren - Lebende Zellen als Sensoren. Forschunsjournal der Westfälischen Wilhelms-Universität Münster:11-17.

Wegener J. 2006. Cell surface interactions. Wiley Encyclopedia of Biomedical Engineering, John Wiley & Sons, Inc.

Wegener J, Janshoff A, Galla HJ. 1998. Cell adhesion monitoring using a quartz crystal microbalance: Comparative analysis of different mammalian cell lines. Eur Biophys J Biophy 28(1):26-37.

Wegener J, Janshoff A, Steinem C. 2001. The quartz crystal microbalance as a novel means to study cell-substrate interactions *in situ*. Cell Biochem Biophys 34(1):121-151.

Wegener J, Keese CR, Giaever I. 2000a. Electric cell-substrate impedance sensing (ECIS) as a noninvasive means to monitor the kinetics of cell spreading to artificial surfaces. Exp Cell Res 259(1):158-166.

Wegener J, Keese CR, Giaever I. 2002. Recovery of adherent cells after in situ electroporation monitored electrically. Biotechniques 33(2):348-357.

Wegener J, Seebach J, Janshoff A, Galla HJ. 2000b. Analysis of the composite response of shear wave resonators to the attachment of mammalian cells. Biophys J 78(6):2821-2833.

Wegener J, Sieber M, Galla HJ. 1996a. Impedance analysis of epithelial and endothelial cell monolayers cultured on gold surfaces. J Biochem Biophys Methods 32(3):151-170.

Wegener J, Sieber M, Galla HJ. 1996b. Impedance analysis of epithelial and endothelial cell monolayers cultured on gold surfaces. J Biochem Bioph Meth 32(3):151-170.

Weiss P. 1945. Experiments on cell and axon orientation in vitro: The role of colloidal exudates in tissue organisation. J Exp Zool 100:353-386.

Welle A. 2004. Competitive plasma protein adsorption on modified polymer surfaces monitored by quartz crystal microbalance technique. J Biomater Sci Polym Ed 15(3):357-370.

Welle A, Gottwald E. 2002. UV-based patterning of polymeric substrates for cell culture applications. Biomed Microdevices 4(1):33-41.

Weng LT, Bertrand P, Lauer W, Zimmer R, Busetti S. 1995. Quantitative surface analysis of styrene-butadiene copolymers using Time-of-Flight Secondary Ion Mass Spectrometry. Surf Interface Anal 23:879-886.

Wenzel RN. 1936. Resistance of solid surfaces to wetting by water. Ind Eng Chem 28(8):988-994.

Whitesides GM, Ostuni E, Takayama S, Jiang X, Ingber DE. 2001. Soft lithography in biology and biochemistry. Annu Rev Biomed Eng 3:335-373.

Wilken R, Holländer A, Behnisch J. 1998. Quantitative comparison between vacuum-ultraviolett irradiation and remote hydrogen plasma treatment of hydrocarbon polymers. Plasmas and Polymers 3(3):165-175.

Wilkinson CDW, Riehle M, Wood M, Gallagher J, Curtis ASG. 2002. The use of materials patterned on a nano- and micro-metric scale in cellular engineering. Mat Sci Eng C-Bio S 19(1-2):263-269.

Williams DF. 1987. Definitions in biomaterials. Amsterdam: Elsevier.

Wilson CJ, Clegg RE, Leavesley DI, Pearcy MJ. 2005. Mediation of biomaterial-cell interactions by adsorbed proteins: A review. Tissue Engineering 11(1-2):1-18.

Winkelmann M, Gold J, Hauert R, Kasemo B, Spencer ND, Brunette DM, Textor M. 2003. Chemically patterned, metal oxide based surfaces produced by photolithographic techniques for studying protein- and cell-surface interactions I: Microfabrication and surface characterization. Biomaterials 24(7):1133-1145.

Wintermantel E, Ha S-W. 2002. Medizintechnik mit biokompatiblen Werkstoffen und Verfahren. Berlin, Heidelberg, New York: Springer-Verlag.

Wozniak MA, Modzelewska K, Kwong L, Keely PJ. 2004. Focal adhesion regulation of cell behavior. Biochim Biophys Acta 1692(2-3):103-119.

Wunsch JR. 2000. Polystyrene - synthesis, production and applications. Dolbey R, editor. Shawbury Shrewsbury: Rapra Technology Limited.

www.media.wiley.com/product_data....pdf.

www.microscopyu.com.

www.mikroskopie.de.

Wyant JC. 2002. White light interferometry. Proc SPIE:1-10.

X/Y/Z

Xia Y, Rogers JA, Paul KE, Whitesides GM. 1999. Unconventional methods for fabricating and patterning nanostructures. Chem Rev 99(7):1823-1848.

Xia YN, Whitesides GM. 1998. Soft lithography. Annu Rev Mater Sci 28:153-184.

Xiao CD, Lachance B, Sunahara G, Luong JHT. 2002. Assessment of cytotoxicity using electric cell-substrate impedance sensing: Concentration and time response function approach. Analytical Chemistry 74(22):5748-5753.

Yang MS, Thompson M. 1993. Multiple chemical information from the thickness shear mode acoustic wave sensor in the liquid phase. Analytical Chemistry 65(9):1158-1168.

Yurchenco PD, Schittny JC. 1990. Molecular architecture of basement membranes. Faseb J 4(6):1577-1590.

Zeng XM, Weng LT, Li L, Chan CM, Liu SY, Jiang M. 2001. ToF-SIMS study of the surface morphology of blends of polystyrene and poly(N-vinyl-2-pyrrolidone) compatibilized by poly(styrene-co-4-vinylphenol). Surf Interface Anal 31(5):421-428.

Ziats NP, Miller KM, Anderson JM. 1988. *In vitro* and *in vivo* interactions of cells with biomaterials. Biomaterials 9(1):5-13.

Zimmerman PA, Hercules DM, Benninghoven A. 1993. Time-of-Flight Secondary Ion Mass-Spectrometry of poly(alkyl methacrylates). Analytical Chemistry 65(8):983-991.

Zinger O, Anselme K, Denzer A, Habersetzer P, Wieland M, Jeanfils J, Hardouin P, Landolt D. 2004. Time-dependent morphology and adhesion of osteoblastic cells on titanium model surfaces featuring scale-resolved topography. Biomaterials 25(14):2695-2711.

Appendix

A Phase Contrast Micrographs of Spin Coated Polymer Films

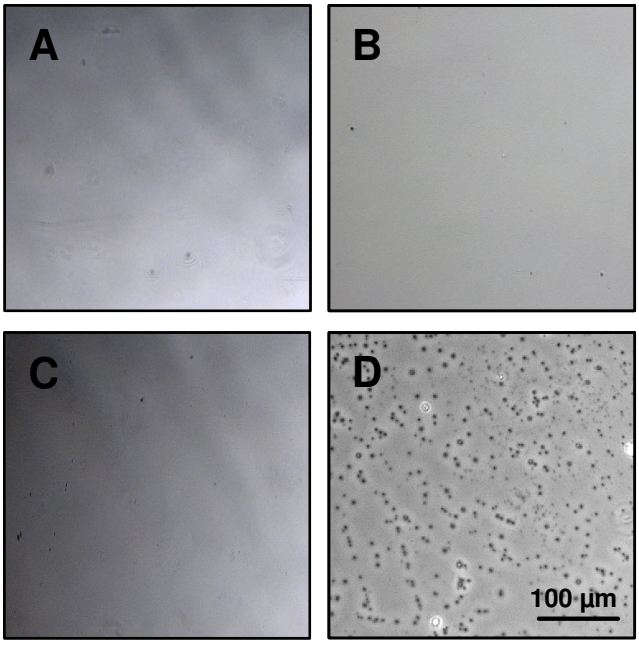

Fig. A.1 Phase contrast micrographs of **A** PS, **B** PMMA, **C** PDMS and **D** PhoP which had been spin coated on coverslips.

B Protein Adsorption upon Polymer Surfaces Using the Active Oscillator Mode QCM

The following diagrams show the results obtained from QCM measurements using the active oscillator mode performed for different proteins during their adsorption upon a polymer surface. The shift in resonance frequency Δf upon protein adsorption is plotted against the respective protein concentration in the bulk solution for each of the proteins under study. The solid line represents the fit according to the Langmuir adsorption isotherm.

1 Polystyrene Surfaces – Unmodified and Plasma Modified

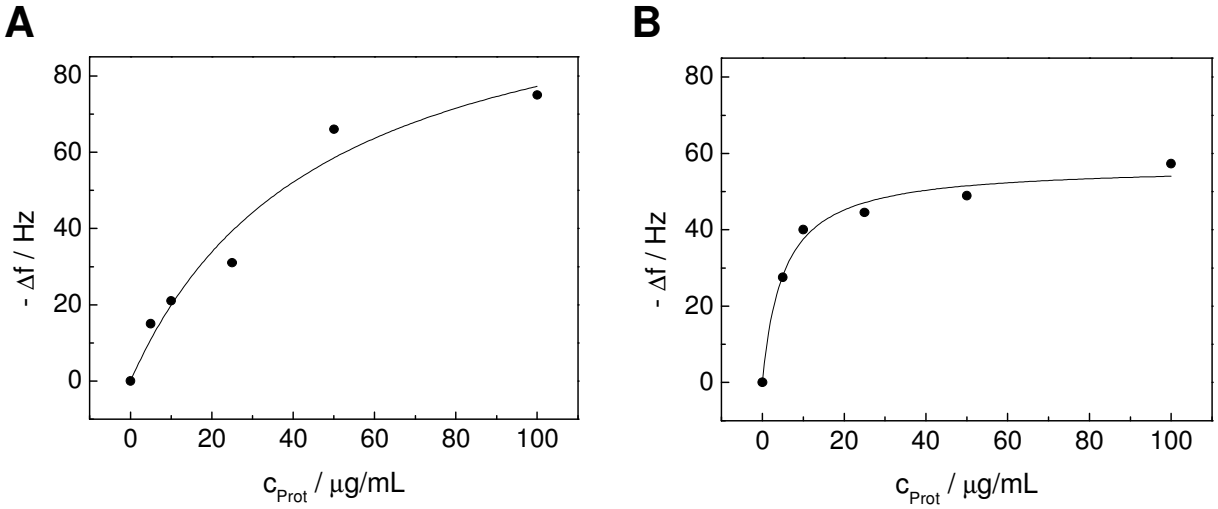

Fig. B.1 Adsorption of BSA on **A** unmodified and **B** plasma modified PS (n = 1).

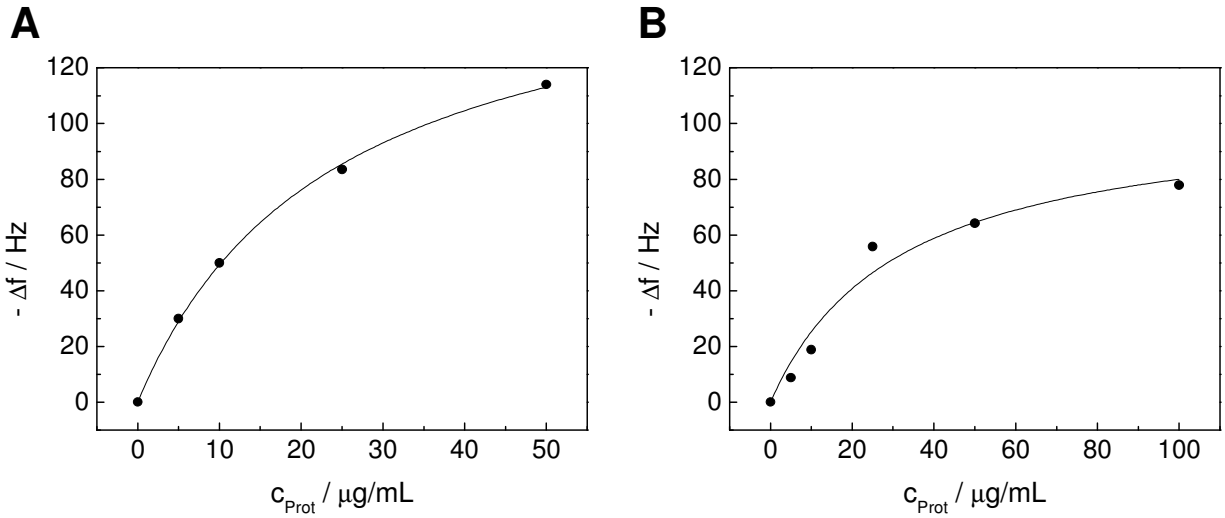

Fig. B.2 Adsorption of Gel on **A** unmodified and **B** plasma modified PS (mean ± SDM; n = 1).

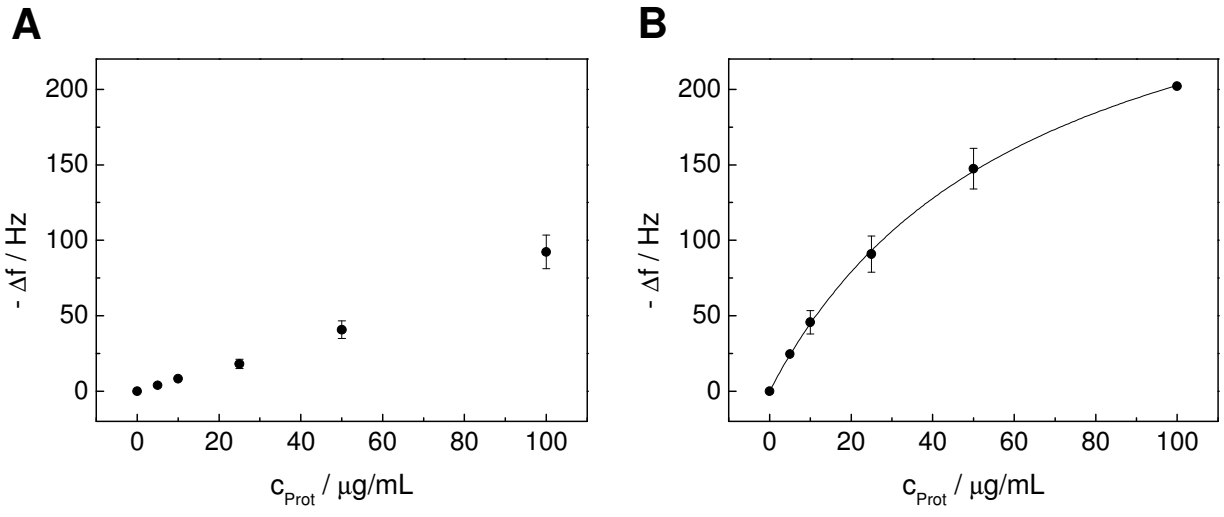

Fig. B.3 Adsorption of Col G on **A** unmodified and **B** plasma modified PS (mean ± SDM; n ≥ 2).

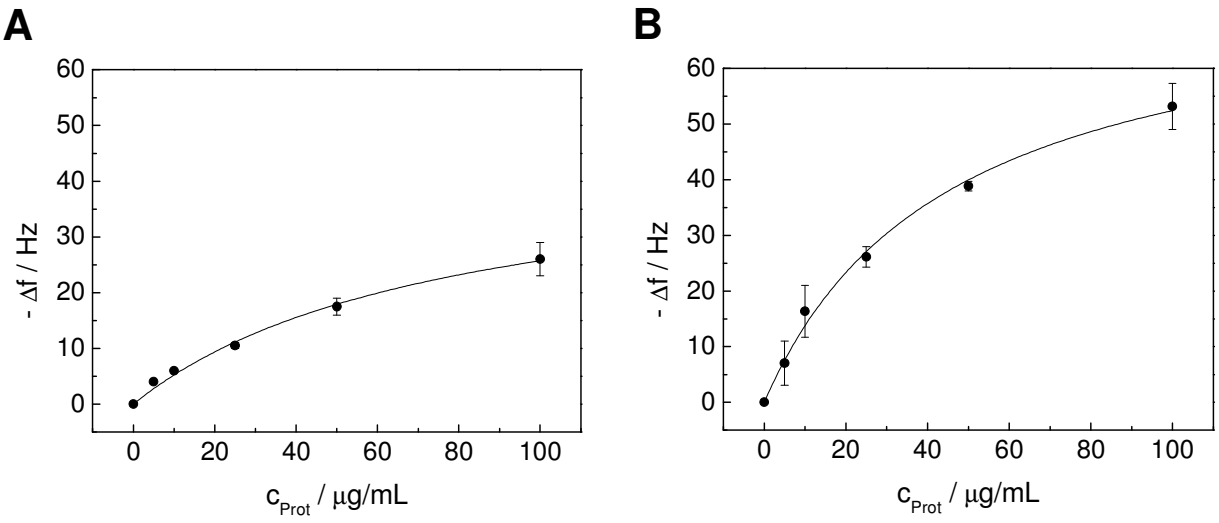

Fig. B.4 Adsorption of Col IV on **A** unmodified and **B** plasma modified PS (mean ± SDM; n = 2).

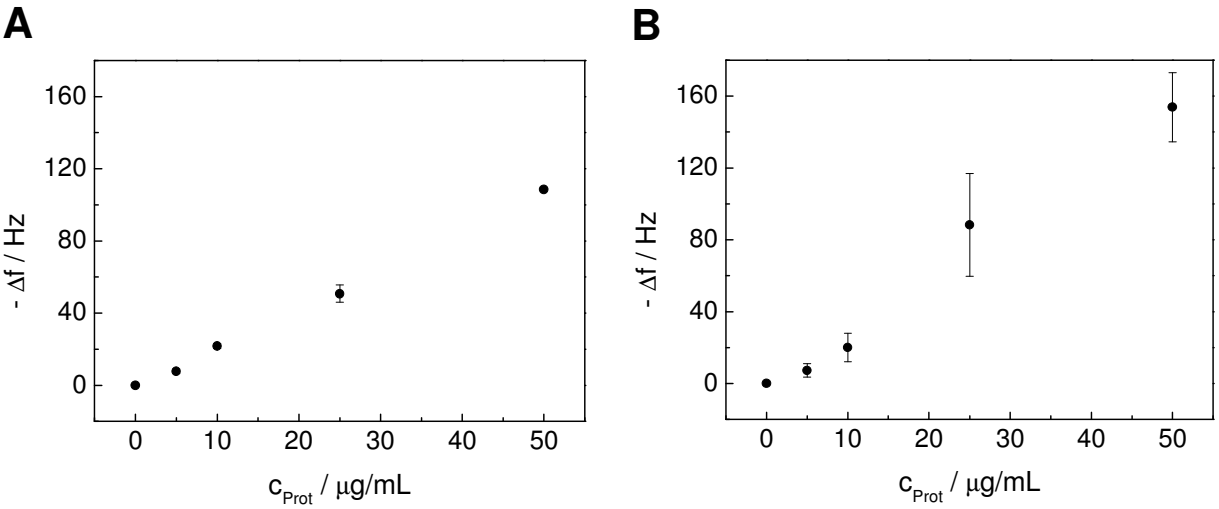

Fig. B.5 Adsorption of Lam I on **A** unmodified and **B** plasma modified PS (mean ± SDM; n = 2).

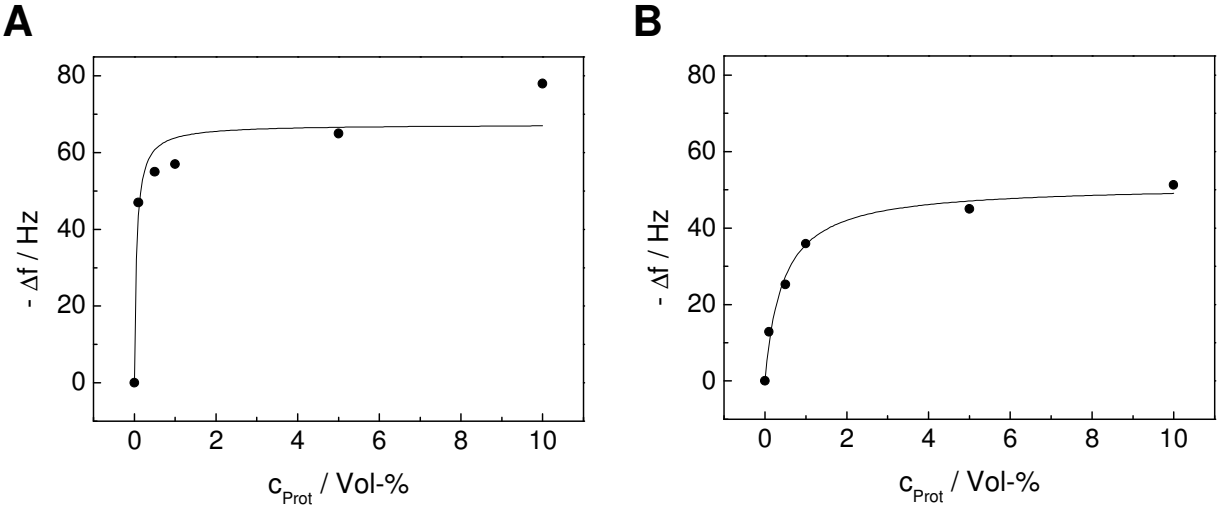

Fig. B.6 Adsorption of NCS on **A** unmodified and **B** plasma modified PS (mean ± SDM; n = 1).

2 PMMA Surfaces – Unmodified and Plasma Modified

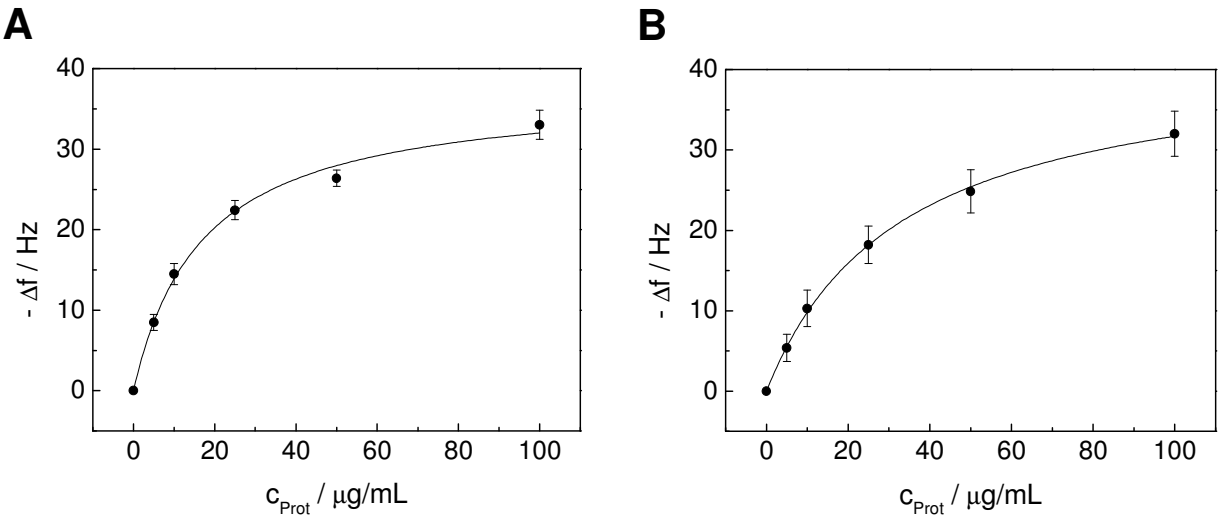

Fig. B.7 Adsorption of BSA on **A** unmodified and **B** plasma modified PMMA (mean ± SDM; n = 5).

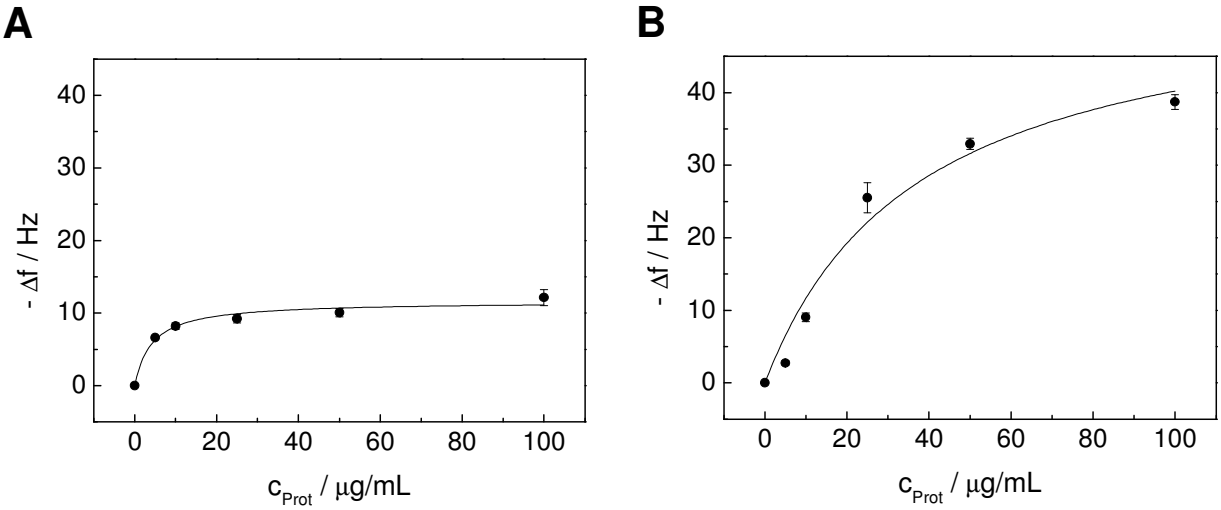

Fig. B.8 Adsorption of Gel on **A** unmodified and **B** plasma modified PMMA (mean ± SDM; n ≥ 3).

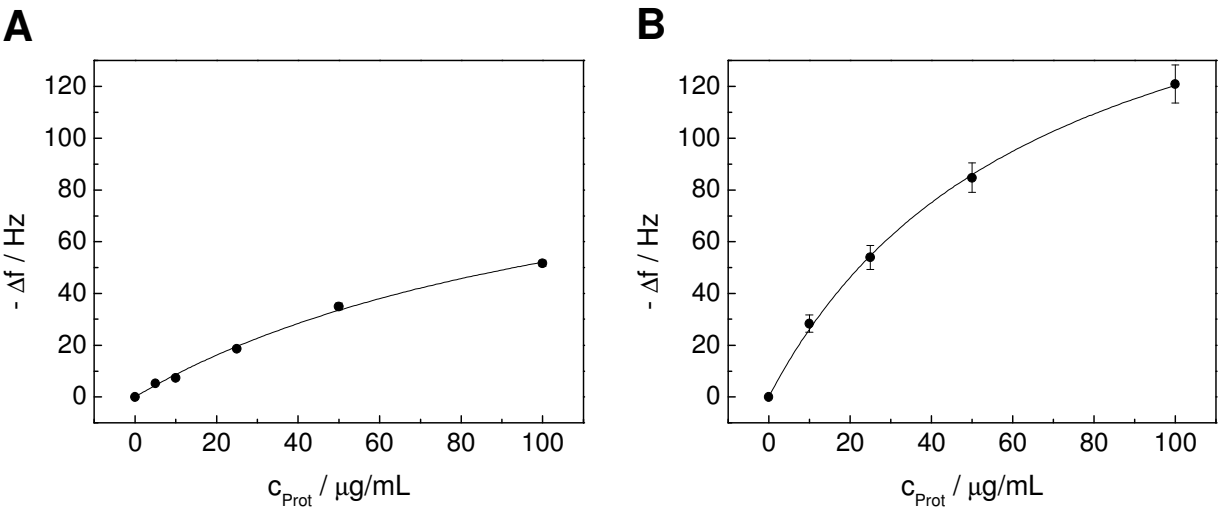

Fig. B.9 Adsorption of Col G on **A** unmodified and **B** plasma modified PMMA (mean ± SDM; n ≥ 4).

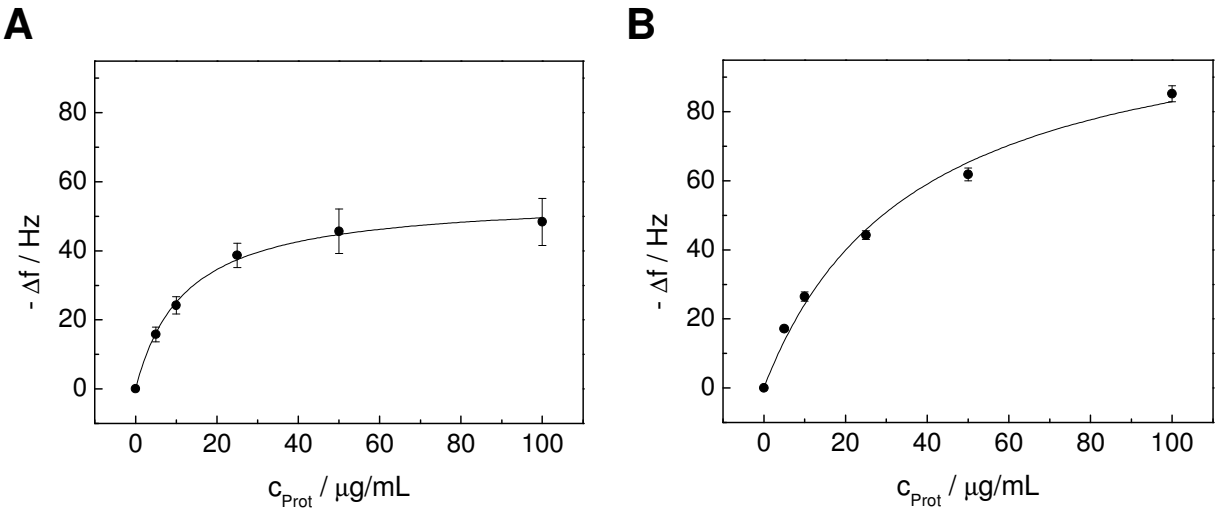

Fig. B.10 Adsorption of Col IV on **A** unmodified and **B** plasma modified PMMA (mean ± SDM; n ≥ 2).

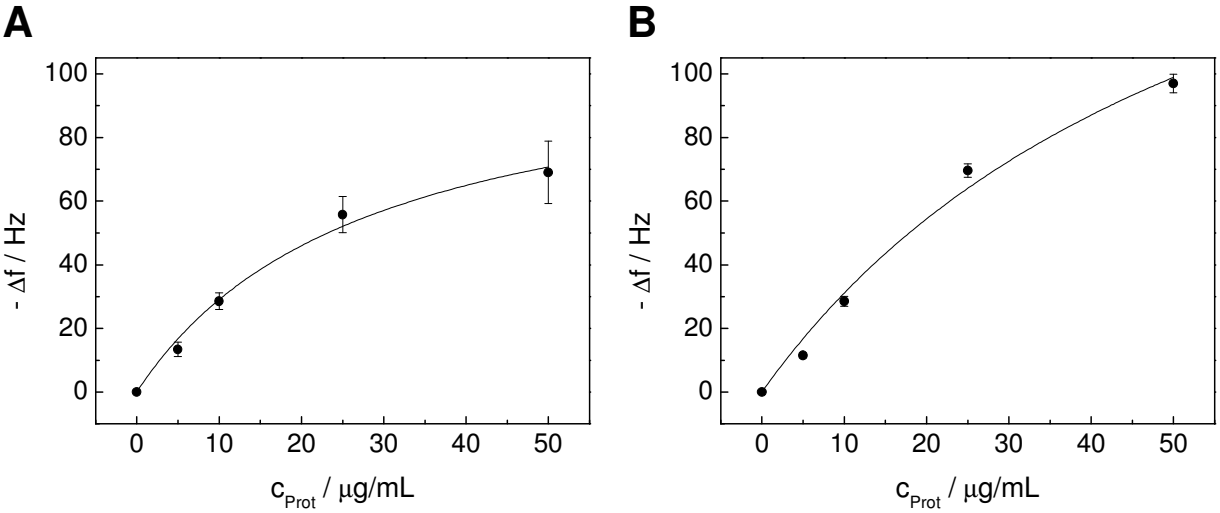

Fig. B.11 Adsorption of Lam I on **A** unmodified and **B** plasma modified PMMA (mean ± SDM; n ≥ 2).

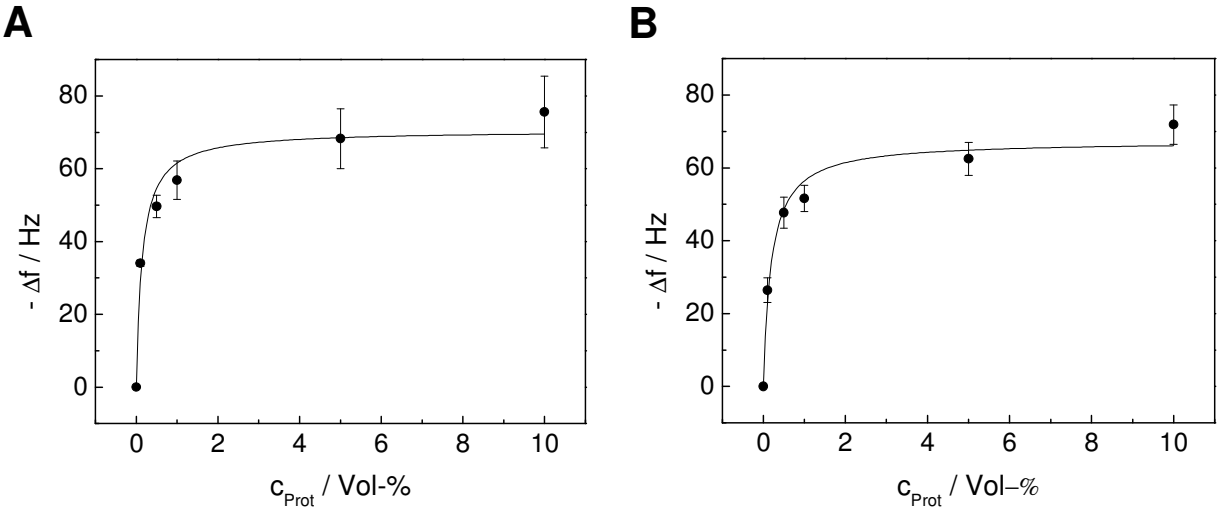

Fig. B.12 Adsorption of NCS on **A** unmodified and **B** plasma modified PMMA (mean ± SDM; n ≥ 2).

3 PDMS Surface – Unmodified

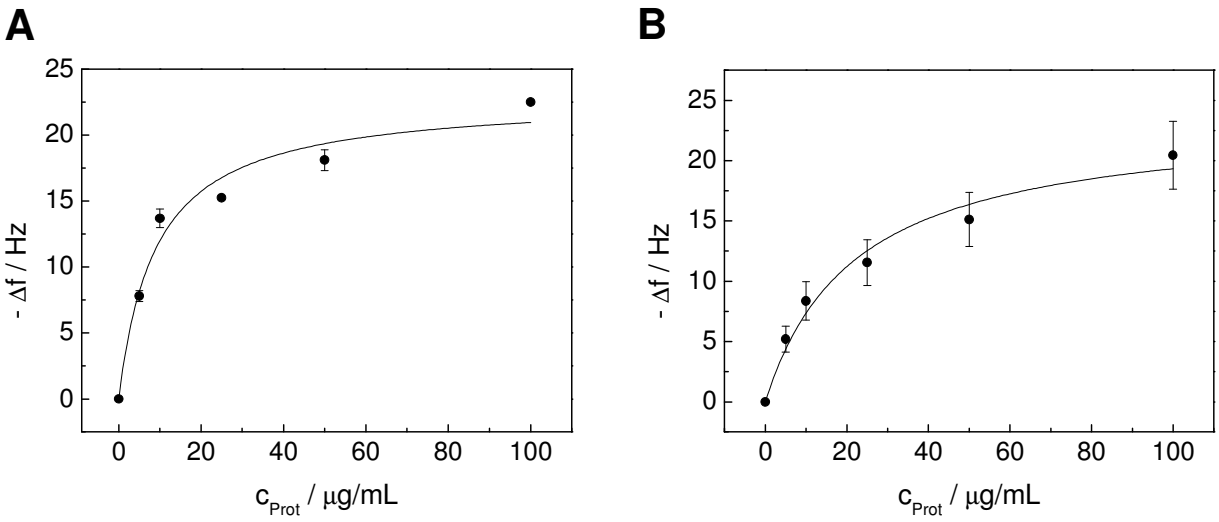

Fig. B.13 Adsorption of **A** BSA and **B** Gel on unmodified PDMS (mean ± SDM; n = 2 (BSA), n = 3 (Gel)).

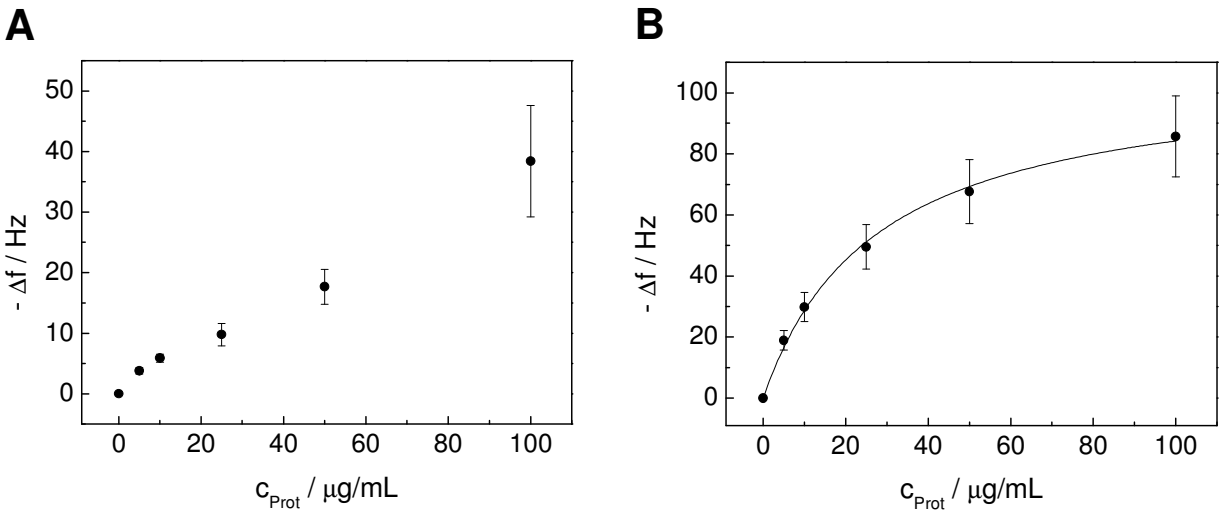

Fig. B.14 Adsorption of **A** Col G and **B** Col IV on unmodified PDMS (mean ± SDM; n = 2).

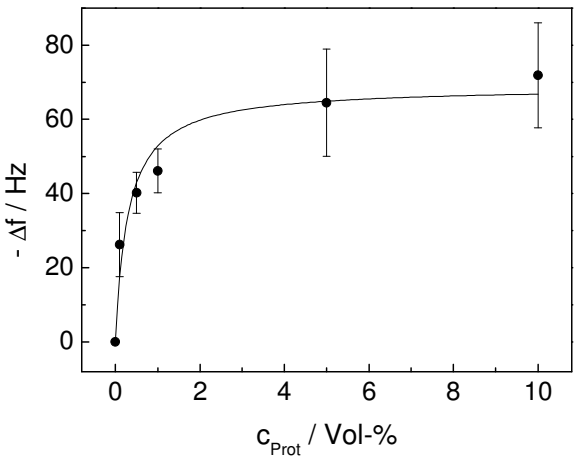

Fig. B.15 Adsorption of NCS on unmodified PDMS (mean ± SDM; n = 2).

4 PhoP Surfaces – Unmodified and Plasma Modified

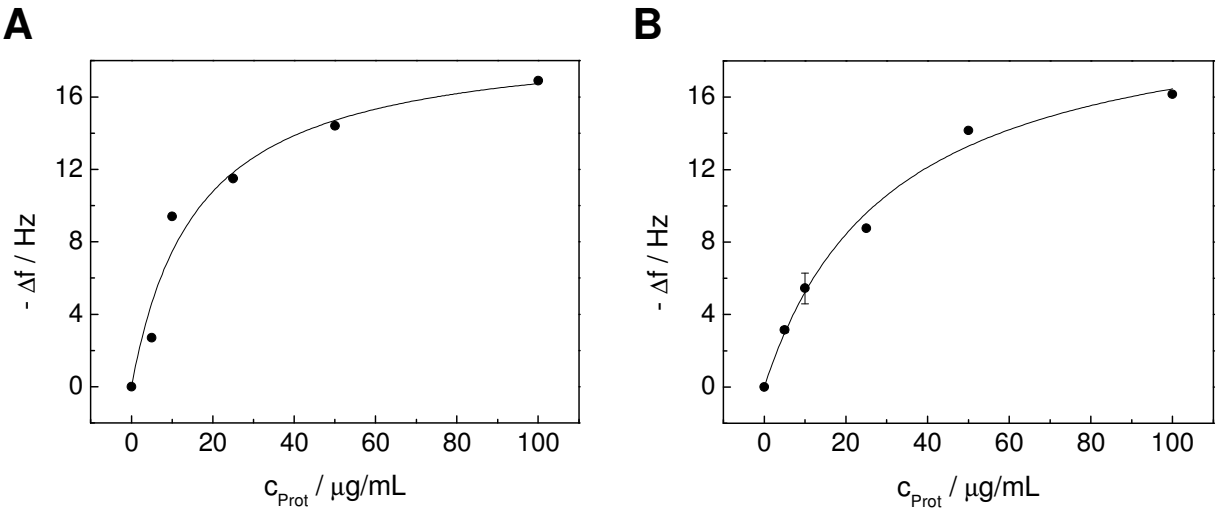

Fig. B.16 Adsorption of BSA on **A** unmodified and **B** plasma modified PhoP (mean ± SDM; n ≥ 1).

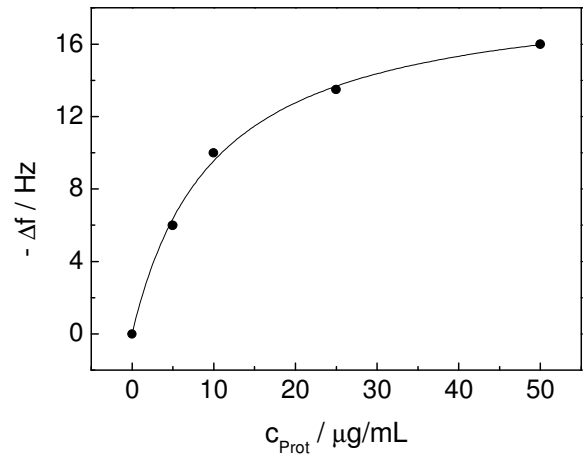

Fig. B.17 Adsorption of Gel on unmodified PhoP (mean ± SDM; n = 1).

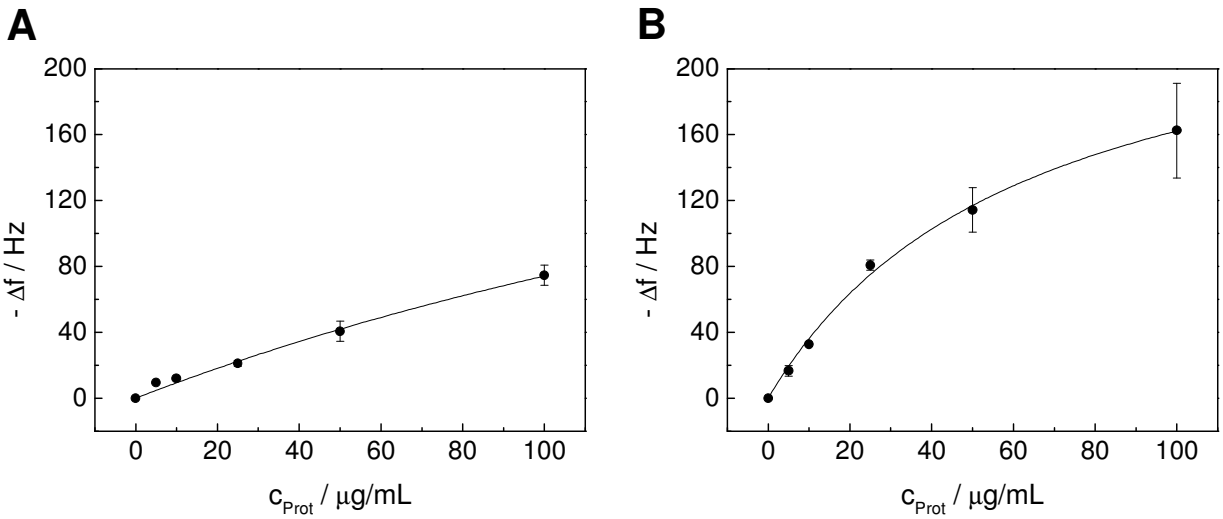

Fig. B.18 Adsorption of Col G on **A** unmodified and **B** plasma modified PhoP (mean ± SDM; n = 2).

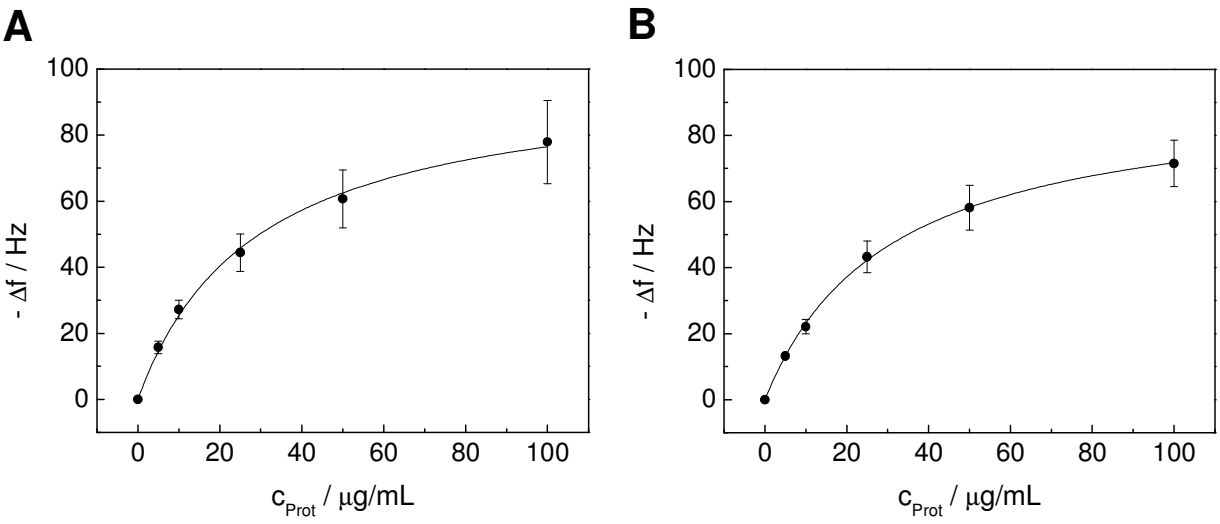

Fig. B.19 Adsorption of Col IV on **A** unmodified and **B** plasma modified PhoP (mean ± SDM; n ≥ 3).

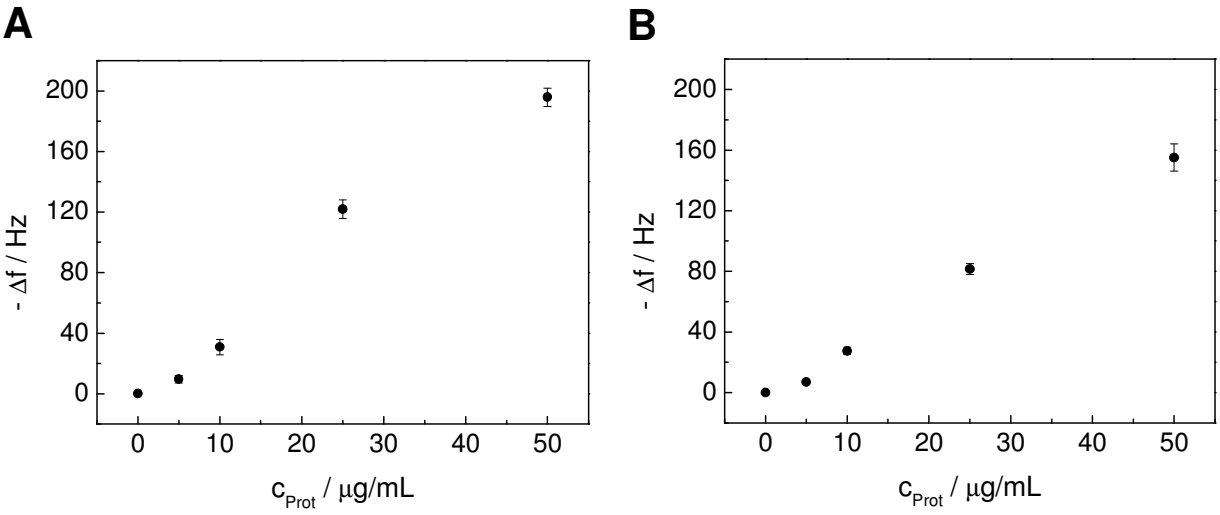

Fig. B.20 Adsorption of Lam I on **A** unmodified and **B** plasma modified PhoP (mean ± SDM; n = 2).

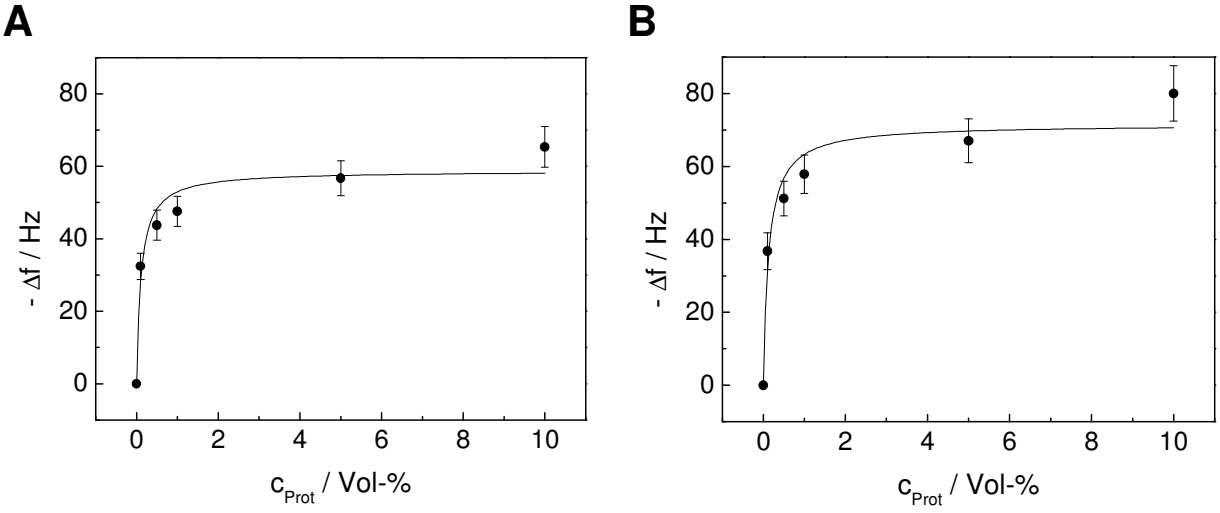

Fig. B.21 Adsorption of NCS on **A** unmodified and **B** plasma modified PhoP (mean ± SDM; n ≥ 4).

C Long-Term Stability of Polymer Films under Physiological Conditions

The polymers' long-term stability was monitored with time using double mode impedance analysis. The following diagrams show the results of the QCM measurements presented in terms of the load resistance ΔR_L and the load reactance ΔX_L, when a polymer coated quartz resonator is exposed to a physiological fluid, i.e. PBS^{--} or SFM, at 37 °C over a period of 20 h. The following polymers were characterized in their unmodified form as well as after argon plasma treatment.

1 Long-Term Stability of PS

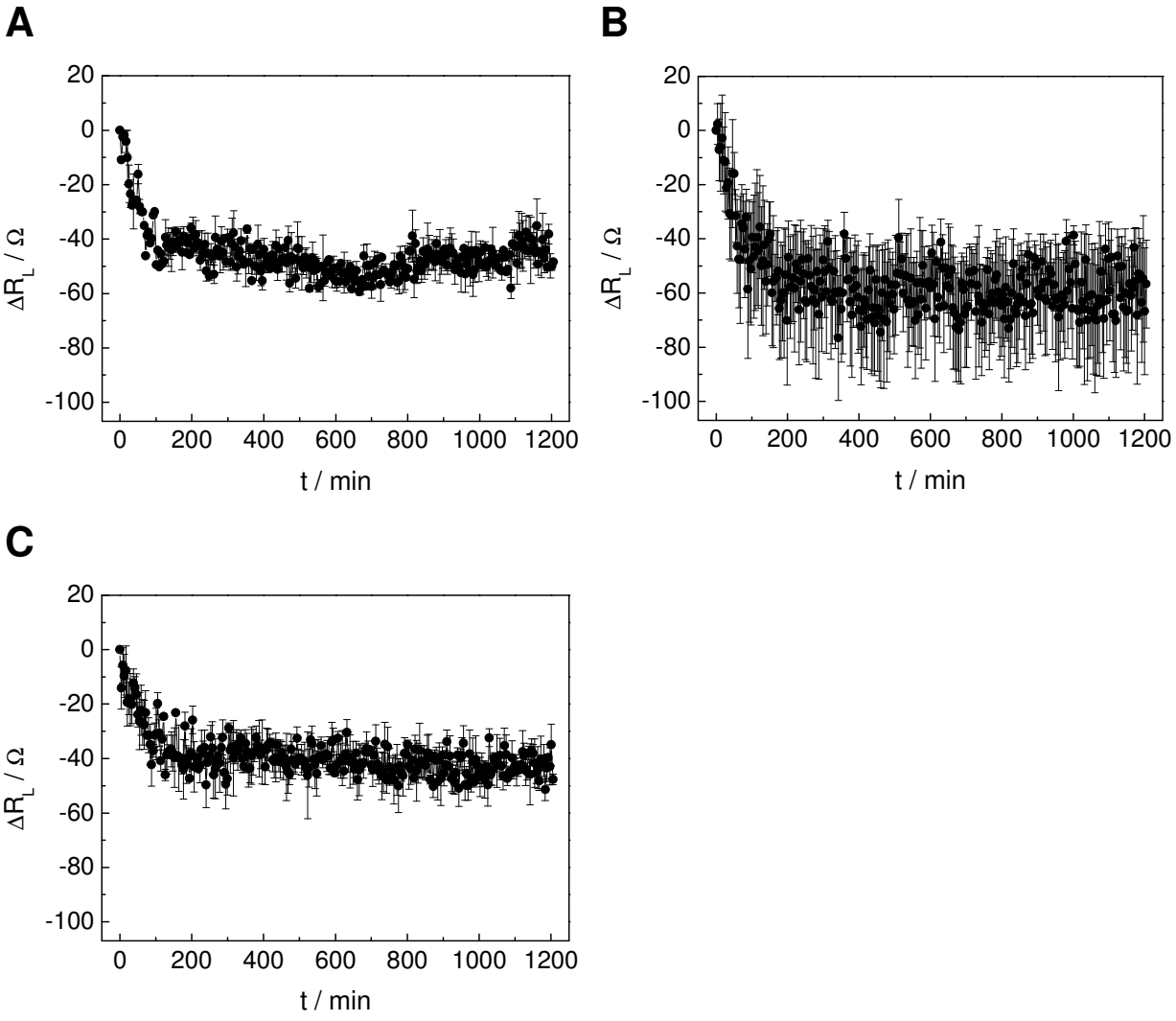

Fig. C.1 Time course of the load resistance ΔR_L during the incubation of a PS coated quartz resonator with a physiological fluid at 37 °C. Changes of the load resistance are given relative to the PS coated resonator directly after addition of fluid. **A** Unmodified + PBS^{--}, **B** plasma modified + PBS^{--}, **C** plasma modified + SFM (mean ± SDM; n = 3).

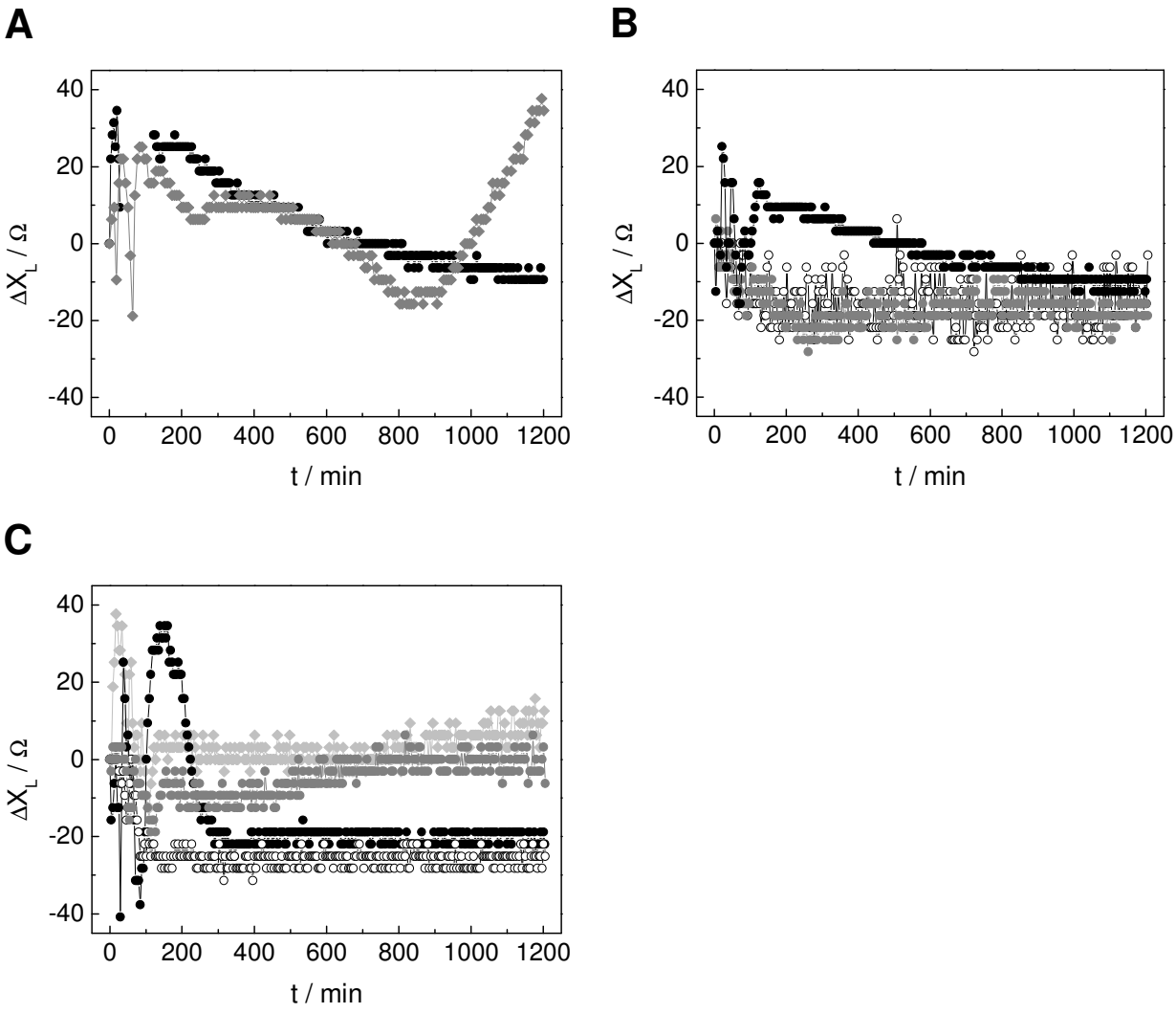

Fig. C.2 Time course of the load reactance ΔX_L during the incubation of a PS coated quartz resonator with a physiological fluid at 37 °C. Changes of the load reactance are given relative to the PS coated resonator directly after addition of fluid. **A** Unmodified + PBS^{--}, **B** plasma modified + PBS^{--}, **C** plasma modified + SFM. The time course of ΔX_L is shown for 2 – 4 individual measurements.

2 Long-Term Stability of PMMA

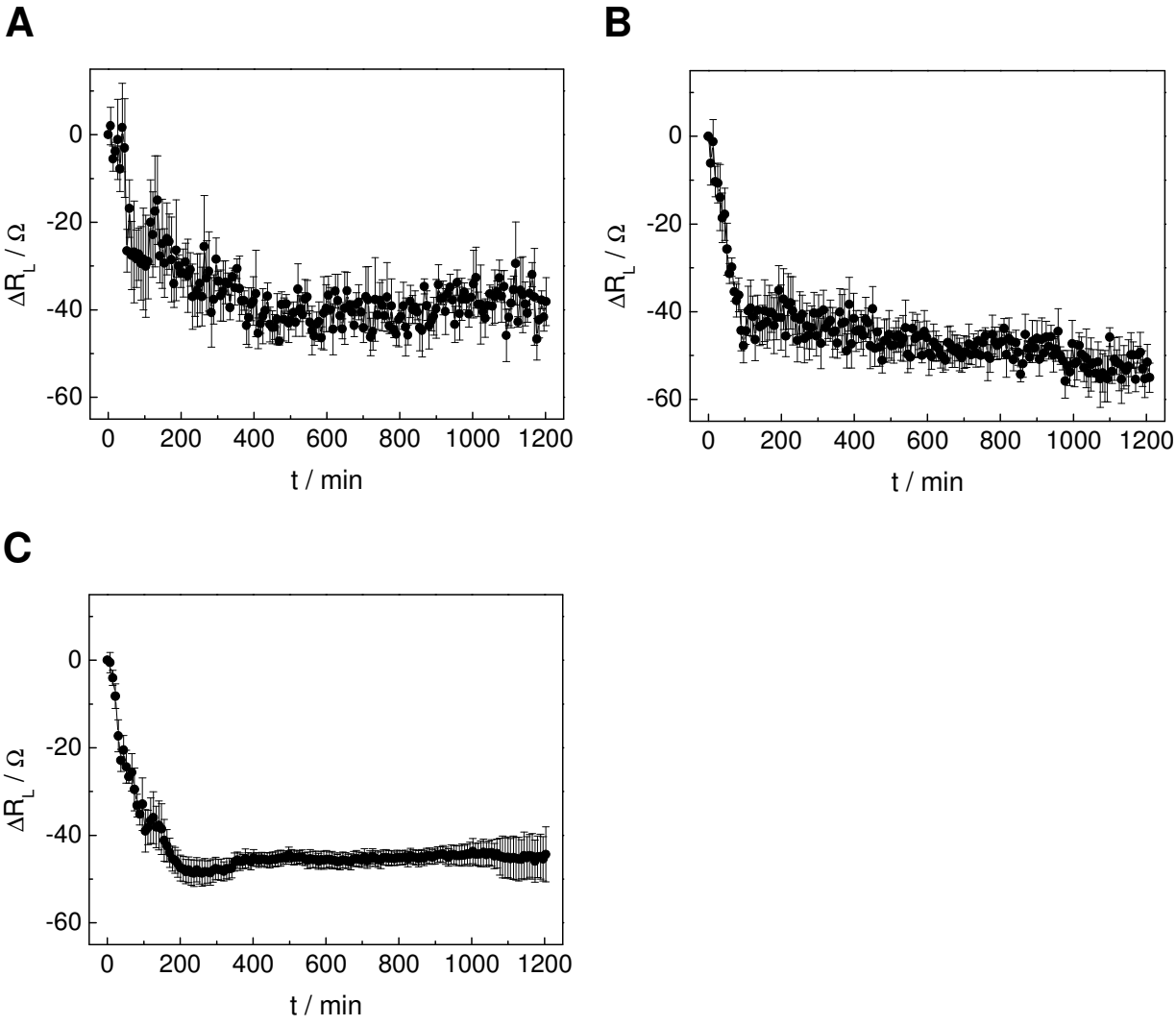

Fig. C.3 Time course of the load resistance ΔR_L during the incubation of a PMMA coated quartz resonator with a physiological fluid at 37 °C. Changes of the load resistance are given relative to the PMMA coated resonator directly after addition of fluid. **A** Unmodified + PBS^{--}, **B** plasma modified + PBS^{--}, **C** plasma modified + SFM (mean ± SDM; n ≥ 4).

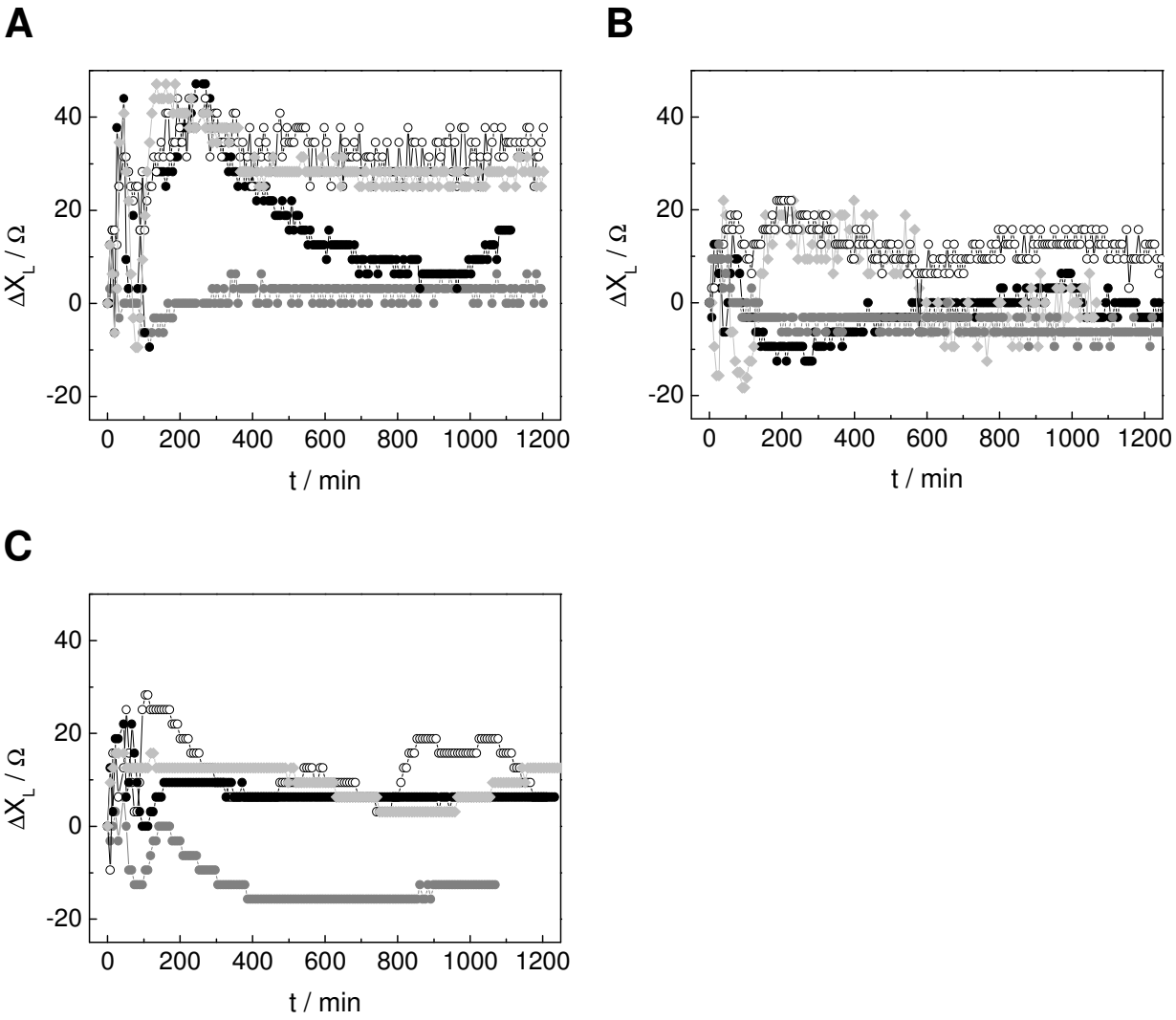

Fig. C.4 Time course of the load reactance ΔX_L during the incubation of a PMMA coated quartz resonator with a physiological fluid at 37 °C. Changes of the load reactance are given relative to the PMMA coated resonator directly after addition of fluid. **A** Unmodified + PBS^{--}, **B** plasma modified + PBS^{--}, **C** plasma modified + SFM. The time course of ΔX_L is shown for n = 4 individual measurements.

3 Long-Term Stability of PhoP

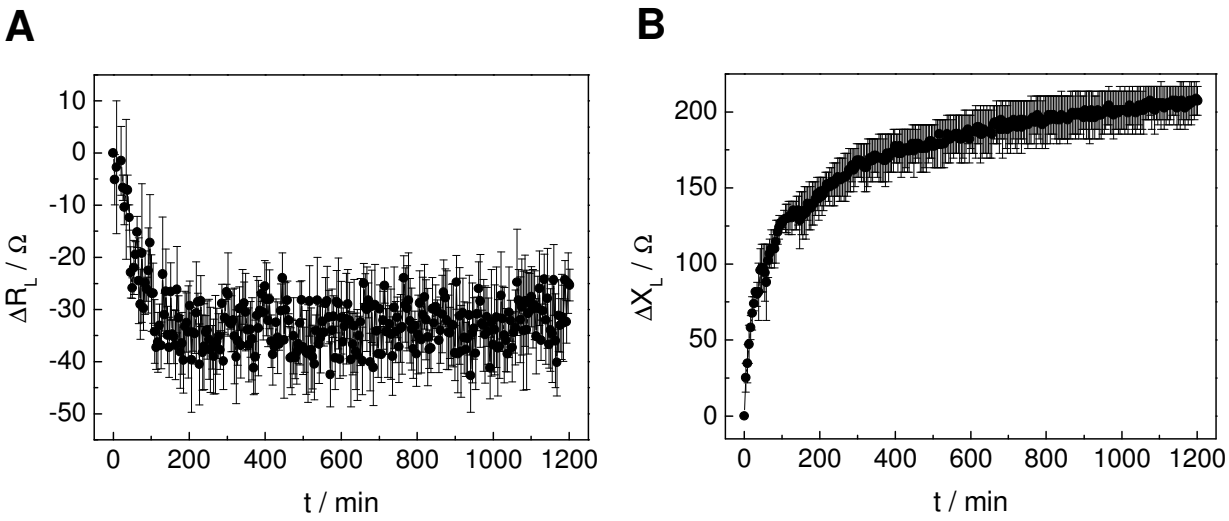

Fig. C.5 A Time course of the load resistance ΔR_L (**A**) and the load reactance ΔX_L (**B**) during the incubation of a PhoP coated quartz resonator with PBS^{--} at 37 °C. Changes of the load parameters are given relative to the PhoP coated resonator directly after addition of PBS^{--} (mean ± SDM; n = 2).

D Cell Attachment and Spreading upon Polymer Films

The following figures present phase contrast micrographs documenting the spreading kinetics of initially suspended MDCK-II or NRK cells upon different polymers at regular time intervals after cell inoculation. The polymer films spin coated upon the surface of glass coverslips were pretreated in a various manner (see caption).

1 Cell Attachment and Spreading upon PS

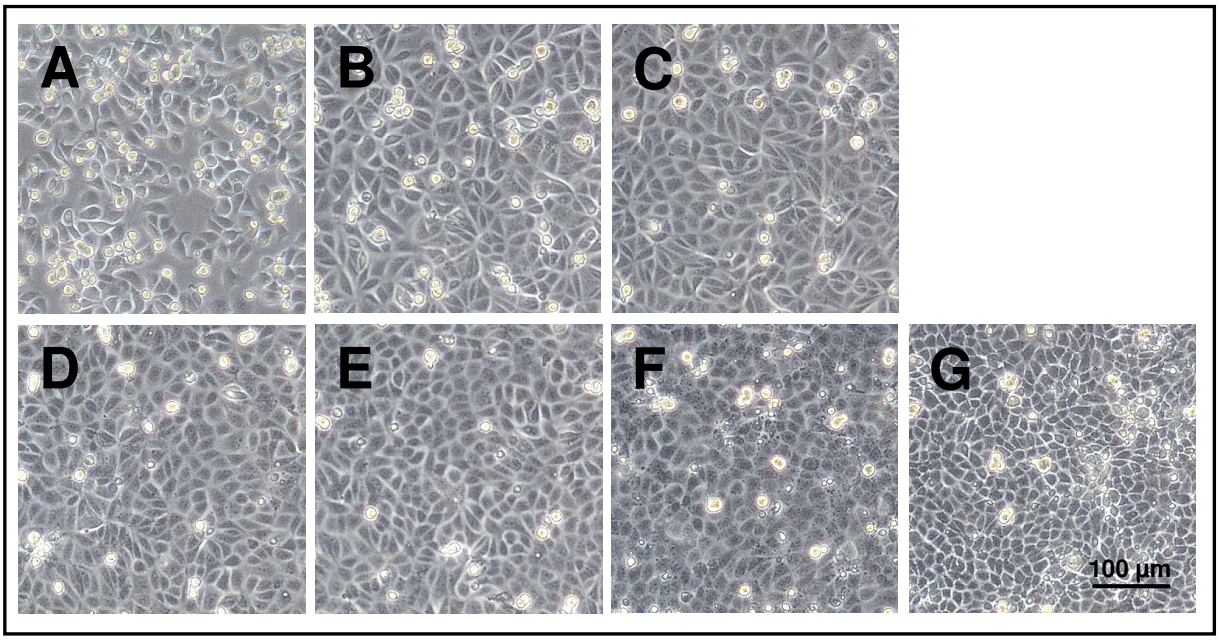

Fig. D.1 Phase contrast micrographs of MDCK-II cells at various time points after inoculation, documenting attachment and spreading upon PS coated coverslips that were argon plasma modified for 1 min followed by an exposure to PBS^{--} for 20 h at 37 °C prior to cell inoculation. The cells were suspended in serum-containing medium with a cell density of 4.5 x 10^5 cm^{-2}. The pictures were taken **A** 2 h, **B** 4 h, **C** 6 h, **D** 8 h, **E** 10 h, **F** 24 h and **G** 48 h after cell inoculation.

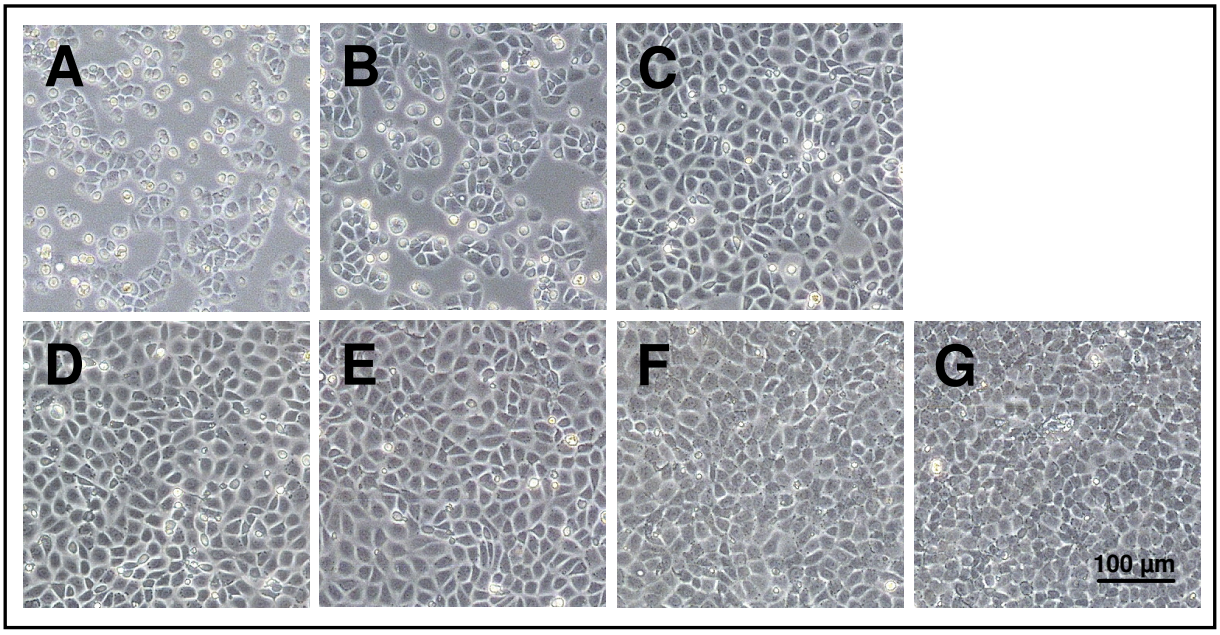

Fig. D.2 Phase contrast micrographs of NRK cells at various time points after inoculation, documenting attachment and spreading upon PS coated coverslips that were argon plasma modified for 1 min followed by an exposure to PBS^{--} for 20 h at 37 °C prior to cell inoculation. The cells were suspended in serum-containing medium with a cell density of 4.5 x 10^5 cm^{-2}. The pictures were taken **A** 2 h, **B** 4 h, **C** 6 h, **D** 8 h, **E** 10 h, **F** 24 h and **G** 48 h after cell inoculation.

2 Cell Attachment and Spreading upon PMMA

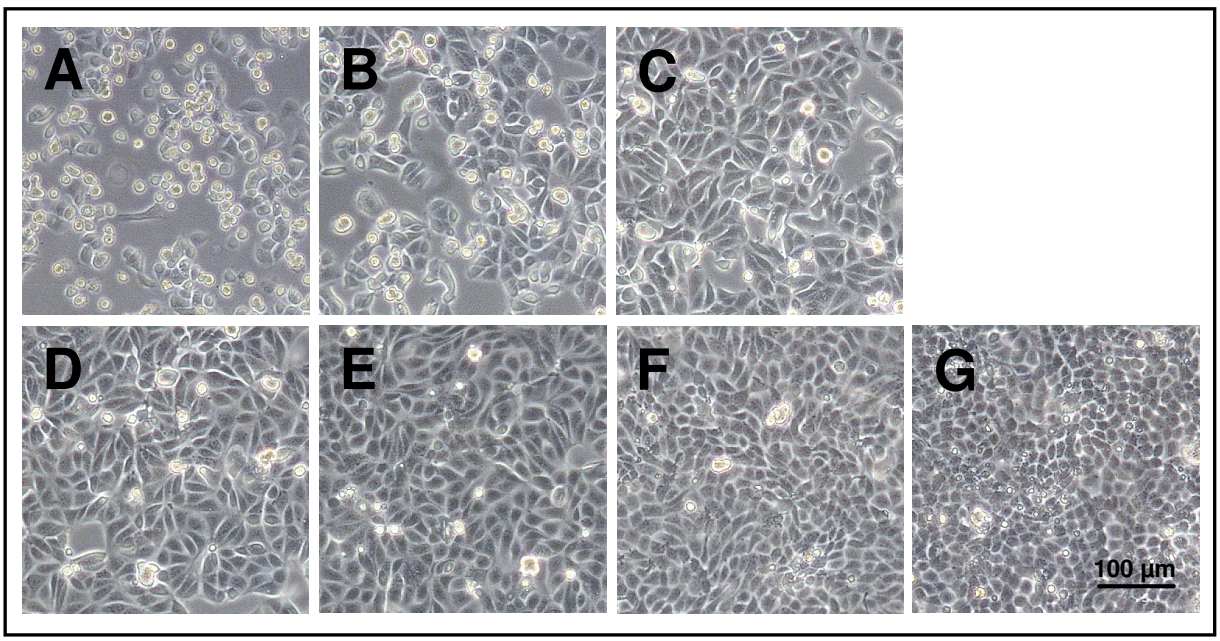

Fig. D.3 Phase contrast micrographs of MDCK-II cells at various time points after inoculation, documenting attachment and spreading upon PMMA coated coverslips that were argon plasma modified for 1 min followed by an exposure to SFM for 20 h at 37 °C prior to cell inoculation. The cells were suspended in serum-containing medium with a cell density of 4.5 x 10^5 cm^{-2}. The pictures were taken **A** 2 h, **B** 4 h, **C** 6 h, **D** 8 h, **E** 10 h, **F** 24 h and **G** 48 h after cell inoculation.

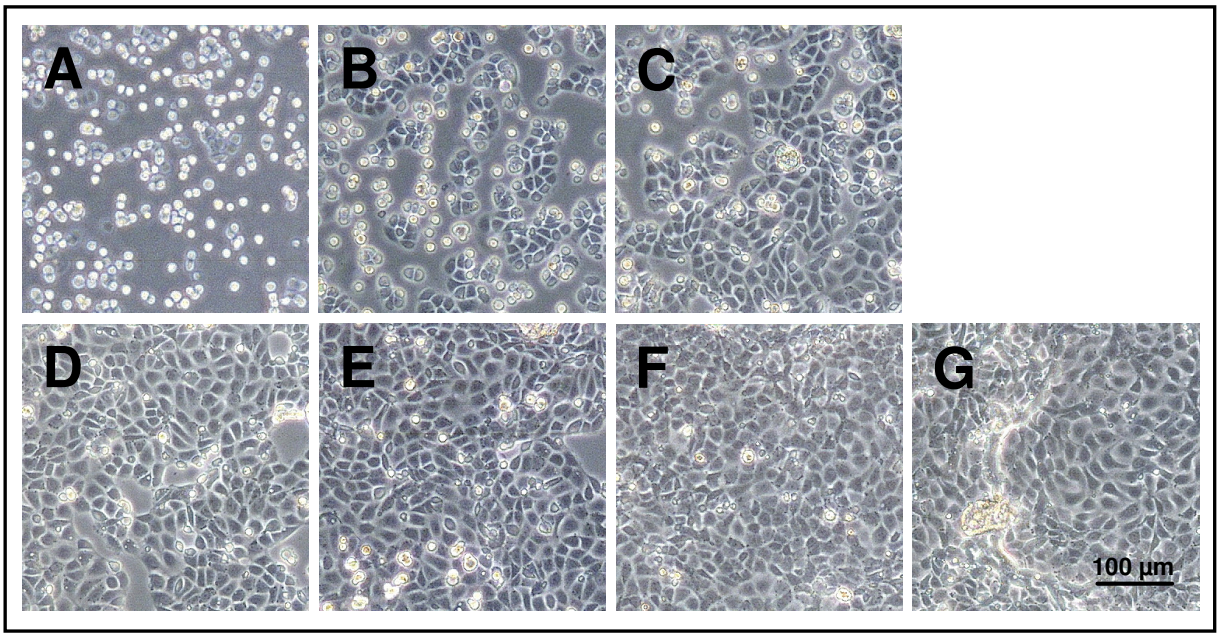

Fig. D.4 Phase contrast micrographs of NRK cells at various time points after inoculation, documenting attachment and spreading upon PMMA coated coverslips that were exposed to PBS^{--} for 20 h at 37 °C prior to cell inoculation. The cells were suspended in serum-containing medium with a cell density of 4.5 x 10^5 cm^{-2}. The pictures were taken **A** 2 h, **B** 4 h, **C** 6 h, **D** 8 h, **E** 10 h, **F** 24 h and **G** 48 h after cell inoculation.

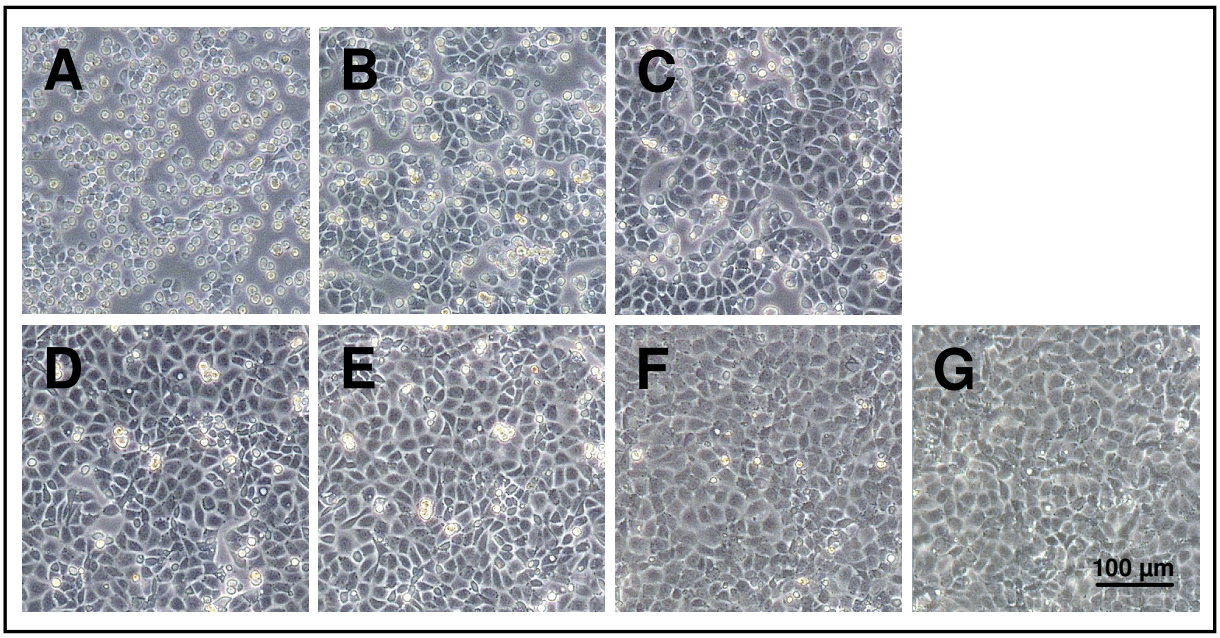

Fig. D.5 Phase contrast micrographs of NRK cells at various time points after inoculation, documenting attachment and spreading upon PMMA coated coverslips that were argon plasma modified for 1 min followed by an exposure to PBS^{--} for 20 h at 37 °C prior to cell inoculation. The cells were suspended in serum-containing medium with a cell density of 4.5 x 10^5 cm^{-2}. The pictures were taken **A** 2 h, **B** 4 h, **C** 6 h, **D** 8 h, **E** 10 h, **F** 24 h and **G** 48 h after cell inoculation.

3 Cell Attachment and Spreading upon PDMS

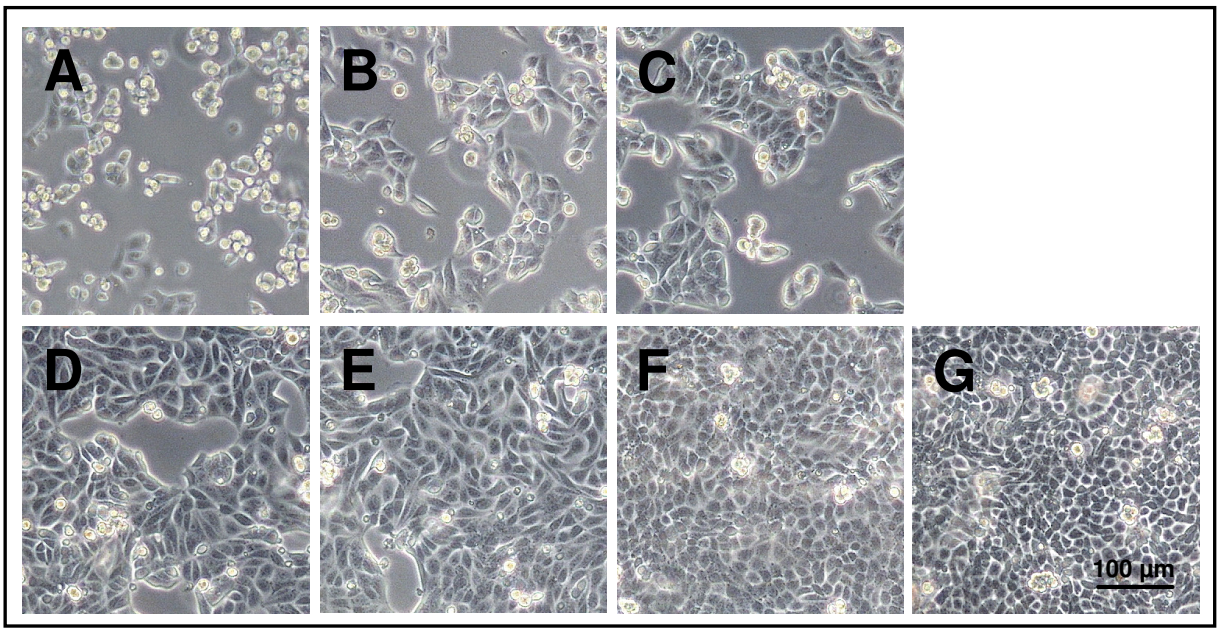

Fig. D.6 Phase contrast micrographs of MDCK-II cells at various time points after inoculation, documenting attachment and spreading upon PDMS coated coverslips that were exposed to PBS^{--} for 20 h at 37 °C prior to cell inoculation. The cells were suspended in serum-containing medium with a cell density of 4.5 x 10^5 cm^{-2}. The pictures were taken **A** 2 h, **B** 4 h, **C** 6 h, **D** 8 h, **E** 10 h, **F** 24 h and **G** 48 h after cell inoculation.

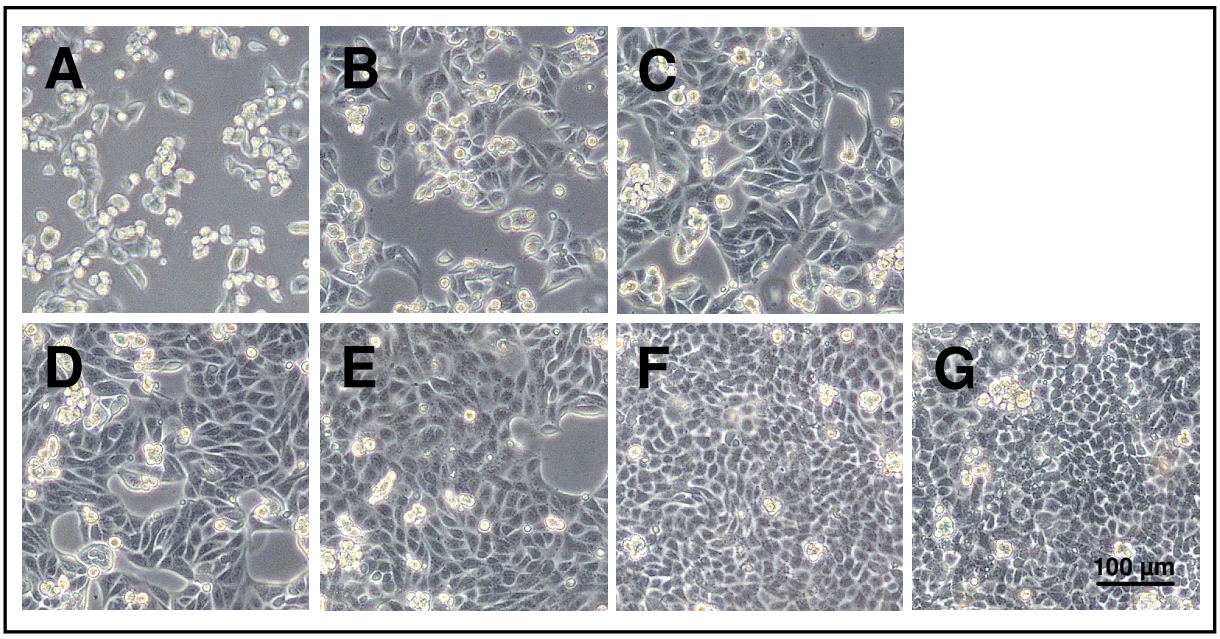

Fig. D.7 Phase contrast micrographs of MDCK-II cells at various time points after inoculation, documenting attachment and spreading upon PDMS coated coverslips that were argon plasma modified for 1 min followed by an exposure to PBS^{--} for 20 h at 37 °C prior to cell inoculation. The cells were suspended in serum-containing medium with a cell density of 4.5 x 10^5 cm^{-2}. The pictures were taken **A** 2 h, **B** 4 h, **C** 6 h, **D** 8 h, **E** 10 h, **F** 24 h and **G** 48 h after cell inoculation.

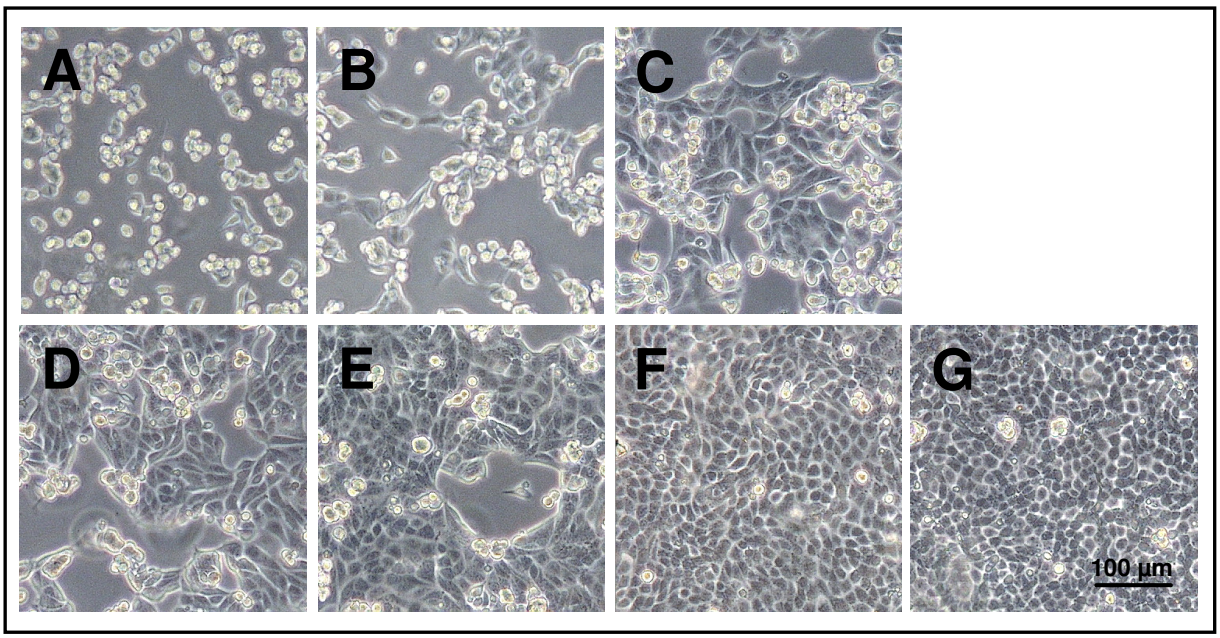

Fig. D.8 Phase contrast micrographs of MDCK-II cells at various time points after inoculation, documenting attachment and spreading upon PDMS coated coverslips that were argon plasma modified for 1 min followed by an exposure to SFM for 20 h at 37 °C prior to cell inoculation. The cells were suspended in serum-containing medium with a cell density of 4.5 x 10^5 cm^{-2}. The pictures were taken **A** 2 h, **B** 4 h, **C** 6 h, **D** 8 h, **E** 10 h, **F** 24 h and **G** 48 h after cell inoculation.

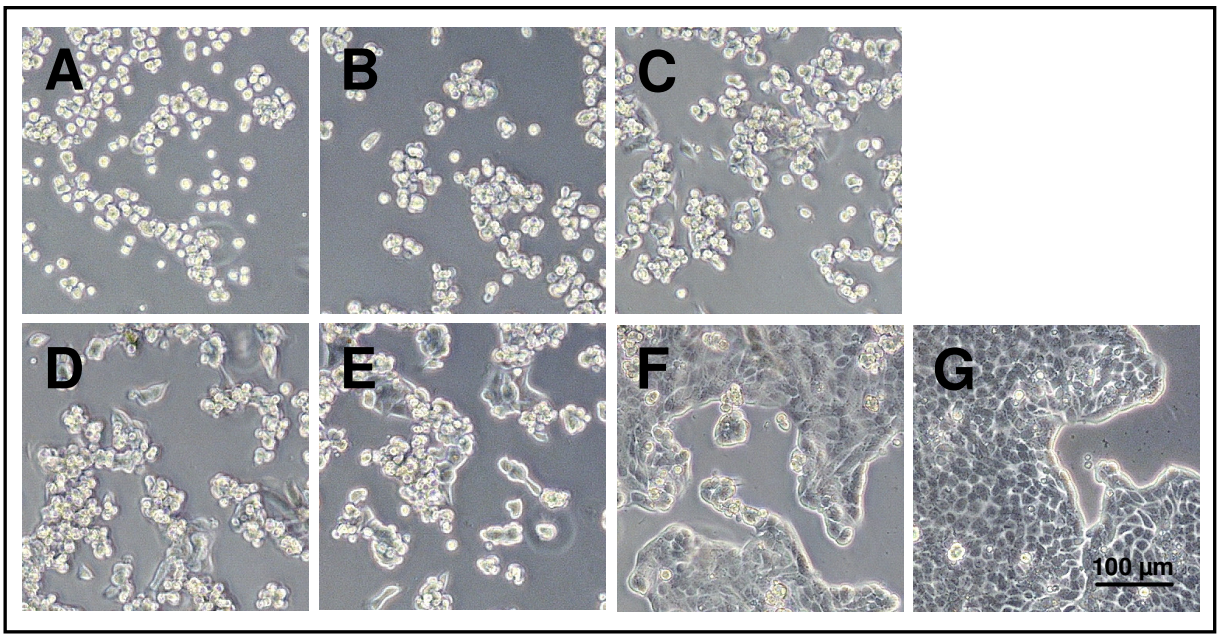

Fig. D.9 Phase contrast micrographs of MDCK-II cells at various time points after inoculation, documenting attachment and spreading upon PDMS coated coverslips that were argon plasma modified for 1 min prior to cell inoculation. The cells were suspended in serum-containing medium with a cell density of 4.5 x 10^5 cm^{-2}. The pictures were taken **A** 2 h, **B** 4 h, **C** 6 h, **D** 8 h, **E** 10 h, **F** 24 h and **G** 48 h after cell inoculation.

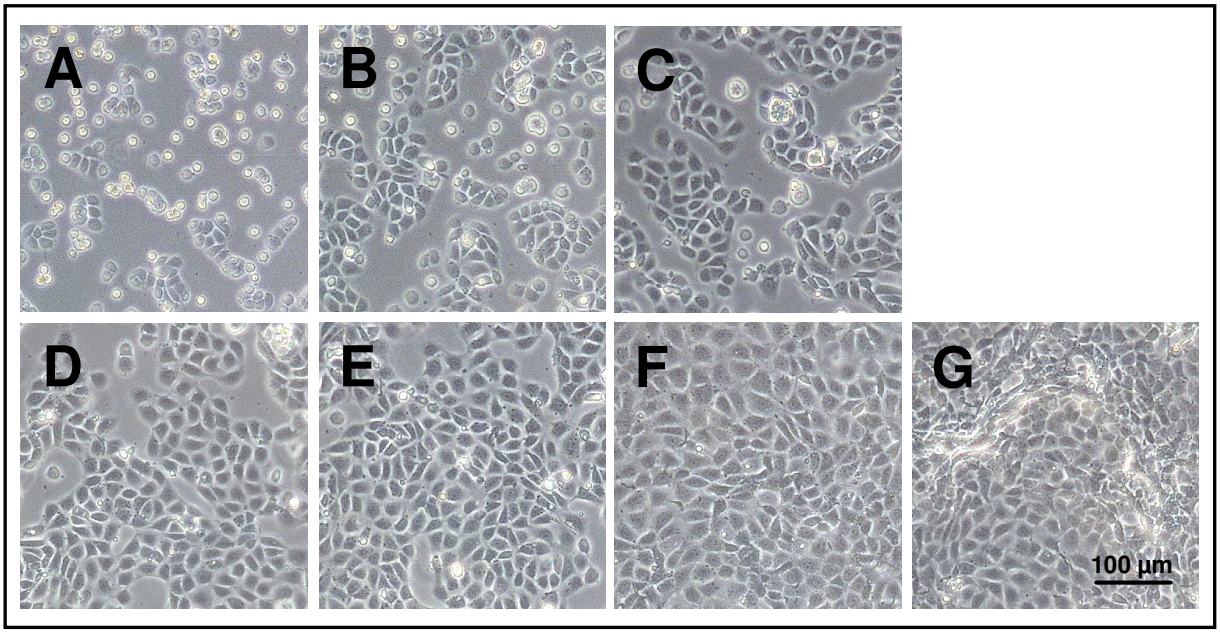

Fig. D.10 Phase contrast micrographs of NRK cells at various time points after inoculation, documenting attachment and spreading upon PDMS coated coverslips that were exposed to PBS^{--} for 20 h at 37 °C prior to cell inoculation. The cells were suspended in serum-containing medium with a cell density of 4.5 x 10^5 cm^{-2}. The pictures were taken **A** 2 h, **B** 4 h, **C** 6 h, **D** 8 h, **E** 10 h, **F** 24 h and **G** 48 h after cell inoculation.

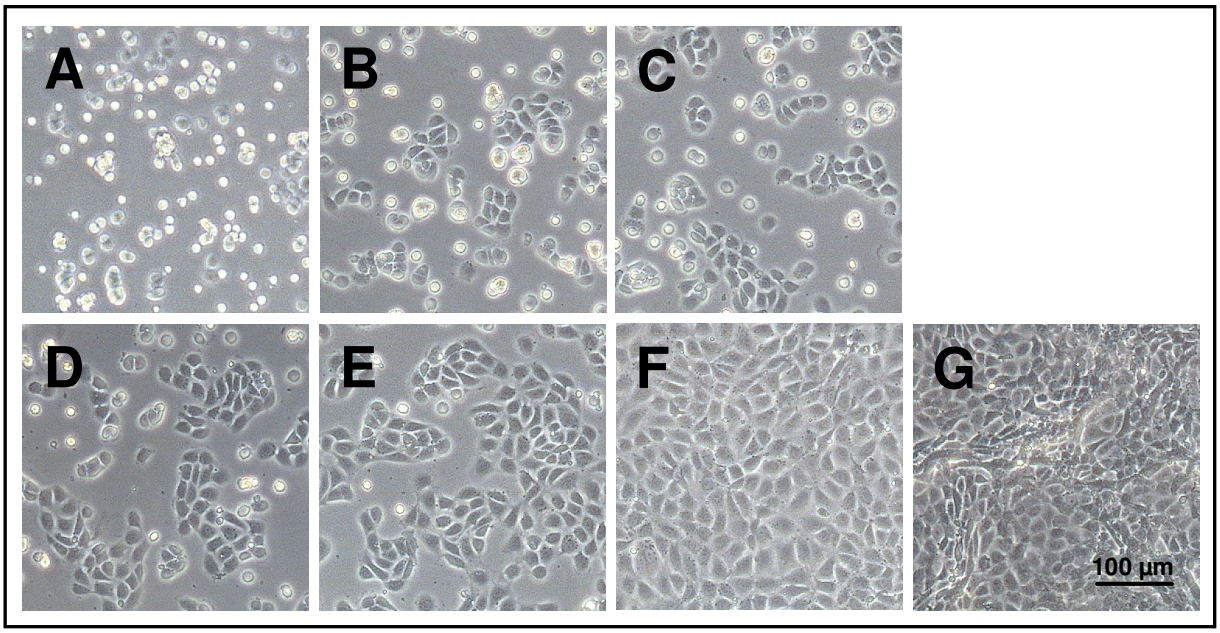

Fig. D.11 Phase contrast micrographs of NRK cells at various time points after inoculation, documenting attachment and spreading upon PDMS coated coverslips that were argon plasma modified for 1 min followed by an exposure to PBS^{--} for 20 h at 37 °C prior to cell inoculation. The cells were suspended in serum-containing medium with a cell density of 4.5 x 10^5 cm^{-2}. The pictures were taken **A** 2 h, **B** 4 h, **C** 6 h, **D** 8 h, **E** 10 h, **F** 24 h and **G** 48 h after cell inoculation.

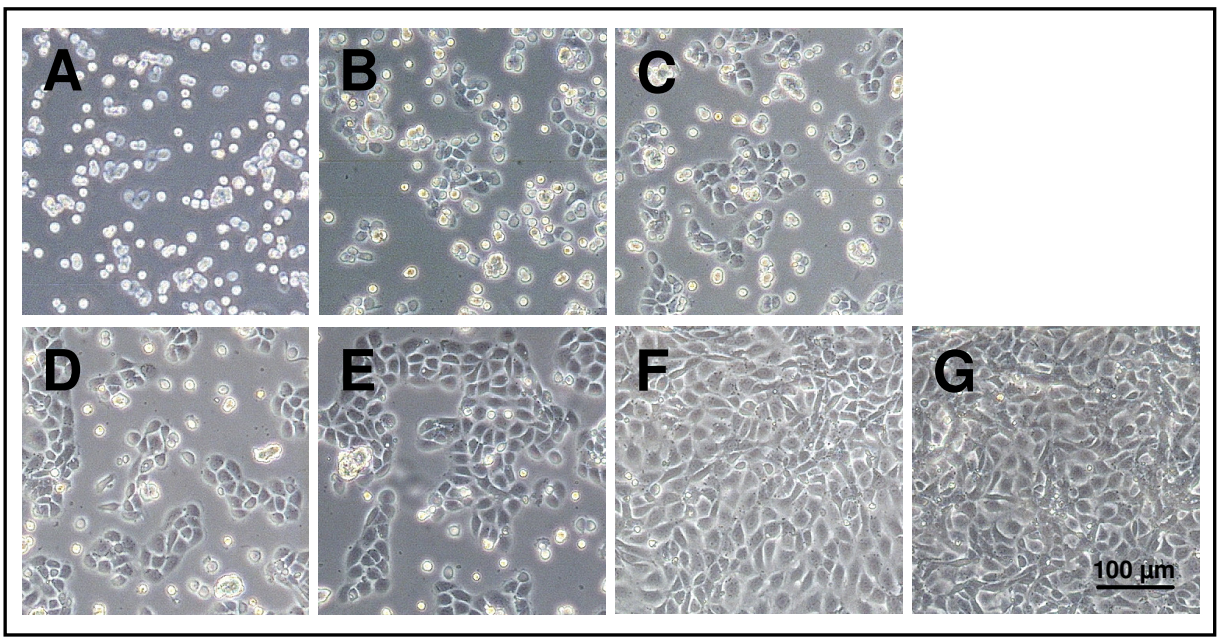

Fig. D.12 Phase contrast micrographs of NRK cells at various time points after inoculation, documenting attachment and spreading upon PDMS coated coverslips that were argon plasma modified for 1 min followed by an exposure to SFM for 20 h at 37 °C prior to cell inoculation. The cells were suspended in serum-containing medium with a cell density of 4.5 x 10^5 cm^{-2}. The pictures were taken **A** 2 h, **B** 4 h, **C** 6 h, **D** 8 h, **E** 10 h, **F** 24 h and **G** 48 h after cell inoculation.

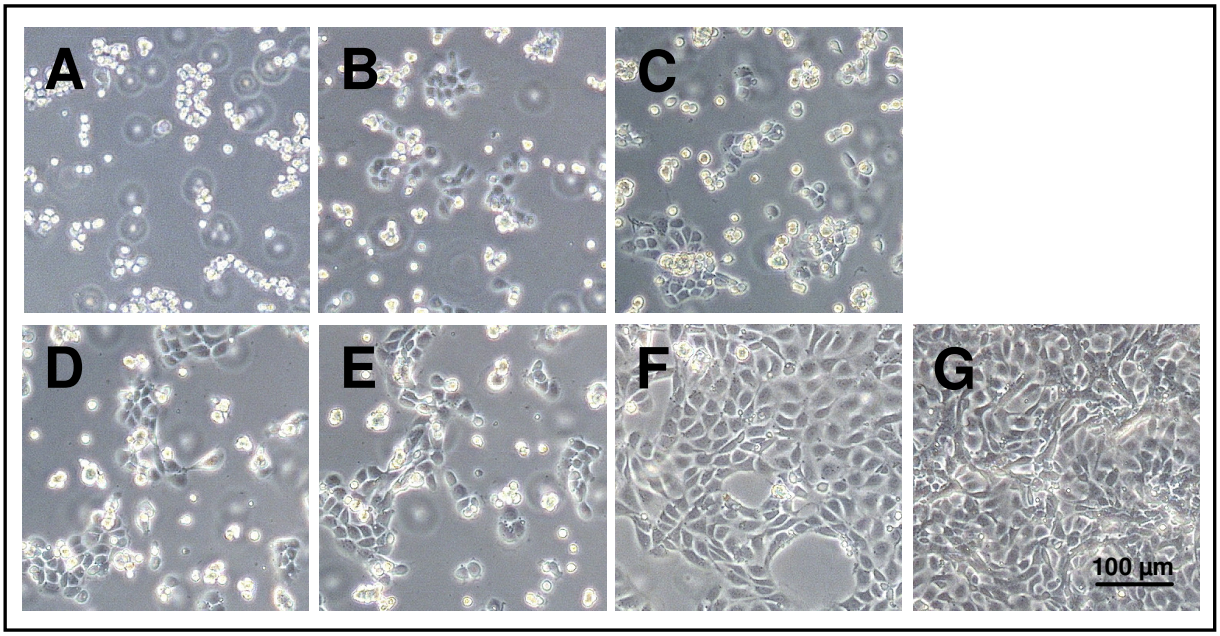

Fig. D.13 Phase contrast micrographs of NRK cells at various time points after inoculation, documenting attachment and spreading upon PDMS coated coverslips that were argon plasma modified for 1 min prior to cell inoculation. The cells were suspended in serum-containing medium with a cell density of 4.5 x 10^5 cm^{-2}. The pictures were taken **A** 2 h, **B** 4 h, **C** 6 h, **D** 8 h, **E** 10 h, **F** 24 h and **G** 48 h after cell inoculation.

4 Cell Attachment and Spreading upon PhoP

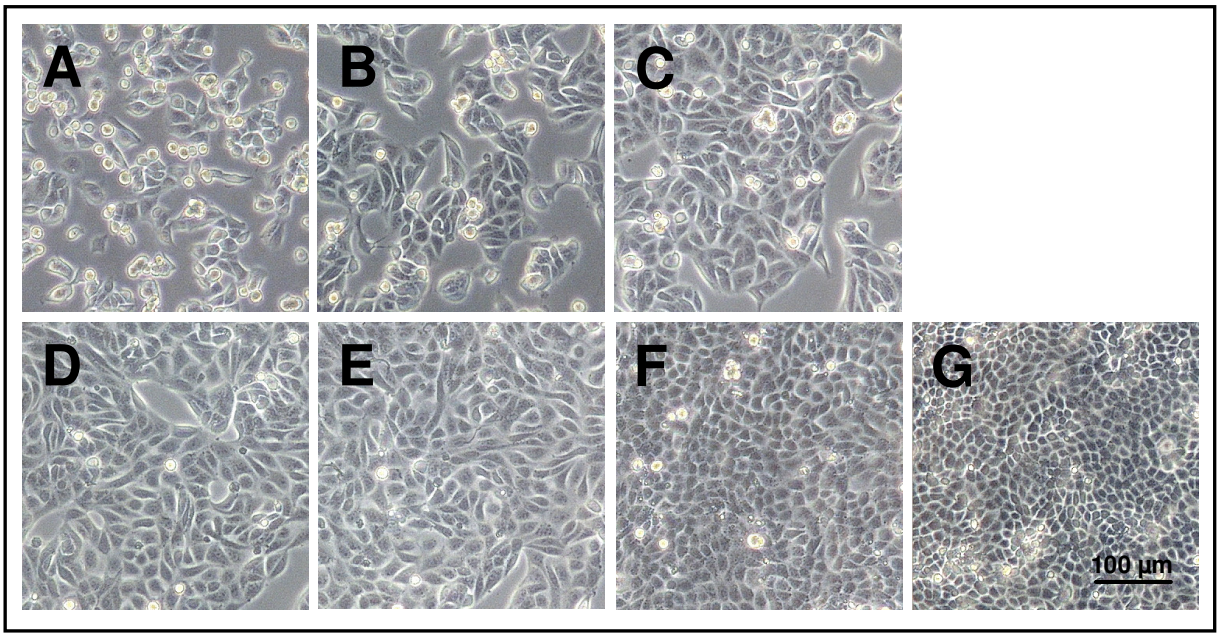

Fig. D.14 Phase contrast micrographs of MDCK-II cells at various time points after inoculation, documenting attachment and spreading upon PhoP coated coverslips that were exposed to PBS^{--} for 20 h at 37 °C prior to cell inoculation. The cells were suspended in serum-containing medium with a cell density of 4.5 x 10^5 cm^{-2}. The pictures were taken **A** 2 h, **B** 4 h, **C** 6 h, **D** 8 h, **E** 10 h, **F** 24 h and **G** 48 h after cell inoculation.

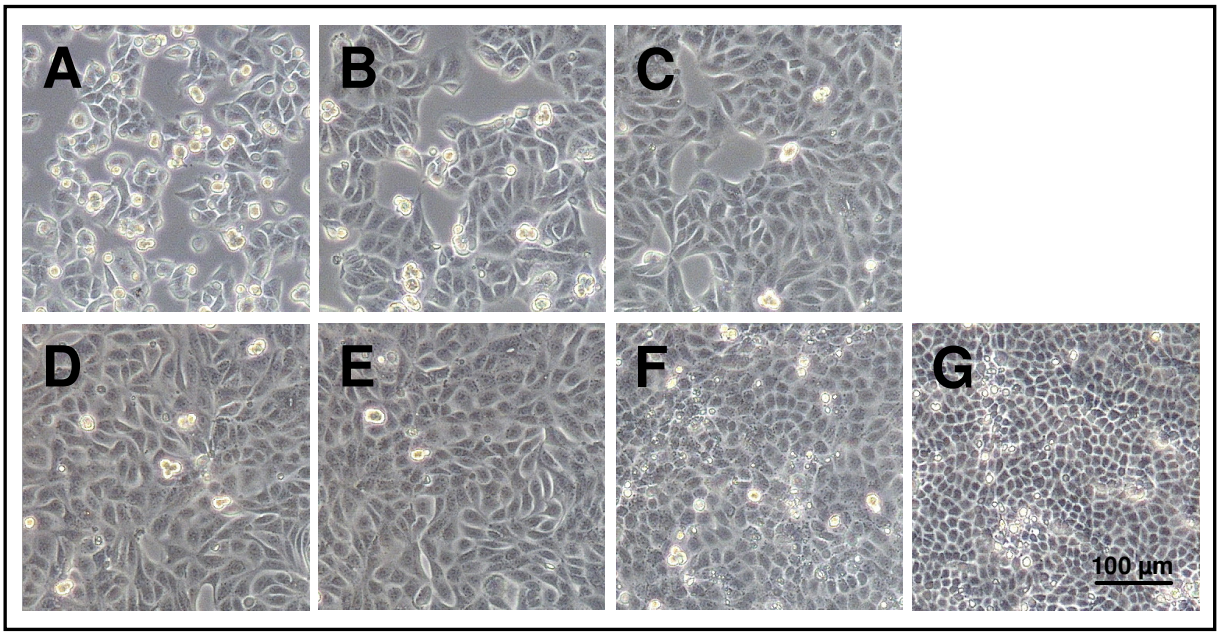

Fig. D.15 Phase contrast micrographs of MDCK-II cells at various time points after inoculation, documenting attachment and spreading upon PhoP coated coverslips that were argon plasma modified for 1 min followed by an exposure to PBS^{--} for 20 h at 37 °C prior to cell inoculation. The cells were suspended in serum-containing medium with a cell density of 4.5 x 10^5 cm^{-2}. The pictures were taken **A** 2 h, **B** 4 h, **C** 6 h, **D** 8 h, **E** 10 h, **F** 24 h and **G** 48 h after cell inoculation.

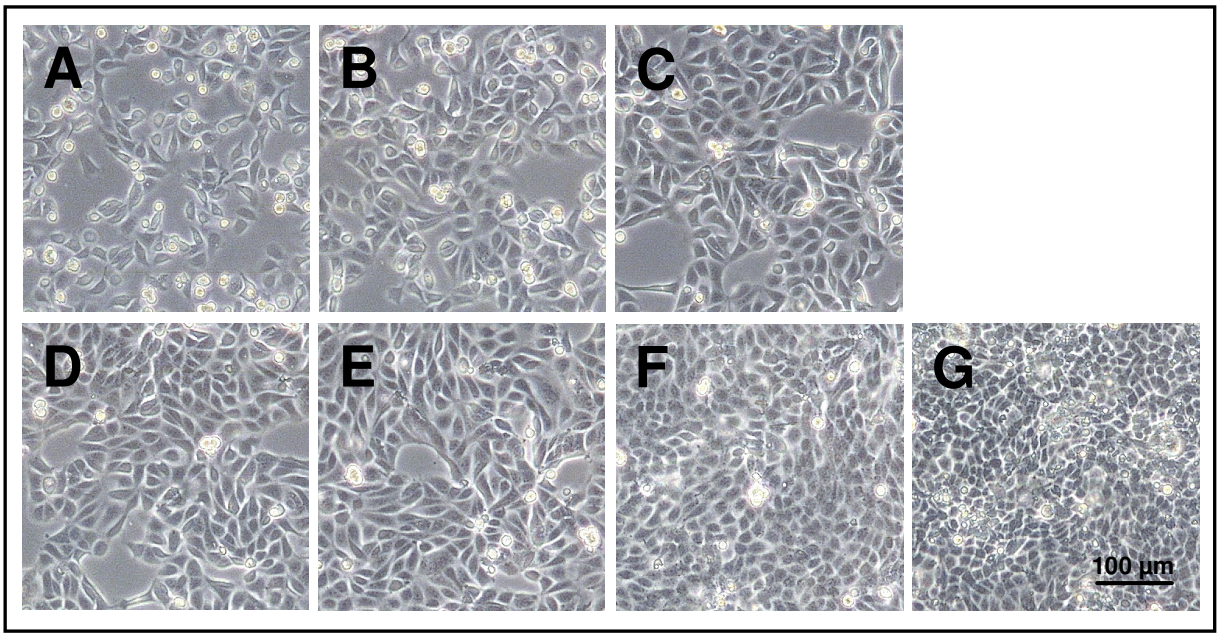

Fig. D.16 Phase contrast micrographs of MDCK-II cells at various time points after inoculation, documenting attachment and spreading upon unmodified PhoP coated coverslips. The cells were suspended in serum-containing medium with a cell density of 4.5 x 10^5 cm^{-2}. The pictures were taken **A** 2 h, **B** 4 h, **C** 6 h, **D** 8 h, **E** 10 h, **F** 24 h and **G** 48 h after cell inoculation.

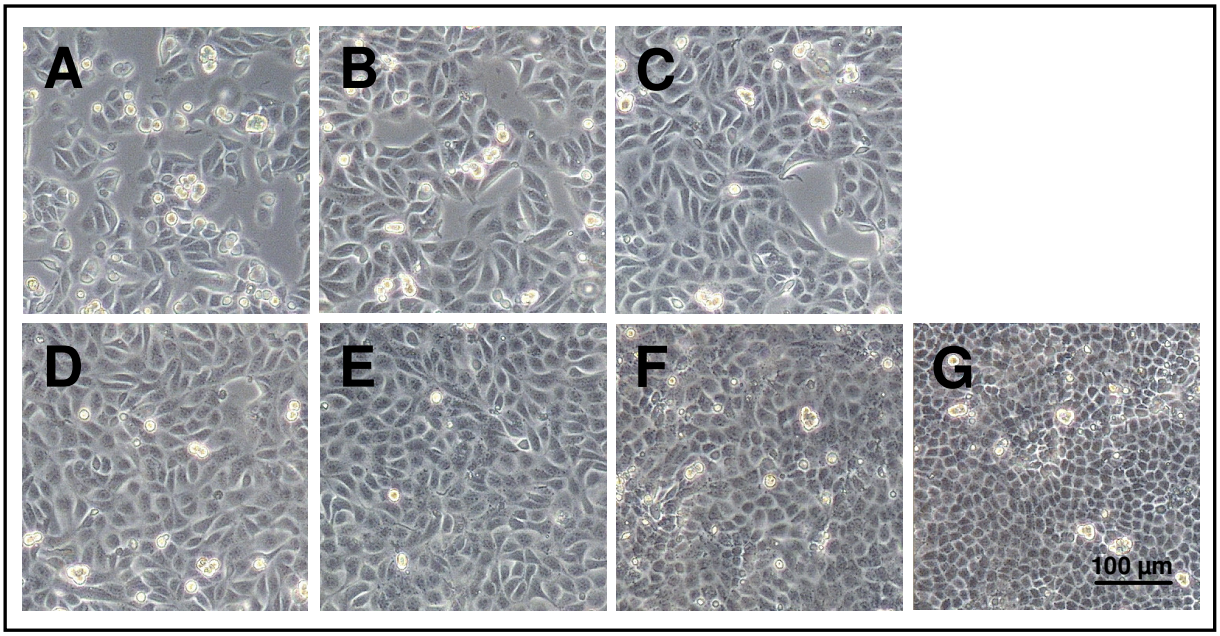

Fig. D.17 Phase contrast micrographs of MDCK-II cells at various time points after inoculation, documenting attachment and spreading upon PhoP coated coverslips that were argon plasma modified for 1 min prior to cell inoculation. The cells were suspended in serum-containing medium with a cell density of 4.5 x 10^5 cm^{-2}. The pictures were taken **A** 2 h, **B** 4 h, **C** 6 h, **D** 8 h, **E** 10 h, **F** 24 h and **G** 48 h after cell inoculation.

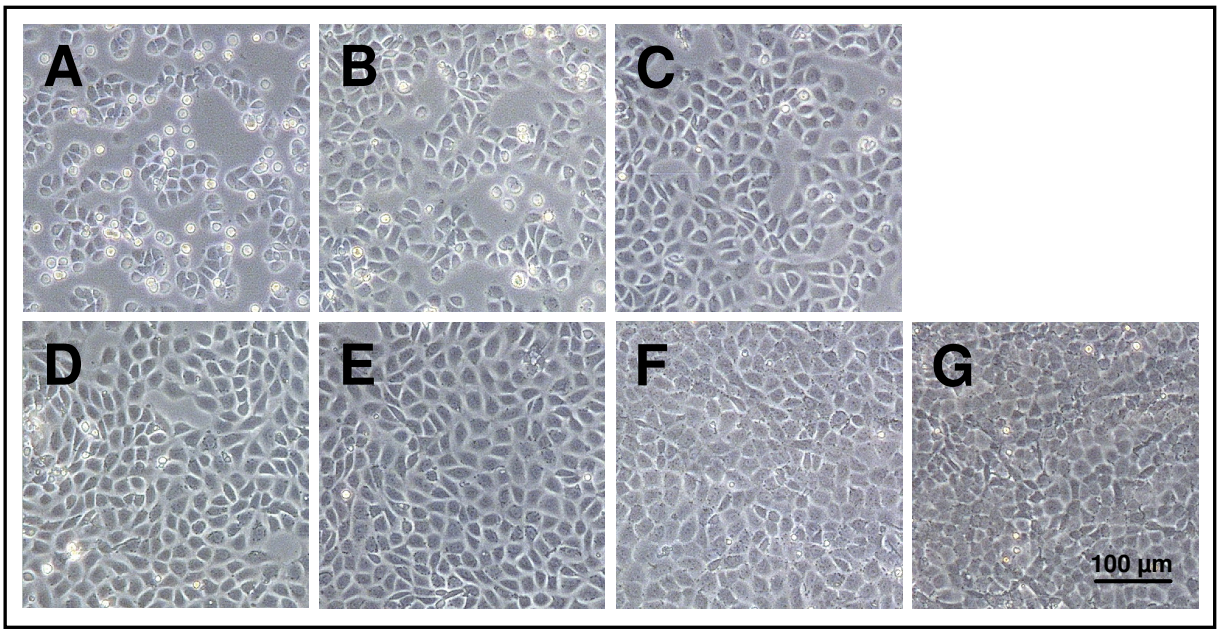

Fig. D.18 Phase contrast micrographs of NRK cells at various time points after inoculation, documenting attachment and spreading upon PhoP coated coverslips that were exposed to PBS^{--} for 20 h at 37 °C prior to cell inoculation. The cells were suspended in serum-containing medium with a cell density of 4.5 x 10^5 cm^{-2}. The pictures were taken **A** 2 h, **B** 4 h, **C** 6 h, **D** 8 h, **E** 10 h, **F** 24 h and **G** 48 h after cell inoculation.

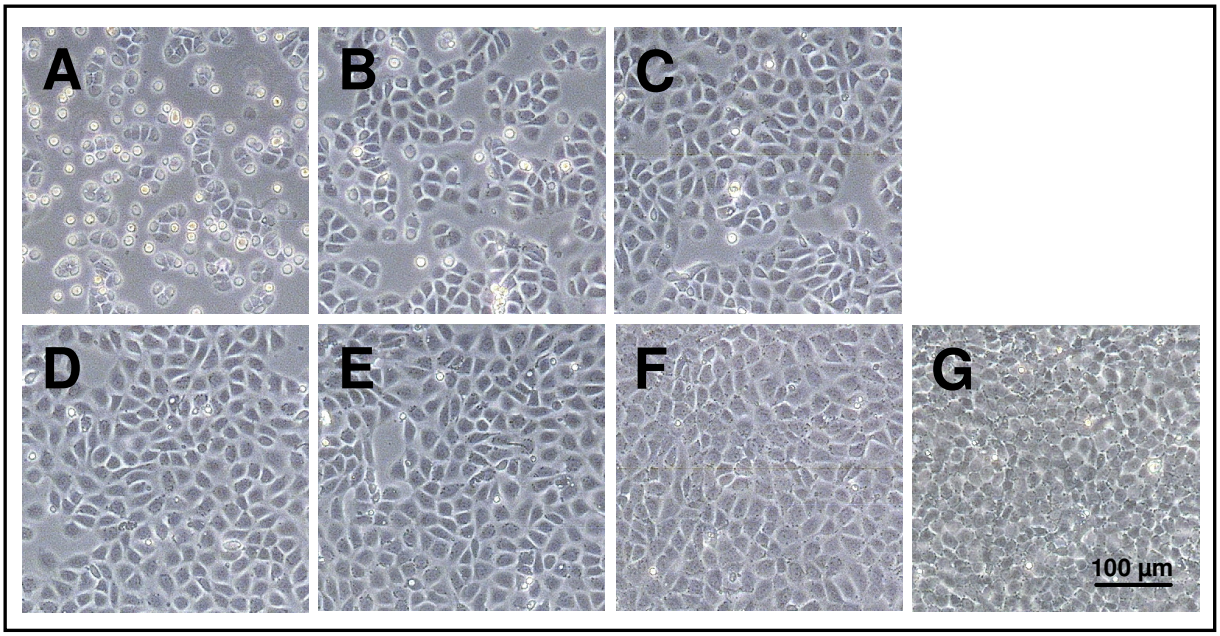

Fig. D.19 Phase contrast micrographs of NRK cells at various time points after inoculation, documenting attachment and spreading upon PhoP coated coverslips that were argon plasma modified for 1 min followed by an exposure to PBS^{--} for 20 h at 37 °C prior to cell inoculation. The cells were suspended in serum-containing medium with a cell density of 4.5×10^5 cm^{-2}. The pictures were taken **A** 2 h, **B** 4 h, **C** 6 h, **D** 8 h, **E** 10 h, **F** 24 h and **G** 48 h after cell inoculation.

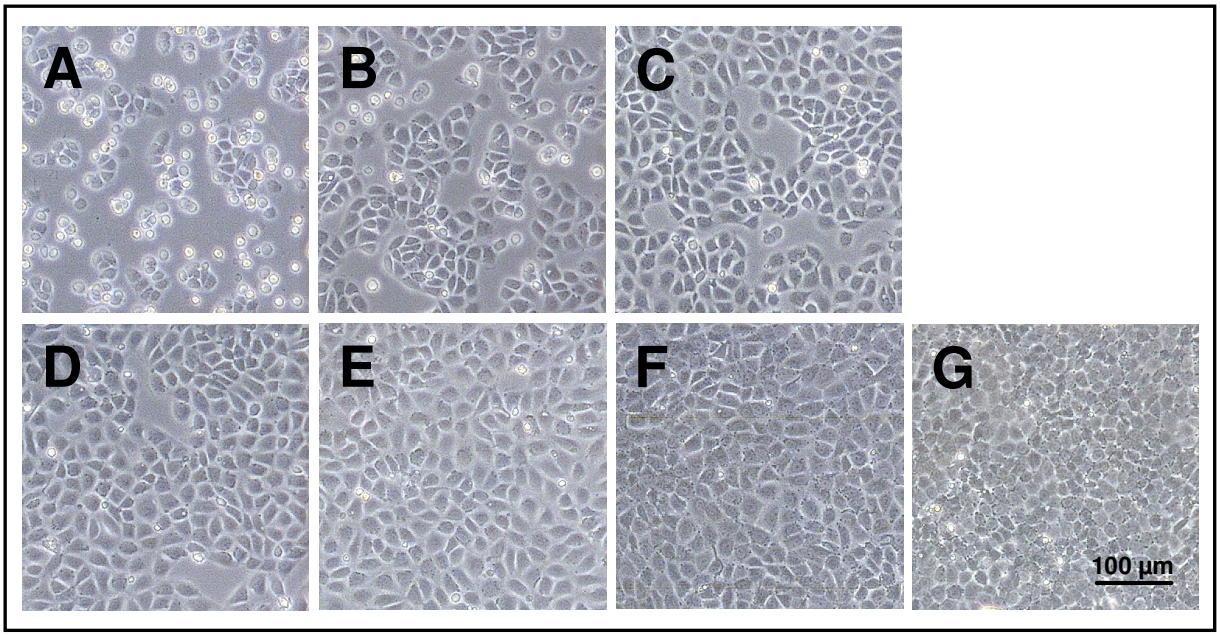

Fig. D.20 Phase contrast micrographs of NRK cells at various time points after inoculation, documenting attachment and spreading upon PhoP coated coverslips that were argon plasma modified for 1 min followed by an exposure to SFM for 20 h at 37 °C prior to cell inoculation. The cells were suspended in serum-containing medium with a cell density of 4.5×10^5 cm^{-2}. The pictures were taken **A** 2 h, **B** 4 h, **C** 6 h, **D** 8 h, **E** 10 h, **F** 24 h and **G** 48 h after cell inoculation.

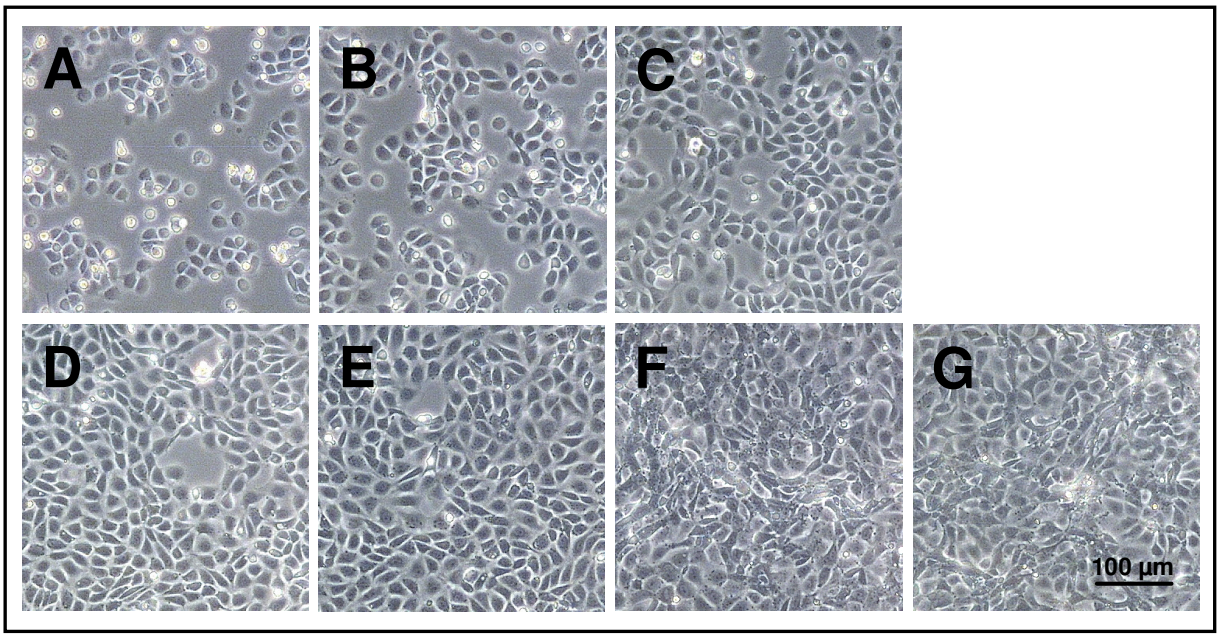

Fig. D.21 Phase contrast micrographs of NRK cells at various time points after inoculation, documenting attachment and spreading upon unmodified PhoP coated coverslips. The cells were suspended in serum-containing medium with a cell density of 4.5 x 10^5 cm^{-2}. The pictures were taken **A** 2 h, **B** 4 h, **C** 6 h, **D** 8 h, **E** 10 h, **F** 24 h and **G** 48 h after cell inoculation.

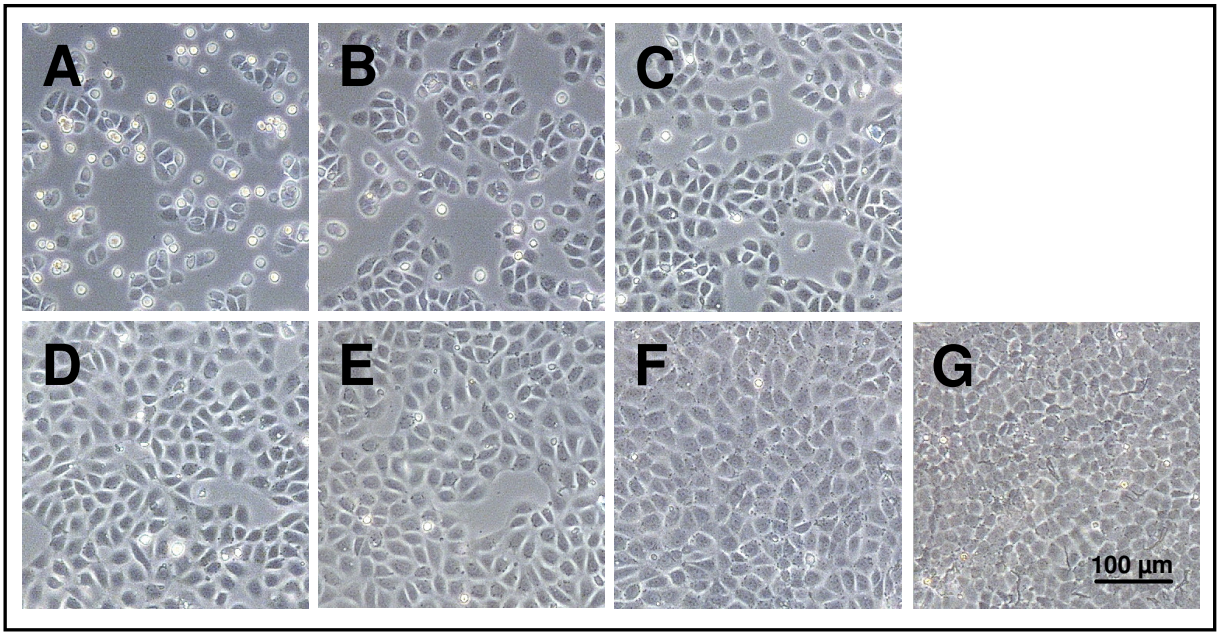

Fig. D.22 Phase contrast micrographs of NRK cells at various time points after inoculation, documenting attachment and spreading upon PhoP coated coverslips that were argon plasma modified for 1 min prior to cell inoculation. The cells were suspended in serum-containing medium with a cell density of 4.5 x 10^5 cm^{-2}. The pictures were taken **A** 2 h, **B** 4 h, **C** 6 h, **D** 8 h, **E** 10 h, **F** 24 h and **G** 48 h after cell inoculation.

E Cell Attachment and Spreading upon Polymer Surfaces Monitored by Piezo-Resonators

The following diagrams show the time course of the minimal impedance $\Delta|Z_{min}|$ recorded by the QCM technique after seeding of initially suspended cells upon polymer coated quartz resonators which had been pre-treated differently.

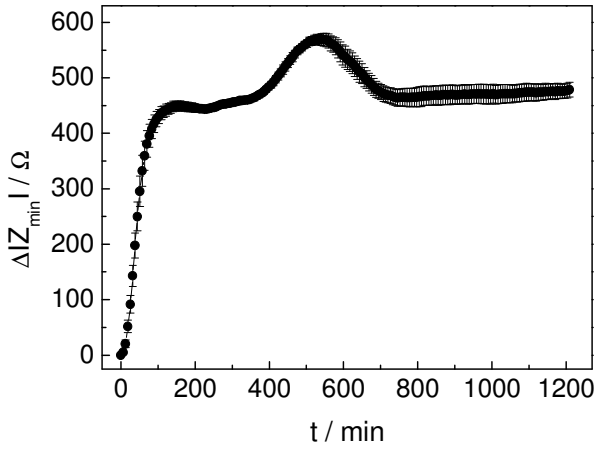

Fig. E.1 Time course of $\Delta|Z_{min}|$ after seeding initially suspended MDCK-II cells on a PS coated quartz resonator at time point zero. The cell density was adjusted to 4.5 x 10^5 cm^{-2}. The PS coated resonator had been argon plasma modified for 1 min followed by an exposure to PBS^{--} for 20 h at 37 °C prior to cell inoculation. The value of $|Z_{min}|$ at the beginning of the experiment was set to zero. (Mean ± SDM, n = 4; T = 37 °C).

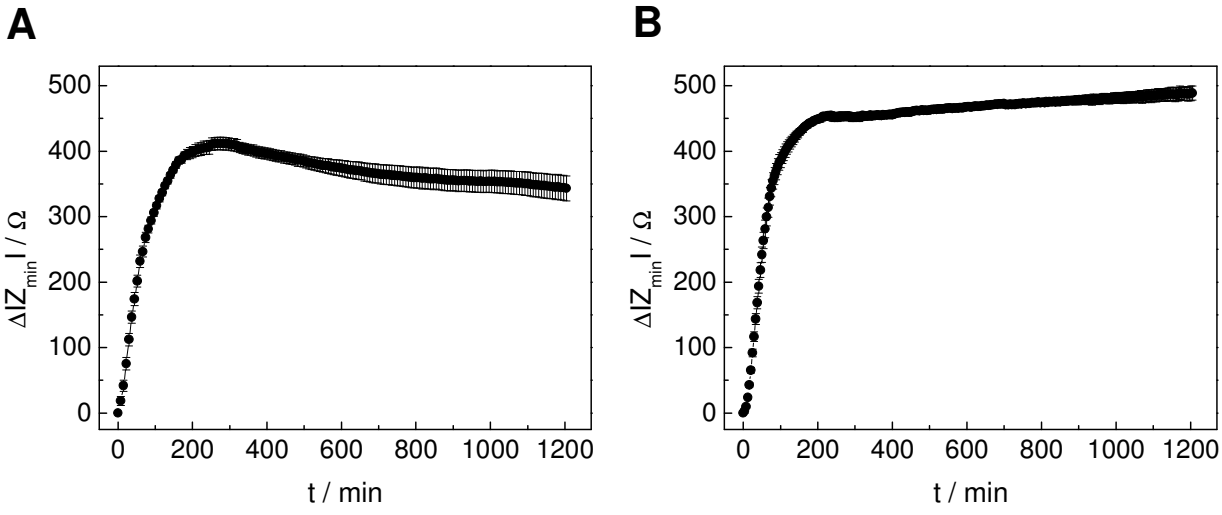

Fig. E.2 Time course of $\Delta|Z_{min}|$ after seeding initially suspended NRK cells on a PS coated quartz resonator at time point zero. The cell density was adjusted to 4.5 x 10^5 cm^{-2}. The PS coated resonator had been pre-treated as follows: **A** Incubation with PBS^{--} for 20 h at 37 °C, **B** argon plasma treatment for 1 min followed by a PBS^{--} incubation for 20 h at 37 °C. The value of $|Z_{min}|$ at the beginning of the experiment was set to zero. (Mean ± SDM, n ≥ 5; T = 37 °C).

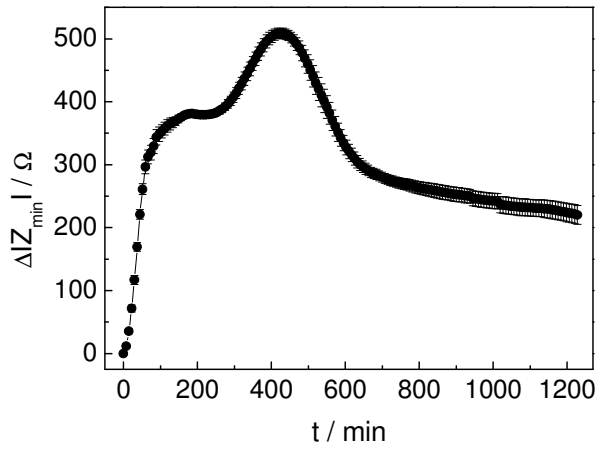

Fig. E.3 Time course of $\Delta|Z_{min}|$ after seeding initially suspended MDCK-II cells on a PMMA coated quartz resonator at time point zero. The cell density was adjusted to 4.5 x 10^5 cm^{-2}. The PMMA coated resonator had been argon plasma modified for 1 min followed by an exposure to SFM for 20 h at 37 °C prior to cell inoculation. The value of $|Z_{min}|$ at the beginning of the experiment was set to zero. (Mean ± SDM, n = 7; T = 37 °C).

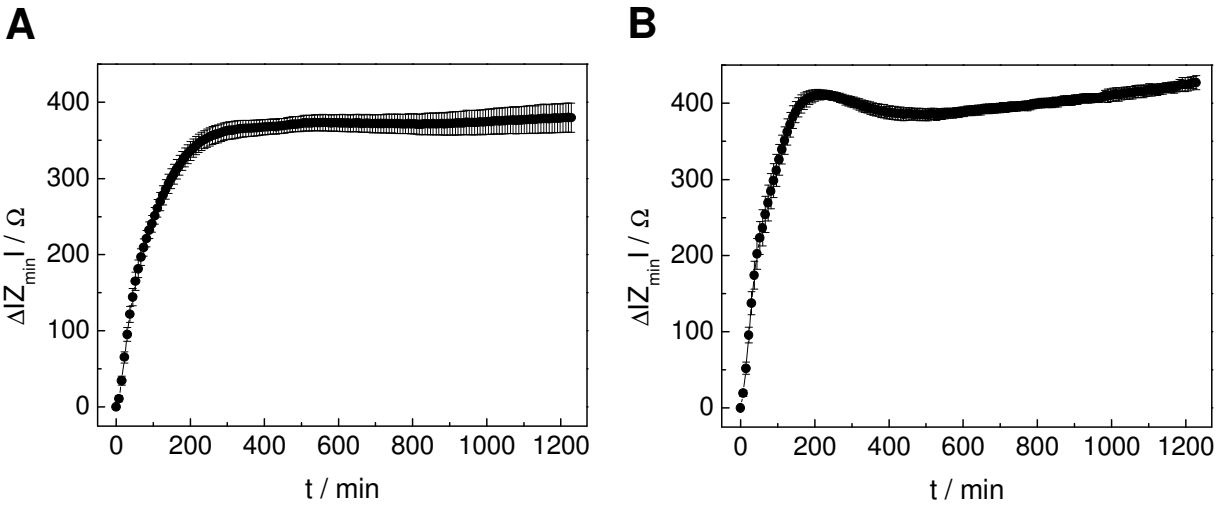

Fig. E.4 Time course of $\Delta|Z_{min}|$ after seeding initially suspended NRK cells on a PMMA coated quartz resonator at time point zero. The cell density was adjusted to 4.5 x 10^5 cm^{-2}. The PMMA coated resonator had been pre-treated as follows: **A** Incubation with PBS^{--} for 20 h at 37 °C, **B** argon plasma treatment for 1 min followed by a PBS^{--} incubation for 20 h at 37 °C. The value of $|Z_{min}|$ at the beginning of the experiment was set to zero. (Mean ± SDM, n ≥ 7; T = 37 °C).

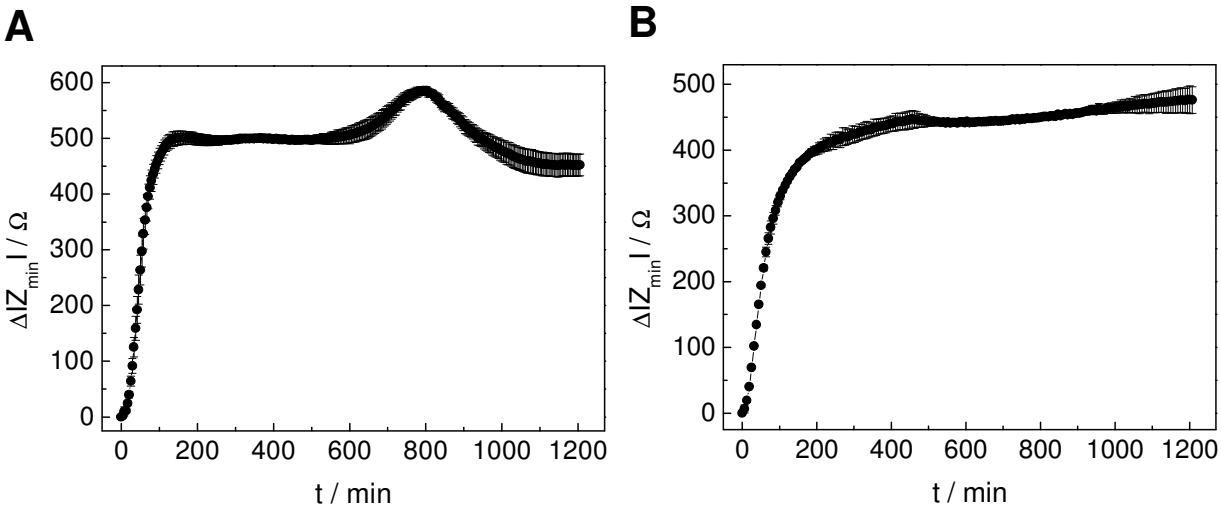

Fig. E.5 Time course of $\Delta|Z_{min}|$ after seeding initially suspended MDCK-II cells (**A**) and NRK cells (**B**) on a PhoP coated quartz resonator at time point zero. The cell density was adjusted to 4.5 x 10^5 cm^{-2}. The PhoP coated resonator had been exposed to PBS^{--} for 20 h at 37 °C prior to cell inoculation. The value of $|Z_{min}|$ at the beginning of the experiment was set to zero. (Mean ± SDM, n ≥ 2; T = 37 °C).

F Abbreviations

AC	Alternating Current
BSA	Bovine Serum Albumin
BVD	Butterworth-van Dyke
CaAM	Calcein Acetoxymethylester
CCD	Charge-Coupled Device
CMO	Common Main Objective
Col	Collagen
CPE	Constant Phase Element
D	Dimension
DI	Deionized
DMEM	Dulbecco's Modified Eagle's Medium
DMSO	Dimethyl Sulfoxide
DSMZ	Deutsche Sammlung von Mikroorganismen und Zellkulturen
ECIS	Electric Cell-Substrate Impedance Sensing
EDTA	Ethylenediamine-Tetraacetic Acid
ECM	Extracellular Matrix

EthD	Ethidium Homodimer
FCS	Fetal Calf Serum
FFT	Fast Fourier Transform
Gel	Gelatin
IC	Internal Conversion
IS	Impedance Spectroscopy
ISC	Intersystem Crossing
Lam	Laminin
LED	Light-Emitting Diode
MDCK	Madin Darby Canine Kidney
MEM	Minimal Essential Medium
mv	Microvilli
NCS	Normal Calf Serum
NRK	Normal Rat Kidney
OPD	Optical Path Difference
PBS^{--}	Phosphate Buffered Saline without divalent cations Ca^{2+} and Mg^{2+}
PBS^{++}	Phosphate Buffered Saline with Ca^{2+} and Mg^{2+}
PC	Personal Computer
PDMS	Poly(dimethyl siloxane)
PFA	Paraformaldehyde
PMMA	Poly(methyl methacrylate)
PhoP	Photopolymer
PS	Polystyrene
QCM	Quartz Crystal Microbalance
rpm	Revolutions per Minute
RT	Room Temperature
SDI	Standard Deviation of the Increments
SDM	Standard Deviation of the Mean
SFM	Serum-Free Culture Medium
SHV	Step Height Value
tj	Tight Junctions
ToF-SIMS	Time-of-Flight Secondary Ion Mass Spectrometry
UV	Ultraviolet
VSI	Vertical Scanning Interferometry

G Symbols

A	Surface Area, Electrical Parameter of the CPE
C	Capacitance
C_m	Specific Cell Membrane Capacitance (ECIS model)
D	Dissipation Factor
E	Energy
F	Force
I	Current
K	Frequency Constant
K_{ad}	Langmuir Adsorption Constant
L	Inductance, Length of Flight Path (ToF-SIMS)
M	Molar Mass
M_w	Molecular Weight
Q	Quality Factor, Amount of Charge
R	Resistance
R_b	Specific Barrier Resistance (ECIS Model)
S_f	Integral Mass Sensitivity
S_0	Electronic Ground Singlet State
S_1	Electronic Excited Singlet State
T	Temperature, Time of Flight (ToF-SIMS)
T_1	Lowest Energy Triplet State
U	Voltage
U_{ac}	Acceleration Potential
X	Reactance
Z	Impedance
c	Concentration
$c_{50\%}$	Concentration at Half-Maximal Surface Coverage
c_{66}	Piezoelectrically Stiffened Elastic Modulus
d	Distance, Thickness
f	Frequency
g	Gravitational Acceleration
h	Height

k	Hooke's Constant
m	Mass
n	Electrical Parameter of the CPE
r	Radius, Dashpot (Friction Coefficient)
q	Fractional Surface Coverage with Adsorbate
t	Time
v	Velocity, Volume
w	Weight
x	Particle Displacement of a Quartz Resonator
z	Charge
Δ	Difference
α	Cell-Substrate Parameter (ECIS Model)
δ	Decay Length of the Shear Wave
ε	Permittivity
φ	Phase Angle between Voltage and Current
γ_{SL}	Interfacial Tension solid/liquid
γ_{SV}	Interfacial Tension solid/vapor
γ_{LV}	Interfacial Tension liquid/vapor
η	Viscosity
λ	Wavelength
ρ	Mass Density, Specific Resistivity
θ	Contact Angle
θ_A	Advancing Contact Angle
θ_R	Receding Contact Angle
ω	Angular Frequency
Ø	Diameter

H Materials for Cell Biological and Biophysical Work

Acetic Acid	Merck KGaA, Darmstadt
Acetone	Sigma-Aldrich GmbH, Steinheim
Alexa Fluor 488 Phalloidin	Invitrogen GmbH, Karlsruhe

Argon	Westfalen AG, Münster
Blu-Tack	Bostik Findley GmbH, Paris (France)
Bovine Serum Albumin	Sigma-Aldrich GmbH, Steinheim
Calcium Chloride	Merck KGaA, Darmstadt
Carbon Dioxide	Westfalen AG, Münster
Collagen G	Biochrom AG, Berlin
Collagen IV	Sigma-Aldrich GmbH, Steinheim
Dimethyl Sulfoxide	Sigma-Aldrich GmbH, Steinheim
Disodium Hydrogen Phosphate	Merck KGaA, Darmstadt
Deionized Water	Sartorius Stedim Biotech GmbH, Göttingen
Ethanol	Merck KGaA, Darmstadt
Ethylenediamine-Tetraacetic Acid	Sigma-Aldrich GmbH, Steinheim
Fetal Calf Serum	Biochrom AG, Berlin
Gelatin	Sigma-Aldrich GmbH, Steinheim
D-Glucose	Sigma-Aldrich GmbH, Steinheim
L-Glutamine	Biochrom AG, Berlin
Hexane	Sigma-Aldrich GmbH, Steinheim
Hot Glue	Henkel AG & Co. KGaA, Düsseldorf
Hydrogen Peroxide (30 %)	Merck KGaA, Darmstadt
Iodine	Sigma-Aldrich GmbH, Steinheim
Isopropyl Alcohol	Merck KGaA, Darmstadt
Laminin I	Tebu-Bio GmbH, Offenbach
Lexan	GE Plastics, München
Live/Dead Viability/Cytotoxicity Kit L3224	Invitrogen GmbH, Karlsruhe
Magnesium Chloride	Merck KGaA, Darmstadt
Medium DMEM	Biochrom AG, Berlin
Medium MEM Earle (1x)	Biochrom AG, Berlin
Mucasol	Merz Consumer Care GmbH, Frankfurt
Nail Polish (Manhattan Top Coat)	Dr. Scheller Cosmetics AG, Eislingen
Nitrogen	Westfalen AG, Münster
Normal Calf Serum	Biochrom AG, Berlin
Paraformaldehyde	Merck Schuchardt OHG, Hohenbrunn
Penicillin	Biochrom AG, Berlin
Photopolymer Microposit SC 1827	Shipley Company, Marlborough, MA (USA)

Poly(methyl methacrylate) (M_w = 120000)	Sigma-Aldrich GmbH, Steinheim
Polystyrene (M_w = 230000)	Sigma-Aldrich GmbH, Steinheim
Potassium Acetate	Sigma-Aldrich GmbH, Steinheim
Potassium Chloride	Merck KGaA, Darmstadt
Potassium Dihydrogen Phosphate	Merck KGaA, Darmstadt
Potassium Iodide	Sigma-Aldrich GmbH, Steinheim
Silicon Glue	Henkel AG & Co. KGaA, Düsseldorf
Silicon Grease	Bayer AG, Leverkusen
Silver Conductive Adhesive	Epoxy GmbH, Fürth/Odenwald
Sodium Chloride	Merck KGaA, Darmstadt
Sodiumhydrogencarbonate	Merck KGaA, Darmstadt
Sodium Hydroxide	Merck KGaA, Darmstadt
Streptomycin	Biochrom AG, Berlin
Sulfuric Acid (96 %)	Acros Organics, Geel (Belgium)
Sylgard 184 Silicone Elastomer Kit	Dow Corning Corporation, Michigan (USA)
TI-Prime	MicroChemicals GmbH, Ulm
Toluene	Acros Organics, Geel (Belgium)
Triton X-100	Sigma-Aldrich GmbH, Steinheim
Trypsin	Biochrom AG, Berlin

I Instrumentation and Consumable

Aluminum Dot Masks	Fine Mechanical Workshop of the Chemical Institute, Münster
Argon Plasma Cleaner PDC 32G-2	Harrick Plasma, New York (USA)
Autoclave	Jürgens, Münster
Bürker Hemacytometer	LO-Laboroptik GmbH, Friedrichsdorf
Cell Culture Dishes	Greiner Bio-One GmbH, Frickenhausen
Cell Culture Flasks (25 cm^2)	Nunc, Roskilde (Denmark)
6-well Cell Culture Plates	Corning Costar GmbH, Bodenheim
12-well Cell Culture Plates	Corning Costar GmbH, Bodenheim
Centrifuge Sepatech Megafuge 1.0	Heraeus, Düsseldorf

Coverslips (round, Ø = 14 mm)	Menzel GmbH & Co. KG, Braunschweig
Cryovials (1.8 mL)	Nunc, Roskilde (Denmark)
Disposable Syringes (1 mL)	Braun Melsungen AG, Melsungen
Disposable Syringes (5 and 20 mL)	Henke-Saas Wolf GmbH, Tuttlingen
Drop Shape Analysis System DSA 100	Krüss GmbH, Hamburg
Fluorescence Microscope DM IRB	Leica Microsystems GmbH, Wetzlar
Fluorescence Microscope TCS SL	Leica Microsystems GmbH, Wetzlar
Freezing Container	Thermo Fisher Scientific, Roskilde (Denmark)
Frequency Generator 33120A	HP-Agilent, Böblingen
Frequency Counter 225 MHz	HP-Agilent, Böblingen
Greiner Tubes (10 mL and 50 mL)	Greiner Bio-One GmbH, Frickenhausen
Heating Cabinet B 6120	Heraeus Holding GmbH, Hanau
Hollow Needles	Neolus, Hamburg
Impedance Analyzer SI-1260	Solartron Instruments, Farnsborough (GB)
Incubator IG 150	Jouan GmbH, Dinslaken
Incubator Ultima II	Revco Technologies, Asheville (USA)
Kalrez Sealing Rings	DuPont Performance Elastomers, Geneva (Switzerland)
Latex Gloves	Roth GmbH & Co. KG, Karlsruhe
Optical 3D Profiling System	Veeco Instruments, New York (USA)
Oven	Memmert GmbH & Co. KG, Schwabach
Parafilm	Pechiney Plastic Packaging Company, Menasha (USA)
Phase Contrast Microscope DM IL	Leica Microsystems GmbH, Wetzlar
Pipette Tips	Sarstedt AG & Co., Nümbrecht
5 MHz AT-Cut Quartz Resonators	KVG GmbH, Neckarbischofsheim
Reaction Tubes (0.5 – 2 mL)	Eppendorf AG, Hamburg
Spin Coater	Institute of Biochemistry, Münster
Sputter Coater SCD 050	Bal-Tec AG, Balzers (Liechtenstein)
SRS QCM200 System	Standford Research Systems, Sunnyvale (Canada)
Stereomicroscope SMZ 1500 C-DSD230	Nikon Instruments Europe, Amstelveen (Netherlands)
Sterile Filters (pore diameter: 0.2 µm)	Sartorius Stedim Biotech GmbH, Göttingen
Sterile Flow Hood	Holten, Gydevang (Denmark)

Sterilizer UT 6120	Heraeus Holding GmbH, Düsseldorf
Thermostat MWG Lauda RM6	Lauda GmbH & Co. KG, Lauda-Königshofen
ToF-SIMS IV Instrument	ION-TOF GmbH, Münster
Ultrasonic Bath RK 255 H	Bandelin Electronic GmbH & Co. KG, Berlin
UV-Light Exposure Unit	Isel Germany AG, Eiterfeld
Water Bath AL18	Lauda GmbH & Co. KG, Lauda-Königshofen

Danksagung

Ich möchte mich ganz herzlich bei den Leuten bedanken, die mich auf dem Weg meiner Promotion begleitet und einen wesentlichen Beitrag zum Gelingen dieser Arbeit geleistet haben.

Zu allererst möchte ich mich bei Herrn Prof. Dr. Joachim Wegener bedanken für die interessante und vielseitige Themenstellung, die hervorragende Betreuung während meiner gesamten Promotion, die vielen wissenschaftlichen Anregungen sowie seine stete Hilfsbereitschaft und Unterstützung in jeglicher Form.

Herrn Prof. Dr. Hans-Joachim Galla danke ich für die freundliche Übernahme des Zweitgutachtens und Herrn Prof. Dr. Eugen J. Verspohl für die Übernahme des Amtes des dritten Prüfers.

Ganz besonders möchte ich mich bei den fleißigen Korrekturlesern meiner Arbeit bedanken: Herrn Dr. Björn Reiß, Frau Dipl.-Biotech. Judith Stolwijk, Frau Dr. Vanessa Heitmann und Herrn Prof. Dr. Joachim Wegener. Vielen Dank für eure hilfreichen Korrekturen und Verbesserungsvorschläge. Es war bestimmt nicht leicht, so eine Masse an Text durchzuarbeiten.

Björn, Christina, Vanessa, Judith und Eva danke ich für die schöne gemeinsame und niemals langweilige Zeit im Labor sowie darüber hinaus. Vielen Dank für eure Unterstützung, für die vielen netten Gespräche zwischendurch sowie etliche fachliche Diskussionen.

Bei Frau Sandra Grunewald bedanke ich mich für ihre Unterstützung und ständige Hilfsbereitschaft besonders bei den Messungen zur Proteinadsorption während der Endphase meiner Arbeit. Ich weiß, die Proteine haben es dir nicht immer leicht gemacht. Vielen Dank auch für die tolle Unterstützung und Organisation in der Zellkultur und bei den Vorbereitungen der Studentenpraktika.

Herrn Dr. Fredrick Höhn danke ich für seine große Hilfsbereitschaft in allen technischen Fragen und Problemen, für die großartige Unterstützung und Aufmunterung und die vielen Diskussionen während der gemeinsamen Mittagessen. Ohne dich wäre die Realisierung des double mode Aufbaus nur schwer möglich gewesen.

Bei Frau Sabine Hüwel und Frau Steffi Wulff möchte ich mich für die Organisation des Arbeitskreises und die angenehmen Arbeitsbedingungen bedanken, die daraus resultierten.

Frau Antje Wiese und Frau Silke Hersping danke ich für ihre stete Hilfsbereitschaft bei den alltäglichen Problemen und ihre Unterstützung in organisatorischen Fragen.

Herrn Dipl.-Ing. Wolfgang Willenbrink danke ich für seine große Hilfsbereitschaft bei computertechnischen Problemen jeglicher Art sowie für die Organisation und das Aufrechterhalten eines tollen institutseigenen EDV Systems.

Herrn Dr. Patrick Zeni danke ich für seine Hilfe und Unterstützung bei allen verwaltungstechnischen Problemen und Aufgaben.

Frau Dipl.-Chem. Lilly Nagel danke ich für die gute Zusammenarbeit im Rahmen ihrer Diplomarbeit.

Ich möchte mich bei allen Mitgliedern des gesamten Instituts für Biochemie, besonders den Mitgliedern des Arbeitskreises Galla, der BHS und den Lipidis, für die angenehme und freundliche Arbeitsatmosphäre und die Hilfsbereitschaft bei jeglichen Problemen bedanken.

Herrn Dr. Daniel Breitenstein von der Tascon GmbH Münster danke ich für die Untersuchung meiner Polymerfilme und die Beantwortung aller Fragen zur ToF-SIMS.

Herrn Dr. Thorsten Reuter und Herrn Dr. Andreas Schäfer von der nanoAnalytics GmbH Münster danke ich für die Durchführung der Schichtdickenbestimmung der Polymerfilme sowie der REM Messungen.

Christina und Vanessa danke ich für unsere legendären Freitags-Mittagessen im UKM. Es war eine sehr schöne Abwechslung zum manchmal stressigen Schreiballtag.

Mira und Kathrin danke ich dass wir uns in unserer gemeinsamen Schreibphase immer gegenseitig motiviert haben und uns bei dem ein oder anderen schönen Besuch samstags auf dem Markt erholt haben, bevor es wieder an den Schreibtisch ging.

Marion Brinks und Susanne Causemann möchte ich danken für die schöne gemeinsame Studienzeit und die daraus entstandene Freundschaft.

Eva Hein danke ich für unsere gemeinsame Zeit auf dem „Ponyhof“, die Freundschaft und das gegenseitige Aufmuntern und Motivieren bei der Fertigstellung unserer Arbeiten. Deine Schokiplätzchen haben mir gut geholfen, wenn ich mal wieder eine Nachtschicht eingelegt habe.

Ein ganz großes Dankeschön gebührt meiner Familie, meinem Vater, meiner Oma und meiner Schwester, die mich während meines Chemiestudiums und der Zeit der Promotion begleitet und immer unterstützt haben. Ohne eure Hilfe wäre vieles nicht möglich gewesen. Papa, danke für den großen Rückhalt und die Kraft, die du mir immer gegeben hast.

Michael, danke dass du mich während der gesamten Zeit in Münster immer unterstützt hast, auch wenn wir uns gerade in der Endphase dieser Arbeit lange nicht mehr gesehen haben. Danke für dein Verständnis und deine Geduld. Du hast mir die nötige Kraft gegeben, diese Arbeit fertig zu stellen.